UCLA
UCLA Electronic Theses and Dissertations

Title
Shock tube kinetics and laser absorption diagnostics for liquid- and hybrid-propellant rocket combustion analysis

Permalink
https://escholarship.org/uc/item/7t8442jx

Author
Bendana, Fabio Andres

Publication Date
2020

Peer reviewed|Thesis/dissertation

eScholarship.org
Powered by the California Digital Library
University of California

UNIVERSITY OF CALIFORNIA
Los Angeles

Shock tube kinetics and laser absorption diagnostics for liquid- and hybrid-propellant rocket combustion analysis

A dissertation submitted in partial satisfaction
of the requirements for the degree
Doctor of Philosophy in Mechanical Engineering

by

Fabio Andres Bendana

2020

© Copyright by
Fabio Andres Bendana
2020

ABSTRACT OF THE DISSERTATION

Shock tube kinetics and laser absorption diagnostics for liquid- and hybrid-propellant rocket combustion analysis

by

Fabio Andres Bendana
Doctor of Philosophy in Mechanical Engineering
University of California, Los Angeles, 2020
Professor Raymond M. Spearrin, Chair

As efforts to access and explore space increase, emerging rocket technologies will undeniably continue to rely on chemical propulsion, as it remains the only feasible way of providing Earth-to-orbit access and has proven invaluable in extending in-space capabilities. Accordingly, advancements are needed to improve combustion performance and the understanding of underlying chemical and physical phenomena governing chemical propulsion systems, as they have a substantial impact on the mission capabilities of flight vehicles and spacecrafts. While modeling efforts have made significant progress in recent years, empirical studies remain a necessity in the development of advanced propulsion systems; however, limits of traditional instrumentation often preclude definitive interpretation of flow-field phenomena in experimental tests and are not suitable for in-situ measurements at the extreme temperatures and pressures present in rocket propulsion systems. As such, optical diagnostics have become an attractive tool in combustion science due to the non-intrusive nature of the measurement and flexibility in the measured properties (temperature, species concentration, pressure, velocity, number density, etc.) inferred via spectroscopic interaction. Therefore, to advance the next generation of chemical propulsion systems, advanced optical diagnostic tools need be developed for characterizing propulsion test facilities and developing/validating computational models for complex chemically reacting flow-fields.

The work herein describes novel advancements in laser absorption spectroscopy for characterizing liquid- and hybrid-propellant rocket combustion systems with support of a new High-Enthalpy Shock Tube (HEST) facility at UCLA. Using the shock tube facility to emulate the high temperatures ($T > 3000$ K) and high pressures ($P > 100$ bar) present in liquid-propellant rocket combustors, a novel laser absorption spectroscopy sensor that exploits line-mixing effects in the infrared spectra was developed for temperature, carbon monoxide (CO), and carbon dioxide (CO_2) measurements. This sensor was then demonstrated on a liquid-propellant rocket combustor at the Air Force Research Laboratory (AFRL) in Edwards Air Force Base with kerosene (RP-2)/oxygen and methane/oxygen propellant combinations. Successful thermochemistry measurements were obtained at pressures up to 105 bar–marking a significant improvement in the pressure capability of optical diagnostic tools. In addition to these liquid-propellant rocket combustor measurements, a unique approach was developed for investigating hybrid rocket propulsion flows. Using laser absorption tomography, spatially-resolved measurements of temperature, carbon monoxide (CO), carbon dioxide (CO_2), and water (H_2O) were obtained in the reaction layer of a hybrid-propellant rocket combustor with poly(methyl methacrylate) (PMMA)/oxygen and high-density polyethylene (HDPE)/oxygen propellant combinations and two injector geometries (single port and axial showerhead). These measurements highlight combustion physics and thermochemical energy conversion in the spatial domain and help identify mechanistic losses in combustion efficiency for different engine configurations. Lastly, in efforts to develop and refine combustion models for real fuels used in chemical propulsion systems, a novel time-resolved, laser absorption spectroscopy technique was developed for measuring the formation of isotopically-labeled carbon monoxide (^{12}CO and ^{13}CO) in shock tube oxidation experiments of isotopically-labeled fuel blends. The technique was demonstrated by examining competitive oxidation of methane (CH_4) with differing C_2 hydrocarbon functional groups (alkane, alkene, alkyne), namely acetylene (C_2H_2), ethylene (C_2H_4), and ethane (C_2H_6). By isotopically-labeling specific fuel components of the overall fuel mixture and simultaneously measuring both ^{12}CO and ^{13}CO, individual reaction pathways and rates are distinguishable, providing kinetic targets for reaction mechanisms used to model fuel blends present in chemical propulsion systems.

The dissertation of Fabio Andres Bendana is approved.

Richard E. Wirz

Xiaolin Zhong

Timothy S. Fisher

Raymond M. Spearrin, Committee Chair

University of California, Los Angeles

2020

Table of Contents

List of Figures

List of Tables

List of Symbols

α	spectral absorbance
$\Delta\nu_{\mathrm{C}}$	collisional halfwidth (FWHM)
$\Delta\nu_{\mathrm{D}}$	Doppler halfwidth (FWHM)
$\dot{m}_p$	total mass flow rate of propellants
γ	specific heat ratio
γ_{i-k}	broadening coefficient between absorbing molecule i and perturbing molecule k
λ	wavelength of light
$\mathscr{M}$	molecular weight
μ	reduced molecular mass
ν	frequency of light
ω_e	fundamental vibrational frequency
ϕ	equivalence ratio
ϕ_j	lineshape function of rovibrational transition j
τ_{ign}	ignition delay time
a	speed of sound
A_{proj}	projected absorbance area
A_j	integrated absorbance area of transitions j
A_t	nozzle throat area
c	speed of light

c^*	characteristic velocity
E''_j	lower state energy of transition j
f_k	uncertainty factor
g_j	degeneracy of transition j
h	Planck's constant
I_0	incident light intensity
I_{sp}	specific impulse
I_t	transmitted light intensity
J	rotational quantum number
K	integrated spectral absorption coefficient
k_ν	spectral absorbance coefficient
k_B	Boltzmann constant
k_s	bond stiffness
L	absorbing path length
M_{S}	incident shock Mach number
M_{S}	reflected shock Mach number
N	number density
n_{i-k}	temperature exponent for γ_{i-k}
P_c	chamber pressure
Q	internal partition function

R	absorbance area ratio
R_u	universal gas constant
$R_{J\rightarrow K}$	population transfer rates between rotational quantum states J and K
S_k^f	sensitivity coefficient
S_j	linestrength of rovibrational transition j
T_ν	fractional transmission
T_c	chamber temperature
u	gas velocity in shock-fixed coordinates
v	gas velocity in laboratory-fixed coordinates
v	vibrational quantum number
W_R	reflected shock speed
W_S	incident shock speed
X_i	mole fraction of species i
$\mathbf{W}$	relaxation matrix
O/F	oxidizer-to-fuel ratio

ACKNOWLEDGMENTS

After 5 years of seemingly non-stop, intense graduate work, nothing else seems more fitting, than having the privilege of finishing my dissertation by thanking the many individuals that have helped me throughout my journey. First and foremost, I am indebted to my advisor, Prof. R. Mitchell Spearrin, for sparking my interest in graduate studies, giving me the opportunity to join the laboratory, and, most importantly, believing in my abilities. I am deeply grateful for your investment in my professional and personal development. You have taught me how to be an ambitious and tactful researcher and have instilled in me a rigor for excellence that I will carry with me throughout the rest of my career. I wish you nothing short of success throughout your career and will surely miss our interactions and, in the summer, your mean barbecue sauce. I would also like to thank all of my committee members, Prof. Richard Wirz, Prof. Xiaolin Zhong, and Prof. Tim Fisher, for their ongoing support and invaluable feedback throughout my graduate studies. Specifically, I would like to thank Prof. Wirz for sparking my curiosity on shock tubes and compressible flows during my first class at UCLA–little did I know I would be tasked with developing a facility a year later. I also thank Prof. Zhong for being my initial graduate advisor and helping me acclimate to graduate school, and Prof. Fisher for taking time out of his role as Department Chair to provide insightful recommendations on my research.

Next, I would like to thank the individuals from external organizations that have collaborated with me to make my time at UCLA an exciting and unforgettable experience. Specifically, I thank Dr. Ashley Karp and Dr. Elizabeth Jens from NASA Jet Propulsion Laboratory (JPL) for giving me the opportunity to showcase my research on hybrid rockets at NASA JPL and always putting so much enthusiasm into our project. I also want to thank Dr. Stephen Schumaker, Dr. Stephen Danczyk, and Dr. William Hargus Jr. from the Air Force Research Laboratory (AFRL) in Edwards Air Force Base for all their help in conducting multiple measurement campaigns on their liquid-propellant rocket combustor facility.

At UCLA, I was surrounded by incredible peers that were instrumental to all my work. I thank Ben Tan and Miguel Lozano for all their assistance in providing access to facilities and resources that made much of the research herein possible. I thank Jose Sanchez and Travis Widick from the UCLA R&D shops for providing an abundance of knowledge on best-practices for manufacturing many of the experimental facilities used throughout my research. Additionally, I thank the Eugene V. Cota-Robles fellowship for supporting underrepresented students and making it possible for me to pursue higher education.

I would now like to thank the amazing people I spent the majority of my time around, members of the Laser Spectroscopy and Gas Dynamics Laboratory. You have all given me countless memories, both in and out of the lab–making you all my second family. Dr. Daniel Lee, Huy Dinh, and Dr. Chuyu Wei, building up a completely new laboratory is no easy task, but having support from all of you made it possible (at least once we built our chairs so we could actually sit somewhere). Kevin Schwarm, David Morrow, and Travis Fujimoto, you all filled my life with excessive laughter, whether it was about what movie or show I never watched, David's most recent Trader Joe's haul, Kevin's lunch, which often consistent of just two avocados, or Travis's...well Travis is just a nice guy. You definitely made graduate school a lot of fun–probably more than it should have been at times. Prof. Daniel Pineda, thank you for all the late nights you stayed in the lab just for support. I deeply appreciate all of the insight you brought to the group and teaching us (by example, of course) the difference between a cookout and a barbecue. Anil Nair, your work ethic and the quality of your work are admirable. You always challenged me to think a little bit different or look at a problem in a different light and I have always appreciated that. More importantly, I appreciate that I knew I could always look at you when I had no idea what David was talking about. Isabelle Sanders, China Hagström, and Josue Castillo, working with the three of you on the hybrid rocket project was such an enjoyable experience–omitting the times we manufactured 30+ fuel-grains in one day or had to use the 'fire stick'. Nonetheless, thank you for all the great memories. Christopher Jelloian, you have taught me how important it is to keep a positive outlook on life regardless of the circumstances and, for that, I thank you. Except for when the DAQ doesn't trigger properly, then it's okay to be a little upset. Nick Kuenning, it has been a huge privilege to have worked with you and have seen your development over the past few years. Thank you for all the help with all shock tube related things. You are a great teacher and I know you'll do amazing things–just don't try to move the diaphragmless shock tube outside of the building again. To everyone else who I've had the privilege of meeting before I left, including Alex Keller, Barathan Jeevaretanam, Alex Lima, and Nora Stacy, I wish our interactions weren't cut so short, but I know you'll all do well from how I've seen you support other people in our group–and I think we finally found someone who loves Trader Joe's more than David.

Finally, these acknowledgements would not be complete if I did not recognize the amazing people behind the scenes that supported me (and had to deal with my stress) once I stepped out of the lab. To my mom, you have always put your children's needs and desires above your own and have always taught me that I can do and be anything. None of this would have been possible if it wasn't for all of your sacrifices and hard work. So this achievement is our achievement. To my dad, you have taught me the value of hard work and that nothing worth having comes easy. Thank you for always supporting me and giving me everything I needed–even if it wasn't what I thought I needed. To Diego, thank you for always being there when I could not. You've always taught me so many things, including how important it is to laugh. To Mike, you have my deepest respect and gratitude for everything you have done for our family. Thank you for always taking so much interest in what I do. To Laura, Carlos, and Alexa, you have always been so selfless in offering your support in any way possible and I know you would do anything to make my life stress-free. Thank you from the bottom of my heart. Now, most importantly, to my sweet Kaelly, who, since the beginning, has always believed in me and my dreams, even when I didn't myself. I owe you the world. You pushed me to embark on this journey (probably without realizing what you just signed up for) and have been by my side every step of the way–through the never-ending nights, the *almost done*'s, and the *be home soon*'s. I could not have asked for a more selfless, loving, and supportive partner throughout the past five years. Thank you. We did it. I love you.

Curriculum Vitae

2010 – 2014	**B.S. in Mechanical Engineering** University of California, Irvine (UCI), Irvine, CA
2010 – 2014	**B.S. in Aerospace Engineering** University of California, Irvine (UCI), Irvine, CA
2015 – 2017	**M.S. in Mechanical Engineering** University of California, Los Angeles (UCLA), Los Angeles, CA
2015 – Present	**Ph.D. Candidate in Mechanical Engineering** University of California, Los Angeles (UCLA), Los Angeles, CA

Peer-Reviewed Publications

[1] Pineda, D. I., **Bendana, F. A.**, & Spearrin, R.M. (2020). Competitive oxidation of methane and C_2 hydrocarbons discerned by isotopic labeling and laser absorption spectroscopy of CO isotopologues in shock-heated mixtures. Combustion and Flame. https://doi.org/10.1016/j.combustflame.2020.11.006

[2] Lee, D. D., **Bendana, F. A.**, Nair, A. P., Danczyk, S. A., Hargus Jr., W. A., & Spearrin, R. M. (2020). Exploiting line-mixing effects for laser absorption spectroscopy at extreme combustion pressures. Proceedings of the Combustion Institute. https://doi.org/10.1016/j.proci.2020.08.037

[3] **Bendana, F. A.**, Sanders, I. C., Castillo, J. J., Hagström, C. G., Pineda, D. I., & Spearrin, R. M. (2020). In-situ thermochemical analysis of hybrid rocket fuel oxidation via laser absorption tomography of CO, CO_2, and H_2O. Experiments in Fluids, 61(9), 190. https://doi.org/10.1007/s00348-020-03004-7

[4] Lee, D. D., **Bendana, F. A.**, Nair, A. P., Pineda, D. I., & Spearrin, R. M. (2020). Line mixing and broadening of carbon dioxide by argon in the v_3 bandhead near 4.2 μm at high temperatures and high pressures. Journal of Quantitative Spectroscopy and Radiative Transfer, 253, 107135. https://doi.org/10.1016/j.jqsrt.2020.107135

[5] **Bendana, F. A.**, Lee, D. D., Schumaker, S. A., Danczyk, S. A., & Spearrin, R. M. (2019). Cross-band infrared laser absorption of carbon monoxide for thermometry and species sensing in high-pressure rocket flows. Applied Physics B, 125(11), 204.
https://doi.org/10.1007/s00340-019-7320-y

[6] **Bendana, F. A.**, Lee, D. D., Wei, C., Pineda, D. I., & Spearrin, R. M. (2019). Line mixing and broadening in the $v(1\rightarrow3)$ first overtone bandhead of carbon monoxide at high temperatures and high pressures. Journal of Quantitative Spectroscopy and Radiative Transfer, 239, 106636. https://doi.org/10.1016/j.jqsrt.2019.106636

[7] Pineda, D. I., **Bendana, F. A.**, Schwarm, K. K., & Spearrin, R. M. (2019). Multi-isotopologue laser absorption spectroscopy of carbon monoxide for high-temperature chemical kinetic studies of fuel mixtures. Combustion and Flame, 207, 379–390.
https://doi.org/10.1016/j.combustflame.2019.05.030

[8] Spearrin, R. M., & **Bendana, F. A.** (2019). Design-build-launch: a hybrid project-based laboratory course for aerospace engineering education. Acta Astronautica, 157, 29–39.
https://doi.org/10.1016/j.actaastro.2018.11.002

[9] Lee, D. D., **Bendana, F. A.**, Schumaker, S. A., & Spearrin, R. M. (2018). Wavelength modulation spectroscopy near 5 μm for carbon monoxide sensing in a high-pressure kerosene-fueled liquid rocket combustor. Applied Physics B, 124(5), 77.
https://doi.org/10.1007/s00340-018-6945-6

CHAPTER 1

Introduction

Chemical propulsion has been the cornerstone of some of the most remarkable human achievements in the last 50 years, from Apollo 11 in 1969 to the commercial launch industry that exists today. During the Apollo era, five F-1 engines powered by liquid oxygen and refined kerosene boosted the Saturn V first stage (S-IC) off the launch pad and on to the moon with over 7,610,000 lbf of thrust [1]. Today, chemical propulsion still remains the only conceivable way of providing Earth-to-orbit access and has proven invaluable in extending in-space capabilities. Currently, there are ongoing efforts by both NASA and private companies, such as Space Exploration Technologies Corporation (SpaceX), Virgin Galactic, and Blue Origin, among others, to reevaluate the way space is accessed, utilized, and explored. Chemical propulsion will continue to play a vital role in emerging technologies; thus, parallel advancements are needed to better understand the underlying chemical and physical phenomena governing these systems.

Chemical propulsion systems use the chemical energy stored in the molecular bonds of the propellant(s) to create thrust. In the combustion chamber, chemical reactions break these molecular bonds and convert the propellant(s) (reactant(s)) into high-temperature, high-pressure gas (products). The thermal energy in the combustor is then turned into useful kinetic energy by expelling the hot gas through a supersonic nozzle–creating thrust. Chemical propulsion systems are typically denoted by their propellant(s) and can be categorized into three major classes: liquid-propellant engines, hybrid-propellant engines, or solid rocket motors, with the main difference being the phase of the propellant(s). Liquid-propellant engines store their propellant(s) in liquid phase, solid rocket motors cast a mixture of solid fuel and solid oxidizer into a grain, and hybrid-propellant engines use a combination of the two, where oxidizer is typically stored in liquid or gas phase and the fuel is cast as a solid fuel grain. Each class has its own strengths and limitations; therefore, mission goals and requirements (safety, performance, reliability, cost, system complexity, ability to throttle/restart, etc.) intimately decide which system is more appropriate. The scope of the work covered herein is mainly relevant to applications utilizing liquid- or hybrid-propellant systems; therefore, solid rocket motors will not be discussed in detail.

1.1 Liquid-propellant rocket combustion

Liquid-propellant rocket engines are a proven means of propulsion that enable both launch and in-space operations. These systems can be further classified into two sub-categories: monopropellants and liquid bi-propellants. Monopropellant engines differ in that they do not require a separate oxidizer. Instead, a single propellant is passed over a catalyst, which initiates a highly exothermic chemical decomposition process that provides enough thermal energy to produce thrust. Liquid bi-propellant systems rely on fuel and oxidizer stored in liquid phase. An injector atomizes, vaporizes, and mixes the propellants as they are fed into the combustion chamber. The homogeneity of propellant mixing is critical to achieving complete combustion and converting the maximum amount of chemical energy into thermal energy.

There is a vast number of propellants ($\sim$170) that have been considered for liquid-propellant rocket engine designs [2]. Of these, over 25 different propellant combinations have actually flown on U.S.-built engines [2]. Since there are extensive options, selecting propellants often involves a compromise between certain advantages and disadvantages and, ultimately, the specific application and mission goals/requirements determine the most suitable combination. Common liquid propellants and their properties are listed in Table 1.1. The following characteristics are desirable in choosing liquid-propellants:

- *High energy release per unit mass of propellant and low molecular weight of combustion species*: The more thrust is produced per unit mass of propellant indicates more efficient chemical-to-thermal energy conversion and results in better combustion performance. Additionally, lower molecular weight of the exhaust gas (products) typically indicates molecules with lower heat capacities (monatomics and diatomics). This means less thermal energy is used up in heating the exhaust gas and more thermal energy is converted to useful kinetic energy (i.e. thrust).

- *Ignition reliability*: Propellants must be able to rapidly ignite once they are introduced into the combustion chamber. Delayed ignition can result in an accumulation of propellants in the chamber, which may then detonate or explode upon being ignited. Additionally, in-space propulsion often requires multiple engine maneuvers, such as orbit transfers, trajectory insertions, and attitude control, where re-ignition is critical to mission success.

- *Combustion stability*: Chamber pressure fluctuations are normally present during engine operation; however, they are typically random in frequency. If combustion becomes unstable, high pressure fluctuations can form and resonate at high or low frequencies. This results in large vibrations of the system, which can lead to engine failure or instrument damage.

- *High propellant density*: Propellants typically comprise the largest mass fraction of the overall launch vehicle; therefore, high density is desired to reduce the required propellant mass and minimize the dry mass of the propellant tanks and feed systems.

- *High specific heat, high thermal conductivity, and high critical temperature*: Typical combustion temperatures are much higher (> 3000 K) than what materials can sustain before melting/deforming. Therefore, to protect the combustion chamber and nozzle, one or both propellants (typically just fuel) is often passed through tubes or channels around these components to cool the engine prior to being injected into the combustion chamber. High specific heat, high thermal conductivity, and high critical temperature allow the propellant to cool the walls more efficiently.

- *Low vapor pressure*: Liquid propellants are often fed into the combustion chamber via turbopumps, which need to spin at very high rates (as high as 30,000+ rpm) to output the necessary flow rates. As a result, the pressure of the propellants may drop significantly at the pump inlet. If this pressure drops below the vapor pressure of the propellants it results in cavitation, which can severely damage turbopump components. As a result, propellants with low vapor pressure are desired to minimize this phenomena.

- *Non-corrosive, non-toxicity*: Propellants must be compatible with engine and seal materials to avoid corrosion and leaks. Additionally, propellants, and the fumes and products they produce, are desired to have low toxicity for health, handling, and storage reasons.
- *Low viscosity*: Propellants with low viscosity help minimize undesired pressure drops and viscous losses through the feed system and injector.

When comparing monopropellants and liquid bi-propellants, the main advantages in using a liquid-monopropellant engine is the reduced complexity and, thus, increased reliability in the system operation. As mentioned previously, monopropellants rely on a single propellant; therefore, the feed system requirements are cut in half compared to a liquid bi-propellant system. This greatly reducing the weight of the vehicle and simplifies feed plumbing, flow control, and injection. Additionally, monopropellants, like hydrazine and hydrogen peroxide, are considered storable propellants, which means they do not require extreme cooling measures to remain liquid (as cryogenics do). This is suitable for spacecraft missions last several years, which may require engine maneuvers throughout the lifetime of the vehicle. Other advantages include high propellant densities, which lowers the dry mass of the vehicle, and clean exhaust, which minimizes soot deposition on optical surfaces (windows, mirrors, solar cells, etc.). Unfortunately, its principal drawback is lower performance when compared to liquid bi-propellant engines and so monopropellants are typically only used as secondary power sources (turbopump gas generator, auxiliary power, attitude control) in rocket engine systems.

Table 1.1: General data on common storable and cryogenic liquid propellants (obtained from [1])

Propellant	Formula	Use[a]	$\mathscr{M}$ [g/mol]	Freezing Pt. [K]	Boiling Pt. [K].	Density [kg/m^3]	Hazards[b]
Hydrogen(L)[c]	H_2	F	2.016	13.9	20.4	710	F
Kerosene (RP-1)[d]	MIL-P-25576C	F	165	219.8	445.4	800	F, U
Methane(L)[c]	CH_4	F	16.04	90.7	111.7	423	F
Ethanol	C_2H_5OH	F	46.07	159.1	351.4	789	F
MMH	$CH_3NH\text{-}NH_2$	F	46.08	220.4	359.3	878	T
UDMH	$(CH_3)_2NNH_2$	F	60.08	215.4	336.5	789	T
Ammonia[c]	NH_3	F	17.03	195.4	239.8	683	T, F
Oxygen(L)[c]	O_2	O	32.00	54.3	90.2	1142	
Nitrous oxide(L)[c]	N_2O	O	44.01	182.4	184.65	1220	U
Nitrogen tetroxide	N_2O_4	O	92.02	261.5	294.3	1440	VT
Nitric acid	HNO_3	O	63.01	231.6	356.2	1550	T
Flourine(L)[c]	F_2	O	38.00	53.2	84.8	1509	VT, F
Oxygen difluoride(L)[c]	OF_2	O	54.00	49.8	89.3	1521	VT, F
Hydrazine	N_2H_4	M	32.05	274.5	386.2	1010	T, F, U
Hydrogen peroxide (98%)	H_2O_2	M	33.42	270.7	421.6	1432	F, U

[a] F: fuel, O: oxidizer, M: monopropellant

[b] VT: very toxic, T: toxic, F: flammable, U: unstable under certain conditions

[c] Cryogenic

[d] Properties given are a low estimate

For these reasons, monopropellants have significant heritage for in-space propulsion applications. They were first introduced between 1947-1966 with hydrogen peroxide and a silver screen catalyst to provide 0.1–100 lbf of thrust [2]. Then, in 1958, hydrazine monopropellant thrusters were developed, which used a granular alumina (aluminum oxide) catalyst bed coated with iridium (Shell-405/S-405) [3, 4]. These systems improved combustion performance by 50% compared to hydrogen peroxide (i.e. 0.1–150 lbf of thrust) [2]. Hydrazine thrusters were first used for the attitude control system of Titan I and Titan II and, because of their start/stop capabilities (up to 100,000+ cycles), were then used for the rapid pulsing operation of the attitude control systems for Pioneer 6, 7, 8, and 9 [2]. Over the years, hydrazine thrusters have proven their reliability and, thus, have flown on numerous missions including the Space Shuttle, Viking 1 and 2, the Pheonix lander, and the Curiosity rover. Although hydrazine thrusters have been widely used across the propulsion industry and exhibit improved performance over other monopropellants, there is currently renewed interest and ongoing research in the use of non-toxic alternatives, such as hydrogen peroxide and hydroxyl ammonium nitrate (HAN) [5, 6].

Liquid bi-propellants are extremely prevalent in the launch industry and can be found in the majority of launch vehicles and numerous in-space systems. As seen by Table 1.1, there are multiple energetic propellant combinations that are available for liquid bi-propellant engines. As a result, their main advantage is the ability to provide high thrust-to-weight with high combustion performance. Additional benefits include the ability to restart and throttle the engine by controlling the feed system of each propellant. This is particularly useful for planetary entry and descent, space rendezvous, orbital maneuvering, and following the most economical thrust curve for optimum vehicle performance [7]. The main drawbacks from using liquid bi-propellants are that it adds system complexity and the highest performing propellants are not easily storable, as seen in Table 1.1. System complexity arises from the fact that many of these engines operate on complex cycles, such as a gas generator, expander, or staged-combustion cycle. These are illustrated in Fig. 1.1 and their benefits and drawbacks are listed in Table 1.2. These cycles vary in complexity, so a trade-study

Table 1.2: Benefits and drawbacks of common liquid-propellant engine cycles

Cycle	**Benefits**	**Drawbacks**	**Vehicles**
Gas generator	Simplicity Lower cost	Lower performance	Saturn V, Delta IV Ariane 5, Falcon 9
Staged combustion	High performance	Increased complexity Increased cost	Space Shuttle Starship
Expander	Good performance Good component life	Power limited	Atlas V Delta IV

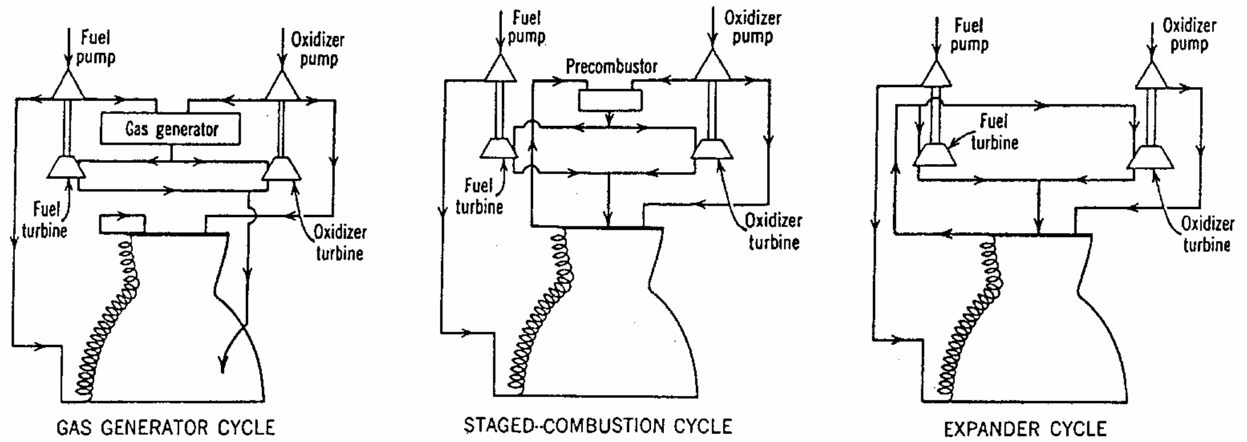

Figure 1.1: Basic cycles for pump-fed liquid-propellant engines (obtained from [8])

is typically conducted early in the design process to determine the most suitable for the given application. In addition to cycle complexity, most of the high energetic propellants are cryogenic liquids, which are liquefied gases with very low boiling points. Cryogenic propellants pose storage and handling problems and often require thermal insulation (added mass) to prevent propellants from boiling off. Additionally, they can lead to ice build-up on system components, which increases operational risks. All things considered, the primary benefit of liquid-propellant engines is that they can be designed over a wide range of thrust values (10^{-2}–10^{6} lbf) and mission profiles [2].

Present day liquid-propellant rocket engines use liquid bi-propellants almost exclusively because of their high combustion performance. The first liquid bi-propellant rocket engine flown was by Robert H. Goddard in 1926 using liquid oxygen and gasoline. The rocket reached an altitude of 41 feet and the flight lasted 2 seconds. Since then, high utilization has significantly matured the technology and pivotal engineering advances have enabled the development of multi-stage liquid bi-propellant rockets that reliably provide access to space. This has led to remarkable achievements, including the Saturn V launch vehicle, which enabled human exploration of the Moon, and the Space Shuttle, which was the first partially reusable low Earth orbital spacecraft and enabled the construction of the Hubble Space Telescope and the International Space Station (ISS). Today, ongoing efforts aim to reduce cost per launch to make space more accessible and commercialize human space transportation.

1.2 Hybrid-propellant rocket combustion

Hybrid-propellant engines differ from other chemical propulsion systems in that oxidizer and fuel are stored in different phases. Typically, engine configurations use a solid fuel grain and gaseous or liquid oxidizer (the opposite configuration has also been tested but is not widely used). Similar to monopropellants, this greatly reduces the complexity of the propellant feed system as only oxidizer has to be fed into the combustion chamber. In these systems, the combustion chamber is predominantly comprised of the fuel grain itself, though many engines also incorporate pre- and post-combustion chambers to promote mixing and complete combustion. An injector atomizes and vaporizes the oxidizer as it is fed into the chamber. Once the propellants are ignited, a diffusion flame is established over the fuel surface and combustion develops within a turbulent boundary layer. Hybrid combustion is typically diffusion limited since solid the fuel has to pyrolyze and vaporize before reacting with the oxidizer.

In choosing hybrid propellants, many of the same characteristics described in Sec. 1.1 are also desirable. Common solid fuels for hybrid-propellant engines are listed in Table 1.3 and can be classified into two categories: classical fuels and liquefying high regression rate fuels– of which the latter has gained recent popularity for its improved combustion performance [9–13]. As the oxidizer is typically gaseous or liquid phase, those listed in Table 1.1 are also primarily considered and used for hybrid systems. As seen by Table 1.3, most hybrid

Table 1.3: General data on common hybrid rocket fuels (obtained from [14, 15])

Fuels	Avg. Formula	$\mathscr{M}$ [g/mol]	Density [kg/m^3]	Heat of Formation [kcal/mol]
PMMA	$(C_5H_8O_2)_n$	100	1180	-102.9
HDPE	$(C_2H_4)_n$	28	959	-53.8
Polyurethane	$(C_{27}H_{36}N_2O_{10})_n$	548	1225	-106.7
HTPB	$(C_{7.337}H_{10.982}O_{0.058})_n$	100	930	-2.97
ABS	$(C_{15}H_{17}N)_n$	211	1060	-55.3
Nylon	$(C_6H_{11}NO)_n$	113	1140	-78.7
Polyethylene wax[a]	$(C_2H_4)_n$	28	940	-53.8
Parrafin wax[a]	$C_{32}H_{66}$	450	925	-224

[a] Liquefying high regression rate fuel

rocket fuels are polymers, which are often fabricated via casting or additive manufacturing. These techniques enable the use of fuel grains with complex geometries, such as multi-port or swirl, energetic fuel additives, such as aluminum or lithium, and mixtures of different fuel combinations to increase performance.

Hybrid rocket engines have intrinsic theoretical cost, safety, and performance advantages over many modern purely liquid- or solid-based systems and thus are attractive for new space propulsion applications. The main advantages are: (1) low cost, which is a result of a simplified propellant delivery system (only the oxidizer needs to be fed into the combustion chamber) and inexpensive paraffin/polymer-based fuels (i.e. low production/operational cost of inert fuels), (2) increased safety as the fuel and oxidizer are inherently separated by both phase and physical location, (3) higher combustion performance than solid rocket motors and comparable performance to liquid-propellant systems, and (4) easily throttleable by controlling the oxidizer flow rate, which enables a wider range of mission profiles. As a result, a number of technology development programs are exploring the feasibility of hybrid propulsion systems for future interplanetary exploration missions [14, 16–19]. However, despite interest from the aerospace sector, the maturation of hybrid rocket technology has been historically hindered by: (1) low regression rate of classical, polymer-based fuels resulting in low combustion performance, (2) performance shift (O/F shift) throughout the burn profile as a result of the changing burn area as fuel regresses, and (3) combustion instabilities.

For the aforementioned reasons, hybrid rockets have historically been at a comparatively low technology readiness level (TRL) and have not been flight proven for most practical applications. The most successful flight of a hybrid rocket was that of SpaceShipOne, an experimental air-launched vehicle with sub-orbital spaceflight capability, which was developed by Scaled Composites and won the Ansari X-Prize. The spacecraft used a four-port HTPB fueled-motor with liquid nitrous oxide oxidizer developed by SpaceDev (now part of Sierra Nevada Corporation) to generate 16,500 lbf of thrust and reach an altitude of 112 km. Currently, the vehicles successor, SpaceShipTwo, uses a polyamide (nylon) fueled-motor with liquid nitrous oxide oxidizer and is being developed by The Spaceship Company for space tourism. These programs along with significant technical advancements have steadily improved hybrid propulsion technology in the last decade and have increased the prospects of implementing these systems on a wide variety of future launch applications.

1.3 Rocket combustion performance

The force, F, imparted on a vehicle by the propulsion system can be described by the momentum thrust and pressure thrust:

$$F = \dot{m}_{\mathrm{p}} V_e + (P_e - P_a) A_e \tag{1.1}$$

where $\dot{m}_{\mathrm{p}}$ is the total mass flow rate propellants, V_e is the exhaust velocity, P_e is the pressure at the nozzle exit, P_a is ambient pressure, and A_e is the area of the nozzle exit. It can be shown that thrust is maximized when the exit pressure and ambient pressure are equal (i.e. when the gas is perfectly expanded). When not perfectly expanded, the pressure contributions must be considered, but it is useful to express Eq. 1.1 in terms of an effective exhaust velocity, c, to evaluate propulsion efficiency.

$$F = \dot{m}_{\mathrm{p}} c \tag{1.2}$$

The performance of a rocket propulsion system is commonly assessed by the specific impulse, I_{sp} [s], which represents the total impulse imparted to the vehicle per unit weight of propellant consumed.

$$I_{\mathrm{sp}} = \frac{F}{\dot{w}_{\mathrm{p}}} = \frac{F}{\dot{m}_{\mathrm{p}} g} \tag{1.3}$$

Here, F [lbf] is the thrust produced by the engine and $\dot{w}_{\mathrm{p}}$ [lb/s] is the total weight flow rate of propellants. $\dot{w}_{\mathrm{p}}$ can easily be expressed in terms of the total mass flow rate of propellants, $\dot{m}_{\mathrm{p}}$, with gravitational constant, g. I_{sp} is directly related to the performance of the overall vehicle by the *rocket equation*:

$$\Delta V = g I_{\mathrm{sp}} \ln\left(\frac{m_0}{m_f}\right) \tag{1.4}$$

where m_0 is the initial vehicle mass, including propellant (wet mass), and m_f is the final vehicle without propellant (dry mass). ΔV represents the velocity increment the vehicle would experience in free space if the engine were firing axially and describes the impulse needed to reach a certain orbit or perform an in-space maneuver. This directly prescribes mission requirements and heavily constrains suitable propellant combinations and other design parameters.

I_{sp} is useful in describing the overall efficiency of the propulsion system (chemical-to-kinetic energy conversion). However, it is often desirable to separate contributions from the combustion efficiency in the chamber (chemical-to-thermal energy conversion) and the product gas expansion performance in the nozzle (thermal-to-kinetic energy conversion). This is done by expressing I_{sp} in terms of the effective exhaust velocity, c, and defining parameters (c^* and C_f) that encompass individual performance contributions.

$$I_{\mathrm{sp}} = \frac{c}{g} = \frac{c^* C_f}{g} \tag{1.5}$$

Here, the characteristic velocity, c^*, is the primary parameter used to assess propellant combustion performance in chemical propulsion systems and C_f is the thrust coefficient, which measures the gas expansion performance through the nozzle. These parameters can be evaluated through the following equations:

$$c^* = \frac{P_c A_t}{\dot{m}_p} = \sqrt{\frac{R_u T_c}{\mathscr{M}\gamma} \left(\frac{\gamma+1}{2}\right)^{\dfrac{\gamma+1}{2(\gamma-1)}}} \tag{1.6}$$

$$C_f = \frac{F}{A_t P_c} \tag{1.7}$$

c^* can be expressed in two forms, where the first is a function of the chamber pressure, P_c, the nozzle throat area, A_t, and the total propellant mass flow rate, $\dot{m}_p$, and the second is a function of the combustion products at the end of the chamber, namely, combustion temperature, T_c, the gas molecular weight, $\mathscr{M}$, and the gas specific heat ratio, γ. C_f reflects product-gas expansion properties and the overall efficiency of the nozzle design; therefore, it can be expressed as the thrust produced by the engine, F, the nozzle throat area, A_t, and the chamber pressure, P_c. Eq. 1.7 shows that C_f compares the force created from expanding the combustion gas through the nozzle to the force created if the chamber pressure solely acted over the throat area. The remainder of this discussion will focus on rocket combustion performance (c^*); therefore, discussion on C_f is limited but can be found in [1].

As seen by Eq. 1.5, combustion performance is a principal factor in determining specific impulse, which directly impacts overall vehicle performance and mission capabilities (Eq. 1.4). By inspection of Eq. 1.6, it is evident that the theoretical combustion performance is solely dependent on a given propellant combination. This is shown in Table 1.4, which compares combustion performance for different liquid-propellant combinations. It is clear through Table 1.4 that although there are some propellant combinations that result in very high combustion performance, other factors, like those listed in Sec. 1.1, need be considered to determine whether a propellant combination is suitable for flight. In real-

Table 1.4: Theoretical performance of rocket propellant combinations (obtained from [1])

Oxidizer	Fuel	I_{sp} [s]	O/F	Bulk density [kg/m^3]	T_c [K]	c^* [ft/s]
$O_2(L)^c$	$H_2(L)^c$	389.4	4.13	290	3013	7927
	$CH_4(L)^c$	309.6	3.21	820	3533	6091
	$C_2H_6^b$	306.7	2.89	900	3593	6038
	$C_2H_4^b$	311.5	2.38	880	3759	6150
	RP-1^a	300.1	2.58	1030	3676	5902
	$N_2H_4^a$	312.8	0.92	1070	3405	6207
$F_2(L)^c$	$H_2(L)^c$	411.8	7.94	460	3962	8385
	$CH_4(L)^c$	348.4	4.53	1030	4191	6786
	$C_2H_6^b$	340.3	3.68	1090	4187	6624
	MMH^a	348.3	2.39	1240	4347	6769
	$N_2H_4^a$	365.3	2.32	1310	4734	7281
	NH_3^a	360.3	3.32	1120	4610	7199
$OF_2(L)^c$	$H_2(L)^c$	409.6	5.92	390	3584	8341
	$CH_4(L)^c$	355.6	4.94	1060	4430	7085
	$C_2H_6^b$	358.3	3.87	1130	4812	7140
	RP-1^a	349.4	3.87	1280	4709	6994
	MMH^a	349.7	2.28	1240	4348	6952
	$N_2H_4^a$	345.0	1.51	1260	4042	6848
$N_2O_4^a$	MMH^a	288.5	2.17	1190	3395	5726
	$N_2H_4^a$	292.0	1.36	1210	3265	5843
	$N_2H_4/\mathrm{UDMH}_{(50/50)}{}^a$	288.9	1.98	1120	3368	5731
IRFNA (III-A)^a	MMH^a	274.5	2.59	1270	3122	5464
	UDMH^a	272.2	3.13	1260	3147	5406
$H_2O_2^a$	MMH^a	284.7	3.46	1240	2993	5663
	$N_2H_4^a$	286.7	2.05	1240	2924	5745

[a] Earth storable: room temperature at 298 K

[b] Space storable: NBP > 123 K

[c] Cryogenic

ity, the actual c^* value of an engine will be lower due to losses associated with incomplete combustion, reaction kinetics, boundary-layer effects, etc.

Due to the substantial impact combustion performance has on the mission capabilities of flight vehicles, spacecrafts, and satellites, there are persistent efforts to increase combustion performance and identify mechanisms that lead to low efficiency. These are active research areas for both liquid- and hybrid-propellant combustion systems. Traditionally, c^* is measured through chamber pressure, P_c, and propellant mass flow rate, $\dot{m}_p$, but, although convenient, this approach globally quantifies the aggregate of multiple processes that occur in the combustion chamber (vaporization, mixing, chemical reaction, etc.). As a result, these types of measurements lack the granularity to identify specific mechanisms that may improve combustion performance. For the aforementioned reasons, optical techniques are favored over traditional measurement methods for studying flow properties in propulsion systems due to the non-intrusive nature of the measurement, which enables diagnostics in harsh environments and does not disrupt the flow-field. Therefore, to better understand the underlying chemical and physical processes governing these propulsion systems and, ultimately, improve combustion performance, parallel advancements are needed in diagnostic capabilities. The work presented herein focuses on extending these capabilities through the development of novel optical diagnostic tools for: (1) thermochemistry measurements at relevant engine conditions (high pressures, high temperatures), (2) thermochemical imaging of the propulsion flow-field for performance assessment, and (3) quantitatively evaluating fuel pyrolysis/oxidation behavior for chemical kinetic models.

1.3.1 Combustion diagnostics

Limits of traditional instrumentation often preclude definitive interpretation of flow-field phenomena in experimental tests and are not suitable for in-situ measurements at the extreme temperatures and pressures present in rocket propulsion systems. As such, combustion diagnostics have come to rely on non-intrusive laser diagnostic tools to characterize propulsion test facilities, validate computational models for complex chemically reacting propulsion flow-fields, and, ultimately, advance the next generation of propulsion systems [20]. A brief review on various optical diagnostic techniques is given below:

- *Laser-induced fluorescence (LIF)*: LIF is a two-step process in which (1) absorption of the laser photon is followed by (2) spontaneous emission. Calibration is required to quantitatively interpret measurement data, but this technique can be used to infer thermophysical flow properties, including: temperature, species concentration, velocity, pressure, and number density. This technique is frequently extended into two-dimensions by using a laser sheet–the resulting method is referred to as Planar laser-induced fluorescence (PLIF). PLIF has been extensively used to visual combustion flow fields; though, quantitative measurement complexity arises at extreme combustion conditions typical of propulsion flows.

- *Coherent anti-Stokes Raman spectroscopy (CARS)*: Raman spectroscopy is based on how a molecule scatters a photon. In anti-Stokes Raman scattering, a molecule will give up energy to a photon, which results in a decrease of its wavelength. CARS targets anti-Stokes Raman spectra by combining multiple light sources to produce a new coherent beam at the anti-Stokes frequency. As a result, these experiments require sophisticated alignment and accurate calibrations, which can make CARS a complex and expensive technique. Nonetheless, high temporal and spatial resolution positions CARS as an attractive diagnostic tool for studying combustion.

- *Laser absorption spectroscopy (LAS)*: LAS exploits the absorption of light at wavelengths resonant with differences in molecular energy levels to infer thermophysical flow properties, such as: temperature, species concentration, pressure, number density, and velocity. Molecules have unique absorbance spectra; therefore, this technique can be used to target numerous species relevant to combustion, including: reactants (CH_4), intermediates (CO, OH, CH), and products (CO_2, H_2O). Unlike the aforementioned techniques, LAS can be calibration-free and strong absorption interactions enable the use of low-power, inexpensive light sources for sensitive measurements. LAS has been more extensively used on practical combustion systems compared to other techniques and demonstrates capabilities for quantitative sensing in harsh environments.

Many of these techniques have been used to characterize combustion devices. Salgues et al. [21] conducted several non-intrusive optical techniques, including OH PLIF, OH^* chemiluminescence, laser light scattering, and shadowgraph imaging, to investigate two different swirl coaxial injectors and a shear coaxial injector using liquid oxygen/gaseous methane propellants. McMillin et al. [22] and Ben-Yakar et al. [23] performed PLIF imaging of NO and OH, respectively, in a model scramjet flow to identify an optimal configuration for flame-holding capabilities with minimal losses. Smith et al. [24] conducted CARS measurements on a liquid oxygen/hydrogen rocket combustor up to 60 bar. Soon after, Grisch et al. [25, 26] also conducted CARS measurements on both a liquid oxygen/hydrogen and a liquid oxygen/methane rocket combustor at pressures up to 65 bar and 56 bar, respectively. Recent work by Goldenstein et al. [27] and Spearrin et al. [28] applied LAS sensors for temperature, H_2O, CO_2, and CO in an ethylene-fueled pulsed detonation combustor. Additionally, Peng et al. [29] developed a novel single-ended mid-infrared LAS sensor for time-resolved measurements of H_2O mole fraction and temperature within the annulus of a hydrogen/air-fed rotating detonation engine.

Per the aforementioned studies, optical diagnostics have become a primary tool in characterizing and interrogating harsh propulsion environments. As the next generation of propulsion systems are designed, parallel advancements are needed in diagnostic and experimental capabilities to inform these flow-fields. Specifically, it is desirable to have experimental facilities capable of emulating these harsh combustion environments (high temperatures, high pressures) in a safe and controlled manner. Typical devices for studying combustion include rapid compression machines, jet-stirred reactors, flat-flame burners, shock tubes, and actual lab-scale engines. Of these, shock tubes are uniquely suited for studying propulsion flow-fields as they can be used to create precisely known test conditions over a wide range of temperatures (600–8000+ K) and pressures (sub-atmospheric–1000 atm)–a detailed discussion on shock tubes is given in Ch. 2. By using a shock tube, optical diagnostic techniques can be developed in a controlled laboratory setting before being implemented on an actual propulsion system, as shown by Nair et al. [30] who used a shock tube facility to develop and validate a mid-infrared laser absorption sensing method for quantifying gas properties (temperature, pressure, and CO column number density) at MHz measurement rates in annular rotating detonation rocket flows. Additionally, shock tubes can be used to create near-zero-dimensional environments, where individual fuel oxidation and pyrolysis behavior can be studied and isolated from the effects of gas dynamics, fluid mechanics, and heat transfer present in actual propulsion flow-fields. As such, the diagnostic techniques developed in this work exploit these advantages and were greatly supported by the design and installation of a new High-Enthalpy Shock Tube (HEST) facility at the University of California, Los Angeles (UCLA)–the details of which are discussed in Appendix D and F.

1.3.2 Chemical kinetics

The combustion performance of real fuels used in chemical propulsion systems is governed by specific physical and chemical kinetic fuel properties. Therefore, understanding and modeling the oxidation and pyrolysis behavior of real fuels are central to combustion research as it has significant implications on how emerging propulsion technologies are developed [20]. As real fuels typically comprise several hydrocarbons as dictated by the distillation process, it is often desirable to formulate surrogate mixtures, which emulate the thermophysical, thermochemical, and chemical kinetic properties of the real fuel, for predictive modeling efforts. An example of two kerosene surrogates (RP-1 and RP-2) proposed by Huber et al. [31] is shown in Table 1.5. Combustion models typically consist of large reaction mechanisms, which encompass hundreds of individual elementary reactions and their associated rates. To accurately describe real combustion systems, reaction mechanisms must be constructed and validated against kinetic targets provided by experimental work. Shock tubes, specifically, are a primary tool for chemical kinetics as they provide a near-instantaneous change in temperature and pressure, while suppressing influences from other processes present in actual propulsion/combustion devices. Additionally, when paired with quantitative opti-

Table 1.5: Multi-component surrogate for RP-1 and RP-2 (obtained from [31])

Species	Formula	Mole Fraction	
		RP-1	RP-2
α-methyldecalin	$C_{11}H_{20}$	0.354	0.354
5-methylnonane	$C_{10}H_{22}$	0.150	0.084
2,4-dimethylnonane	$C_{11}H_{24}$	–	0.071
n-dodecane	$C_{12}H_{26}$	0.183	0.158
heptylcyclohexane	$C_{13}H_{26}$	0.313	0.333

cal diagnostic tools, such as laser absorption spectroscopy, shock tubes can be used for high-fidelity time-resolved measurements of species and gas properties. This enables measurements of three functional types of kinetic targets, including ignition delay times, species time-histories, and elementary reaction rates, which serve as internal constraints on combustion kinetics model. A detailed discussion on laser absorption spectroscopy methods is given in Ch. 3.

The implementation of laser absorption diagnostics in shock tubes has enabled accurate measurements of elementary reaction rates and provided critical kinetic targets for evaluating detailed reaction mechanisms for pyrolysis and oxidation of fuels and fuel surrogates [20]. Hong et al. [32, 33] used ultraviolet and infrared laser absorption to measure OH and H_2O time-histories in various H_2/O_2 systems, such as H_2 oxidation, H_2O_2 decomposition, and shock-heated H_2O/O_2 mixtures, to develop an improved H_2/O_2 reaction mechanism at high temperatures (950–3000 K). Additionally, several studies have focus on measuring methane pyrolysis and oxidation, as it is an important intermediate in the combustion of hydrocarbon fuels. Hidaka et al. [34] used infrared laser absorption to measure the decay of methane and CO_2 production in methane pyrolysis and oxidation reactions behind reflected shock waves. As these kinetic targets are vital to characterizing combustion systems and shock tubes provide an excellent means of measuring them, there exists an abundance of data in the combustion community. However, studies on practical fuels, such as kerosenes and jet fuels, and their surrogates, create new challenges for shock tube experiments. As many of these fuels have very low vapor pressures (for practical reasons discussed in Sec. 1.1), they are typically liquid phase at room temperature. This presents challenges in uniformly distributing the mixture and often requires heating shock tubes to temperatures greater than 100°C to vaporize the fuel. Several studies use this approach, including works by Vasu et al. [35], Shao et al. [36], and Shen et al. [37] who measured ignition delay times for *n*-dodecane oxidation under practical engine conditions to provide kinetic targets for the refinement of jet fuel mechanisms. More recently, a novel aerosol shock tube by Davidson et al. [38] was developed to introduce uniform micrometer-sized aerosol mixtures into a shock tube, enabling new kerosene and jet fuel studies that are difficult to produce in the purely vapor phase.

Despite these recent advancements in chemical kinetics, there continues to be a need to accurately model real fuels, especially those used in chemical propulsion systems. Due to the complex fuel composition comprising hundreds of hydrocarbon species, during pyrolysis, these large hydrocarbons, and mixtures thereof, will typically decompose into smaller molecular fuel fragments (CH, CH_3, CH_4, C_2H_2, C_2H_4, C_2H_6, etc.), which then oxidize to form the final combustion products. This heterogeneity makes it difficult to identify kinetic targets for individual reactions as significant coupling exists between different fuel components and fuel components often form similar intermediates and products. To address this ambiguity, the work herein presents a novel time-resolved, laser absorption spectroscopy technique that isotopically-labels specific fuel components of the overall fuel mixture and simultaneously detects multiple isotopologues as the isotopically-labeled fuel components oxidize. This distinguishes contributions of individual fuel components, discerns individual reaction pathways and rates, and sets kinetic targets for combustion kinetics models.

1.4 Scope and organization

This dissertation describes novel advancements in laser absorption spectroscopy for characterizing liquid- and hybrid-propellant rocket combustion systems. Key achievements include: (1) the development of diagnostic capabilities (temperature and species concentration) for liquid-propellant combustors at relevant operating conditions ($T>3000$ K, $P>100$ bar)–

more than double the previous pressure capability of existing techniques, (2) thermochemical imaging of a hybrid rocket reaction layer, which highlights spatial gradients in combustion physics and efficiency and enables the assessment of different engine configurations, and (3) a time-resolved, laser absorption spectroscopy technique capable of distinguishing individual reaction pathways and rates of fuel blends, providing kinetic targets for real fuels used in chemical propulsion systems.

This work is structured into ten chapters. Chapters 1–3 provide an introduction and background to the techniques and methods used herein. Specifically, Chapter 2 provides an overview of shock tubes and their role in advancing chemical propulsion systems and Chapter 3 reviews laser absorption spectroscopy, which enables quantitative measurements in extreme combustion environments. Chapters 4–8 discuss direct implementations of the preceding methods and techniques. Chapters 4 introduces a time-resolved, laser absorption spectroscopy technique for developing and validating chemical kinetic mechanisms of fuel blends found in chemical propulsion systems. Chapter 5 describes a direct application of Chapter 4 for examining competitive oxidation of methane with different hydrocarbon fuel fragments in shock tube studies. Chapter 6 introduces a tomographic imaging technique to spatially-resolve the thermochemical flow-field in a hybrid rocket reaction layer. Chapter 7 extends the discussion on laser absorption spectroscopy to thermodynamic conditions relevant to propulsion systems and introduces a novel sensing approach, which exploits line-mixing effects in the infrared spectra for high-temperature and high-pressure thermochemistry measurements. Chapter 8 describes an application of the spectral line-mixing sensor from Chapter 7 for a liquid-propellant rocket combustor with kerosene/oxygen and methane/oxygen propellant combinations. Finally, Chapter 9 summarizes the work of this dissertation and suggests directions for future research.

CHAPTER 2

Background on shock tubes

This chapter serves as a brief introduction to shock tubes as it relates to combustion research. Although the operating principles for conventional, pressure-driven shock tubes [39] and the fundamentals of unsteady wave propagation [40, 41] can be readily found in literature, a brief discussion is included here to provide context for the reader. This is followed by a description of common challenges encountered when operating/designing shock tubes and a review of existing facilities. The chapter concludes with a discussion on shock tube applications for advancing diagnostic capabilities in propulsion environments (high temperatures, high pressures) and combustion chemistry (chemical kinetics).

2.1 Principles of shock tube operation

In its simplest form, a pressure-driven shock tube is a device that produces a planar moving shock wave by rupturing a diaphragm that separates high-pressure and low-pressure gas [42], as seen in Fig. 2.1. The high-pressure gas is commonly referred to as the driver and the low-pressure gas as the driven. Upon rupturing, a series of finite compression waves form and quickly coalesce into an incident shock wave, which propagates into the driven section. Notably, formation of a planar shock wave requires a finite amount of time and is largely dependent on the diaphragm breaking process and the length-to-diameter (L/D) ratio of the tube [43, 44]. Simultaneously, a series of expansion (or rarefaction) waves form and travel in the opposite direction, into the driver. The driver and driven gases are separated by a contact surface, which propagates into the driven section, behind the shock front.

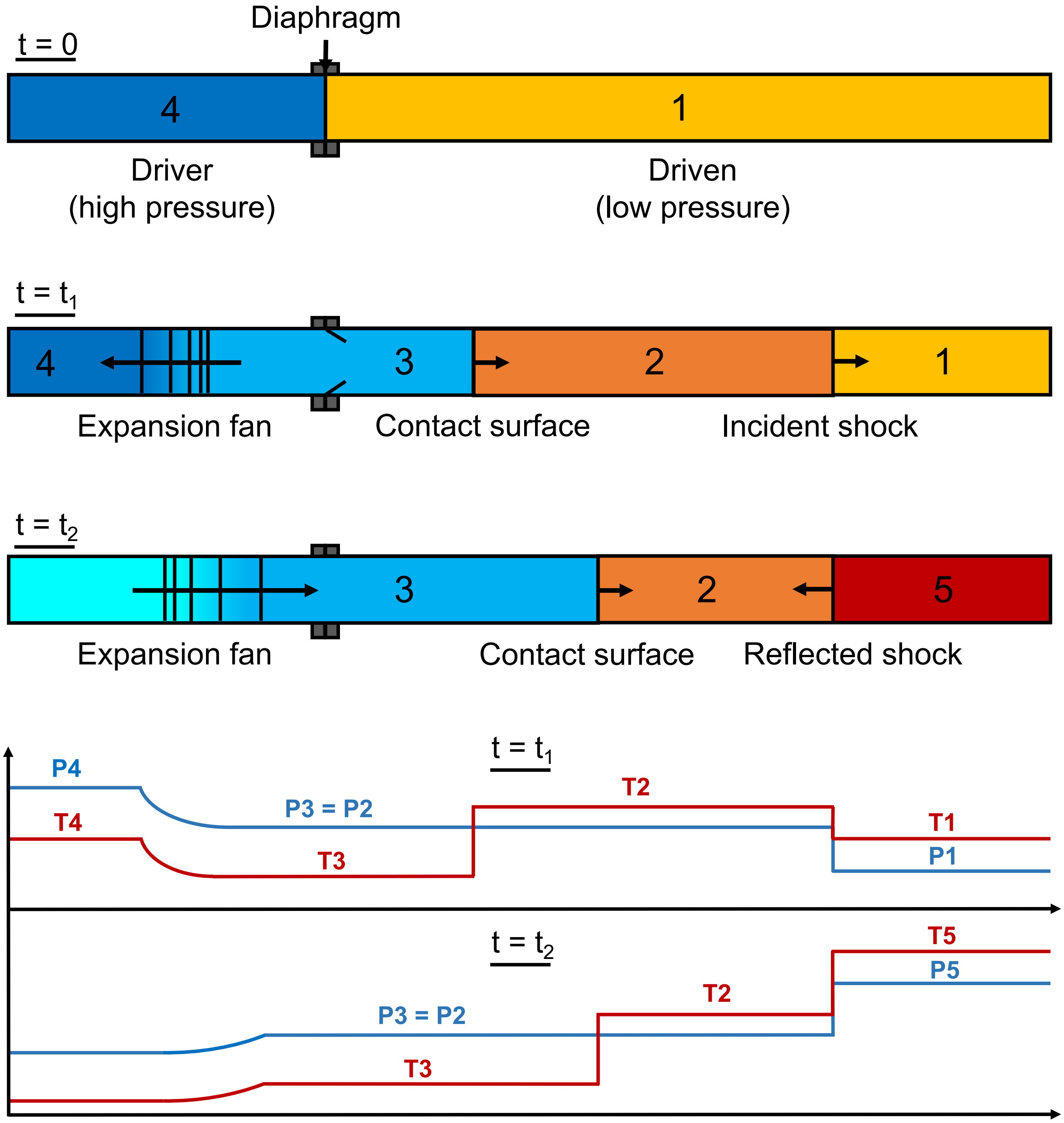

Figure 2.1: Schematic of conventional shock tube operation with graphical depictions of the unsteady wave motion. Representative pressure and temperature traces are shown at the bottom

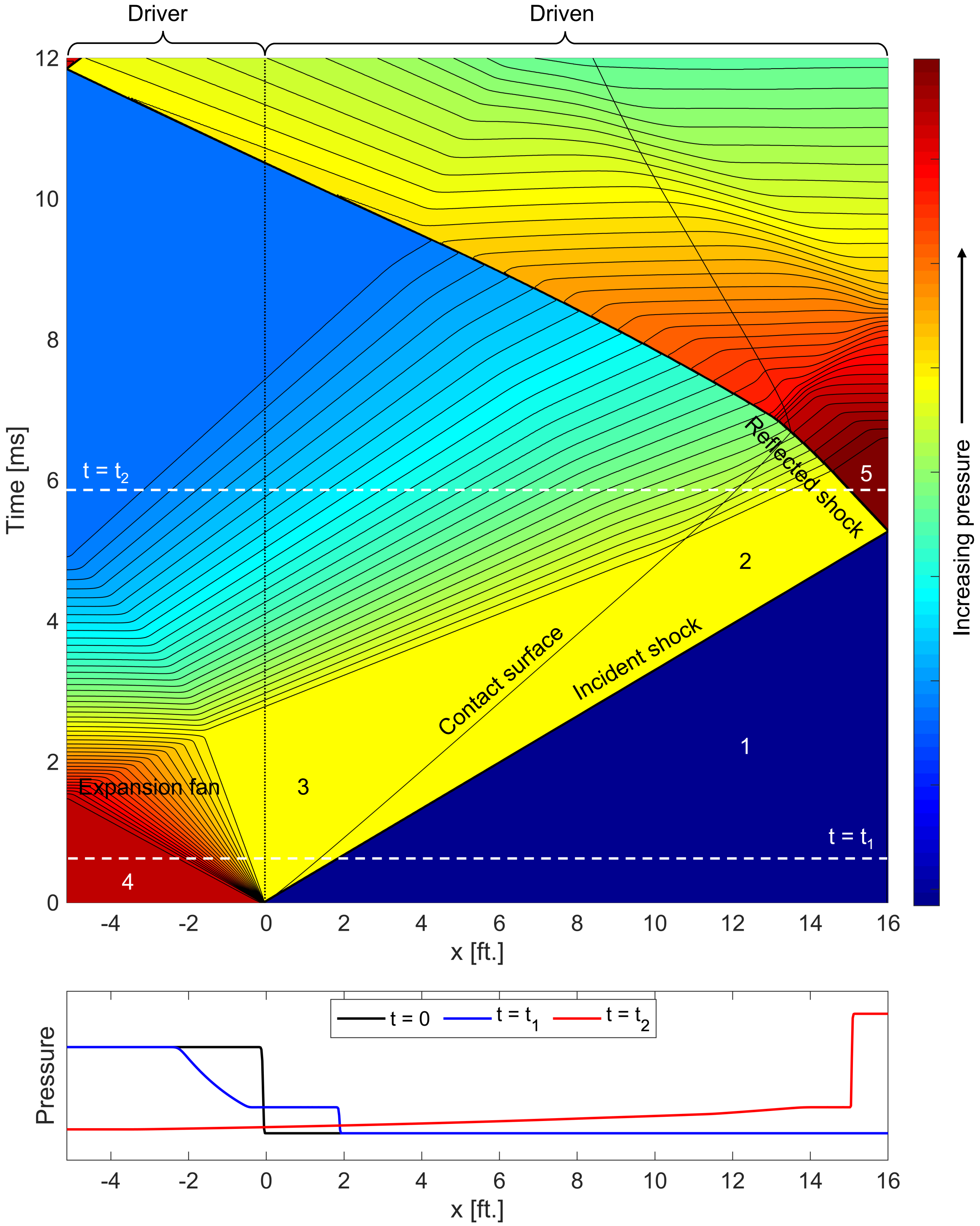

Figure 2.2: x-t diagram with pressure contours illustrating shock tube wave propagation. Representative pressure traces are shown at two times post diaphragm rupture. Simulations were modeled using the Wisconsin Shock Tube Laboratory (WiSTL) code [45]

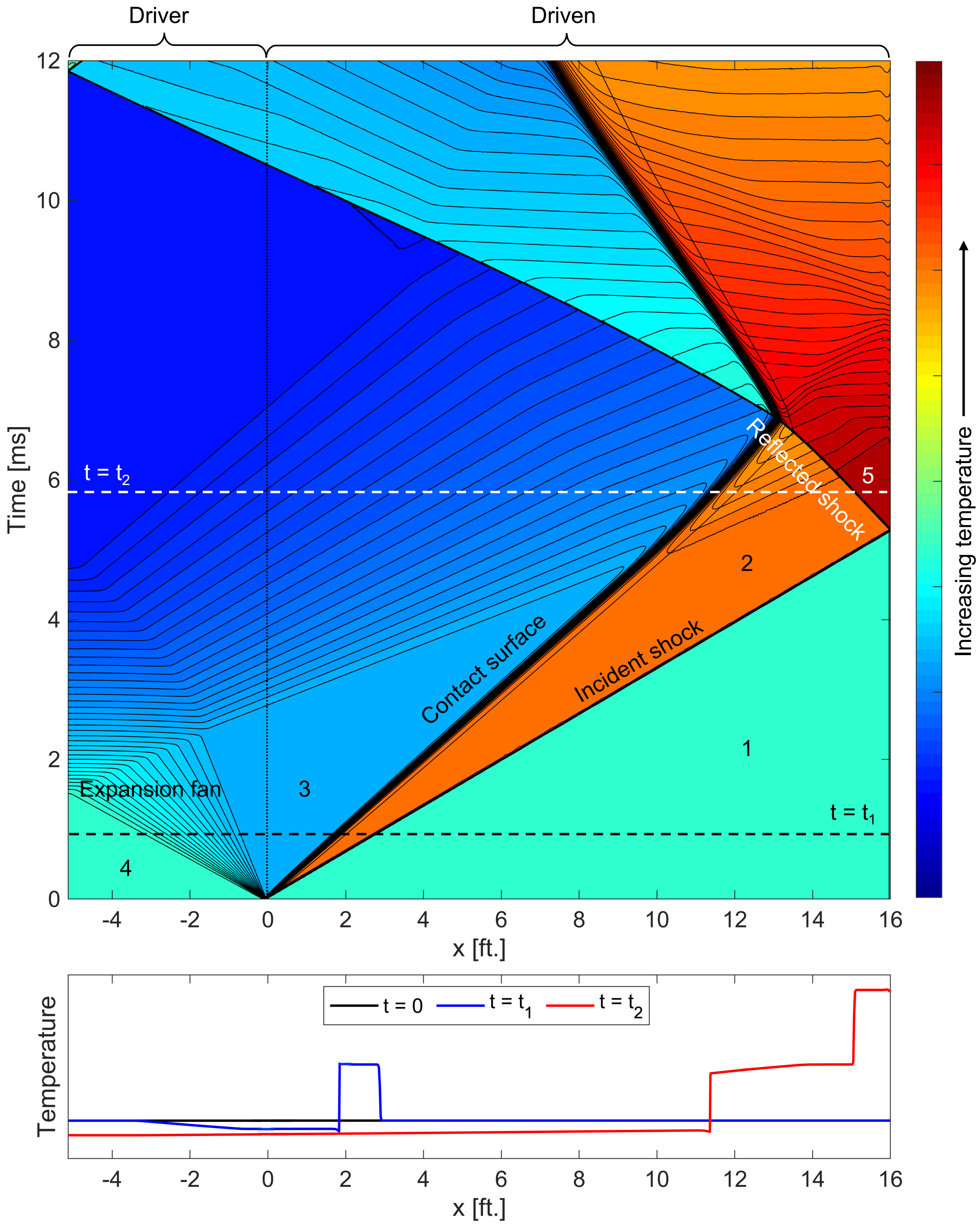

Figure 2.3: x-t diagram with temperature contours illustrating shock tube wave propagation. Representative temperature traces are shown at two times post diaphragm rupture. Simulations were modeled using the Wisconsin Shock Tube Laboratory (WiSTL) code [45]

A convenient method of representing this flow-field is through an x-t (position-time) diagram, as shown in Fig. 2.2 and Fig. 2.3. This diagram illustrates waves created by the diaphragm rupture and the corresponding thermodynamic conditions (T, P) at times t_1 and t_2. At t_1, the undisturbed driven gas (region 1) is at the initial temperature and pressure, T_1 and P_1. As the shock wave travels through the driven section (region 2), it near-instantaneously compresses and heats the gas to T_2 and P_2 and imposes a bulk velocity in the direction of the moving shock. On the opposing end, the high-pressure driver gas (region 4) is at the initial temperature and pressure, T_4 and P_4, where often $T_4 = T_1$ for simplicity. The rarefaction waves isentropically expand the gas (region 3), dropping the temperature and pressure to T_3 and P_3. The contact surface separates region 3 and region 2, such that $P_3 = P_2$ but $T_3 < T_2$. At later test times, t_2, the incident shock wave reaches the end of the driven section and reflects off the endwall. The reflected shock wave stagnates the flow-field–compressing and heating the gas even further (region 5) to T_5 and P_5–and creates a near zero-dimensional reactor (excluding a thin boundary layer), which can be properly modeled using constant-volume or constant-pressure constraints [46, 47].

2.2 Fundamentals of unsteady wave motion

This section describes the physical processes involved in the formation and propagation of shock waves and rarefaction waves through an ideal gas. A brief mention of the considerations for real gas effects is also given at the end.

2.2.1 Moving normal shock waves

A sound wave is propagated through a gas in the form of a weak isentropic adiabatic compression via collisions between neighboring molecules. Under these conditions, there is no bulk velocity imposed on the fluid with the passage of the wave and the process is reversible. The rate at which information is transmitted is the speed of sound, a, in the gas:

$$a = \sqrt{\frac{\gamma P}{\rho}} = \sqrt{\frac{\gamma R_u T}{\mathscr{M}}} \tag{2.1}$$

where γ, P, and ρ are the specific heat ratio, pressure, and density of the gas, respectively. By applying the ideal gas equation, a can also be related to the temperature T, and molecular weight $\mathscr{M}$, of the gas (where R_u is the universal gas constant). Since a sound wave is transmitted via collisions, a disturbance that propagates at a speed higher than the characteristic speed of sound at which molecules communicate is known as a shock wave. Shock waves can form when multiple weak compression waves (sound waves), initiated by a disturbance (diaphragm rupture), coalesce into a single steep wave front, as is the case in shock tube devices.

Once a shock wave forms, it propagates into the undisturbed gas ($v_1 = 0$) with a velocity, W_S, relative to the tube and imposes a velocity, v_2, on the gas behind the wave. Fig. 2.1 is shown in a laboratory-fixed coordinate reference frame (i.e. shock tube at rest), but it is often convenient to consider the shock-fixed coordinates (i.e. shock wave at rest), as seen in Fig. 2.4. Here, u is the gas velocity measured in shock-fixed coordinates and v is that measured in laboratory-fixed coordinates. The two coordinates may then be related through:

$$u_1 = W_\mathrm{S} - v_1 \tag{2.2}$$

$$u_2 = W_\mathrm{S} - v_2 \tag{2.3}$$

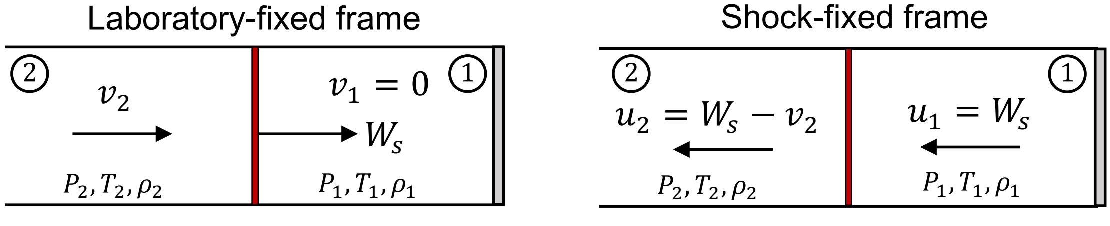

Figure 2.4: Incident shock velocity in laboratory-fixed and shock-fixed coordinates

Now, in the shock-fixed reference frame, the conservation of mass, momentum, and energy can be used to relate the change in thermodynamic gas properties through a static shock front.

$$\rho_1 u_1 = \rho_2 u_2 \tag{2.4}$$

$$P_1 + \rho_1 u_1^2 = P_2 + \rho_2 u_2^2 \tag{2.5}$$

$$H_1 + \frac{1}{2}u_1^2 = H_2 + \frac{1}{2}u_2^2 \tag{2.6}$$

Here, H is the enthalpy of the gas and Eq. 2.6 assumes no heat exchange in the shock wave–a reasonable assumption as most experiments are on the order of milliseconds, making heat losses due to conduction negligible.

In general, Eqs. 2.4–2.6 must be solved numerically when considering temperature dependent specific heats, dissociation, or ionization; however, in the special case of a calorically perfect gas (i.e. constant C_p and C_v), Eqs. 2.4–2.6 can be rearranged to obtain the Rankine-Hugoniot equations:

$$\frac{T_2}{T_1} = \frac{P_2}{P_1}\left[\frac{\dfrac{\gamma+1}{\gamma-1} + \dfrac{P_2}{P_1}}{1 + \dfrac{\gamma+1}{\gamma-1}\left(\dfrac{P_2}{P_1}\right)}\right] \tag{2.7}$$

$$\frac{\rho_2}{\rho_1} = \frac{1 + \dfrac{\gamma+1}{\gamma-1}\left(\dfrac{P_2}{P_1}\right)}{\dfrac{\gamma+1}{\gamma-1} + \dfrac{P_2}{P_1}} \tag{2.8}$$

Eqs. 2.7–2.8 express the temperature and density ratio across a shock wave to the pressure ratio. It is convenient to express these relations as a function of the incident shock wave Mach number, M_{S}, as this is often the measured parameter in shock tube experiments. Hence, the Mach number of the incident shock wave (in laboratory-fixed coordinates) is expressed as:

$$M_{\mathrm{S}} = \frac{u_1}{a_1} = \frac{W_{\mathrm{S}}}{a_1} \tag{2.9}$$

where $u_1 = W_{\mathrm{S}}$ when the gas ahead of the shock is stationary ($v_1 = 0$). Eq. 2.9 can now be used to relate thermodynamic changes across a moving shock to the shock Mach number.

$$\frac{P_2}{P_1} = \frac{2\gamma M_{\mathrm{S}}^2 - (\gamma - 1)}{\gamma + 1} \tag{2.10}$$

$$\frac{T_2}{T_1} = \frac{\left(\gamma M_{\mathrm{S}}^2 - \dfrac{\gamma - 1}{2}\right)\left(\dfrac{\gamma - 1}{2} M_{\mathrm{S}}^2 + 1\right)}{\left(\dfrac{\gamma + 1}{2}\right)^2 M_{\mathrm{S}}^2} \tag{2.11}$$

$$\frac{\rho_2}{\rho_1} = \frac{u_1}{u_2} = \frac{(\gamma + 1) M_{\mathrm{S}}^2}{(\gamma - 1) M_{\mathrm{S}}^2 + 1} \tag{2.12}$$

Curves for the above relationships are shown in Fig. 2.5 for an ideal gas with $\gamma = 5/3$. Again, these relationships are only applicable for gases with constant specific heats–the conditions for real molecular gases deviate rapidly due to the dependence of γ on temperature. Notably, these equations do predict the behavior of inert monatomic gases exactly up to fairly high temperatures ($\sim$ 8000 K), before ionization and electronic excitation need be considered [42].

2.2.2 Reflected shock waves

When the incident shock wave reaches the end of the driven section, it will reflect back into the gas which was already heated and compressed by the initial passage (region 2). As a result, the reflected shock wave stagnates the flow-field ($v_5 = 0$) and further increase the temperature, pressure, and density of the gas, which is referred to as region 5. Reflected shock waves are thus able to achieve much higher effective temperatures than incident shock

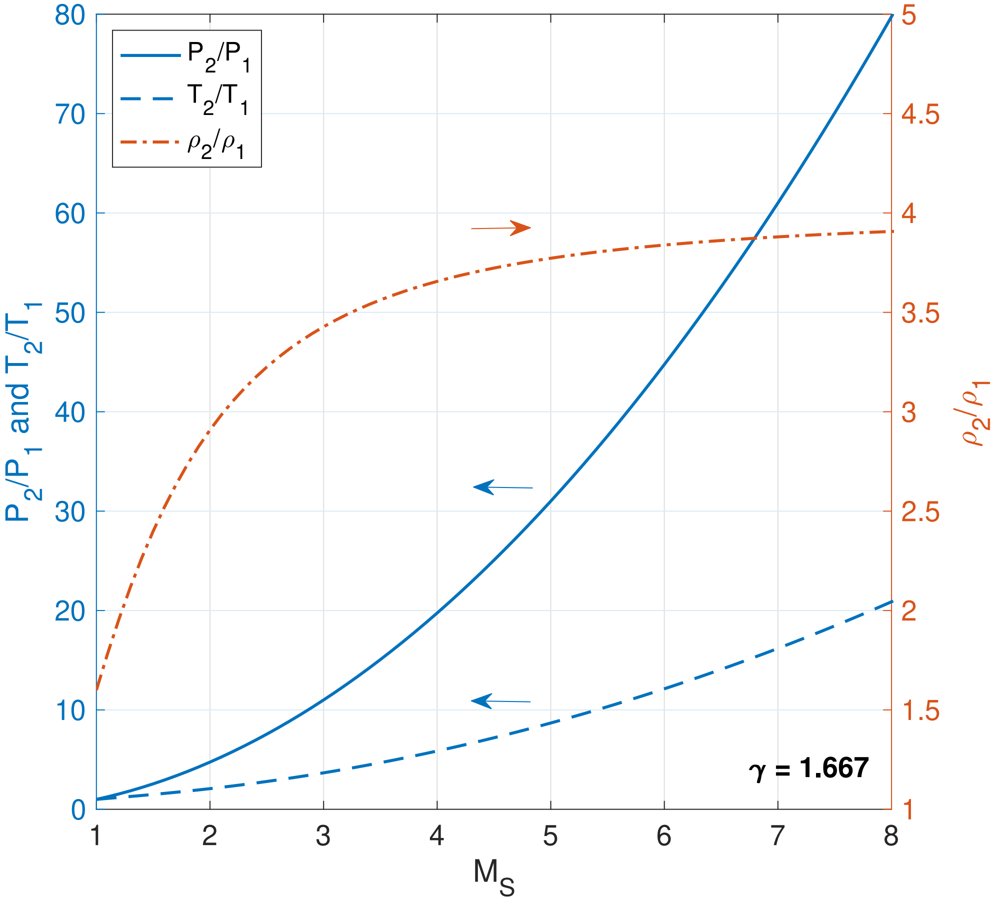

Figure 2.5: Theoretical increase in pressure, temperature, and density versus incident shock Mach number for an ideal gas with $\gamma = 1.667$

waves since the gas gives up the entirety of its kinetic energy and higher pressures suppress the effects of dissociation. As will be discussed in Sec. 2.4, the high temperatures and high pressures attainable in the reflected shock region favor its use in the development of diagnostic sensors for rocket combustion analysis, flow characterization around re-entry vehicles, and chemical kinetics.

Similar to the incident shock wave analysis, laboratory-fixed and shock-fixed coordinates can be established for the reflected shock wave, as illustrated in Fig. 2.6. Here, the reflected shock speed in laboratory-fixed coordinates is given by W_R and is related to the shock-fixed coordinates through the following:

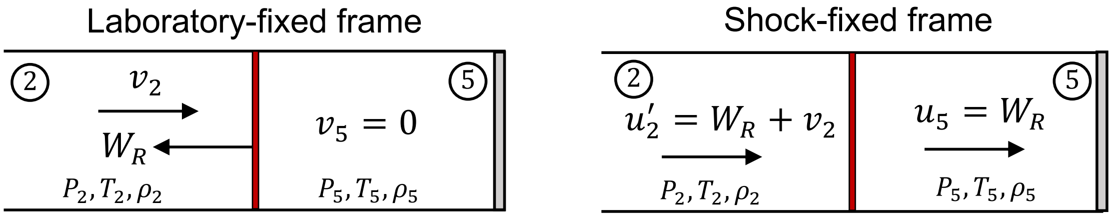

Figure 2.6: Reflected shock velocity in laboratory-fixed and shock-fixed coordinates

$$u_5 = W_{\mathrm{R}} - v_5 \tag{2.13}$$

$$u_2' = W_{\mathrm{R}} + v_2 \tag{2.14}$$

where $v_5 = 0$ due to the shock tube wall. As a result, the reflected shock Mach number is defined by:

$$M_{\mathrm{R}} = \frac{u_2'}{a_2} = \frac{W_{\mathrm{R}} + v_2}{a_2} \tag{2.15}$$

To obtain the thermodynamic conditions achieved in the reflected shock region, it is often desirable to relate the reflected shock Mach number, M_{R}, to the incident shock Mach number, M_{S}, as this is more commonly measured directly. This relation can be obtained for a calorically perfect gas by using the conservation of mass, momentum, and energy given by Eqs. 2.4–2.6:

$$\frac{M_{\mathrm{R}}}{M_{\mathrm{R}}^2 - 1} = \frac{M_{\mathrm{S}}}{M_{\mathrm{S}}^2 - 1}\sqrt{1 + \frac{2(\gamma - 1)}{(\gamma + 1)^2}(M_{\mathrm{S}}^2 - 1)\left(\gamma + \frac{1}{M_{\mathrm{S}}^2}\right)} \tag{2.16}$$

Combining Eq. 2.16 with the incident shock relations derived in Sec. 2.2.1, the thermodynamic conditions in region 5 can be directly related to the initial conditions:

$$\frac{P_5}{P_1} = \left[\frac{2\gamma M_{\mathrm{S}}^2 - (\gamma - 1)}{\gamma + 1}\right]\left[\frac{(3\gamma - 1)M_{\mathrm{S}}^2 - 2(\gamma - 1)}{(\gamma - 1)M_{\mathrm{S}}^2 + 2}\right] \tag{2.17}$$

$$\frac{T_5}{T_1} = \frac{[2(\gamma-1)M_\mathrm{S}^2 + (3-\gamma)][(3\gamma-1)M_\mathrm{S}^2 - 2(\gamma-1)]}{(\gamma+1)^2 M_\mathrm{S}^2} \tag{2.18}$$

To illustrate the benefits of using reflected shock waves to achieve extreme thermodynamic conditions, Table 2.1 compares attainable pressure and temperature ratios over a range of incident shock Mach numbers. Notably, the pressure and temperature increases in the reflected shock region are limited to finite values in the case of an infinitely strong incident shock. Again, these results are derived for ideal gases; however, a similar trend is observed when real gases are considered.

Table 2.1: Theoretical increase in pressure and temperature versus incident and reflected shock Mach number for ideal gases with $\gamma = 1.4$ and $\gamma = 1.667$

	$\gamma = 1.4$					$\gamma = 1.667$				
M_S	M_R	$\frac{P_2}{P_1}$	$\frac{P_5}{P_1}$	$\frac{T_2}{T_1}$	$\frac{T_5}{T_1}$	M_R	$\frac{P_2}{P_1}$	$\frac{P_5}{P_1}$	$\frac{T_2}{T_1}$	$\frac{T_5}{T_1}$
1.5	1.43	2.46	5.43	1.32	1.68	1.40	2.56	5.61	1.49	2.08
2.0	1.73	4.50	15.00	1.69	2.50	1.65	4.75	14.93	2.08	3.44
2.5	1.95	7.13	30.40	2.14	3.52	1.81	7.56	29.02	2.80	5.15
3.0	2.10	10.33	51.67	2.68	4.75	1.91	11.00	47.67	3.67	7.22
4.0	2.30	18.50	111.00	4.05	7.88	2.04	19.75	97.71	5.86	12.48
5.0	2.41	29.00	191.40	5.80	11.88	2.10	31.00	163.86	8.68	19.24
8.0	2.55	74.50	550.65	13.39	29.22	2.18	79.75	454.69	20.87	48.50

2.2.3 Incident and reflected expansion waves

As discussed in Sec. 2.1, a conventional shock tube utilizes a diaphragm to separate high- and low-pressure gases. When the diaphragm ruptures, a series of expansion waves form and propagate into the driver gas with local velocities $v - a$ for left-running waves and $v + a$ for right-running waves. Fig. 2.2 and Fig. 2.3 show both left-running and right-running expansion waves. The left-running expansion waves form directly after the diaphragm rupture ($t = 0$), where the first wave (referred to as the head) has a velocity $-a_4$ since the mass-motion velocity of region 4 is zero. As the incident expansion waves travel into the undisturbed driver gas, they induce a flow velocity, v, in the opposing direction of the wave propagation (i.e. a left-running wave will induce velocity directed towards the right). As a result, each consecutive wave propagates at a slower velocity–causing the expansion waves to spread out as they travel down the tube, with the last wave (referred to as the tail) having a velocity $v_3 - a_3$. Since the incident expansion waves propagate into a uniform region (region 4), they are referred to as *simple waves*. When the head reaches the driver endwall, it will reflect and interact with the remaining oncoming waves. This region is now a mix of left- and right-running waves, as seen in Fig. 2.2 and Fig. 2.3, and is referred to as a *nonsimple region*.

The properties for the incident and reflected expansion waves (in both the nonsimple and simple regions) can be determined numerically by applying *the method of characteristics* and using the boundary condition $v = 0$ at the wall. Notably, the thermodynamic conditions in the simple region can be expressed in closed analytical form at any local point through the following equations:

$$\frac{a}{a_4} = 1 - \frac{\gamma - 1}{2}\left(\frac{v}{a_4}\right) \tag{2.19}$$

$$\frac{T}{T_4} = \left[1 - \frac{\gamma - 1}{2}\left(\frac{v}{a_4}\right)\right]^2 \tag{2.20}$$

Since the flow is isentropic, Eqs. 2.19–2.20 can be combined with isentropic relations ($P/P_4 = (\rho/\rho_4)^\gamma = (T/T_4)^{\gamma/(\gamma-1)}$) to obtain equations for changes in pressure and density:

$$\frac{P}{P_4} = \left[1 - \frac{\gamma - 1}{2}\left(\frac{v}{a_4}\right)\right]^{\dfrac{2\gamma}{\gamma - 1}} \tag{2.21}$$

$$\frac{\rho}{\rho_4} = \left[1 - \frac{\gamma - 1}{2}\left(\frac{v}{a_4}\right)\right]^{\dfrac{2}{(\gamma - 1)}} \tag{2.22}$$

Eqs. 2.19–2.22 can now be used to calculate thermodynamic conditions at any point across the incident expansion waves with local velocity v. Additionally, it can be shown through the method of characteristics that v changes linearly with x across the incident expansion waves, which, for left-running waves, can be expressed as:

$$v = \frac{2}{\gamma + 1}\left(a_4 + \frac{x}{t}\right) \tag{2.23}$$

Using Eq. 2.23, the thermodynamic properties across the incident expansion waves can also be expressed in terms of x and t.

2.2.4 Shock tube relations

In order to accurately predict test conditions in a shock tube experiment, it is desirable to relate the strength of the incident/reflected shock waves and expansion waves to the initial driver and driven gas conditions. The strength of the waves initiated by rupturing a diaphragm is dependent on the pressure ratio, P_4/P_1, across the diaphragm and the physical properties ($\mathscr{M}$, γ) of the two gases. By using the equations discussed in Secs. 2.2.1–2.2.3 and relating the gas properties across the contact surface ($v_2 = v_3$ and $P_2 = P_3$) the incident shock strength can be related to the diaphragm pressure ratio through the following:

$$\frac{P_4}{P_1} = \frac{2\gamma_1 M_\mathrm{S}^2 - (\gamma_1 - 1)}{\gamma_1 + 1}\left[1 - \frac{a_1}{a_4}\left(\frac{\gamma_4 - 1}{\gamma_1 + 1}\right)\left(M_\mathrm{S} - \frac{1}{M_\mathrm{S}}\right)\right]^{\dfrac{-2\gamma_4}{(\gamma_4 - 1)}} \tag{2.24}$$

or, in terms of the incident shock pressure ratio:

$$\frac{P_4}{P_1} = \frac{P_2}{P_1}\left\{1 - \frac{(\gamma_4 - 1)\left(\dfrac{a_1}{a_4}\right)\left(\dfrac{P_2}{P_1} - 1\right)}{\sqrt{2\gamma_1\left[2\gamma_1 + (\gamma_1 + 1)\left(\dfrac{P_2}{P_1} - 1\right)\right]}}\right\}^{\dfrac{-2\gamma_4}{(\gamma_4 - 1)}} \tag{2.25}$$

Although difficult to see, by inspection of these two equations, the strength of the incident shock, for a given diaphragm pressure ratio, P_4/P_1, is largely dependent on the specific heat ratio and speed of sound–with the strongest possible shock ($P_4/P_1 \to \infty$) obtained when:

$$M_\mathrm{S} \to \frac{a_4}{a_1}\left(\frac{\gamma_1+1}{\gamma_4-1}\right) = \sqrt{\frac{\gamma_4\mathscr{M}_1 T_4}{\gamma_1\mathscr{M}_4 T_1}}\left(\frac{\gamma_1+1}{\gamma_4-1}\right) \tag{2.26}$$

As a result, the strongest shocks are obtained by using a driver gas with a high speed of sound and low specific heat ratio and a driven gas with a low speed of sound and high specific heat ratio. Fig. 2.7 shows the variation in attainable incident shock Mach numbers, and

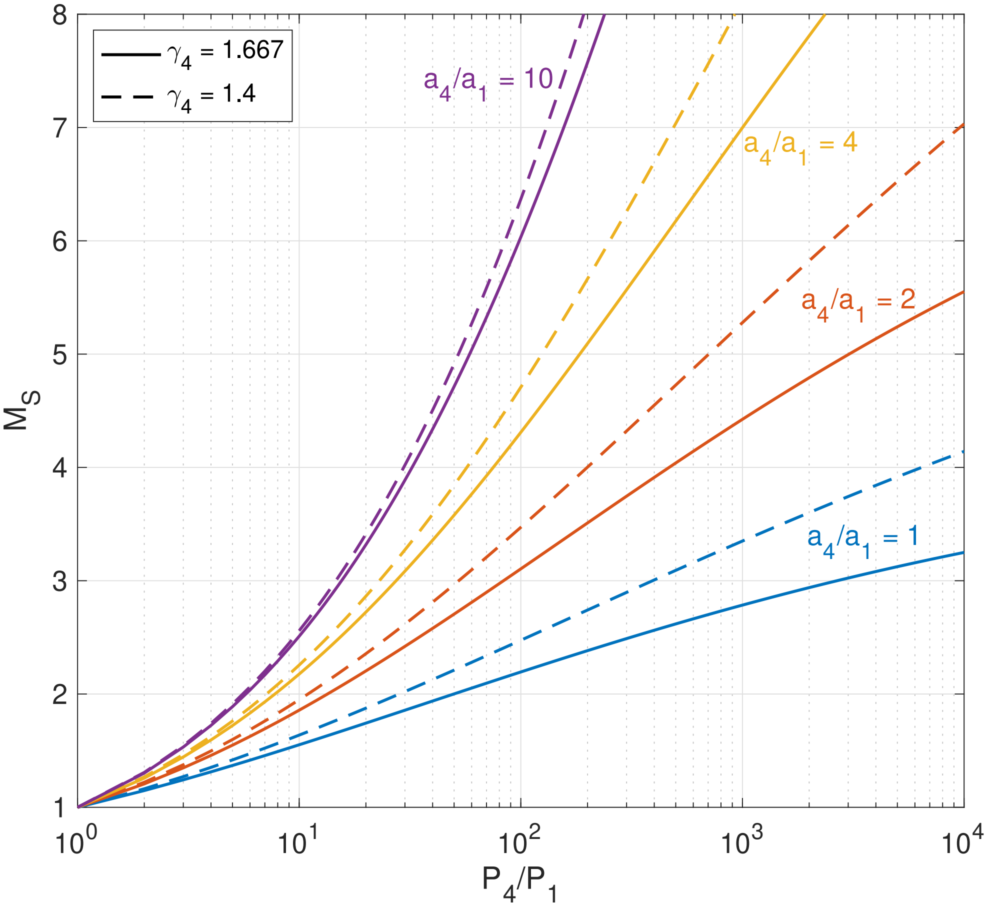

Figure 2.7: Theoretical incident shock Mach number M_S obtained over a range of diaphragm pressure ratios P_4/P_1 and sound speed ratios a_4/a_1 with a driven gas of $\gamma_1 = 1.667$ and driver gases of $\gamma_4 = 1.667$ and $\gamma_4 = 1.4$

its sensitivity to driver and driven gases, over a range of diaphragm pressure ratios. The most common (and simple) way of realizing these benefits is using a driver gas with a low molecular weight, such as hydrogen or helium, and a driven bath gas with a high molecular weight, such as argon. Another way of increasing the speed of sound ratio is by increasing the temperature of the driver gas (T_4). This is typically done by either: (1) externally heating the shock tube walls with an electric heater [48], (2) placing solid heating elements inside the driver section [49], (3) combustion of the driver gas mixture (H_2/O_2 diluted in He) [50–53], (4) adiabatically compressing the driver gas with a piston [54–56], or (5) discharging an electric current through the driver gas [57–63]. Each of these methods requires some level of modification to the shock tube and, depending on the desired thermodynamic conditions, some methods may be more limiting than others. However, they have all been successfully implemented in existing facilities to produce strong shock waves.

2.2.5 Shock tube pressure trace

Pressure measurements are commonly used to identify the different thermodynamic regions and test time during shock tube experiments. This is typically done by placing a fast-response pressure transducer on the sidewall of the driven section within 2 cm of the endwall or on the driven endwall directly. Placing the pressure transducer on the sidewall of the driven section is commonly done as it enables the pressure measurement and any other line-of-sight measurements, which are often transverse to the shock tube, to be on the same measurement plane. Measuring pressure directly on the driven endwall can be done to mitigate boundary layer effects (as discussed in Sec. 2.3) that may impact sidewall pressure measurements. A representative $x-t$ diagram indicating the sidewall measurement location and the corresponding pressure trace are shown in Fig. 2.8. From the $x-t$ diagram, it is evident that measuring near the driven endwall helps maximize the reflected shock wave test time–where a majority of shock tube studies are conducted due to the high temperatures and high pressures that are attainable. However, this minimizes the available test time behind the incident shock wave.

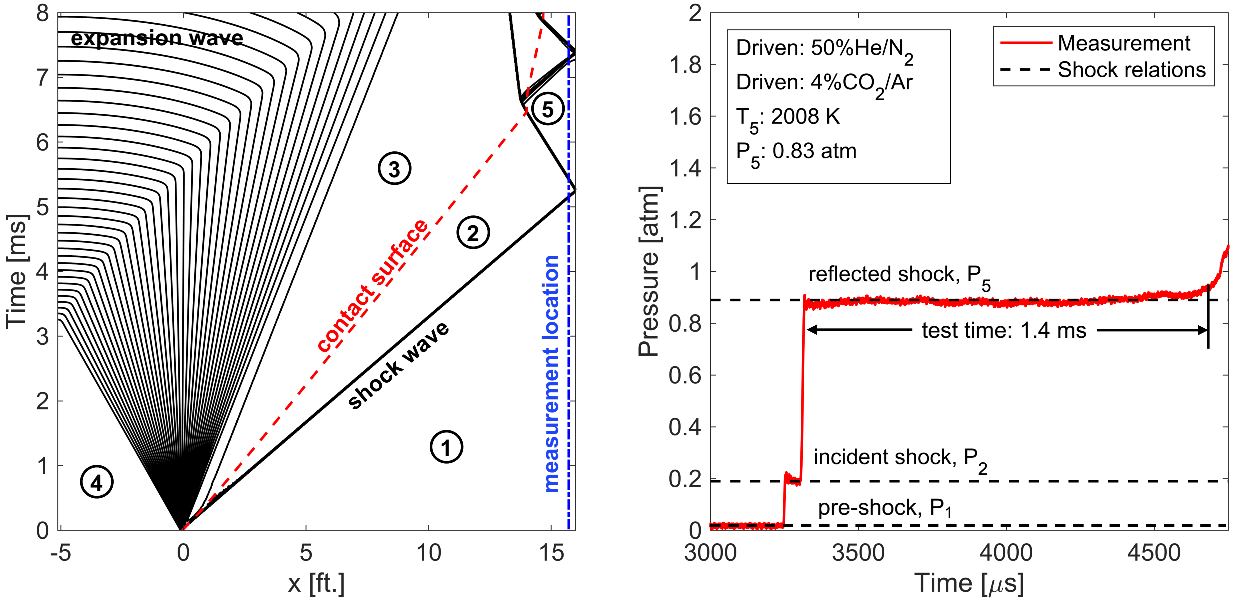

Figure 2.8: Representative $x-t$ diagram indicating the measurement location shown alongside the corresponding measured pressure trace

The increase in pressure (and corresponding increase in temperature) due to the arrival of the incident (region 2) and reflected shock (region 5) wave are clearly seen in the measured pressure trace. The test time for each region is defined by the quasi-steady thermodynamic conditions achieved behind each wave. In addition to the aforementioned pressure measurements, multiple piezoelectric transducers are often placed at different axial distances along the driven section to measure the incident shock Mach number M_S. Knowing M_S and the initial conditions of the shock tube (region 4 and region 1), Eq. 2.10 and Eq. 2.17 can be used to determine the theoretical pressure behind the incident (P_2) and reflected shock waves (P_5). As seen in Fig. 2.8, the pressures obtained from shock relations can be compared to the measured pressure trace. It should be noted that Eq. 2.10 and Eq. 2.17 do not account for non-ideal gas phenomena (i.e. vibrational relaxation, boundary layer effects, real gas effects, etc.); however, when properly accounted for, shock relations can determine post-shock conditions with $< 1\%$ uncertainty [64].

2.3 Shock tube challenges

2.3.1 Real gas effects

Accurate prediction of the thermodynamic conditions produced by shock waves is highly desirable for studying combustion chemistry and high-temperature physical processes in shock tube facilities. The discussion in the preceding sections has implicitly assumed that the molecules in these experiments can be adequately described by the ideal gas law, where intermolecular forces are negligible. Under certain conditions, namely high pressures ($>$ 100 atm), real gas effects must be considered when determining the temperature, pressure, and density behind incident or reflected shock waves. Generally, real gas effects result in a decrease in temperature and an increase in pressure and density compared to ideal gas relations. The extent of these effects on monatomic, diatomic, and polyatomic species can be seen in Fig. 2.9, which shows the compressibility factor, Z, as a function of pressure and temperature for argon, carbon monoxide, carbon dioxide, and methane. Notably, Fig. 2.9 illustrates that at elevated temperatures and relatively low pressures, ideal gas theory is sufficient to describe the state of the system. However, as pressure increases, the non-ideal effects increase nearly linearly, resulting in lower incident and reflected shock temperatures and pressures.

Because of the Arrhenius behavior of many chemical reactions, small variations in either temperature or pressure can significantly affect chemical kinetics. As an example, a 10% increase in temperature at 1100 K can lead to a 90% increase in the reaction rate for $H + O_2 \rightarrow OH + O$ [32, 33]. Consequently, studying combustion chemistry and high-temperature physical processes requires well-known thermodynamic conditions. When real gas effects are present, determining post-shock conditions typically involves numerically solving the shock wave equations with a real gas equation of state (EOS) and temperature-dependent specific heat capacities and enthalpies, which can be obtained through the 7-coefficient NASA polynomials or the NIST-JANAF thermochemical tables. Commonly used equations of state include the Van der Waals (Eq. 2.27) or Peng-Robinson EOS (Eq. 2.28),

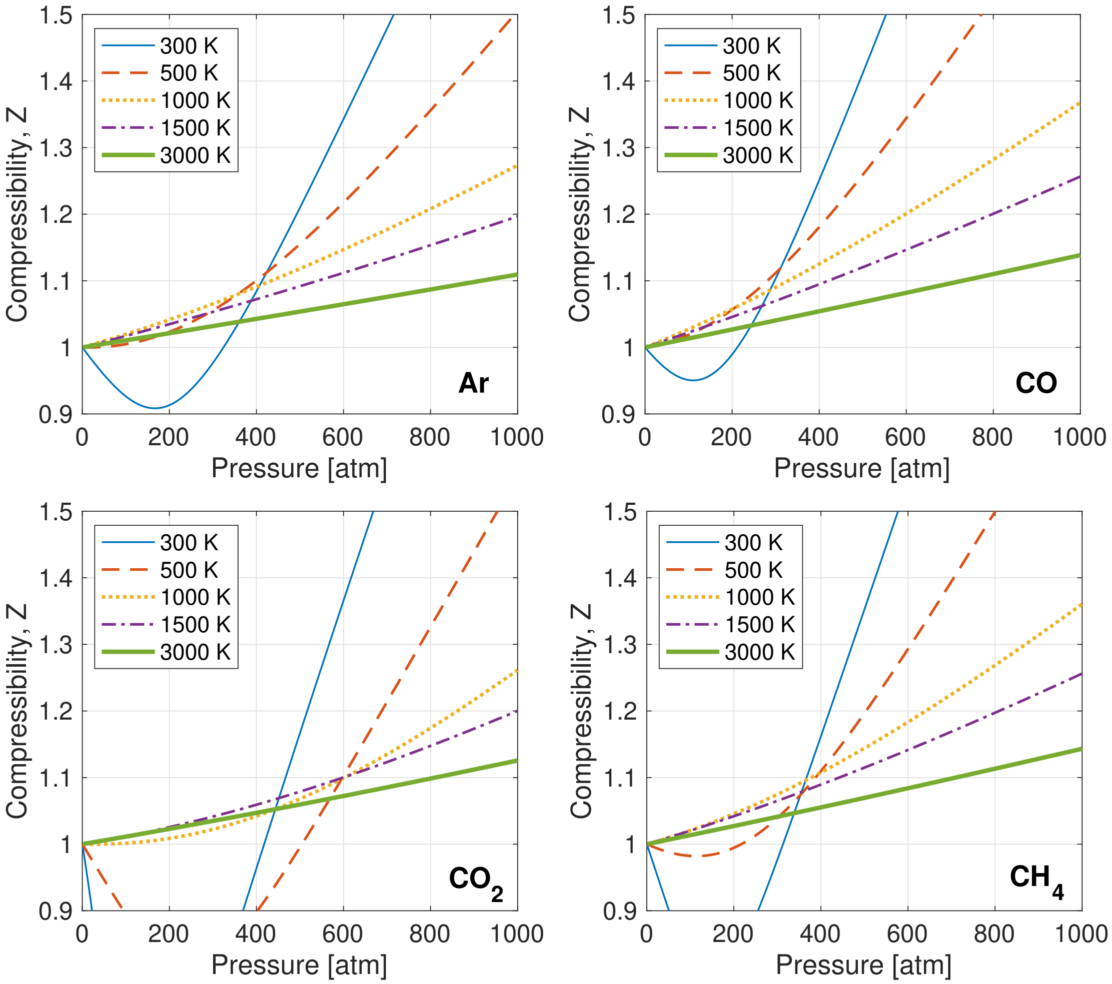

Figure 2.9: Variation in compressiblity with temperature and pressure for argon (Ar), carbon monoxide (CO), carbon dioxide (CO_2), and methane (CH_4) calculated by Van der Waals EOS

which use a third-order polynomial with empirically determined factors, a and b, to estimate the compressibility.

$$P = \frac{RT}{v-b} - \frac{a}{v^2} \tag{2.27}$$

$$P = \frac{RT}{v-b} - \frac{a}{v^2 + 2vb - b^2} \tag{2.28}$$

Several algorithms for accurate calculations of post-shock conditions with real gas effects have been developed, including the work by Mitchell and Kee [65], who developed a code to predict chemical changes behind incident and reflected shock waves with allowances for real gas behavior, boundary layer effects, and detailed finite rate chemistry, and Davidson and Hanson [66] who developed a routine, RGFROSH, to find post-shock temperature corrections using several real gas EOS. Notably, the work by Davidson and Hanson determined that the Peng-Robinson EOS captures the real-gas behavior of argon at high pressures and that results predicted by ideal gas and real gas equations are very similar for $T > 1000$ K and $P < 100$ atm, validating the use of ideal gas relations for most experiments.

2.3.2 Relaxation processes

The temperature of a gas is a measure of the fractional population distribution (commonly assumed to be Boltzmann) in different quantum energy levels. When a shock wave passes through a gas, there is an immediate increase in energy imparted on the molecules. This energy is redistributed among a molecule's degrees of freedom via intermolecular energy transfers (rotational-translational, vibrational-translational, vibrational-vibrational) and changes the fractional population distribution (i.e. changes temperature) of different energy modes. For monatomic molecules with only translation energy, this redistribution occurs within a few collisions and the molecules reach thermal equilibrium rather quickly [67]. However, for diatomic and polyatomic molecules with rotational and vibrational energy, this redistribution occurs on a longer time scale. In this case, most of the energy will initially go into translation. Within a few collisions, equilibrium with rotational energy will occur and eventually, vibrational equilibrium will follow [67]. Rotational-translational energy transfers are very efficient; therefore, equilibrium between these modes occurs rather quickly. Vibrational energy transfers are not as efficient and can take, in some instances, orders of magnitude longer to reach equilibrium with the other energy modes. The time delay between the initial impart of energy from the shock and when the system reaches thermal equilibrium is known as relaxation. This relaxation time decreases at high temperatures, where kinetic energy increases (increased collisional energy), and high pressures, where collision frequency increases, or when molecules with very efficient energy transfers, such as helium, water, or large hydrocarbons, are present.

Much of a shock tube's value is in its ability to produce well-known thermodynamic conditions. To determine these properties, assumptions must be made on the vibrational state of the post-shock gas mixture–mainly, whether it can be considered frozen or in thermal equilibrium. Campbell et al. [64] conducted a detailed investigation using a program called FROSH on the dependence of these assumptions and their uncertainties on post-shock conditions for incident and reflected shock wave experiments. Here, the frozen assumption is implemented by decoupling vibrational energy from translational/rotational energy, "freezing" the vibrational energy modes across the shock wave so that the post- and pre-shock vibrational energy is the same, and only allowing rotational/translational energy modes to equilibrate to post-shock temperatures. Similarly, the equilibrium assumption allows all three energy modes (translation, rotation, vibration) to equilibrate to post-shock temperatures. With proper consideration of the vibrational state of the gas, this method can be used to predict post-shock temperatures with $< 1\%$ uncertainty for both frozen and equilibrated cases [64].

To estimate, or avoid, vibrational relaxation effects in shock tube experiments, relaxation times can be pre-determined for a given mixture at the target test conditions using widely-available semi-empirical correlations [68–73]. These values are typically reported as $p\tau$ and scale linearly with $T^{-1/3}$. Here, p is pressure, T is temperature, and τ is the relaxation time. These correlations can be used to estimate the relaxation time of a mixture, τ_{mix}, through the following equation:

$$(\tau_{\text{mix}})^{-1} = \sum_{B} X_B(\tau_{A-B})^{-1} \tag{2.29}$$

where X_B is the mole fraction of species B in the mixture. Note that self contributions ($B = A$) must be accounted for. The estimated relaxation time can then be compared to the available test time behind the incident or reflected shock wave to determine whether frozen or equilibrium assumptions are appropriate in determining post-shock properties.

2.3.3 Shock wave attenuation

The previous discussion on shock propagation and theoretical shock strength relies heavily on two major assumptions: (1) the diaphragm separating the high-pressure (region 4) and low-pressure (region 1) gases is removed instantaneously and the resulting waves (shock waves/expansion waves) are immediately planar and fully developed and (2) the resulting flow-field is one-dimensional, adiabatic, and inviscid. In reality, the diaphragm opening process is gradual and can take hundreds of microseconds [74], which ultimately affects shock formation distance and the measured shock trajectory [43, 44, 75]. Additionally, viscosity and heat conduction causes a side-wall boundary layer to form, which decelerates the incident shock wave as it propagates down the tube and accelerates the contact surface [76], as seen in Fig. 2.10. Consequently, this also results in lower available test times compared to theory due to the aforementioned non-ideal wave interactions [77]. During experiments, incident shock speed is typically measured by piezoelectric pressure transducers or time-of-arrival sensors close to the driven end wall. Therefore, shock wave attenuation is often measured directly and is generally well-represented as a linear regression with attenuation values reported as a percent change in shock velocity per unit length (%/m)–typical values being between 0–4%/m [78, 79]. Together, these effects result in a shock trajectory that exhibits a lower speed near the diaphragm due to non-ideal rupture, a peak in speed once fully-developed and planar at some L/D, and then a decrease in speed due to viscous losses. These effects are more pronounced in smaller diameter shock tubes [80] and, combined, result in an attenuation of the shock wave and, ultimately, a deviation from the predicted shock strength and thermodynamic calculations given by theory.

Since shock attenuation is measured directly, a linear extrapolation is often used to determine the shock velocity at the driven end wall. This can then be used to accurately predict post-shock conditions using theoretical shock relations. However, since these non-idealities have implications on theoretical driver efficiencies, chemical kinetics rate constants, and ignition behavior, there have been several efforts to quantify and correlate these effects. Drewry and Walenta [81] presented a relationship to characterize the opening time of a

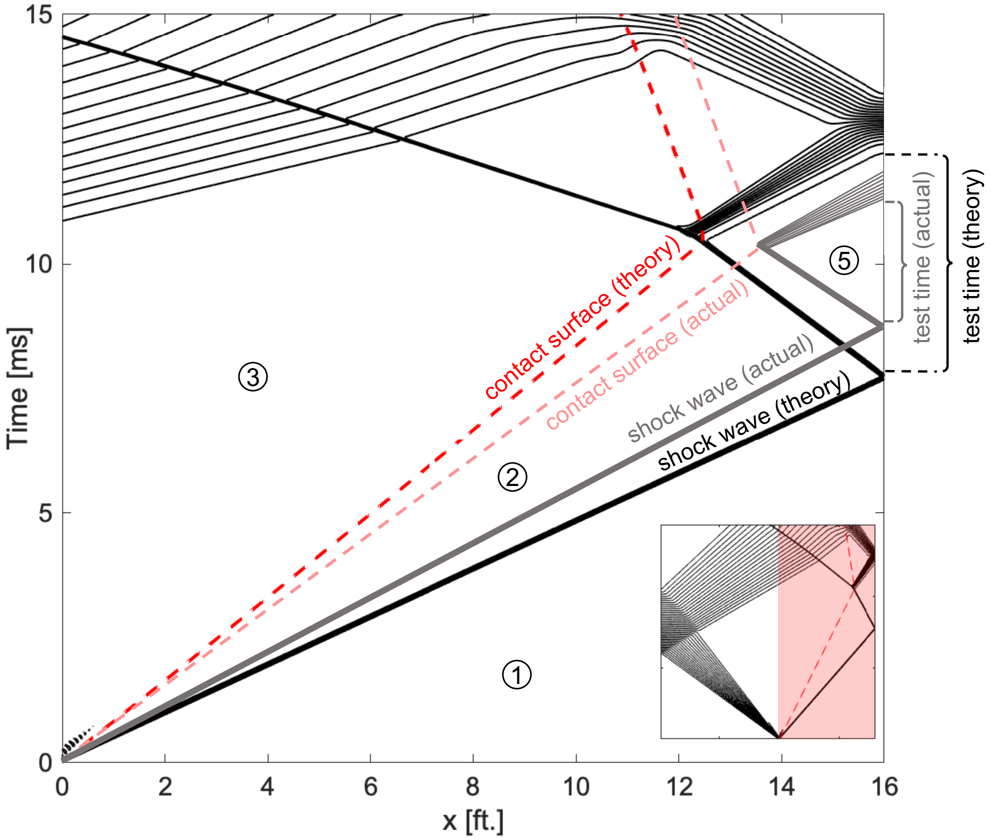

Figure 2.10: Representative boundary layer effects on shock tube wave propagation and the available test time behind the reflected shock wave

diaphragm that ruptures instantaneously without any material deformation. They found that the rupture time, t_r, is related to the diaphragm petal thickness, τ, the material density, ρ, the length of the petal base, b, the rupture pressure, P_4, and an empirical constant, K.

$$t_r = K\sqrt{\frac{\rho b \tau}{P_4}} \tag{2.30}$$

The constant K was found to be 0.93 by Drewry and Walenta [81], 0.91 by Simpson et al. [75], and 0.95 by Duntsova et al. [82]. Although some experimental studies presented deviations from this relationship [44], Rothkopf and Low [74] found that, if the initial tearing time of the diaphragm is neglected (as much as 50% of the total opening time) and that the rupture time starts when 5% of the aperture is open, Eq. 2.30 well represents the rupture time for diaphragms made of different materials (aluminum, copper, brass). Additionally, Tajima et al. [83] found that the formation distance of the incident shock wave is typically 20 times the tube diameter and becomes longer at larger diaphragm pressure ratios (P_4/P_1) and lower driven gas pressures. Notably, if the formation distance at certain conditions is longer than the driven section, the shock velocity will accelerate over the full length of the tube. Supporting the findings from Tajima et al. [83], Petersen and Hanson [79] determined that wall viscous effects comprise approximately 70% of their total shock attenuation, while non-ideal shock formation (i.e. non-ideal diaphragm ruptures) contributed the remaining 30%. By incorporating their experimental results with the attenuation theory of Mirels [77, 84–86], they were able to provide a correlation for incident shock attenuation for the High Pressure Shock Tube at Stanford University, which has an inner diameter of 5 cm (Eq. 2.31). Nativel et al. [78] attained similar correlations for shock tubes with inner diameters of 8–9 cm (Eq. 2.32) and 15–16 cm (Eq. 2.33) from the University of Duisburg-Essen and Texas A&M University, respectively.

$$\text{Attenuation (\%/m)} = 0.32 + 2.34 P_1^{-0.14}\sqrt{M_\text{S}} \tag{2.31}$$

$$\text{Attenuation (\%/m)} = -0.53 + 1.32 P_1^{-0.14}\sqrt{M_\text{S}} \tag{2.32}$$

$$\text{Attenuation (\%/m)} = 0.48 + 0.13 P_1^{-0.14}\sqrt{M_\text{S}} \tag{2.33}$$

It should be noted that P_1 is in [atm] and the attenuation theory of Mirels [77, 84–86] does not account for non-ideal diaphragm rupture and only incorporates viscous losses. This results in a pressure and Mach number dependence of $P_1^{-0.14}$ and $\sqrt{M_\text{S}}$ due to friction and boundary-layer growth, respectively. Nonetheless, there is a clear increase in the slope between these correlations, which emphasizes the dependence of wave attenuation on shock tube diameter (smaller diameters exhibiting higher attenuation rates). To better characterize viscous losses, Jones [87] observed that the resulting attenuation for a given shock strength was twice as high with a hydrogen driver gas compared to helium, concluding that the viscous losses may be more dependent on the driver gas than the test gas. Therefore, to minimize attenuation it is desirable to minimize the sound speed of the driver gas. However, from shock relations, this will inevitably also decrease the shock strength for a given diaphragm pressure ratio and so a compromise between the two is needed.

2.3.4 Reflected-shock bifurcation

As previously mentioned, viscous effects behind the incident shock wave result in the formation of a side-wall boundary layer. When the shock wave reaches the driven end wall, the reflected shock wave will interact with the boundary layer and, depending on the incident shock Mach number and the composition of the driven gas, may result in boundary layer separation and shock bifurcation. This phenomena was first observed in schlieren images by Mark [89] and Strehlow and Cohen [90], who developed models to predict bifurcation characteristics. These studies observed that a shock bifurcation occurs when the boundary layer does not have enough momentum to pass through the reflected wave. In other words, if

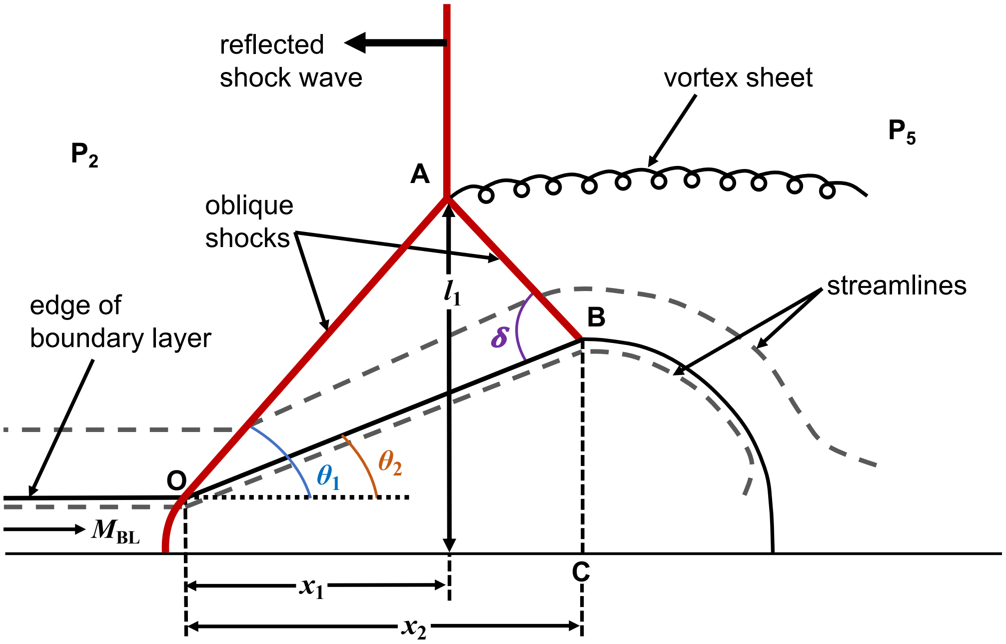

Figure 2.11: Schematic of reflected-shock bifurcation (adopted from [88, 89])

a low-energy boundary layer has a stagnation pressure, $P_{0,\mathrm{BL}}$, much lower than the reflected-shock pressure, P_5, the boundary layer cannot pass through and, as a result, will separate from the shock tube wall. A schematic of this interaction is shown in Fig. 2.11. Characteristic bifurcation features include two oblique shocks, AO and AB, and a shear layer (slip line). The energy-deficient boundary layer collects behind the first oblique shock, AO, which turns the flow around the separated gas, and the second oblique shock, AB, returns the flow parallel to the wall. Since the gas molecules that encounter the two oblique shocks retain more forward momentum and exhibit lower entropy than the molecules that interact with the planar reflected shock, a vortex sheet forms. Moreover, Davies and Wilson [88] extended Mark's work to include an estimate of the growth rate of this interaction.

When conducting reflected shock wave experiments, it is of interest to understand and estimate the severity of these effects, as they directly impact molecular behavior. The investigation conducted by Mark [89] looked into characterizing the onset of bifurcation–based on the incident shock Mach number and gas composition–and the resulting bifurcated foot geometry. Using his approach, the Mach number in the boundary layer, M_{BL}, is related to the incident shock Mach number, M_{S}, in shock-fixed coordinates, through the following relationship:

$$M_{\mathrm{BL}} = \frac{2(\gamma-1)M_{\mathrm{S}}^2 + (3-\gamma)}{(\gamma+1)M_{\mathrm{S}}} \tag{2.34}$$

The boundary layer stagnation pressure, $P_{0,\mathrm{BL}}$, can then be evaluated to estimate whether or not shock bifurcation would occur.

$$\frac{P_{0,\mathrm{BL}}}{P_2} = \begin{cases} \left[1+\dfrac{(\gamma-1)}{2}M_{\mathrm{BL}}^2\right]^{\dfrac{\gamma}{\gamma-1}}, & \text{if } M_{\mathrm{BL}} < 1 \\ \left[\dfrac{2\gamma}{\gamma+1}M_{\mathrm{BL}}^2 - \left(\dfrac{\gamma-1}{\gamma+1}\right)\right]^{\dfrac{1}{1-\gamma}} \left[\dfrac{(\gamma+1)}{2}M_{\mathrm{BL}}^2\right]^{\dfrac{\gamma}{\gamma-1}}, & \text{if } M_{\mathrm{BL}} > 1 \end{cases} \tag{2.35}$$

Fig. 2.12 illustrates attainable boundary layer Mach numbers and compares the reflected shock pressure to the boundary layer stagnation pressure as a function of incident shock

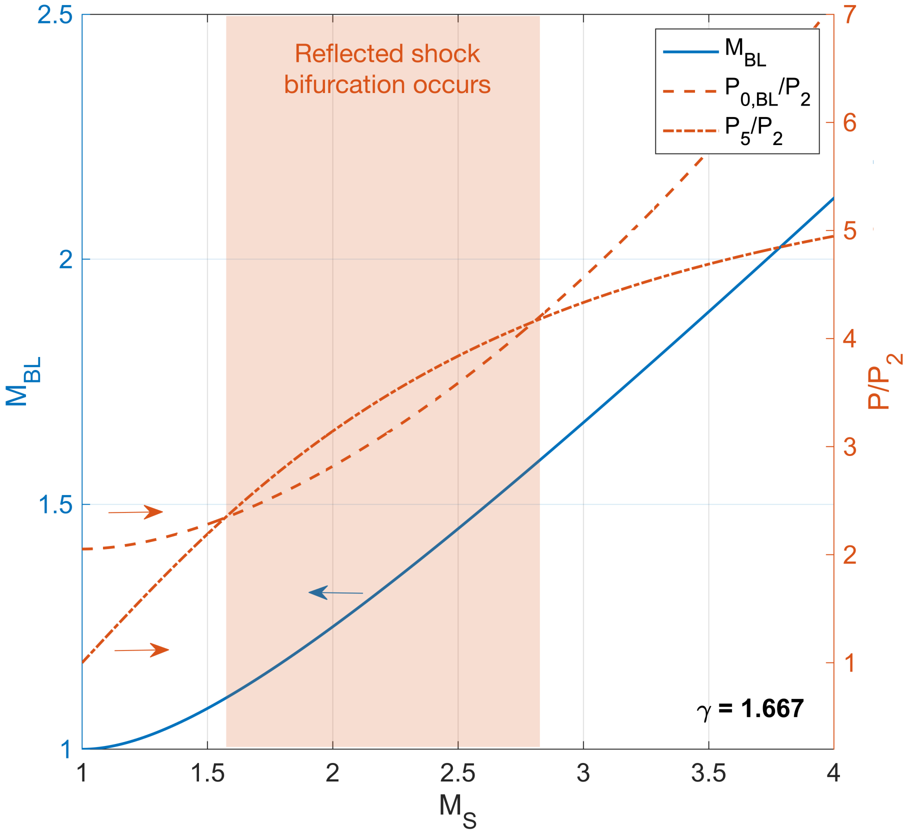

Figure 2.12: Incident shock Mach number M_{S} versus the boundary layer Mach number M_{BL} and the associated pressure ratios in the boundary layer and reflected shock regions. The range of M_{S} for which reflected shock bifurcation occurs is denoted for $\gamma = 1.667$

Mach number. Notably, for $1.57 > M_{\mathrm{S}} > 2.8$ and $\gamma = 1.67$, the boundary layer stagnation pressure is higher than the reflected shock pressure; therefore, in this regime, the boundary layer can pass continuously under the foot of the shock and into the reflected shock region. Outside these bounds, the boundary layer stagnation pressure is lower than the reflected shock pressure and, as a result, boundary layer separation and shock bifurcation is likely to occur. Additionally, the critical pressure ratio, $P_{0,\mathrm{BL}}/P_5$, below which shock bifurcation will occur, was suggested to be $P_{0,\mathrm{BL}}/P_5 < 0.8$ by Mark, but found to be as high as $P_{0,\mathrm{BL}}/P_5 < 0.95$ by Byron and Rott [91], who carried out a similar analysis using a more realistic model for the boundary layer given by Rott and Hartunian [92].

In addition to whether or not a bifurcation occurs, it is important to understand the

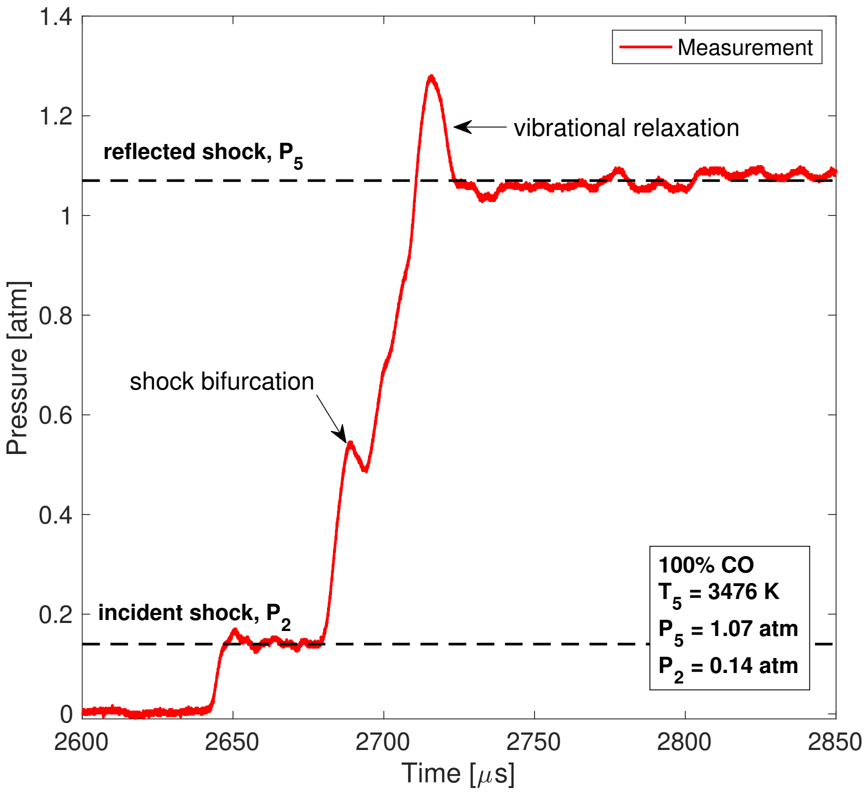

Figure 2.13: Example of reflected shock bifurcation in a sidewall pressure measurement for 100% CO. CO additionally exhibits observable vibrational relaxation at the given conditions.

severity of the disruption. During shock tube experiments, a shock bifurcation appears as a step in the measured pressure trace upon the reflected shock wave arrival. This is illustrated in Fig. 2.13, which shows an example sidewall pressure measurement for a shock tube experiment with 100% CO. Petersen and Hanson [93] investigated the magnitude of the reflected-shock bifurcation over a wide range of pressure and gas composition. Their results showed that the likelihood of bifurcation increases with the level of diatomic and polyatomic molecules in the gas mixture–previously observed in other studies. To characterize the severity of the bifurcation, Petersen and Hanson used a fast-response pressure transducer and schlieren imaging to determine the geometry of the bifurcation features shown in Fig. 2.11. The height of the bifurcation disturbance, l_1, can be determined using the lengths (x_1 and x_2) and angles (θ_1, α, δ) of the oblique shocks (where $\alpha = \delta - \theta_2 + \pi/2$).

$$l_1 = x_1 \tan\theta_1 \tag{2.36}$$

$$\frac{x_1}{x_2} = \frac{1+\tan\theta_1\tan\alpha}{1+\tan\delta\tan\alpha} \tag{2.37}$$

The length of the oblique shock, x_1, was calculated using the incident shock velocity and the time between the bifurcation arrival and the planar shock front, Δt_{AO}. The oblique shock angle, θ_1, can be found from the reflected shock strength, M_{R}, and the boundary layer stagnation pressure.

$$M_{\mathrm{R}}^2 \sin^2\theta_1 = \frac{(\gamma+1)\dfrac{P_{0,\mathrm{BL}}}{P_2} + \gamma - 1}{2\gamma} \tag{2.38}$$

By conducting extensive experiments over a range of mixtures and conditions, Petersen and Hanson found bifurcation height, l, varied from 2–8 mm and Δt_{AO} ranged from 5–30 μs in a 5 cm shock tube. From the measurement data, they determined empirical correlations for the bifurcation height and the arrival time of the planar shock front based of the incident shock Mach number, M_{S} and gas composition ($\mathscr{M}$ [g/mol] and γ).

$$l(\mathrm{mm}) = 7.5 M_{\mathrm{S}}^{1.07}\gamma_2^{-2.66}\mathscr{M}^{-0.37} \tag{2.39}$$

$$\Delta t_{AO}(\mu\mathrm{s}) = 4.6 M_{\mathrm{S}}^{0.66}\gamma_2^{-7.1}\mathscr{M}^{0.57} \tag{2.40}$$

This indicates that stronger incident shock waves and molecules with smaller γ result in a larger bifurcation height and duration and that larger fractions of diatomic and polyatomic molecules in the mixture lead to a larger disturbance. Notably, the results were found to be insensitive to pressure and, thus, these empirical correlation can be used on both high- and low-pressure shock tubes to correct for reflected shock arrival time and spatial non-uniformities. Additional empirical correlations on the duration of the bifurcation waves can be found in their original work [93].

2.3.5 Test times

The shock tube's ability to create spatially-homogeneous, near-constant test conditions has made it invaluable for studying combustion chemistry. However, for reflected shock experiments, the available test time (constant temperature and pressure) is often limited to 1–5 ms due to non-ideal wave interactions and geometric constraints. Incident shock experiments are limited to even shorter test times (< 100 μs) due to the arrival of the reflected shock wave. Figure 2.14 illustrates several $x - t$ diagrams to visualize these limitations. After the incident shock reaches the driven end wall, it reflects back towards the driver and initiates the test time. The test time ends when either the expansion fan reaches the test section or the contact surface interacts with the reflected shock wave and transmits a shock or expansion wave back towards the test section. Assuming $\gamma_2 = \gamma_3$, the contact surface and reflected shock wave interaction will transmit a shock if the sound speed in region 2 is greater than region 3 ($a_2 > a_3$) and an expansion wave if the opposite occurs ($a_2 < a_3$). These events make it particularly difficult to study low-temperature (<1000 K) kinetics, where processes have much longer timescales. Because of the Arrhenius behavior of chemical reactions, the time required for ignition exponentially increases at lower temperatures. Since ignition delay decreases with increasing pressure, relatively high pressures (>10 atm) are required to study low-temperature chemistry [94–98]. Consequently, one of the challenges encountered when conducting shock tube experiments is studying the low-temperature ignition behavior of many fuels due to the limited test time.

To counteract these non-ideal wave interactions, driver extensions [99–101] or driver gas tailoring [102, 103] are commonly used. Driver extensions simply increase the length of the driver section; thereby, delaying the arrival of the expansion wave to the test section. However, laboratories are often limited in space and so driver extensions may not always be feasible (a compact driver extension design is discussed in Appendix D). It should be noted

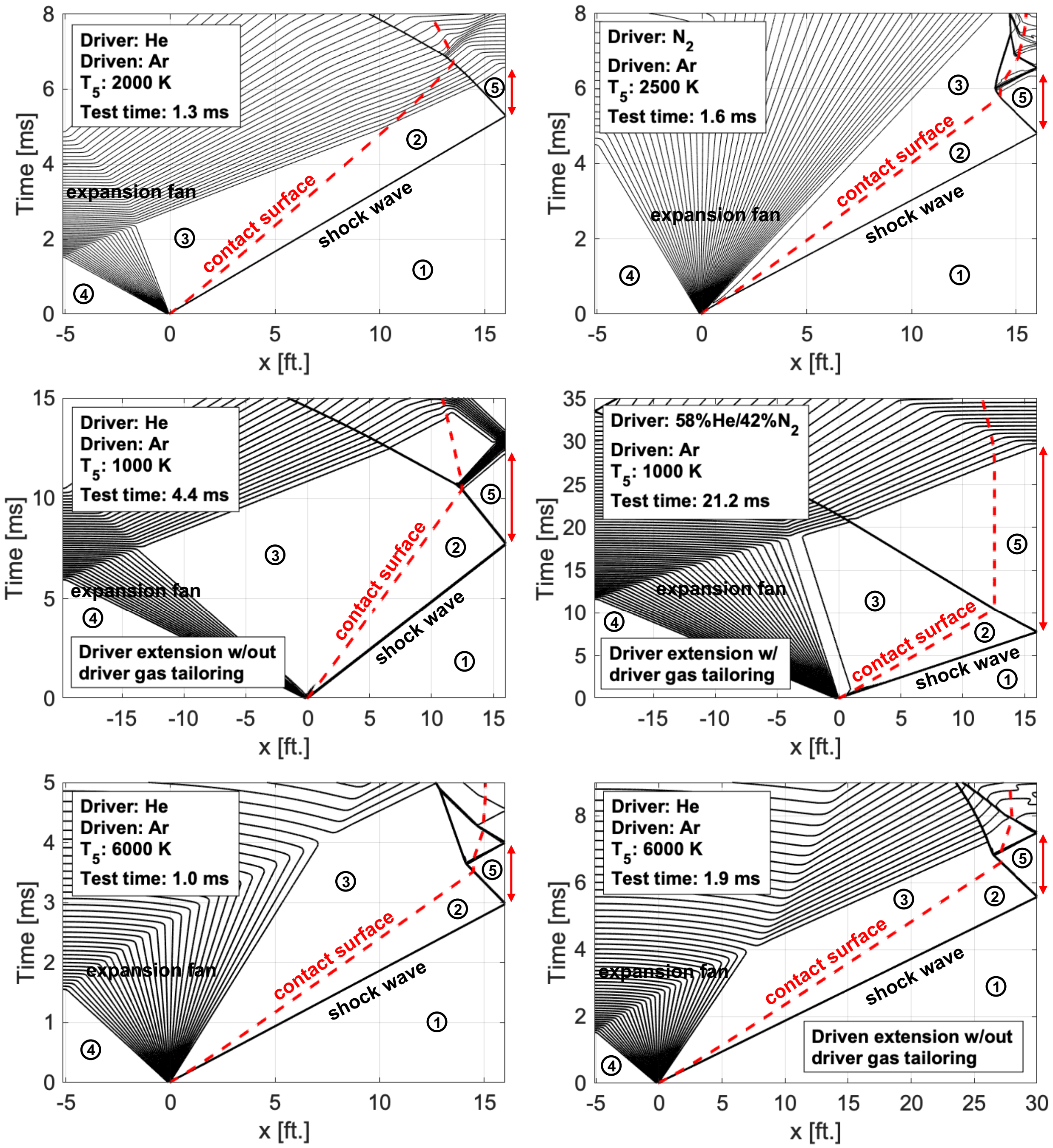

Figure 2.14: *x-t* diagrams modeled using the Wisconsin Shock Tube Laboratory (WiSTL) code [45]. *Top*: Typical reflected shock test times limited by the expansion fan arrival or contact surface-shock wave interaction. *Middle*: Attainable test times using driver extensions with and without driver gas tailoring. *Bottom*: Attainable test times with and without driven extensions at high reflected-shock temperatures when driver gas tailoring is not possible.

that extending the driver section does not impact the contact surface-reflected shock wave interaction. In other words, if the test time is limited by the contact surface-reflected shock wave interaction, extending the driver section further will have no impact. In this case, driver gas tailoring can be used to match the sound speeds, and resulting pressures, on each side of the contact surface after the passage of the reflected shock wave (i.e. $a_2 = a_3$ and $P_2 = P_3$). This is achieved by strategically blending a lower speed of sound gas, like nitrogen, with a higher speed of sound gas, like helium. As seen in Fig. 2.14, this stagnates the contact surface and no wave is transmitted to the test section. As a result, the test time will now be limited by the expansion wave arrival, which can be delayed by using driver extensions. Under some conditions, mainly high reflected-shock temperatures, driver gas tailoring is not possible because of the sound speed required to equilibrate the pressure across the contact surface. Nevertheless, test times at high temperatures are typically sufficient because of the increased rates in physical and chemical processes. If longer test times are desired at these conditions, they can be achieved by extending the driven section length, which delays the arrival of any transmitted waves from the contact surface-reflected shock wave interaction Several studies have focused on extending shock tube test times by implementing a variety of techniques,

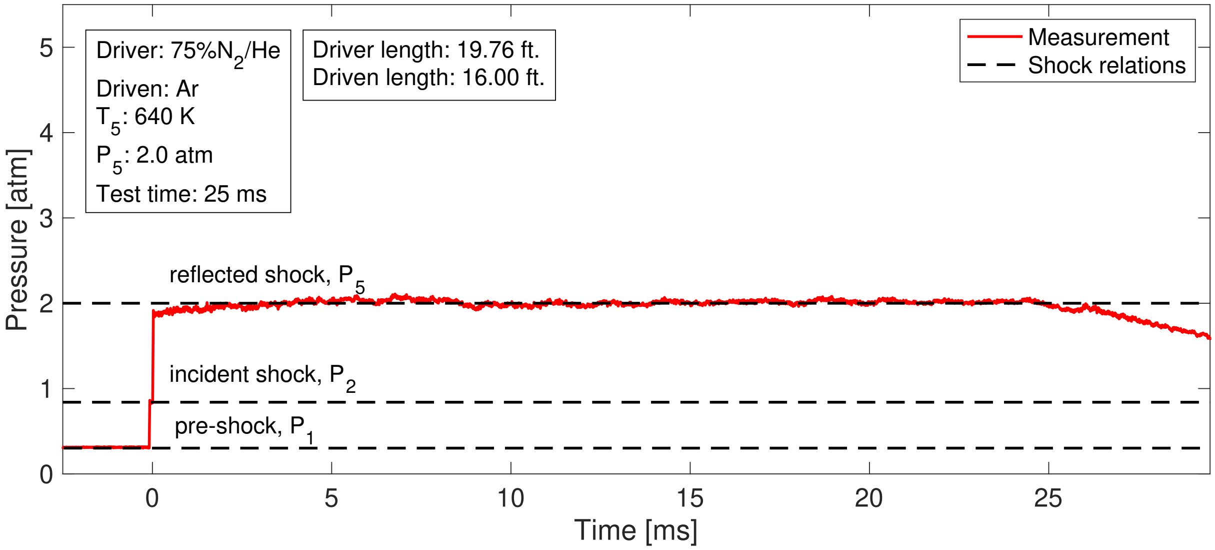

Figure 2.15: Demonstration of combined test time extension techniques (driver gas tailoring, driver extensions, driver inserts) on the high-enthalpy shock tube facility at UCLA

such as driver gas tailoring [102, 103], driver extensions [99–101], driver inserts [104], and staged driver gas filling [105]. Notably, by combining these techniques, the Constrained Reaction Volume (CRV) shock tube [106] at Stanford University demonstrated reflected shock test times up to 102 ms at 524 K [39], marking the longest constant-pressure test time achieved in a reflected shock experiment. Similarly, by combining driver gas tailoring, driver extensions, and driver inserts, the high-enthalpy shock tube facility at UCLA is able to achieve reflected shock test times up to 25 ms at 640 K, as shown in Fig. 2.15.

2.3.6 Non-uniform test conditions

The non-ideal behaviors discussed in the preceding sections (shock wave attenuation, boundary layer growth, diaphragm-bursting mechanics) often lead to non-uniform test conditions behind reflected shock waves. This is most commonly observed as variations in the reflected shock pressure trace. To minimize these non-idealities, it is desirable to be able to recognize the different types of phenomena that may occur. Two post-shock effects most frequently observed in the reflected shock pressure trace are a gradual (linear) pressure increase throughout the test time and a pressure bump, the latter which mainly occurs for long test times. A sample pressure trace illustrating these effects is shown in Fig. 2.16.

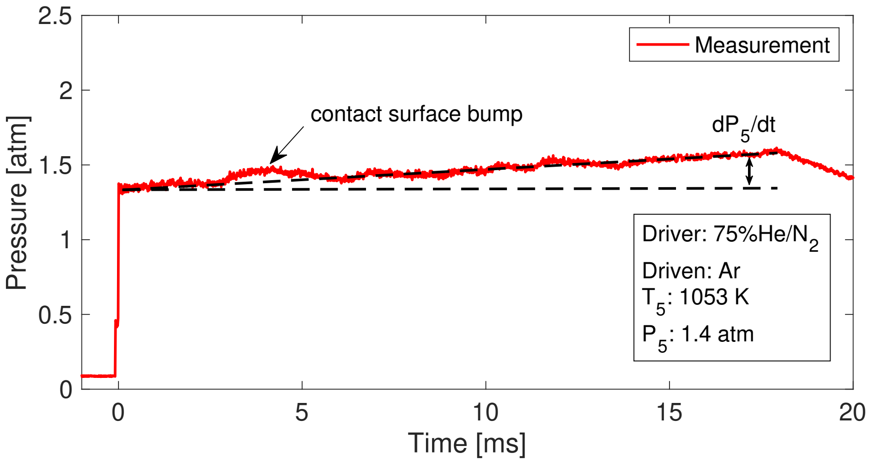

Figure 2.16: Example of a shock tube experiment with non-uniform test conditions in the reflected shock pressure trace

The gradual pressure increase is referred to as $\mathrm{d}P_5^*/\mathrm{d}t$ and is often expressed as a percent change in pressure per millisecond test time.

$$\frac{\mathrm{d}P_5^*}{\mathrm{d}t}(\%/\mathrm{ms}) = \frac{\left(\dfrac{\mathrm{d}P_5}{\mathrm{d}t}\right)}{P_5} \tag{2.41}$$

where P_5 is the initial reflected shock pressure calculated by the incident shock Mach number and the initial pressure and temperature of the driven gas. Pressure changes during the test time are undesirable as they are accompanied by changes in temperature, T_5. This change in temperature is typically accounted for by assuming isentropic compression of the gas

$$T = T_0 \left(\frac{P}{P_0}\right)^{\dfrac{\gamma - 1}{\gamma}} \tag{2.42}$$

Recent work by Nativel et al. [78] highlights how $\mathrm{d}P_5^*/\mathrm{d}t$ can vary depending on shock-tube facility and is largely influenced by incident shock Mach number and shock tube inner diameter. Typical values range from $0 < \mathrm{d}P_5^*/\mathrm{d}t < 10$ %/ms. By comparing different shock tube facilities, Nativel et al. was able to develop an empirical correlation between $\mathrm{d}P_5^*/\mathrm{d}t$ and incident shock Mach number, initial driven gas pressure in [Pa], shock tube inner diameter in [m], and gas composition.

$$\frac{\mathrm{d}P_5^*}{\mathrm{d}t}(\%/\mathrm{ms}) = \exp(-3.55) P_1^{-0.04} M_\mathrm{S}^{3.13} \mathrm{ID}^{-1.00} \gamma_1^{0.37} \tag{2.43}$$

This illustrates that $\mathrm{d}P_5^*/\mathrm{d}t$ is expected to increase with decreasing shock tube diameter and initial fill pressures and increasing incident shock Mach number and γ. Additional investigations on how to eliminate $\mathrm{d}P_5^*/\mathrm{d}t$ altogether have been conducted by Dumitrescu [107] and Hong et al. [104]. Here, pressure increases in the reflected shock test time were compensated by placing variable-area inserts into the driver section of the shock tube. During an experiment, the expansion waves travelling towards the driver end wall, will interact with the surface of the driver inserts and partially reflect expansion waves towards the driven section. The partially-reflected expansion waves will then reach the driven end wall and compensate for the pressure rise ($\mathrm{d}P_5^*/\mathrm{d}t$) caused by non-ideal effects.

Another commonly observed non-uniformity in the reflected shock pressure trace is a small pressure bump, as shown in Fig. 2.16. This is effect is typically seen at longer test times when using a tailored driver gas. As mentioned in Sec. 2.3.5, driver gas tailoring mixes a lower speed of sound gas, like N_2, with a higher speed of sound gas, like He, to match the pressures and sound speeds across the contact surface when the contact surface and reflected shock wave interact. This stagnates the contact surface and eliminates the transmission of any waves back to the test section, enabling longer test. In reality, the contact surface is not a discrete partition but a mixing zone (between driver and driven gas) that has some finite thickness [102, 108, 109]. The pressure bump occurs when the reflected shock wave interacts with this mixing zone, transmitting partially reflected waves back to the test section. The condition for what type of wave is transmitted (expansion or compression) has been explained by Hong et al. [102] and Polachek and Seeger [108] by the concept of shock impedance.

$$z = \frac{1}{a}\sqrt{\gamma\left[(\gamma+1)+(\gamma-1)\right]\left(\frac{P_5}{P_2}\right)^{-1}} \tag{2.44}$$

where a is the sound speed and P_5/P_2 is the shock strength. Polachek and Seeger showed that when a planar shock wave propagates into an interface of two gaseous media with a larger impedance, z, a compression wave is reflected. Therefore, using a lightweight gas (such as helium) as a buffer between the driver and driven gases, reduces the impedance of the interface and the pressure bump is diminished. Likewise, using a heavier gas (such as nitrogen) as a buffer, will increase the impedance and augment the pressure bump. Campbell et al. [39] demonstrated this technique by filling a small amount of helium gas (2–10%) into the driven section next to the diaphragm. This eliminated the contact surface pressure bump and produced a constant pressure test time with $\mathrm{d}P_5^*/\mathrm{d}t = 0$.

2.3.7 Repetition rate and repeatability

One of the primary disadvantages of using a conventional shock tube facility is the cycle time between tests and the single-shot nature of the experiment The cycle time for a single shock is typically on the order of 30–60+ min. The main time-consuming aspects of running an experiment are replacing the burst diaphragm that separated the driver and driven sections and waiting for the facility to vacuum down, which, in certain cases, can take several hours if a low ultimate pressure ($< 10^{-6}$ torr) is desired. Additionally, although conventional shock tubes can accurately predict the post-shock conditions with $< 1\%$ uncertainty [64], reliably obtaining repeatable shocks can be a challenge due to the influence the diaphragm rupture has on shock wave development and post-shock conditions. Diaphragm rupture is commonly controlled by use of a cutter [110, 111] or cross-scribing [74, 75, 81, 112]; however, inconsistencies in the rupture mechanics are still often present. These limitations are highly undesirable as most investigations often require numerous shocks (15+) for a single study and small variations in either temperature or pressure can significantly affect chemical kinetics.

To alleviate these drawbacks, there have been several investigations into the design and operation of diaphragmless shock tubes [113–116] where the diaphragm is replaced by a fast-acting valve [117]. Notably, Tranter and Giri [118] developed a diaphragmless shock tube (DFST) for high temperature kinetic studies. This method enables repeated shocks at near-similar conditions with a cycle time as low as ~ 1 min. A recent study by Randazzo and Tranter [119] greatly improves the equipment lifetime and test repeatability of this facility by slightly modifying the fast acting valve. With these modifications, Randazzo and Tranter were able to achieve 50 near-identical experiments with $< 1\%$ change in post-shock temperature and pressure from test to test. Extending this concept to produce even faster cycle times, Tranter and Lynch [120] developed a miniature high-repetition-rate shock tube capable of producing repeatable tests up to 100 bar with a 4 Hz cycle time.

2.4 Shock tube applications

Shock tubes are uniquely suited for studying combustion phenomona as they can be used to create precisely known test conditions over a wide range of temperatures (600–8000+ K) and pressures (sub-atmospheric–1000 atm)–emulating the harsh environments found in many modern propulsion applications. By combining shock tubes with optical diagnostics, sensors can be developed and validated in a controlled laboratory setting at the expected thermodynamic conditions prior to being implemented on actual combustion devices. Additionally, shock tubes can be used to create near-zero-dimensional environments, where individual fuel oxidation and pyrolysis behavior can be studied and isolated from gas dynamics, fluid mechanics, and heat transfer effects present in actual propulsion flow-fields.

2.4.1 High temperatures and high pressures

Shock tubes are remarkably effective tools for producing high temperature and high pressure environments typifying modern combustion devices. To illustrate the shock tube's ability to produce high-temperature conditions, Fig. 2.17 compares theoretical temperatures between shock heating and isentropic heating at similar compression ratios, P_2/P_1 (comparable to shock strength). This shows that over all conditions, shock heating can produce similar temperatures with significantly lower compression ratios (i.e. shock strength)–especially at temperatures greater than 2000 K where the pressure requirement is more than five times less. Furthermore, it is nearly impossible to achieve temperature conditions greater than 2000 K via isentropic compression due to the extremely high compression ratios that would be required. As such, shock tubes have become a primary tool in characterizing propulsion test facilities and developing/validating computational models for complex chemically reacting flow-fields.

In real shock tubes, deviations from ideal gas-dynamic behavior, such as those described in Sec. 2.3, can significantly impact shock tube performance and attainable post-shock conditions [78]. As a result, shock tube capabilities depend greatly on their design and

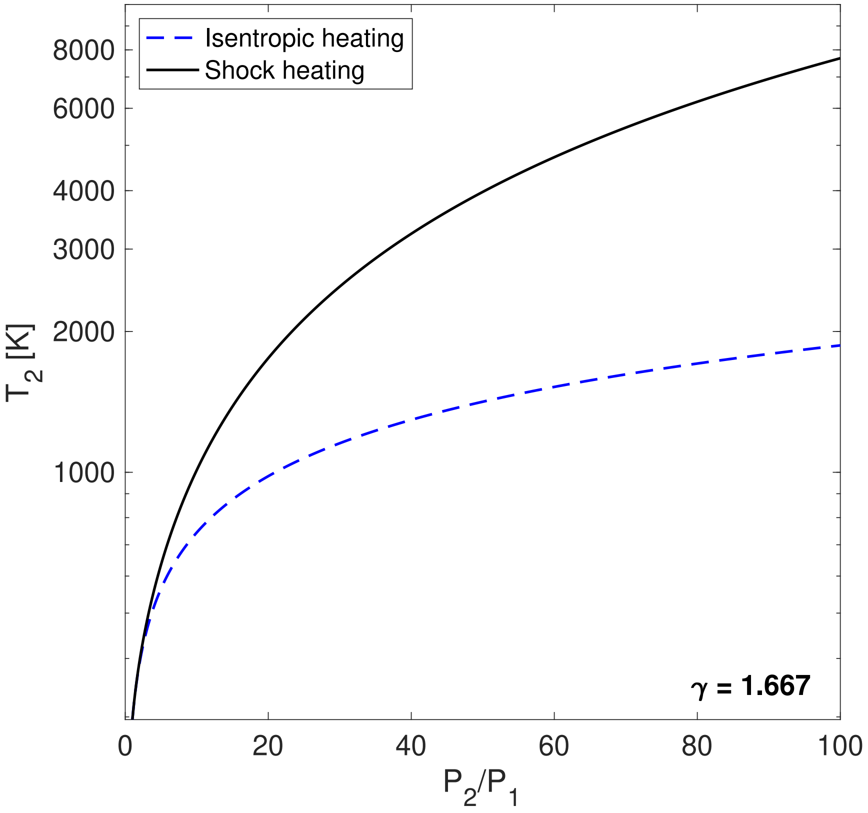

Figure 2.17: Comparison of temperatures achieved T_2 via isentropic heating and shock heating of room temperature ($T_1 = 296$ K) gas for a wide range of compression ratios P_2/P_1

specific research applications. A brief review of notable achievements in high-temperature and high-pressure studies is given here while a more complete list of existing facilities can be found in Table 2.2. For high-purity, high-pressure chemical kinetics experiments, the High Pressure Shock Tube (HPST) at Stanford University is able to produce reflected-shock pressures up to 1000 atm [121] and has been used extensively for ignition delay time studies and kinetic modeling [35, 96, 97, 99, 104, 122–125]. Similarly, the High Pressure Single Pulse Shock Tube at the University of Illinois at Chicago can also achieve post-shock pressures up to 1000 atm [126] and has been used to investigate the high-pressure pyrolysis and oxidation behavior of various hydrocarbon species and aromatics via gas chromatography and mass spectrometry [127–133]. Furthermore, shock tubes are also capable of producing extreme temperature environments to characterize real gas phenomena, such as thermal non-equilibrium, ionization, and dissociation, relevant to planetary entry or hypersonic vehicles.

Table 2.2: Dimensions of several shock tube facilities

Institution	Description	Country/State	Driver Section Diameter [cm]	Driver Section Length [m]	Driver Section L/D	Driven Section Diameter [cm]	Driven Section Length [m]	Driven Section L/D
Stanford University	CRVST	California	16.05	13.42	83.6	11.53	9.73	84.4
Stanford University	HPST	California	7.62	3.00	39.4	5.00	5.00	100
Stanford University	KST	California	14.13	7.12	50.4	14.13	8.54	60.4
Stanford University	NASA Tube	California	15.24	7.55	49.5	15.24	10.51	68.9
Caltech	T5	California	9.00	12.00	133.3	30.00	30.00	100.0
Caltech	–	California	15.24	6.19	40.6	15.24	11.28	74.0
NASA's Ames Research Center	EAST	California	10.00	1.37	13.7	10.00	12.00	120.0
NASA's Ames Research Center	EAST	California	10.00	1.37	13.7	60.00	21.00	35.0
KAUST	HPST	Saudi Arabia	10.00	7.00	70.0	10.00	7.00	70.0
KAUST	LPST	Saudi Arabia	14.00	9.00	64.3	14.00	9.00	64.3
RWTH Aachen	–	Germany	8.70	5.30	60.9	8.70	6.30	72.4
RWTH Aachen	–	Germany	14.00	4.50	32.1	14.00	11.00	78.6
University of Illinois at Chicago	HPST	Illinois	5.08	1.52	29.9	2.54	4.10	161.4
University of Illinois at Chicago	LPST	Illinois	10.16	1.52	15.00	6.35	3.05	48.0
KIT	–	Germany	3.14	1.98	63.1	3.14	2.97	94.6
McGill University	–	Quebec	5.00	3.00	60.0	5.00	4.20	84.0
RPI	–	New York	5.70	2.59	45.4	5.70	4.11	72.1
NUI Galway	–	Ireland	6.30	3.03	50.2	6.30	5.73	95.0
University of Duisburg-Essen	–	Germany	9.00	6.10	67.8	9.00	6.40	71.1
Texas A&M University	HPST	Texas	7.62	4.93	64.7	15.24	4.72	31.0
Texas A&M University	AST	Texas	7.62	3.25	42.7	16.20	7.88	48.6
University of Central Florida	–	Florida	7.62	3.50	45.9	16.20	10.70	66.0

In particular, the Electric Arc Shock Tube (EAST) Facility at NASA Ames Research Center generates conditions for measurements of spectrally resolved radiance and kinetics of shock-heated gases for atmospheric entry. By using an electric discharge, the driver gas can be heated to 8000–10,000 K, producing shock velocities up to 46 km/s [63, 134]. The facility has been used to help characterize the aerothermal environment encountered during lunar return of the Orion Command Module and planetary entry of Mars, Earth, Venus, and other celestial bodies [135–139].

2.4.2 Chemical kinetics

Despite the aforementioned challenges, shock tubes have been an invaluable tool for studying combustion chemistry [47, 140]. Behind reflected shock waves, reactive mixtures are near-instantaneously heated/pressurized in a spatially-uniform, stagnant flow-field–creating a near-ideal reactor for studying chemical processes. Specifically, when combined with non-intrusive, laser-based diagnostics, shock tubes can provide accurate determinations of ignition delay times, species time-histories, and elementary reaction rates. These types of measurements have been conducted for many different fuels over a wide range of conditions and have been used to develop and validate widely-used combustion reaction mechanisms.

Ignition delay time is the time it takes a reactive mixture, subjected to an instantaneous increase in temperature, to experience an exponential increase in its overall reaction rate and, thereby, igniting. In shock tubes, this is the time interval between the reflected shock wave arrival and ignition. Accurately determining the time at which both of these events occur demands careful consideration to any non-ideal effects (boundary layer growth, shock attenuation, shock bifurcation) influencing the measurement [141]. The arrival of the reflected shock wave (”time zero”) is commonly determined by the step rise in pressure at the measurement location. Care should be taken if severe reflected shock bifurcation is present. In this case, the true ”time zero” should be adjusted based off the arrival of the planar shock front and not the bifurcation event [93]. The onset of ignition is commonly determined by the rapid increase in pressure, OH^*, or CH^*, though some indicators are only appropriate under certain conditions. The ignition time is defined by locating the time of steepest rise in pressure, OH^*, or CH^* and linearly extrapolating back to the baseline. The three indicators generally agree to within 2% [141]; however, for dilute mixtures with low concentration of reactants, the pressure rise may not be substantial enough to make a reliable measurement. Overall, knowledge of a fuel's ignition delay time provides a global target for model validation and refinement since it encompasses the full combustion reaction.

Species time histories track the formation and extinction of individual molecules (fuels, products, or intermediates) throughout the reaction process. Since these measurements provide quantitative species evolution, they enforce strong constraints on the rate constants and reaction pathways used by kinetic mechanisms to model these processes. Laser absorption spectroscopy provides a sensitive, quantitative, non-intrusive method of measuring species time histories behind reflected shock waves. This diagnostic method has been used extensively for multi-species detection [140] and has enabled the development of kinetic mechanisms through species time histories of reactants, radicals, intermediates, and products.

Elementary reactions are single step processes describing the break-up/formation of new bonds in a chemical reaction. The reaction rate is the speed at which this process occurs and is often expressed as a rate of reactant consumption or product formation, as shown in Eq. 2.45.

$$aA + bB \xrightarrow{k} cC + dD$$

$$\text{rate} = \frac{\mathrm{d}[A]}{\mathrm{d}t} = -k[A]^a[B]^b \tag{2.45}$$

$$k = A \exp\left(\frac{-E_a}{RT}\right) \tag{2.46}$$

Their rate constants, k, can be expressed by the empirical Arrhenius equation, shown in Eq. 2.46, where A is an empirical factor representing the frequency of collision and E_a is the reaction's activation energy. In practice, rate constants are determined by designing experiments that kinetically isolate reactions and measuring a species time-history that is primarily sensitive to the reaction rate constant of interest. For a single experiment at some temperature, an individual species time-history can be used to determine the rate constant, k, via Eq. 2.45. A and E_a can be determined by conducting several experiments over a wide range of temperatures and plotting $\ln k$ versus $1/T$. A linear regression can then be used to find the slope, $-E_a/R$, and y-intercept, $\ln A$. Rate constants are the primary input for detailed kinetic mechanisms, which can easily contain hundreds of species and thousands of elementary reactions. Examples include GRI-MECH 3.0 [142] with 325 elementary reactions and 53 species, USC MECH II [143] with 784 elementary reactions and 111 species, AramcoMech 2.0 [144] with 2716 elementary reactions and 493 species, and LLNL gasoline surrogate [145] with 1389 species and 5935 elementary reactions. As is evident by the number of reactions considered, developing, validating, and optimizing these models is a laborious task and often requires the collaborative effort of several institutions. These efforts help advance the understanding of fuel oxidation/pyrolysis behavior and expand the capabilities of future combustion systems.

CHAPTER 3

Basics of infrared laser absorption spectroscopy

Over the last two decades, laser absorption spectroscopy (LAS) has become an attractive tool for characterizing complex, chemically-reacting flow-fields for its ability to provide high bandwidth, calibration-free, in-situ measurements of various thermophysical flow properties (temperature, species concentration, pressure, number density, velocity, etc.). Additionally, recent advancements in optical equipment have extended the capabilities of LAS sensing in combustion environments. Namely, the advent of quantum cascade lasers (QCLs) and interband cascade lasers (ICLs) have made the mid-infrared more easily accessible. The mid-infrared contains spectral transitions that are orders of magnitude stronger compared to the near-infrared, enabling the development of highly sensitive diagnostic tools for numerous species relevant to combustion science, including reactants (CH_4), intermediates (CO, OH,

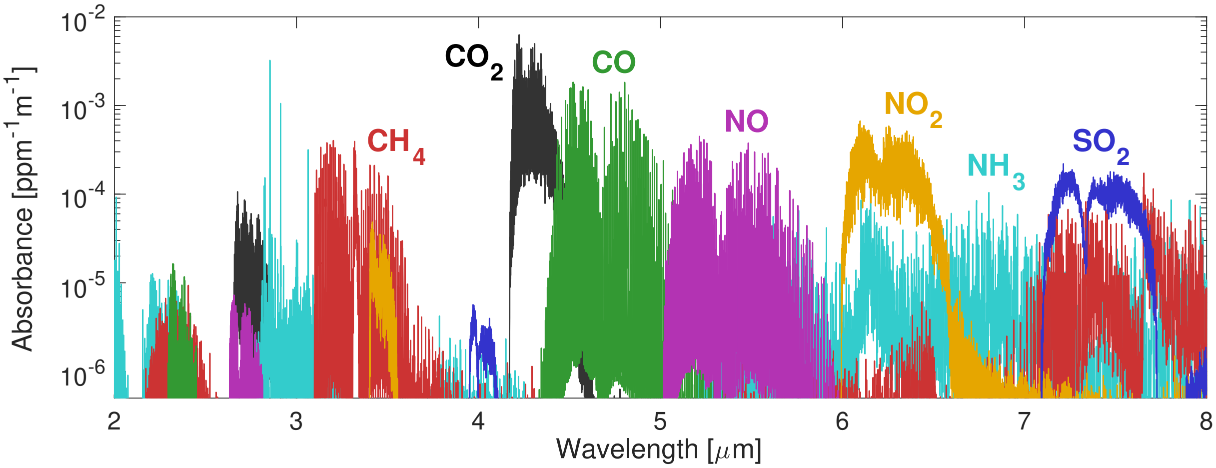

Figure 3.1: Broadband spectral survey of select combustion relevant species accessible via laser absorption spectroscopy (obtained from [146])

CH), and products (CO_2, H_2O). Select species accessible by LAS are shown in Fig. 3.1. This chapter introduces the basics of LAS sensing and discusses fundamental techniques used for thermometry and species measurements in chemical propulsion flows. More thorough reviews of laser absorption spectroscopy and techniques can be found in [147, 148].

3.1 Fundamentals

Absorption occurs when an atom or molecule changes quantum energy states from a lower to higher energy state by absorbing a photon. Atoms and molecules with *intrinsic* dipole moments can absorb radiation when the photon energy (frequency) resonates with (i.e. matches) the spacing between two discrete quantum states. In the infrared, absorption occurs between rovibrational states–indicating a change in both rotational and vibrational quantum energy levels. Different quantum energy levels are commonly discerned by their respective quantum numbers, where J is the quantum number for total angular momentum and v is the vibrational quantum number. Additionally, prime ($'$) and double prime ($''$) are commonly used to denote upper and lower energy levels, respectively. As seen in Fig. 3.1, this leads to a unique spectrum of discrete rovibrational absorption *transitions* for different molecules across the infrared. The relationship between the frequency of the absorbed photon and a molecule's quantum energy spacing is given by Planck's Law:

$$\Delta E = E_{\text{upper}} - E_{\text{lower}} = h\nu = \frac{hc}{\lambda} = hc\bar{\nu} \tag{3.1}$$

where E is the energy of a given quantum state, h is Planck's constant $h = 6.63 \times 10^{-34}$ J·s, ν is the frequency of light in units of Hz, MHz, GHz, or THz, c is the speed of light $c = 3 \times 10^8$ m/s, λ is the wavelength of light in units of nm or μm, and $\bar{\nu}$ is frequency of light given in wavenumbers, which typically has units of cm^{-1}.

For a monochromatic light source tuned to some frequency ν, the amount of light transmitted through an absorbing gas medium with uniform gas properties is governed by the Beer-Lambert Law:

$$T_\nu = \left(\frac{I_t}{I_0}\right)_\nu = \exp\left(-k_\nu L\right) \tag{3.2}$$

where T_ν is the fractional transmission, I_t and I_0 are the transmitted and incident light intensities, respectively, k_ν [cm^{-1}] is the spectral absorbance coefficient, and L [cm] is the absorbing path length. The combined quantity $k_\nu L$ is known as the spectral absorbance α_ν. By targeting a specific rovibrational transition j of some absorbing molecule i, the measured absorbance can be related to thermophysical flow properties using:

$$\alpha_\nu = -\ln\left(\frac{I_t}{I_0}\right)_\nu = \sum_j PX_iS_j(T)\phi_j(\nu, T, P, X_i)L \tag{3.3}$$

where P [atm] is pressure, X_i is the mole fraction of the absorbing species i, $S_j(T)$ [cm^{-2}atm^{-1}] is the temperature-dependent linestrength of rovibrational transition j, and ϕ_j [cm] is the lineshape function of rovibrational transition j. For combustion gases, the lineshape function is typically modeled as a Voigt profile, which encompasses both Doppler and collisional broadening effects (discussed later); however, under certain conditions, more advanced lineshape functions may be required [148]. Regardless of which profile is chosen, by definition, the integral of the lineshape function is:

$$\int_{-\infty}^{+\infty} \phi \mathrm{d}\nu = 1 \tag{3.4}$$

This simplifies Eq. 3.3, such that the integrated absorbance area A_j of the transition is only a function of thermophysical flow properties.

$$A_j = \int_{-\infty}^{+\infty} \alpha_\nu \mathrm{d}\nu = PX_iS_j(T)L \tag{3.5}$$

This prompts a technique known as two-line thermometry, where temperature is measured by taking the absorbance area ratio R of two rovibrational transitions 1 and 2. This eliminates the pressure, mole fraction, and path length dependence, which allows temperature to be inferred directly from R.

$$R = \frac{A_1}{A_2} = \frac{PX_iS_1(T)L}{PX_iS_2(T)L} = \frac{S_1(T)}{S_2(T)} = f(T) \tag{3.6}$$

With temperature known, mole fraction can be easily determined using either of the transitions assuming the pressure and absorbing path length are measured independently.

$$X_i = \frac{A_1}{PS_1(T)L} = \frac{A_2}{PS_2(T)L} \tag{3.7}$$

In conducting two-line thermometry, it is desirable to design a sensitive sensor for the temperature range of interest. Temperature sensitivity can be assess by taking the derivative of R with respect to temperature, which can be approximated as [147]:

$$\left|\frac{dR/R}{dT/T}\right| \approx \left(\frac{hc}{k_B}\right)\frac{|E_1'' - E_2''|}{T} \tag{3.8}$$

where k_B [J/K] is the Boltzmann constant $k_B = 1.38 \times 10^{-23}$ J/K and E_j'' [cm^{-1}] is the lower state energy of rovibrational transition j. Notably, Eq. 3.8 indicates that temperature sensitivity is greater for transition pairs with large difference in lower state energies (typically $|E_1'' - E_2''| > 2000$ cm^{-1}). This ultimately influences the line-selection process to ensure sufficient sensitivity for the desired application.

In order to infer temperature in Eq. 3.6, the temperature dependent linestrength $S_j(T)$ must be known. For a gas in thermal equilibrium ($T_{\text{tr}} = T_{\text{rot}} = T_{\text{vib}}$), $S_j(T)$ [cm^{-2}atm^{-1}] can be calculated by:

$$\begin{aligned} S_j(T) = S_j(T_0)\frac{Q(T_0)}{Q(T)}\left(\frac{T_0}{T}\right)\exp\left[-\frac{hcE_j''}{k_B}\left(\frac{1}{T} - \frac{1}{T_0}\right)\right] \\ \times\left[1 - \exp\left(-\frac{hc\nu_{0,j}}{k_BT}\right)\right]\left[1 - \exp\left(-\frac{hc\nu_{0,j}}{k_BT_0}\right)\right]^{-1} \end{aligned} \tag{3.9}$$

where T_0 [K] is the reference temperature (typically 296 K), $\nu_{0,j}$ [cm^{-1}] is the transition line center, and $Q(T)$ is the internal partition function of the absorbing species. Note Eq. 3.9 gives $S_j(T)$ in units of [cm^{-2}atm^{-1}], some databases provide units of [cm^{-1}/(molecule·cm^{-2}]. Converting between the two can be done as follows:

$$S_j(T)[\mathrm{cm}^{-2}\mathrm{atm}^{-1}] = \frac{S_j^{*}(T)\ [\mathrm{cm}^{-1}/(\mathrm{molecule}\cdot\mathrm{cm}^{-2}] \times 1013250\ [\mathrm{dynes}/(\mathrm{cm}^2\mathrm{atm})]}{k_B T} \tag{3.10}$$

where k_B is the Boltzmann constant $k_B = 1.38 \times 10^{-16}$ erg/K. $S_j(T_0)$, $\nu_{0,j}$, and $Q(T)$ can be found in line-by-line spectroscopic databases, such as HITRAN [149], HITEMP [150], PNNL/NIST [151], and GEISA [152], among others. The internal partition function $Q(T)$ can also be calculated through:

$$Q(T) = \sum_j g_j \exp\left(-\frac{hcE_j''}{k_B T}\right) = Q_{\mathrm{rot}} Q_{\mathrm{vib}} Q_{\mathrm{elec}} Q_{\mathrm{nuc}} \tag{3.11}$$

where g_j is the degeneracy of quantum state j. Using Eq. 3.6 and Eq. 3.9, the temperature of the absorbing gas medium can be found iteratively with known absorbance area ratio R.

As mentioned previously, the vast majority of combustion applications use a Voigt lineshape function to model spectral transitions since it encompasses both Doppler and collisional broadening effects and typically yields residuals within 5%. Doppler broadening occurs when a molecule has a velocity component in the same (or opposite) direction of the photon propagation causing absorbance to occur at a Doppler-shifted frequency. For gas molecules following a Maxwellian velocity-distribution function and in the absence of other broadening mechanisms (high temperatures, very low pressures), the absorption lineshape may be described by the Gaussian profile:

$$\phi_{D,j}(\nu, T) = \frac{2}{\Delta\nu_{D,j}} \left(\frac{\ln 2}{\pi}\right)^{1/2} \exp\left[-4\ln 2\left(\frac{\nu - \nu_{0,j}}{\Delta\nu_{D,j}}\right)^2\right] \tag{3.12}$$

where $\Delta\nu_{D,j}$ [cm^{-1}] is the Doppler halfwidth (FWHM), given by:

$$\Delta\nu_{D,j}(T) = \nu_{0,j}(7.1623 \times 10^{-7})\sqrt{\frac{T}{\mathscr{M}}} \tag{3.13}$$

where T [K] is temperature and $\mathscr{M}$ [g/mol] is the molecular weight of the absorbing molecule. Eq. 3.13 demonstrates that $\Delta\nu_{D,j}$ scales linearly with the transition line center $\nu_{0,j}$ and $\sqrt{T/\mathscr{M}}$; therefore, Doppler width increases with temperature and is relatively larger for higher frequencies and lighter molecules.

Collisional broadening occurs when: (1) inelastic collisions reduce a molecule's lifetime in the absorbing state, (2) elastic dephasing collisions perturb the molecular rotation and/or vibration, or (3) elastic angular-momentum altering collisions re-orient the angular momentum vector of the dipole [148]. At high gas densities (high collision frequency) and in the absence of other broadening mechanisms, the absorption lineshape is accurately described by a Lorentzian profile:

$$\phi_{L,j}(\nu, T, P, X_i) = \frac{1}{2\pi}\left[\frac{\Delta\nu_{C,j}}{(\nu - \nu_{0,j})^2 + \left(\frac{\Delta\nu_{C,j}}{2}\right)^2}\right] \tag{3.14}$$

where $\Delta\nu_{C,j}$ [cm^{-1}] is the collisional halfwidth (FWHM), given by:

$$\Delta\nu_{C,j}(T, P, X_i) = P\sum_k X_k 2\gamma_{(i-k),j} \tag{3.15}$$

Here, P [atm] is pressure, $\gamma_{(i-k),j}$ [cm^{-1}/atm] is the broadening coefficient between the absorbing molecule i and a perturbing molecule k for rovibrational transition j, and X_k is the mole fraction of the perturbing species. Note, contributions due to self-broadening ($i = k$) need be considered as well. Eq. 3.15 indicates the collisional broadening increases linearly with pressure. The temperature dependence of the broadening coefficient is commonly modeled using the power law:

$$2\gamma_{(i-k),j}(T) = 2\gamma_{(i-k),j}(T_0)\left(\frac{T_0}{T}\right)^{n_{(i-k),j}} \tag{3.16}$$

where $n_{(i-k),j}$ is the temperature exponent (typically ranging from n =0.5–0.8) and $\gamma_{(i-k),j}(T_0)$ is the broadening coefficient at some reference temperature T_0, usually 296 K. $\gamma_{(i-k),j}(T_0)$ and $n_{(i-k),j}$ have some dependence on the rovibrational transition j but are usually tabulated in spectroscopic databases as a function of quantum number. Ch. 7 discusses methods on how to measure $\gamma_{(i-k),j}$ and $n_{(i-k),j}$ if not found in literature.

The Voigt lineshape function is a convolution of both the Gaussian and Lorentzian profiles in Eq. 3.12 and Eq. 3.14, respectively, and accounts for both Doppler and collisional broadening.

$$\phi_{V,j}(\nu, T, P, X_i) = \phi_{D,j}(\nu_{0,j})V(a, w) = \phi_{D,j}(\nu_{0,j})\frac{a}{\pi}\int_{-\infty}^{+\infty}\frac{\exp(-y^2)\mathrm{d}y}{a^2 + (w-y)^2} \tag{3.17}$$

where $V(a, w)$ is the *Voigt function*, a indicates the relative significance of Doppler and collisional broadening, w is a measure of distance from the line center $\nu_{0,j}$, and y is an integration variable.

$$a = \frac{\sqrt{\ln 2}\Delta\nu_{C,j}}{\Delta\nu_{D,j}} \tag{3.18}$$

$$w = \frac{2\sqrt{\ln 2}(\nu - \nu_{0,j})}{\Delta\nu_{D,j}} \tag{3.19}$$

$$y = \frac{2u\sqrt{\ln 2}}{\Delta\nu_{D,j}} \tag{3.20}$$

Due to the computational cost of evaluating the Voigt function directly, numerical approximations are commonly used. Two of the most common and quickest algorithms developed for calculating the Voigt lineshape profile are those by Humlíček [153] (later enhanced by [154] and corrected by [155]) and McClean et al. [156].

3.2 Collisional line mixing

Line mixing is a collisional effect present at high number densities, which causes a change in rotational energy (usually within the same vibrational energy level) and must be accounted for to accurately model infrared absorption spectra. Line mixing occurs when inelastic collisions transfer molecules between two rotational states of an absorbing transition (i.e. collision-induced population transfers). This results in a shift in absorption intensity from weakly absorbing regions to strongly absorbing regions and leads to a narrowing of the spectral structure [157], as seen in Fig. 3.2. Additionally, line mixing is most pronounced when the spacing between neighboring rotational energy levels is small, such that molecular collisions can easily transfer enough energy to impart a change in the rotational state. When line-mixing effects are present, the spectrum is no longer well-represented by a sum of individual transitions as done in Eq. 3.3 and models accounting for these effects are necessary. Modeling techniques are discussed further in Ch. 7.

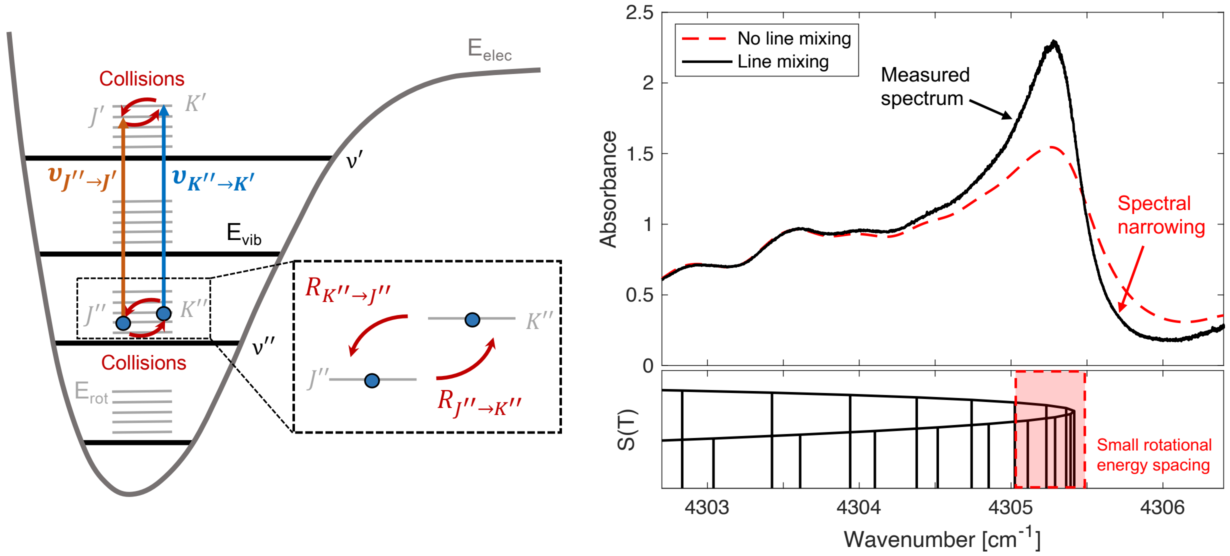

Figure 3.2: *Left*: Diagram illustrating rotational energy transfers between neighboring energy states as a result of collisional line-mixing effects (adapted from [157]). *Right*: Representative data showing narrowing of the spectral structure due to line mixing, which is more pronounced when rotational energy spacing is small.

To illustrate this phenomenon, consider two rovibrational transitions depicted in Fig. 3.2:

$$(v'', J'') \rightarrow (v', J')$$
$$(v'', K'') \rightarrow (v', K')$$

located at frequencies $\nu_{J''\rightarrow J'}$ and $\nu_{K''\rightarrow K'}$, respectively, where J and K denote different rotational energy levels within the same vibrational band ($v'' \rightarrow v'$). In the presence of radiation, a molecule in energy level (v'', J'') can be excited to (v', J') by a photon at frequency $\nu_{J''\rightarrow J'}$. When line mixing is present, a molecule in energy level (v'', J'') can be transferred to energy level (v'', K'') via collisions, then be excited to level (v', K') by absorbing a photon at frequency $\nu_{K''\rightarrow K'}$, and finally relax from (v', K') to (v', J') via collisions [157]:

$$(v'', J'') \rightarrow (v'', K'') \rightarrow (v', K') \rightarrow (v', J')$$

This path from (v'', J'') to (v', J') via (v'', K'') and (v', K') shows that a molecule initially at (v'', J'') can contribute to the absorption intensity located at $\nu_{K''\rightarrow K'}$ by collision-induced population transfers between neighboring energy states. Population transfers of the reverse path are also possible. For collision-induced population transfers to have a significant effect on the vibrational band structure (i.e. transfer intensity between line positions), the follow criteria must generally be satisfied as described in [157]:

1. $(v'', J'') \leftrightarrow (v'', K'')$ and $(v', K') \leftrightarrow (v', J')$ collisional transfers must be allowed; therefore, no line mixing can occur between transitions of different molecules or of different isotopologues of a given species.
2. The transitions must be similar in upper and lower state energy levels, such that collisional transfers are purely rotational jumps.
3. Nuclear spin changes through spin-rotation interactions are very slow; therefore, transitions must be identical in nuclear spin.

4. Finally, if line mixing is possible, collision-induced population transfers only have a significant effect on the spectral shape if the collision-broadened linewidths are greater than the line space: $\Delta\nu_C \geq |\nu_{J''\rightarrow J'} - \nu_{K''\rightarrow K'}|$. This last criterion reflects the scaling with gas density and collision frequency. Accordingly, at very high gas densities, line mixing can significantly affect the intensity distribution of a vibrational band.

3.3 Methods

3.3.1 Scanned-wavelength direct absorption

Scanned-wavelength direct absorption is one of the most widely-used spectroscopic methods for measuring thermophysical flow properties due to its simplicity, wide applicability, and relatively simple data processing. In this technique, the light source, typically a distributed feedback (DFB) diode, interband-, or quantum-cascade laser, is scanned in wavelength via injection-current tuning (usually a sinusoid, sawtooth, or triangle waveform), as seen in Fig. 3.3. The specific tuning range is chosen such that the output wavelength scans across one or more absorption transitions to resolve the spectrum of interest. The light is pitched across the gas medium and collected on the opposing end with a photodetector. Absorbance is obtained

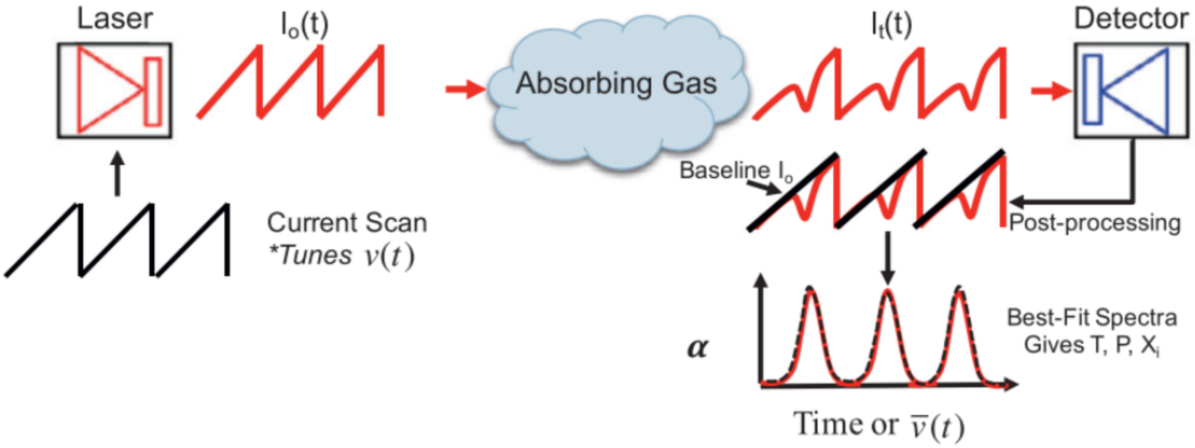

Figure 3.3: Schematic for scanned-wavelength direct absorption technique (obtained from [148])

using Eq. 3.3 via the incident and transmitted light intensities, I_0 and I_t, respectively. Afterwards, the absorbance is fit with a lineshape function (typically a Voigt as discussed previously) to obtain the absorbance area. Gas properties are then obtained through the absorbance areas as shown in Eq. 3.6 and Eq. 3.7. This technique is used in the chemical kinetic studies discussed in Ch. 4 and Ch. 5.

3.3.2 Scanned-wavelength modulation spectroscopy

In harsh combustion environments, mechanical noise, beam steering, emission, and scattering can lead to low signal-to-noise (SNR) using a simple scanned-wavelength direct absorption approach. In these flow-fields, a more sophisticated sensing technique known as scanned-wavelength modulation spectroscopy (scanned-WMS) can be used as its insensitive to broadband interference and baseline uncertainty. In scanned-WMS, the laser is injection-current scanned with a high-frequency (10 kHz–1 MHz) sinusoid superimposed on a low-frequency sinusoid (50 Hz–1 kHz), which shifts absorption information to the harmonics of the modulation frequencies. Similarly, the light is pitched across the gas medium and collected on the opposing end with a photodetector, as shown in Fig. 3.4. The measured signal is post-processed through a lock-in amplifier and frequency filter to extract the first ($1f$) and second

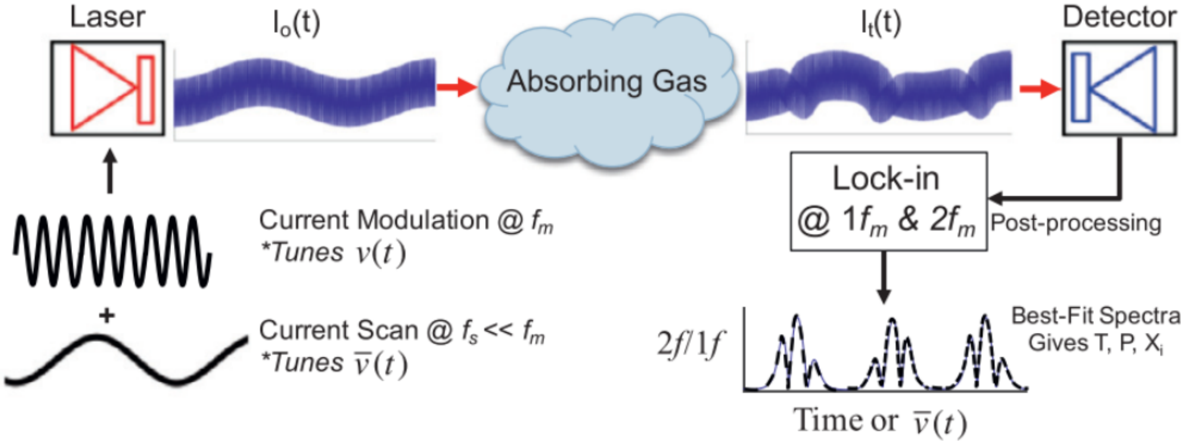

Figure 3.4: Schematic for scanned-wavelength modulation spectroscopy technique (obtained from [148])

($2f$) harmonics. The second harmonic signal is sensitive to the absorbance lineshape curvature (differential absorption) and can be normalized by the first harmonic to eliminate intensity variations caused by beam steering, window fowling, etc. Gas properties are inferred by compared the measured $2f/1f$ signal to a spectral model. This technique is used in the liquid-propellant rocket combustor studies discussed in Ch. 8.

3.3.3 Laser absorption tomography (1D)

Laser absorption tomography is an imaging technique that involves reconstructing distributions of gas properties from multiple projected (lines-of-sight) absorption measurements. This is a common approach in measuring non-uniform flow-fields. Similar to Eq. 3.3, absorbance can be related to thermophysical flow properties through the Beer-Lambert Law; however, for a non-uniform flow-field, the equation takes the following form:

$$\alpha_\nu = -\ln\left(\frac{I_t}{I_0}\right)_\nu = \int_0^L \sum_j PX_i(l)S_j(T(l))\phi_j(\nu, T, P, X_i)\mathrm{d}l \tag{3.21}$$

Axially-symmetric distributions are frequently encountered in combustion applications. This greatly simplifies the reconstruction technique as the gas properties are only a function of the flow-field radius r and can be reconstructed from a single projection angle [158]. Under this assumption, the projected absorbance measurements described in Eq. 3.21 can be integrated over the spectral domain to obtain projected integrated absorbance areas $A_{j,\mathrm{proj}}$ [cm^{-1}]. $A_{j,\mathrm{proj}}$ measurements can be obtained at discrete locations y [cm], from the axis of symmetry and can be related to the radial distribution of the integrated spectral absorption coefficient $K_j(r)$ [cm^{-2}] using Abel's integral equation [159, 160]. This process is described by Eq. 3.22 and further illustrated in Fig. 3.5.

$$\begin{aligned} A_{j,\mathrm{proj}}(y) = \int_{-\infty}^{+\infty} \alpha_\nu \mathrm{d}\nu = \int_0^{L(y)} K_j(l)\mathrm{d}l = \int_0^{L(y)} PX_i(l)S_j(T(l))\mathrm{d}l \\ = 2\int_y^R \frac{K(r)r}{\sqrt{r^2-y^2}}\mathrm{d}r = 2\int_y^R \frac{PX_i(r)S_j(T(r))r}{\sqrt{r^2-y^2}}\mathrm{d}r \end{aligned} \tag{3.22}$$

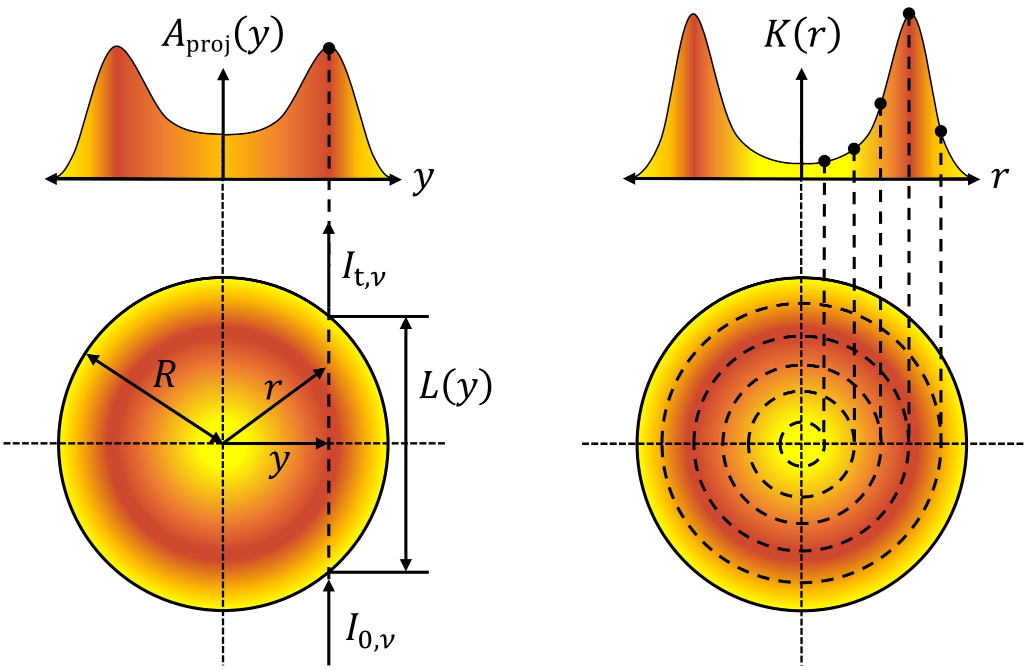

Figure 3.5: Deconvolution geometry for line-of-sight measurements in an azimuthal symmetric flow-field. Abel's integral equation enables $A_{\text{proj}}(y)$ to be related to the radial distribution of K, as shown in Eq. 3.22. Figure adapted from [161].

To obtain radially-resolved temperature and species profiles, the line-of-sight absorption data $A_{j,\text{proj}}(y)$ is related to the radially-resolved integrated spectral absorption coefficient $K_j(r)$ through Abel's integral equation [159, 160]:

$$P(y) = 2\int_y^R \frac{f(r)r}{\sqrt{r^2 - y^2}}\mathrm{d}r \tag{3.23}$$

where R is the field radius and y is a given distance from the axis of symmetry. Here, $P(y)$ is representative of the measured projected absorbance area $A_{j,\text{proj}}(y)$ and $f(r)$ is the radial distribution of the integrated spectral absorption coefficient $K_j(r)$, as seen in Eq. 3.22. In practice, the Abel inversion is implemented numerically [162], and the field distribution $f(r)$ is approximated by implementing the three-point Abel (TPA) transform [163]. This enables

Eq. 3.22 to be written at every radial location r, giving rise to a system of linear equations:

$$\mathbf{A_{TPA}}\mathbf{f} = \mathbf{P} \tag{3.24}$$

where $\mathbf{f} = [f_0,\ f_1, \ldots f_{N-1}]^T$ and $\mathbf{P} = [P_0,\ P_1, \ldots_{N-1}]^T$ contain values of $K_j(r)$ and $A_{j,\mathrm{proj}}(y)$, respectively, at every radial location and $\mathbf{A_{TPA}}$ is the projection matrix. To solve Eq. 3.24 and address the inherent ill-conditioned nature of $\mathbf{A_{TPA}}$, a Tikhonov-regularization [162] is adopted.

The Tikhonov method imposes a regularization parameter λ that controls the relative importance of accuracy and smoothness in the solution to the inversion. This regularization can be represented as an additional set of equations that constrain the solution:

$$\lambda \mathbf{L_0}\mathbf{f} = 0 \tag{3.25}$$

where $\mathbf{L_0}$ $(N \times N)$ is a discrete gradient operator that characterizes the smoothness of the solution:

$$\mathbf{L_0} = \begin{bmatrix} 1 & -1 & 0 & \ldots & 0 \\ 0 & 1 & -1 & \ddots & 0 \\ \vdots & \ddots & \ddots & \ddots & \vdots \\ 0 & 0 & 0 & \ldots & -1 \\ 0 & 0 & 0 & \ldots & 1 \end{bmatrix} \tag{3.26}$$

An appropriate value for λ is determined for each reconstruction based on the L-curve method [164, 165]. A least-squares solution of the field distribution $f(r)$ can now be determined by combining Eq. 3.24 and Eq. 3.25:

$$\mathbf{f}_\lambda = \arg\min \left\| \begin{bmatrix} \mathbf{A_{TPA}} \\ \lambda \mathbf{L_0} \end{bmatrix} \mathbf{f} - \begin{bmatrix} \mathbf{P} \\ 0 \end{bmatrix} \right\| \tag{3.27}$$

The technique described above enables reconstruction of the integrated spectral absorption coefficient, $K_j(r)$, from the measured projected absorbance areas, $A_{j,\mathrm{proj}}(y)$. Examples of these reconstructions are discussed in Ch. 6. To infer the radial distribution of temperature $T(r)$, $K_j(r)$ can be obtained for two absorbance features, where the ratio between $K_1(r)$ and $K_2(r)$ is only dependent on $T(r)$:

$$R(r) = \frac{K_1(r)}{K_2(r)} = \frac{PX_iS_1(T(r))}{PX_iS_2(T(r))} = \frac{S_1(T(r))}{S_2(T(r))} = f(T(r)) \tag{3.28}$$

With knowledge of pressure and the radial distribution of temperature, the radial distribution of mole fraction, $X_i(r)$, can be evaluated directly from $K_j(r)$ of either absorbance feature:

$$X_i(r) = \frac{K_1(r)}{PS_1(T(r))} = \frac{K_2(r)}{PS_2(T(r))} \tag{3.29}$$

CHAPTER 4

Multi-isotopologue sensing of CO for high-temperature chemical kinetics studies of fuel blends

The contents of this chapter have been submitted to the journal ***Combustion and Flame*** *under the full title 'Multi-isotopologue laser absorption spectroscopy of carbon monoxide for high-temperature chemical kinetics studies of fuel mixtures' [166]*

4.1 Introduction

Optical sensing of carbon monoxide (CO) is important for a variety of applications, including environmental health safety monitoring and combustion efficiency characterization. In regards to combustion, CO is a significant intermediate species, measurements of which are often used to validate and develop chemical kinetic models for combustion applications [140]. Particularly, laser absorption spectroscopy (LAS) is a common method for quantitatively measuring concentration of combustion species—including CO [167–174]—at high time resolution during combustion reactions behind reflected shock waves, providing valuable experimental constraints on kinetic models of hydrocarbon decomposition and oxidation. Most of these measurements have been made using 'neat' mixtures comprising a single fuel; practical fuels used in real combustion devices are typically blends of many different hydrocarbons with similar intermediates and products [175]. During the initial fuel pyrolysis prior to oxidation, these fuel molecules tend to decompose into a small number of similar C_1-C_4 intermediates, the kinetics of which largely dictate the evolution of the rest of the reaction [176, 177]. These intermediates compete with one another in oxidation reactions, making it difficult to charac-

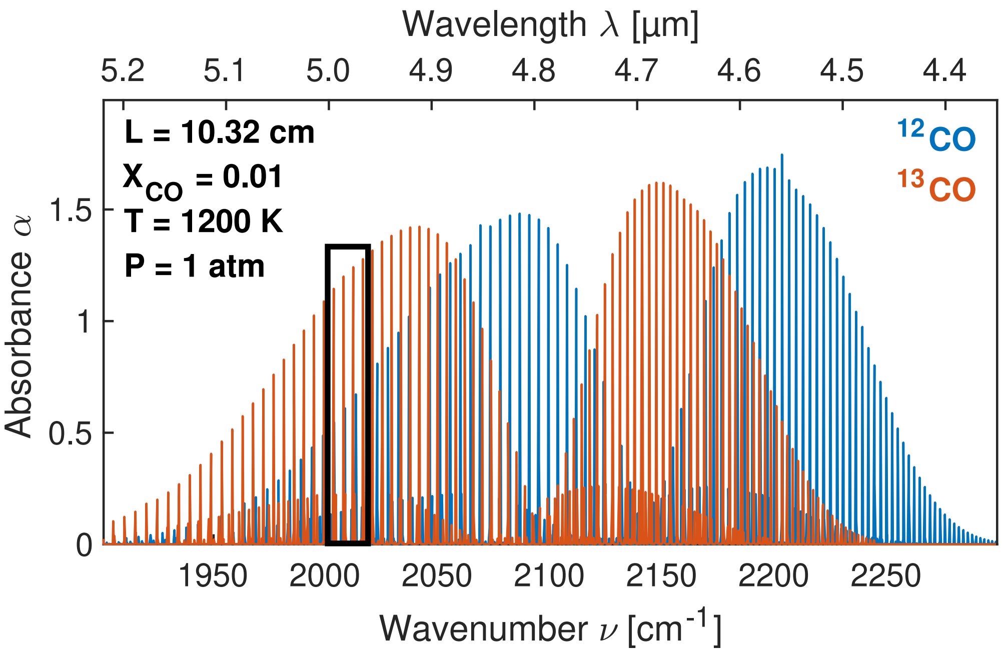

Figure 4.1: Simulated spectra of ^{12}CO and ^{13}CO calculated at conditions relevant to combustion. Targeted spectral region outlined in black. Spectral line parameters taken from HITEMP database [150].

terize the contributions of a particular fuel component on overall combustion behavior when probing a single kinetic parameter.

To experimentally constrain complex kinetics models, an increased number of parameters must be measured in controlled studies. Deliberately labeled isotopologues, particularly those that contain isotopes of hydrogen atoms, are commonly used in physical organic chemistry research to distinguish reaction pathways [178, 179]. Here we focus on carbon as a shared element in fuels and the intermediate CO, which can be readily measured by infrared absorption. Roughly 1.1% of all carbon on Earth is ^{13}C [180, 181], making it one of the more common stable isotopes available for use in isotopic tagging techniques [178, 180] and representing an opportunity for combustion kinetics investigations [179]. Accordingly, this work targets the infrared absorption spectra of the two most abundant isotopologues of CO, ^{12}C^{16}O and ^{13}C^{16}O, as shown in Fig. 4.1.

In this article, we describe a laser absorption sensor that simultaneously probes the distinct spectra of $^{12}C^{16}O$ and $^{13}C^{16}O$ (abbreviated in this work as ^{12}CO and ^{13}CO, respectively) to recover mole fraction and temperature in high-temperature shock tube kinetics studies. The technique is coupled with isotopic labeling of fuel components with either a ^{12}C or ^{13}C to discern the influence of specific fuels on the aggregate combustion behavior of fuel mixtures. We present the sensor development by first discussing the influence of isotopic labeling and substitution on molecular spectra in the context of wavelength selection. After establishing the theoretical foundations of the technique, we detail our experimental methodology, including the optical setup, experimental apparatus, and data processing techniques required to obtain temperatures and mole fractions from our absorption measurements. We describe both a scanned-wavelength direct absorption (scanned-DA) method for simultaneous multi-isotopologue detection and a fixed-wavelength direct absorption (fixed-DA) method for high-speed sensing of ^{13}CO. Validation measurements in non-reactive shock tube experiments are followed by demonstration of the capabilities of multi-isotopologue LAS in reacting mixtures of isotopically labeled fuels at high temperatures. The paper concludes with an example analysis highlighting the unique utility of the technique to help distinguish chemical kinetic pathways.

4.2 Isotopic effects on molecular spectra

Absorption spectra for ^{12}CO and ^{13}CO are shown in Fig. 4.1. For a diatomic molecule approximated as a harmonic oscillator, the fundamental vibrational frequency ω_e is dependent on the bond stiffness k_s and the reduced molecular mass μ [182]:

$$\omega_e \propto \sqrt{\frac{k_s}{\mu}} \tag{4.1}$$

The spacing between rovibrational transition frequencies, set by the rotational constant B, is also dependent on μ:

$$B \propto \frac{1}{\mu} \tag{4.2}$$

For an isotopologue, changes in nuclear mass of a molecule without a change in the number of protons does not strongly affect bond length r_e or the bond stiffness k_s [147]. As a result, ω_e changes as μ changes; an increase in reduced mass shifts the center of the overall vibrational band to lower frequencies, seen in Fig. 4.1, by about 50 cm^{-1} for CO. Additionally, the rotational constant B is also affected—albeit less obviously—as seen in Fig. 4.1, in which the line spacing between rovibrational transitions reduces by approximately 0.17 cm^{-1}. These isotopic substitution effects provide a basis for understanding the ability to spectrally distinguish ^{12}CO and ^{13}CO isotopologues using LAS, and provides a basis for their independent detection in oxidation experiments of isotopically labeled fuels.

4.3 Spectral line selection

Line selection for LAS sensing is typically influenced by the strength, isolation, and temperature sensitivity of accessible rovibrational transitions. For multi-isotopologue sensing, relative proximity of transitions for both ^{12}CO and ^{13}CO is also an important consideration. Ideally, the spectral domain should exhibit minimal interference from neighboring ^{12}CO$_2$ and ^{13}CO$_2$ lines, but the lines should be in sufficient proximity that they can be accessed within the tuning depth of a single narrowband light source tuned at a high scan rate (to achieve a correspondingly high measurement rate). The strongest absorption in ^{12}CO and ^{13}CO occurs in the fundamental bands centered near 4.65 μm (2150 cm^{-1}) and 4.76 μm (2100 cm^{-1}), respectively, and this mid-infrared domain has recently become accessible with compact, tunable, room-temperature quantum cascade lasers (QCLs) [169, 170].

The P-branches of both ^{12}CO and ^{13}CO contain many strong rovibrational absorption lines that are favorable for low-interference measurements at moderate pressures (∼1 atm) [169, 170]. The high-temperature spectra of H$_2$O, while overlapping those of both CO isotopologues, is less crowded and possesses larger spacing between lines in the wavelength domain of the P-branches of the CO isotopologues compared to the domain of the R-branches. Additionally, in the P-branches, there is minimal interference from the high-temperature spectra

Table 4.1: Examined rovibrational transitions in the present work. All linestrengths from the HITRAN database [149] have a reported uncertainty of 2%, except the ^{13}CO P(2,10) and ^{12}CO P(2,20) lines, which have 5% reported uncertainty.

Freq. ν_i [cm^{-1}]	Species	Line (v'',J'')	$S_i(T_0)$ [cm^{-2}/atm]	E''_i [cm^{-1}]
2007.877	^{13}CO	P(0,22)	$5.56{\cdot}10^{-3}$	928.582
2007.944	^{13}CO	P(2,10)	$4.20{\cdot}10^{-15}$	4365.33
2008.422	^{12}CO	P(2,20)	$2.85{\cdot}10^{-9}$	5051.74
2008.525	^{12}CO	P(0,31)	$6.62{\cdot}10^{-3}$	1901.13
2008.626	^{13}CO	P(1,16)	$2.50{\cdot}10^{-6}$	2591.13

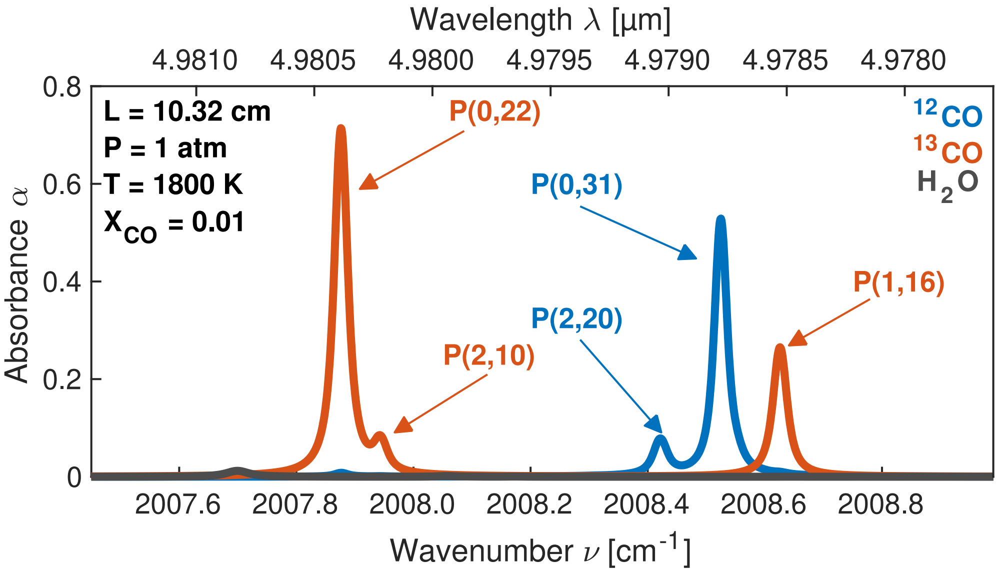

Figure 4.2: Examined spectral range noted in Fig. 4.1 showing the ^{12}CO and ^{13}CO transitions of interest. Absorbance simulated at expected conditions behind a reflected shock with HITEMP 2010 [150].

of both CO_2 isotopologues. A close inspection of the P-branches within 1900–2100 cm^{-1} reveals several isolated absorption features near 2008 cm^{-1} as attractive targets. Fig. 4.2 shows simulated spectra of ^{12}CO and ^{13}CO in this domain of interest along with H_2O at combustion-relevant shock tube conditions using the latest HITEMP [150] database for an optical pathlength of $L = 10.32$ cm, temperatures of $T = 1200$ K, and mole fractions of $X_{\text{CO}} = 0.01$ and

$X_{H_2O} = 0.02$. The spectra comprises two rovibrational transitions for ^{12}CO and three for ^{13}CO, allowing for multiple two-line thermometry options. For ^{12}CO, the P(31) line in the $v(0 \rightarrow 1)$ fundamental band provides the dominant contribution, while the P(20) line in the $v(2 \rightarrow 3)$ hot band contributes more significantly at the higher end of the temperature range. These ^{12}CO lines are also used for measurements in high-temperature, high-pressure rocket engine combustion conditions [183] and atmospheric pressure flames [184, 185], and more details about their selection and application can be found in previous work. For ^{13}CO, the strong P(22) line in the $v(0 \rightarrow 1)$ fundamental band provides the only transition observable at room-temperature for the expected mole fractions, while the P(16) line in the $v(1 \rightarrow 2)$ hot band contributes more significantly above 600 K. Lastly, the P(10) line in the $v(2 \rightarrow 3)$ hot band contributes above 1000 K, although this feature blends with the P(22) line at pressures above ~1.5 atm. Table 4.1 details the ^{12}CO and ^{13}CO rovibrational transitions of interest. A comparison of the different possible combinations of ^{13}CO lines for two-line thermometry

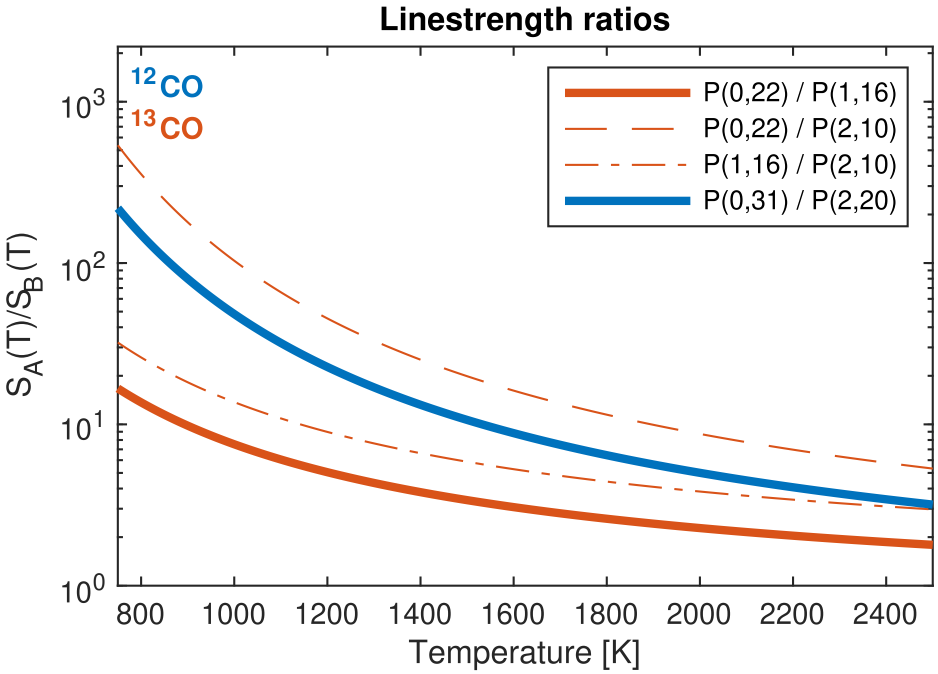

Figure 4.3: Calculated linestrength ratios as a function of temperature for the different combinations of the P(0,22), P(1,16), and P(2,10) lines of ^{13}CO and P(0,31) and P(2,20) lines of ^{12}CO. Lines used for thermometry in this work are bolded.

using Eqn. 3.6 is shown in Fig. 4.3. Although including the P(2,10) line ratios show more sensitivity in the higher temperature range, the tendency of this weak line to overlap with neighboring strong lines at low temperatures and higher pressures limits utility. Additionally all the transitions in the domain have linestrength $S_i(T_0)$ uncertainties reported in the HITRAN database [149] as 2%, except the ^{13}CO P(2,10) and ^{12}CO P(2,20) lines, which have 5% reported uncertainty. As a result of these considerations, the P(0,22)/P(1,16) combination with $\Delta E''$=1662.5 cm^{-1} is the most favorable for a wide range of conditions, despite greater line separation in the ^{13}CO spectra. Likewise, owing to its strong absorption over the range of expected temperatures (1100–2200 K) at expected concentrations ($\sim$0.5%), we utilize the ^{13}CO P(0,22) line for high-speed (>1 MHz) fixed-DA measurements of ^{13}CO mole fraction.

4.4 Sensing methodology

This section describes aspects of the sensing methods necessary for successful implementation in the targeted combustion environments. Here we discuss the selection of the light source, laser control and tuning parameters, and the relevant optical setups. We also discuss the spectral data processing methods associated with interpreting the absorbance measurements, including requisite measurements of select line broadening parameters. Estimates of uncertainty regarding all measurements are discussed in detail in Appendix A.

4.4.1 Optical setup

For the light source, a continuous-wave distributed-feedback (DFB) quantum cascade laser (QCL) (ALPES Lasers) is used to access the two ^{12}CO and three ^{13}CO lines of interest. The QCL is tunable from 2001 to 2014 cm^{-1}, with a typical power of 50 mW at 4.9 μm. In the scanned-wavelength operating mode, a 50 kHz triangle waveform of injection current tunes the QCL across a wavenumber range of $\sim$1.2 cm^{-1} capturing the CO transitions of interest, as depicted in Fig. 4.4. This effectively yields absorbance area measurements at 100 kHz, counting the up-scan and down-scan. The injection current $i(t)$ is also scanned below the lasing threshold to allow for measurement of the transient thermal emission. The wavelength tuning of the QCL was stable enough to capture the targeted ^{12}CO and ^{13}CO transitions with repeatable signal-to-noise ratios (SNR) from scan to scan. For fixed-wavelength measurements, the injection current is held constant and the QCL is fixed at the linecenter of the ^{13}CO P(0,22) line (2007.8767±0.00025 cm^{-1}), monitored by a wavemeter (Bristol 671B) before and after each shock tube experiment.

For light collection, the transmitted laser radiation is passed through a bandpass spectral filter (Spectrogon, 4960±148 nm) to minimize thermal emission before being focused onto a thermo-electrically cooled photovoltaic (PV) detector (Vigo PVI-4TE-5). For each measurement I_t, a corresponding background I_0 is recorded without a mixture present to establish a baseline for calculation in Eqn. 3.3. For scanned-wavelength measurements, the relative frequency of the laser light is determined using a germanium etalon with a free spectral range of 0.0241 cm^{-1}. For all tests, the detector is sampled at its maximum bandwidth of 15 MHz for an equivalent measurement rate of 7.5 MHz.

4.4.2 Shock tube experiments

The high-enthalpy shock tube (Fig. 4.4) used in this work is of a weldless flange design–details of which are included in Appendix D and Appendix F. The shock tube is connected to vacuum pumps, an agitated mixing tank, and a gas delivery manifold used to barometrically prepare the mixtures of interest for all experiments. The test section of the shock tube has an internal diameter of $L = 10.32$ cm, and is circumscribed by interchangeable ports which can hold sensors or optical windows 2 cm from the end wall. For these experiments, two half-inch sapphire windows are used to allow transmission of the laser light into and out of the tube. A dynamic pressure transducer (Kistler 601B1) is also mounted in one of the ports and records the pressure trace of the incident and reflected shock wave through a charge amplifier (Kistler 5018A). Five time-of-arrival sensors (Dynasen, Inc.) provide a means for determining the incident shock velocity, from which the reflected shock test conditions

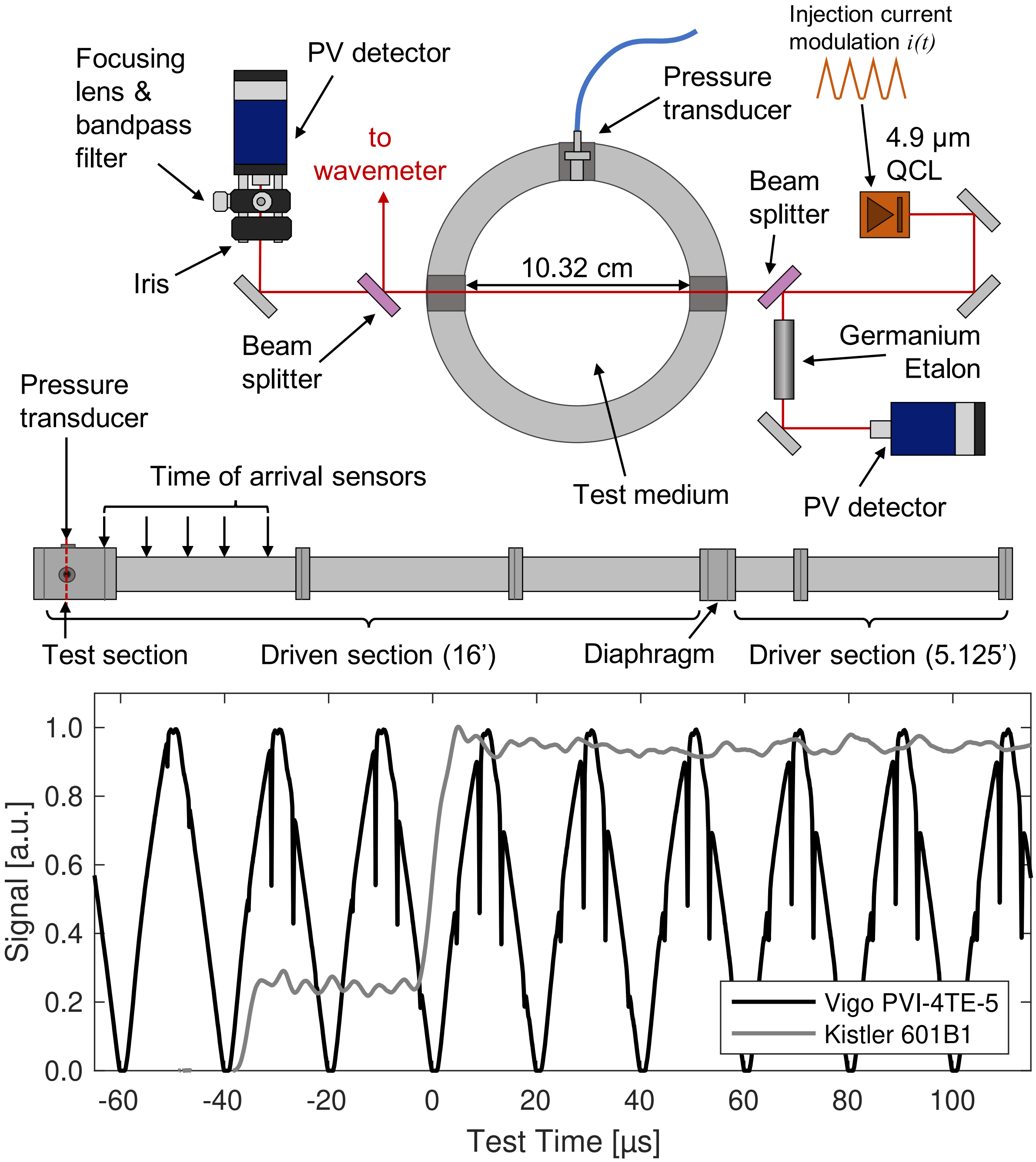

Figure 4.4: *Top*: Cross-section of the shock tube test section showing windows for optical access and laser/detector setup. *Middle*: Side view of the shock tube showing the location of the test section at the end of the driven section of the tube. *Bottom*: Example raw detector and pressure transducer signals during non-reactive shock heating of ^{12}CO and ^{13}CO in a He/Ar bath gas.

(T_5, P_5) are determined [40]. Uncertainty in reflected shock temperature and pressure are typically about 1% when properly accounting for vibrational relaxation of all components of the test gas [64]. Once the QCL and detector were aligned and operational, a series of argon (Ar) shocks were performed to ensure that no beam-steering was present, which would complicate the baseline fitting discussed in Section 4.4.3.1. Data from the detector at 15 MHz using a PicoScope 4000 series data acquisition module, which was triggered to record by the time-of-arrival sensors.

^{12}CO and ^{13}CO thermometry and concentration measurements at 100 kHz were conducted in the shock tube over a range of combustion-relevant temperatures (1100–2300 K) and near-atmospheric pressures (0.5–1.5 atm) using scanned-DA techniques. For the non-reactive thermometry and concentration studies, equal concentrations of ^{12}CO and ^{13}CO were prepared with different bath gas mixtures of argon (Ar) and helium (He) for measurements at temperatures between 1100 and 2300 K. These experiments provided validation of simultaneous ^{12}CO and ^{13}CO thermometry and mole fraction measurement. For reactive studies, mixtures of Ar, O_2, and combinations of $^{12}CH_4$, $^{13}CH_4$, and $^{12}C_2H_4$ were prepared for oxidation experiments at temperatures from 1400–1800 K, measured with both scanned-DA and fixed-DA methods. These experiments validated the ability of the shock tube to produce

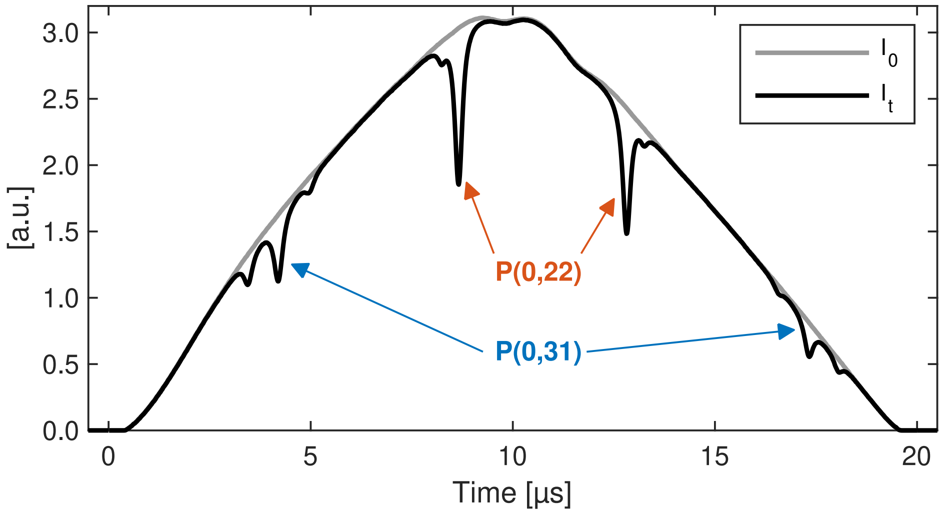

Figure 4.5: Example scanned-wavelength detector signal in the shock tube.

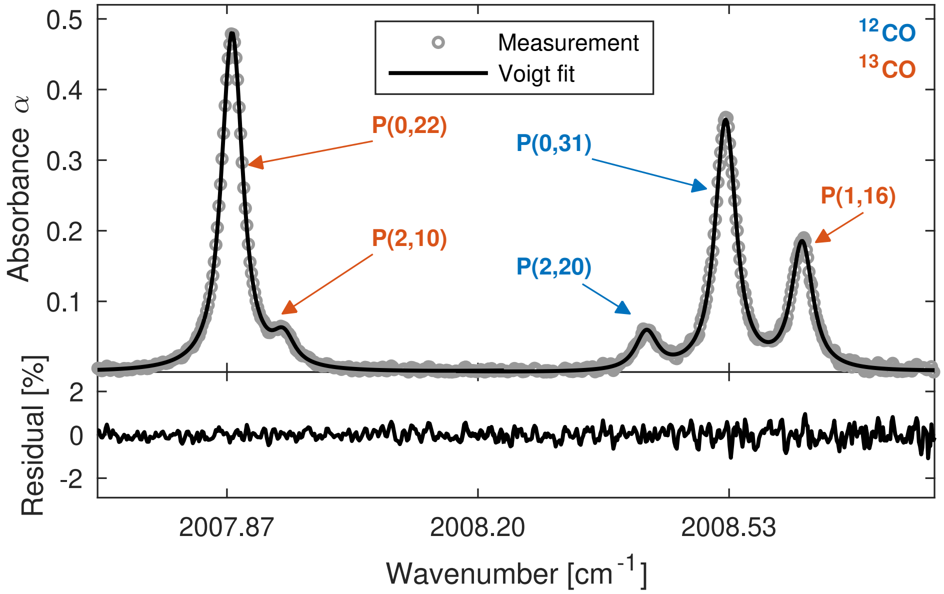

Figure 4.6: Example scanned-wavelength Voigt fitting of data in a high enthalpy shock tube experiment.

repeatable species time-histories in oxidation studies with a fuel (CH_4) that has well-known ignition behavior [186]. Finally, we demonstrated the ability of the sensor to simultaneously resolve production and destruction of both CO isotopologues during ignition of a binary fuel mixture in which one of the fuels was isotopically labeled. These experiments validated the sensor's ability to perform time resolved multi-isotopologue species measurements for combustion studies.

4.4.3 Data processing

4.4.3.1 Scanned-wavelength direct absorption (100 kHz)

Raw detector voltage data, such as those shown in Figs. 4.4 and 4.5, are processed using Eqn. 3.3 to obtain spectral absorbance α_ν, such as shown in Fig. 4.6. The spectral domain is then divided into two regions; the first containing the P(0,22) and P(2,10) lines of ^{13}CO and the second containing the P(2,20) and P(0,31) lines of ^{12}CO and the P(1,16) line of ^{13}CO. A two-line least-squares fitting routine was used for the first region, while a three-line fitting routine was used for the second region. All lines in this work were fit using the Voigt lineshape profile with absorbance area A_i and collisional width Δv_c as free parameters, while Doppler width Δv_D was fixed independently using temperatures estimated from ideal shock relations [40]. Residuals from the fitting were all within 2% during the shock tube experiments, confirming the appropriateness of the Voigt lineshape for this study.

Example calculated absorbance areas from a non-reactive shock tube experiment containing $X_{^{12}\mathrm{CO}} = X_{^{13}\mathrm{CO}} = 0.0075$ are shown in Fig. 4.7. Some vibrational relaxation is visible immediately after the incident and reflected shocks, but the absorbance area calculations for all transitions are shown to be stable in time. Moreover, the absorbance areas calculated

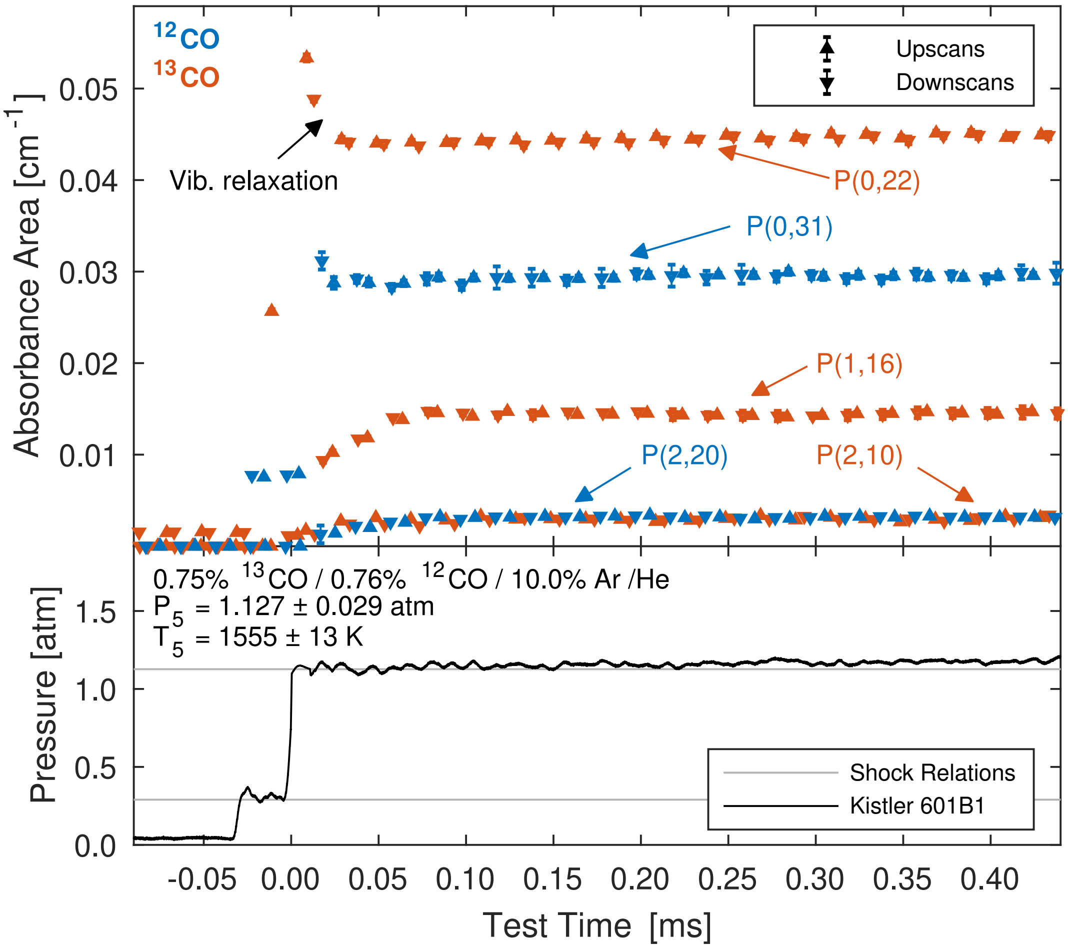

Figure 4.7: *Top*: Example scanned-wavelength absorbance area measurement during a non-reacting shock of ^{12}CO and ^{13}CO. *Bottom*: Pressure time history for corresponding shock.

from the upscan of the triangle wave agree with the absorabance areas calculated from the downscan of the triangle wave, highlighting the ability of the sensor to perform measurements at 100 kHz. As seen in Fig. 4.7, the P(0,22) and P(1,16) lines of ^{13}CO and P(0,31) line of and ^{12}CO show favorable absorbance area with 0.75% ^{12}CO and ^{13}CO seeded in the bath gas. These absorbance areas are used to infer temperature and mole fraction of both CO isotopologues using Eqns. 3.6 and 3.7, respectively, and the results are discussed in Sections 4.5 and 4.6.

4.4.3.2 Fixed-wavelength direct absorption (>1 MHz)

To enable high time resolution (>1 MHz) fixed-DA measurements, a spectral model accounting for collisional broadening is necessary to simulate linecenter absorbance, which is then used to infer mole fraction from measured linecenter absorbance using Eqn. 3.3. Our shock tube studies are carried out with He and/or Ar as the bath gas, for which collisional broadening parameters are unavailable in the current HITRAN [149] and HITEMP databases [150]. For the aforementioned scanned-DA measurements, these broadening parameters are not a prerequisite to employ the two-line thermometry methods discussed in Section 3.1, since Eqns. 3.5 and 3.6 are independent of the lineshape function $\phi_i(\nu)$. However, for a given oxidation experiment utilizing fixed-DA, both the broadening parameters $\gamma_Y(T_0)$ and n as well as the temperature of the medium must be known independently to model $\phi_i(\nu)$ and interpret the absorbance measurements. To determine the He- and Ar-broadening parameters of the P(0,22) line of ^{13}CO, high-temperature (>1000 K) absorbance measurements were made during the non-reacting shock tube experiments described previously, while lower-temperature (300–1000 K) measurements of broadening parameters for the P(0,22) line of ^{13}CO were taken using a high-temperature optical static cell at pressures varying from 40–100 Torr. The relative temperature and pressure uncertainty in the cell is approximately ±0.3%, and ±0.125%, respectively. More details about the mechanical design and thermal analysis of the cell are available in another work [146]. For the shock tube broadening measurements in Ar, some He was added (10%) to the bath gas to accelerate vibrational relaxation of CO behind

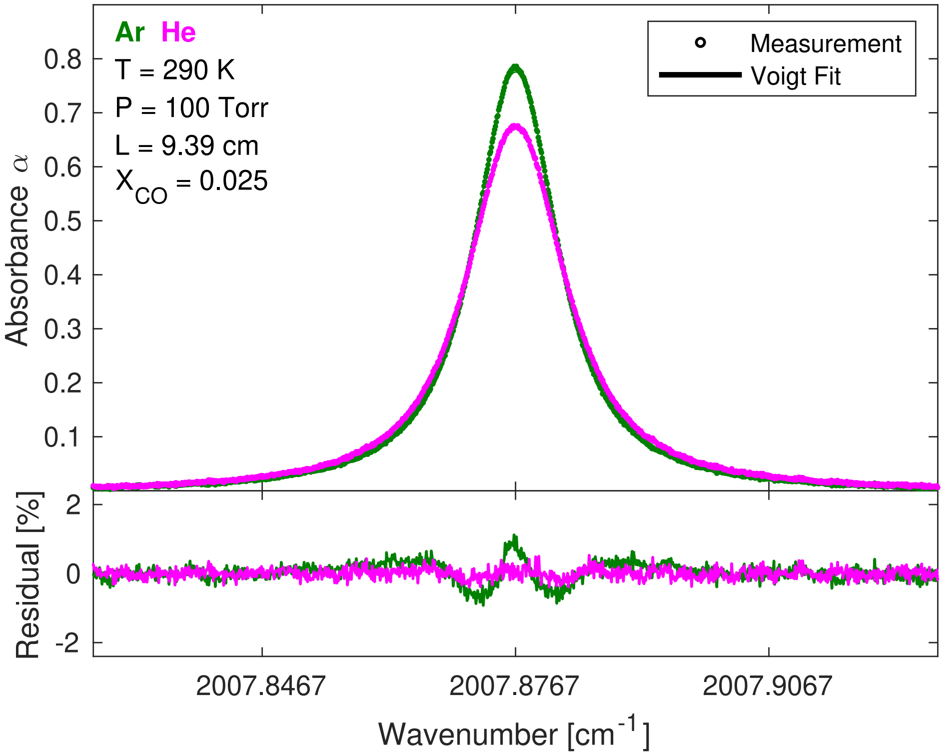

Figure 4.8: Example absorbance spectra and spectral fits of the P(0,22) ^{13}CO line for both He and Ar collision partners in a high temperature optical cell.

the reflected shock wave, necessitating independent knowledge of He broadening parameters.

For measurements in the optical static cell, the QCL was scanned at 70 kHz from 2007.82–2007.96 cm^{-1} to cover the entire P(0,22) line, and data was collected from the detector at 7.5 MHz using a PicoScope 5000 series data acquisition module. Figure 4.8 shows example scanned measurements of the P(0,22) line using the DFB QCL with both He and Ar as bath gases. For temperatures in which the spectra exhibited substantial collisional narrowing [187] (residuals $> 3\%$), only higher pressure (> 80 Torr) measurements are used, and the error in measured $\Delta\nu_c$ is larger, resulting in larger uncertainty in $2\gamma_Y(T)$ for those temperatures. Measurements of broadening coefficients $2\gamma_{^{13}\mathrm{CO}-Y}(T)$ of the P(0,22) line from both the shock tube and gas cell experiments of ^{13}CO are shown in Fig. 4.9. Also shown is a least-squares fit [188] of Eqn. 3.16 to estimate both the temperature-dependent exponents n_{He}, $\gamma_{\mathrm{He}}(T_0)$, n_{Ar}, and $\gamma_{\mathrm{Ar}}(T_0)$, as well as their respective uncertainties, Δn_{He}, $\Delta\gamma_{\mathrm{He}}(T_0)$,

Table 4.2: Spectral modeling parameters for the P(0,22) ^{13}CO line

Y	$2\gamma_{^{13}\mathrm{CO}-Y}(T_0)$ [cm^{-1}/atm]	$n_{^{13}\mathrm{CO}-Y}$	Range [K]
He	0.0953 ± 0.0023	0.494 ± 0.024	296–1863
Ar	0.0767 ± 0.0017	0.595 ± 0.026	296–2312

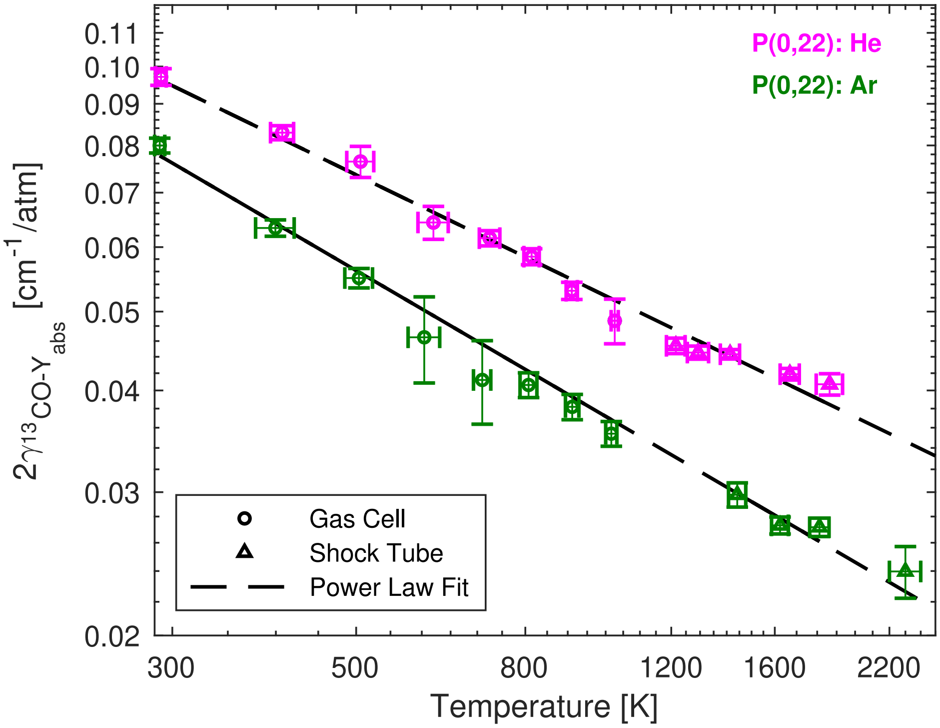

Figure 4.9: He- and Ar-broadening coefficients for the P(0,22) ^{13}CO line with power law fits for 300–2300 K. High-temperature gas cell data marked with circles. Data from shock tube measurements marked with triangles.

Δn_{Ar}, and $\Delta\gamma_{\mathrm{Ar}}(T_0)$. The resulting broadening parameters are given in Table 4.2.

To obtain high-speed measurements of ^{13}CO mole fraction in a reacting mixture, we perform a fixed-DA measurement during the reaction behind a reflected shock as well as a companion scanned-DA measurement with the same mixture composition at the same reflected shock conditions to obtain a temperature time-history using two-line thermometry. Using the measured reflected shock pressure and calculated temperature, as well as the parameters in Table 4.2, we calculate $\phi_i(\nu_{i,0})$ using a Voigt lineshape profile [147] and subsequently determine mole fraction from Eqn. 3.3, as shown in Section 4.6. By accounting for the temperature change in the collisional broadening during the reaction, we reduce the uncertainties associated with the mixture's exothermicity [174], allowing for more accurate measurements of CO mole fraction. Results are provided in Section 4.6.

4.5 Validation results

The main objective of this work is to provide the ability for accurate simultaneous temperature and concentration measurements of both CO isotopologues at concentrations sensitive enough to distinguish competitive oxidation between different components of fuel mixtures. This section discusses the performance of the sensor in high-temperature environments typical of shock tube oxidation studies. For a comprehensive uncertainty analysis on the measurements of temperature and mole fraction reported here, the reader is referred to Appendix A.

The temperature for each reflected shock is calculated from the incident shock velocity measured by the time-of-arrival sensors and is treated as the known temperature, while the known mole fractions of both CO isotopologues for non-reacting shocks are calculated from the barometric mixture preparation. Known reflected shock temperature and CO mole fractions are overlaid with measured values during a representative shock tube experiment in Fig. 4.10, showing excellent agreement. Typical uncertainty in temperature measured using two-line thermometry on the upscan (50 kHz) absorbance areas for each CO isotoplogue is approximately 2% over the test time (∼1 ms) of the non-reacting shock. It can also be seen that the mole fraction values calculated from the upscan absorbance agrees with those calculated from the downscan absorbance, enabling 100 kHz mole fraction measurements. Several of these experiments were conducted for a temperature range relevant to combustion kinetic studies. The accuracy of the sensor over 1100–2250 K is shown in Fig. 4.11, in which the measured temperatures and mole fractions of ^{12}CO and ^{13}CO are compared with the expected temperature from shock relations and the concentrations recorded barometrically during mixture preparation. The sensor is shown to reliably determine temperature and mole fraction for various concentrations of ^{12}CO and ^{13}CO in different bath gas mixtures

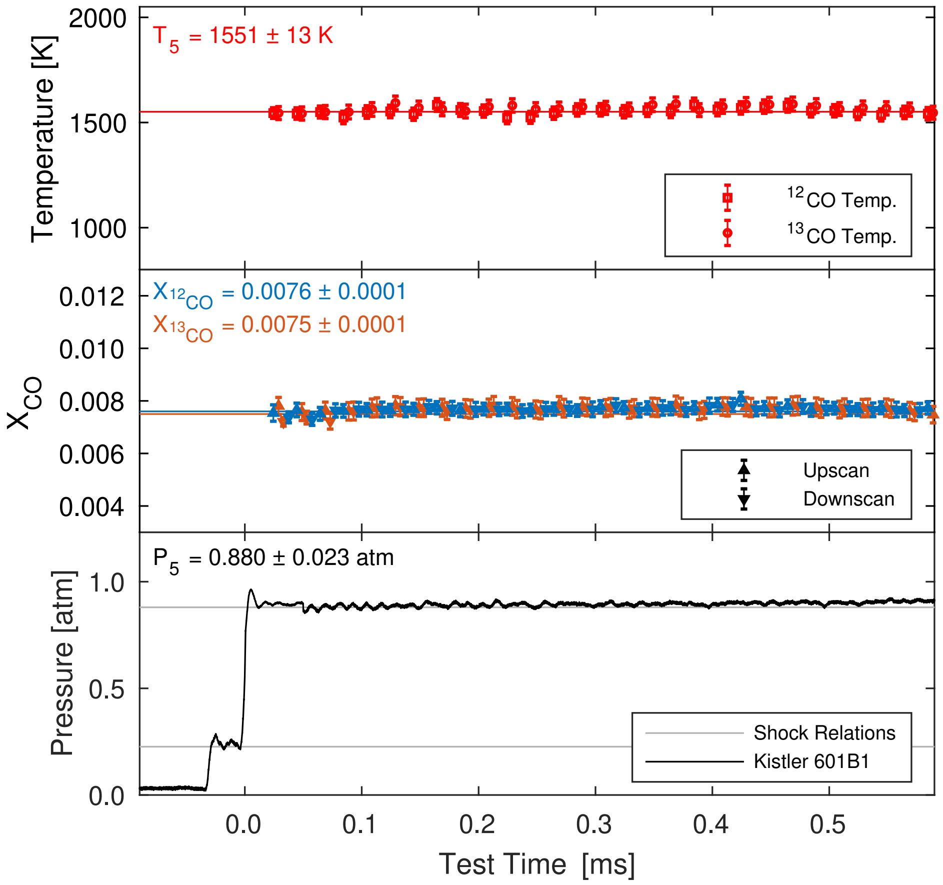

Figure 4.10: Measured temperature and mole fraction of ^{13}CO and ^{12}CO based on two-line thermometry for a non-reactive ^{13}CO/^{12}CO/Ar/He shock with comparison to calculations from ideal shock relations and known mixture concentrations.

of He and Ar. At lower temperatures (<1300 K) and higher pressures (>1.5 atm), the P(2,10) line of ^{13}CO and the P(2,20) line of ^{12}CO were too broadened to make reliable measurements of the absorbance areas for those transitions. However, in these conditions, the P(0,22) and P(1,16) line of ^{13}CO and the P(0,31) line of ^{12}CO are still distinguishable enough for thermometry and mole fraction measurements of ^{13}CO, as shown in Fig. 4.11 for the points at 1200 and 1300 K. Assuming temperature from ideal shock relations, ^{12}CO and ^{13}CO exhibited detection limits of 150 ppm and 160 ppm, respectively, using scanned-DA methods at 1500 K. The corresponding ^{13}CO detection limit using fixed-DA methods was approximately 21 ppm at 1620 K.

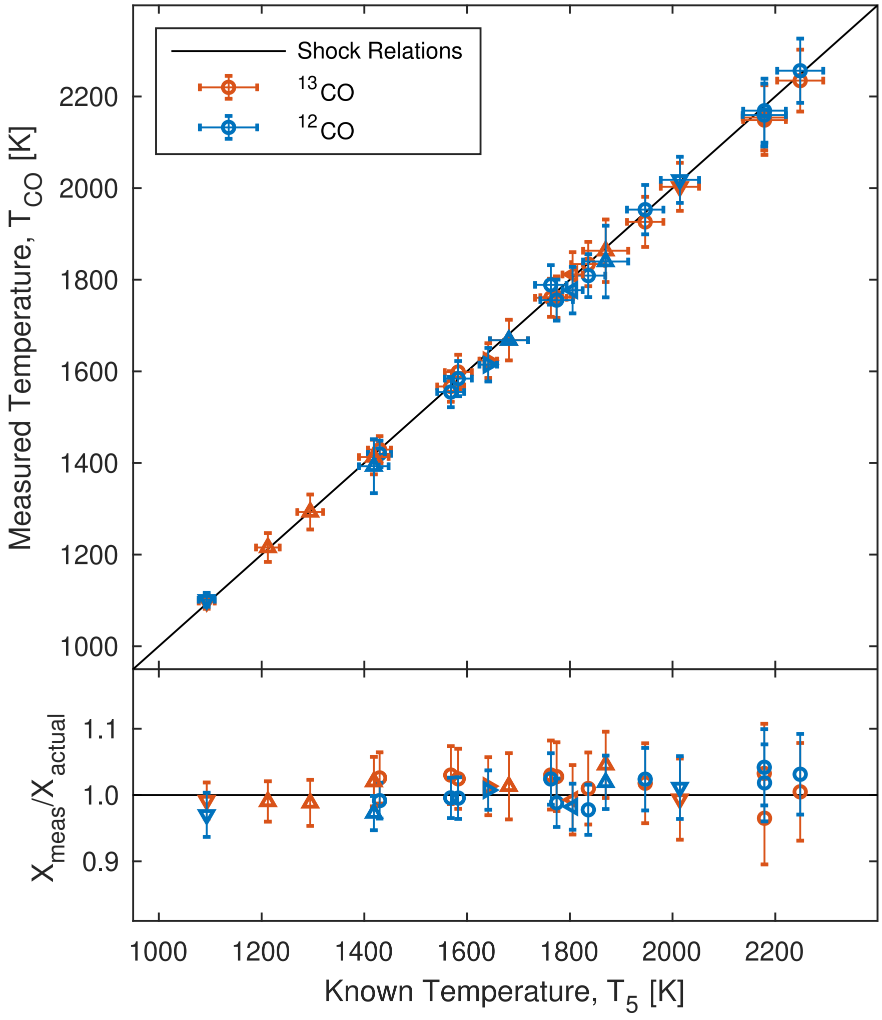

Figure 4.11: Comparison of multi-isotopologue thermometry and concentration measurements with known quantities in high-enthalpy shock tube from 1100–2250 K. Different markers indicate distinct $^{12}CO/^{13}CO/Ar/He$ mixtures.

To validate both the experimental apparatus and the similarities of the reaction rates associated with isotopologues of fuels, we performed shock tube oxidation experiments at approximately the same conditions (nominally $T_5 = 1758 \pm 10$ K and $P_5 = 0.764 \pm 0.025$ atm) for two different stoichiometric ($\phi = 1$) mixtures of 1.25% CH_4 / 2.50% O_2 / 96.5% Ar; one with $^{12}CH_4$ and another with $^{13}CH_4$. The ignition behavior of CH_4 is one of the most well-known among fuels, and for which there are several established kinetic mechanisms; these experiments (at conditions for which much data exists in the literature) serve to validate

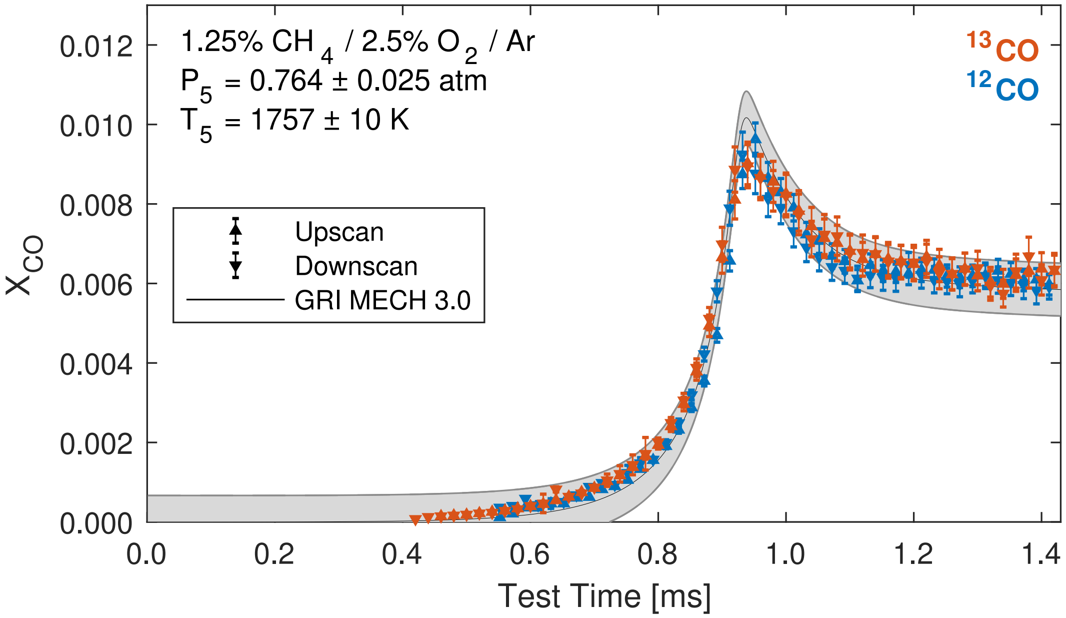

Figure 4.12: Mole fractions of ^{12}CO and ^{13}CO from two shock oxidation experiments using $^{12}CH_4$ and $^{13}CH_4$ as the fuel. Shaded regions indicate uncertainty in model predictions due to uncertainties in reflected shock conditions.

the measurement technique as well as the facility used to prepare and react the mixtures. The mole fractions of both CO isotopologues from these experiments are shown in Fig. 4.12, along with a chemical kinetic simulation performed using Cantera [189] with an unmodified GRI-MECH 3.0 mechanism [142]. The mole fraction results of the independent experiments agree with one another and with the kinetic model for methane combustion, highlighting the similarities in ignition behavior of the isotopically labeled fuels. Further discussion regarding the kinetic effects of isotopic substitution is provided in Appendix C.

4.6 Demonstration results

In order to conclusively demonstrate the ability of the technique to discern competitive oxidation between different components of a fuel mixture, a representative combination of fuels and reflected shock environments must be determined. A well-established and tractable chemical kinetic mechanism, GRI MECH 3.0 [142], was chosen for modification accounting for isotopic labeling of carbon atoms. We used this modified mechanism to survey and downselect temperature and pressure regimes of interest for ignition of isotopically-labeled fuel mixtures, with particular attention to smaller carbon-number species relevant to real fuel oxidation [176, 177]. Owing to all the possible permutations of carbon atoms in the molecules possessing more than one carbon atom, this modification increased the number of species in the mechanism from 53 to 117 and the number of reactions from 325 to 886.

Two fuels with distinctly different structure (and hence, ignition behavior), methane (CH_4) and ethylene (also known as ethene, C_2H_4), were chosen for inclusion in reactive mixtures for the initial competitive oxidation tests. Shock tube oxidation experiments were performed with different mixtures of $^{13}CH_4$, $^{12}C_2H_4$, O_2, and Ar to validate the sensor's ability to measure both species during a reaction. Although known as the simplest hydrocarbon, CH_4 often requires higher temperatures than other hydrocarbons at stoichiometric equivalence ratios to ignite in a comparable amount of time [190, 191]. For example, at atmospheric pressure, a temperature of about 1700 K is required for successful ignition within the shock tube test times demonstrated in this work ($\sim$2 ms). The addition of C_2H_4 into the fuel mixture reduces this temperature requirement, and a stoichiometric mixture of 67% CH_4/33% C_2H_4 will ignite at 1500 K within this test time. Notably, this particular ratio of $^{13}CH_4$ to $^{12}C_2H_4$ results in a nearly equal number of carbon atoms corresponding to each carbon isotope.

4.6.1 Multi-isotopologue CO sensing in reacting mixtures

To specifically test competitive oxidation in oxygen-starved environments, a fuel-rich mixture ($\phi = 1.5$) of 67% CH_4/33% C_2H_4 and O_2 was prepared in an Ar bath gas. Example results in Fig. 4.13 show the mole fraction results of two scanned-DA experiments with this mixture under similar shock-heated pressures (0.744 ± 0.02 atm) and different temperatures (1726 ± 9 K and 1504 ± 8 K), along with the modified kinetic simulation prediction. It can be seen that at higher temperatures (>1700 K), the time histories of the mole fractions of both ^{12}CO and ^{13}CO are both similar, tracking with one another. This indicates that the carbon

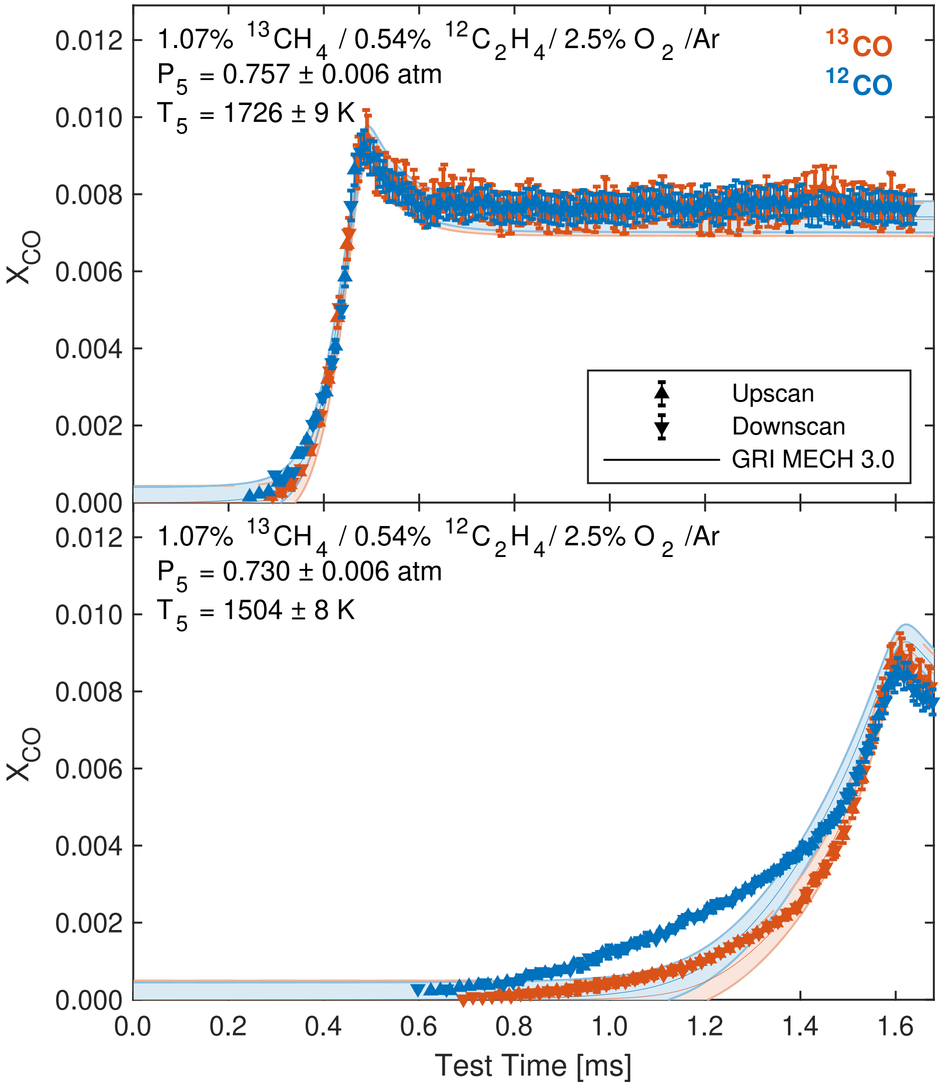

Figure 4.13: Measured CO mole fraction during ignition of fuel/O_2 mixture diluted in Ar at 1726 K (*top*) and at 1504 K (*bottom*) alongside chemical kinetic predictions. Shaded regions indicate uncertainties in kinetic model due to uncertainty in mixture composition and reflected shock conditions.

atoms from both $^{12}C_2H_4$ and $^{13}CH_4$ are oxidizing at similar rates in these conditions. This particular observation agrees with the modified chemical kinetic prediction quite well. At lower temperatures, however (∼1500 K), a separation of reaction timescales is visible between ^{12}CO and ^{13}CO—^{12}CO appears earlier and in higher quantities than ^{13}CO. This indicates that the carbon atoms from $^{12}C_2H_4$ and $^{13}CH_4$ are oxidizing at different rates in these conditions, at least initially. Moreover, the degree to which the timescales are initially separated is underpredicted by the modified kinetic mechanism, which shows the mole fractions agreeing within the model uncertainty. Notably, the experimental mole fraction results for ^{12}CO and ^{13}CO disagree with one another beyond what is explicable with experimental uncertainty.

4.6.2 High-speed (MHz) ^{13}CO sensing

Since high-speed ^{12}CO sensing using transitions in the P-branch of the fundamental band has already been demonstrated by other researchers [169, 192], we focus the discussion of our fixed-DA measurements on ^{13}CO. To demonstrate the ability of the sensor to measure

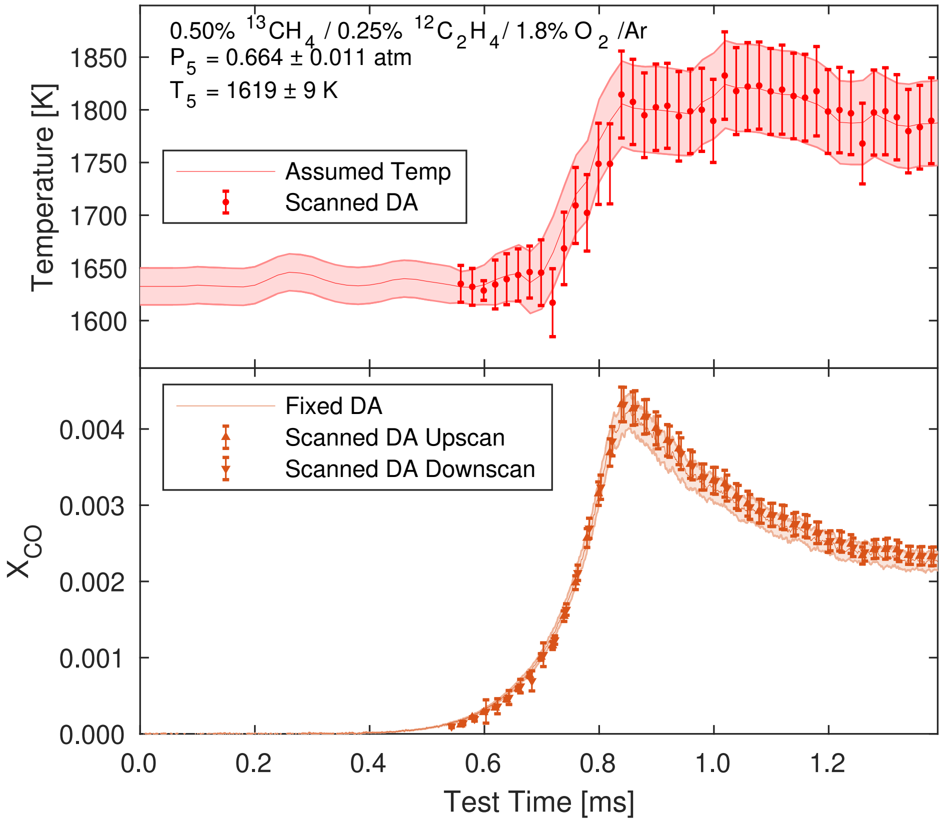

Figure 4.14: *Top*: Measured (scanned-DA) and assumed (fixed-DA) temperature for oxidation experiments in identical reflected shock conditions. *Bottom*: CO mole fraction during scanned-DA (markers) and fixed-DA (smooth line) experiments. Shaded regions indicate fixed-DA uncertainties.

mole fraction of ^{13}CO at a time resolution (>1 MHz) suitable for chemical kinetic studies at higher temperatures (>1800 K), a stoichiometric mixture ($\phi = 1$) of 67% CH_4/33% C_2H_4 and O_2 was prepared in an Ar bath gas. Fig. 4.14 shows the mole fraction results of two independent shock tube oxidation experiments—one scanned-DA and one fixed-DA—with nearly identical reflected shock conditions. The two-line thermometry temperature time history from the scanned-DA experiment, shown in red markers with error bars, was used to estimate a temperature time history for the corresponding fixed-DA experiment, shown as a line with shaded error region. The mole fraction results from the fixed-DA measurements show excellent agreement with the results from the scanned-DA measurements, building confidence in both the precision and versatility of the sensor and in the accuracy of the broadening parameters we report in Table 4.2.

4.7 Discussion

In Section 4.6, we demonstrated the ability of multi-isotopologue laser absorption spectroscopy to unambiguously identify the parent fuel sources of intermediate oxidation species. The technique represents a starting point of a new avenue towards anchoring and constraining detailed reaction mechanisms of fuel mixtures using laser absorption spectroscopy. In many modern kinetic mechanisms in the literature, significant uncertainties exist in several key elementary reactions involved in the production of CO, particularly reactions involving the formyl (HCO) and ketenyl (HCCO) radicals [144, 172, 174], which we touch on here.

As an example of the type of analysis that can be made with this experimental technique, we performed a reaction pathway analysis using the GRI-MECH 3.0 mechanism [142] modified for isotopic tracking for a constant pressure ideal gas reactor simulation in Cantera [189] for the low-temperature ignition condition in Fig. 4.13. The reaction pathway analysis yielded some insights into the mechanism potentially responsible for disagreement between the experiment and the model. During the onset of CO formation for both isotopologues (∼1.1 ms in the lower plot of Fig. 4.13), the primary pathway for the generation of

^{13}CO is through the methyl radical (CH_3) and formaldyhyde (CH_2O):

$$HO_2 + CH_3 \longleftrightarrow OH + CH_3O \tag{R119}$$

$$O + CH_3 \longleftrightarrow H + CH_2O \tag{R10}$$

$$H + CH_2O + M \longleftrightarrow CH_3O + M \tag{R57}$$

$$CH_2O + H \longleftrightarrow HCO + H_2 \tag{R58}$$

$$HCO + M \longleftrightarrow H + CO + M \tag{R167}$$

For reader convenience, we have labeled the reactions according to their reaction number in GRI MECH 3.0. In the oxidation of C_2H_4, HCO is also comparably produced via direct O atom attack,

$$O + {}^{12}C_2H_4 \longleftrightarrow {}^{12}CH_3 + H^{12}CO \tag{R25}$$

and, in conjunction with reaction R167, this represents the dominant pathway to CO for C_2H_4 during this stage of the oxidation. Another comparable path to HCO occurs through the reaction of the vinyl (C_2H_3) radical with O_2, a reaction which is known to have many possible pathways [193]:

$$^{12}C_2H_3 + O_2 \longleftrightarrow H^{12}CO + {}^{12}CH_2O \tag{R173}$$

These additional pathways to $H^{12}CO$ and ^{12}CO production require $^{12}C_2H_4$ and so are not available to ^{13}CO, because the only ^{13}C in the system must ultimately come from $^{13}CH_4$, and $^{13}CH_3$ recombination and downstream production of $^{13}C_2H_3$ is not competitive under these conditions. It should be noted that at this time (~1.1 ms), a significant pathway for the vinyl radical reaction with O_2 produces ketene (CH_2CO):

$$^{12}C_2H_3 + O_2 \longleftrightarrow O + {}^{12}CH_2{}^{12}CHO \tag{R294}$$

$$H + {}^{12}CH_2{}^{12}CO + M \longleftrightarrow {}^{12}CH_2{}^{12}CHO + M \tag{R304}$$

However, at ~1.1 ms, ketene is not yet reacting appreciably.

A bit later in the reaction (~1.3 ms in the lower plot of Fig. 4.13), the aforementioned pathway to CO through the methyl radical and formaldehyde stays dominant for ^{13}CO and becomes dominant for ^{12}CO. Additionally, for the formation of ^{12}CO from $^{12}C_2H_4$, a significant pathway through the ketenyl (HCCO) radical becomes available as ketene undergoes hydrogen abstraction:

$$H + {}^{12}CH_2{}^{12}CO \longleftrightarrow H^{12}C^{12}CO + H_2 \tag{R80}$$

$$H^{12}C^{12}CO + O_2 \longleftrightarrow OH + {}^{12}CO + {}^{12}CO \tag{R176}$$

As with earlier, this CO pathway is unavailable to ^{13}CO, since it ultimately comes from $^{12}C_2H_3$. From these two snapshots in time of the reaction paths for the GRI mechanism, it is clear that there are many more paths to ^{12}CO than to ^{13}CO, and this is validated by our experimental results. Since the results in Fig. 4.13 show that there is a larger separation of timescales between the appearance of ^{13}CO and ^{12}CO than predicted by the model, however, it is reasonable to suggest that the reaction rates of the pathways exclusive to $^{12}C_2H_4$ should be increased relative to the pathway shared by both $^{12}C_2H_4$ and $^{13}CH_4$.

This reaction analysis on an established kinetic mechanism is an example of how multi-isotopologue laser absorption spectroscopy can provide a unique experimental constraint for efforts to optimize kinetic models of fuel mixtures undergoing competitive oxidation given inherent uncertainties in reaction rate constants [176, 177]. Analyses of more modern chemical kinetic mechanisms under active development and optimization are the subject of forthcoming investigations.

4.8 Summary and potential improvements

A mid-infrared laser absorption sensor was developed for simultaneous temperature and concentration measurements of two CO isotopologues at 100 kHz, enabling novel chemical kinetic studies of isotopically labeled fuel mixtures at combustion-relevant temperatures and near-atmospheric pressures. To the authors' knowledge, these are the first simultaneous time-resolved measurements of multiple CO isotopologues originating from intentionally isotopically-labeled fuels in a reacting mixture. Using the method, we provide initial experimental evidence revealing distinct competitive oxidation in a relevant fuel mixture. In doing so, we also provide the first time-resolved LAS measurements of ^{13}CO for high-temperature shock tube kinetics studies. The technique shows potential to improve understanding of competitive oxidation in multi-component fuel mixtures to distinguish reaction pathways and respective rates by unambiguously identifying the parent fuels of intermediate species. We provide an example of the type of reaction pathway analysis that can be facilitated through use of this method, which can aid combustion kinetics investigations. To facilitate the use of the sensor in combustion environments in which CO is created and destroyed more quickly than can be satisfactorily measured at 100 kHz, broadening parameter measurements with relevant collision partners He and Ar were conducted and utilized for fixed-DA measurements of the temporal evolution of ^{13}CO at 7.5 MHz, limited only by the bandwidth of the available PV detector (15 MHz). Additional broadening parameters associated with other combustion-relevant species—such as CO_2, H_2O, O_2, and particularly N_2—must be performed before fixed-DA measurements of ^{13}CO can be performed in atmospheric flames or other non-diluted reactive mixtures.

CHAPTER 5

Competitive oxidation of CH_4 and C_2 hydrocarbons discerned by isotopic sensing in shock-heated mixtures

The contents of this chapter have been published in the journal ***Combustion and Flame*** *under the full title 'Competitive oxidation of methane and* C_2 *hydrocarbons discerned by isotopic labeling and laser absorption spectroscopy of CO isotopologues in shock-heated mixtures' [194]*

5.1 Introduction

Accurate and computationally-efficient chemical kinetic models are desired to design practical combustion systems operating with real fuels (usually blends of several different hydrocarbons) to meet performance and emissions targets in the transportation and power sectors [175]. In several advanced energy conversion devices,such as Homogeneous Charge Compression Ignition (HCCI) engines, ignition is governed by reaction kinetics and the overall reactivity of the fuel-air mixtures is much more sensitive to system thermochemistry (temperature, pressure, mixture composition) and fuel molecular structure than in traditional combustion systems [195, 196]. This represents a significant challenge for modeling and system design, particularly at lower combustion temperatures (< 1500 K) where reaction kinetics can be more complex and are generally less well-understood. This study leverages a novel diagnostic method to examine kinetic behavior of select hydrocarbon mixtures, with a particular focus on discerning competitive oxidation at temperatures below 1200 K, relevant to real fuel combustion.

Modeling real fuels such as diesels or kerosenes remains a challenge in part due to the complex fuel compositions that may include hundreds of species of varying carbon number and functional group. Despite this heterogeneity, large hydrocarbons and mixtures thereof have been shown to decompose into a relatively smaller pool of similar fuel fragments [197–199]; the reactions of these fuel fragments are the rate-limiting steps in the combustion of higher hydrocarbons [172, 176, 177]. Although in principle this increases the tractability of the modeling problem, significant challenges remain in characterizing the combustion behavior of blends of even the smallest C_1–C_2 hydrocarbons at lower temperatures, as significant coupling exists between the intermediates of different fuel components [144]. To examine this coupling, several investigators have studied the effects of blending small C_1–C_2 fuels together through a variety of experiments including but not limited to measurements of flame speeds [200–202], as well as of ignition delay times behind reflected shock waves [203–208]. Despite this experimental work and concurrent progress in chemical mechanisms, many reaction models which predict similar time-evolution of combustion species at high temperatures ($>$1800 K) yield significantly different predictions of time-to-ignition at lower temperatures ($<$1500 K), though peak CO mole fraction remains similarly predicted amongst the models. An example of this is shown in Fig. 5.1 for predictions of the time-evolution of CO, a key intermediate in the energy conversion process, during combustion of a methane-ethylene fuel blend.

Accurate prediction of CO formation and oxidation in combustion systems is critical for the development of practical energy-conversion devices, owing to its importance in the determination of heat release and extinction behavior [172, 209]. The predictive capability of reaction models for fuel oxidation can be evaluated through comparison with time-resolved species measurements behind reflected shock waves, often through optically-based measurement methods. Quantitative species time-histories can provide an additional granular constraint on kinetic models along with ignition delay times and flame speeds, which are aggregate measurements of overall combustion behavior [140]. Several experimental studies have reported measured species time-histories of CO during oxidation of

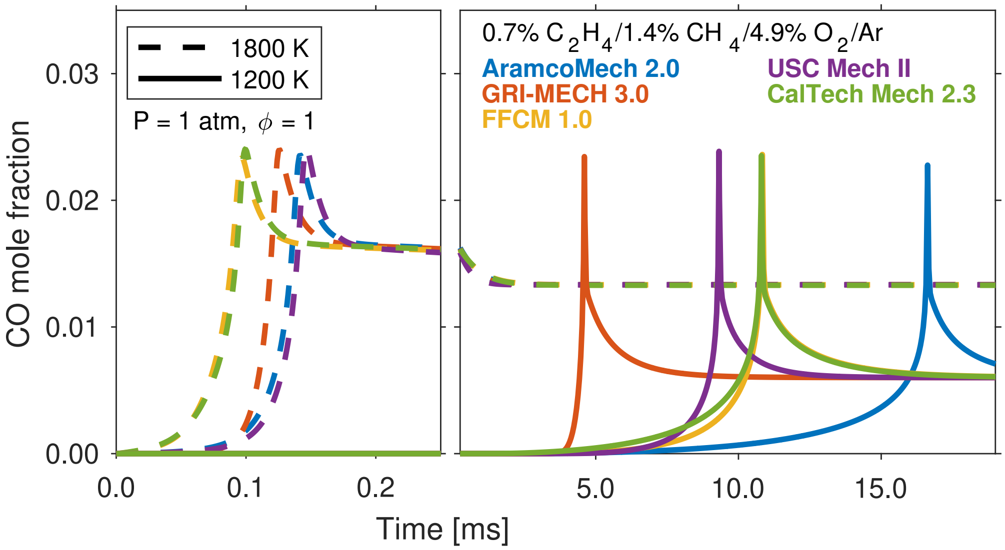

Figure 5.1: Predictions of CO mole fraction evolution during constant-volume reaction of 0.7% C_2H_4, 1.4% CH_4, and 4.9% O_2 ($\phi \approx 1$) in Ar by various chemical kinetic mechanisms at 1 atm and 1800 K and 1200 K. Simulations performed using CANTERA 2.4.0 [189].

.

hydrocarbons behind reflected shock waves, including many using laser absorption-based measurements [168, 169, 171–174, 210–214], providing valuable experimental constraints and validation benchmarks with which to compare chemical reaction models. However, only a few of these studies considered fuel mixtures [173, 211, 212, 214]; in many modern chemical reaction models available in the literature, significant uncertainties remain in several key elementary reactions involved in the production of CO at low temperatures, particularly reactions involving the formyl (HCO), vinyl (C_2H_3), and ketenyl (HCCO) radicals [144, 172, 174, 193, 215, 216]. These species are prominent in the oxidation of small C_1–C_2 fuel mixtures, including CH_4 and C_2H_4, as seen in the simplified reaction pathways shown in Fig. 5.2. These species participate in a much larger set of reactions and the relative contribution (i.e. branching fractions) of various fuel components in a mixture to the measured CO species time-histories becomes less clear when additional fuel components are added.

To address this ambiguity, the authors have developed a time-resolved laser absorption

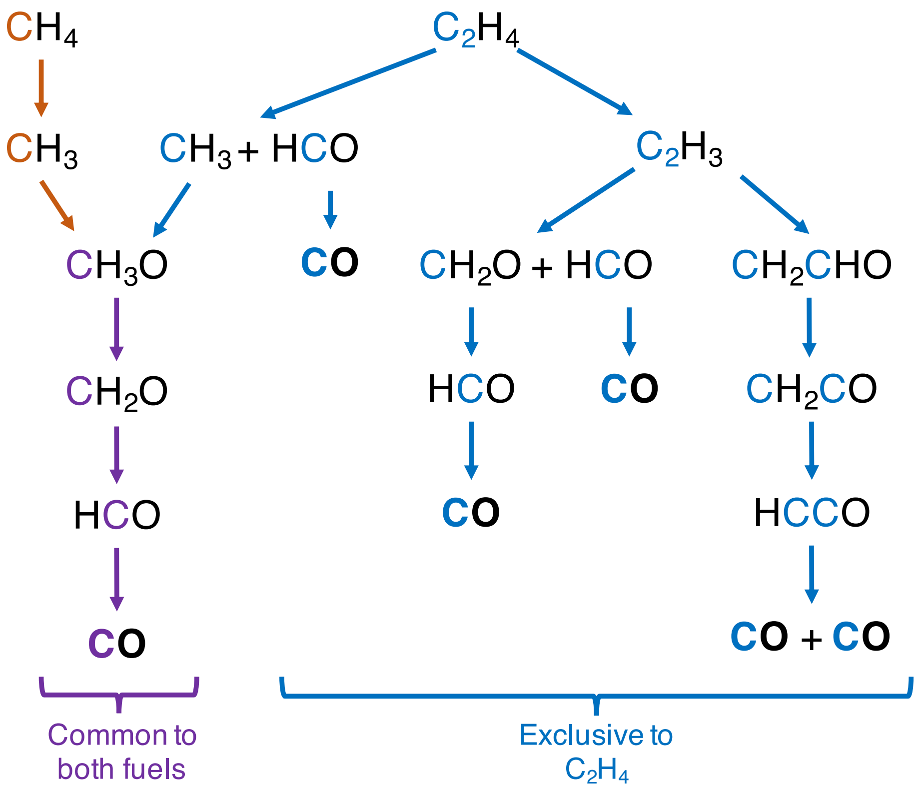

Figure 5.2: Simplified reaction pathway for the oxidation of a CH_4/C_2H_4 blend into CO, with carbon atoms color-coded to correspond to source fuel molecule. CH_4-exclusive pathways shown in orange, C_2H_4-exclusive pathways shown in blue, and common pathways shown in purple.

spectroscopy (LAS) measurement technique for simultaneous detection of multiple isotopologues to discern individual contributions of fuel components to the production of CO in the oxidation of multi-component fuel blends [166]. By isotopically-labeling specific component fuels of the overall fuel mixture and simultaneously measuring both ^{12}CO and ^{13}CO, we can distinguish reaction pathways and respective rates by unambiguously identifying the parent fuels of intermediate species. Fig. 5.2 shows competing reaction pathways for the oxidation of CH_4 and C_2H_4 into CO—Many more pathways to CO are observed for C_2H_4 than are observed for CH_4, and the carbon atoms are color-coded to highlight the utility of the multi-isotopologue LAS technique in providing more information about specific reaction pathways. In previous work [166], we observed that ^{12}CO (from $^{12}C_2H_4$) was produced both earlier than

^{13}CO (from $^{13}CH_4$) and earlier than predicted by an isotopically-labeled GRI-MECH 3.0 [142] reaction model in shock tube oxidation experiments performed at temperatures of 1500 K. In this work, we examine an expanded set of oxidizing fuel mixtures behind reflected shock waves at temperatures ranging from 1000–1800 K, incorporating mixtures that include additional C_2 hydrocarbons: the alkane ethane (C_2H_6) and the alkyne acetylene (C_2H_2). We primarily target the fuel-rich domain to force competitive oxidation among the component fuels, and for its relevance in fuel pyrolysis and soot formation.

The following sections of this paper describe the shock tube experimental setup and isotopic labeling and detection methods, followed by a presentation of the novel dataset capturing competitive oxidation of methane and C_2 hydrocarbons. The approach to modifying specific chemical mechanisms for isotopic labeling is also presented, and simulation results are compared to experimental data. A more detailed examination of the modified FFCM 1.0 mechanism is given for CH_4-C_2H_4 blends, including reaction pathway and sensitivity analysis, while opportunities for mechanistic improvements are identified to capture kinetic behavior of blends with the other C_2 hydrocarbons.

5.2 Methods

This section describes the methods used to examine competitive oxidation of methane and different C_2H_X hydrocarbons behind reflected shock waves. We first detail the spectroscopic sensing methodology as well as the shock tube facility used for all experiments. Additionally, we describe the adaptation of chemical mechanisms for measurement comparison. Estimates of the measurement uncertainty and model sensitivity are discussed in detail in Sec. 5.4.

5.2.1 Multi-isotopologue CO spectroscopy

The mole fractions of two isotopologues of carbon monoxide were measured here using a continuous wave (cw) distributed feedback quantum cascade laser (DFB-QCL, ALPES Lasers) targeting the P(0,31) and P(2,20) transitions of $^{12}C^{16}O$ and the P(0,22) and P(1,16) transitions of $^{13}C^{16}O$ near 4.9 μm [166]. A scanned-wavelength direct absorption technique was employed to rapidly scan over the spectral domain of interest, enabling integration in ν over each individual rovibrational transition. This yields a spectrally-integrated absorbance area A_j [cm^{-1}] for each transition j, as shown previously in Eq. 3.5. Upon measuring multiple A_j for a given species, gas temperature can be determined through two-line thermometry via Eq. 3.6. Once T is known, the Beer-Lambert relation in Eq. 3.7 can be used to determine absorbing species mole fraction X_i, assuming independent knowledge of the pressure. Herein, temperature and mole fraction were measured spectroscopically once the signal-to-noise ratio (SNR) of the spectral transitions was high enough to perform the aforementioned two-line thermometry technique. Prior to this, temperature was obtained using shock relations and assuming isentropic compression of the measured pressure trace. As demonstrated in prior work [166], good agreement in the initial post-shock conditions is achieved with the two methods. Both temperature values are reported in the proceeding data.

The optical setup for the present work is shown in Fig. 5.3. The laser light pitch and catch system, including the QCL, photodetector (Vigo PVI-4TE-5), optical bandpass filter (Spectrogon, 4960±148 nm), and lens is the same as in prior work targeting these CO isotopologues [166], with a notable exception: To increase the modulation depth of the QCL at high scan rates (and subsequently the robustness in baseline fitting), we employ a diplexed RF modulation technique developed by our group using bias-tee circuitry [30]. In this work, we injection-current modulate the QCL with a sine wave at 50 kHz, resulting in an effective temperature and species measurement rate of 100 kHz when performing spectral fitting on both the upscan and downscan. Representative detector signal waveforms illustrating this modulation during a shock tube oxidation experiment are shown in the top right of Fig. 5.3. Employing the bias-tee circuitry at a 50 kHz scan rate results in a modulation depth of approximately 1.2 cm^{-1}, capturing the $^{12}C^{16}O$ and $^{13}C^{16}O$ transitions of interest. A representative plot of experimentally-measured spectral absorbance for a single laser scan period is shown in Fig. 5.4 for the upscan. A corresponding spectral fit using the Voigt lineshape model for the targeted transitions is also shown, yielding low residuals ($< 2\%$) for

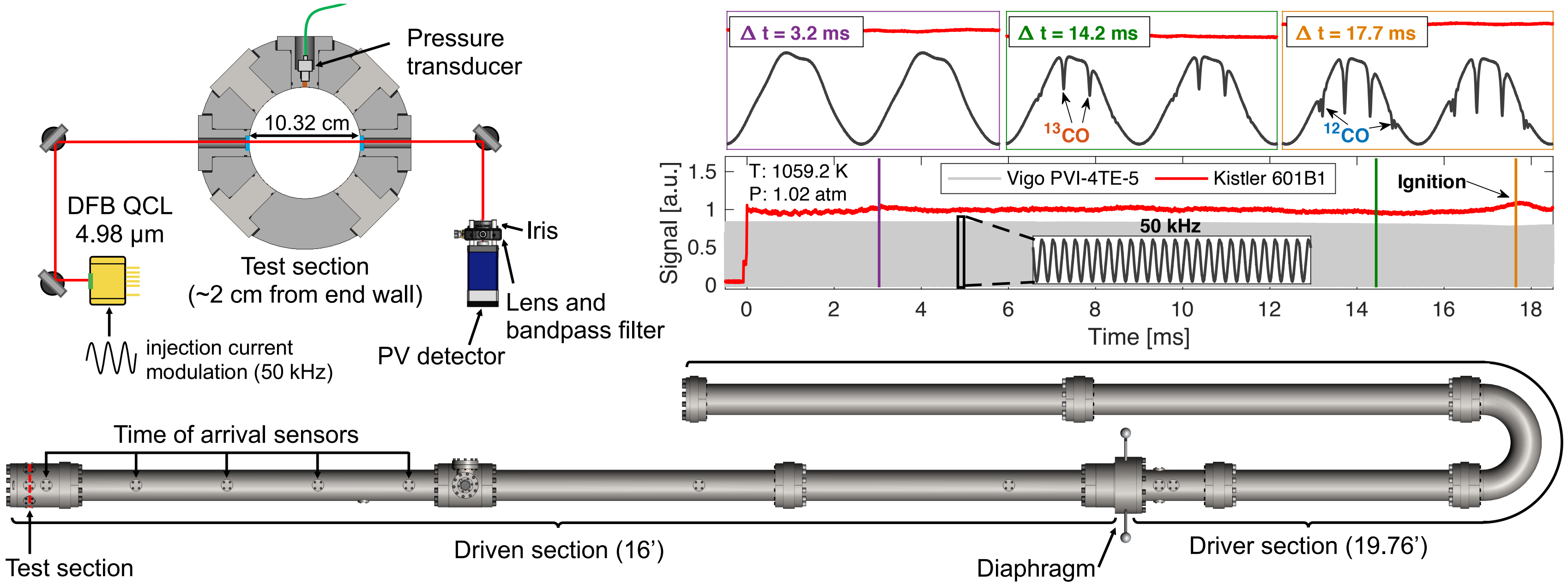

Figure 5.3: Shock tube facility with driver extension used for extended test times. A cross-section of the test section with optical setup is shown alongside representative test data for a reacting mixture of 1.14% $^{13}C_2H_4$, 1.14% $^{12}C_2H_6$, 5.71% O_2, and 18.4% He in argon. Example pressure and detector data highlight the diagnostic techniques ability to discern competitive oxidation, via ^{12}CO and ^{13}CO measurements, for fuel blends at low temperatures

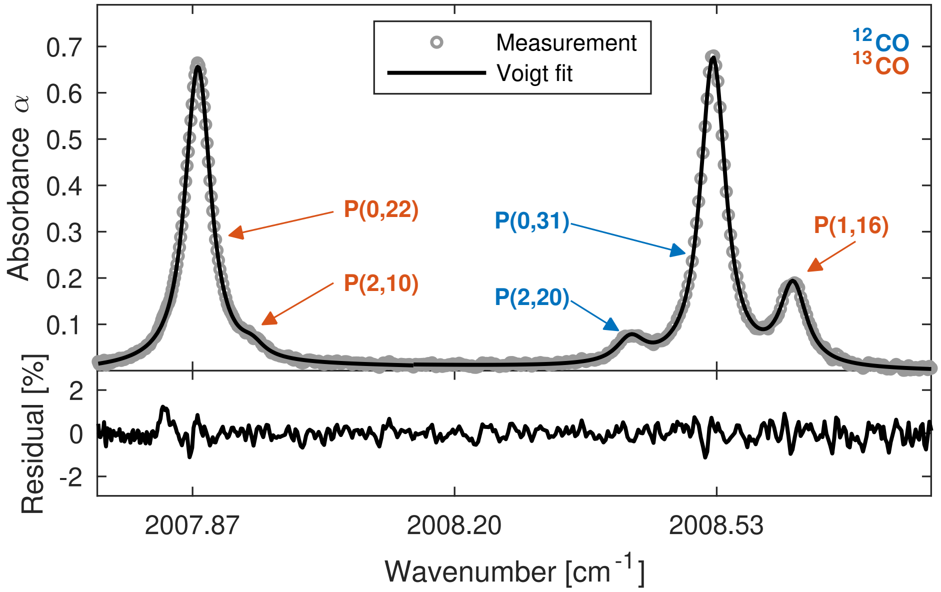

Figure 5.4: Example scanned-wavelength Voigt fitting of data in a shock tube oxidation experiment.

all experiments performed for this study. Lastly, all measurement uncertainties shown in this study are computed using the approach outlined in the appendix of our previous work [166].

5.2.2 Shock tube experiments

Here we use a shock tube facility to serve as a near constant-volume reactor to observe chemical kinetics with minimal influence of fluid dynamics. Because of the Arrhenius behavior of many chemical reactions in combustion, examining lower-temperature (1100–1200 K) ignition behavior and kinetic rates requires significantly longer test times compared to high-temperature combustion (>1800 K). Additionally, variations in either temperature or pressure during a test can significantly affect the observed kinetics. As an example, a temperature increase as small as 1% at 1500 K can lead to a 25% error in the measured rate coefficient for the dissociation of NO_2 [217]. Consequently, conducting low-temperature chemical kinetics experiments requires both extended test times ($>$ 5 ms) and well-controlled and characterized thermodynamic conditions. In a conventional shock tube, the reflected shock wave creates a near-instantaneous and spatially-homogenous high-temperature reactor with precisely known thermodynamic conditions (typically $< \pm 1\%$ in pressure and temperature) [218]; however, the usable test time is often limited to 1–3 ms [140] due to physical dimensional constraints that lead to wave interactions or non-ideal gas dynamics such as boundary layer growth [79]. To extend test times, such that low-temperature combustion kinetics are observable, conventional shock tubes may require physical modification of the geometry and/or gas mixture optimization to mitigate effects that terminate constant pressure test times. A notable distinction in the present shock tube study from our prior work [166] is the implementation of a 19.76 ft. driver extension, variable-area driver inserts, and tailored driver gases; the judicious combination of which enable significantly longer duration test times (up to 30 ms) than are achievable in the shock tube's standard configuration [39].

The high-enthalpy shock tube used in this study is shown in Fig. 5.3 and is also described in previous work by the authors [166, 219, 220]. The facility consists of a high-pressure driver section and a low-pressure driven (test gas) section, which are separated by either a polycarbonate or metal diaphragm. When the diaphragm ruptures due to pressure-induced strain, an incident shock wave forms and propagates into the driven section–compressing and heating the test gas and imposing a bulk velocity in the direction of the moving shock. Additionally, an expansion wave travels into the driver and the contact surface between the driver and driven gases propagates into the driven section (although at a much lower velocity). When the incident shock wave reaches the end wall of the driven section, it reflects back towards the driver, stagnating the flow and compressing and heating the test gas even further. This creates near-constant temperature and pressure conditions and initiates the test time for the kinetics experiments conducted in this work.

The pressure time history at the measurement location (near end-wall) determines the test time and can be used to assess uniformity of the thermodynamic conditions during a test. The test time typically ends when either the expansion fan reflects off the driver end wall and returns to the driven section–changing the thermodynamic conditions at the measurement location–or the contact surface and reflected shock wave interact, sending another shock or expansion wave back towards the measurement test section. To delay the reflected expansion fan arrival and extend the total test time, a 19.76 ft. driver extension, shown in Fig. 5.3, was used for all the measurements conducted in this study. The use of the driver extension enables reflected shock test times up to 30 ms, ideal for studying low-temperature combustion chemistry. Additionally, more uniform thermodynamic conditions were achieved by using a tailored driver gas mixture (75%He/N_2) to mitigate contact surface-reflected shock wave interactions along with variable-area driver inserts to minimize the pressure rise, $\mathrm{d}P/\mathrm{d}t$, (and the associated temperature rise [221]) caused by factors such as boundary layer growth and shock attenuation. Driver gas tailoring can minimize expansion or compression at the test section when the reflected shock wave interacts with the contact surface. This is achieved by blending a lower speed-of-sound gas, such as N_2, with He, such that the pressures across the contact surface following the passage of the reflected shock wave, are identical. To minimize $\mathrm{d}P/\mathrm{d}t$, variable-area driver inserts were designed [104] to partially reflect expansion waves back to the test section where the chemical kinetic studies are being conducted. The pressure decrease from the expansion waves helps offset the pressure rise caused by non-idealities in the test section. Combined, these modifications result in an approximate factor of 5 increase in the achievable test times compared to our standard shock tube configuration and are particularly useful for studying low-temperature combustion chemistry, where reaction rates are relatively slow. The results can be directly observed in Fig. 5.3, where ignition at 1059.2 K and 1.02 atm occurs on the order of 18 ms, with pre-ignition chemistry observed as early as 8 ms.

To conduct experiments, the driver and driven sections of the shock tube are connected to rotary vane roughing pumps (Alcatel Adixen 2021i) and a turbomolecular pump (Varian V550) to reach ultimate pressures $< 1 \times 10^{-4}$ torr and remove trace amounts of any contaminating species. The driven and driver sections are then filled with the test gas mixture and tailored gas, respectively. The tailored driver gas contained 75% He balanced in N_2 and was supplied by Airgas. Test gas mixtures were barometrically prepared with capacitance manometers (Baratron 627D) with an uncertainty of 0.12% of reading in an agitated mixing tank. All test gas mixtures were prepared in an Ar or 18.4%He/Ar bath gas and targeted a nearly equal number of carbon atoms corresponding to each carbon isotope (67%CH_4/33%C_2H_X, where X $= 2, 4, 6$). $^{12}CH_4$, $^{12}C_2H_2$, $^{12}C_2H_4$, $^{12}C_2H_6$, O_2, He, and Ar gases were supplied by Airgas with purities of 99.97%, 99.6%, 99.9995%, 99.99%, 99.994%, 99.997%, and 99.999%, respectively. $^{13}CH_4$ and $^{13}C_2H_4$ gases were supplied by Sigma-Aldrich with purities of 99% and 99%. Competitive oxidation experiments were conducted over a range of temperatures (1000–1800 K) at near-atmospheric pressures (0.5–1.5 atm). Combustion kinetics were compared and analyzed based off the thermometry and species measurements discussed in Sec. 5.2.1. Additionally, ^{12}CO and ^{13}CO production rates assisted in evaluating the validity and sensitivity of several chemical kinetic models (GRI-MECH 3.0 [142] and FFCM-1 [222]) for the different fuels and conditions considered herein.

5.2.3 Chemical kinetic modeling

For model comparison and evaluation, we modified both the GRI-MECH 3.0 [142] mechanism and the Foundational Fuel Chemistry Model (FFCM-1) [222] to account for isotopic labeling of carbon atoms. In GRI-MECH 3.0, this increased the number of species from 53 to 117 and the number of reactions from 325 to 886. For FFCM-1, the number of species increased from 38 to 85 and the number of reactions increased from 291 to 926. We initially examine these somewhat reduced models as they possess a small enough number of reactions and species so as to be tractable for isotopic labeling. These mechanisms include the various fuel components of interest, but it should be noted that the models were primarily developed for predicting methane combustion and have had little to no validation against C_2 fuel blends. Additional larger mechanisms are also employed for comparison of the global kinetic timescales (i.e. ignition delay times).

In addition to the chemical model, the simulation technique for a shock tube experiment can affect the quality of comparison with measurements. Measurements of ignition experiments behind reflected shock waves are often compared with zero-dimensional reactor models, assuming a constant internal energy / volume (constant U, V) or a constant enthalpy

/ pressure (constant H, P) thermochemical process. These models are only valid in reflected shock wave experiments for reacting mixtures with minimal heat release, and so these experiments are typically highly diluted in inert gas, such as argon. It is often desirable to increase the concentration of reactants in these experiments, either to enable the mixture to ignite within the test time allowed by the shock tube, or to increase absorbance for a more robust species measurement. To enable model comparison with experiments utilizing higher concentrations of reactants, we employ a split-timestep reactor model in CANTERA [189] similar to that developed for CHEMKIN by Li et al [46]. At the beginning of each time step, the zero-dimensional mixture is at an initial temperature T, pressure P, and composition X. During the first part of each timestep, the mixture is allowed to react while holding volume V and internal energy U constant, resulting in new values of temperature T', pressure P', and composition X'. Following this constant volume reaction, the mixture is isentropically expanded (or compressed) assuming a frozen mixture composition X' from the model-predicted pressure P' to the experimentally measured pressure P_{meas}:

$$V_{final} = V' \left(\frac{P_{meas}}{P'} \right)^{1/\gamma} \tag{5.1}$$

This is performed using CANTERA's `wall()` function, and has the effect of isentropically increasing or decreasing the mixture temperature to a value T_{final}, which is used as initial temperature T for the next timestep. A representative assessment of the split-timestep reactor model's performance is shown in Fig. 5.5 for a reactive $CH_4/C_2H_4/O_2/Ar$ mixture at approximately 1500 K and 0.73 atm. The modified split-timestep reactor model displays an enhanced accuracy relative to both the constant-volume and constant-pressure reactor models in predicting the temperature evolution of the system.

For the split-timestep reactor model currently implemented in CANTERA 2.4.0, a small computational performance impact is observed for reactor simulations without sensitivity analyses, but this impact is magnified significantly for reactor simulations utilizing sensitivity analyses. Sensitivity analyses of the FFCM-1 reaction model were conducted using multiple

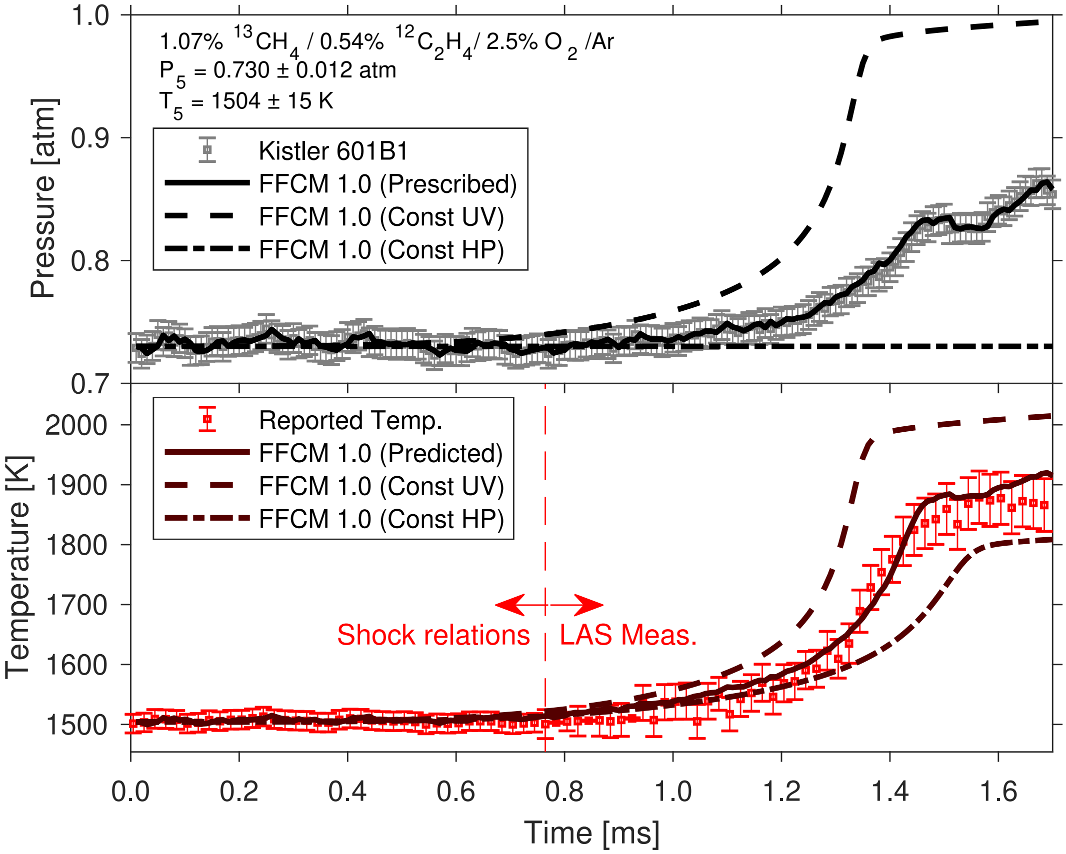

Figure 5.5: Pressure (*top*) and temperature (*bottom*) prescribed / predicted by models and measured in experiments in a shock tube oxidation experiment. 0.54% C_2H_4, 1.07% CH_4, and 2.5% O_2 ($\phi \approx 1.5$) in argon.

reactor simulations. For each experiment, a full sensitivity analysis considering all 926 reactions for a constant volume reactor model was first conducted to determine time-resolved normalized sensitivity coefficients for each ^{12}CO and ^{13}CO concentration with respect to reaction rate constants k_i:

$$S_{k,\mathrm{CO}} = \frac{k_i}{\mathrm{CO}} \cdot \frac{\partial \mathrm{CO}}{\partial k_i} \tag{5.2}$$

This constant UV reactor model is initiated with the experimentally-determined reflected shock conditions T_5 and P_5, as well as the molar composition X. The Foundational Fuel Chemistry Model effort provides uncertainty factors for each reaction, f_k [222]. We can utilize these f_k values to weight our normalized sensitivity coefficients, so as to specifically highlight reactions that deserve more attention when comparing model predictions with experimental measurements:

$$S^f_{k,\mathrm{CO}} = f_k \cdot S_{k,\mathrm{CO}} \tag{5.3}$$

We rank the reactions by their uncertainty-weighted sensitivity, and consider the top 50 in a subsequent sensitivity analysis utilizing the split-timestep reactor model discussed previously. We use these sensitivity analyses to identify key reactions which can be isolated by the multi-isotopologue LAS method.

5.3 Results

5.3.1 Competitive oxidation of methane with ethylene

The oxidation of methane (CH_4) and ethylene (C_2H_4) mixtures were investigated behind reflected shock waves at multiple temperatures for both fuel-rich ($\phi = 1.5$) and stoichiometric ($\phi = 1.0$) equivalence ratios. The experiments are performed at reflected shock temperatures between 1000–1800 K and pressures between 0.5–1.5 atm. In most cases, included those shown here, the initial mole fractions of each fuel component were adjusted to give an equal number of carbon atoms, such that at longer time scales approaching equilibrium, the mole fractions of carbon monoxide are expected to equalize according to simulations. This provided a quantitative check on the magnitudes of each measured isotopologue. The convergence of the measurements at longer times can be readily observed in the figures throughout this section.

Temperature and species time-histories of ^{12}CO and ^{13}CO during shock tube oxidation experiments for fuel-rich ($\phi = 1.5$) mixtures of $^{13}CH_4$ and $^{12}C_2H_4$ are shown in Fig. 5.6 for a series of post-shock temperatures. As initial temperature progressively decreases, the oxidation process slows overall and timescales of the component fuels increase in separation. At 1726 ± 19 K, $^{13}CH_4$ and $^{12}C_2H_4$ are experimentally observed to oxidize into ^{13}CO and ^{12}CO at very similar rates. At 1504 ± 15 K, the reaction timescales are separated, with

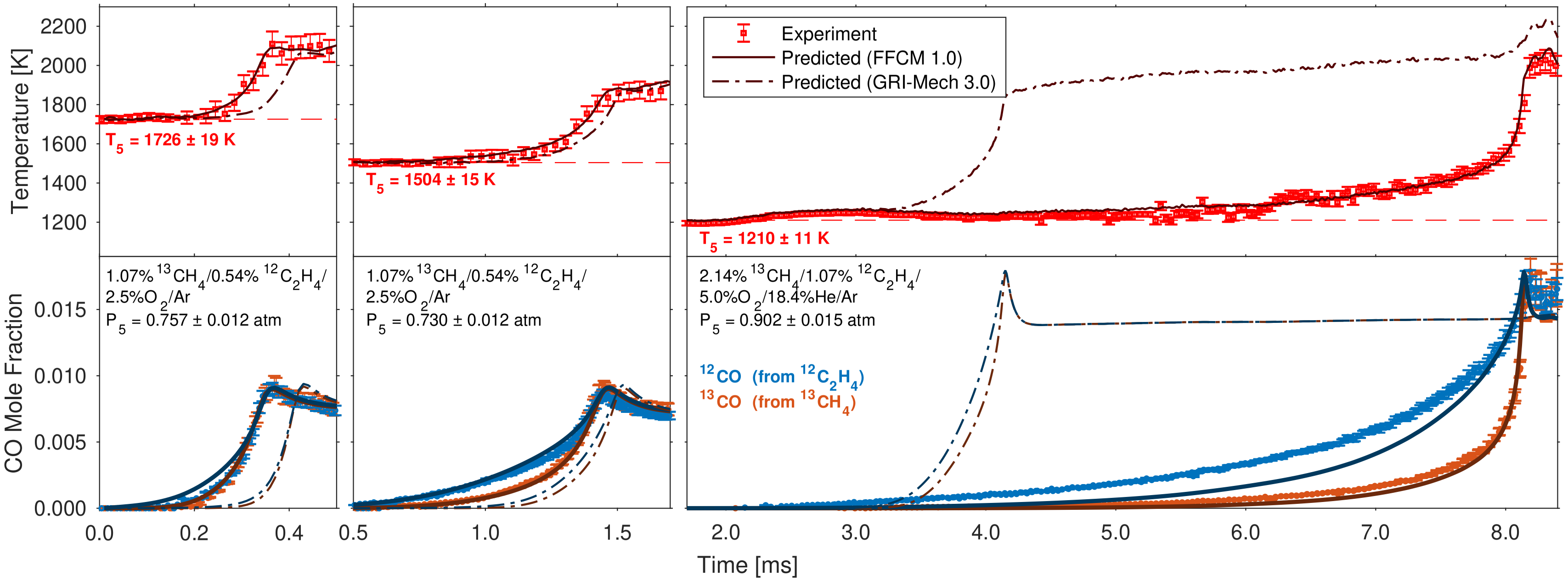

Figure 5.6: Measurements and predictions of temperature (*top*) and CO mole fraction evolution (*bottom*) during oxidation behind reflected shock waves of $C_2H_4/CH_4/O_2$ reactive mixtures ($\phi \approx 1.5$) in Ar and Ar/He bath gases. $t = 0$ denotes passage of reflected shock. Some data points are omitted for reader clarity, and reflected shock temperatures decrease from left to right. The data are plotted at different x axis scales to better examine temperature and CO evolution.

$^{12}C_2H_4$ oxidizing into ^{12}CO earlier than $^{13}CH_4$ and at a faster rate. At 1210 ± 11 K, the reaction timescale separation widens further, such that the concentration of ^{12}CO reaches a value greater than seven times that of ^{13}CO at half the ignition delay time. At the lower two initial temperatures of 1504 ± 15 K and 1210 ± 11 K, there is an eventual convergence in magnitude and rate of ^{12}CO and ^{13}CO production at $\approx$1.3 ms and $\approx$7.9 ms, respectively, indicating a transition from lower-temperature oxidation to rapid ignition behavior. In all cases, rapid rise in concentration of the CO isotopologues is accompanied by a corresponding rise in temperature. Overall, the results support established understanding that ethylene possesses an increased ability to consume oxygen relative to methane at lower temperatures, increasing mixture reactivity and reducing ignition delay in fuel mixtures [200, 202, 207].

The measurement data is overlaid with CO isotopologue simulations from both the modified FFCM-1 and GRI-MECH 3.0 models. We first note that measured peak values of CO match very well with both mechanisms. The increasing separation in reaction timescale is predicted by both reaction models, though the FFCM-1 model more accurately predicts the extent of the increasing separation than the GRI-MECH 3.0 model. The ignition delay time is also much better predicted by FFCM-1. To better compare the time-resolved model predictions with measured species time-histories prior to ignition, we slightly time-shift experimental profiles via adjustment of initial temperature/pressure within experimental uncertainty) such that the measured peak mole fractions of CO correspond to the numerical peak mole fractions predicted by FFCM-1 [166, 174]. FFCM-1 slightly overpredicts the early ^{12}CO production at 1726 ± 19 K and 1504 ± 15 K despite accurately predicting the production of ^{13}CO within experimental uncertainty. By contrast, FFCM-1 underpredicts the oxidation rate of ^{12}CO from $^{12}C_2H_4$ at 1210 ± 11 K, despite qualitatively capturing the fuel-specific behavior of low- and high-temperature oxidation. In general, the isotopically-labeled FFCM-1 chemical kinetic model outperforms the isotopically-labeled GRI-MECH 3.0 model at all temperatures examined, particularly at lower temperatures. This is unsurprising, as the GRI-MECH effort largely did not target temperatures much below 1200 K [142] and was not validated against C_2H_4. For this reason, as well as the availability of uncertainty factors

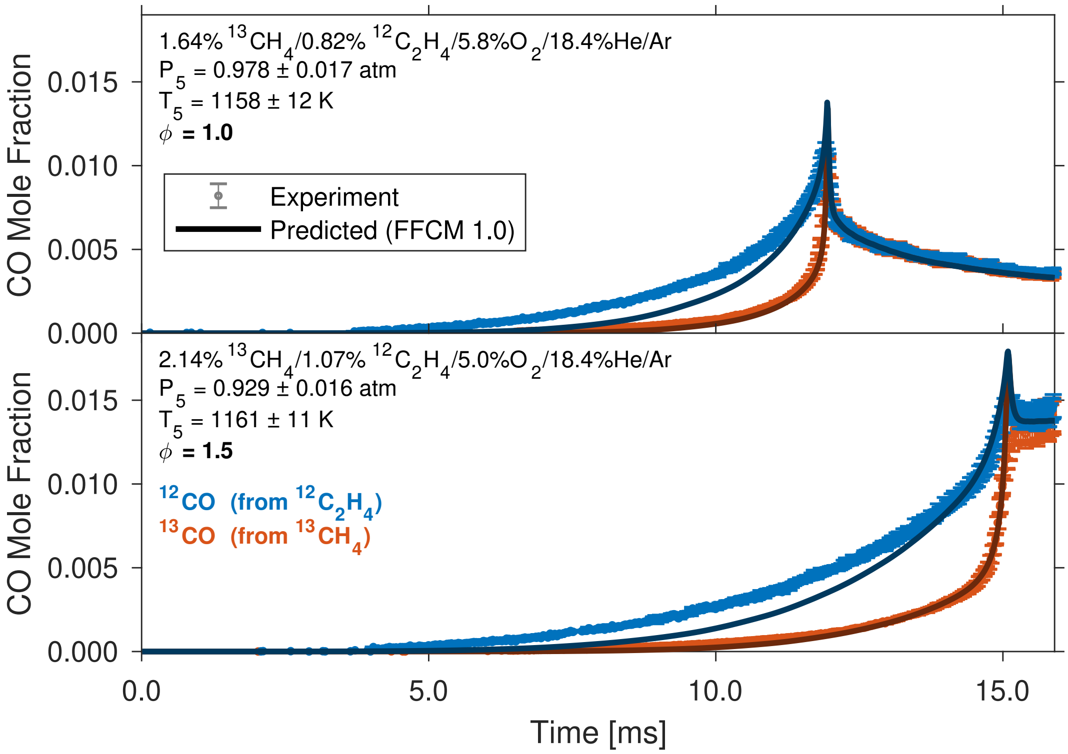

Figure 5.7: Measurements and predictions of CO mole fraction evolution during oxidation behind reflected shock waves of both stoichiometric ($\phi = 1.0$) and fuel-rich ($\phi = 1.5$) $C_2H_4/CH_4/O_2$ reactive mixtures in an Ar/He bath gas.

for each reaction in FFCM-1 (facilitating subsequent sensitivity analysis), we restrict our detailed modeling comparisons to FFCM-1 in the rest of this work.

The competitive oxidation behavior of the different fuel components persists in the increased availability of oxygen. Fig. 5.7 compares the results of two shock tube oxidation experiments at similar temperatures of ≈ 1160 K but with different equivalence ratios. During oxidation of stoichiometric mixtures of $^{12}C_2H_4$ and $^{13}CH_4$, ^{12}CO appears earlier than ^{13}CO, just as in the fuel-rich mixtures, demonstrating that the reaction pathways of oxidation are not unique to fuel-rich competitive oxidation conditions. As with the fuel-rich condition, the FFCM-1 reaction model accurately predicts the formation of ^{13}CO, while slightly under-predicting ^{12}CO in the earlier stages of ignition. The reduction in absolute magnitude of CO concentration for both isotopologues is well predicted by the model at both equivalence ratios.

Overall the FFCM-1 model predictions are in relatively good agreement with the results, and the temporal evolution of ^{12}CO is largely captured despite underprediction of early CO formation at lower temperatures. It should be noted that FFCM-1 was not optimized with C_2H_4 as a target [172, 222], and has explicitly not been recommended for use beyond H_2, H_2/CO, CH_2O, and CH_4 combustion [222]. However, the reaction model remarkably appears to capture the kinetic behavior of the CH_4/C_2H_4 mixtures quite well, especially for the predicted time to peak CO concentration.

5.3.2 Competitive oxidation of CH_4 with different C_2 fuels

To examine the effect of functional group on the competitive oxidation behavior of CH_4/C_2H_X fuel mixtures, mixtures of CH_4 with the alkane C_2H_6, the alkene C_2H_4, and the alkyne C_2H_2 were prepared, maintaining a constant ratio of carbon-to-oxygen across the different fuel combinations. Time-histories of both CO isotopologues for two shock tube oxidation experiments of near-stoichiometric mixtures of $^{13}CH_4/^{12}C_2H_4$ ($\phi = 1.00$) and $^{13}CH_4/^{12}C_2H_6$ ($\phi = 1.07$) are shown in Fig. 5.8 for similar temperatures of $\approx$ 1200 K. Note that although the equivalence ratios are different, the carbon/oxygen ratios, O_2 concentration, and dilution of reactants for the two tests are the same. The $^{13}CH_4/^{12}C_2H_6$ mixture is observed to ignite slightly later than the $^{13}CH_4/^{12}C_2H_4$ mixture despite higher pressures, highlighting the greater reactivity of C_2H_4 under near-stoichiometric conditions. While both C_2H_6 and C_2H_4 promote earlier oxidation of CH_4 at lower temperatures than would be observed on its own, the effect of each C_2H_X fuel is distinctly different. In the $^{13}CH_4/^{12}C_2H_6$ mixture, ^{13}CO initially appears at very similar concentrations as ^{12}CO, indicating that both fuels are oxidizing to CO at similar rates in the earlier stages of combustion. After about 5 ms, however, the concentration of ^{12}CO outpaces that of ^{13}CO, although not to the same extent that is observed for the $^{13}CH_4/^{12}C_2H_4$ mixture. The FFCM-1 reaction model significantly overpredicts the oxidation rate of the CH_4/C_2H_6 alkane fuel blend, beyond which is explained by experimental uncertainty—overprediction of peak CO concentration by state-of-the-art reaction models at the stoichiometric condition was also noted by Mathieu et al. in their

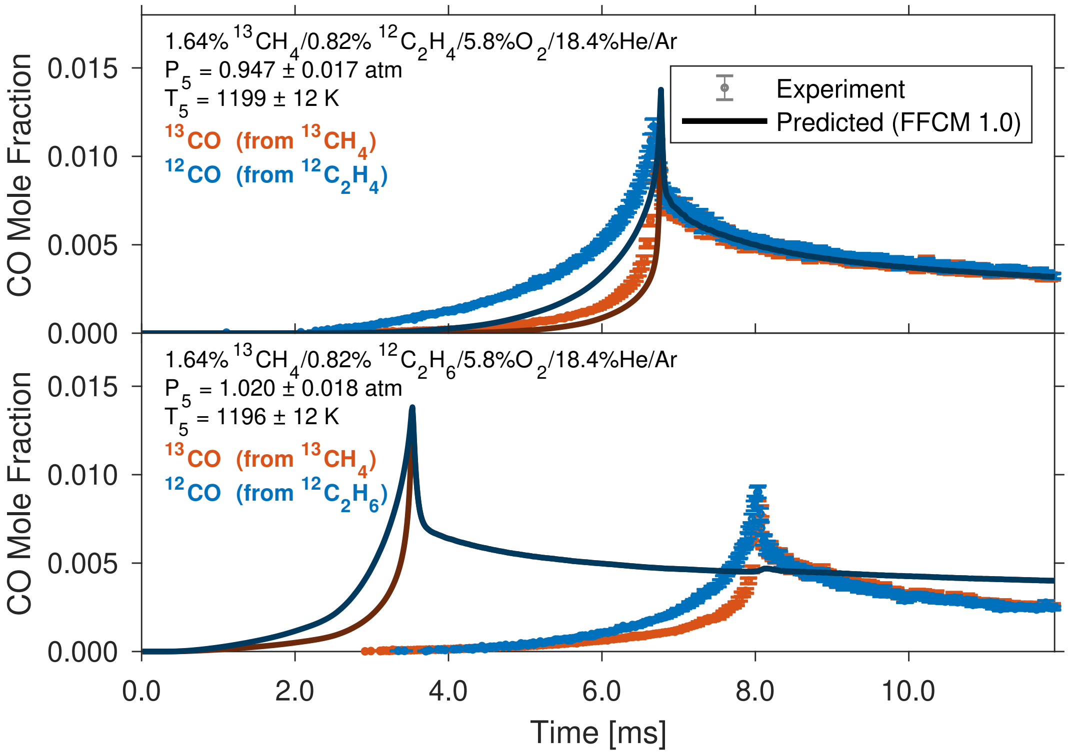

Figure 5.8: Measurements and predictions of CO mole fraction evolution during oxidation behind reflected shock waves of near-stoichiometric reactive mixtures of $C_2H_4/CH_4/O_2$ (*top*) and $C_2H_6/CH_4/O_2$ (*bottom*) in an Ar/He bath gas.

investigation of CH_4 oxidation [174]. Notably, the difference of ignition delays between the two mixtures examined here is less pronounced than that predicted by the model.

In fuel-rich conditions, competition for available O_2 is greater, magnifying the distinct behavior of each C_2H_X fuel on the overall evolution of both CO isotopologues. Time-histories of temperature and both CO isotopologues for three shock tube oxidation experiments of fuel-rich mixtures of $^{13}CH_4/^{12}C_2H_4$ ($\phi = 1.50$), $^{13}CH_4/^{12}C_2H_6$ ($\phi = 1.60$), and $^{13}CH_4/^{12}C_2H_2$ ($\phi = 1.40$) are shown in Fig. 5.9 for similar temperatures of $\approx$ 1150 K. As with the near-stoichiometric experiments shown in Fig. 5.8, the carbon/oxygen ratio, O_2 concentration, and reactant dilution are the same among the three tests shown. Unlike in the near-stoichiometric experiments, however, the $^{13}CH_4/^{12}C_2H_6$ mixture is observed to ignite slightly earlier than the $^{13}CH_4/^{12}C_2H_4$ mixture. Additionally, the $^{13}CH_4/^{12}C_2H_6$ mixture is observed to ignite at a similar time as the $^{13}CH_4/^{12}C_2H_2$ mixture, although uncertainties in initial temperature pre-

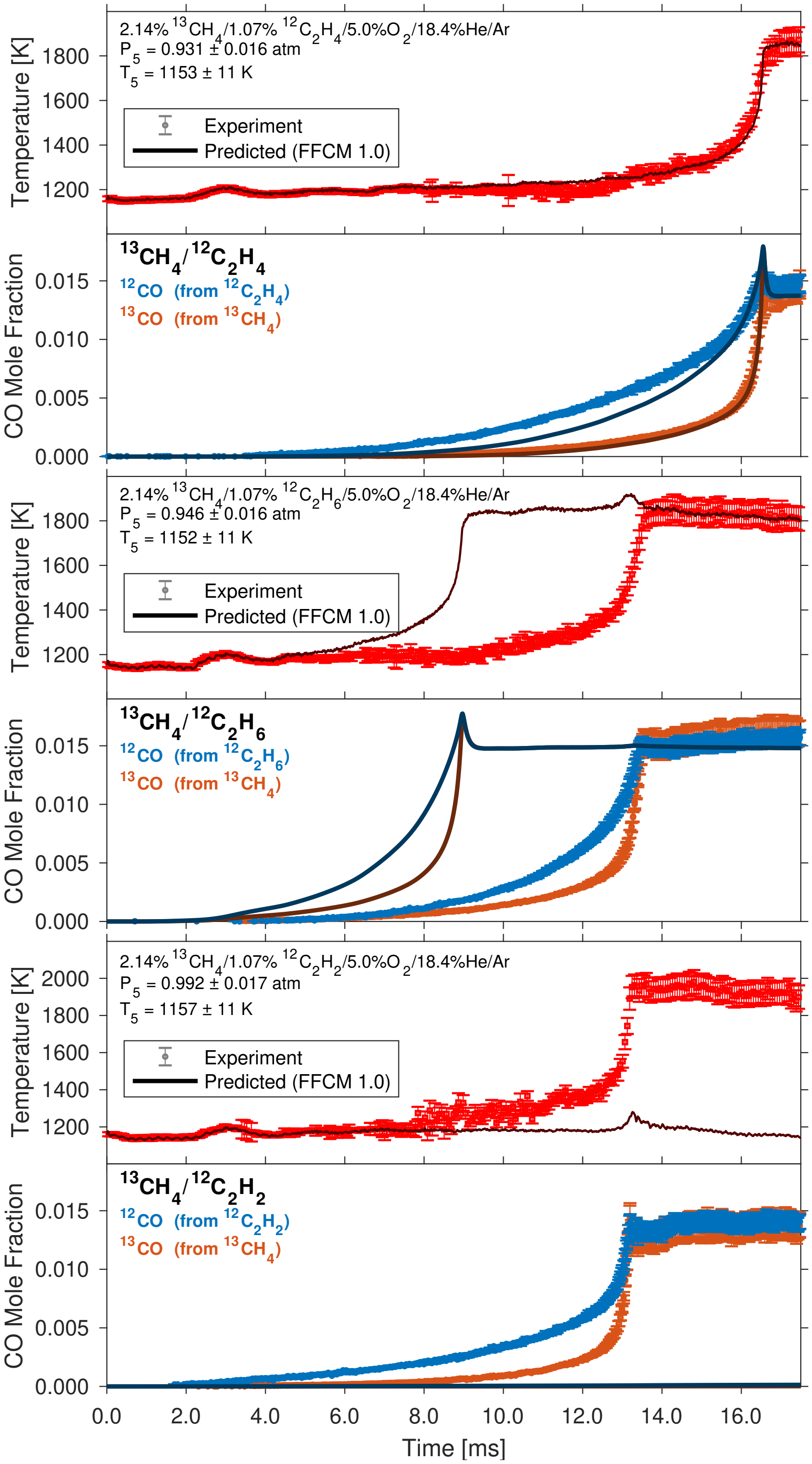

Figure 5.9: Measurements and predictions of temperature and CO mole fraction evolution during oxidation behind reflected shock waves of fuel-rich reactive mixtures of $C_2H_4/CH_4/O_2$ (*top*), $C_2H_6/CH_4/O_2$ (*middle*), and $C_2H_2/CH_4/O_2$ (*bottom*) in an Ar/He bath gas.

clude a definite conclusion. The $^{13}CH_4/^{12}C_2H_2$ mixture displays the earliest temperature rise and earliest ^{12}CO formation, indicating more pre-ignition heat release than the other mixtures at these temperatures. The largest separation in oxidation timescales between the two CO isotopologues is observed for the $^{13}CH_4/^{12}C_2H_4$ mixture, followed by the $^{13}CH_4/^{12}C_2H_2$ and the $^{13}CH_4/^{12}C_2H_6$ mixture. As was observed in the near-stoichiometric cases for the alkane mixture containing $^{12}C_2H_6$, ^{13}CO initially appears at very similar concentrations as ^{12}CO, indicating that the reactions involved in $^{12}C_2H_6$ oxidation also serve to promote the oxidation of $^{13}CH_4$. Additionally, the FFCM-1 significantly over-predicts the oxidation rate of the alkane mixture while under-predicting the oxidation rate of the $^{13}CH_4/^{12}C_2H_2$ mixture. As C_2H_2 was not a target fuel and only a limited set of C_2H_6 was included in the FFCM-1 optimization effort [222], the disagreement is not unexpected.

To check whether or not isotopic effects may be occurring on the timescales associated with the measurements presented in this study, a mixture of $^{13}C_2H_4$ and $^{12}CH_4$—analogous to the fuel-rich ($\phi = 1.5$) mixture shown previously in Figs. 5.6, 5.7, and 5.9—was prepared to compare species evolution behind reflected shock waves. The results of a representative shock tube oxidation experiment at $\approx$ 1160 K are shown in Fig. 5.10. The results show evolution

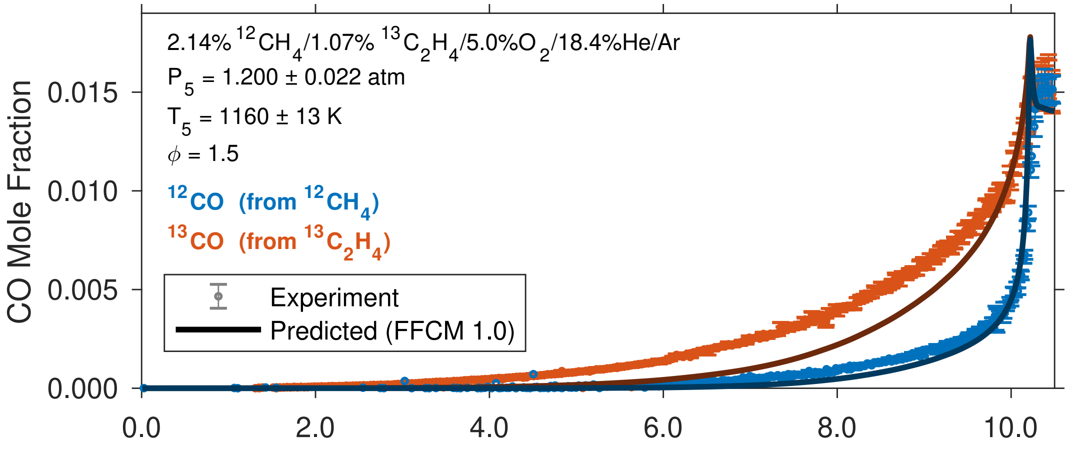

Figure 5.10: Measurements and predictions of CO mole fraction evolution during oxidation behind reflected shock waves of a fuel-rich ($\phi = 1.5$) $^{13}C_2H_4/^{12}CH_4/O_2$ reactive mixture in an Ar/He bath gas.

of both CO isotopologues that is reversed from the previous tests: ^{13}CO now appears earlier and in higher concentrations than ^{12}CO, suggesting that the $^{13}C_2H_4$ is oxidizing earlier and more rapidly than $^{12}CH_4$, and—most importantly—that this behavior prior to ignition is unaffected by any observable isotopic effects. Additionally, the isotopically-labeled FFCM-1 reaction model generally captures the relative oxidation of the two CO isotopologues. The time to ignition is observed to be shorter than the analogous experiment in Fig. 5.9; this is attributed to a difference in initial pressure in the experiments.

The results shown in this section highlight representative data from each mixture. A total of 40 shock tube tests were run over a range of conditions and trends are examined more holistically in the following section.

5.4 Discussion

Here we examine global kinetic scales (ignition delay times) and more granular reaction pathways via the time-resolved multi-isotopologue species measurements. A focused sensitivity analysis is performed on the CH_4/C_2H_4 mixtures, and some future research directions are suggested.

5.4.1 Ignition delay times

To take advantage of the availability of larger detailed mechanisms (for which isotopic labeling is outside the scope of this investigation), we examine measured global kinetic timescales and compare several modern detailed chemical reaction models against experimental data for binary fuel mixtures, several of which—particularly those of CH_4/C_2H_4—have not previously been reported for these temperatures, pressures, mixture and equivalence ratios, even without isotopic labeling. Besides FFCM-1 [222], these models include USC Mech II [143], AramcoMech 2.0 [223], and Caltech Mech 2.3 [224]. For these comparisons, the time-resolved summation of both CO isotopologue mole fractions is assumed to behave the same as an unlabeled mixture. We compare an ignition delay time, τ_{ign}, defined here as the time between the passage of the reflected shock and the time of peak CO concentration. This readily quantifiable metric facilitates comparison between model predictions and experimental observations in this work.

To examine the different models' predictive capability relative to one another for the temperature range of interest, constant volume reactor ignition simulations were performed for several examined mixtures assuming an initial pressure—averaged across all experiments for a given test gas composition as $P_{\mathrm{avg,mix}}$—isentropically compressed using an averaged $\mathrm{d}P/\mathrm{d}t$ pressure rise (1.5%/ms). This scaling of the initial pressure and temperature accounts for the pre-ignition pressure rise associated with the energetic mixtures examined in this study while reducing the influence of test-specific pressure behavior, allowing for easier comparison amongst model predictions. Constant-volume reactor τ_{ign} predictions for different $^{13}CH_4/^{12}C_2H_X/O_2/Ar/He$ mixtures at constant carbon-to-oxygen ratio (C/O = 0.856) are shown in the top of Fig. 5.11 alongside measured τ_{ign}. In the top plot of Fig. 5.11, the experimentally-determined $\tau_{\mathrm{ign,Meas}}$ is simply scaled by $(P_{\mathrm{5,Meas}}/P_{\mathrm{avg,mix}})$ to facilitate test-to-test comparison across a range of pressures:

$$\tau_{\mathrm{ign}} = \left(\frac{P_{\mathrm{5,Meas}}}{P_{\mathrm{avg,mix}}}\right)\tau_{\mathrm{ign,Meas}} \tag{5.4}$$

Note that this is a relatively small correction as most tests were near atmospheric pressure (1 atm), and at these elevated temperatures, $\tau_{\mathrm{ign}} \propto 1/P$. Beyond this, we do not attempt to determine any scaling laws for the experimental data. As mentioned previously, the carbon/oxygen ratio, O_2 concentration, and reactant dilution are the same across tests, with the goal to examine variations associated with fuel structure.

Somewhat surprisingly, in the experimental global kinetic timescale data shown in Fig. 5.11, there are no obvious fuel-specific effects, suggesting that—at least for the binary mixtures, temperatures, and pressures examined in this study—the structure of C_2H_X hydrocarbons does not strongly affect overall τ_{ign}. This contrasts with several reaction models that predict a much greater influence of fuel components on the ignition delay than is experimentally ob-

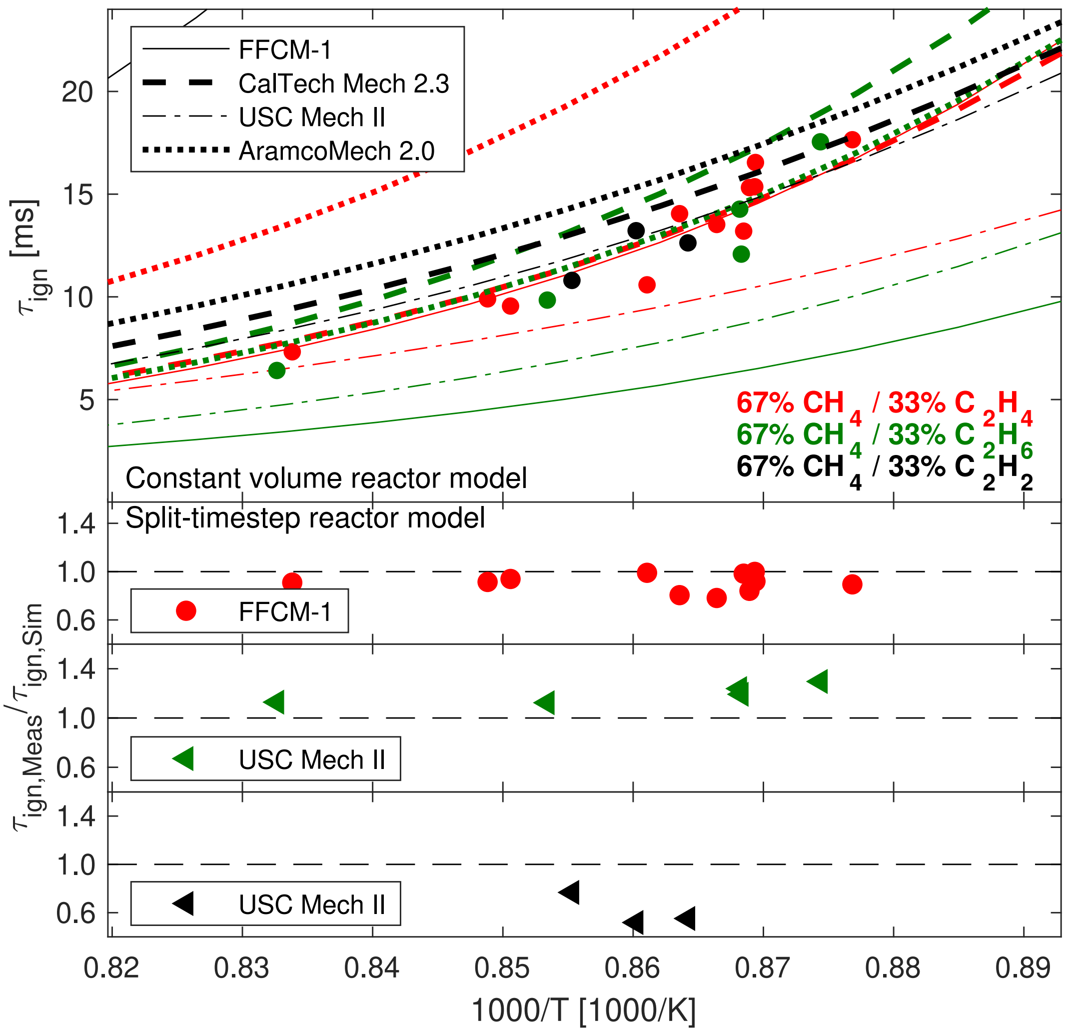

Figure 5.11: Temperature dependence of predicted and experimentally observed global kinetic timescales for different mixtures of CH_4/C_2H_X hydrocarbons assuming constant volume ignition (*top*) alongside relative predictive capability of various reaction models when using the split-timestep reactor model described in Section 5.2.3 (*bottom*).

served. FFCM-1 predicts shorter ignition delay times for mixtures containing C_2H_6 than for those containing C_2H_4, which are predicted to ignite much more quickly than mixtures containing C_2H_2. USC Mech-II predicts the same fuel-ordering in τ_{ign}, though the fuel-specific influence is reduced. Similarly, AramcoMech 2.0 predicts that mixtures containing C_2H_6 ignite faster than the others, although it predicts that those containing C_2H_4 react most slowly. Of the models examined, the Caltech Mech 2.3 reaction model predicts the most similar τ_{ign} behavior among the binary fuel mixtures, and the predictions for the CH_4/C_2H_4 mixture are nearly identical to those of FFCM-1 for the temperature range examined.

For an assessment of the ability of the models to predict CO time history and ignition delay while considering shock tube non-idealities such as pressure variation, we use the split-timestep reactor model developed in Section 5.2.3 to determine $\tau_{\text{ign,Sim}}$ predicted by each chemical model. Relative predictive capability of the most accurate models with respect to $\tau_{\text{ign,Meas}}$ are shown in the bottom of Fig. 5.11 for all CH_4/C_2H_X mixtures as a ratio of observed versus predicted values. In this analysis, the data are not time-shifted to compare time-resolved speciation of CO. Of the reaction models, FFCM-1 is observed to best capture both the quantitative and qualitative temperature-dependent ignition behavior of the fuel-rich $^{13}CH_4/^{12}C_2H_4$ fuel mixtures, which was shown in Section 5.3. Despite the overprediction relative to FFCM-1 shown for the constant-volume simulations of $^{13}CH_4/^{12}C_2H_6$ mixtures, USC Mech-II is observed to best capture their behavior when considering experimental pressure variation, although the disagreement increases at lower temperatures. When considering time-varying pressure in the shock tube experiments, nearly all of the models significantly underpredict the reactivity of the $^{13}CH_4/^{12}C_2H_2$ fuel mixtures for the tests shown, exhibiting a delayed formation of CO relative to experimental observations, similar to what was observed in Fig. 5.9. Of the models, USC Mech-II is observed to have the best relative predictive capability, as shown in the bottom plot of Fig. 5.11. Overall, the best model for acetylene mixture underpredicts reactivity, the best model for ethane overpredicts reactivity, while for ethylene mixtures the best model (FFCM-1) very closely predicts the ignition delay.

To gain more insight with respect to competitive oxidation, we can further examine a single binary fuel combination, $^{13}CH_4/^{12}C_2H_4$. Constant-volume reactor τ_{ign} predictions for $^{13}CH_4/^{12}C_2H_4/O_2/Ar/He$ mixtures at two different equivalence ratios ($\phi = 1.0, 1.5$) are shown in the top of Fig. 5.12 alongside measured τ_{ign}. A distinct separation in reaction timescales is observed between the fuel-rich and stoichiometric mixtures of the fuel blends, with the stoichiometric mixtures igniting earlier than the fuel-rich mixtures. As expected, there is an increase in ignition delay as temperatures decrease, accompanied by a diver-

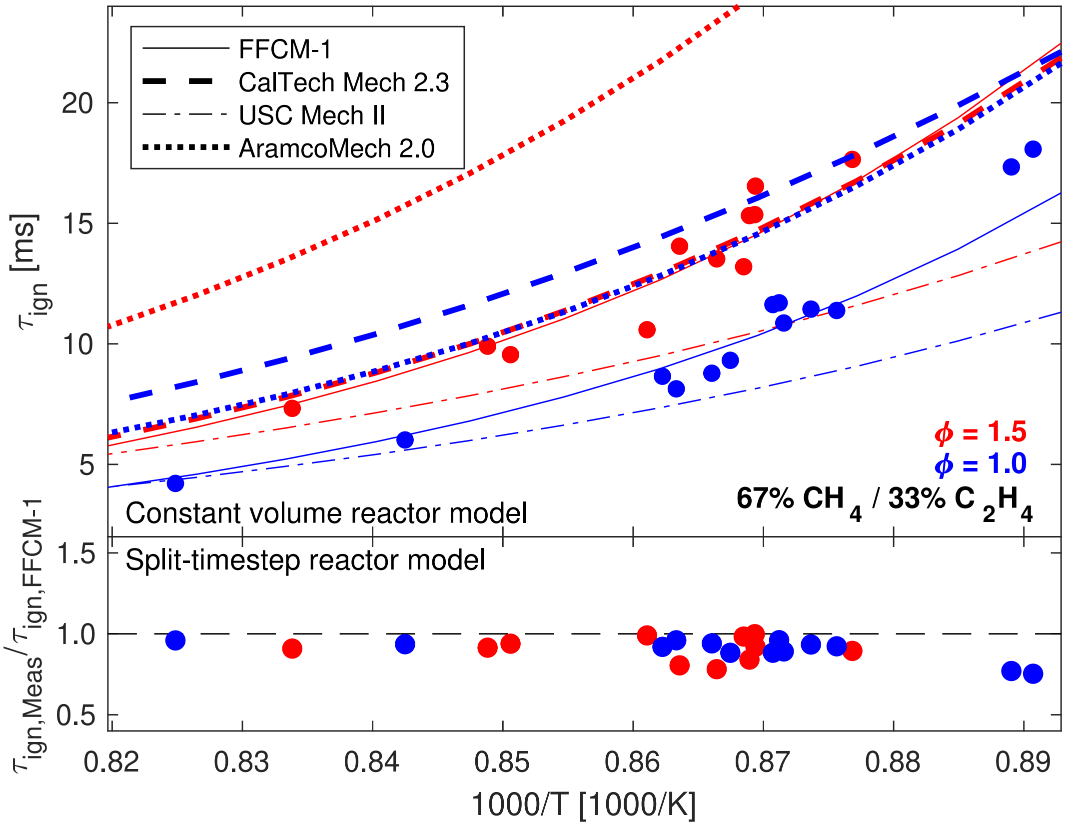

Figure 5.12: Temperature dependence of predicted and experimentally observed global kinetic timescales for binary CH_4/C_2H_4 mixtures at two different equivalence ratios assuming constant volume ignition (*top*) alongside relative predictive capability of various reaction models when using the split-timestep reactor model described in Section 5.2.3 (*bottom*).

gence in τ_{ign} predicted by the models. Most of the models, with the exception of Caltech Mech 2.3, predict faster ignition for the stoichiometric equivalence ratio. For the fuel-rich mixtures, Caltech Mech 2.3 and FFCM-1 predict similar ignition behavior with respect to temperature-dependence, while the other models either underpredict (USC Mech-II) or overpredict (AramcoMech 2.0) ignition delay at lower temperatures. Relative predictive capability of FFCM-1 with respect to $\tau_{\mathrm{ign,Meas}}$ is shown in the bottom of Fig. 5.12 for both fuel-rich and stoichiometic mixtures as a ratio of observed versus predicted values. As was shown in Section 5.3, the FFCM-1 reaction model generally demonstrates excellent agreement with experimental observations for binary CH_4/C_2H_4 mixtures, with many tests exhibiting agreement of ignition delay time within 5%. It should be noted that the increase in measurement scatter in the top of Fig. 5.12 relates to variation of initial test pressure and variation throughout the test time. When incorporating the split-timestep model, as shown in the residual plot, scatter is reduced and trends are more clear. While the FFCM-1 model performs quite well, there is a somewhat increasing overprediction of the ignition delay time with decreasing temperature that is outside of measurement scatter, though additional measurements at lower temperatures are needed to confirm this trend.

5.4.2 CH_4–C_2H_4 oxidation pathway analysis

The generally good agreement in ignition delay between the predictions of the split-timestep reactor model using FFCM-1 and the measured CO time-histories for binary fuel mixtures of CH_4/C_2H_4 enables a more granular sensitivity analysis of CO production, examining the different isotopologues to identify reactions responsible for disagreement during early oxidation. As CO is near the end of the overall oxidation process, many reactions common to the oxidation of all fuels—including those with large uncertainty factors f_k—are expected to be revealed as sensitive to its production; however, the ability to track each carbon isotope independently enables isolation of reactions which can be prioritized for further optimization. For example, experiments for which ^{13}CO mole fraction agrees with numerical predictions, while ^{12}CO mole fraction is lower than numerical predictions, prompt investigation into specific reactions for which increasing rates would produce relatively more ^{12}CO than ^{13}CO. To identify these reactions, we calculate the uncertainty-weighted sensitivity coefficients for the difference between ^{12}CO and ^{13}CO:

$$S^{f}_{k,\Delta \mathrm{CO}} = \frac{f_k \cdot k_i}{^{12}\mathrm{CO} - {}^{13}\mathrm{CO}} \cdot \frac{\partial \left(^{12}\mathrm{CO} - {}^{13}\mathrm{CO} \right)}{\partial k_i} \tag{5.5}$$

This can be expressed in terms of the sensitivity coefficients defined previously in Eqs. 5.2 and 5.3:

$$S^f_{k,\Delta\mathrm{CO}} = \frac{{}^{12}\mathrm{CO} \cdot S^f_{k,{}^{12}\mathrm{CO}} - {}^{13}\mathrm{CO} \cdot S^f_{k,{}^{13}\mathrm{CO}}}{{}^{12}\mathrm{CO} - {}^{13}\mathrm{CO}} \tag{5.6}$$

Time-resolved uncertainty-weighted isotopologue-difference sensitivity coefficients of selected reactions in the FFCM-1 chemical model for high temperature oxidation—spanning almost the entire duration of the experiment shown in the left of Fig. 5.6—are shown in Fig. 5.13. In the high-temperature experiment, the concentration of ^{12}CO just prior to ignition was slightly overpredicted by the model. Reactions with relatively uncertain rate constants that are candidates for adjustment include a few containing the formyl (HCO) and vinylidene (H_2CC) radicals:

$$\mathrm{H_2{}^{12}C{}^{12}C + O_2 \longleftrightarrow 2\,H{}^{12}CO} \tag{R185}$$

$$\mathrm{{}^{12}C_2H_2 + M \longleftrightarrow H_2{}^{12}C{}^{12}C + M} \tag{R176}$$

$$\mathrm{{}^{12}C_2H_4 + M \longleftrightarrow H_2 + H_2{}^{12}C{}^{12}C + M} \tag{R237}$$

For reader convenience, we label the selected reactions in the text according to their reaction number in the original unlabeled FFCM-1 reaction model. At the peak CO concentration, the denominator in Eq. 5.6 drops to zero as the predicted concentrations of ^{12}CO and ^{13}CO become nearly equal, and the sensitivity analysis provided by $S^f_{k,\Delta\mathrm{CO}}$ becomes less informative. After the peak CO concentration, the uncertainty-weighted isotopologue-difference sensitivity coefficients of the reactions for both CO are very similar, and so and neither isotopologue is significantly more sensitive than the other to any of the reaction rates, and $S^f_{k,\Delta\mathrm{CO}}$ drops to zero, though this is not shown in Fig. 5.13.

At lower temperatures, different reactions become much more significant. Fig. 5.14 shows the uncertainty-weighted isotopologue-difference sensitivity coefficients of selected reactions for low temperature oxidation, corresponding to the experiment shown in the top of Fig. 5.7. In this plot, we highlight the region of the experiment near 10 ms, since that is where

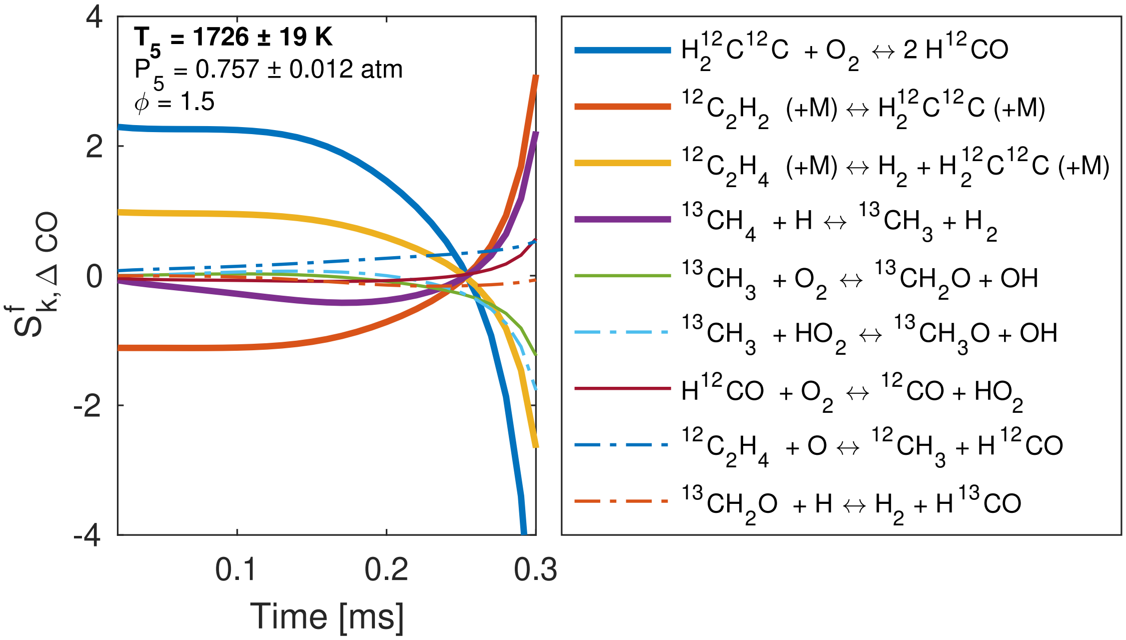

Figure 5.13: Time-resolved $S^f_{k,\Delta\mathrm{CO}}$ for selected reactions in an oxidation experiment at 1726 K. Dash/line styles simply help distinguish the respective reactions.

the greatest model disagreement is observed. In this experiment, the concentration of ^{12}CO prior to ignition was largely underpredicted by FFCM-1, while the concentration of ^{13}CO was predicted to within experimental uncertainty, allowing for identification of the the following reactions:

$$^{12}\mathrm{C_2H_4} + \mathrm{OH} \longleftrightarrow {}^{12}\mathrm{C_2H_3} + \mathrm{H_2O} \tag{R243}$$

$$^{12}\mathrm{C_2H_3} + \mathrm{O_2} \longleftrightarrow {}^{12}\mathrm{CH_2}{}^{12}\mathrm{CHO} + \mathrm{O} \tag{R205}$$

$$^{12}\mathrm{CH_3} + \mathrm{HO_2} \longleftrightarrow {}^{12}\mathrm{CH_4} + \mathrm{O_2} \tag{R104}$$

$$^{12}\mathrm{C_2H_4} + \mathrm{H} \longleftrightarrow {}^{12}\mathrm{C_2H_3} + \mathrm{H_2} \tag{R239}$$

Some key reactions involving the vinyl ($\mathrm{C_2H_3}$) radical are observed. Notably, $S^f_{k,\mathrm{CO}}$ for reaction R205 is large for both ^{12}CO and ^{13}CO (at 10 ms, 6.619 and 4.794, respectively).

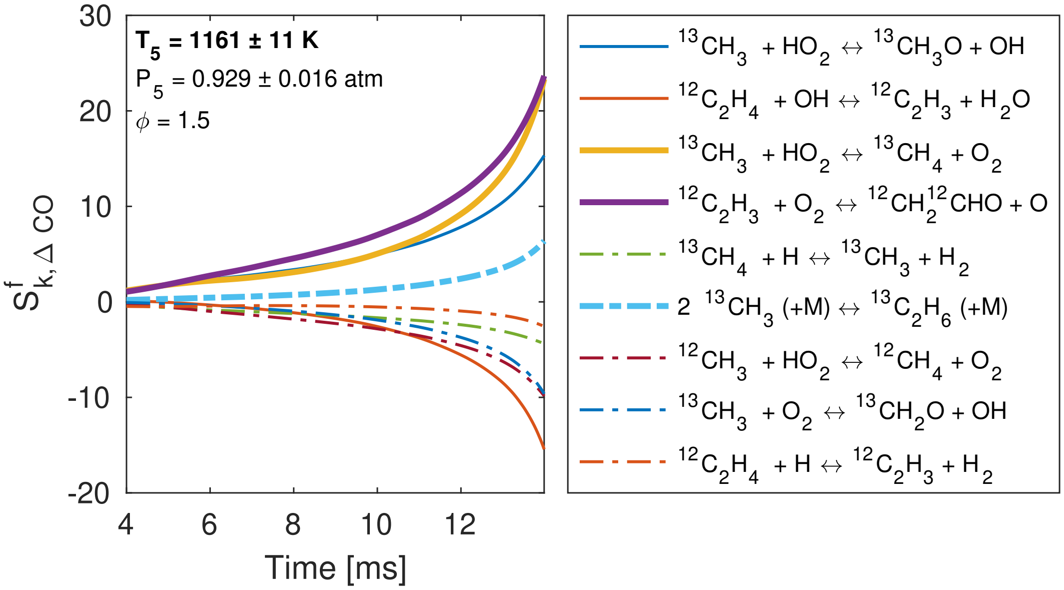

Figure 5.14: Time-resolved $S^f_{k,\Delta\mathrm{CO}}$ for selected reactions in an oxidation experiment at 1161 K. Dash/line styles simply help distinguish the respective reactions.

A reaction pathway analysis of the FFCM-1 chemical model near the same point in the ignition process (10 ms) shows that most (>60%) of the ^{12}C from $^{12}C_2H_4$ follows a path through the vinyl (C_2H_3) radical. Most of this is by reaction R243 with OH (≈72%), followed by reaction R239 with H (≈20%), and both of these reactions have been identified in the sensitivity analysis. Once C_2H_4 becomes C_2H_3, about 24% of this C_2H_3 reacts with O_2 to form CH_2CHO in reaction R205. Reaction R205 is one of several of C_2H_3 with O_2; these have been investigated by Goldsmith et al. [193], who determined that uncertainties in barrier heights on the $C_2H_3O_2$ potential energy surface result in a significant uncertainty in the temperature at which reaction R205 dominates all other competing reaction pathways.

While increasing the relatively uncertain rate of reaction R205 would increase ^{12}CO more than ^{13}CO, doing so without consideration of other sensitive reactions would cause ^{13}CO to be overpredicted by the model. Other prominent reactions in Fig. 5.14 include low temperature pathways for $^{13}CH_4$ oxidation:

$$^{13}CH_3 + HO_2 \longleftrightarrow {}^{13}CH_4 + O_2 \tag{R104}$$

$$2\,^{13}\mathrm{CH_3} + \mathrm{M} \longleftrightarrow {}^{13}\mathrm{C_2H_6} + \mathrm{M} \tag{R112}$$

Adjusting these rates could increase the difference between ^{12}CO and ^{13}CO concentration (currently underpredicted in the experiment); however, this would do so by decreasing ^{13}CO concentration rather than increasing ^{12}CO concentration. Since ^{13}CO concentration is well-predicted by the model, other rates should be prioritized in model optimization.

Notably, reactions containing ^{13}C are often observed to have high sensitivity coefficients with respect to ^{12}CO production, and vice-versa—this is often because these reactions consume or produce other species, such as the radicals OH, O, H, or HO_2, which are highly influential to the oxidation of all fuels. In this way, the multi-isotopologue technique provides increased granularity in the sensitivity analysis.

5.5 Summary

The competitive oxidation kinetics of methane (CH_4) with C_2 hydrocarbons of differing functional groups (alkane, alkene, and alkyne) was investigated via time-resolved measurements of carbon monoxide isotopologues (^{12}CO and ^{13}CO) in shock-heated isotopically-labeled fuel mixtures. Fuel-rich mixtures of methane with acteylene (C_2H_2), ethylene (C_2H_4), and ethane (C_2H_6) were examined by isotopically labeling one of the fuels with ^{13}C. Shock tube autoignition experiments were conducted over a range of temperatures from 1100–1800 K and near-atmospheric pressures (0.5–1.5 atm). In aggregate this has yielded a novel dataset with more granular constraints than prior efforts (including, to the authors' knowledge, the first species time history measurements for these binary mixtures) that may be used as validation targets in mechanism refinement. In particular, recent studies in the HyChem effort [172, 176, 177] have shown that large fuel pyrolysis produces large amounts of methane and ethylene, further promoting the relevance of the reported measurements. In order to compare chemical models to measurement data, two mechanisms for small hydrocarbons fuels (GRI-MECH and FFCM-1) were modified in this work to include isotopically-labeled reactions and species. A modified mechanism—available in the supplementary material of the original publication for FFCM1—may be used to identify reactions for future investigation, including those which may exhibit isotope effects. Other larger mechanisms were also employed to evaluate the global kinetics (ignition delay). When holding carbon/oxygen ratio and dilution constant, it was found that the different fuel-rich binary mixtures exhibited very similar ignition delay times, contrasting the stronger divergence predicted by the models. A similar convergence has been observed for larger real fuel blends of highly variable composition [225].

The Foundational Fuel Chemistry Model was found to be in very good agreement for ignition delay of the CH_4/C_2H_4 fuel mixtures at both stoichiometric and fuel-rich conditions, extending the validation range of the mechanism; however, the modified mechanism consistently under-predicted initial CO formation from ethylene oxidation at lower temperatures. A rigorous sensitivity analysis was performed to identify key reactions that may be responsible for the disagreement weighted by their uncertainty in the mechanism. While this work stops short of adjusting the rate constants, a framework is presented for future work towards mechanism refinement using the isotopic labeling approach, and additional validation data—complete with measurement uncertainties–are included as supplementary material in the original publication.

CHAPTER 6

Thermochemical imaging of the oxidation reaction layer in hybrid-propellant rocket combustors

The contents of this chapter have been published in the journal ***Experiments in Fluids*** *under the full title 'In-situ thermochemical analysis of hybrid rocket fuel oxidation via laser absorption tomography of CO, CO_2, and H_2O' [226]*

6.1 Introduction

Hybrid rockets (typically involving a solid fuel and liquid or gaseous oxidizer) have received increased interest by industry and government agencies in recent years due to potential advantages in safety, performance, and cost over traditional liquid or solid rocket propulsion systems [227]. More pointedly, several technology development programs have been initiated to prove the feasibility of hybrid propulsion systems for future interplanetary exploration missions [14, 16–19]. Despite well-known theoretical advantages over solid- or liquid-propellant combustion systems, notable challenges remain to mature hybrid rocket technology. Critically, sub-optimal combustion performance from low-regression-rate, polymer-based fuels has hindered the development of hybrid propulsion systems for many applications [227, 228]. This key limitation has prompted investigations to increase engine performance through both physical and chemical adaptations of hybrid rocket systems, such as multi-port fuel grains [229, 230], swirled flows [231], solid-fuel additives [232], and paraffin-based fuels [9, 11, 233]. To properly recognize the effects of such variations in hybrid rocket motor design, it is important to understand the underlying mechanisms (multi-phase thermochemistry, diffusive mixing, turbulence, etc.) governing the combustion performance.

The traditional flame structure inherent to hybrid combustion is characterized by complex multi-physical phenomena involving a competition of heat and mass transfer, chemical kinetics, and fluid dynamics. While hot-fire testing is frequently utilized to develop and refine more efficient hybrid motors, most experiments assess combustion performance based on global metrics, such as thrust, chamber pressure, and aggregate regression rate, which, although convenient, provide little granularity to the complex physics. Complementary numerical models for hybrid combustion can provide such granularity [234–237], but considerable uncertainty remains in the input data and assumptions regarding interactions of the underlying mechanisms. To better inform predicted physical behavior, several lab-scale combustion experiments have been devised using non-intrusive optical diagnostic tools, including Schlieren and chemiluminescence imaging, to investigate the flame structure of different hybrid propellants (paraffin, PMMA, HDPE, etc.) [12, 238–240]. While such optical methods provide quantitative spatial information, the thermochemical evolution of the hybrid fuel oxidation layer can only be understood qualitatively with these techniques. In this work, we develop a quantitative in-situ method to discern the thermochemical structure of a hybrid fuel reaction layer based on laser absorption spectroscopy, with the goal of providing granular data that can be compared to hybrid rocket combustion models and used to discern variations in combustor design.

Laser absorption spectroscopy (LAS) is an optical method known for its quantitative species-specific measurement capability in harsh environments [148]. The development of rapidly-tunable, room-temperature semiconductor lasers enables convenient access to strong mid-infrared absorption bands of many major hydrocarbon combustion species. Specifically, Fig. 6.1 shows the fundamental vibrational bands of CO, CO_2, and H_2O, which exhibit wavelength regions that are both well isolated and sufficiently strong for sensing over short optical path lengths. Here we present a strategy for probing multiple rovibrational transitions in these regions to achieve sensitive thermometry and speciation measurements in the combustion zone of a cylindrical solid fuel burning at the internal surface with an oxygen cross-flow

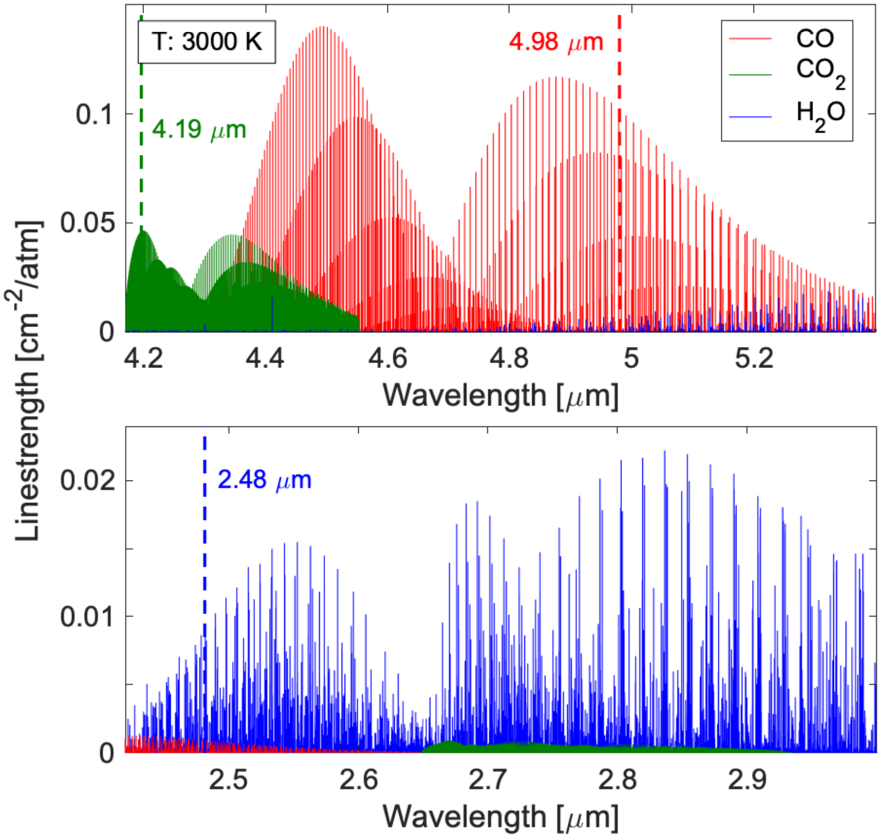

Figure 6.1: Absorption linestrengths for the CO, CO_2, and H_2O fundamental bands at 3000 K. Simulations use the HITRAN [241] and HITEMP [150] spectral databases. Targeted wavelengths are indicated as dashed lines.

(relevant to common hybrid rocket motor geometries). We combine this experimental method with tomographic reconstruction techniques [162, 163] to enable multi-dimensional imaging of the gaseous reaction layer assuming azimuthal symmetry of the core flow.

The key contribution in this work is the laser absorption tomography method (discussed in Sec. 3.3.3) and its coupling with the solid fuel oxidation experiment. The method builds on previous work from our group, imaging two-dimensional turbulent jet flames [185, 242, 243], and extends to additional species, new thermodynamic conditions, and a different experimental interface, which result in a unique sensor design and configuration. In this paper we describe the three key elements of the novel methodology, including (1) the laser absorption spectroscopy approach comprising wavelength and line selection for multi-species detection and thermometry; (2) the solid fuel oxidation experiment, designed for variable fuels, injector designs, and physical translation to spatially-scan a fixed laser beam across the exit plane at different heights; and (3) the tomographic reconstruction methods used to invert the line-of-sight absorption data to obtain radially-resolved thermochemistry, illustrating two-dimensional progression of fuel oxidation by way of CO, CO_2, H_2O, and temperature measurements. Example results are shown for two propellant combinations, PMMA/GOx and HDPE/GOx, and two injector designs (port and showerhead) to highlight the ability of the method to discern variations in hybrid rocket combustor design. In addition to enabling more granular and fundamental understanding of solid-gas combustion physics, it is envisioned that this technique can ultimately be used for increasing hybrid rocket technical readiness by optimizing hybrid motor designs and refining computational models.

6.2 Methods

6.2.1 Wavelength selection

Wavelength selection for LAS is influenced by the absorption strength, spectral isolation, and temperature sensitivity of the transitions (called *lines*) at the expected flow-field conditions. In order to develop a rigorous sensing approach suitable for a variety of hybrid rocket systems, a range of operating conditions was estimated through thermochemical equilibrium calculations [189, 244] for multiple hybrid rocket fuels (PMMA, HDPE, paraffin, etc.). These results provided upper bounds on the theoretical maximum temperature and species concentrations in the flow-field, which helps in simulating and surveying the rovibrational spectra of the target molecules.

Fig. 6.1 illustrates broadband simulations of CO, CO_2, and H_2O spectra in the mid- and near-wave infrared at expected combustion temperatures. For CO and CO_2, the strongest rovibrational transitions with minimal H_2O interference occur in the fundamental bands centered near 4.7 μm and 4.3 μm, respectively. However, in this region, the R-branch of CO and the P-branch of CO_2 interfere significantly with one another near 4.4 μm, making it dif-

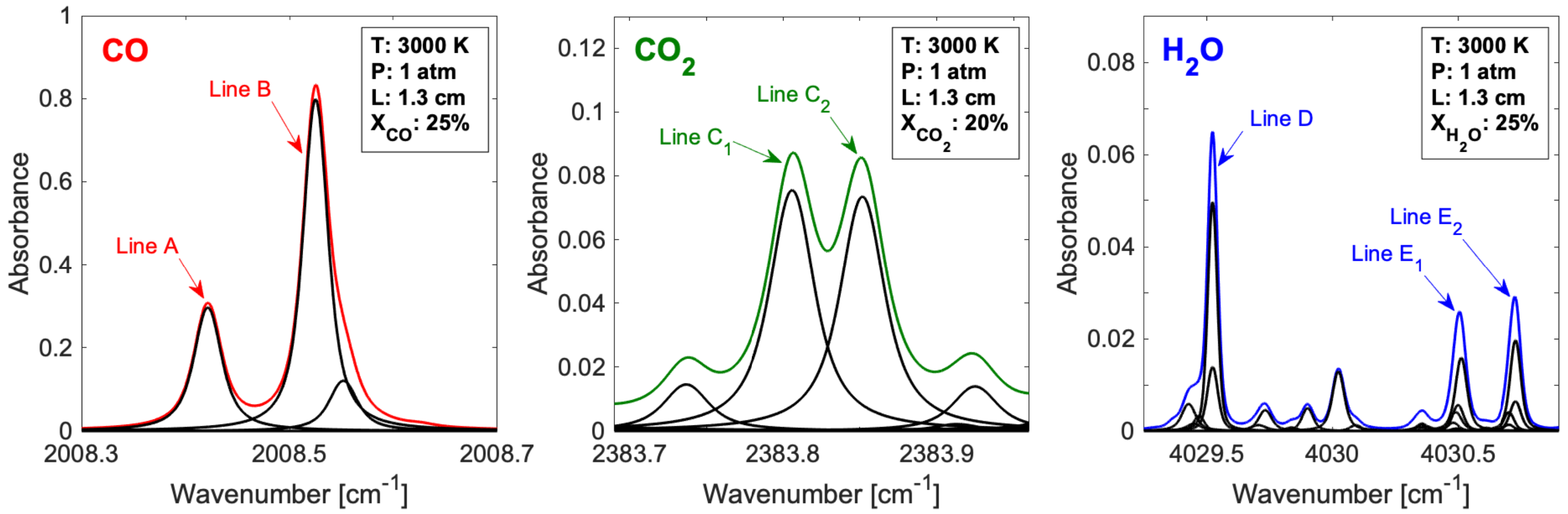

Figure 6.2: Absorbance simulations at expected atmospheric combustion conditions for CO, CO_2, and H_2O thermochemistry measurements. Each feature is labeled as it is referred to in the manuscript. The individual transitions comprising each feature are shown in black

Table 6.1: Spectroscopic parameters for targeted CO, CO_2, and H_2O transitions

Line	Species	Wavenumber [cm^{-1}]	E'' [cm^{-1}]	S(296 K) [$cm^{-1}/(molec \cdot cm^{-2})$]
A	CO^a	2008.42	5051.74	$1.149 \times 10^{-28(2)}$
B	CO^a	2008.53	1901.13	$2.669 \times 10^{-22(1)}$
C_1	$CO_2{}^a$	2382.81	4677.40	$4.659 \times 10^{-27(1)}$
C_2	$CO_2{}^a$	2383.85	4762.90	$3.105 \times 10^{-27(1)}$
D	H_2O^a	4029.52	2660.94	$4.570 \times 10^{-24(1)}$
E_1	H_2O^b	4030.48	7193.51	$3.285 \times 10^{-34(3)}$
E_1	H_2O^b	4030.49	5949.22	$2.019 \times 10^{-31(3)}$
E_1	H_2O^a	4030.50	4902.61	$9.679 \times 10^{-29(3)}$
E_2	H_2O^b	4030.70	8916.25	$4.788 \times 10^{-37(4)}$
E_2	H_2O^a	4030.73	4889.49	$1.154 \times 10^{-28(3)}$

[a] Values taken from HITRAN 2016 [241]

[b] Values taken from HITEMP 2010 [150]

Uncertainty codes: $^{(1)}$1–2%, $^{(2)}$2–5%, $^{(3)}$10–20%, $^{(4)}$>20%

ficult to target spectrally-isolated transitions. Consequently, absorption features in the more isolated P-branch of CO near 4.98 μm and R-branch of CO_2 near 4.19 μm were chosen for thermochemistry measurements [170, 192]. The absorption spectra of H_2O, which is present throughout most of the infrared, is strongest at the fundamental vibrational frequencies (important for probing short pathlengths). The fundamental band of H_2O near 2.48 μm offers spectral windows of relatively strong well-isolated transitions suitable for LAS sensing [245]. Fig. 6.2 shows simulated spectra of the specific rovibrational lines chosen for CO, CO_2, and H_2O sensing at expected hybrid rocket combustion temperatures and concentrations. Line pairs A and B from CO and line pairs D and E_1 plus E_2 from H_2O are utilized to obtain gas temperature in addition to mole fraction distributions of the flow-field. With the temperature field known, CO_2 mole fraction is then obtained through lines C_1 and C_2. The relevant spectroscopic parameters for the selected transitions, as well as associated uncertainties and source databases, are detailed in Table 6.1.

As discussed previously, the temperature distribution of the flow-field is obtained through CO and H_2O absorption. In order to assess the temperature sensitivity of the line pairs, the linestrengths, $S(T)$, of each transition are plotted in Fig. 6.3. It should be noted that the linestrengths of line E_1 and line E_2 exhibit a very similar temperature dependence; therefore, to simplify the analysis and increase the robustness of the thermometry measurement, the two values were summed and treated as a single transition (i.e. line group E). The same procedure was done for line C_1 and line C_2 (line group C). The temperature sensitivity, $(\mathrm{d}R/R)/(\mathrm{d}T/T)$, of each line pair was evaluated numerically through Eq. 3.8 over the temperature range of interest. The large difference in lower state energies, $\Delta E''$, between the paired transitions (shown in Table 6.1) results in high temperature sensitivity at the expected combustion temperatures, reducing the uncertainty of the resulting profiles obtained from tomographic reconstruction [246].

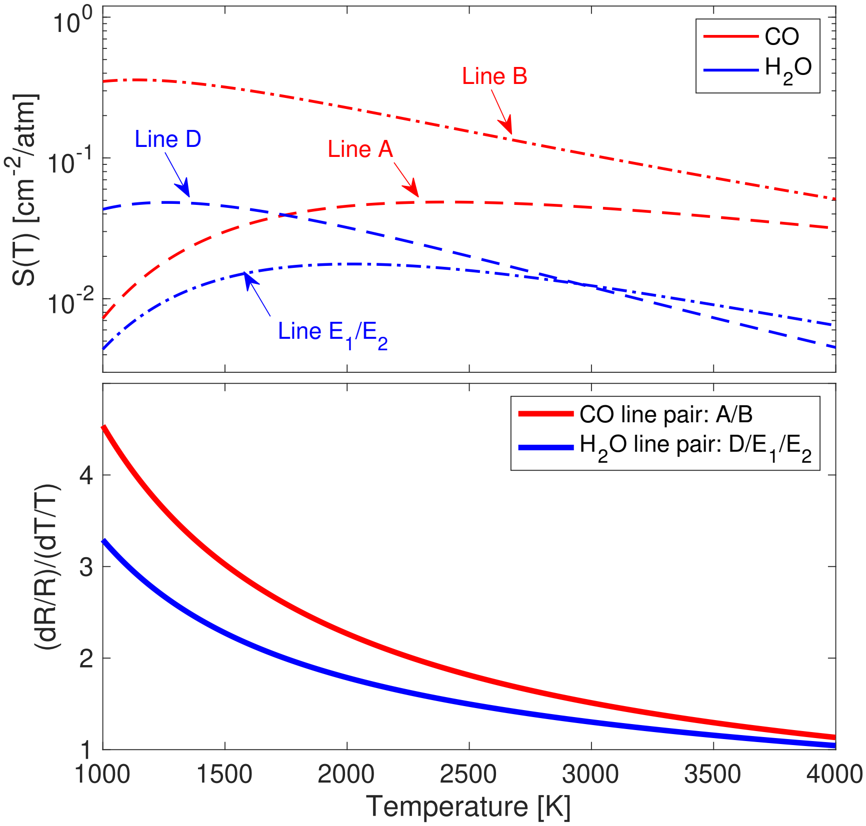

Figure 6.3: Linestrength, $S(T)$, and temperature sensitivity, $(\mathrm{d}R/R)/(\mathrm{d}T/T)$, as a function of temperature for the CO and H_2O line pairs used in this study

6.2.2 Solid fuel oxidation

6.2.2.1 Hybrid combustion

This section details the design of the experimental apparatus used to analyze the combustion behavior of hybrid rocket fuels using the previously discussed spectroscopic method. We first note that caution should be exercised when burning polymers and other materials in pure oxygen as they commonly produce toxic gases in substantial quantities. All experiments shown in this study were located in a high-efficiency low-volume laboratory fume hood (Kewaunee Scientific: Supreme Air LV) that rapidly exhausts the combustion products at a rate of ∼1150 cfm.

Fig. 6.4 illustrates the vertical test stand, which was designed to accommodate solid cylindrical fuel grains with an outer diameter up to 50.8 mm and lengths varying from 25.4 mm to 203.2 mm. The fuel grains can be manufactured to incorporate different fuel port geometries; however, an axially symmetric profile is required for the tomographic reconstruction techniques discussed herein. The setup enables in-situ measurements of the combustion zone by providing an unobstructed optical line-of-sight at the exit-plane of the fuel grain (referred to as measurement plane). In order to minimize the effects of entrainment/thermal boundaries on the measurement, the measurement plane is located within ∼0.5 mm of the fuel-grain exit, and assumed to be primarily determined by upstream flow conditions. Spatially-resolved measurements are obtained by mounting the vertical test stand on a motorized translation stage (Thorlabs NRT100) that moves horizontally at 5 mm/s during the experiment. To conduct measurements at multiple axial locations for a spatially-resolved image, modular blocks can be added/removed to allow different fuel grain lengths to be burned. This also minimizes the amount of optical adjustments between experiments. The mass of each fuel grain and diameter of the exit is measured before and after each test to estimate overall equivalence ratio and regression rate.

During the experiment, gaseous oxygen is introduced into the center of a graphite pre-combustion chamber with an internal diameter of 17.8 mm. The injector exit is located

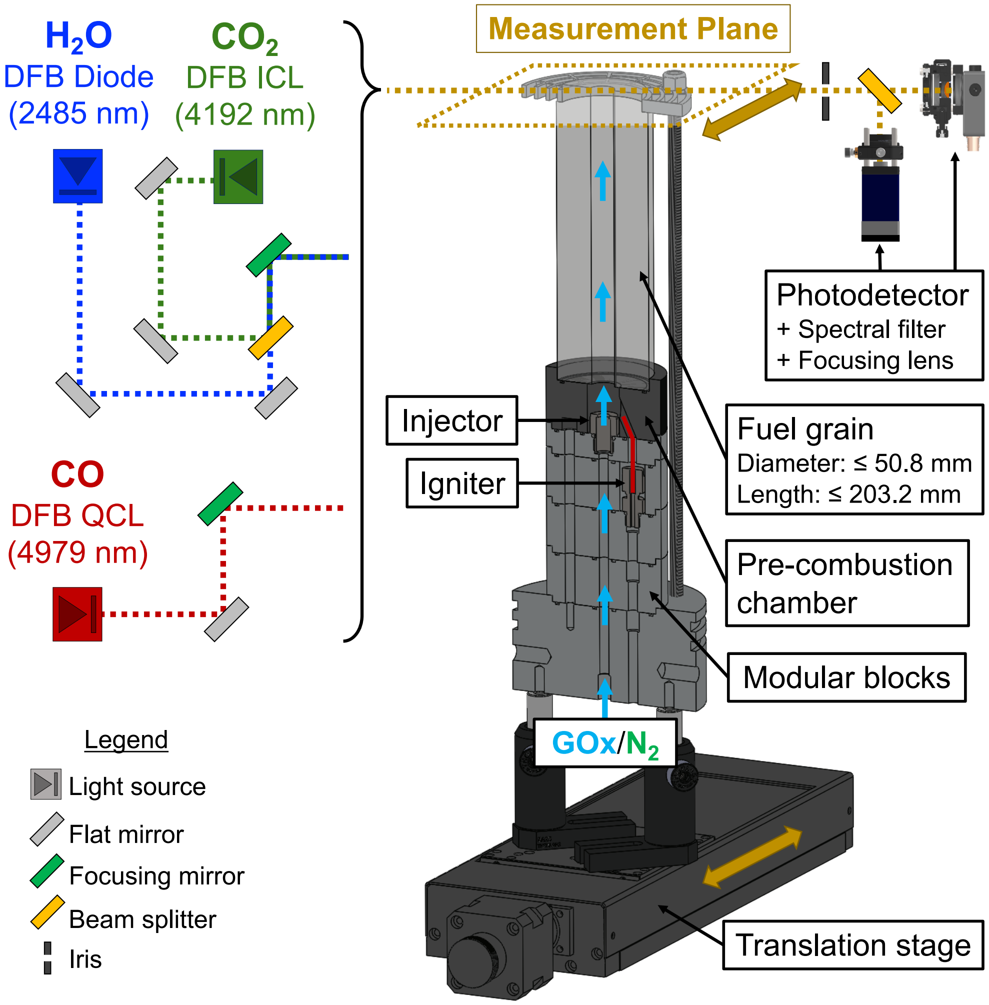

Figure 6.4: Vertical test stand utilized for exit-plane temperature and species measurements. Optical setup is shown for both CO and CO_2/H_2O configurations

15.2 mm from the front end of the fuel grain and is designed to be easily interchangeable to facilitate experiments with different injection geometries. Remote ignition is achieved via an electrical igniter located in the precombustion chamber. After each hot-fire, a gaseous nitrogen (N_2) purge system clears the lines of any excess oxygen and extinguishes the flame. Oxygen and nitrogen flow rates are measured using a sonic orifice ($\varnothing = 1.27$ mm) with a discharge coefficient of $C_\mathrm{d} = 0.85$ and an upstream pressure transducer (Setra 225G), both of which can be interchanged to target different flow rates. Further information on plumbing and instrumentation can be found on the schematic in Fig. 6.5. We note here that all

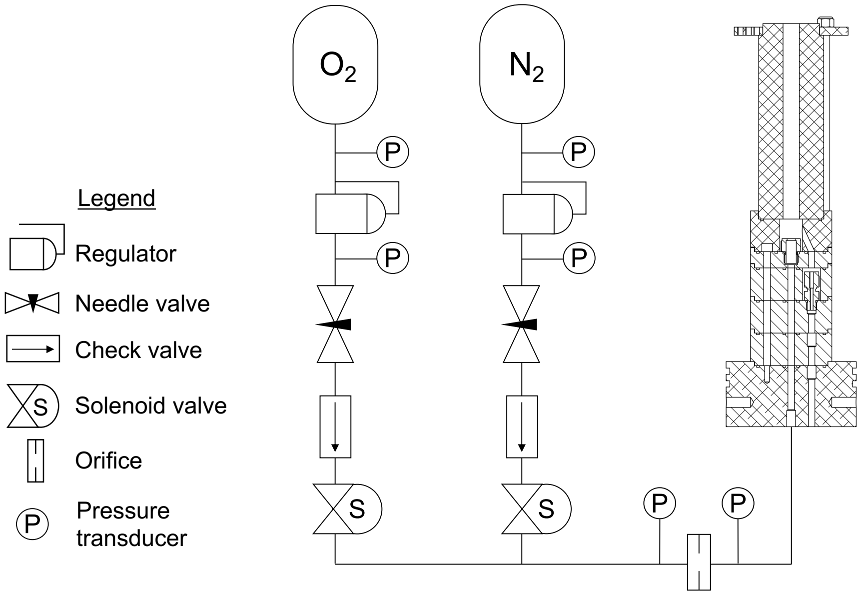

Figure 6.5: Piping and instrumentation diagram illustrating both GOx and N_2 gas delivery systems. Flow rates for all experiments are regulated using a sonic orifice

combustion experiments to date have been conducted at ambient exhaust pressure with no downstream nozzle.

6.2.2.2 Optical interface

Fig. 6.4 illustrates the optical setup designed to interface with the vertical test stand for in-situ thermochemistry measurements. To probe the CO transitions listed in Table 6.1, we utilized a quantum cascade laser centered near 4.98 μm with ~50 mW output power. Similarly, to measure CO_2 and H_2O, an interband cascade laser and a diode laser, both with ~5 mW output power, were used to target features near 4.19 μm and 2.48 μm, respectively. In order to maximize signal-to-noise ratio (SNR), experiments were constrained to two light sources per test, which limits the amount of power loss associated with combining and splitting the wavelengths. Consequently, hot-fires were conducted twice for each condition, alternating between CO and CO_2/H_2O. Test repeatability was confirmed for all experiments and more details are discussed in Sec. 6.3.1.

To facilitate optical alignment, two optical breadboards were used to swap between CO and CO_2/H_2O measurement configurations. High spatial resolution in the radial direction was achieved by pitching the laser beams across the flow-field using a focusing mirror (f = 200 mm) that reduced beam waist. This resulted in a beam diameter of ~0.5 mm that was located within ~0.5 mm of the fuel-grain exit-plane. For the CO_2/H_2O configuration, the light sources were made colinear using a CaF_2 50/50 beam splitter prior to focusing the beam. The transmitted light was then passed through a ~4.0 mm diameter iris to mitigate the influence of thermal emission. For CO measurements, the light was then spectrally filtered (4960 ± 148 nm) before being focused onto a thermo-electrically cooled photovoltaic (PV) detector (VIGO PVI-4TE-5) using a CaF_2 plano-convex lens. For CO_2 and H_2O measurements, the transmitted light was split using another beam splitter. Half of the light was spectrally filtered for CO_2 (4210 ± 42 nm) and focused onto a PV detector (VIGO PVI-4TE-5), while the other half was focused onto a photodetector (Thorlabs PDA10D) that is only sensitive to wavelengths < 2.6 μm, effectively filtering out the longer wavelengths.

6.2.2.3 Test procedure

All of the light sources in this study were scanned in wavelength by modulating the injection current at a frequency of 2 kHz using a sawtooth waveform, as seen in Fig. 6.6. In order to correct for thermal emission during the experiment, each laser was also scanned below its lasing threshold to provide a baseline for the detector. A germanium etalon with a free spectral range of 0.0231 cm^{-1} was used to find the relative frequency in the time domain. Data were collected on a data acquisition card (NI PXI-6115) at a sample rate of 2.5 MHz with every 100 scans binned for averaging and statistical analysis, as detailed further in Sec. 6.2.3.1. For a translational motion of 5 mm/s, 100 scans yield an effective measurement resolution of 0.25 mm in the radial direction (half the beam diameter). Thus, the radial spatial resolution can be approximated by the beam diameter.

Fig. 6.6 illustrates representative transmitted, I_t, and incident intensities, I_0, recorded on each detector. In order to measure I_0 appropriately, background measurements were taken while horizontally translating the test stand—as is done during a hot-fire test—and

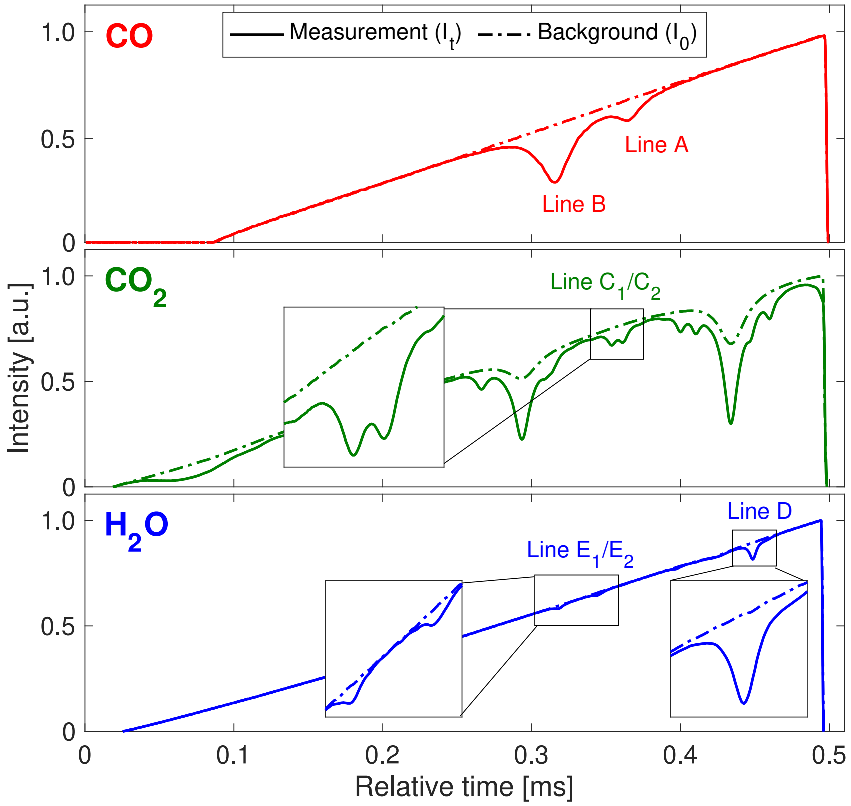

Figure 6.6: Representative direct-absorption scans for targeted CO, CO_2, and H_2O transitions, I_t. The dashed lines indicate the background signals, I_0, taken with the flame off and a N_2 purge through the fuel-grain core

purging N_2 gas through the fuel grain. These background measurements effectively correct for ambient water vapor and/or CO_2 present in the targeted flow field that would otherwise interfere with the transmitted intensity. It should be noted that the selected absorption lines are weakly active at room temperature, thus having little ambiguity when measured in the high-temperature combustion exhaust. Data collection and horizontal translation during a hot-fire test commenced once a repeatable quasi-steady-state was reached (typically < 1 s after ignition). The system was translated 30 mm to ensure measurements over the full combustion zone and aid tomographic reconstruction efforts. Transient effects inherent to hybrid combustion systems were found to be negligible during the measurement time. This, along with test repeatability, is discussed further in Sec. 6.3.1.

In order to demonstrate the optical technique to discern thermochemical changes between different propellants and injection schemes, the aforementioned procedure was conducted to evaluate both PMMA and HDPE fuel grains with two different oxidizer injectors. The oxidizer flow rate was kept constant at 1.2 g/s across these experiments. All of the fuel grains had an outer diameter of 50.8 mm with a 12.7 mm diameter cylindrical port, and spatially-resolved images were obtained by conducting measurements for varying fuel grain lengths from 25.4–139.7 mm in 12.7 mm increments.

6.2.3 Tomographic imaging

6.2.3.1 Spectral line fitting

The measured absorbance, $\alpha(\nu)$, was obtained through Eq. 3.21 using the incident and transmitted light intensities shown in Fig. 6.6. As mentioned previously, the measured absorbance for every 100 scans were averaged prior to calculating the projected absorbance areas, $A_{\mathrm{proj}}(y)$, through Eq. 3.22. This procedure was done throughout the horizontal scan to reduce environmental noise (vibrations, beam steering, etc.) and allowed for statistical analysis of the signals. A 95% confidence interval was obtained for each 100-scan average and was used, along with the reported HITRAN and HITEMP uncertainties in Table 6.1, to propagate uncertainties to the inferred results of temperature and mole fraction.

A Voigt line shape function was least-squares fit to the measured absorbance spectra, as shown in Fig. 6.7, to obtain $A_{\mathrm{proj}}(y)$. The Voigt profile is a convolution of a Lorentzian profile and a Gaussian profile, accounting for both collisional and Doppler broadening, respectively [147]. For the fitting routine, we used an estimated temperature from chemical equilibrium to fix the Doppler width, $\Delta\nu_D$, independently and solved for $A_{\mathrm{proj}}(y)$ and collisional width, $\Delta\nu_C$. The resulting $A_{\mathrm{proj}}(y)$ was then used to calculate a path-integrated temperature using the two-line thermometry technique shown in Eq. 3.28. Afterwards, the Doppler width was recalculated using the path-integrated temperature and this procedure was iterated until the resulting temperature converged. For CO_2, we utilized the projected two-line thermometry

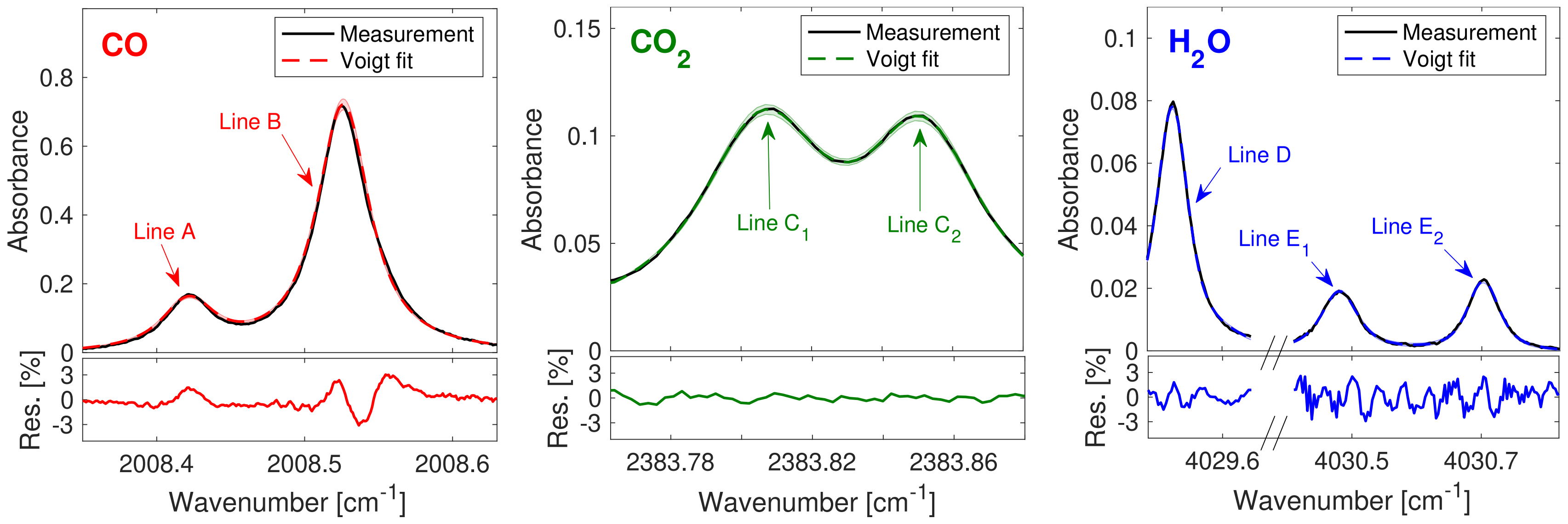

Figure 6.7: Measured absorbance averaged over 100 scans versus wavenumber. The corresponding Voigt fits illustrate a 95% confidence interval of the measured data. Reasonable residuals for each fit confirm appropriateness of a Voigt line shape model

results from H_2O to fix $\Delta\nu_D$. It is critical to note that the temperature used for $\Delta\nu_D$ is simply a line-of-sight value averaged over the path-length, not a radially-resolved measurement.

For several of the line fits, the absorbance data was truncated in the wavelength domain to avoid biasing influence of neighboring lines (this can be seen in the spectral windows of Fig. 6.7). Moreover, due to direct overlap of multiple transitions at several of the line positions (see Fig. 6.2) and the thermochemical gradients along the lines of sight, it should be noted that the lineshapes are not expected to strictly follow a Voigt profile. However, fitting the lines with a Voigt function proved to be an efficient approach for recovering projected line areas and separating the overlapping areas of the more prominent features with relatively low residual error [185, 242]. We note that the fractional residual was typically less than 3% for CO, less than 2% for CO_2, and less than 3% for H_2O, supporting the appropriateness of the Voigt line fitting routine for this application.

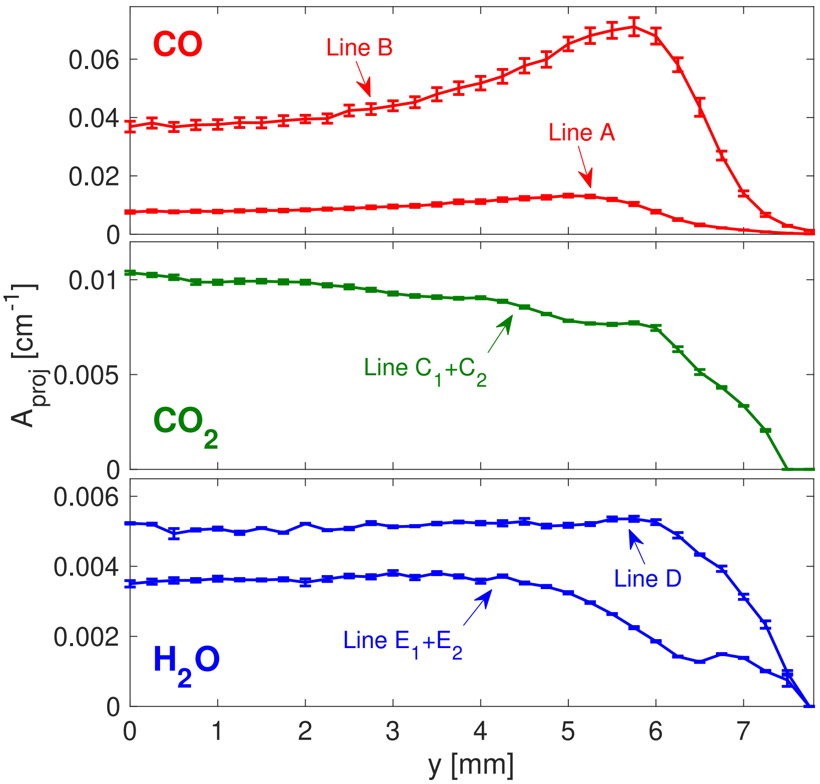

Figure 6.8: Projected absorbance areas, $A_{\text{proj}}(y)$, for the targeted lines at discrete distances, y, from the center of the fuel grain ($y = 0$ mm)

6.2.3.2 Data inversion

After fitting the absorbance spectra, we obtained projected absorbance areas, $A_{\text{proj}}(y)$, at every fuel grain length. Fig. 6.8 illustrates $A_{\text{proj}}(y)$ for each transition as a function of distance, y, from the center of the fuel grain ($y = 0$ mm) for a length of 139.7 mm. It should be noted that the projected absorbance areas of line C and line E represent the sum of the individual contributions from multiple transitions, as discussed in Sec. 6.2.1. To determine the center of the fuel grain, measurements were taken across the entire reaction zone and the results for $A_{\text{proj}}(y)$ were mirrored and averaged about $y = 0$ mm. Notably, minimal differences were observed when mirroring the results for each experiment, confirming axisymmetry of the burn profile and quasi-steady operation during the measurement time.

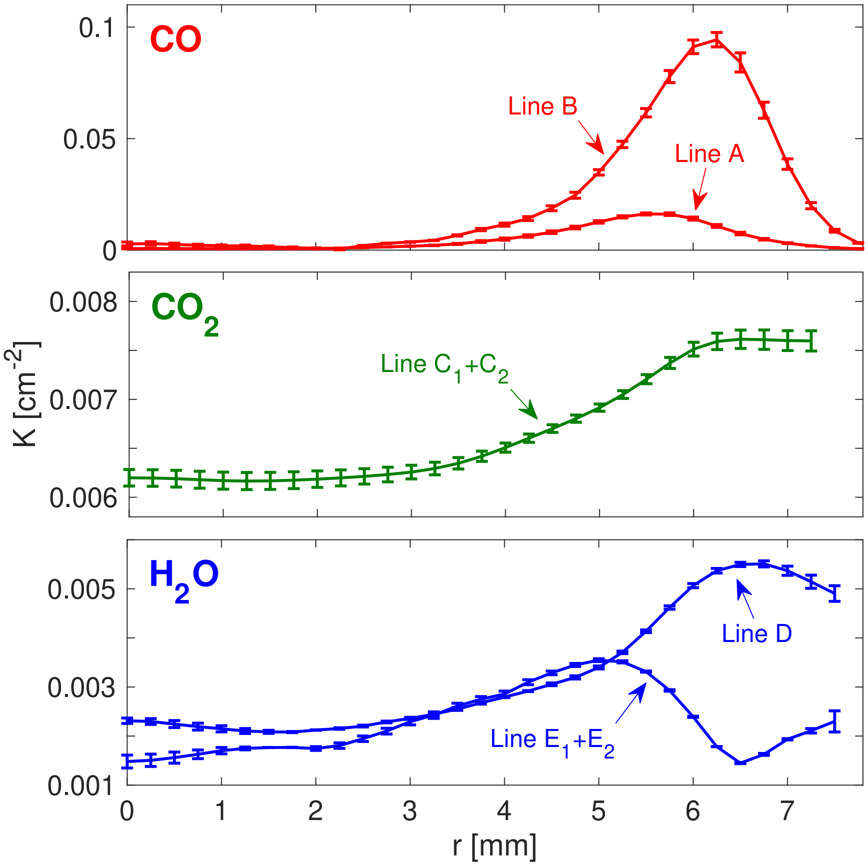

Figure 6.9: Abel-inverted integrated absorption coefficient, $K(r)$, for the targeted lines versus radial distance, r, from the center of the fuel grain ($r = 0$ mm)

Once $A_{\text{proj}}(y)$ was known, the Tikhonov-regularized Abel inversion scheme discussed in Sec. 3.3.3 was implemented to obtain radially-resolved profiles of the integrated absorption coefficient, $K(r)$. Fig. 6.9 illustrates $K(r)$ for each transition at a fuel grain length of 139.7 mm. With $K(r)$ known, radially-resolved thermochemical flow-field properties were obtained through Eq. 3.28 and Eq. 3.29.

6.3 Results

6.3.1 Experiment repeatability

As discussed in Sec. 6.2.2.2, hot-fire tests were limited to two light sources per test; therefore, each experimental condition was tested twice, alternating between CO and CO_2/H_2O optical measurements. Test repeatability was evaluated using two independent methods. First, $A_{\text{proj}}(y)$ measurements were compared for multiple tests targeting the same condition (with the same laser configuration), shown in Fig. 6.10, demonstrating that measurements from separate hot-fire tests can produce repeatable results within the associated uncertainties. The Pearson correlation coefficient, ρ, between these two experiments was calculated to be $\rho > 0.97$ for both CO_2 and H_2O transitions, indicating highly correlated results [247].

The second method for confirming test-to-test repeatability and measurement consistency compares CO and H_2O thermometry results for two hot-fires at the same condition. Fig. 6.11 illustrates the radially-resolved temperature fields obtained from each species at two different fuel grain lengths, each tested twice with different laser configurations. Temperature from both species show good agreement within experimental uncertainty, further reinforcing the repeatability of this experiment.

6.3.2 Thermochemistry measurements

Example radially-resolved profiles of temperature and species for PMMA/GOx propellants with a single-port injector geometry are shown in Fig. 6.11. As discussed in the previous section, the temperature field was obtained from both CO and H_2O (top of Fig. 6.11) to

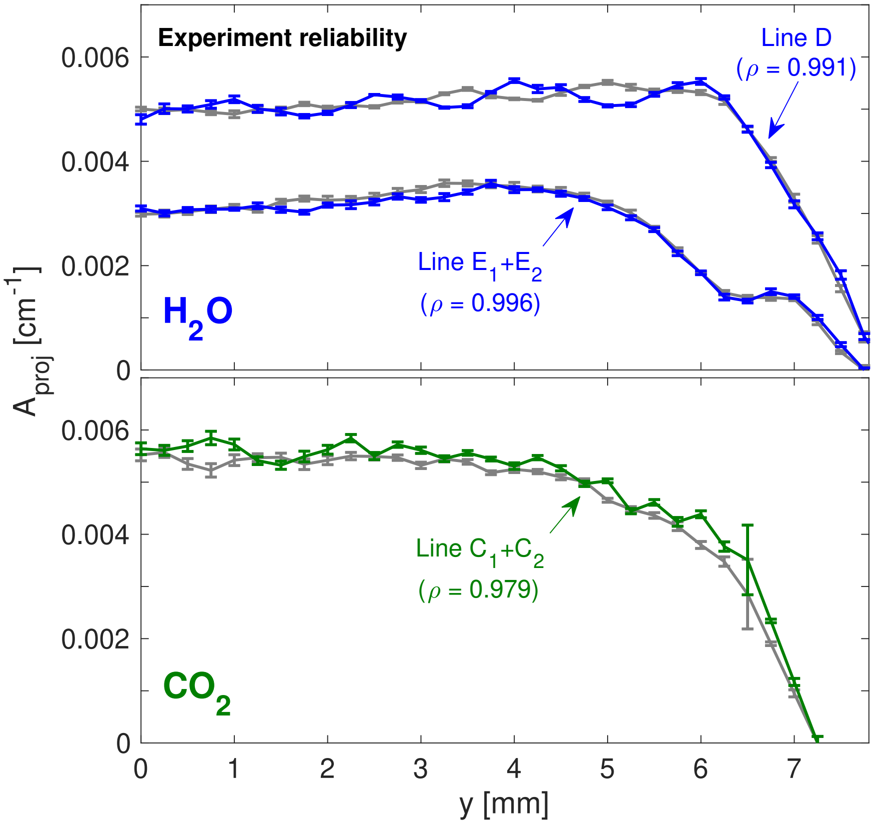

Figure 6.10: Measured projected absorbance areas, A_{proj}, for H_2O and CO_2 transitions from two experiments (gray and color) to demonstrate test-to-test reliability. High Pearson correlation coefficient ($\rho > 0.97$) indicates reliable measurements

ensure consistency between repeated experiments and build confidence in the thermometry measurements. Unlike H_2O, there was minimal CO present in the core ($r = 0$ mm) of this flow-field due to oxidation to CO_2; therefore, CO thermometry could not be obtained throughout the entire radial domain (typical of the shorter axial distances). However, where CO is sufficiently abundant, the two independent temperature measurements exhibit very good agreement. The top of Fig. 6.11 also illustrates thermochemical variation of the radial profiles with fuel grain length. As combustion progresses along the axis of flow, the peak temperature in the flow-field remains fairly constant (as expected with a diffusion flame), but the core temperature increases as a result of mixing and the reaction layer growth. These one-dimensional radial profiles highlight the granularity of the results which can be

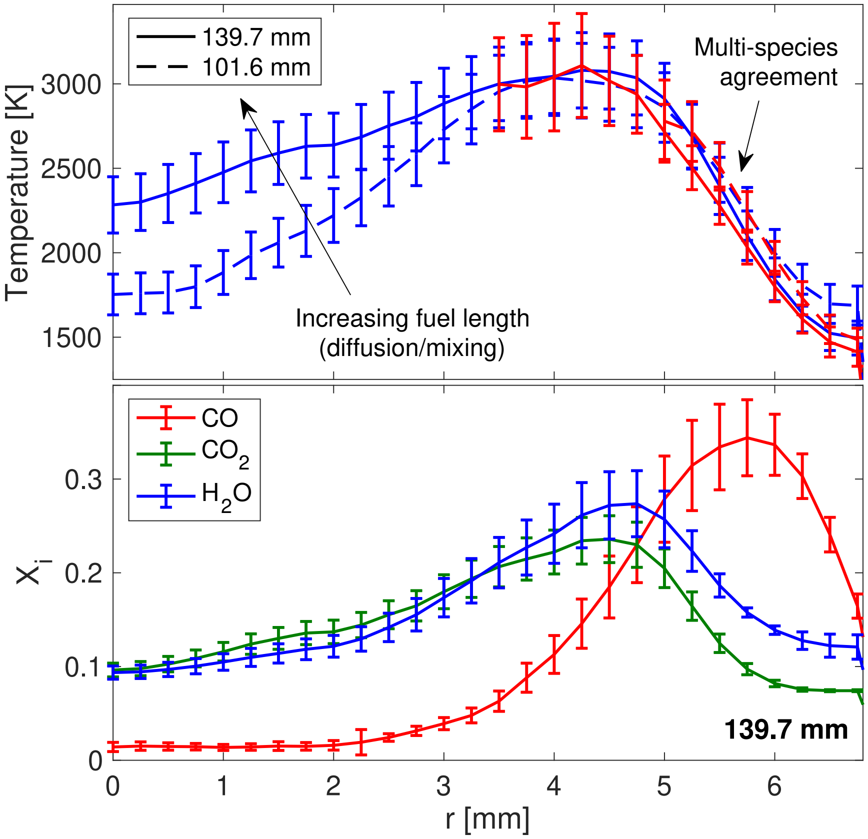

Figure 6.11: *Top*: Radially-resolved CO and H_2O temperature profiles measured using two-line thermometry for two fuel grain heights with single-port injection. *Bottom*: Radially-resolved CO, CO_2, and H_2O mole fraction profiles obtained using the measured temperatures

compared to numerical multi-physical models.

When possible, thermometry results from both species were averaged to determine radially-resolved species profiles. When only H_2O thermometry was available, as in Fig. 6.11, H_2O temperature was used for all speciation results. The bottom of Fig. 6.11 shows CO, CO_2, and H_2O mole fractions at a fuel grain height of 139.7 mm. CO is both an intermediate and product species in rocket applications, forming in large quantities owing to typically fuel-rich operation. This duality is pronounced in hybrid combustion, where the reaction zone is typically characterized as a diffusion flame, resulting in a wide range of effective equivalence ratios in the spatial domain. Fig. 6.11 clearly illustrates the physics involved, as CO peaks rather quickly near the fuel grain wall ($r \approx 6.8$ mm), where combustion can be considered fuel-rich. Towards the core, CO oxidizes and forms CO_2, defining a heat release boundary where the peak temperature in the flow-field occurs. Further away from the fuel grain surface, both H_2O and CO_2 mole fractions peak. Within the core of the flow, combustion is sufficiently fuel-lean that CO fully oxidizes and CO_2 mole fraction surpasses H_2O. All product species are further diluted by oxygen in the core flow.

The uncertainties in the temperature and mole fraction profiles have been determined by propagating systematic uncertainties in spectral properties (i.e. linestrength) and using a 95% confidence interval on the measured absorbance. Further details on the calculation of uncertainties are discussed in the Appendix A.4, Appendix A.6, and the Appendix of Wei et al. [185]. Typical temperature uncertainties were approximately ±100 K near the fuel grain wall and up to ±200 K near the core, while typical mole fraction uncertainties were approximately 5% near the fuel grain wall and up to 10% near the core. Error bars have been added to Fig. 6.11 to illustrate these estimated uncertainties in the spectroscopic method.

To better visualize the thermochemical structure of the solid-fuel reaction layer, Fig. 6.12 depicts an assembly of the single-plane measurements at different axial distances to form two-dimensional images for some example test conditions. Temperature and species (CO, CO_2, and H_2O) results are shown for PMMA/GOx propellants with a single-port injector geometry. Additionally, to highlight the technique's ability to discern mechanistic influences on the reaction layer growth, CO mole fraction results are also shown for an HDPE/GOx propellant combination with an axial showerhead injector geometry. The two cases were conducted with an equivalent oxidizer mass flux and all speciation images are shown on the same scale for purposes of comparison.

Consistent with the previously shown radial profiles (Fig. 6.11), temperature is observed in these 2D images to both increase in magnitude and diffuse/mix into the fuel grain core along the central axis of oxidizer flow. This is also observed in all the species measurements, although diffusion into the core is less pronounced in CO mole fraction results. For the single-port injector, the temperature in the core of the flow stays relatively low (compared to the peak temperature) and nearly all the species are contained in a thin region near

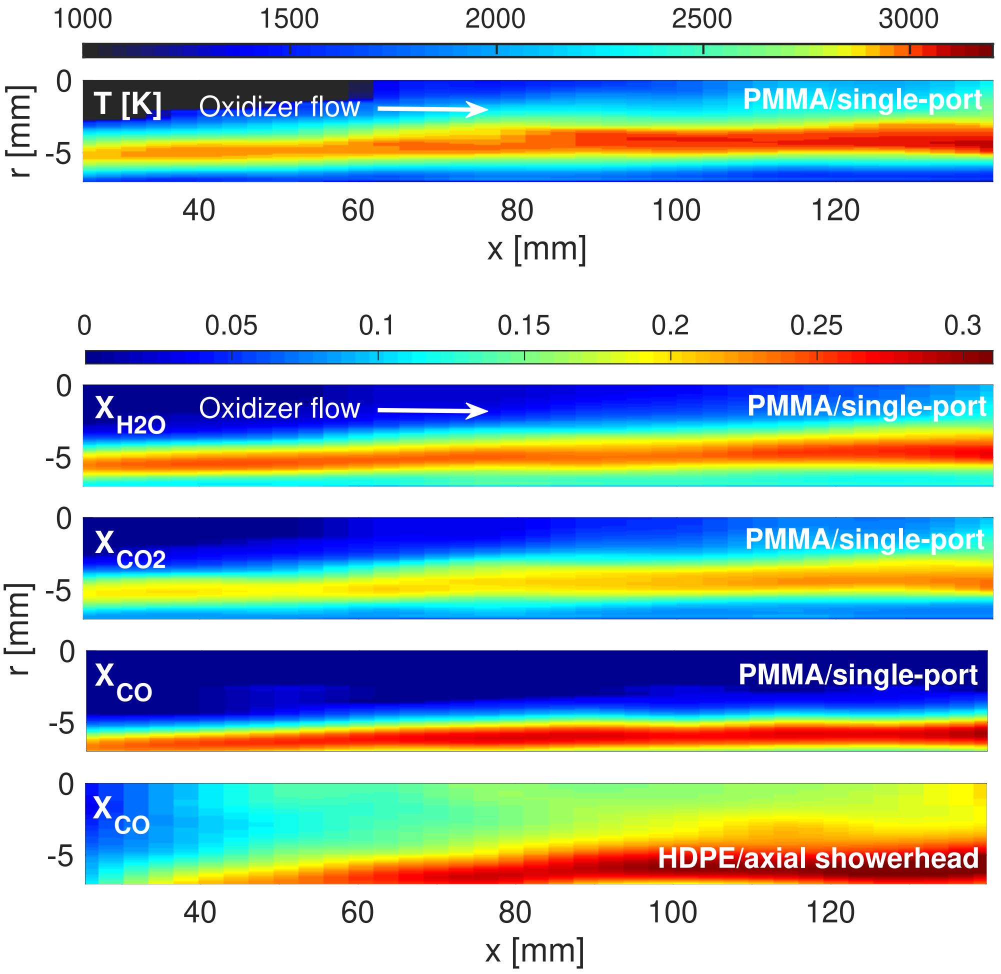

Figure 6.12: Two-dimensional thermochemistry measurements demonstrating combustion progress for PMMA/GOx with a single-port injector geometry. Results for HDPE/GOx with an axial showerhead injector shown to highlight differences in combustion physics

the fuel surface over the range of lengths considered here. Most of the chemical reaction occurs in this region, which is representative of the flame location in the flow-field. The cool oxidizer core indicates that much of the oxidizer propellant is not participating in the reaction, resulting in lower combustion efficiencies in practical applications. By contrast, when comparing a different propellant combination (HDPE/GOx) with an axial showerhead injector, there is significantly more CO present in the core, indicating a larger mixing layer and better oxidation of the fuel per unit axial length. These results suggest that there is a characteristic downstream distance for attaining complete combustion and it is highly dependent on propellant combination and oxidizer injection configuration.

This prompted the investigation of oxidizer injector influence on hybrid-propellant rocket combustion. The aforementioned techniques were used to compares two canonical hybrid rocket oxidizer injector designs via spatially-resolved measurements of temperature and mole fractions of CO, CO_2, and H_2O. The two test cases were conducted at the same oxidizer mass flow rates to isolate the influence of injector design. Dramatic differences between the thermochemical flow-fields of the two injectors were observed and are shown in Fig. 6.13 and Fig. 6.14. Fig. 6.13 shows the radial spatial evolution of the temperature and species (CO, CO_2, H_2O) field for both injector designs at multiple downstream distances. The radial distance associated with the boundary of the gaseous core and fuel grain surface involves some ambiguity due to phase-change and the lack of combustion products in the initial fuel pyrolysis, but is estimated to be within 0.5–1 mm of the termination of the data array, supported by post-test measurements of grain diameter. The right side of Fig. 6.13 plots equilibrium temperature and species versus equivalence ratio, ϕ, for PMMA/GOx combustion at atmospheric conditions for reference. While equivalence ratio is determined globally by the fixed oxidizer mass flux and corresponding burn rate, it is expected that the developing reaction layer is characterized by a range of local equivalence ratios. Of most immediate note, it is observed that the maximum expected equilibrium temperature over the range of ϕ ($T_{eq} \approx 3060$ K), matches very well with the local maxima of each radial profile, with the exception of the lowest axial distances for the single-port injector, wherein the combustion zone appears to be developing and is likely diluted. For both injector designs, there is a progressive shift of the local maximum temperature towards the core with increasing axial distance, representative of radial diffusion and mixing. However, the two injectors exhibit distinct radial profiles, with higher core temperatures (at $r = 0$ mm) observed at much shorter axial distances for the showerhead injector relative to the single-port injector, suggesting that the core flow remains lean for the single-port at longer axial distances.

Similar to the temperature fields, all product species (CO, CO_2, H_2O) appear to diffuse radially inward with increasing axial length. When comparing the two injector designs,

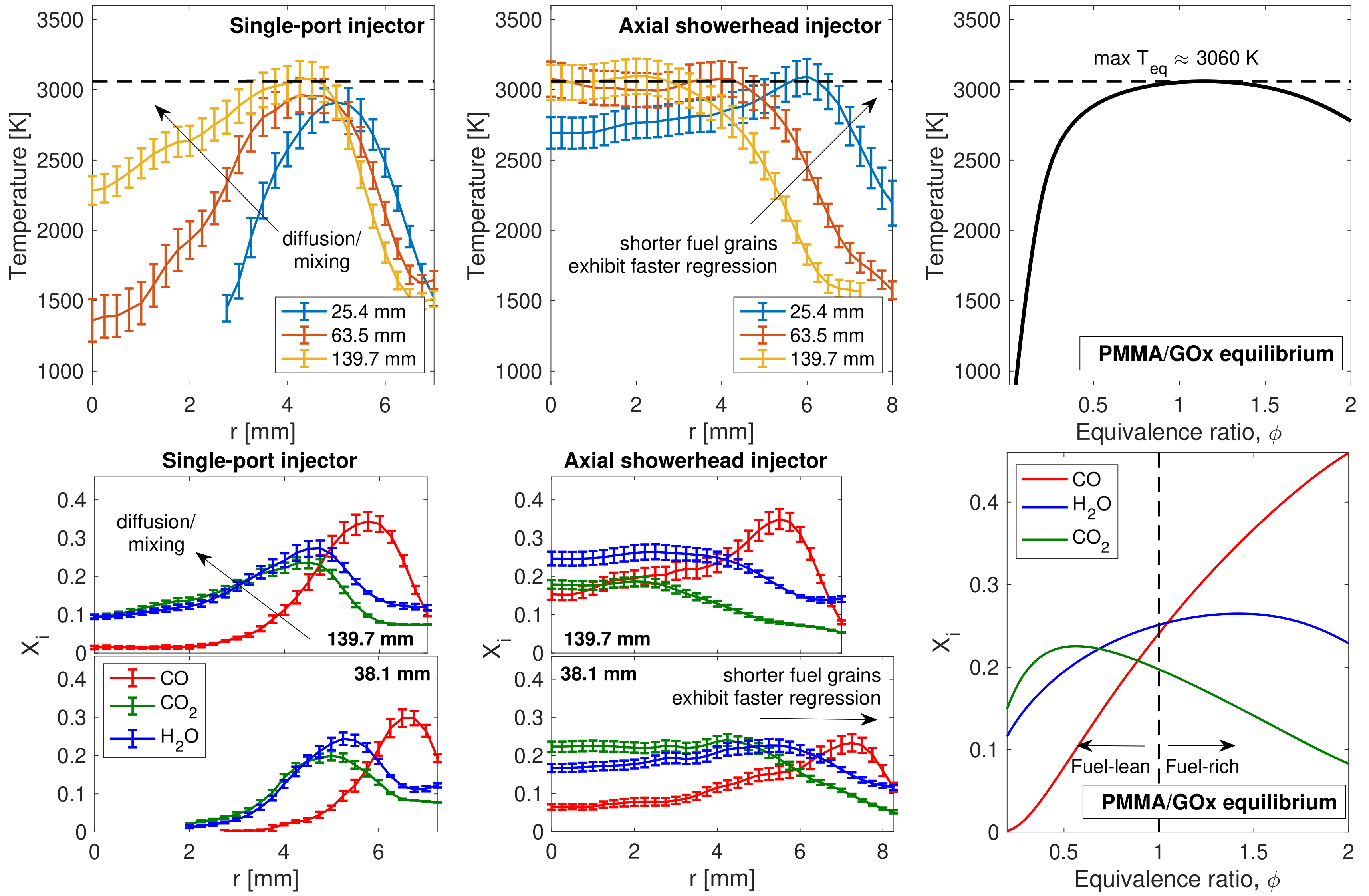

Figure 6.13: Comparison of measured temperatures and mole fractions for the single-port and axial showerhead injectors. Chemical equilibrium temperature and mole fractions versus equivalence ratio, ϕ, are shown for PMMA/GOx combustion

the showerhead injector shows an increased presence of combustion species in the core of the flow-field at any given axial distance, while the species distributions for the single-port injector peak closer to the fuel surface. The relative magnitudes of the species mole fractions are also notable. For CO and H_2O, the peak mole fraction and width of the distribution tends to increase with increasing fuel-grain length. This trend is similar for CO_2 with single-port injection, but differs with the showerhead design. Though the radial distribution of CO_2 for the showerhead injector suggests a high relative abundance, peak CO_2 mole fraction is observed to decrease as fuel-grain length increases. Quantitative mole fractions are also compared with the equilibrium values at varying equivalence ratios.

The mole fraction magnitudes for all measurements are within the range expected from chemical equilibrium. The species measurements for the single-port injector well-represent a radial distribution of varying local equivalence ratios, with a fuel-lean region in the core due to high oxidizer dilution and a fuel-rich region closer to the fuel-grain surface. Approaching the fuel-grain surface, CO peaks and higher concentrations of H_2O are present when compared to CO_2, as anticipated from fuel-rich chemical equilibrium. Towards the oxidizer core, CO_2 and H_2O peak and CO decreases as it is oxidized to CO_2. Within the core of the flow, combustion is sufficiently fuel-lean such that CO fully oxidizes and CO_2 mole fraction surpasses H_2O. This cross-over (CO_2 mole fraction exceeding H_2O mole fraction) is observed in the chemical equilibrium simulation at an equivalence ratio of approximately $\phi = 0.65$. All product species are further diluted by oxygen in the core flow. When comparing the two fuel-grain lengths (38.1 mm and 139.7 mm) using the single-port injector, the species-distribution is observed to behave very similarly, albeit with slightly higher peak magnitudes and a distribution shift towards the core at the longer axial position. The cross-over of the CO and H_2O mole fractions, which corresponds to near stoichiometric fuel to oxidizer balance ($\phi = 1$), shifts from $r = 6$ mm at $x = 38.1$ mm to $r = 5$ mm at $x = 139.7$ mm.

For the axial showerhead injector, the radial variation of species (at the same axial distances) is considerably diminished relative to the single-port injector distributions. This is most evident in the core of the flow ($r = 0 - 4$ mm), where the species concentrations are relatively constant. Some radial variation remains near the fuel-grain boundary. The showerhead injector flow-field reveals a more distinct axial change in mole fractions. Specifically, the CO and H_2O mole fraction distributions increase in magnitude, while CO_2 mole fraction decreases with increasing fuel-grain length. This is consistent with a reduction in the global O/F as the fuel-grain length increases due to additional fuel regression and constant oxidizer mass flow rate. Lastly, the radial scales for the plots in Fig. 6.13 are different, reflecting greater aggregate fuel regression with the showerhead injector and a larger axial variation in regression rate.

The two-dimensional images for the single-port injector indicate that the temperature in the core of the flow stays relatively low (compared to the peak temperature) and nearly all the species are contained in the thin boundary layer region near the fuel surface. Over the range of lengths considered here, most of the chemical reaction occurs in this region, which grows in width and shifts slightly towards the core as axial distance increases. The relatively cool core and lack of combustion product species near $r = 0$ mm indicates that much of the oxidizer propellant is not participating in the reaction even at the furthest axial distance. Conversely, the axial showerhead injector achieves a core temperature near the maximum equilibrium temperature at a relatively short fuel-grain length ($x < 50$ mm) and it is sustained throughout the rest of the axial distance. An axial progression of O/F from fuel-lean to fuel-rich is noticeably evident. At lower fuel-grain lengths where the O/F is high (fuel-lean), CO_2 mole fraction dominates, followed by H_2O and trace amounts of CO. As combustion progresses and fuel is added axially, the O/F reduces and the concentration of CO_2 decreases while concentrations of both H_2O and CO continue to increase. The incremental addition of CO appears primarily from radial diffusion. It should also be noted that as the highly fuel rich near-surface boundary layer grows, the lowest temperatures are seen near the wall. Overall, the results presented here serve as a demonstration that the method developed in this work can be utilized to elucidate combustion physics for a solid fuel in a gaseous oxidizer cross-flow by capturing quantitative, spatially-resolved species and temperature fields in the reaction layer.

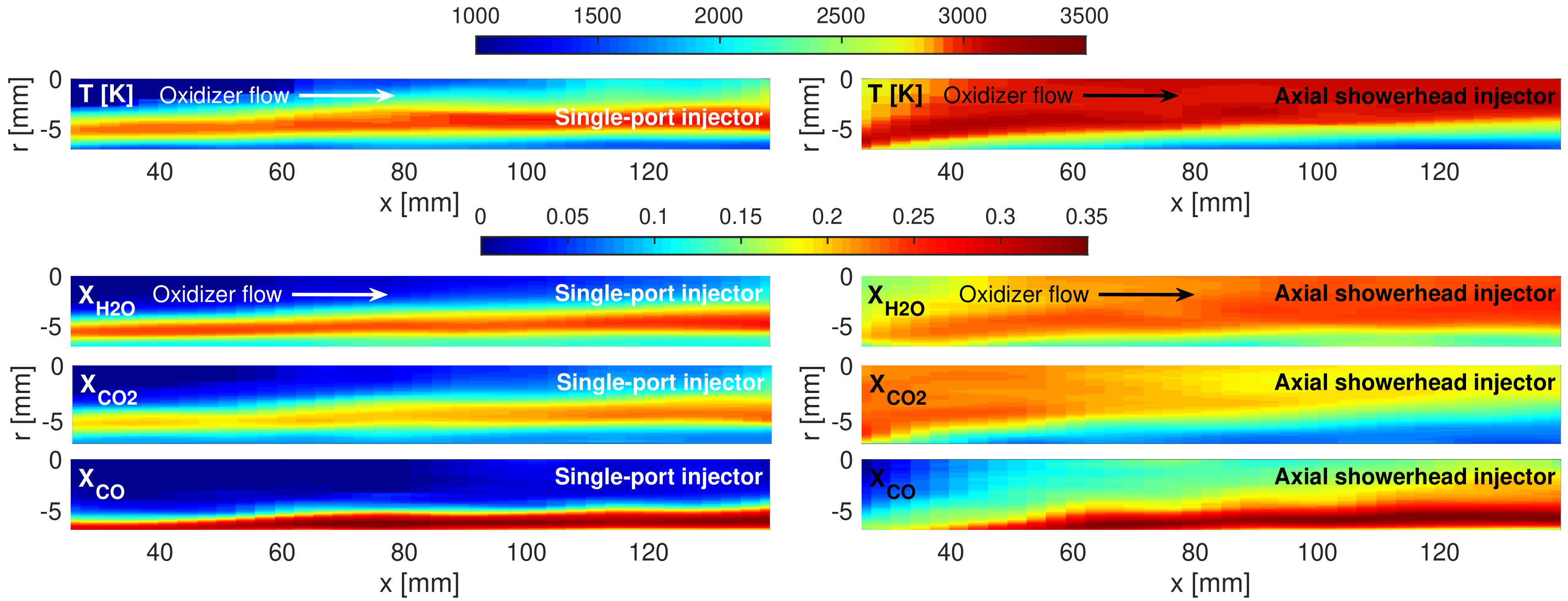

Figure 6.14: Two-dimensional thermochemistry measurements comparing PMMA/GOx combustion progress for a single-port injector (*left*) and an axial showerhead injector (*right*). The fuel-grain core is located at $r = 0$ mm and the fuel-grain surface is located at $r \approx -6.8$ mm

6.3.3 Spatially-resolved combustion performance

The thermochemistry results in the preceding section provide significant insight into hybrid rocket combustion physics and highlight the performance impacts of different hybrid rocket injector designs. To better quantify the differences in combustion performance, the thermochemistry measurements in Fig. 6.13 and Fig. 6.14 can be used to determine spatially-resolved characteristic velocity. As discussed in Sec. 1.3, characteristic velocity c^*, is the primary parameter used to assess propellant combustion performance in chemical propulsion systems. Typically c^* is determined through chamber pressure P_c and propellant mass flow rate $\dot{m}_p$ measurements:

$$c^* = \frac{P_c A_t}{\dot{m}_p} = \sqrt{\frac{R_u T_c}{\mathscr{M}\gamma}\left(\frac{\gamma+1}{2}\right)^{\dfrac{\gamma+1}{2(\gamma-1)}}} \tag{6.1}$$

However, chamber pressure and mass flow rate are more global parameters that do not capture more complex combustion processes; especially, in hybrid rockets, where fuel and oxidizer are stored in separate states–resulting in high spatial gradients in thermochemical properties. Consequently, pressure and mass flow rate do little to inform the specific loss mechanisms that may lead to low combustion performance. To provide a more granular approach for measuring c^* efficiency, spatially-resolved thermochemistry measurements can be used to better reflect chemical-to-thermal energy conversion in these combustion devices.

As shown in Eq. 6.1, knowledge of temperature (T_c) and species ($\mathscr{M}$, γ) can be used to evaluate c^*. Spatially-resoled temperature is obtained directly from the spectroscopic measurements described previously (shown in Fig. 6.13). The local molecular weight $\mathscr{M}(r)$ and the specific heat ratio $\gamma(r)$ distributions are determined by comparing the measured CO, CO_2, and H_2O mole fractions to expected values from chemical equilibrium of PMMA and gaseous oxygen combustion. Fig. 6.15 illustrates the distribution in species mole fractions, molecular weight, and specific heat ratio at chemical equilibrium for a range of equivalence ratios at the hybrid rocket conditions where spectroscopic measurements were obtained. Using the spatially-resolved CO, CO_2, and H_2O measurements in Fig. 6.13, a local equivalence

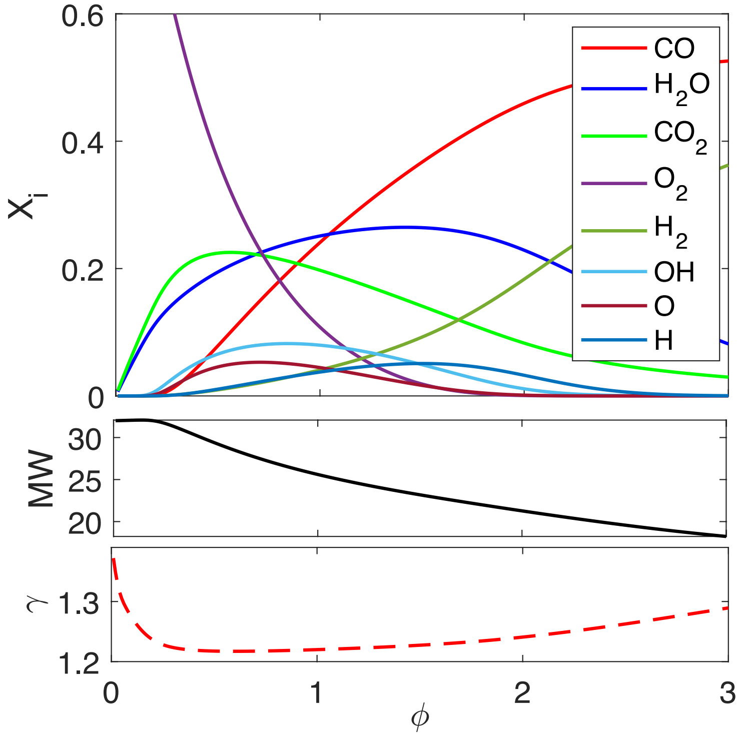

Figure 6.15: Expected species mole fractions, molecular weights, and specific heat ratios at chemical equilibrium versus equivalence ratio for combustion of PMMA and gaseous oxygen

ratio $\phi(r)$ (assuming local chemical equilibrium) can be established as a function of radial distance r. With local equivalence ratio known, radially-resolved molecular weight $\mathscr{M}(r)$ and specific heat ratio $\gamma(r)$ can be determined–enabling c^* to be calculated directly from Eq. 6.1.

Fig. 6.16 shows radially-resolved c^* for both single-port and axial showerhead injectors at various downstream distances obtained using the aforementioned technique. Similar to the spatially-resolved thermochemistry measurements, an increase in combustion performance is observed as downstream distance from the injector increases. This trend is more subtle in the axial showerhead injector, which attains peak combustion performance earlier on. For the single-port injector, combustion performance peaks near $r \approx 5$ mm and decreases near the core. The local maxima in combustion performance was found to occur at a similar radial distance as the peak combustion temperature, per Fig. 6.13. For the axial showerhead injector, combustion performance also peaks near $r \approx 5$ mm; however, performance is sustained

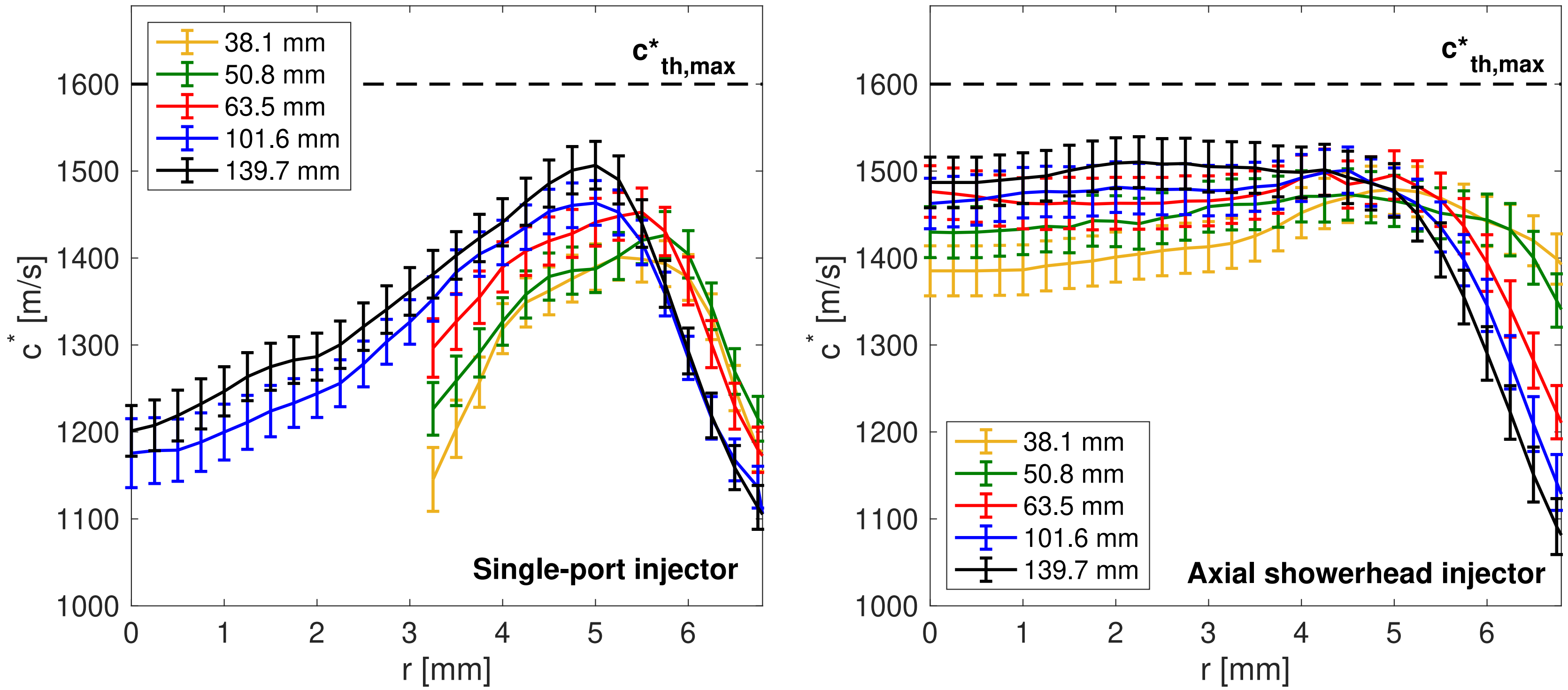

Figure 6.16: Spatially-resolved c^* measurements for the single-port and axial showerhead injector geometries compared to the maximum theoretical value obtained from chemical equilibrium

throughout the core of the flow-field. Additionally, the measured c^* values can be compared to the theoretical maximum performance given by chemical equilibrium, $c^*_{\text{th,max}} = 1600$ m/s. Notably, all of the measured c^* values are below $c^*_{\text{th,max}}$, as expected; however, the axial showerhead injector demonstrates c^* values slightly closer to $c^*_{\text{th,max}}$, indicating better combustion performance. The radially-resolved c^* measurements in Fig. 6.16 can be compiled into two-dimensional images, as shown in Fig. 6.17, to better illustrate differences and highlight trends in combustion performance. Similar to the temperature distribution, Fig. 6.17 shows how c^* peaks in a rather thin region of the flow-field for the single-port injector. This is highly undesirable for hybrid rocket systems as it ultimately results in a longer combustion chamber (added mass) to obtain the desired performance. In contrast, the showerhead injector demonstrates higher performance–closer to $c^*_{\text{th,max}}$–throughout the majority of the flow-field. This demonstrates the significant impact oxidizer injector geometry/design can have on combustion performance and highlights the techniques ability to discern mechanistic losses in hybrid rocket combustion devices.

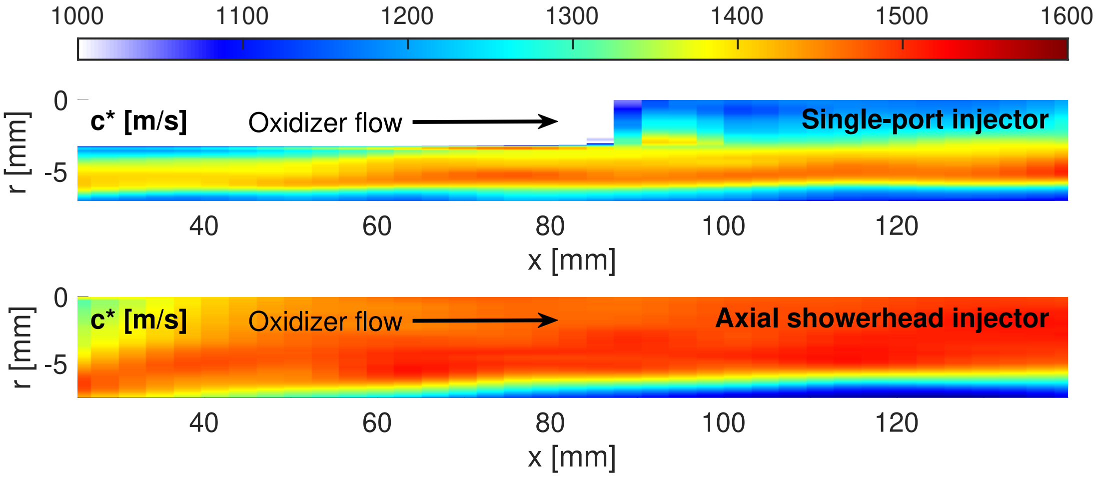

Figure 6.17: Two-dimensional c^* measurements comparing PMMA/GOx combution performance for single-port and axial showerhead injector designs. The fuel-grain core is located at $r = 0$ mm and the fuel-grain surface is located at $r \approx -6.8$ mm

6.4 Summary

This work details the development of an in-situ absorption spectroscopy method enabling quantitative, spatially-resolved temperature, species (CO, CO_2, H_2O), and characteristic velocity (c^*) measurements for studies of hybrid rocket fuel oxidation. The method involves a novel combination of multi-species infrared laser absorption spectroscopy, a modular solid fuel oxidation experiment, and tomographic data processing to facilitate the unique application. For the spectroscopic strategy, strong and well-isolated rovibrational transitions of the target molecules are selected to provide for species-specific detection over a wide range of equivalence ratios and at the short optical pathlengths of the reaction layer. Line-pairs were selected for sensitive thermometry for CO and H_2O within the scan range of available semi-conductor lasers. An experimental apparatus with cylindrical fuel geometry and central oxidizer flow was mounted to a horizontal translation stage to enable scanning of the laser beams across the exit-plane of the fuel grain during a hot-fire test to collect spatially-resolved absorption data. An Abel inversion with Tikhonov regularization was used to process the line-of-sight absorption data and produce radially-resolved temperature and species profiles for a given fuel grain length. Planar measurements at different distances from the oxygen injector were compiled to form two-dimensional images of the thermochemical structure of the oxidation layer. Example results are shown for two propellant combinations and two injector geometries as a demonstration to highlight sensitivity of the method to changes in experimental parameters. To the authors' knowledge, these results are the first in situ quantitative 2D measurements of temperature, species (CO, CO_2, H_2O), and c^* in the oxidation layer of a hybrid rocket fuel. It is envisioned that the method can be used to constrain complex multi-physics models of solid-fuel oxidation and inform design considerations for hybrid rocket motors.

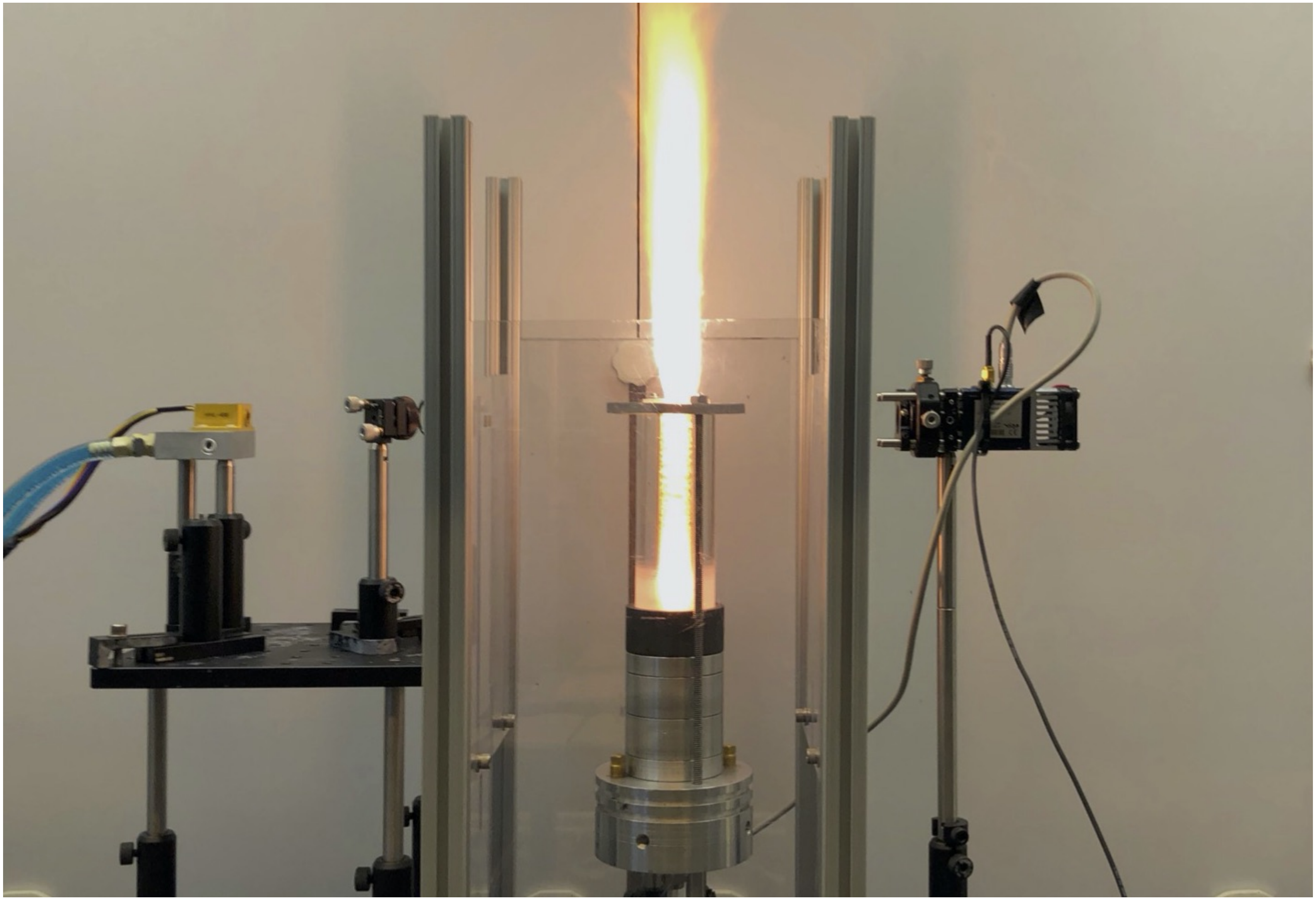

Figure 6.18: Hot-fire of the hybrid-propellant rocket combustor where optical measurements were conducted. Image illustrates a test with PMMA/O_2 propellant combination

CHAPTER 7

Line-mixing effects in the infrared spectral bandheads of CO at high temperatures and high pressures

The contents of this chapter have been published in the journal ***Journal of Quantitative Spectroscopy and Radiative Transfer*** *under the full title 'Line mixing in the $v(1 \rightarrow 3)$ first overtone bandhead of carbon monoxide at high temperatures and pressures' [219].*

7.1 Introduction

Carbon monoxide (CO) is an important molecule in both atmospheric and combustion chemistry. Absorption spectroscopy of CO is relevant in ground-based measurements (e.g. smog regulations) of on-road vehicle emissions [248], satellite-based remote sensing of pollutants for climate science [249], time-resolved characterization of combustion dynamics [250], and thermal radiation modeling in the development of planetary entry and propulsion systems [251]. In all such cases, accurate spectroscopic data with appropriate thermodynamic scaling across relevant conditions provides a basis for quantitative simulation and analysis. This work experimentally investigates the CO spectra near 2.3 μm at high-temperature conditions relevant to combustion and planetary entry over a broad range of pressures (up to 60 atm), with the goal of developing an accurate model of the target spectral domain capturing relevant collisional effects.

Notably, the first overtone band of CO near 2.3 μm has been utilized extensively for combustion gas sensing via laser absorption methods. Several works have targeted rovibrational transitions in the $v(0 \rightarrow 2)$ band for CO measurements to monitor syngas composition

(T < 400 K, P < 20 atm) [252] and combustion-based power plant exhausts (T < 1200 K, P ∼ 1 atm) [253]. More recently, this domain was exploited by our group for in-chamber rocket combustion gas sensing at much higher temperatures and pressures (T > 3000 K, P > 100 atm) [183, 254]. At these extreme combustion temperatures, transitions with higher rotational energies and vibrational hot bands, such as the $v(1 \rightarrow 3)$ band, become more prominent. Moreover, at such extreme combustion conditions, transitions comprising the bandhead regions exhibit local absorption peaks with high differential absorption, attractive for sensing. At high gas densities, spectrally crowded bandhead regions become susceptible to collisional line mixing [255]. In this work, we examine line broadening and mixing in argon and carbon monoxide bath gases for 17 high-energy transitions ($J'' = 42-58$)

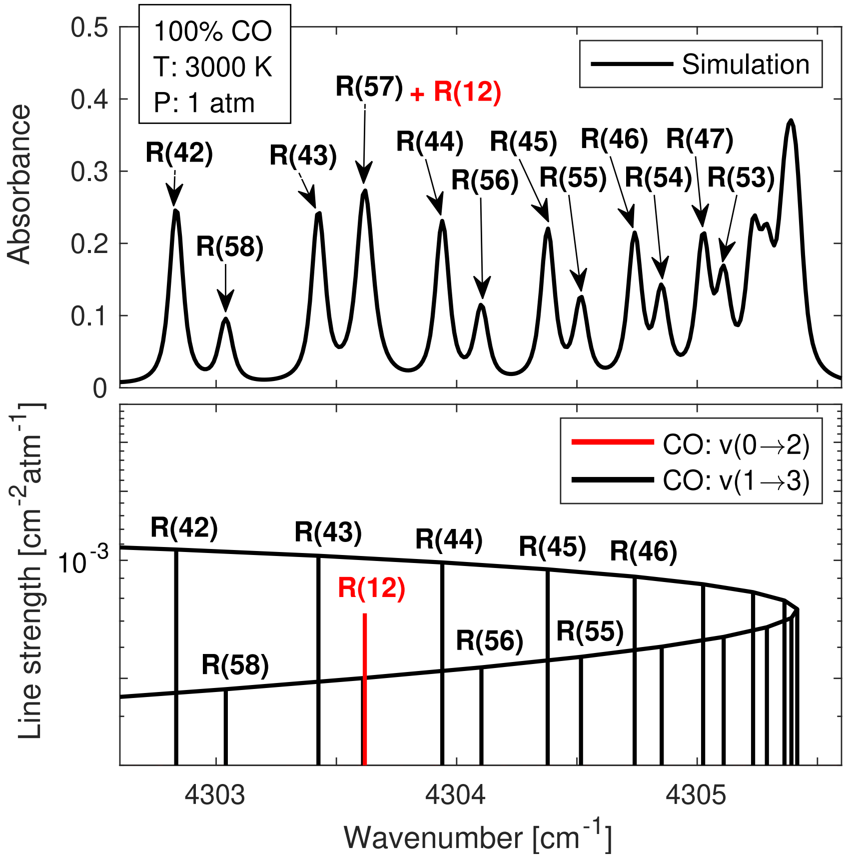

Figure 7.1: *Top*: Spectral absorbance simulation of the $v(1 \rightarrow 3)$ first overtone bandhead of CO at 3000 K and 1 atm for pure CO. *Bottom*: Line strength positions and magnitudes of the spectral transitions relevant to this work.

near the $v(1 \rightarrow 3)$ bandhead of CO, identified in Fig. 7.1.

Line broadening of carbon monoxide has been shown to have weak vibrational energy dependence, with stronger dependence on rotational energy. Though much progress has been made in quantifying and modeling CO line broadening in the $v(0 \rightarrow 1)$ [169, 256, 257], $v(0 \rightarrow 2)$ [257–263], and $v(0 \rightarrow 3)$ [264–266], a dearth of line-broadening data exists for rotational quantum number transitions larger than $J'' > 31$ of any vibrational band, as noted in Fig. 7.2. This is primarily because most measurements of line broadening coefficients for CO have been conducted at or near room temperature [262, 267], corresponding to the lower rotational energy transitions. We focus this experimental study to a temperature range of 1200–3750 K to access lines with higher rotational energies.

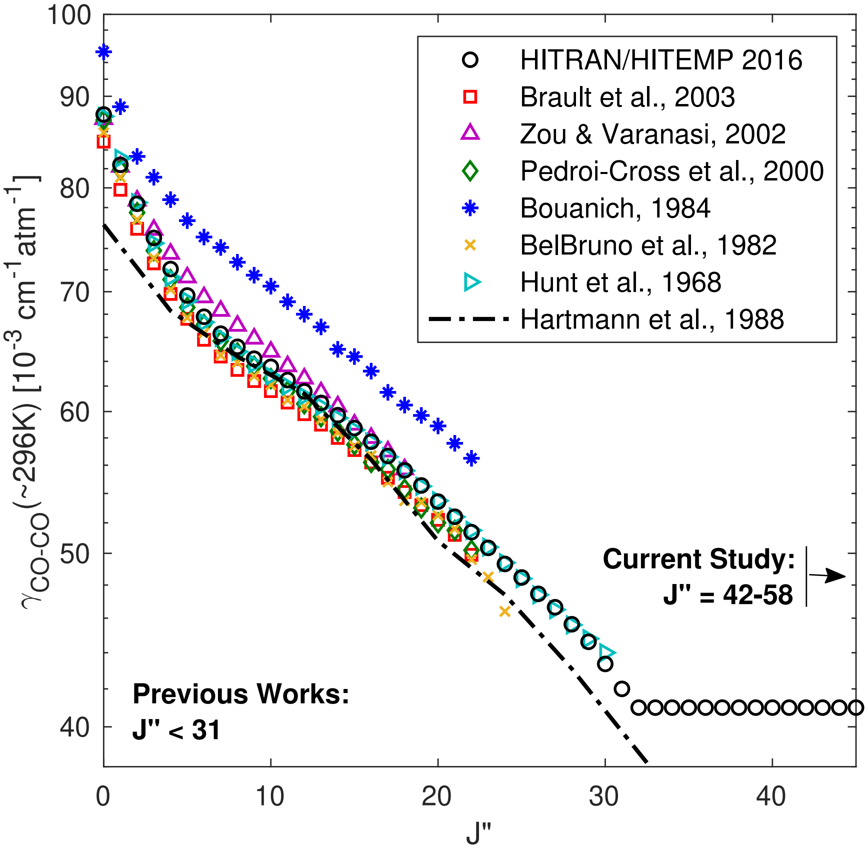

Figure 7.2: Experimental self-broadening coefficients for CO transitions obtained by previous works. The current study focuses on higher rotational quantum number transitions ($J'' = 42 - 58$) to extend diagnostic capabilities at extreme temperatures and pressures.

Line mixing is a band narrowing effect that occurs at high pressures, resulting from local population transfers when collisional linewidths are on the order of line spacing [157]. Line mixing is often observed in bandheads where line spacing becomes very small. Q-branches that have bandheads at lower rotational energies are often observed to have line mixing near ambient temperatures [157]. Here we study line mixing in the R-branch bandhead of the $v(1 \rightarrow 3)$ overtone band of CO at pressures up to 60 atm. A spectral simulation of the target bandhead considered herein is shown in Fig. 7.1.

This paper describes the experimental measurements and modeling of the aforementioned line broadening and mixing effects in the $v(1 \rightarrow 3)$ first overtone bandhead of CO at high temperatures and high pressures, with Ar and CO collision partners. After establishing the theoretical framework, we present our experimental methods, including the optical setup, experimental apparatus, and data processing techniques required to obtain broadening parameters from laser absorption measurements at moderate pressures (P < 2.5 atm). We then discuss how these broadening parameters were used to develop the complimentary line-mixing model based on high-pressure (up to 60 atm) spectrally-resolved CO absorption measurements in a shock tube. The combination of broadening and mixing models provides a basis for spectral simulation of CO near 2.3 μm over a broad range of temperatures and pressures.

7.2 Theory

7.2.1 Absorption spectroscopy and line broadening

The basic theory of laser absorption spectroscopy is detailed in Ch. 3, but a brief review is provided here for context within this application. In the spectral vicinity of *a single transition*, the spectral absorbance, defined in Eq. 3.3, can also be written in terms of total number density of the absorbing species N [molec $\cdot$ cm^{-3}]:

$$\alpha_\nu = -\ln\left(\frac{I_t}{I_0}\right)_\nu = S(T)NL\phi(\nu) \tag{7.1}$$

where $S(T)$ [cm^{-1}/(molec $\cdot$ cm^{-2})] is the line strength of the transition, L [cm] is the path length, $\phi(\nu)$ [cm] is the line shape function, and N [molec $\cdot$ cm^{-3}] is the total number density of the absorbing species, given by:

$$N = \frac{PX_i}{k_B T} \cdot 10^{-6} \tag{7.2}$$

Here, P is the pressure with units of [Pa], X_i is the mole fraction of the absorber i, k_B [J/K] is the Boltzmann constant, and T [K] is the temperature. Based on the compressibility factors for CO and Ar, deviations from the ideal gas assumption implied in Eq. 7.2 are not expected to exceed 1% for any condition in this study [268]. The spectral line shape $\phi(\nu)$ can be modeled using a Voigt profile [157], as described in Ch. 3. Each broadening mechanism is characterized by full width at half maximum (FWHM) parameter; $\Delta\nu_C$ [cm^{-1}] for collisional broadening and $\Delta\nu_D$ [cm^{-1}] for Doppler broadening, given by Eq. 3.15 and Eq. 3.13 , respectively. Collisional broadening scales linearly with pressure and often leads to an additive blending of neighboring lines, with the temperature dependence of $\gamma_{(i-k),j}(T)$ modeled as a power law expression, given in Eq. 3.16:

As lines become more closely spaced together, the spectral absorbance α_ν at a given wavenumber ν is no longer a function of just one spectral transition, but is rather a summation of all neighboring transitions as demonstrated in the bandhead shown in Fig. 7.1. In this work, we report measured values of $\gamma_{\mathrm{CO-CO}}$ and $\gamma_{\mathrm{CO-Ar}}$ at a reference temperature of 1500 K along with their respective temperature exponents, $n_{\mathrm{CO-CO}}$ and $n_{\mathrm{CO-Ar}}$, for 17 transitions in the $v(1 \rightarrow 3)$ band of CO (described in Sec. 7.1). The reported values are considered most appropriate for a temperature range of 1500–4000 K.

7.2.2 Line mixing

To model line-mixing effects, we implement the relaxation matrix formalism [269] to account for collisional effects on the molecular spectra. For brevity, lower state rotational energy levels, J'' and K'', are written as J and K for the proceeding equations. The absorbance, α_ν, for overlapping transitions can be written within the impact approximation [270] in the following form:

$$\alpha_\nu = \frac{NL}{\pi}\,\mathrm{Im}(\mathbf{d} \cdot \mathbf{G}^{-1} \cdot \boldsymbol{\rho} \cdot \mathbf{d}) \tag{7.3}$$

where $\boldsymbol{\rho}$ is a diagonal matrix with nonzero elements ρ_J defined by the lower state Boltzmann population fraction [271]:

$$\rho_J = \frac{N_J}{N} = \frac{g''_J}{Q}\exp\left(- \frac{hcE''_J}{k_B T}\right) \tag{7.4}$$

where N_J [molec $\cdot$ cm^{-3}] is the number density, g''_J is the lower state degeneracy, E''_J [cm^{-1}] is the lower state energy, Q is the total internal partition function, h [J $\cdot$ s] is Planck's constant, and c [cm/s] is the speed of light. $\mathbf{d}$ [cm^{-1}/(molec $\cdot$ cm^{-2})]$^{\frac{1}{2}}$ is a vector of transition amplitudes with elements d_J given as [272]:

$$d_J = \sqrt{\frac{S_J(T)}{\rho_J}} \tag{7.5}$$

Another commonly used form of Eq. 7.3 is shown in B, where the temperature dependence of $\mathbf{d}$ is removed. The dependence on wavenumber ν [cm^{-1}] in Eq. 7.3 is within $\mathbf{G}$ [cm^{-1}], a complex matrix defined as:

$$\mathbf{G} = \nu\mathbf{I} - \mathbf{H} \tag{7.6}$$

where $\mathbf{I}$ is the identity matrix and a frequency-independent matrix $\mathbf{H}$ [cm^{-1}] is defined as:

$$\mathbf{H} = \boldsymbol{\nu}_0 + iP\mathbf{W} \tag{7.7}$$

$\boldsymbol{\nu}_0$ [cm^{-1}] is a diagonal matrix of transition frequencies and $\mathbf{W}$ [cm^{-1}/atm] is the relaxation matrix [269]. Note that in Eq. 7.7, total pressure P is in units of [atm]. $\mathbf{H}$ can be diagonalized using a similarity transform [273] to obtain a diagonal eigenvalue matrix $\boldsymbol{\Omega}$ [cm^{-1}] with diagonal elements ω_J [cm^{-1}] such that:

$$\boldsymbol{\Omega} = \mathbf{A}^{-1} \cdot \mathbf{H} \cdot \mathbf{A} \tag{7.8}$$

Since $\mathbf{G}$ only differs from $\mathbf{H}$ by a constant diagonal matrix, $\mathbf{G}^{-1}$ is also diagonalized by $\mathbf{A}$. Eq. 7.3 can now be written as a function of ν spanning all relevant spectral transitions J:

$$\alpha_\nu = \frac{NL}{\pi} \operatorname{Im} \left[\sum_J \frac{(\mathbf{d} \cdot \mathbf{A})_J (\mathbf{A}^{-1} \cdot \boldsymbol{\rho} \cdot \mathbf{d})_J}{(\nu - \omega_J)} \right] \tag{7.9}$$

The relaxation matrix is implemented to model line-mixing effects in the spectra and is given by:

$$\mathbf{W}_{JK} = \begin{cases} \gamma_J + i\Delta\nu_{0,J} & \text{if } J = K \\ -R_{J\to K} & \text{if } J \neq K \end{cases} \tag{7.10}$$

where the real diagonal elements of $\mathbf{W}$ are the broadening coefficients γ_J discussed in Sec. 7.2.1 and the imaginary diagonal elements are the pressure shifts $\Delta\nu_{0,J}$ [cm^{-1}/atm] (termed "δ" in the HITRAN database [149]). The real off-diagonal elements represent the state-specific population transfer rates, $R_{J\to K}$ [cm^{-1}/atm], between two states, J and K. Notably, for linear molecules, broadening coefficients can also be expressed in terms of total depopulation rates through Eq. 7.11 [157].

$$\gamma_J = \sum_{J\neq K} R_{J\to K} \tag{7.11}$$

The imaginary off-diagonal components of $\mathbf{W}$ represent contributions from rotational dephasing [274]. Previous work has found the effect of these terms to be negligible for collisionally-narrowed infrared spectra at both low and high densities [275]. Consequently, the rotational dephasing contributions are approximated as zero for all transitions in the relaxation matrix. It is noteworthy that if the population transfer rates are set to zero for all transitions, Eq. 7.3 simply represents the sum of the Lorentzian lines with no line-mixing effects. When multiple collision partners are present, the full relaxation matrix is written as a summation of the individual perturber contributions:

$$\mathbf{W} = \sum_{B} X_B \mathbf{W}_{A-B} \tag{7.12}$$

In this study, we model $R_{J \to K}$ using a modified-exponential-gap (MEG) law [276, 277] to construct the real part of the relaxation matrix. The MEG law takes the following form:

$$R_{J \to K} = a_1(T) \left[\frac{1 + a_4 \left(\dfrac{E''_J}{a_2 k_B T} \right)}{1 + a_4 \left(\dfrac{E''_J}{k_B T} \right)} \right]^2 \times \exp \left[\frac{-a_3 \left(E''_K - E''_J \right)}{k_B T} \right] \tag{7.13}$$

where $a_1(T)$ [cm^{-1}/atm], a_2, and a_3 are species-specific MEG law coefficients obtained by fitting measured absorbance data to the model using a least-squares fitting routine. a_4 describes the collision duration [276] based on distance of closest approach [278] and is set to $a_4 = 2$ as an estimate for CO-CO collisions [279, 280]. It is important to note that the value of a_4 is not critical in the ability of the MEG law to fit the measurement data [279, 280]; therefore, it was kept constant for all experiments in this study.

This empirically-derived MEG law formulation has been successfully implemented for other linear molecules [271, 279] using absorption spectroscopy techniques to account for line mixing. Since collisions promote the Boltzmann population distribution, the upward and downward population transfer rates, $R_{J \to K}$ and $R_{K \to J}$, respectively, can be related through the detailed-balance principle [281]:

$$\rho_K R_{K \to J} = \rho_J R_{J \to K} \tag{7.14}$$

This completes the real part of the relaxation matrix and indicates that starting from the less populated energy level is the more probable of the two counter processes. This suggests that line mixing favors population transfers from weak transitions to strong transitions, inducing a narrowing of the spectral structure and enhancing high absorbing regions.

Only a single set of measured absorbance data is needed to obtain the species-specific MEG law coefficients for a given temperature [282]. To determine the temperature dependence of the population transfer rates, $a_1(T)$ can be modeled as a power law expression:

$$a_1(T) = a_1(T_0)\left(\frac{T_0}{T}\right)^m \tag{7.15}$$

where we define a temperature exponent m obtained by fitting multiple sets of absorbance data at different temperatures, and $a_1(T_0)$ is the MEG law coefficient at a reference temperature T_0.

Similar to the reported broadening coefficients $\gamma_{\mathrm{CO}-B}$, we report measured values of MEG law coefficients for both $a_{i,\mathrm{CO-CO}}$ and $a_{i,\mathrm{CO-Ar}}$ with their respective temperature exponents, $m_{\mathrm{CO-CO}}$ and $m_{\mathrm{CO-Ar}}$ at a reference temperature of 1500 K. We show that these parameters can model line-mixing effects in the $v(1 \rightarrow 3)$ bandhead of CO at high pressures (> 5 atm) over a temperature range of 2000–3600 K.

7.3 Experimental Setup

We first note that extreme caution should be exercised when handling mixtures with high concentrations of CO, due its acute toxicity. All CO was stored in a ventilated toxic gas cabinet and transported to the experimental apparatuses in lines that had been thoroughly checked for leaks with inert gases. After each measurement, each device described in this section was vacuumed and diluted with N_2 to eliminate residual CO before the next measurement.

The experiments in this work were conducted using the high-enthalpy shock tube facility illustrated in Fig. 7.3 with some supporting collisional broadening measurements conducted in a heated static optical gas cell described in previous work [146]. The shock tube has a constant 10.32 cm inner diameter, a 4.88 m long driven section, and a 1.56 m long driver section. The test section is circumscribed with interchangeable port plugs, which integrate different sensors or optical windows, located ∼2 cm from the driven endwall. Incident shock speeds are determined by five fast-response, piezoelectric time-of-arrival sensors (Dynasen, Inc.) located at equidistant intervals over the last 170 cm of the driven section, as shown in the bottom of Fig. 7.3. Initial reflected shock conditions are determined by the incident shock speed with a typical uncertainty of ∼1% in temperature when properly accounting for vibrational relaxation of the gas mixture [64]. Prior to each experiment, a roughing pump (Alcatel Adixen 2021i) was used to vacuum down the shock tube to $< 1 \times 10^{-3}$ Torr. Test gas mixtures were barometrically prepared in a 12.5 L agitated mixing tank using a heated capacitance manometer (MKS 627D Baratron) with a full-scale pressure range of 1000 Torr and an uncertainty of 0.12% of the reading. All gases were supplied by Airgas, Inc. with purity levels of 99.9% for CO, 99.999% for Ar, and 99.995% for He. Two different mixtures were prepared for collisional broadening and line mixing investigations: 100% CO for CO-CO measurements and 30% CO/Ar for CO-Ar measurements.

The $v(1 \rightarrow 3)$ bandhead of CO near 2.3 μm was spectrally resolved by current-tuning a continuous-wave distributed-feedback (DFB) laser (Norcada, Inc.) with ∼10 mW output power. The DFB laser is temperature- and current-tunable from 4290–4325 cm^{-1}. A 10 kHz triangle waveform, shown in Fig. 7.3, was implemented to injection-current-tune the light source over a wavenumber range of ∼4.5 cm^{-1} between 4302–4306.5 cm^{-1}. Additionally, the injection current was scanned below the lasing threshold to account for transient thermal emission during the measurements. The relative frequency of the laser light during the scan was determined using a germanium etalon with a free spectral range of 0.0231 cm^{-1}. During the experiments, the incident light was pitched across the shock tube through two 0.5° wedged sapphire windows with a 9.5 mm aperture, as shown in Fig. 7.3. The transmitted light was passed through a bandpass spectral filter (Spectrogon, 2320±20 nm) and an iris to mitigate thermal emission, and was focused onto a thermo-electrically cooled photodetector (Thorlabs PDA10D) using a CaF$_2$ plano-convex lens. Incident and reflected shock pressures

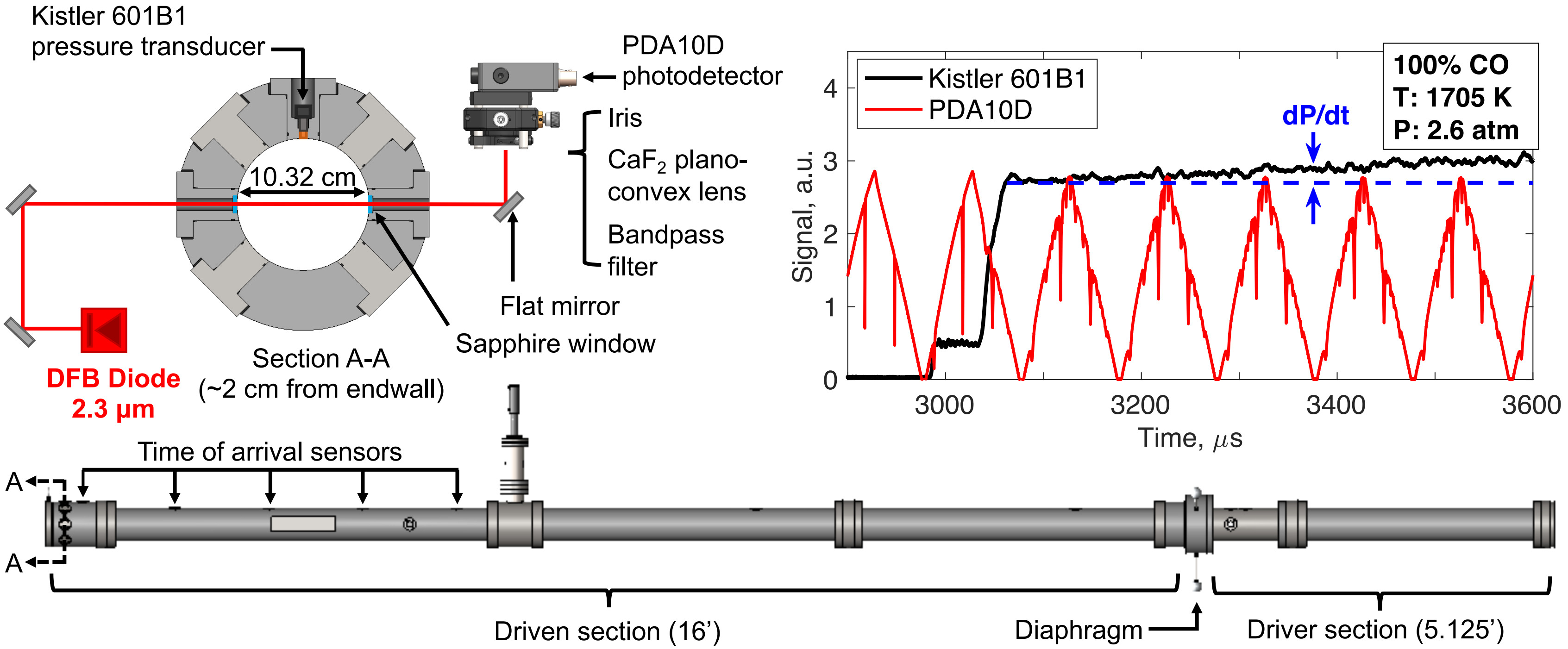

Figure 7.3: *Top left*: Cross-section of the shock tube test section showing windows for optical access and laser/detector setup. *Top right*: Example raw detector and pressure transducer signals during non-reactive shock heating of pure CO. *Bottom*: Side view of the shock tube showing lengths of the driven and driver sections of the tube as well as the locations of the time-of-arrival sensors.

were measured using a dynamic pressure transducer (Kistler 601B1) mounted in one of the test section port plugs, which was connected to a charge amplifier (Kistler 5018A). Pressure and detector data were collected on a PicoScope 4000 series data acquisition module at 80 MHz while detector data were sampled at the maximum detector bandwidth of 10 MHz, yielding an equivalent measurement rate of 5 MHz.

Representative raw time-resolved signals from a shock tube experiment are shown in Fig. 7.3. Prior to the incident shock arrival, the R(12) feature from the $v(0 \rightarrow 2)$ first overtone band of CO is visible at 296.3 K and 23.8 Torr. Following the passage of the incident and reflected shocks, R(42)–R(58) appear as the high temperatures more densely populate the $v(1 \rightarrow 3)$ first overtone hot band. Throughout the test time, a non-ideal pressure rise was often observed and accounted for by assuming isentropic compression of the test gas. This method has shown to be a valid assumption for correcting thermodynamic conditions behind reflected shock waves [46]. For a single scan interval, the change in temperature and pressure are less than 0.3% and 1.2%, respectively, when pure CO was used, and 0.2% and 0.6% when the 30%CO/Ar mixture was used; thus, the thermodynamic properties were assigned at the scan mid-point and assumed to be constant during each scan.

Shock tube experiments for line-broadening parameters of pure CO were conducted over a temperature range of 1700–3750 K and a pressure range of 0.5–2.5 atm. Moderate pressures were targeted for line-broadening experiments to minimize spectral blending amongst neighboring transitions and resolve the line-specific broadening and temperature coefficients discussed in Section 7.2.1. For the 30%CO/Ar mixtures, the lower end of the temperature range was limited to 2000 K due to decreased absorption in the $v(1 \rightarrow 3)$ band, precluding reliable line-broadening measurements; however, the pressure range (< 2.5 atm) was kept similar. Shock-heated CO requires a finite amount of time to attain vibrational equilibrium; estimates of vibrational relaxation time for the mixtures used in these studies are shown in Fig. 7.4, with empirical correlations from Millikan and White [68]. Pure CO experiments have a faster vibrational relaxation time compared to CO/Ar mixtures, owing to argon's poor collision efficiency. Lower temperature (< 2500 K) line-broadening experiments were

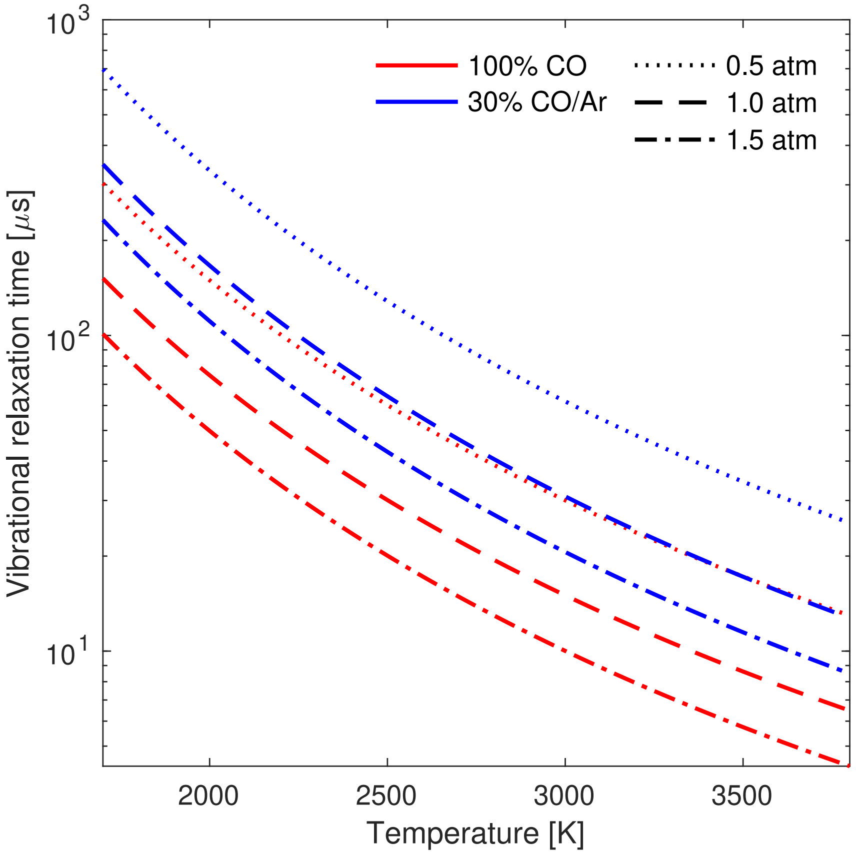

Figure 7.4: Vibrational relaxation times for mixtures and conditions considered in this work, using calculations of Millikan & White [68]

conducted at higher pressures ($>$ 1.5 atm) to reduce vibrational relaxation time. At lower temperatures, reflected shock test times were typically ~600 μs, allowing sufficient time for CO to vibrationally relax. Processed laser scans were typically acquired at least 100 μs after the estimated vibrational relaxation time. Shock tube experiments for line-mixing parameters covered a temperature and pressure range of 2000–3600 K and 5–60 atm, respectively, for both pure CO and 30%CO/Ar. Higher pressures were targeted for line-mixing experiments in order to determine MEG law coefficients and prove pressure scalability.

For each experiment, absorbance α_ν was determined through Eq. 7.1 via measurements of incident and transmitted intensity, I_0 and I_t. The incident laser light intensity through the shock tube was measured without a mixture present prior to each shock experiment to provide a baseline I_0 for calculation of α_ν. Each scan of the transmitted laser intensity, I_t, was corrected for detector offset from both emission and dark current noise by tuning below the lasing threshold. Minimal emission was observed throughout the test, as seen in the representative data from Fig. 7.3. For broadening experiments, the absorbance profile was least-squared fit with Voigt lineshape functions positioned at the line center of each transition with the broadening coefficients set as the free parameters. For higher-pressure line-mixing experiments, the MEG law coefficients were set as free parameters with the diagonals of the relaxation matrix assigned with the pre-determined broadening coefficients.

7.4 Results and discussion

Temperature dependent line-broadening and line-mixing coefficients of CO with CO and Ar are reported for seventeen transitions in the $v(1 \rightarrow 3)$ first overtone hot band between 4302–4306.5 cm^{-1}. Values for the transition line centers ν_0, line strengths $S_J(T_0)$, and lower state energy levels E''_J were taken from the HITEMP database [150]. Quantum number assignments and lower state energies are noted in Table 7.1. The following two subsections detail the line-broadening and line-mixing results, respectively.

7.4.1 Line broadening

Laser absorption measurements were made behind reflected shocks and in the heated optical cell to gather line broadening data from 1200–3750 K for R(42)–R(58). A representative single-scan absorbance measurement from a shock tube experiment with corresponding Voigt line fits is shown in Fig. 7.5. Generally, the Voigt fits produced low peak residuals (1–4%). At high temperatures and low pressures both CO-broadening and Ar-broadening experiments exhibited some evidence of collisional narrowing (gull-wing residual) likely due to a reduction in Doppler broadening from velocity-changing collisions [187]. Fig. 7.5 also provides evidence of line mixing effects where the Voigt lineshape summation is unable to properly fit the measured absorbance near the bandhead.

As discussed previously, line-broadening experiments targeted lower pressures (< 2.5 atm) to minimize spectral blending from neighboring transitions, which become more significant near the bandhead and complicates the fitting routine. Despite the low pressures of the experiments, the R(48)–R(54) transitions near the bandhead are too closely spaced to reliably extract broadening information. Instead, the broadening coefficients from transitions before and after the bandhead—R(42)–R(47) and R(53)–R(58)—were used to establish a J'' dependency and estimate the broadening coefficients of the bandhead transitions for the Voigt line shape model.

As previously mentioned, self-broadening measurements were conducted on a high-temperature gas cell at 1226±10 K over a pressure range of 0.6–1.0 atm to extend the temperature range of the reported broadening parameters. This data served to reduce uncertainty in

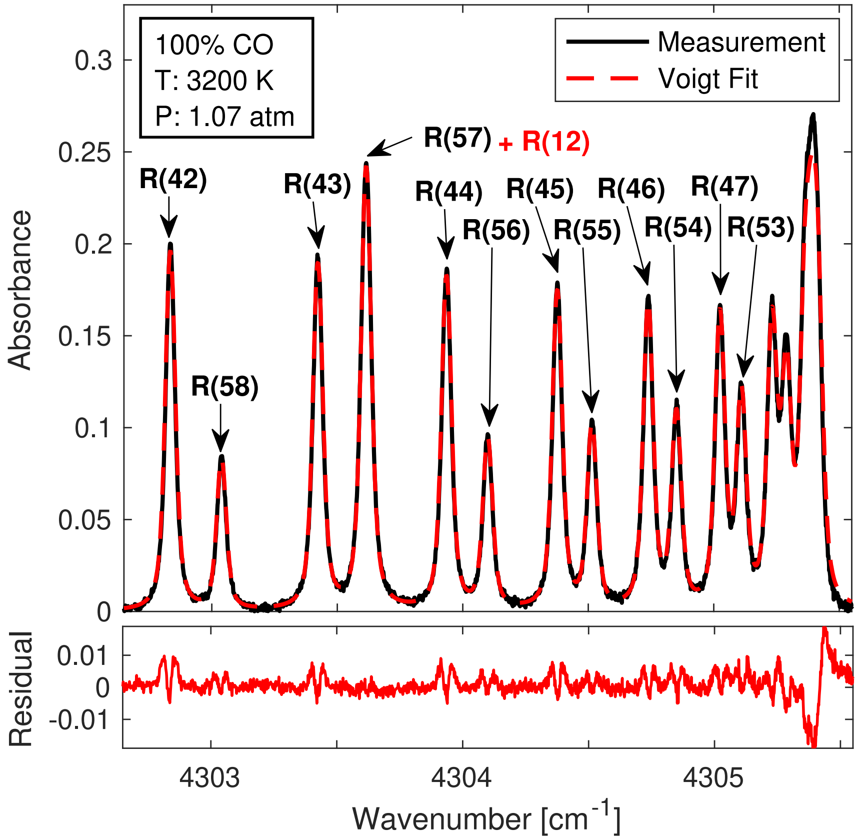

Figure 7.5: *Top*: Absorbance of the first overtone bandhead of CO at 3200 K and 1.07 atm with corresponding Voigt fits. *Bottom*: Residuals of the Voigt fit, showing larger disagreement at the bandhead.

the temperature-dependence exponent, and to check that acquired data had negligible facility dependence. As with the shock tube measurements, the detectable transitions in the absorbance spectra were fit with simultaneous Voigt line shape functions positioned at the line center of each transition with broadening coefficient, $\gamma_{\mathrm{CO}-B}(T)$, as the free parameter using a least squares fitting routine. Representative collision width measurements from these experiments are shown as a linear function of pressure in Fig. 7.6. At these lower temperatures (1226 ± 10 K), the absorbance from each of the transitions after the bandhead was too weak ($\alpha_\nu < 0.005$) to recover reliable collision widths and not factored into $\gamma_{\mathrm{CO}-B}(T)$. Consequently, to help establish temperature dependence for the higher energy lines after the bandhead, R(53)–R(58), we incorporate estimates of room-temperature broadening in the

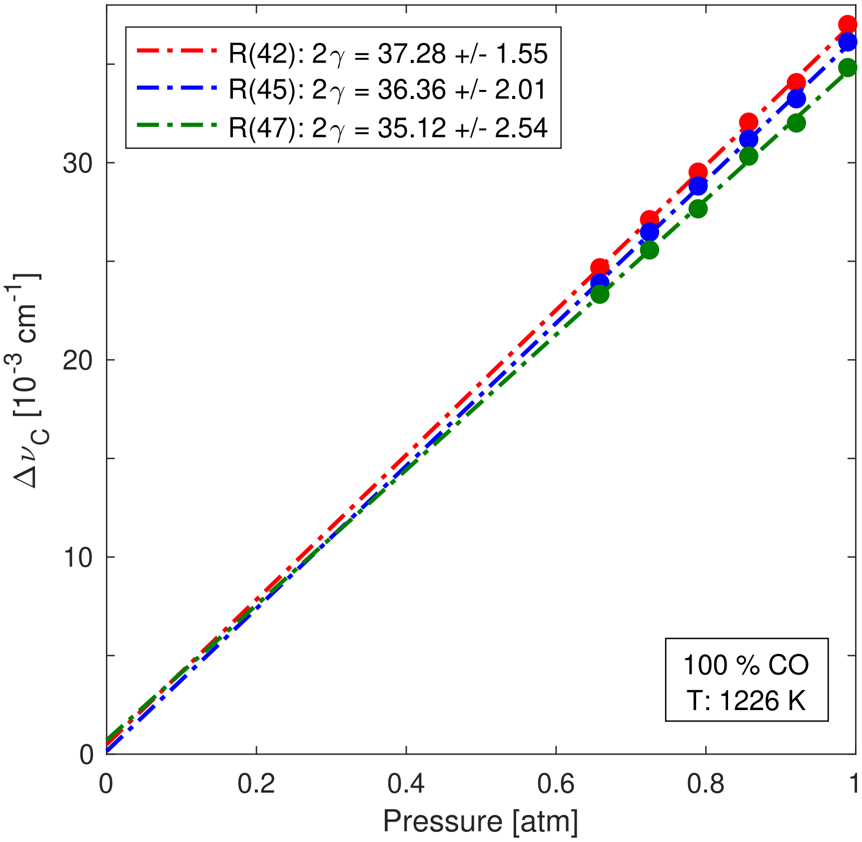

Figure 7.6: Collisional width Δv_C versus pressure for rovibrational transitions in the $v(1 \rightarrow 3)$ first overtone bandhead: R(42), R(45), and R(47) (markers) along with best fits (dashed lines) recorded in the static optical cell experiments at 1226 K.

power law fit from an existing model [283] validated for lower J'' transitions [149]. The resulting broadening coefficients referenced to 1500 K and temperature-dependence exponents are reported in Table 7.1.

Owing to weak expected absorbance at the maximum temperatures achievable by the heated optical cell, CO-Ar broadening measurements were not conducted, considering these experiments would require significant dilution of the CO. Therefore, as with the aforementioned R(53)–R(58) lines in pure CO, a room-temperature estimation of Ar-broadening coefficient [284] is incorporated into the power law fit for all transitions before and after the bandhead (R(42)–R(47) and R(53)–R(58)). Room-temperature Ar-broadening estimations were obtained by extrapolating existing measurements that have been validated at lower J''

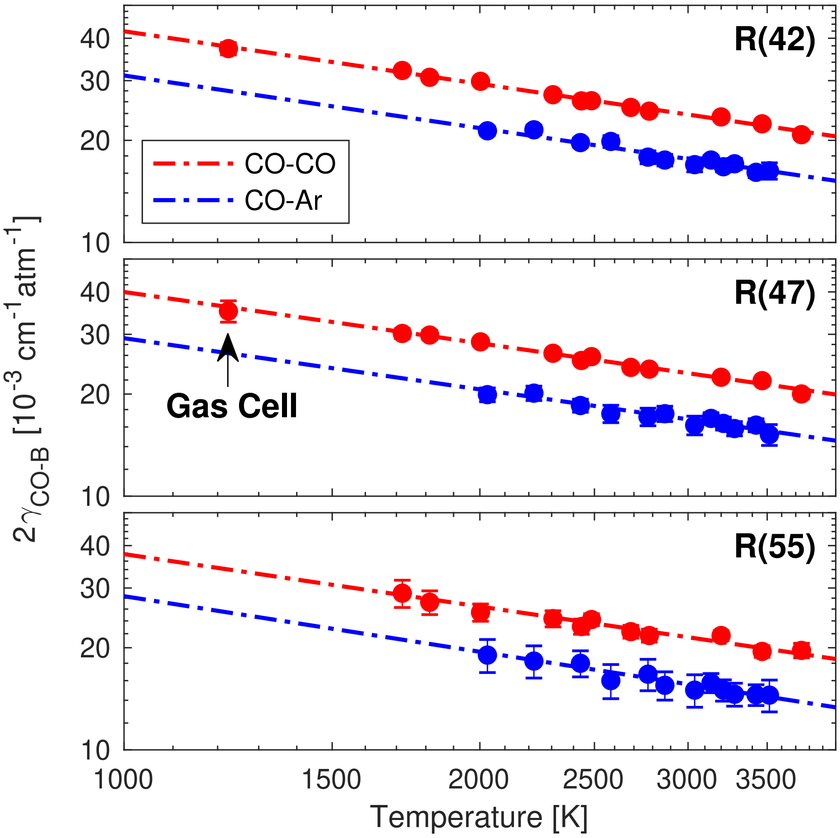

Figure 7.7: CO- and Ar-broadening coefficients for the transitions of interest with power law fits for 1000–4000 K. High-temperature optical cell data at 1226 K annotated, all other points from shock tube experiments.

transitions [284].

Fig. 7.7 shows broadening data versus temperature for representative transitions before and after the bandhead, representing all relevant test conditions. The measured broadening coefficients were fit with a power law to obtain the temperature exponent n for each transition, using 1500 K as the reference temperature T_0. Details regarding the uncertainties associated with this procedure are provided in Appendix A.1 and A.2. With measured broadening coefficients before and after the bandhead, we infer the broadening coefficients for transitions located at the bandhead—R(47)–R(53)—via linear interpolation, as shown in Fig. 7.8. It is important to note that R(57) is blended with R(12) from the $v(0 \rightarrow 2)$

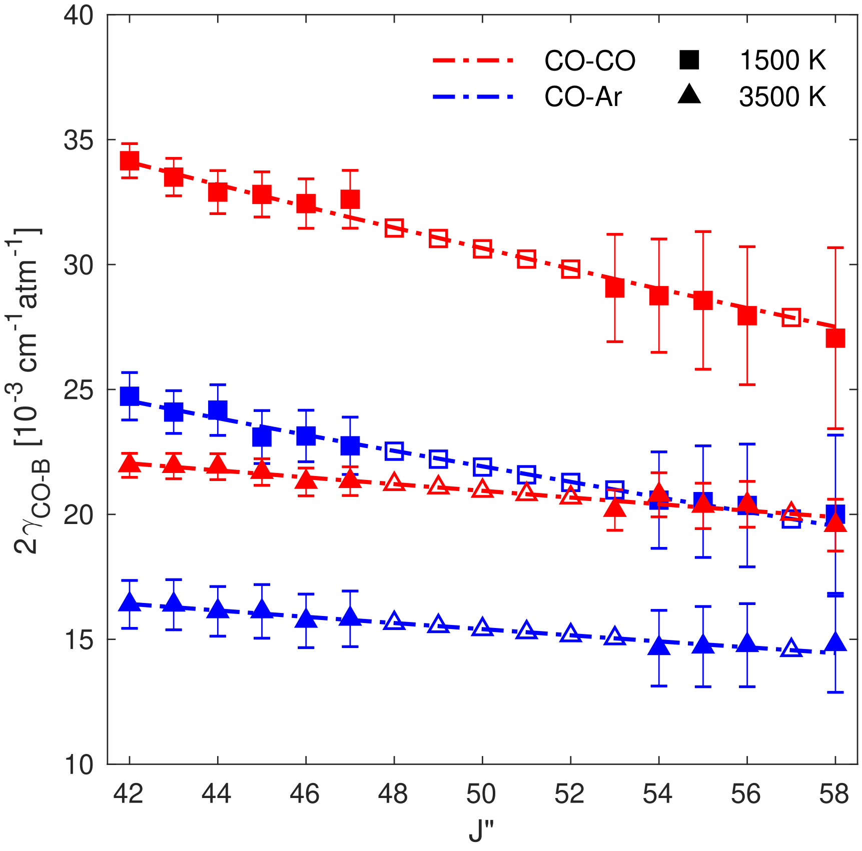

Figure 7.8: Measured broadening coefficients $2\gamma_{\mathrm{CO}-B}$ (markers) for $J'' = 42$–58 for CO (red) and Ar (blue) at 1500 K (squares) and 3500 K (triangles). Least-squares exponential fits (lines) of the measured (filled markers) are used to estimate $2\gamma_{\mathrm{CO}-B}$ for J'' too interfered to measure directly (open markers).

first overtone band, and therefore broadening parameters for this transition also required interpolation. Temperature-dependent exponents n for the interpolated transitions are determined by similarly fitting the inferred broadening coefficients $\gamma_{\mathrm{CO}-B}(T)$ over the range of test temperatures. The broadening parameters for all seventeen transitions and their uncertainties are listed in Table 7.1. Subscripts in the table indicate if the reported parameter is an interpolated value or if it incorporates any high-temperature gas cell data or room-temperature estimations. Power-law fits of all measured broadening coefficients versus temperature (similar to the subset shown in Fig. 7.7) are provided in Sec. 7.6.

Table 7.1: Self- and Ar-broadened line parameters for the $v(1 \rightarrow 3)$ band of CO

Transition (v'', J'')	E''_J [cm^{-1}]	$\gamma_{\mathrm{CO-CO}}$(1500 K) [10^{-3} cm^{-1}atm^{-1}]	$n_{\mathrm{CO-CO}}$	$\gamma_{\mathrm{CO-Ar}}$(1500 K) [10^{-3} cm^{-1}atm^{-1}]	$n_{\mathrm{CO-Ar}}$
R(1,42)	5563.82	17.08 ± 0.35[a]	0.521 ± 0.023[a]	12.36 ± 0.45[b]	0.485 ± 0.036[b]
R(1,43)	5725.71	16.75 ± 0.38[a]	0.500 ± 0.025[a]	12.05 ± 0.49[b]	0.455 ± 0.037[b]
R(1,44)	5891.27	16.45 ± 0.41[a]	0.480 ± 0.026[a]	12.09 ± 0.48[b]	0.478 ± 0.037[b]
R(1,45)	6060.50	16.40 ± 0.46[a]	0.488 ± 0.028[a]	11.55 ± 0.52[b]	0.425 ± 0.038[b]
R(1,46)	6233.39	16.22 ± 0.52[a]	0.497 ± 0.031[a]	11.57 ± 0.52[b]	0.455 ± 0.039[b]
R(1,47)	6409.92	16.31 ± 0.60[a]	0.501 ± 0.034[a]	11.37 ± 0.59[b]	0.429 ± 0.040[b]
R(1,48)	6590.11	15.72 ± 0.64[c]	0.465 ± 0.046[c]	11.26 ± 0.66[c]	0.429 ± 0.065[c]
R(1,49)	6773.93	15.51 ± 0.71[c]	0.456 ± 0.045[c]	11.10 ± 0.71[c]	0.422 ± 0.064[c]
R(1,50)	6961.38	15.30 ± 0.79[c]	0.448 ± 0.045[c]	10.94 ± 0.76[c]	0.414 ± 0.063[c]
R(1,51)	7152.46	15.09 ± 0.88[c]	0.439 ± 0.044[c]	10.78 ± 0.82[c]	0.406 ± 0.062[c]
R(1,52)	7347.15	14.89 ± 0.98[c]	0.431 ± 0.043[c]	10.62 ± 0.88[c]	0.398 ± 0.061[c]
R(1,53)	7545.45	14.53 ± 1.13[b]	0.431 ± 0.037[b]	10.47 ± 0.94[c]	0.390 ± 0.060[c]
R(1,54)	7747.36	14.38 ± 1.19[b]	0.383 ± 0.037[b]	10.29 ± 0.98[b]	0.401 ± 0.043[b]
R(1,55)	7952.85	14.28 ± 1.40[b]	0.401 ± 0.038[b]	10.25 ± 1.12[b]	0.393 ± 0.044[b]
R(1,56)	8161.93	13.98 ± 1.40[b]	0.372 ± 0.039[b]	10.18 ± 1.23[b]	0.379 ± 0.044[b]
R(1,57)	8374.60	13.91 ± 1.64[c]	0.389 ± 0.038[c]	9.88 ± 1.26[c]	0.359 ± 0.056[c]
R(1,58)	8590.82	13.53 ± 1.82[b]	0.382 ± 0.041[b]	10.00 ± 1.55[b]	0.355 ± 0.045[b]

[a] Power law fit incorporates high-temperature gas cell data

[b] Power law fit incorporates room-temperature broadening estimation (discussed in Sec. 7.4.1)

[c] Interpolation based on J''-dependence (reference Fig. 7.8)

7.4.2 Line mixing

As discussed in Sec. 7.2.2, the relaxation matrix, $\mathbf{W}$, accounts for the collisional rates that result in line mixing in the spectra. The real diagonal elements of $\mathbf{W}$ are the broadening coefficients, γ_J, the imaginary diagonal elements are the pressure shifts, $\Delta\nu_{0,J}$, the real off-diagonal elements represent the state-specific population transfer rates, $R_{J\rightarrow K}$, and the imaginary off-diagonal components are set to zero. The reported broadening coefficients in Table 7.1 and the pressure shift coefficients from the HITEMP database [149] are used to complete the real and imaginary diagonal elements of $\mathbf{W}$, respectively. The MEG law described by Eq. 7.13 is implemented to model the population transfer rates. To find the MEG law coefficients, a_i, high pressure absorbance data measured using the shock tube facility are least-squares fit with the absorbance model, given by Eq. 7.3, with a_1, a_2, and a_3 set as the free parameters. It should be noted that since line mixing only occurs within the same vibrational band, as described in Sec. 7.2.2, transitions not belonging to the $v(1 \rightarrow 3)$ first overtone hot band were simulated using the HITEMP database and removed from the measured absorbance data prior to the fitting routine. This procedure was initially carried out using pure CO in order to determine the population transfer rates associated with CO-CO collisions, and then repeated with test gas mixtures of 30%CO/Ar to obtain the appropriate rates for CO-Ar collisions using Eq. 7.12.

A comparison of representative high-pressure absorbance data collected in the shock tube at 25 atm and 3350 K is shown in Fig. 7.9 with various simulated results from the line mixing model. Without line mixing, the simulated spectra poorly represents the measured spectra near the bandhead, where most population transfers occur. Implementing the fitting routine described above, allows for a high fidelity reconstruction of the spectra with a max residual $< 3\%$. This compares to a disagreement of nearly 50% at the bandhead peak without accounting for line mixing. As expected, away from the bandhead, the line mixing model still agrees well with both the measured absorbance and the simulated spectra without any line mixing. Notably, with the MEG law coefficients established, we can adjust the a_1 parameter to vary the degree of line mixing and visualize the associated changes in the

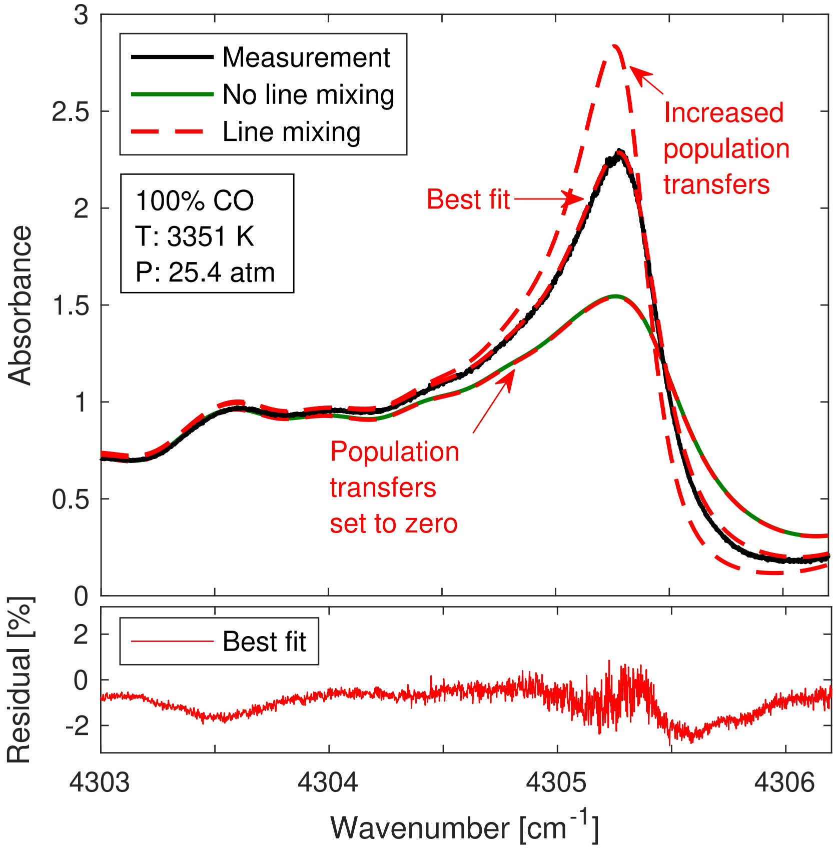

Figure 7.9: Absorbance measurement of the $v(1 \rightarrow 3)$ first overtone bandhead of CO at 3351 K and 25.4 atm with spectral simulations using Eq. 7.1 (green), Eq. 7.3 (red) with no population transfers ($a_1 = 0$), too many population transfers, and best-fit population transfers.

spectra. As population transfer rates increase, line mixing favors population transfers from weak absorption regions to strong absorption regions; consequently, narrowing the spectral structure and increasing the differential absorption near the bandhead.

It is informative to compare the transfer rates of different transitions as a function of ΔJ. Fig. 7.10 shows the rates for select transitions given by the line mixing model at two conditions. Since collision-induced transfers across larger rotational levels require more energy, $R_{J \rightarrow K}$ decays as ΔJ increases. Accordingly, Fig. 7.10 illustrates that at higher temperatures, the population transfers from larger ΔJ become more significant. This can be described through Eq. 7.7 and Eq. 7.13. It should be noted that the relaxation matrix scales

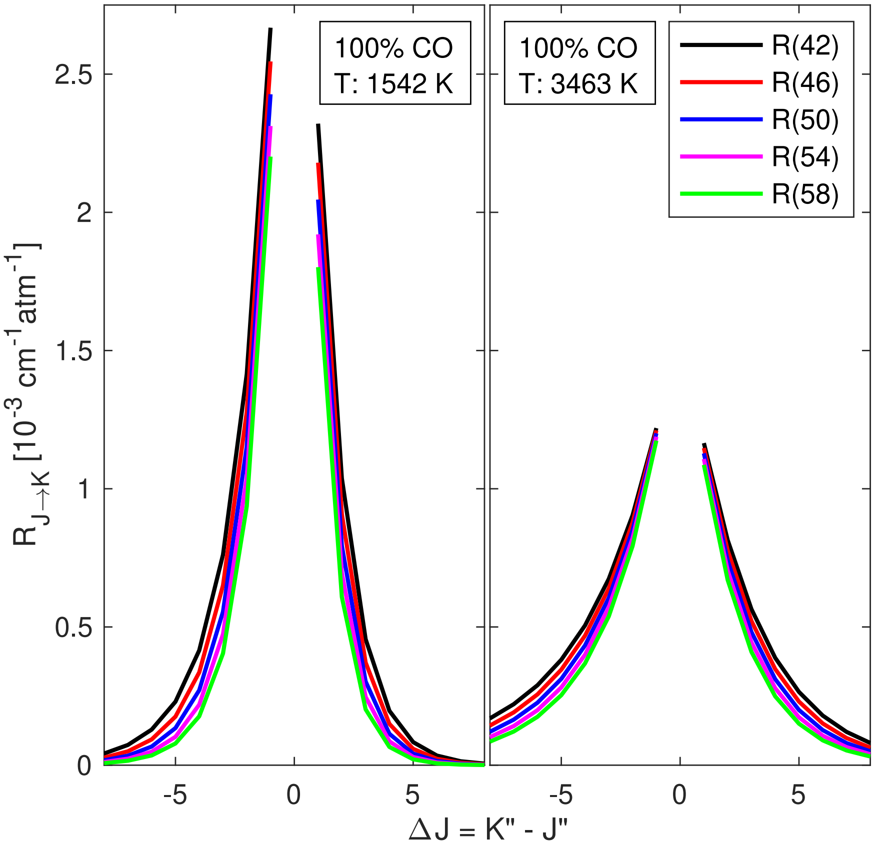

Figure 7.10: Population transfer rates $R_{J\to K}$ given by the MEG model, from selected initial states J''= 42, 46, 50, 54, and 58 to final K'' states, plotted as $\Delta J = K'' - J''$.

linearly with pressure, but the relative probability of collision-induced transfers between a given ΔJ is only dependent on temperature. Previous studies have implemented the MEG model at room temperature and shown that collision transfer rates occur predominantly at $\Delta J = \pm 1$ [285, 286]. However, at the high temperatures ($>$ 1500 K) investigated in this work, population transfers with larger ΔJ significantly contribute to the population redistribution.

With the MEG law coefficients inferred empirically at various conditions, the temperature dependence of $a_1(T)$ was found through Eq. 7.15 by fitting experimental data at different temperatures, while holding a_2 and a_3 constant. The temperature dependence of the relaxation matrix is captured in Fig. 7.11 for both CO-CO and CO-Ar collisions. Notably, the temperature exponents for the off-diagonal components of the relaxation matrix are larger

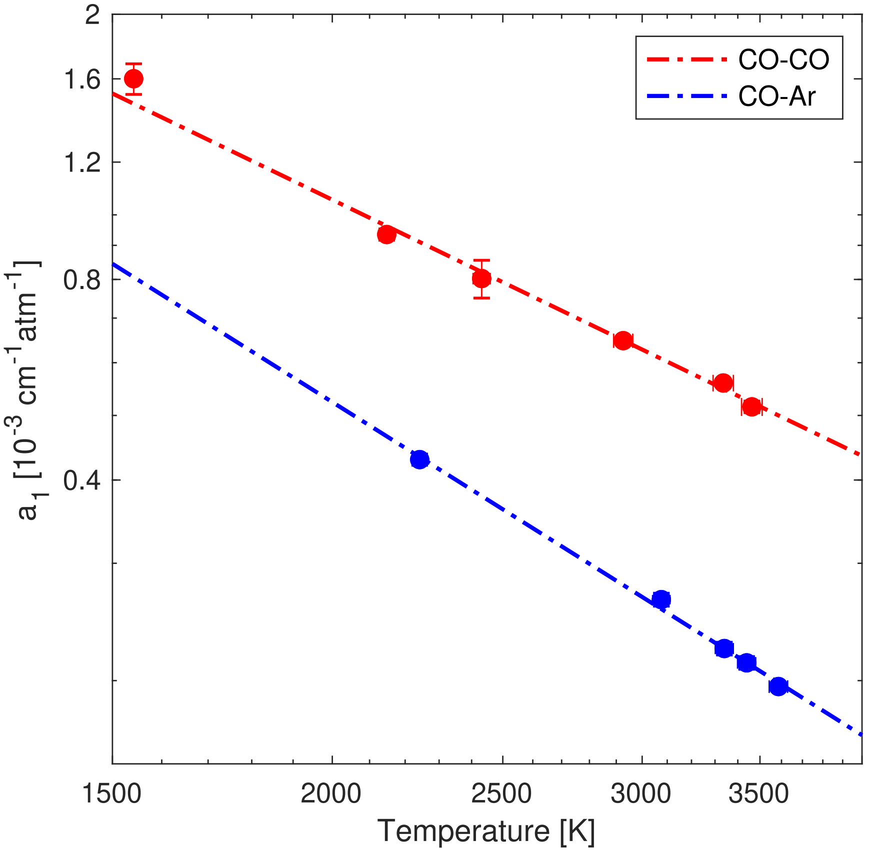

Figure 7.11: Best-fit determinations of a_1 for different temperatures (markers) with power law fits (dashed line) for both CO-CO (red) and CO-Ar (blue) collisional line mixing.

than those of the corresponding broadening coefficients. For CO-CO collisions, a_2 and a_3 were obtained at 3463 K and 18.7 atm with a_1 reported at a reference temperature of 1500 K. Similarly, for CO-Ar collisions, a_2 and a_3 were obtained at 3586 K and 28.3 atm with $a_1(T)$ reported at a reference temperature of 1500 K. The reported MEG law coefficients can be found in Table 7.2. It is important to note that the specific transfer rates obtained by the reported MEG law coefficients do not in themselves sum up to the broadening coefficient (as shown in Eq. 7.11) as there are other state-changing collisions not accounted for in the modeled absorbance. As such, caution should be exercised in using these inferred population transfer rates beyond modeling the target absorption spectra, as the absolute values have not been normalized.

With an established temperature dependence for $R_{J\rightarrow K}$ and γ_J, the full relaxation matrix

Table 7.2: Temperature-dependent MEG law parameters determined in this work

	a_1(1500 K) [10^{-3} cm^{-1}atm^{-1}]	a_2	a_3	a_4	m
CO-CO	1.52 ± 0.15	0.51 ± 0.05	5.21 ± 0.10	2	1.28 ± 0.06
CO-Ar	0.85 ± 0.13	0.30 ± 0.04	7.46 ± 0.15	2	1.66 ± 0.09

can be calculated over a wide range of temperatures and pressures. To validate the pressure scalability of the line mixing model, a series of shock tube experiments were conducted from 5–25 atm for pure CO and 25–60 atm for 30%CO/Ar at similar temperatures, respectively, as shown in Fig. 7.12 and Fig. 7.13. At all pressures, the line mixing model exhibits excellent agreement with the measured absorbance spectra. More specifically, in these figures, the a_i

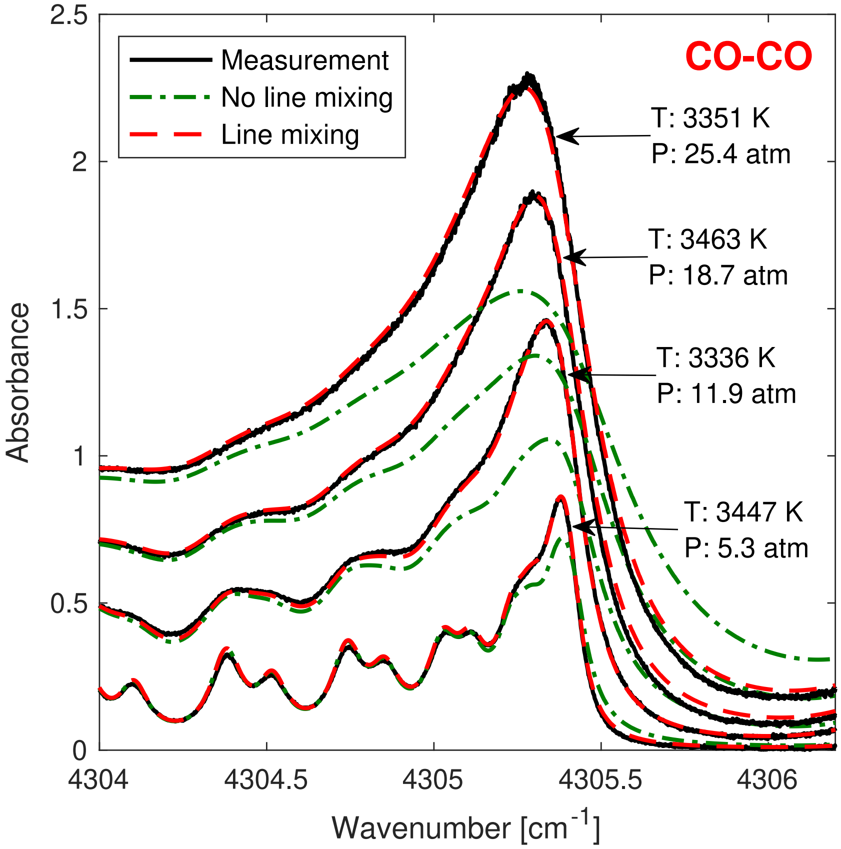

Figure 7.12: CO-CO: measured spectral absorbance compared to the developed MEG model used capture line-mixing effects over a range of pressures. The simulated spectral absorbance with no line mixing is illustrated for reference.

parameters were obtained at a single pressure and then used to calculate the spectra at the other pressures; therefore, validating the pressure scalability of the MEG law model. It should be noted that below 5 atm we found the simulated spectral shape could no longer accurately represent the measured spectra, a limit associated with the Lorentzian lineshape assumption in Eq. 7.3. An additional Voigt convolution step with the Gaussian function is required to capture the less prominent line mixing at lower pressures.

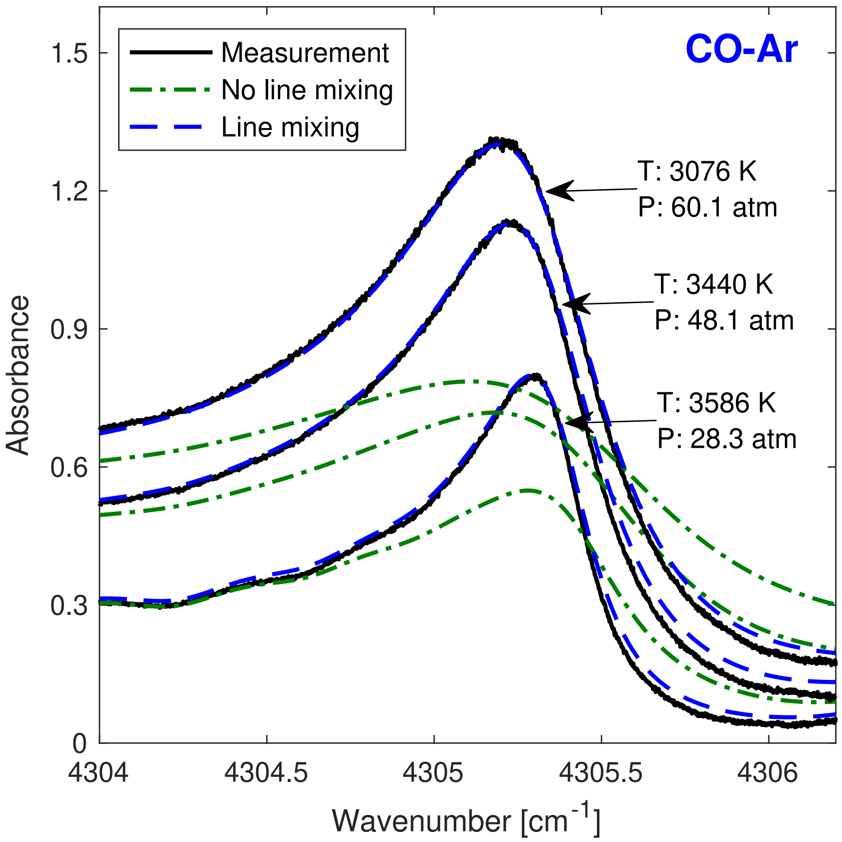

Figure 7.13: CO-Ar: measured spectral absorbance compared to the developed MEG model used capture line-mixing effects over a range of pressures. The simulated spectral absorbance with no line mixing is illustrated for reference.

7.5 Summary

Self- and Ar-broadening coefficients and temperature-dependent exponents for CO have been measured and reported for 17 rovibrational transitions, R(42)–R(58), in the $v(1 \rightarrow 3)$ first overtone hot band of CO near 2.3 μm. Experiments were conducted over a wide range of temperatures, 1200–3750 K, utilizing a shock tube facility and a heated gas cell. To the authors' knowledge, this work represents the first experimental study of these very high rotational energy transitions ($E'' = 5500$–8600 cm^{-1}), extending the spectroscopic knowledge base of temperature-dependent broadening for CO. With broadening parameters established, a modified exponential gap model was developed to evaluate the thermodynamic scaling of state-specific collisional transfer rates associated with line mixing. The line-mixing model developed in this work quantitatively resolves the spectral domain over a range of extreme temperatures and pressures, 2000–3600 K and 5–60 atm, relevant to combustion and planetary entry.

7.6 Supplementary material

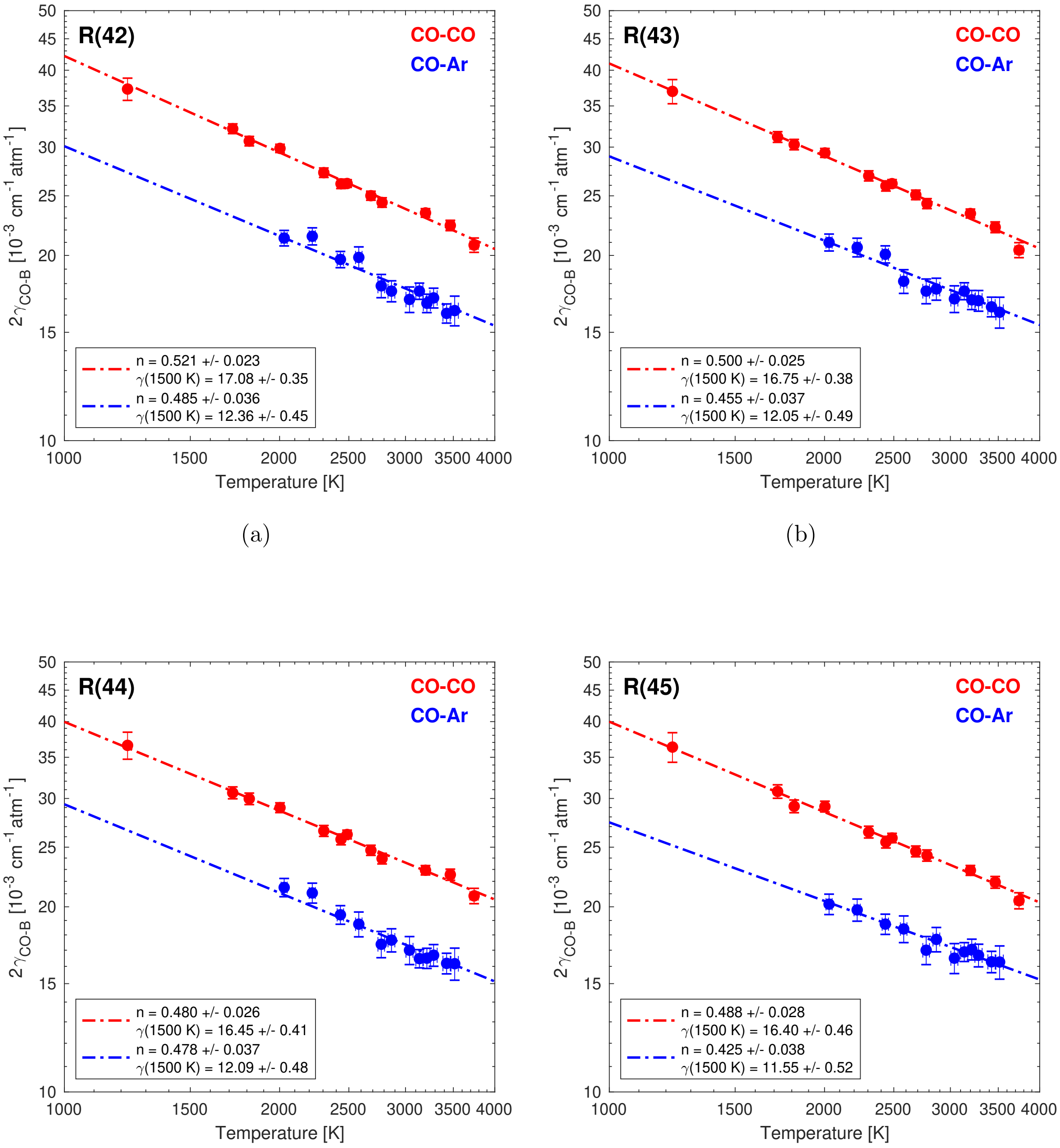

(a) (b) (c) (d)

Figure 7.14: CO- and Ar-broadening coefficients and temperature exponents for (a) R(42), (b) R(43), (c) R(44), and (d) R(45) with power-law fits for 1000–4000 K. Units of γ(1500 K) given in $[10^{-3}\ \mathrm{cm}^{-1}\mathrm{atm}^{-1}]$.

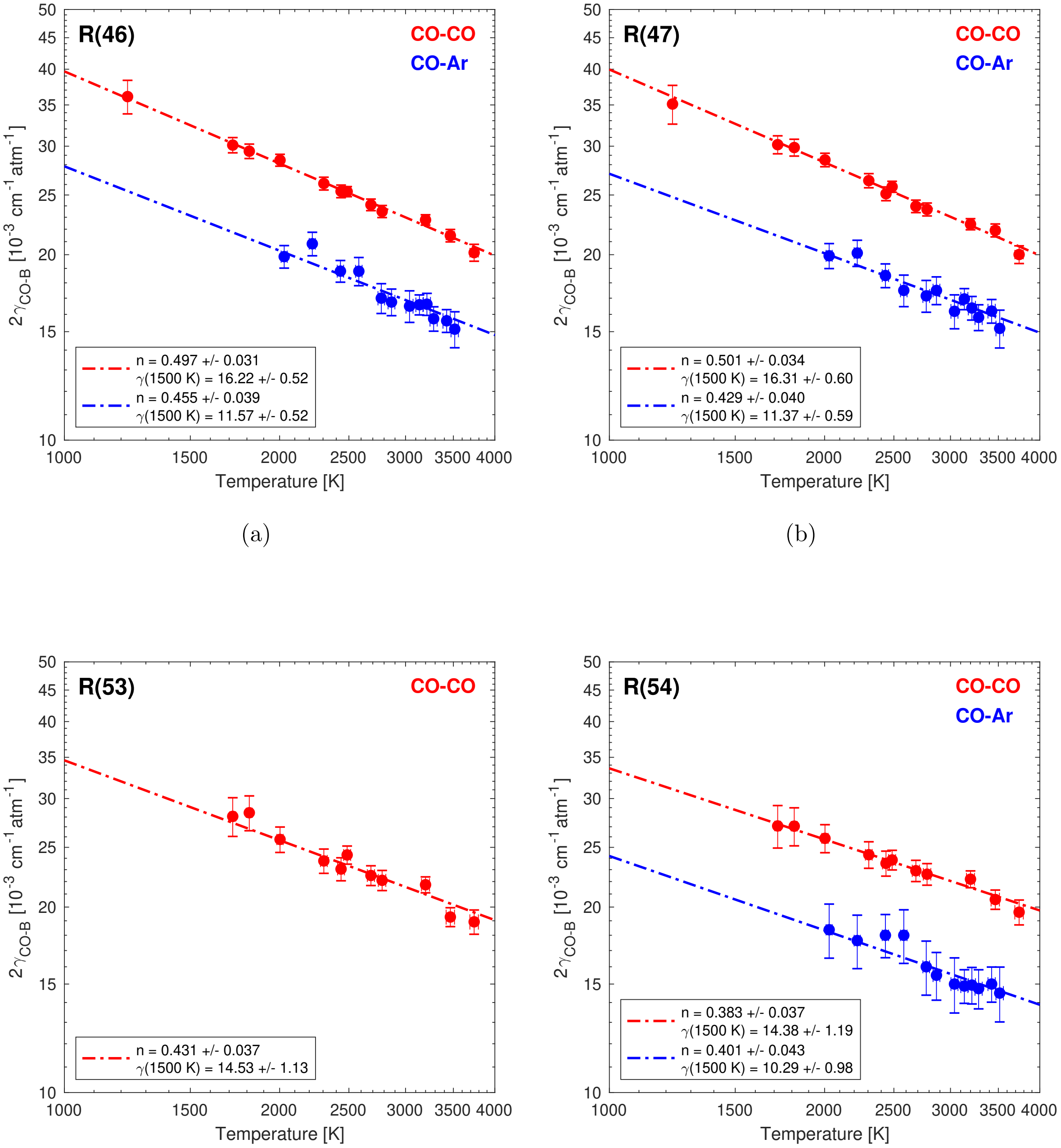

(a) (b) (c) (d)

Figure 7.15: CO- and Ar-broadening coefficients and temperature exponents for (a) R(46), (b) R(47), and (d) R(54). CO-broadening coefficient and temperature exponent for (c) R(53). Power-law fits for 1000–4000 K and units of $\gamma(1500\text{ K})$ given in $[10^{-3}\text{ cm}^{-1}\text{atm}^{-1}]$.

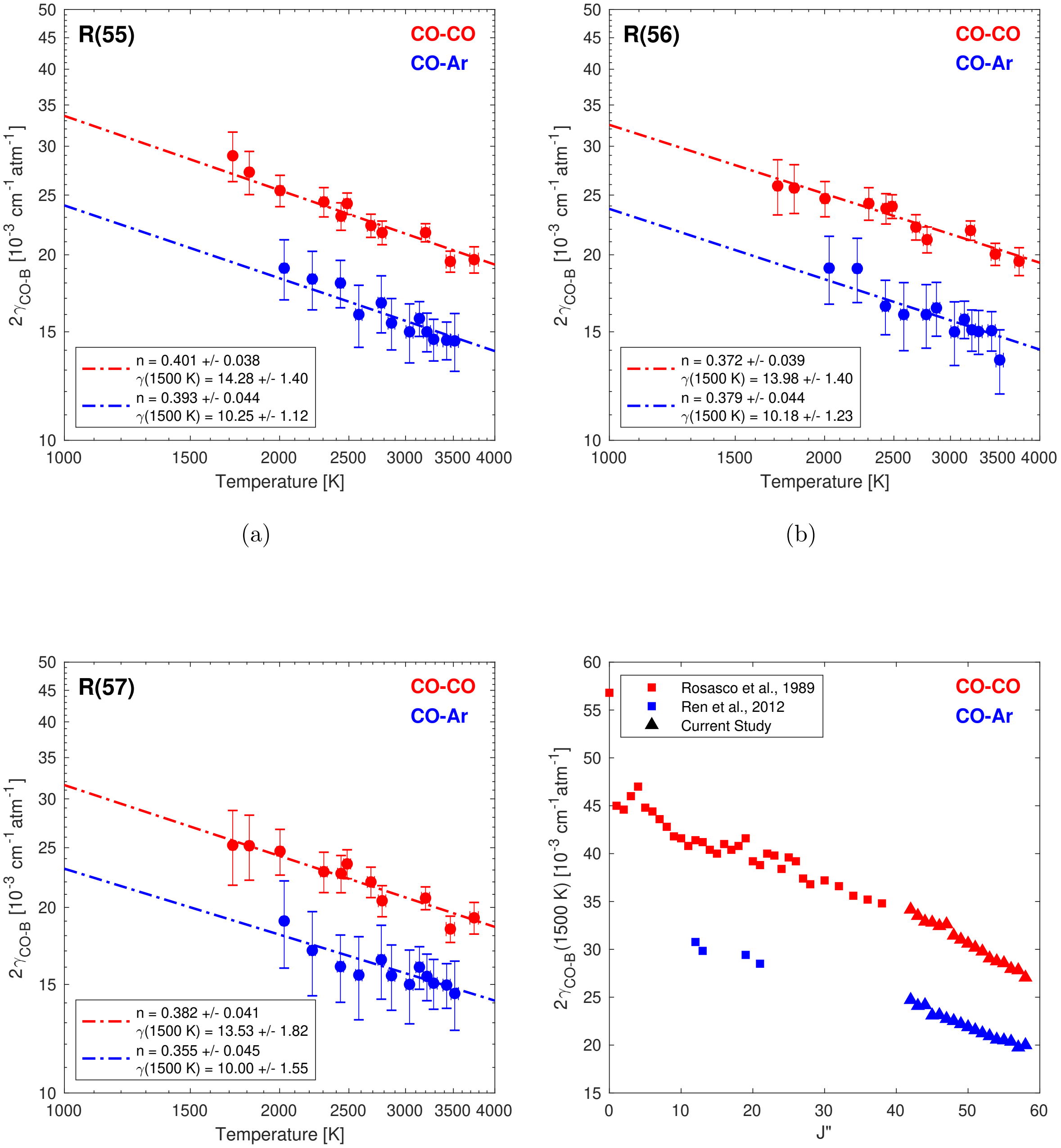

(a) (b)

(c) (d)

Figure 7.16: CO- and Ar-broadening coefficients and temperature exponents for (a) R(55), (b) R(56), and (c) R(57) with power-law fits for 1000–4000 K. Units of γ(1500 K) given in [10^{-3} cm^{-1}atm^{-1}]. (d) CO- and Ar-broadening coefficients at 1500 K for R(42)–R(58) (current study) compared to previous works [169, 279]

CHAPTER 8

Thermochemistry measurements in high-pressure liquid-propellant rocket combustors

The contents of this chapter have been published in the journal ***Applied Physics B*** *under the full title 'Cross-band infrared laser absorption of carbon monoxide for thermometry and species sensing in high-pressure rocket flows' [287]*

8.1 Introduction

For chemical rockets, combustion chamber pressure directly influences mass-specific thrust, or specific impulse, which is a critical factor to enabling higher payload mass fractions and mission capability. Higher combustion pressures increase specific impulse via two primary mechanisms: (1) high pressures suppress dissociation of major products, yielding higher combustion temperatures and characteristic velocities, and (2) higher pressure ratios between the chamber and exhaust yield a higher nozzle thrust coefficient. Due to these factors, considerable effort has been placed in maximizing combustion chamber pressure in rockets. As a point of reference, Space Exploration Technologies Corporation (SpaceX) recently announced a combustion chamber pressure record of 269 bar in the new Raptor CH_4/O_2 rocket engine, which is currently in development [288]. To assess combustion performance and support research and development of the next generation of chemical rockets, diagnostics capable of operating in high-pressure environments on this order of magnitude are needed.

Rocket combustor performance is typically evaluated through c^* efficiency, $\eta = c^*/c^*_{ideal}$, where $c^* = p_0 A^*/\dot{m}$ and involves measurement of the chamber pressure and total propellant mass flow rate. As discussed in Sec. 1.3, such measurements provide a convenient global assessment of the conversion of chemical energy to thermal energy but, because pressure is nominally constant in a combustor, they lack any information on specific internal mechanisms that may cause low combustion performance. A more granular approach would be to measure and track the changes in gas composition and temperature along the axis of flow [289]. The spatial variation of these parameters internal to a rocket combustion chamber reflect the evolution of mixing, evaporation, and chemical kinetics that dictate overall performance. Unfortunately, the extreme thermodynamic operating conditions typical of liquid-propellant rocket combustion ($T > 3000$ K, $P > 50$ bar) and sooting propensity associated with hydrocarbon fuel-rich combustion present a challenging environment for measuring temperature and species in situ [148].

Laser absorption spectroscopy (LAS) has been utilized for quantitative in situ measurements of species and temperature for a variety of harsh combustion environments, including some applications to rockets. Several works have been dedicated to LAS measurements in rocket plumes near ambient pressure [290, 291], while a limited number of in-chamber measurements at elevated pressures have also been demonstrated. Specifically, Locke et al. conducted near-infrared absorption measurements of water vapor in a GH_2/GOx rocket combustor up to 8 bar [292], and Zeng et al. performed infrared absorption measurements of N_2O, NO, and CO in an ammonium-dinitramide based rocket thrust chamber near 7 bar [293]. It can be noted that these pressures (< 10 bar) are quite low by rocket standards. At high pressures (> 50 bar), collisional broadening and blending of the spectra significantly reduces the number of prospective wavelengths for conducting thermometry and species measurements, as seen in Fig. 8.1, presenting unique challenges for sensor design. Recently, our research group utilized a wavelength modulation spectroscopy technique in the mid-infrared to measure CO mole fraction in a kerosene-fueled liquid rocket combustor at pressures up to 70 bar, marking a breakthrough in relevant pressure capability [183, 294]. Here, we build on this prior work, introducing a novel multi-wavelength strategy that adds in situ temperature measurement capability at practical rocket combustion pressures.

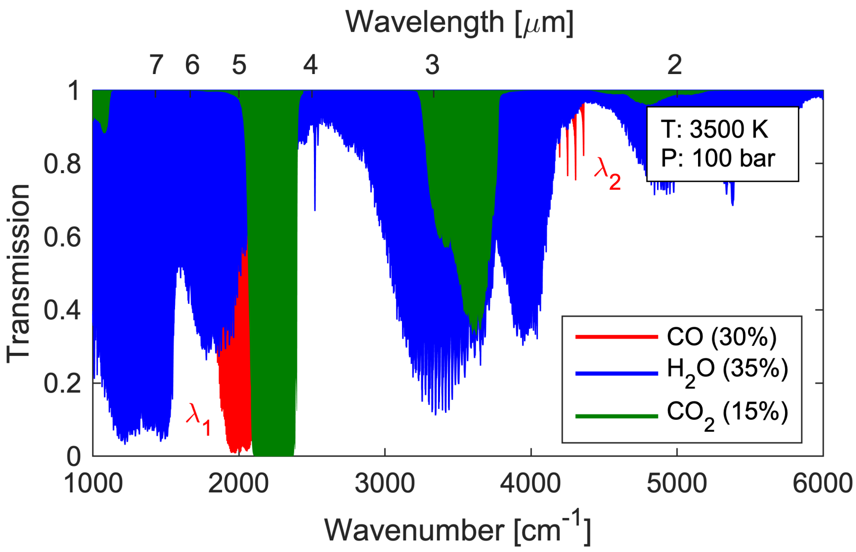

Figure 8.1: Spectral transmission of CO, H_2O, and CO_2, highlighting targeted wavelengths for the cross-band sensing strategy. Simulated conditions are representative of a liquid-propellant rocket combustor with an optical pathlength of 2.5 cm.

This paper describes the development and deployment of a unique cross-band infrared laser absorption spectroscopy (LAS) sensing strategy for in situ temperature and species measurements in high-pressure rocket flows. Key elements of novelty and significance include: (1) wavelength selection strategy, (2) high-pressure range capability, and (3) application to a relevant rocket combustion environment. The measurement technique simultaneously probes transitions in both the fundamental (4.98 μm) and first overtone (2.32 μm) infrared bands of nascent carbon monoxide (CO), indicated in Fig. 8.1, exploiting the distinct temperature dependencies at disparate wavelengths to achieve a broad range of sensor operability (at high pressures). Notably, deviations in spectral behavior (i.e. line mixing) at the high gas densities targeted in this work are shown to require changes in spectroscopic modeling methods to enable quantitative data interpretation. To demonstrate capability, the cross-band thermometry and species sensing method is deployed on a single-element-injector rocket combustor operating on RP-2/GOx and CH_4/GOx propellant combinations, reaching pressures up to 105 bar.

8.2 Sensor design

8.2.1 Wavelength selection

Rocket combustors typically operate fuel-rich and at relatively extreme thermodynamic conditions (P > 50 bar, T > 3000 K). For a hydrocarbon fuel and oxygen, the equilibrium combustion product mixture includes a large fraction (%) of infrared active diatomic species (OH, CO) as well as the major products (CO_2, H_2O). High concentrations of carbon monoxide ($X_{CO} > 30\%$) provide an attractive target to track changes in gas composition and thermodynamic state as a measure of combustion progress. CO has smaller collisional cross-sections than the larger polyatomic products (e.g. CO_2, H_2O) and therefore can have substantially less spectral broadening at high pressures, as discussed in Sec. 3.1 [147]. This fundamental spectroscopic characteristic helps preserve differential absorption and lessens interference at elevated pressures, providing a basis for the development of an LAS thermometry technique above the pressure limits (∼50 bar) of previous work [192]. Accordingly, this effort targets carbon monoxide absorption in the infrared.

Gas temperature and species mole fraction are commonly inferred using a two-wavelength absorption technique [147]. Wavelength-pair selection criteria include: (1) absorbance between optically thin and thick limits, (2) minimal interference from other absorbing species, and (3) high temperature sensitivity. All three of these criteria become more challenging to meet at high gas pressures. As aforementioned, collisional broadening scales linearly with pressure and blends transitions. This reduces differential absorbance and increases interference. Moreover, due to scaling of absorbance with gas density, the stronger vibrational bands can become optically thick at relatively short pathlengths in high-pressure environments. Fig. 8.1 highlights these issues, showing simulated transmission through a 2.5 cm optical path for a representative hydrocarbon rocket combustion product mixture at 100 bar. Due to extreme line broadening, spectral interference by H_2O and CO_2 is prevalent throughout the infrared. The CO spectra (shown in red) can be accessed in the P-branch of the fundamental band near 4.98 μm and in the R-branch bandheads of the first overtone near 2.32 μm, with minimal but not entirely avoidable interference. Zoomed in regions of this domain can be seen in Fig. 8.2. The wavelength region near 4.98 μm is dominated by the P($J = 31$) line of the ground state fundamental band, but also includes contributions from other neighboring hot band lines [183]. The first overtone bandhead near 2.32 μm consists of multiple transitions ($J = 40$–60) belonging to the $v(1\rightarrow3)$ hot band, with some overlapping contributions from the ground state $v(0\rightarrow2)$ first overtone band [219].

For thermometry, ideally two neighboring lines or wavelengths can be accessed with a single light source and/or shared detection optics. Unfortunately, at very high pressures the local spectra within a band becomes sufficiently blended that wavelengths in close proximity have increasingly similar temperature dependence, determined by the aggregate line strengths and lower state energy levels of the many overlapping transitions. This results in

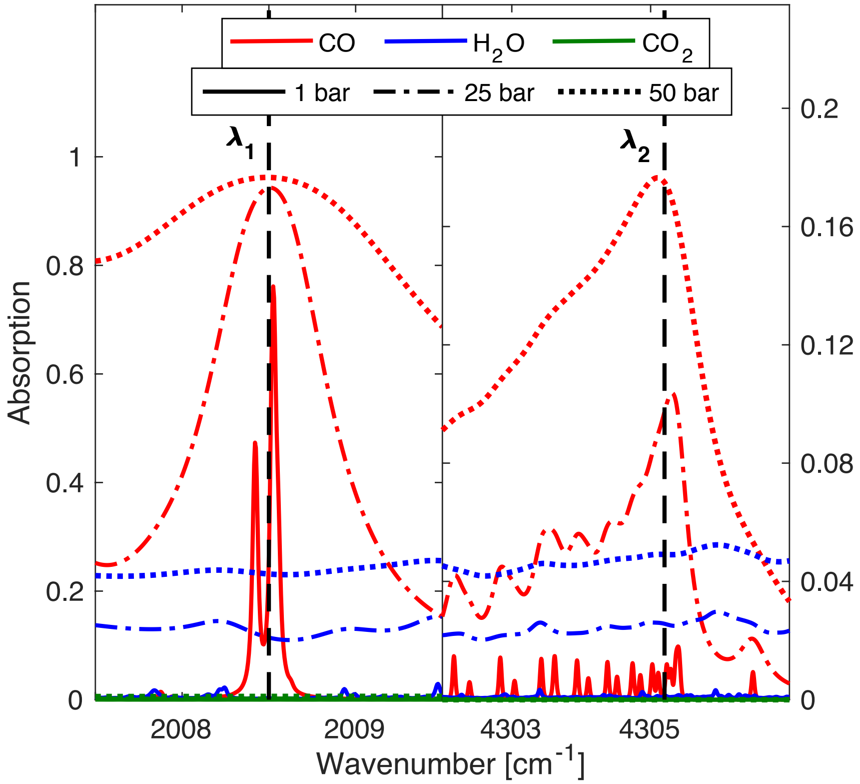

Figure 8.2: Simulated absorption spectra in CO's fundamental band and first overtone band, illustrating collisional effects at high pressures. Simulated conditions: T = 3500 K, $X_{\mathrm{CO}} =$ 30%, $X_{\mathrm{H_2O}} =$ 30%, $X_{\mathrm{CO_2}} =$ 10%

accessible wavelength pairs within the same band having poor temperature sensitivity, which reduces thermometry range and accuracy. This effect is quantified and shown in Fig. 8.3. A candidate intra-band wavelength pair was selected within the accessible low-interference region of the fundamental band near 4.98 μm. However, the temperature sensitivity of the local peak absorbance ratio, $R = \alpha(\lambda_1)/\alpha(\lambda_2)$, was found to be undesirably low. To resolve this limitation, a cross-band wavelength pair from the disparate fundamental (λ_1: 4.98 μm) and first overtone (λ_2: 2.32 μm) bands of carbon monoxide was considered, and proved to yield superior temperature sensitivity at high pressures, consistent with other cross-band techniques [170, 246, 295]. The specific wavelength selections are shown in Fig. 8.2.

Spectral interference from other major infrared-active hydrocarbon combustion products is minimal at both wavelengths relative to the surrounding domain, but significant on an absolute basis. A scanned-wavelength modulation spectroscopy technique employing normalized second harmonic detection is utilized to recover signals related to the differential absorption at each wavelength in the harsh rocket environment, similar to our prior

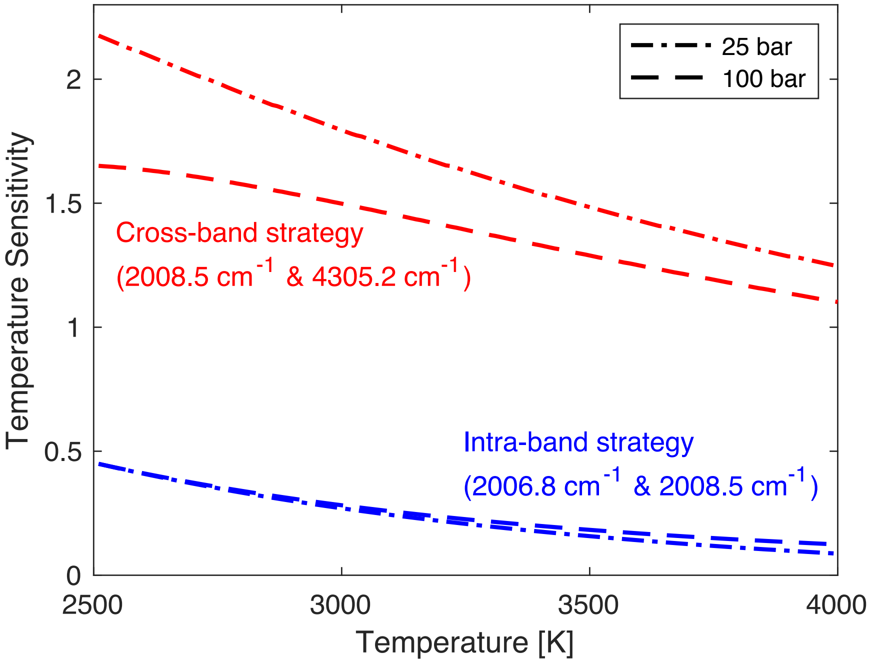

Figure 8.3: Temperature sensitivity $(\mathrm{d}R/R)/(\mathrm{d}T/T)$ of the cross-band sensing strategy compared to more traditional intra-band sensing strategies at elevated pressures.

work [183]. This approach generally negates the influence of baseline signal changes including attenuation associated with spectrally-flat absorption such as the H_2O interference noted in Fig. 8.2 [296, 297].

8.2.2 Optimizing laser tuning parameters

As mentioned, the scan and modulation depths (a_S and a_M) and associated tuning frequencies (f_S and f_M) of the optical output can be adjusted to optimize the quality of the WMS harmonic signals for a target gas condition and measurement environment. A model of the WMS harmonics based on laser-specific tuning characteristics is utilized to inform parametric optimization [297]. For this sensor, optimum modulation depth is deemed the value at which the WMS-$2f$ signal is maximized. Although the $2f$ and $1f$ signals are typically not maximized at the same modulation depth, maximizing $2f$ generally increases the signal-to-noise of the normalized WMS-$2f/1f$ measurement. In probing high-pressure spectra, rapidly-tunable semi-conductor lasers are often unable to achieve an optimal modulation depth and the $2f$ monotonically increases with a_M until it reaches a maximum limit. SNR can be further influenced by modulation frequency. Modulating at higher frequencies enables high time resolution measurements and typically suppresses noise. Common noise sources (vibrations, beam steering, etc.) in engine applications usually occur at relatively low frequencies (< 10 kHz) and can be mitigated by modulating at much higher frequencies and filtering around those frequencies. Unfortunately, modulation frequency has an inverse relationship with modulation depth (see Fig. 8.4 (*top*)) and thus a compromise is required between the competing demands of signal quality and time resolution. Additionally, adding a low frequency waveform to the high frequency modulation further reduces the maximum modulation depth available. The low frequency scan is added to ensure that the local absorption peak is measured, allowing for some uncertainty in the pressure shift of the targeted transitions. However, since it is not necessary to fully resolve the harmonic spectra to interpret measurement data, the scan depth of the low frequency waveform can be minimized in order to maximize the modulation depth.

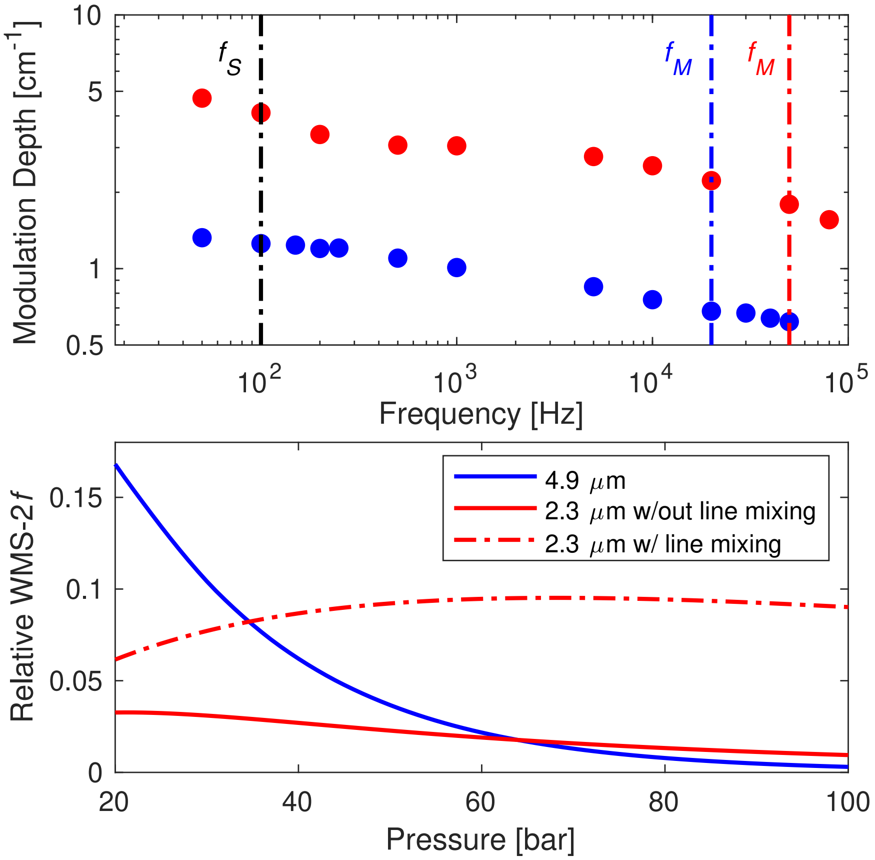

Figure 8.4: *Top*: Maximum modulation depth over a range of frequencies for the QCL near 4.98 μm and the DFB diode near 2.32 μm. *Bottom*: Simulated WMS-2f signals ($a_M = 0.5$ cm^{-1}) over a range of pressures.

Fig. 8.4 (*top*) illustrates the maximum modulation depth at different frequencies for the two lasers chosen for the cross-band technique. To target CO's fundamental band near 4.98 μm and first overtone band near 2.32 μm, a distributed feedback (DFB) quantum cascade laser (QCL) and DFB diode laser are utilized, respectively. The maximum modulation depth is determined by injecting the maximum allowable current range at a given frequency and measuring the corresponding change in relative wavenumber with a germanium etalon. For both light sources, maximum modulation depth is shown to decrease logarithmically as frequency increases. Fig. 8.4 (*bottom*) also illustrates the simulated WMS-2f signals ($a_M = 0.5$ cm^{-1}) for both lasers over a range of pressures at the targeted wavelengths for a representative rocket combustion condition. As pressure increases and the spectra broadens, the second harmonic signal generally decreases due to its sensitivity to line-shape curvature, which is diminishing. As a result, it is desired to utilize a large modulation depth at high pressures to fully capture the spectral shape and maximize pressure range capability. When comparing the two wavelengths, the WMS-$2f$ from the fundamental band starts higher but decreases at a much faster rate than the overtone band. This relates to the favorable characteristics of the bandhead in retaining spectral structure at extreme conditions. Furthermore, the bandhead region is subject to high-pressure line-mixing effects, which induce a spectral narrowing of the vibrational band and preserves differential absorption. Consequently, accounting for line mixing results in a higher WMS-$2f$ signal across all pressures in the first overtone band. The benefit of exploiting this phenomenon increases with increasing pressure. Fig. 8.4 (*bottom*) shows that at 100 bar, line mixing results in nearly an order of magnitude gain in the WMS-$2f$ signal relative to the simulation that ignores line mixing (discussed further later).

For the present work, a scan depth of 0.13 cm^{-1} at 100 Hz was chosen for the QCL near 4.98 μm. The remaining injection-current budget was allocated to a modulation depth of 0.50 cm^{-1} at 20 kHz. For the DFB diode laser centered near 2.32 μm, a scan depth of 2.55 cm^{-1} at 100 Hz was utilized. Similar to the QCL, the remaining injection-current budget was devoted to a modulation depth of 0.48 cm^{-1} at 50 kHz. These parameters were selected as a compromise of the competing demands aforementioned, aiming to achieve high WMS-$2f$ signal quality (SNR) over a pressure range of 20–100 bar.

8.2.3 Optical interface

Fig. 8.5 above illustrates the optical configuration for the cross-band absorption sensing technique and hardware interface for conducting measurements at a fixed axial location on the target liquid bi-propellant rocket combustor. To probe the fundamental CO absorption band near 4.98 μm and the first overtone band near 2.32 μm, a DFB QCL with ∼50 mW output power and a DFB diode laser with ∼5 mW output power are utilized, respectively. An inherent challenge presented by this approach is the wavelength-specific nature of many optical components (e.g. detectors, fibers) that potentially increases sensor complexity. To

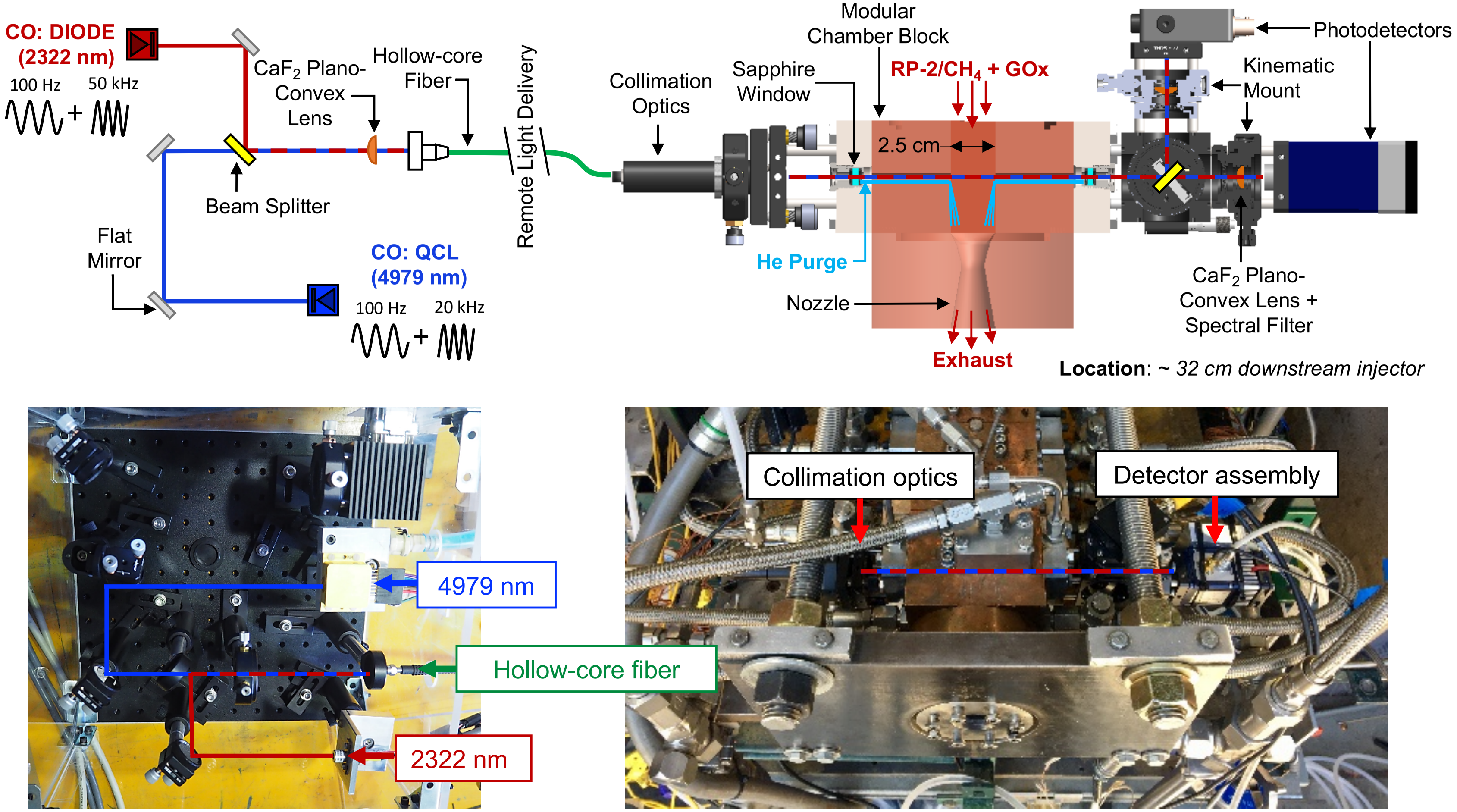

Figure 8.5: Optical interface for high-pressure CO sensing measurements in a liquid-propellant rocket combustor. Key features include a hollow-core fiber for remote light delivery and a He/N2 purge system to maintain clear optical access

reconcile this, both incident beams are free-space coupled into one hollow-core fiber with broad transmissivity (300 μm diameter) [298]. The fiber output is then re-collimated using another $\mathrm{CaF_2}$ lens and is transmitted across the combustion chamber through two wedged sapphire windows (3/8 in. diameter with 1° wedge). The sapphire windows have an aperture of 4 mm and are recessed $\sim$5 cm from the combustion flow path. A beam splitter separates the transmitted light so that each beam can be spectrally filtered for its respective wavelength (Spectrogon, 2320±20 nm and 4960±148 nm) before being collected on distinct thermoelectrically cooled photodetectors. An InGaAs photodetector (Thorlabs PDA10D) with 15 MHz bandwidth is utilized for 2.32 μm light and a MCT photovoltaic detector (Vigo PVI-4TE-5-1) with 10 MHz bandwidth is utilized for 4.98 μm light. Measurements are taken across a 2.5 cm transverse optical pathlength located $\sim$32 cm downstream of the single-element injector. Raw detector data were typically collected at a sample rate of 10 MHz for 5 s intervals with hot-fires spanning 2–3 s in duration.

The optical setup described above included mechanical mounts for beam pointing and translation, which were used to optimize alignment and maximize the transmitted light intensity during the experiment. A number of complementary hardware-related elements, including a N_2 purge system in the fiber-optic and pitch assembly and a He purge system in the chamber, were implemented to mitigate signal-convoluting factors in the test environment. The N_2 purge system displaces excessive water vapor in the optical path that can spectrally interfere with CO. The He purge system aims to minimize soot deposition on the sapphire windows by keeping the optical path clear while minimizing the penetration depth of He into the chamber [299]. Laser tuning and signal processing methods discussed in Sec. 8.2.2 were also chosen to mitigate environmental noise.

8.3 Experimental results

8.3.1 Initial sensor demonstration

A series of measurements over a range of pressures and mixture ratios (MR) were conducted on a single-element-injector rocket combustor with both CH_4/GOx and RP-2/GOx as propellants. The test facility is located at the Air Force Research Laboratory on Edwards Air Force Base. These measurements built on prior research from our group conducted at the same facility by introducing the cross-band thermometry that enables in situ temperature measurement capability at practical rocket combustion pressures [183]. For the tests discussed here, the modular chamber block with optical access was located at the furthest location downstream of the injector (∼32 cm), where complete combustion and mixing is most likely to occur. Measurements using CH_4/GOx were conducted at pressures and MR ranging from 25–105 bar and 2.2–4, respectively, while pressures and MR using RP-2/GOx ranged from 25–75 bar and 2.5–4.5, respectively. The details discussed below focus on experiments using CH_4/GOx as propellants but are generally representative of all datasets.

Raw optical signals at both wavelengths were processed through a digital lock-in amplifier to extract the WMS harmonics, from which gas properties could be interpreted. Fig. 8.6 shows the pressure evolution in time for an example test with corresponding WMS-$2f/1f$ signals at 4.98 μm and 2.32 μm for a steady-state chamber condition of 28 bar and MR of 2.33. The WMS-$2f/1f$ signals are background subtracted, with the background taken prior to ignition. The initial rise in pressure around 0.3 s is associated with the purge gas. An abrupt increase in both the pressure and WMS-$2f/1f$ signals around 1.3 s corresponds to the introduction of propellants and ignition, indicating CO presence in the combustor. As chamber pressure increases towards steady-state, the WMS-$2f/1f$ signals slightly decrease due to spectral broadening and reduced differential absorption (more pronounced in 4.98 μm signal). At steady state, 100 Hz oscillations, corresponding to the scan frequency of each laser, become clearly evident in both the 4.98 μm and 2.32 μm signals. As mentioned in Sec. 8.2.3, hot-fire tests typically span a 2–3 s duration with detector data sampled for 5 s.

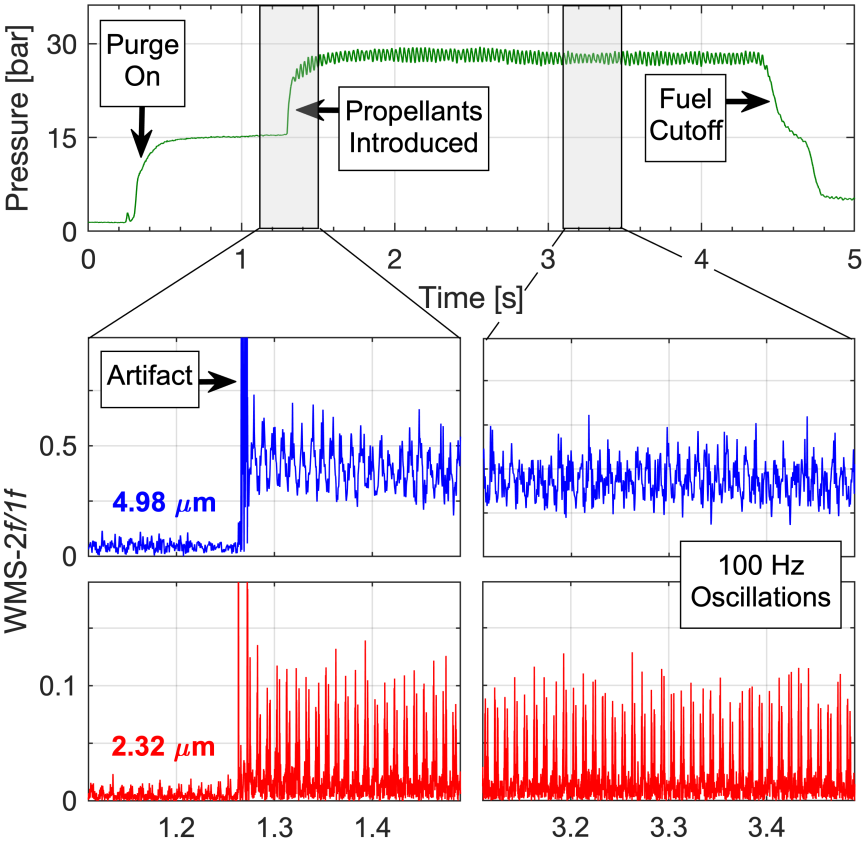

Figure 8.6: Time evolution of chamber pressure and corresponding WMS-$2f/1f$ signals (background subtracted) for 4.98 μm and 2.32 μm.

Fig. 8.7 and Fig. 8.8 compare measured WMS-$2f/1f$ signals to WMS-$2f/1f$ simulations assuming chemical equilibrium for mixture composition and temperature and the HITEMP database [150] for spectral parameters for both 4.98 μm and 2.32 μm. The WMS harmonics are extracted by using a digital lock-in amplifier and a 2 kHz passband filter, then averaged over ∼50 cycles throughout the steady-state chamber condition. Fig. 8.7 illustrates the measurement at the fundamental band for two conditions: 29 bar with a MR of 2.86 and 73 bar with a MR of 2.91. The 100 Hz oscillations from the laser scan (present in Fig. 8.6) are more clearly evident in these zoomed-in WMS-$2f/1f$ signals. The measurements conducted near 4.98 μm demonstrated relatively close agreement with the simulated model at chemical equilibrium. At higher pressures, spectral broadening and reduced differential absorption lowers the SNR of the fundamental band; however, a measurement is still discernible at pressures up to 75 bar, consistent with our prior work [183]. Fig. 8.8 illustrates the measurement at the first overtone bandhead for two conditions: 28 bar with a MR of 2.33 and 105 bar with a MR of 2.93. Notably, the SNR only modestly decreases across this wide pressure range. However, the measured and simulated WMS-$2f/1f$ signals exhibit substantial disagreement, beyond typical uncertainties, in both magnitude and spectral shape, indicating a fundamental error in the spectroscopic modeling of the first overtone band. This was suspected to be a consequence of line-mixing effects (discussed in Sec. 3.2), which occur in spectrally-dense regions [157], such as the bandhead, and were unaccounted for in the original model. In Fig. 8.8, estimates of broadening-related error ($\gamma_{mix} \pm 10\%$) are added to the spectral simulation to elucidate the extent of the disagreement.

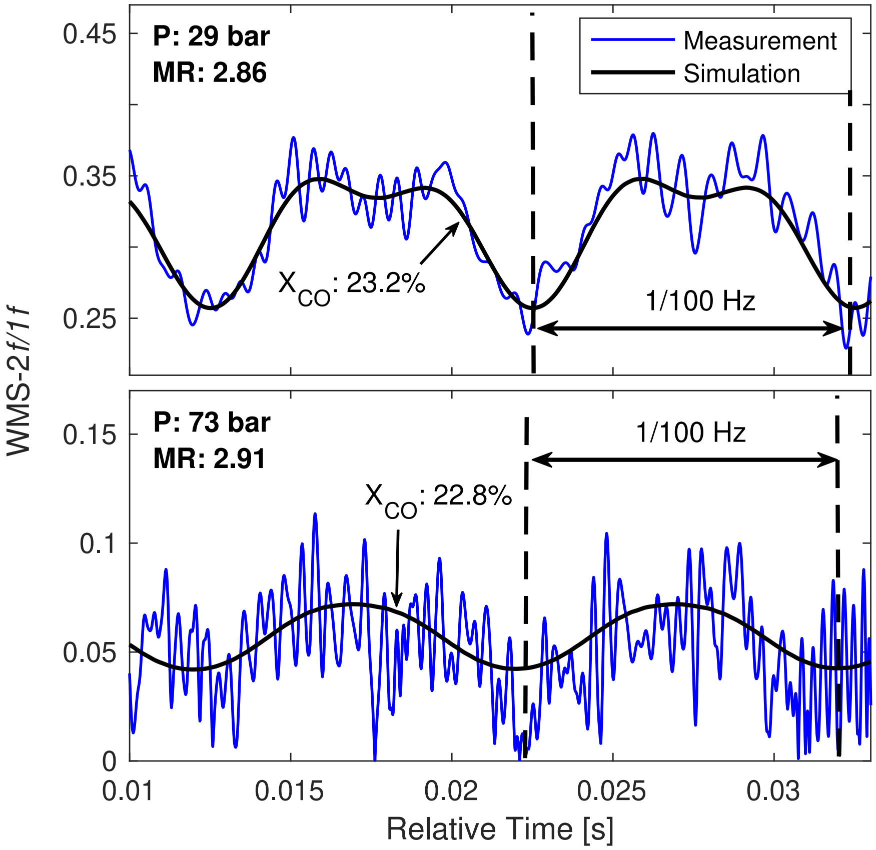

Figure 8.7: Measured WMS-$2f/1f$ signals near 4.98 μm compared to a chemical equilibrium simulation at two chamber pressures and mixture ratios.

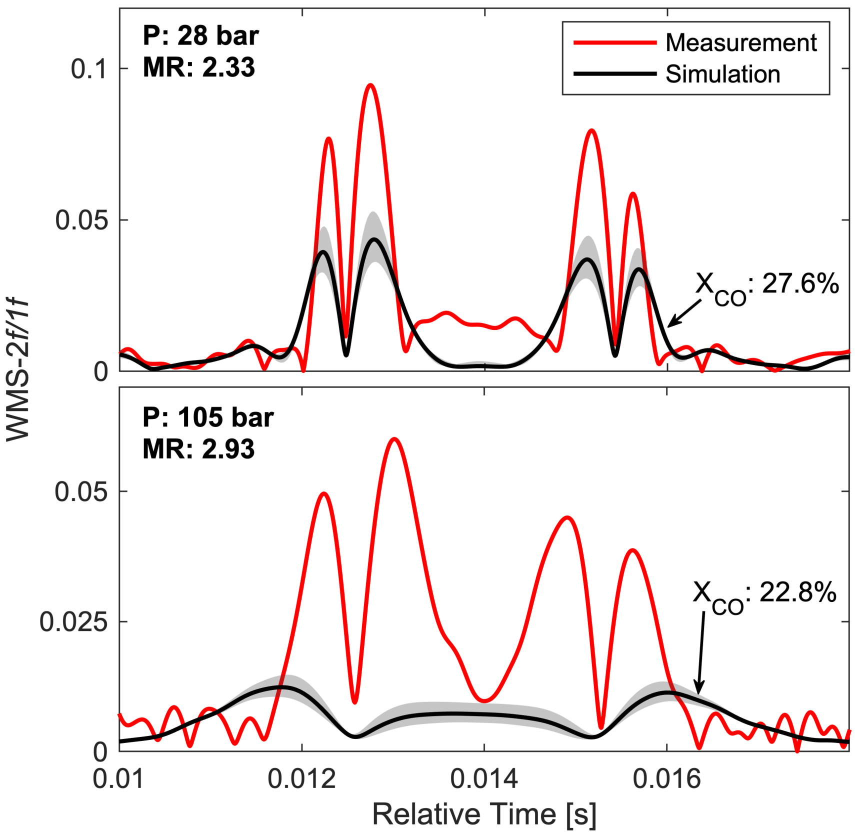

Figure 8.8: Measured WMS-$2f/1f$ signals near 2.32 μm compared to a chemical equilibrium simulation with initial estimates of spectroscopic uncertainty ($\gamma_{mix} \pm 10\%$) bound in grey at two chamber pressures and mixture ratios.

Similar data analysis was carried out for a series of test conditions represented in Fig. 8.9, which highlights trends in SNR and accuracy of the initial simulation model. Measured WMS-$2f/1f$ signals are normalized by simulated WMS-$2f/1f$ signals and plotted over the range of pressures and MR conducted. As mentioned previously, the simulated WMS-$2f/1f$ signal assumes chemical equilibrium for temperature and composition and the HITEMP database parameters with Voigt lineshapes for spectral properties. The WMS signals at 4.98 μm show good agreement with NASA's Chemical Equilibrium with Applications (CEA) software [244, 300] and HITEMP up to 75 bar. However, as pressure increases, collisional-broadening effects in the fundamental band cause the targeted absorption features to broaden and the differential absorption to diminish (see Fig. 8.2). This results in a diminishing SNR

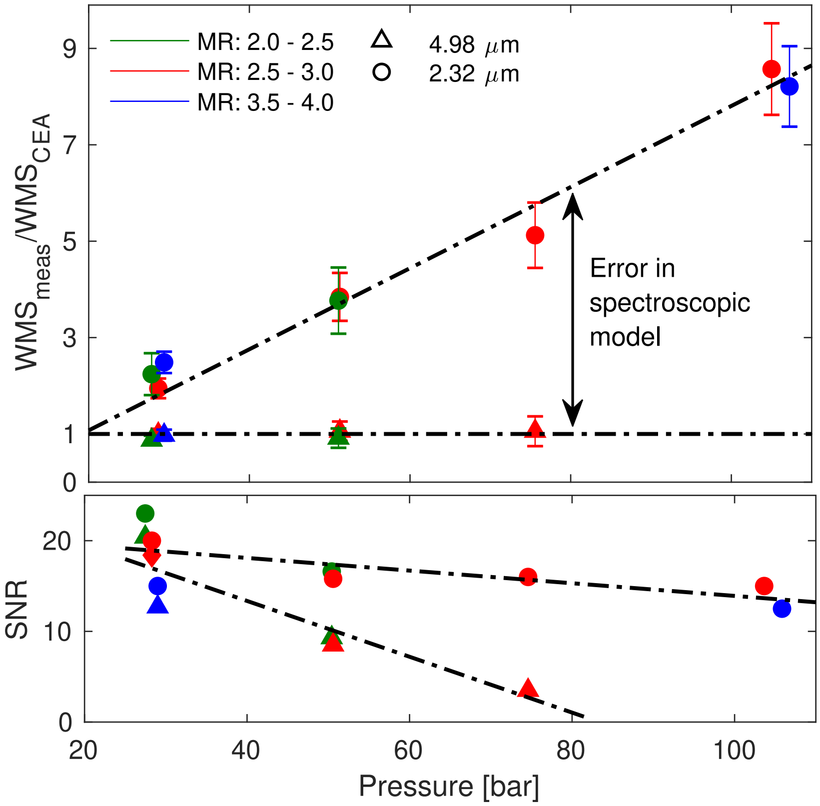

Figure 8.9: Measured WMS-$2f/1f$ signals with SNR compared to chemical equilibrium simulations for both 4.98 μm and 2.32 μm over relevant mixture ratios and pressures.

that approaches unity around 80 bar, deeming any measurements at extended pressures unreliable. The measured WMS signal at 2.32 μm demonstrated adequate signal quality (SNR > 10) at pressures up to 105 bar, as seen in Fig. 8.8. However, disagreement between the simulated and measured signals was substantial, increasing nearly linearly with pressure to almost an order of magnitude disagreement at the highest pressures. As discussed previously, such disagreement was deemed well beyond the typical uncertainties in the simulation, and hypothesized to be a more fundamental error in the spectroscopic model assumptions. It can be noted that by assuming a temperature, the fundamental band measurement near 4.98 μm could solely be used to infer CO concentration, as demonstrated in previous works [183, 294]. To measure temperature, both wavelengths are needed. Therefore, to reconcile the large disagreement between the simulated and measured signals near 2.32 μm, a deeper investigation of the spectral characteristics of the targeted CO $v(1 \rightarrow 3)$ bandhead was initiated.

8.3.2 Interpretation of line-mixing effects

Line-mixing effects in the $v(1\rightarrow3)$ first overtone bandhead of CO at high temperatures and high pressures have been recently studied by our research group on a high-enthalpy shock tube [219]. Direct absorption measurements of CO near 2.32 μm were conducted behind reflected shock waves over a range of pressures (5–60 bar) and temperatures (1200–3750 K) relevant to liquid-propellant rocket combustors. An example of the spectroscopic data highlighting the non-ideal phenomena and modeling at these conditions is discussed briefly here, while a more comprehensive dataset and discussion is available in another paper by the authors [219]. As seen in Fig. 8.10, the measured absorption spectra at a representative rocket condition demonstrates large disagreement when compared to a simulated spectra with no line-mixing effects. The translation of this disagreement to the WMS-$2f/1f$ signal can also be observed. At high gas densities, collision-induced rotational energy transfers within the same vibrational band induce a spectral narrowing effect that amplifies high-absorbing regions. This results in larger differential absorption (i.e. larger WMS-$2f/1f$) in the measured spectra, as observed in the initial sensor demonstration in Fig. 8.8. In order to model the collision-induced population transfers between transitions near the bandhead, a modified-exponential gap (MEG) rate law was adopted [271, 280, 285] (discussed in Ch. 4). The adjustable parameters in the MEG law were obtained by implementing a least-squares fitting routine to the measured data. This allowed line-mixing effects to be accounted within the absorption modeling framework. Measurements over a range of pressures and temperatures further provide for scaling over the full range of relevant thermodynamic conditions present in a rocket combustion chamber. Fig. 8.10 illustrates that the simulated spectra using the MEG law can accurately represent CO absorption in first overtone bandhead. Similarly, the updated spectroscopic line-mixing model in Fig. 8.10 shows the improved agreement in WMS-$2f/1f$ signal that can be achieved by accounting for line-mixing effects.

The controlled shock tube investigation provided concrete support of the line-mixing hypothesis for the initial disagreement observed in the field data and, with appropriate estimates for the population transfer rates, provides a critical new framework for quantitative interpretation of the CH_4/GOx and RP-2/GOx rocket combustor data. The shock tube study focused on quantifying collisional transfer rates and broadening for pure CO and CO perturbed by Ar. In order to account for species-dependent collisional broadening and line mixing in the rocket gas mixtures, additional assumptions were required. Notably, chemical equilibrium was assumed to dictate the composition for the range of mixture ratios and pressures tested. Species-specific spectral parameters and MEG law coefficients were used where available in the literature for other perturbers [280, 301–303], and otherwise scaled with ratios of broadening coefficients consistent with Eq. 7.11. The modified absorption model was integrated into the WMS harmonic simulations to interpret the high-pressure rocket combustor data.

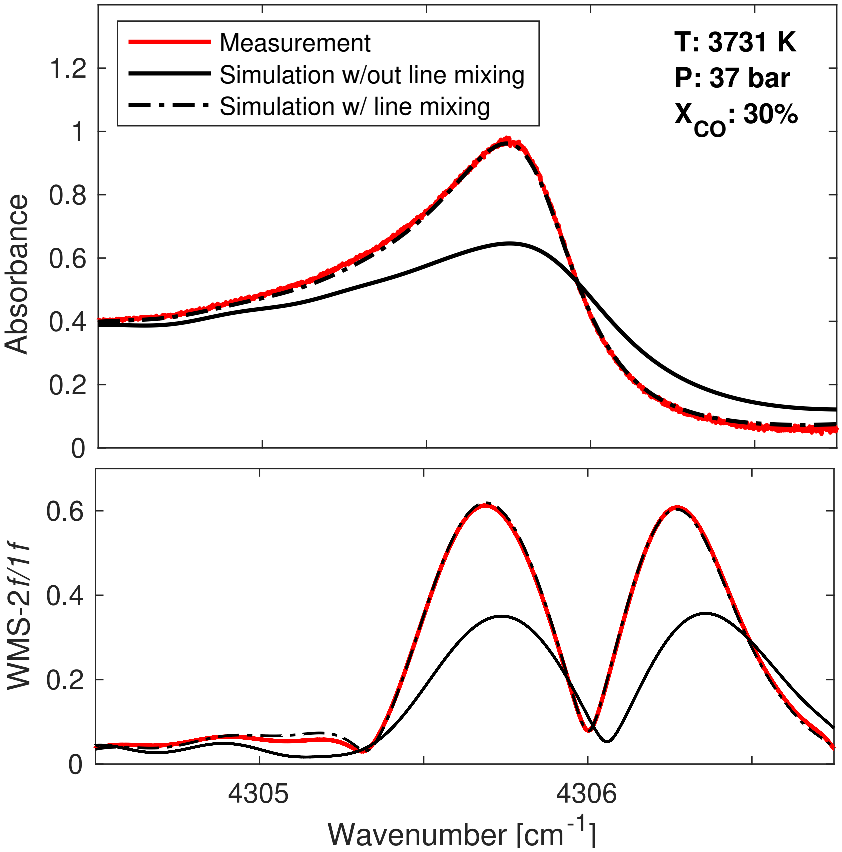

Figure 8.10: CO absorbance measurement of the first overtone bandhead near 2.32 μm with corresponding WMS-$2f/1f$ signals compared to an empirical MEG law model accounting for line-mixing effects and a spectral simulation with no line mixing.

8.3.3 High-pressure rocket characterization

With a modified absorption model to account for line-mixing effects at high pressures, the WMS signal from CO's first overtone band (shown in Fig. 8.8) can be interpreted and utilized with the fundamental band (shown in Fig. 8.7) to quantitatively infer temperature and CO mole fraction. Temperature is obtained by taking the ratio of the measured peak WMS-$2f/1f$ signals from the two wavelengths and comparing to simulated values. With temperature known, CO concentration can be inferred from absolute WMS-$2f/1f$ signal magnitude [183, 297]. Fig. 8.11 compares measured temperatures and mole fractions to chemical equilibrium. The chemical equilibrium results are bounded by the highest and lowest pressures measured, 105 bar and 28 bar, respectively, and shown for reference. In order to obtain mole fraction measurements above 100 bar, where the SNR at 4.98 μm drops below unity, the chemical equilibrium temperature was assumed, and the first overtone bandhead (2.32 μm), which exhibited promising signal quality (SNR $>$ 10) even at the highest pressures ($>$ 100 bar), was solely used to infer mole fraction.

Representative error bars in temperature and mole fraction based on the standard deviation of the measured harmonic signals are shown in Fig. 8.11. Temperature precision for all CH_4/GOx and RP-2/GOx tests ranged from 5–14% and 5–9%, respectively, while mole fraction precision ranged from 6–12% for both fuels. The highest potential error (worst precision) occurs at the highest pressures, as expected. The inferred temperatures from all tests followed the expected trends but were slightly lower (generally by 100–300 K) than equilibrium temperature, indicative of incomplete combustion, poor mixing, or possibly a cold boundary layer. For inferred CO mole fraction, more distinct differences have been observed between the two fuels. Species measurements from CH_4/GOx tests were consistently less than chemical equilibrium while measurements from RP-2/GOx testing were nearly equivalent or slightly higher. This discrepancy may be attributed to the differences in single-element injector designs and performance, suggesting lower performance with the CH_4/GOx configuration. It should also be noted that modest uncertainty remains in the spectroscopic model related to composition-dependent collisional broadening and line mixing. Even with these

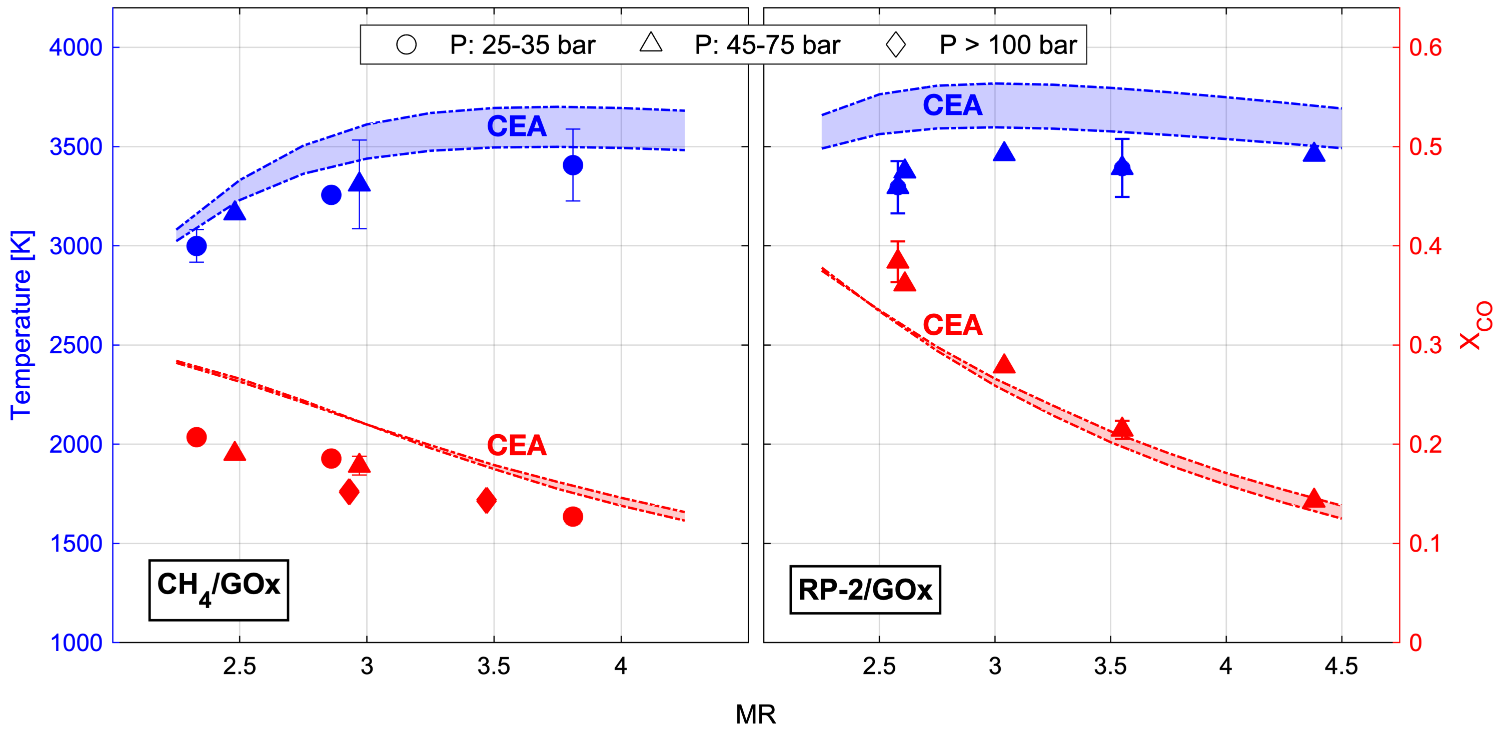

Figure 8.11: Temperature and species measurements with representative error bars at steady-state combustor conditions for CH_4/GOx and RP-2/GOx up to 105 bar. Measured temperature and mole fractions are compared to chemical equilibrium over a range of mixture ratios and pressures.

uncertainties, mole fraction measurements for both fuels follow the trend anticipated from chemical equilibrium in close proximity. The differences observed between fuel and injector combinations support the utility of the sensor in evaluating rocket combustion performance.

8.4 Summary

A novel cross-band infrared laser absorption sensing strategy probing carbon monoxide at the vibrational bands near 4.98 μm and 2.32 μm was developed and deployed to quantitatively measure temperature and species concentration in high-pressure rocket combustion environments. The initial target application for the diagnostic technique was a single-element-injector rocket combustor at the U.S. Air Force Research Laboratory, Edwards. Measurements were performed by collecting and interpreting harmonics of wavelength modulation (WMS-$2f/1f$) related to absorption at each target wavelength over a range of pressures and mixture ratios for both CH_4/GOx and RP-2/GOx propellant combinations. The method exhibited an ability to overcome challenges associated with the extreme thermodynamic conditions and sooting propensity of the rocket combustor. Data collected at the fundamental vibrational band (4.98 μm) showed reliable signal quality up to 75 bar, while data from the first overtone bandhead (2.32 μm) exhibited favorable SNR up to 105 bar, with the clear potential to conduct measurements at even higher pressures.

In order to interpret the signals from the first overtone bandhead, a modified spectroscopic model was developed to account for the temperature- and pressure-dependent line-mixing effects occurring at high gas densities. Using the modified absorption model, temperatures in the rocket combustor were successfully inferred to be in the 2900–3600 K range for the various tests, showing similar but consistently lower values than equilibrium predictions by 3–12%. Quantitative characterization of temperature and species in the rocket combustion gases for the CH_4 and RP-2 fuels identified possible differences in injection/mixing performance that likely cause the disagreements with equilibrium predictions. Notably, the injector appeared to perform worse for the CH_4/GOx configuration, most pronounced by relatively low CO mole fraction values suggesting incomplete combustion. To the authors' knowledge, these measurements represent new limits in pressure capability for non-intrusive temperature and species combustion diagnostics. More importantly, the unique pressure-capability of the sensing strategy provides for a useful method for evaluating combustion efficiency/performance at practical rocket operating conditions and novel datasets that can be compared to reacting flow computational models.

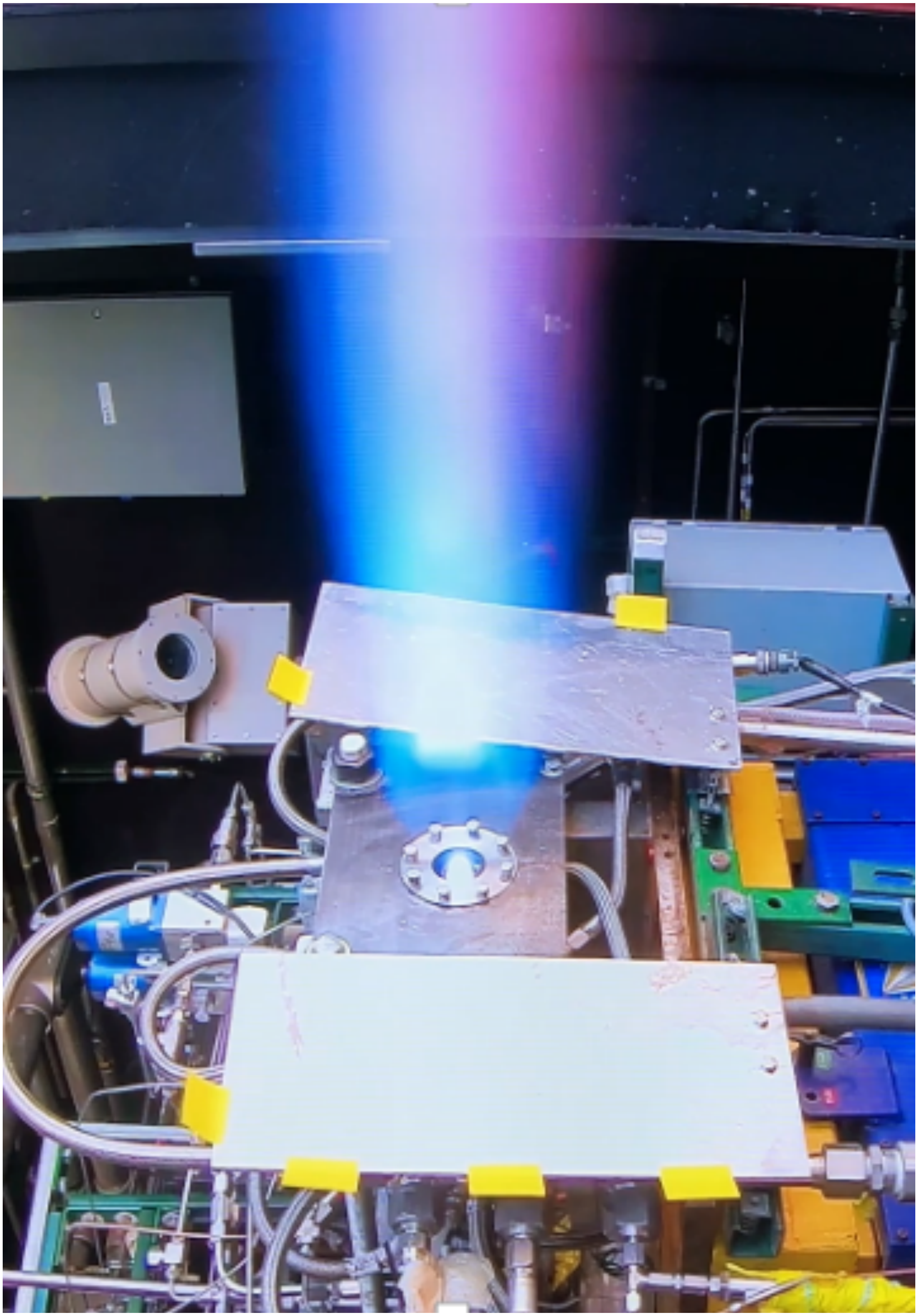

Figure 8.12: Hot-fire of the liquid-propellant rocket combustor where optical measurements were conducted. Image illustrates a test with CH_4/O_2 propellant combination. Credit: U.S. Air Force Research Laboratory

CHAPTER 9

Conclusions

The research presented herein demonstrates novel advancements in laser absorption spectroscopy for characterizing liquid- and hybrid-propellant rocket combustion systems with support of a new High-Enthalpy Shock Tube (HEST) facility at UCLA. The work has leveraged the non-intrusive nature and flexibility of optical diagnostics for characterizing propulsion test facilities and providing novel experimental data to aid the development/validation of computational models for complex chemically reacting flow-fields.

9.1 Shock tube kinetics research

In efforts to develop/refine combustion models for real fuels used in chemical propulsion systems, a laser absorption diagnostic technique, probing the mid-infrared vibrational bands of $^{12}C^{16}O$ and $^{13}C^{16}O$ near 4.9 μm, was developed for sensitive multi-isotopologue temperature and concentration measurements in high-temperature gaseous systems. Time-resolved multi-isotopologue thermometry performance was validated in a shock tube over a range of temperatures (1100–2400 K) relevant to combustion kinetics investigations. The technique was utilized in shock-heated oxidation experiments with isotopically labeled fuel mixtures, simultaneously measuring both carbon monoxide isotopologues throughout the reactions. These results demonstrate the first use of carbon isotope labeling with laser absorption spectroscopy to observe distinct competitive oxidation among different fuel components. This technique presents a starting point of a new avenue towards anchoring and constraining detailed reaction mechanisms of fuel mixtures using laser absorption spectroscopy. Significant uncertainties exist in key elementary reactions involved in the production of CO, particularly involving the formyl (HCO) and ketenyl (HCCO) radicals.

To provide additional kinetic targets for anchoring these kinetic models, the competitive oxidation of methane with C_2 hydrocarbons of differing functional groups (alkane, alkene, and alkyne) was examined experimentally via combustion of isotopically-labeled fuel mixtures and laser absorption spectroscopy of carbon monoxide isotopologues. Quantitative species time-histories of the ^{12}CO and ^{13}CO isotopologues were measured simultaneously and in situ using laser absorption spectroscopy behind reflected shock waves, used for near-instantaneous heating and auto-ignition of binary mixtures containing equal carbon fractions of the different fuels. Tested fuel mixtures were primarily fuel-rich to force the competition of carbon oxidation between the fuel components. The novel dataset of multi-isotopologue species time-histories were compared to available chemical mechanisms, revealing insights on the influence of each C_2 fuel on methane ignition. The GRI-MECH 3.0 and Foundational Fuel Chemistry Model (FFCM-1) reaction models were modified to incorporate ^{13}C reactions and species. Detailed comparison of the measurement data with FFCM-1 simulations revealed generally good agreement at elevated temperatures (>1500 K), with increasing divergence at lower temperatures, particularly for mixtures involving ethane and acetylene. Reaction pathway and sensitivity analysis of the variance between data and the modified mechanisms reveal key reactions likely responsible for the disagreements. This research has yielded a novel dataset with more granular constraints than prior efforts that may be used as validation targets in more modern chemical kinetic mechanisms under active development and optimization.

9.2 Liquid- and hybrid-rocket propulsion research

Many modern liquid-propellant rocket systems have placed considerable effort into maximizing combustion chamber pressure, as it directly influences specific impulse, which is a critical factor to enabling higher payload mass fractions and mission capability. To support the research and development of the next generation of chemical rockets, diagnostics capable of operating in high-pressure environments are needed. As a result, this research focused on developing a novel cross-band laser absorption spectroscopy technique for quantitative measurements of gas temperature and carbon monoxide (CO) in high-pressure, high-temperature rocket combustion flows. The strategy enables a broad range of sensor operability by simultaneously probing rovibrational transitions in both the fundamental and first overtone bands of CO near 4.98 μm and 2.32 μm, respectively, which sustain large differences in temperature dependence despite collisional broadening. Initial experiments using the cross-band thermometry technique were conducted on a single-element-injector rocket combustor with RP-2/GOx and CH_4/GOx propellant combinations at pressures up to 105 bar. To account for collisional effects at high gas densities, empirical models for line mixing, developed via shock tube studies, were employed to enable quantitative interpretation of measured signals for temperature and CO mole fraction in the rocket combustor. These measurements now represent new limits in pressure capability for non-intrusive temperature and species combustion diagnostics. Notably, the technique developed herein provides for a useful method for evaluating combustion efficiency/performance at practical operating conditions and novel datasets that can be compared to reacting flow computational models.

In addition to liquid-propellant rocket systems, several technology development programs have been initiated to prove the feasibility of hybrid propulsion systems for future interplanetary exploration missions due to their intrinsic theoretical cost, safety, and performance advantages over many modern purely liquid or solid based systems. Despite interest from the aerospace sector, the maturation of hybrid rocket technology has been hindered by significant obstacles, a crucial one of which is sub-optimal combustion performance from low-regression-rate, polymer-based fuels. This limitation has motivated research into hybrid rocket motor design variations and their effects on combustion efficiency, or c^* efficiency, which linearly impacts specific impulse. However, to properly recognize the effects of such variations, it is important to understand the underlying mechanisms (multi-phase thermochemistry, diffusive mixing, turbulence, etc.) governing combustion performance. As such, this research focused on developing a laser absorption tomography (LAT) technique for investigating the thermochemical structure of hybrid rocket combustion systems. The measurement strategy utilizes tunable infrared lasers to target rovibrational transitions of three major combustion species: carbon monoxide (CO), carbon dioxide (CO_2), and water (H_2O). Spectrally- and spatially-resolved absorption data was collected by translating co-linear laser beams across the exit plane of a fuel cylinder with an oxidizer core flow at various fuel-grain lengths. Planar measurements at different axial distances were compiled to form two-dimensional images, spatially-resolving the thermochemical structure downstream of the oxygen injector. The results presented in this work clearly indicate a strong dependence of hybrid motor combustion performance on oxidizer injector design and the intensity of viscous forces in the incipient flow-fields that induce downstream mixing and radial diffusion. This work represents the first quantitative in-situ measurements of species, temperature, and characteristic velocity in a hybrid rocket reaction layer. It is envisioned that continued efforts employing these experimental methods can be used to further inform hybrid rocket motor design and anchor numerical models, including reacting flow simulations.

9.3 Current and future research directions

9.3.1 Diaphragmless shock tube facility

Developing optical diagnostics for propulsion devices or high temperature chemical kinetics requires experimental facilities that can produce controlled, high temperature and high pressure environments. As discussed in Ch. 2, this is typically achieved using a shock tube, as it provides a near-instantaneous change in temperature and pressure and can operate over a wide range of conditions representative of many practical combustion devices. Two primary disadvantages of using a conventional shock tube facility are the cycle time between tests and the single-shot nature of the experiment. The manual changing of burst diaphragms that separated the driver and driven sections and waiting for the facility to vacuum down can, in certain cases, take several hours if a low ultimate pressure ($< 10^{-6}$ torr) is desired. Additionally, although conventional shock tubes can predict post-shock conditions with $< 1\%$ uncertainty [64], reliably obtaining repeatable experiments can be challenging due to the influence of diaphragm rupture on shock wave development and post-shock conditions. These limitations are highly undesirable for new sensor development or kinetics studies as numerous experiments (15+) are often required. Specifically for chemical kinetics studies, the Arrhenius behavior of many chemical reactions signifies small variations in temperature or pressure can significantly affect combustion behavior. As an example, a 10% increase in temperature at 1100 K can lead to a 90% increase in the reaction rate for $\mathrm{H} + \mathrm{O_2} \rightarrow \mathrm{OH} + \mathrm{O}$ [32, 33]. Consequently, studying combustion chemistry and high-temperature physical processes requires well-known and repeatable thermodynamic conditions.

To address these limitations and extend the capabilities of the high-enthalpy shock tube (HEST) facility at UCLA, a new diaphragmless driver section, shown in Fig. 9.1 and Fig. 9.2 has been designed and manufactured. The diaphragmless driver relies on a fast-actuating valve to produce a shock wave. The poppet (shown in red in Fig. 9.2) is actuated by a bellows valve, which can be pressurized to close the poppet or exhausted to open. At the

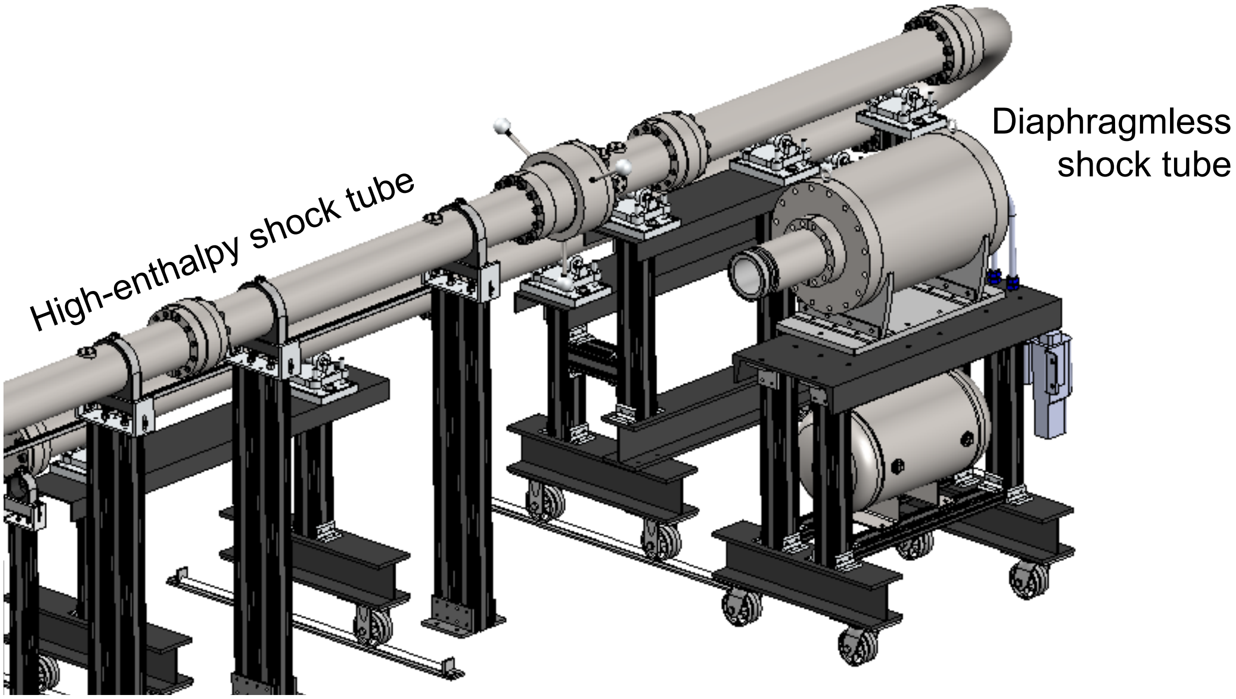

Figure 9.1: Diaphragmless shock tube driver next to the existing high-enthalpy shock tube facility at UCLA

beginning of a new experiment, the poppet will be closed, separating the driver and driven sections as a diaphragm normally would, by slightly pressurizing the bellows. The driver and the bellows volume are also mechanically separated; therefore, the driver and driven sections can now be vacuumed down to reach the desired ultimate pressure and eliminate any trace gases. The driven section is then filled with the test gas to the the initial pressure P_1. Now, while keeping the poppet closed, the driver section can be filled to the desired "burst pressure" P_4. In contrast to a conventional shock tube, where the burst pressure is determined by strain-induced failure of the diaphragm, this approach enables precise control

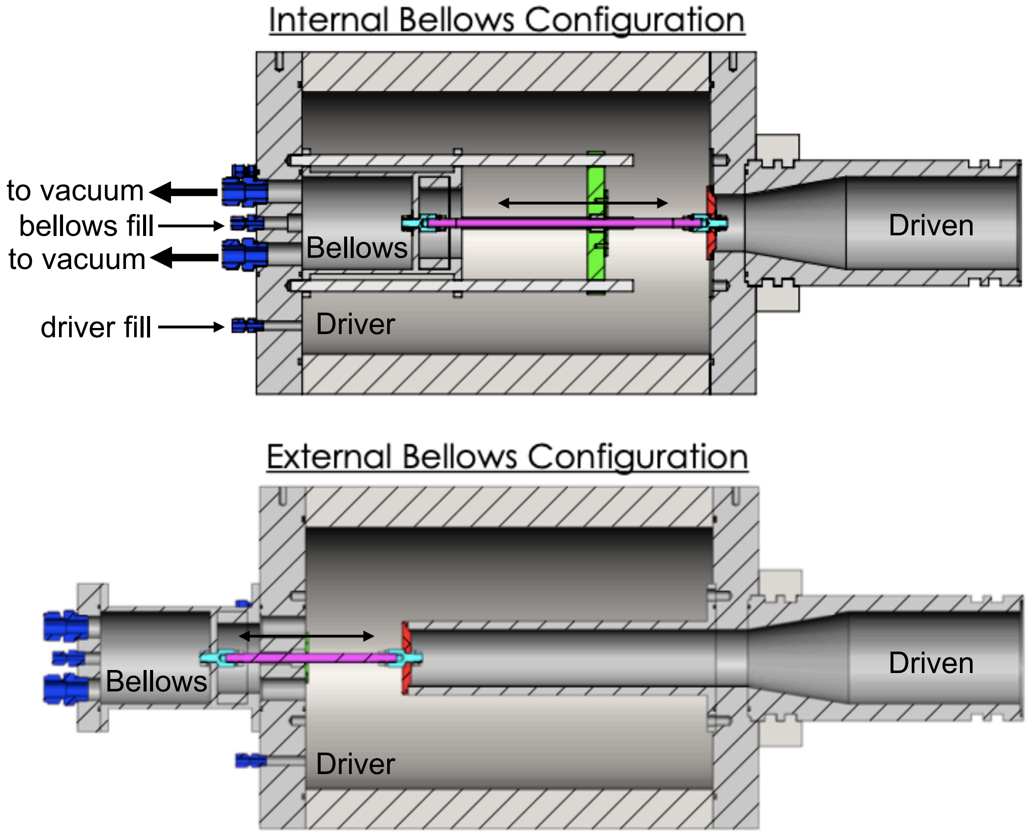

Figure 9.2: Diaphragmless shock tube cross-section shown in two configurations. Pressurizing the bellows closes the poppet (shown in red), which separates the driver and driven sections. Driver and driven sections are filled to the desired pressures. Bellows is exhausted to vacuum, which rapidly opens the poppet and creates an incident shock wave that propagates into the driven section

of the driver fill pressure and, ultimately, the shock strength and thermodynamic conditions. Once the driver and driven sections are filled to the desired pressures, the bellows valve can be exhausted to vacuum, which rapidly opens the poppet, creating an incident shock wave that propagates into the driven section. After the test, the shock tube can be vacuumed down for the next test without the need to disassemble or open as would done in a conventional shock tube to replace the burst diaphragm. Maintaining a closed system also facilitates the time needed to vacuum down as there is no air introduced to the shock tube, which contains water, among other molecules, that tend to stick to the shock tube walls and slow down the vacuuming process.

The diaphragmless shock tube facility will enable highly repeatable experiments over a wide range of operating conditions (sub-atmospheric$< P <$ 100 bar, 600 $< T <$ 4000+K), as the driver and driven pressures can be precisely set, and greatly reduce the typical cycle time of conventional shock tube experiments. The repetition rate has been estimated by calculating the time required for each step limited by infrastructure capabilities (e.g. exhaust flow rate, vacuum pumping speed/capacity) and shock tube geometry (volume). Vent, vacuum, and fill times are longest (all other steps sub-second). For a post-reflected shock pressure of 100 bar and tube volume of 3 ft^3 , post-test vent time is estimated at ∼20-s vacuum from atmosphere to 0.05 torr at ∼15-s, and simultaneous driver and driven section fill at ∼10-s. In total, automated test turnaround of approximately 50 seconds (or repetition rate of ∼1 test/min) is estimated for a 100 bar test. Adjustable parameters include vacuum pump strength and vent orifice diameter.

It is envisioned that this new facility will facilitate the development of new diagnostics in combustion science. With fast cycle times and precise repeatability, the time it takes to develop a sensor in the lab to when its deployed on an actual test rig can be greatly reduced. Additionally, incorporating the multi-isotopologue sensing strategy developed in this work with this new facility can greatly advance the modeling efforts of real fuels and their surrogates by providing a multitude (due to high cycle time) of precise (due to test repeatability) kinetic targets (ignition delay times, species time histories, elementary reaction rates) to refine and validate new and existing reaction mechanisms. The full drawing package for the diaphragmless shock tube facility can be found in Appendix G.

9.3.2 High-pressure hybrid-propellant combustion characterization

Though hybrid-propellant rocket engines have intrinsic cost, safety, and performance advantages over many modern liquid-propulsion systems, their usage in practical systems has been largely hindered by slow-burning, low-regression-rate fuels. This limitation has prompted numerous research efforts to increase engine performance through both physical and chemical adaptations of hybrid rocket systems, such as multi-port fuel grains, swirled flows, solid-fuel

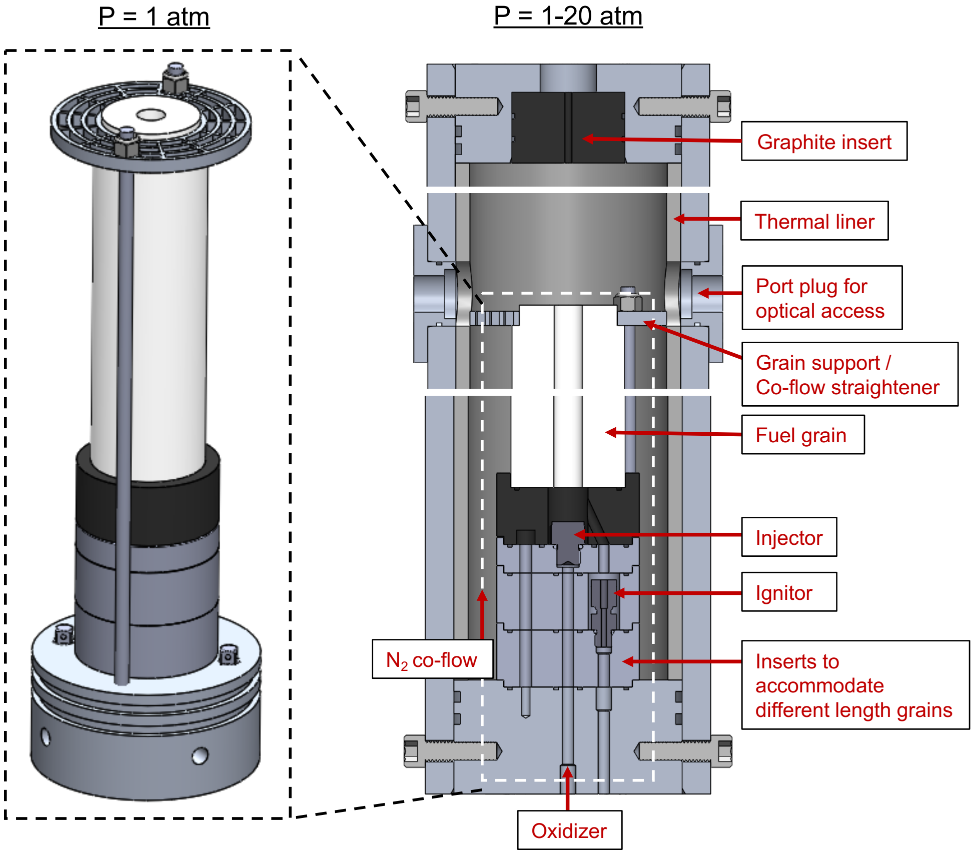

Figure 9.3: Diagram of the high-pressure hybrid-propellant combustion chamber with optical access for thermochemical imaging technique. The high-pressure chamber design incorporates the current setup used for atmospheric measurements

additives, and paraffin-based fuels. The novel thermochemical imaging technique developed in this work, helps gain insight into the underlying mechanism (multi-phase thermochemistry, diffusive mixing, turbulence, etc.) that governs combustion performance. As discussed in Ch. 6, this technique enables a more granular and fundamental understanding of solid-gas combustion physics and can be used to identify mechanistic combustion losses across different engine configurations. It is envisioned that this technique can ultimately be used for increasing hybrid rocket technical readiness by optimizing hybrid motor designs and refining computational models.

The measurements conducted in Ch. 6 were at atmospheric pressure while ongoing work aims to extend this technique to higher pressures (20 atm) representative of actual operating

Figure 9.4: Parts manufactured and tested for the high-pressure hybrid-propellant combustion chamber. *From left to right*: end cap with graphite nozzle, combustion chamber with optical access for thermochemistry measurements, fiberglass phenolic insulation, and the current assembly described in Ch. 6 with a burnt PMMA fuel grain

conditions. To achieve this a high-pressure hybrid-propellant combustion chamber, shown in Fig. 9.4 and Fig. 9.3, was designed with optical access to enable laser-based diagnostics. As shown in Fig. 9.3, the current motor assembly is simply placed inside the chamber assembly, enabling similar measurements to those reported in Ch. 6, only at higher pressures. The high-pressure assembly incorporates a fiberglass thermal liner, a nitrogen co-flow, and a graphite nozzle. All parts have been designed, manufactured, and tested at UCLA. An image of the complete assembly/parts is shown in Fig. 9.4.

Conducting spectroscopic measurements at high pressures may require a revised spectroscopic approach to mitigate collisional-broadening effects. To achieve this, the line-mixing models developed in Ch. 4 and applied to liquid-propellant rocket combustors in Ch. 5, may be utilized. It is envisioned this facility will help characterize combustion performance at high pressures, which can be used to anchor and refine complex chemically-reacting models. This will continue to advance hybrid rocket technology readiness level and provide further insights into hybrid combustion physics and optimized engine configurations.

9.3.3 Methyl methacrylate (MMA) kinetics

Chemical kinetic mechanisms greatly influence the design and development of modern combustion systems. Therefore, accurately characterizing the combustion behavior of real fuels is critical for the advancement of future propulsion technologies. For hybrid-propellant rockets, a fuel of interest has been poly(methyl methacrylate) (PMMA), which motivated the thermochemical imaging of PMMA/O_2 combustion in Ch. 6. To further refine computational models and reaction mechanisms used to model hybrid-propellant combustion, the pyrolysis and oxidation behavior of methyl methacrylate can be studied behind reflected shock waves. By studying methyl methacrylate in shock heated mixtures, we can gain insight into the pyrolysis and oxidation behavior present in the reaction layer of a hybrid-propellant combustor.

APPENDIX A

Uncertainty Analysis

Unless otherwise noted, the Taylor series method (TSM) of uncertainty propagation [304] is implemented, in which the uncertainty of a variable r, Δr, is given by:

$$(\Delta r)^2 = \left(\frac{\partial r}{\partial x_1}\Delta x_1\right)^2 + \left(\frac{\partial r}{\partial x_2}\Delta x_2\right)^2 + \cdots \tag{A.1}$$

where x_i are dependent variables and Δx_i are their respective uncertainties.

A.1 Thermodynamic state variables

Reported parameters are determined from measurements made at various thermodynamic conditions, uncertainties of which ultimately affect the temperature- and pressure-dependence of the associated models.

Uncertainty in pressure, ΔP is generally dominated by two sources. For both shock tube and heated optical cell experiments, uncertainty in the pressure transducer/capacitance manometer measurements ΔP_{meas} leads to uncertainties in broadening parameters. For the shock tube experiments, uncertainty in the reflected shock pressure P_5 due to uncertainties associated with the shock relations ΔP_5 contribute.

$$\left(\frac{\Delta P}{P}\right)^2 = \left(\frac{\Delta P_{meas}}{P_{meas}}\right)^2 + \left(\frac{\Delta P_5}{P_5}\right)^2 \tag{A.2}$$

For the heated optical static gas cell experiments, ΔP_5 is taken to be zero, and ΔP_{meas} is

0.012% of the measurement reported by the capacitance manometer, while for the shock tube experiments, ΔP_{meas} is 0.18% of the measurement reported by the pressure transducer.

Uncertainty in temperature, ΔT, is different for each of the devices. For the shock tube measurements, the uncertainty in temperature is simply the uncertainty in reflected shock temperature T_5, ΔT_5. For the sake of brevity, the uncertainties ΔP_5 and ΔT_5 will not be discussed here in further detail; however, we note that significant contributors include uncertainties in the composition of the driven gas (from the barometric mixture preparation), uncertainties in the time-of-arrival measurements, and small uncertainties in the initial pressure P_1 and temperature T_1. Further information regarding uncertainties in reflected shock conditions can be found in the work by Campbell et al. [64]. Temperature uncertainty in the static optical cell is governed by the thermocouple measurements taken on the outside surface of the cell. The thermocouples used herein have an uncertainty of 0.75% of reading. More detail about the optical cell used in this paper is provided in previous research [146].

A.2 Broadening coefficient

The uncertainties in collisional broadening coefficient (for absorber i by perturber k) $\gamma_{(i-k),j}(T_0)$, $\Delta\gamma_{(i-k,)j}(T_0)$, and temperature-dependent exponent $n_{(i-k),j}$, $\Delta n_{(i-k),j}$, are determined from applying a linear regression to Eq. 3.16. In this case, the standard errors of the slopes and intercepts of the fitted lines are $\Delta n_{(i-k),j}$ and $\Delta\gamma_{(i-k,)j}(T_0)$, respectively. In our linear regressions, we follow the approach of York et al. [188], incorporating variable uncertainties in both x and y to provide slope and intercept standard errors more reflective of variable measurement quality amongst the data. In practice, this enables measurements from different devices in the same regression (as shown in Fig. 7.7), despite that each of these devices has different measurement uncertainties in thermodynamic state variables.

$\Delta\gamma_{(i-k,)j}(T_0)$ and $\Delta n_{(i-k),j}$ have uncertainty dependence on ΔT and $\Delta\gamma_{(i-k,)j}(T)$. $\Delta\gamma_{(i-k,)j}(T)$ can be determined by applying Eq. A.1 to Eq. 3.15 after rearranging to solve for $\gamma_{(i-k,)j}(T)$:

$$\begin{aligned}\left(\frac{\Delta\gamma_{(i-k,)j}(T)}{\gamma_{(i-k,)j}(T)}\right)^2 &= \left(\frac{\Delta(\Delta v_C)}{2PX_k}\right)^2 + \left(\frac{\Delta v_C \Delta P}{2P^2X_k}\right)^2 \\ &+ \left(\frac{\Delta v_C \Delta X_k}{2PX_k^2} - \frac{\Delta X_k}{X_k}\sum_y X_y\gamma_{i-y}(T)\right)^2 \\ &+ \left(\frac{1}{X_k}\sum_y \Delta X_y\gamma_{i-y}(T)\right)^2 \\ &+ \left(\frac{1}{X_k}\sum_y X_C\Delta\gamma_{i-y}(T)\right)^2\end{aligned} \tag{A.3}$$

Eq. A.3 describes the uncertainty dependence of the broadening coefficient of absorber i by perturber k, $\gamma_{(i-k,)j}(T)$, on the uncertainties in collisional width Δv_C, total pressure P, mole fraction of perturber k, X_k, and broadening influences of any other perturbers y (which includes self-broadening by i). For self-broadening, $X_k = X_i \approx 1$ and $X_y = 0$, and so the last few terms of Eq. A.3 drop out. When considering only a single perturber k, $y = i$ to account for the influence of self-broadening. ΔP is given by Eq. A.2, and mole fraction uncertainties ΔX_i are determined based on the barometric mixture preparation uncertainties. Collisional width Δv_C is determined from a Voigt fit of the measured absorbance spectra, and so $\Delta(\Delta v_C)$ is conservatively estimated by multiplying the maximum residual of the Voigt fit by Δv_C, typically less than 3%.

Thus, the uncertainty dependencies of $\Delta\gamma_{(i-k,)j}(T_0)$ and $\Delta n_{(i-k),j}$ are all accounted for. Some sensitivity is observed in the preceding equations regarding the mole fraction of perturber k, such that lower mole fractions of k lead to higher uncertainties in $\Delta\gamma_{(i-k,)j}(T)$ for a given transition, as demonstrated in Figs. 7.7 and 7.8.

A.3 MEG law coefficients (line mixing)

Because the MEG law is an empirical model [276, 277], the coefficients $a_1(T)$, a_2, and a_3 for each experiment are determined by a nonlinear least-squares fit, and so their uncertainties cannot be interpreted as meaningfully through physical relationships as described by Eq. A.1. Thus, we estimate uncertainties for this model in a manner consistent with how the model will be used; i.e., to make predictions of absorption spectra in the range of thermodynamic conditions described in this work. The uncertainties in $a_1(T)$, a_2, and a_3 for each high-pressure shock tube experiment were determined by varying the wavenumber range over which the least-squares fit was made. The differences between the values of a_i determined from the simulating the wavelength range of the measured experiment and the values of a_i determined from simulating the wavelength range of the entire band were taken to be a conservative estimate of Δa_i. This represents the uncertainty associated with using experimental data gathered from a limited spectral range to model the line mixing behavior of the entire band.

The uncertainties for $a_1(T)$, $\Delta a_1(T)$, are shown as error bars in Fig. 7.11. Together with ΔT, these are used in the linear regression determination of $a_1(T_0)$ and m to obtain their respective uncertainties $\Delta a_1(T_0)$ and Δm using the same approach of York et al. [188] as described for $\Delta\gamma_{(i-k,)j}(T_0)$ and Δn. Δa_i are observed to be similar for line-mixing in argon despite the lower signal-to-noise ratios in the measurements; this is because the MEG law coefficients a_i determined for pure CO are used to determine a_i for argon through Eq. 7.12. Since these coefficients are treated as fixed for this second least-squares fitting procedure, the additional constraints on the fit reduce the variation in suitable a_i. As such, the MEG law coefficients presented in Table 7.2 for CO-Ar should not be interpreted independently from those for CO-CO.

A.4 Temperature uncertainty for scanned-wavelength direct absorption

For the two-line thermometry methods used in this work, temperature is given by [147]:

$$T = \frac{\frac{hc}{k_B}(E_2'' - E_1'')}{\ln(R) + \ln\left(\frac{S_2(T_0)}{S_1(T_0)}\right) + \frac{hc}{k_B}\frac{(E_2'' - E_1'')}{T_0}} \tag{A.4}$$

Uncertainty in temperature as expressed in Eqn. A.4 depends only on the uncertainties of the reference temperature linestrengths in the HITRAN/HITEMP database, $\Delta S_i(T_0)$, and the uncertainty in the ratio of calculated absorbance areas ΔR:

$$\left(\frac{\Delta T}{T}\right)^2 = \frac{\left(\frac{\Delta R}{R}\right)^2 + \left(\frac{\Delta S_1(T_0)}{S_1(T_0)}\right)^2 + \left(\frac{\Delta S_2(T_0)}{S_2(T_0)}\right)^2}{\left[\frac{hc}{k_B}\left(\frac{E_2'' - E_1''}{T_0}\right) + \ln(R) + \ln\left(\frac{S_2(T_0)}{S_1(T_0)}\right)\right]^2} \tag{A.5}$$

The largest contributor to Eqn. A.5 is usually ΔR, given by the expression:

$$\left(\frac{\Delta R}{R}\right)^2 = \left(\frac{\Delta A_1}{A_1}\right)^2 + \left(\frac{\Delta A_2}{A_2}\right)^2 \tag{A.6}$$

ΔA_i can be conservatively assumed to be equal to the maximum value of the residual multiplied by the absorbance area A_i calculated from the Voigt fitting procedure.

A.5 Mole fraction uncertainty for scanned-wavelength direct absorption

For the scanned-DA measurements, the mole fraction uncertainty in depends on the uncertainties of A_i, $S_i(T)$, P, and L:

$$\left(\frac{\Delta X}{X}\right)^2_{\text{SDA}} = \left(\frac{\Delta A_i}{A_i}\right)^2 + \left(\frac{\Delta S_i(T)}{S_i(T)}\right)^2 + \left(\frac{\Delta P}{P}\right)^2 + \left(\frac{\Delta L}{L}\right)^2 \tag{A.7}$$

As mentioned earlier, ΔA_i is calculated based on the residuals of the Voigt fit. The pathlength L of the shock tube is known to a high precision; $\Delta L/L$ is assumed to be much smaller than the other terms in Eqn. 3.7 and so it is not included in our uncertainty analysis. However, for the high temperature gas cell, the pathlength changes a small amount with the thermal expansion of the cell, and so $\Delta L = 1$ mm for those experiments.

Uncertainty in pressure, ΔP is dominated by two sources. For all experiments, uncertainty in the pressure transducer / capacitance manometer measurements ΔP_{meas} leads to uncertainties in mole fraction and broadening parameters. For the shock tube experiments, uncertainty in the reflected shock pressure P_5 due to uncertainties associated with the shock relations ΔP_5 contribute.

$$\left(\frac{\Delta P}{P}\right)^2 = \left(\frac{\Delta P_{meas}}{P_{meas}}\right)^2 + \left(\frac{\Delta P_5}{P_5}\right)^2 \tag{A.8}$$

For the sake of brevity, these uncertainties will not be discussed in detail; however, we note that significant contributors to ΔP_5 include uncertainties in the composition of the driven gas (from the barometric mixture preparation), uncertainties in the time-of-arrival measurements, and small uncertainties in the initial pressure P_1 and temperature T_1. Further information can be found in the work by [64].

This leaves the uncertainty in temperature-dependent linestrength $S_i(T)$. The two uncertainties we are primarily concerned with are the reference temperature linestrength uncertainty $\Delta S_i(T_0)$ and the uncertainty in temperature-dependent linestrength due to uncertainty in temperature $\Delta S_{i,T}(T)$. In short, ΔT (from the uncertainty in ΔR) affects the $S_i(T)$ used to calculate mole fraction. The following expression can be obtained for the uncertainty in linestrength due to uncertainty in observed temperature, ΔT:

$$\begin{aligned}\Delta S_{i,T}^2(T) = S_i^2(T)\Delta T^2 \Bigg(&-\frac{\partial Q(T)/\partial T}{Q(T)} - \frac{1}{T} + \frac{hcE_i''}{k_B T^2} \\ &+\frac{hc\nu_{0,i}}{k_B T^2}\left(\frac{\exp\left(-hc\nu_{0,i}/k_B T\right)}{1-\exp\left(-hc\nu_{0,i}/k_B T\right)}\right)\Bigg)^2\end{aligned} \tag{A.9}$$

This expression is consistent with the analysis presented by [305]. The total uncertainty in the linestrength $S_i(T)$ can now be calculated:

$$\Delta S_i^2(T) = \Delta S_i^2(T_0) + \Delta S_{i,T}^2(T) \tag{A.10}$$

Thus, all uncertainty dependencies of X as given in Eqn. 3.7 are accounted for and ΔX can be calculated using Eqn. A.7.

A.6 Mole fraction uncertainty for fixed-direct absorption

For fixed-DA measurements at the linecenter $\nu_{i,0}$, the mole fraction is calculated by:

$$X = \frac{\alpha_\nu}{S_i(T) P \phi_i(\nu_0) L} \tag{A.11}$$

which is spectrally dependent on lineshape $\phi_i(\nu)$. The uncertainty in X depends on the uncertainties of α_ν, $S_i(T)$, P, $\phi_i(\nu_0)$, and L:

$$\begin{aligned}\left(\frac{\Delta X}{X}\right)^2_{\text{FDA}} = \left(\frac{\Delta \alpha_\nu}{\alpha_\nu}\right)^2 + \left(\frac{\Delta S_i(T)}{S_i(T)}\right)^2 + \left(\frac{\Delta P}{P}\right)^2 \\ + \left(\frac{\Delta L}{L}\right)^2 + \left(\frac{\Delta \phi_i(\nu_0)}{\phi_i(\nu_0)}\right)^2\end{aligned} \tag{A.12}$$

The uncertainties ΔP and ΔL remain the same as previously. Since we estimate T from a scanned-DA experiment to calculate both $S_i(T)$ and $\phi_i(\nu_0)$ for a fixed-DA experiment at nearly identical conditions, the uncertainties $\Delta S_i(T)$ and ΔT also remain the same. Measurement uncertainty in wavelength-dependent absorbance α_ν, as determined by Eqn. 3.3, is influenced by noise in the intensity of the laser light on the detector. We estimate the absorbance uncertainty $\Delta\alpha_\nu$:

$$\Delta \alpha_\nu = -\ln\left(\frac{I_t \pm \Delta I}{I_0 \pm \Delta I}\right) \tag{A.13}$$

where ΔI is the 95% confidence interval associated with the laser and detector noise for both the incident light I_0 and transmitted light I_t, determined from a measurement of I_0 prior to shock heating the test gas. The uncertainty in lineshape $\phi_i(\nu)$ depends on the spectral model used. When using the Voigt lineshape, consideration must be given to both Doppler width $\Delta\nu_D$ [cm^{-1}] (which is dependent on temperature T) and collisional width $\Delta\nu_c$ [cm^{-1}]. For brevity, we omit the details of the Voigt profile uncertainty derivation and provide a conservative approximate uncertainty dependence:

$$\left(\frac{\Delta\phi_i(\nu_0)}{\phi_i(\nu_0)}\right)^2 = 2\left(\frac{\Delta(\Delta\nu_D)}{\Delta\nu_D}\right)^2 + \left(\frac{\Delta(\Delta\nu_c)}{\Delta\nu_c}\right)^2 \tag{A.14}$$

The uncertainty dependence in the Doppler width $\Delta\nu_D$, $\Delta(\Delta\nu_D)$, can be obtained as:

$$\left(\frac{\Delta(\Delta\nu_D)}{\Delta\nu_D}\right)^2 = \left(\frac{\Delta\nu_{0,i}}{\nu_{0,i}}\right)^2 + \frac{1}{4}\left(\frac{\Delta T}{T}\right)^2 \tag{A.15}$$

where $\Delta\nu_{0,i}$ can be determined by the stability of the wavemeter measurement, in this work ±0.00025 cm^{-1}. During fixed-DA shock tube studies, collisional width $\Delta\nu_c$ is modeled according to Eqn. 3.15, and the resulting expression for its uncertainty can be calculated:

$$\begin{aligned}\left(\frac{\Delta(\Delta\nu_c)}{\Delta\nu_c}\right)^2 = \left(\frac{\Delta P}{P}\right)^2 + \left(\frac{\Delta X_Y}{X_Y}\right)^2 + \left(\frac{\Delta\gamma_Y(T_0)}{\gamma_Y(T_0)}\right)^2 \\ + n^2\left(\frac{\Delta T}{T}\right)^2 + (\ln(n)\Delta n)^2\end{aligned} \tag{A.16}$$

The uncertainties in collisional broadening coefficient (in bath gas Y) $\gamma_Y(T_0)$, $\Delta\gamma_Y(T_0)$, and temperature-dependent exponent n, Δn, are determined from the linear regressions applied to Eqns. 3.15 and 3.16, respectively, which account for independent measurement uncertainty in multiple dimensions [188]. The mole fraction of the non-reacting bath gas Y (in this work, Ar) is assumed not to change appreciably throughout the experiment, and its uncertainty ΔX_Y is calculated from the barometric mixture preparation. Notably, the temperature-dependent pressure-induced line shift [147] of the ^{13}CO P(0,22) line is not considered when tuning the laser to 2007.8767 cm^{-1}. Assuming $\delta(T_0) = -0.003$ cm^{-1}/atm [306, 307] and a temperature-dependent exponent of $M \approx 1$ [308], this results in a line shift of $\delta \approx -0.00035$ cm^{-1} and a $\approx 0.03\%$ underestimation of α_ν at the tested conditions, which is added to the overall uncertainty $\Delta\alpha_\nu$. Thus, all uncertainty dependencies of X as given in Eqn. A.11 are accounted for and ΔX can be calculated using Eqn. A.12.

A.7 Ignition delay timing

In the oxidation experiments shown in this paper, the modeled and experimental ignition delay times were observed to occur within the margin of error resulting from the uncertainty in the reflected shock temperature and pressure. Given this agreement, we slightly shift the timing of the modeled results (within the calculated uncertainty) so that the peak CO mole fractions align in time with the experimental results in order to focus comparison on the remainder of the species time-history profiles. In particular this adjustment allows for improved comparison of species evolution/shape before primary ignition.

Likewise, there are small shock-to-shock variations in ignition delay related to the stochastic nature of the diaphragm bursts. The peaks of CO mole fraction and absorbance from the respective scanned-DA and fixed-DA oxidation experiments shown in Fig. 4.14 were found to agree within the time of one scanned-DA scan, and were similarly synchronized to provide the temperature profile estimate used to determine X_{CO} for the fixed-DA experiment.

APPENDIX B

Unifying line-mixing equations

Within the impact approximation, the absorption coefficient for overlapping lines can be written as:

$$k_\nu = \frac{N}{\pi}\,\mathrm{Im}(\mathbf{d}\cdot\mathbf{G}^{-1}\cdot\boldsymbol{\rho}\cdot\mathbf{d}) \tag{B.1}$$

In this form, solving for k_ν can be significantly time consuming, especially if considering mixing between multiple transitions, as it requires a matrix inversion for each frequency. The computation of k_ν is simplified considerably by following the procedure discussed in Sec. 7.2.2, as shown by Gordon and McGinnis [273] and Koszykowski et al. [309]. The resulting expression for k_ν is shown in Eq. B.2.

$$k_\nu = \frac{N}{\pi}\,\mathrm{Im}\left[\sum_J \frac{(\mathbf{d}\cdot\mathbf{A})_J(\mathbf{A}^{-1}\cdot\boldsymbol{\rho}\cdot\mathbf{d})_J}{(\nu-\omega_J)}\right] \tag{B.2}$$

Note that Eq. B.2 is still an exact expression for k_ν and involves no approximations.

In this form, $\mathbf{d}$ represents a vector of transition amplitudes with a temperature dependence given by:

$$d_J = \sqrt{\frac{S_J(T)}{\rho_J}} \tag{B.3}$$

where $S_J(T)$ [$\mathrm{cm}^{-1}/(\mathrm{molec}\cdot\mathrm{cm}^{-2})$] is the transition line strength and ρ_J is the Boltzmann population fraction given by Eq. 7.4. It is often of interest to express $\mathbf{d}$ in terms of temperature independent molecular properties. This can be done by letting $S_J(T)$ take the following form:

$$S_J(T) = I_a \frac{A_J}{8\pi c \nu_0^2} \frac{g'_J \exp\Big(-\frac{hcE''_J}{k_B T}\Big)\Big[1 - \exp\Big(-\frac{hc\nu_0}{k_B T}\Big)\Big]}{Q} \tag{B.4}$$

where I_a is the natural terrestrial isotopic abundance, g'_J is the upper state degeneracy, E''_J [cm^{-1}] is the lower state energy, Q is the total internal partition function, and A_J [s^{-1}] is the Einstein coefficient for spontaneous emission. The Einstein-A coefficient is independent of temperature and, for electric dipole transitions, can be related to the weighted transition-moment squared $\mathfrak{R}_J^2$ [Debye^2] through Eq. B.5:

$$A_J = \frac{64\pi^4}{3h} \nu_0^3 \frac{g''_J}{g'_J} \mathfrak{R}_J^2 \tag{B.5}$$

where g''_J is the lower state degeneracy. Substituting Eq. B.5 into Eq. B.4 yields:

$$S_J(T) = I_a \frac{8\pi^3}{3hc} \nu_0 \rho_J \Bigg[1 - \exp\Bigg(-\frac{hc\nu_0}{k_B T}\Bigg)\Bigg] \mathfrak{R}_J^2 \tag{B.6}$$

Finally, combining Eq. B.2 with Eq. B.5 and Eq. B.6 produces an expression for absorption coefficient accounting for line mixing frequently seen in literature:

$$k_\nu = I_a \frac{8\pi^2}{3hc} \nu \Bigg[1 - \exp\Bigg(-\frac{hc\nu}{k_B T}\Bigg)\Bigg] \sum_J \sum_K N_J \mathfrak{R}_J \mathfrak{R}_K \mathrm{Im}\{\langle\langle J \big| [\mathbf{\Sigma} - \mathrm{L}_\mathbf{0} - iP\mathbf{W}]^{-1} \big| K \rangle\rangle\} \tag{B.7}$$

where $\mathbf{\Sigma}$, $\mathrm{L}_\mathbf{0}$, and $\mathbf{W}$ are operators in Liouville line space. $\mathbf{\Sigma}$ and $\mathrm{L}_\mathbf{0}$ are diagonals associated with the wavenumber of the calculation ν and the transition line center ν_0, respectively. All collisional influences on spectral shape are contained in the relaxation matrix $\mathbf{W}$, as discussed in Sec. 7.2.2.

APPENDIX C

Isotopic effects on chemical reactions

In many fields of chemistry, isotopic substitution is used—particularly with hydrogen—for its ability to produce observably different reaction rates as a means to distinguish reaction pathways. In this study, however, we assume that the reaction rates of ^{12}C- and ^{13}C-containing fuels and fuel fragments are indistinguishable enough to have minimal effects on the ignition behavior of the fuels. A brief justification of this assumption follows.

The change in observed reaction rate due to isotopic substitution is related the change in vibrational frequencies of the bonds associated with the transition state of the reaction [178]. The changes in vibrational frequencies are, in turn, dependent on the change in the reduced mass of the atoms in the bonds. As such, reactions involving isotopes of hydrogen have some of the largest observable changes in reaction rates due to its relatively small atomic mass—deuterium has a mass that is twice that of hydrogen, a 100% increase. However, ^{13}C is only 8% more massive than ^{12}C, which has a less significant effect on its respective reduced masses that control the vibrational frequencies of the bonds involved in reactions. An expression for estimating kinetic isotope effects is given in Eq. C.1,

$$\frac{k_{^{12}\mathrm{C}}}{k_{^{13}\mathrm{C}}} = \exp\left\{ \left(\frac{hc(\bar{\nu}_{^{12}\mathrm{C}} - \bar{\nu}_{^{13}\mathrm{C}})}{2k_B T} \right) \right\} \tag{C.1}$$

in which k_i is the rate coefficient of a reaction for isotope i, T is temperature, and ν_i is the vibrational frequency associated with the relevant bond to the reaction. For a typical reaction that involves breaking a C$-$H bond in the stretch coordinate ($\bar{\nu}_{^{12}\mathrm{C}} \approx 3000$ cm^{-1}), substituting ^{13}C ($\bar{\nu}_{^{13}\mathrm{C}} \approx 2991.10$ cm^{-1}) results in a reaction rate ratio $k_{^{12}\mathrm{C}}/k_{^{13}\mathrm{C}}$ of 1.00493.

This assumes the bond is fully broken without any activated complexes (such as would normally exist in a hydrogen abstraction reaction), and so the actual isotope effect will be smaller [178].

This calculation, along with the results shown in Fig. 4.12, suggest that carbon isotopologues of the fuels in this study can be treated as kinetically indistinguishable, facilitating analysis in chemical kinetic studies utilizing multi-isotopologue laser absorption spectroscopy. Lastly, it should be noted that all the shock tube experiments in this work are carried out with significant dilution ($>96\%$) with small quantities ($<2\%$) of fuels, rendering the effect of naturally occurring ^{13}C during oxidation of ^{12}C-containing fuels negligible.

APPENDIX D

The high-enthalpy shock tube facility

Shock tubes are uniquely suited for studying high temperature chemical and physical processes as they can create precisely-known, homogeneous, test conditions over a wide range of temperatures (600–8000+ K) and pressures (sub-atmospheric-1000 atm). As a result, shock tubes have become a primary tool in the development of advanced optical diagnostics for informing combustion chemistry models (chemical kinetics), characterizing complex chemically-reacting flows (aerospace propulsion systems, planetary entry vehicles, internal combustion engines, etc.), and optimizing practical energy systems (incinerators, power plants, etc.) [20]. Due to the diverse nature of shock tube research, shock tube capabilities greatly depend on the target application; however, most facilities still conform to some of the same design considerations. This chapter will detail the design, operation, and performance of the High-Enthalpy Shock Tube (HEST) facility in the Laser Spectroscopy and Gas Dynamics Laboratory at UCLA. The general principles included herein are widely applicable to other shock tube facilities as well.

The High-Enthalpy Shock Tube facility was designed with the following goals and considerations in mind:

1. Produce precisely controlled, high-temperature test conditions up to 8000 K relevant to planetary-entry vehicles

2. Produce precisely controlled, high-pressure test conditions up to 200 bar relevant to chemical propulsion devices (i.e. rockets)

3. Test section must have an inner diameter (ID) greater than 8 cm (3.14 in.) to minimize

boundary layer effects (discussed in Ch. 2) and enable optical diagnostics at sub-ppm concentration levels (longer absorbing optical path length)

4. Obtain test times up to 25 ms to study low-temperature chemical kinetics (down to 600 K), where reaction rates are much slower
5. Test region must have optical access for the development of laser-based diagnostic tools
6. Diaphragm loading mechanism must be easily accessible to minimize the cycle time in between experiments
7. Shock tube sections must be modular enough to reconfigure the assembly for optimal test times under different target conditions
8. Additional consideration must be given to manufacturing feasibility (to minimize cost) and constraints set by the physical space in the laboratory

These performance targets and considerations intimately governed design choices and, ultimately, the design that satisfied all of these was the most suitable for this application.

D.1 Shock tube design

D.1.1 Optimizing test time and diaphragm location

The reflected shock wave produces the highest pressures and temperatures in shock tube experiments, as seen in region 5 of Fig. 2.2 and Fig. 2.3, and creates spatially-homogeneous, zero-dimensional, near-constant test conditions. As a result, optical diagnostic techniques commonly target this region for sensor development and kinetics studies. Therefore, it is of interest to maximize the allowable test time for which the thermodynamic conditions remain constant. As discussed in Sec. 2.2.3, the test time starts when the reflected shock wave passes the measurement location (typically 2 cm from the end wall) and ends when non-ideal wave interactions disturb the flow-field. These disturbances can come from either the arrival of the expansion fan or the reflected shock-contact surface interaction depending on the shock tube geometry and test conditions. Thus, it is desirable to model the unsteady wave propagation present in an experiment to optimize the shock tube geometry, such that the test time is maximized over a given range of conditions. This provides a suitable starting point in the design process as maximizing test time helps size general shock tube dimensions/geometry.

To do this, a 2nd order, Muscl-Hancock-Method finite volume code with an exact Riemann solver was used to illustrate shock, expansion wave, and contact surface propagation and interactions in the shock tube. This code was developed by the Wisconsin Shock Tube Laboratory (WiSTL) [45] and can be used to produce x-t diagrams like those shown in Fig. 2.2 and Fig. 2.3. The WiSTL code can be run through MATLAB but requires an operating system capable of running .exe files (i.e. Windows). To run the program, the following inputs are required: driver length, driven length, initial driver temperature T_4, initial driven temperature T_1, driver gas composition, driven gas composition, and a thermodynamic file (can be obtained from Sandia, NASA, etc.) Additionally, the user needs to specify: (1) either the desired reflected shock temperature T_5 or the desired incident Mach number M_S and (2) either the desired reflected shock pressure P_5 or the initial driven fill pressure P_1. With these inputs the program will produce x-t diagrams, which can be easily used to determined the available test time at the measurement location. It should be noted that the program does not account for non-ideal wave phenomena (shock attenuation, boundary-layer interactions, etc.), but these effects can be incorporated into the program if desired. Nonetheless, the ideal x-t diagrams provide a suitable representation of the actual test conditions.

By inspection of Eq. 2.18 and through use of the WiSTL code, it is evident that, for a given initial temperature T_1, the shock strength M_S is primarily a function of the desired reflected shock temperature T_5. The initial temperature of the driver and driven sections, T_4 and T_1, do not tend to vary in conventional shock tubes (unless heating is desired); therefore, higher reflected shock temperatures are simply achieved by stronger incident shocks. Therefore, the desired reflected shock temperature T_5 will determine the velocity of the incident shock, which dictates when the test time begins. In an ideal shock tube, pressure poses minimal constraints on the start of the test time. In other words, since the initial fill pressure P_1

is allowed to vary, a wide range of reflected shock pressures P_5 is attainable for a given shock strength M_S (i.e. a given reflected shock temperature T_5), as seen in Eq. 2.17. The rupture pressure required for a given test temperature T_5 and pressure P_5 can then be found via Eq. 2.24. This is not the case if T_4 and T_1 are varied, which can also be used to increase the shock strength and is desirable for certain test conditions, as discussed in Sec. 2.2.4. Additionally, in reality, variations in pressure have significant impact on non-ideal wave phenomena, such as boundary-layer growth, shock formation, etc., which is not captured by the numerical simulation.

With these stipulations in mind, an initial design considering ideal conditions still provides a reasonable starting point. Using the WiSTL program, the driver and driven lengths can be easily changed to assess the impact on the reflected-shock test time over a range of conditions. This can be done by simply changing the desired reflected shock temperature T_5, which, as mentioned, determines the beginning of the test time, for a range of driver and driven length combinations. For certain temperatures, the contact surface-reflected shock wave interaction will end the test time while for others the arrival of the expansion fan will end the test time. If the contact surface-reflected shock wave interaction ends the test time, driver gas tailoring may be possible, which mitigates any reflections back towards the test section. Driver gas tailoring can also be incorporated into the WiSTL code to visualize these effects. If the expansion fan ends the test time, the main constraint is the driver length and driver speed of sound, which determines how quickly the expansion fan reaches the test section.

Often times, a large constraint on shock tube design is the available space in the laboratory, as shock tube length commonly corresponds to longer test times. For the high-enthalpy shock tube facility, the total length was constrained to 22 ft., this allowed 1.5 ft. between either end of the shock tube and the wall, a set regulation in case of emergency egress. A novel way of extending the shock tube length past the permitted laboratory space was the addition of a compact, U-extension on the driver section, (more details provided in a later section). Using the approach described above, and the physical constraints set by the labora-

Table D.1: High-enthalpy shock tube configurations

Configuration	1	2	3
Driver Length [ft]	5.13	19.76	16.13
Driven Length [ft]	16.00	16.00	19.63
Test Time [ms] at 800 K	5.1[a]	25.3[a]	19.2[a]
Test Time [ms] at 3000 K	2.2[a]	11.6[a]	8.9[a]
Test Time [ms] at 8000 K	0.7	0.7	0.9

[a] Assumes driver gas tailoring

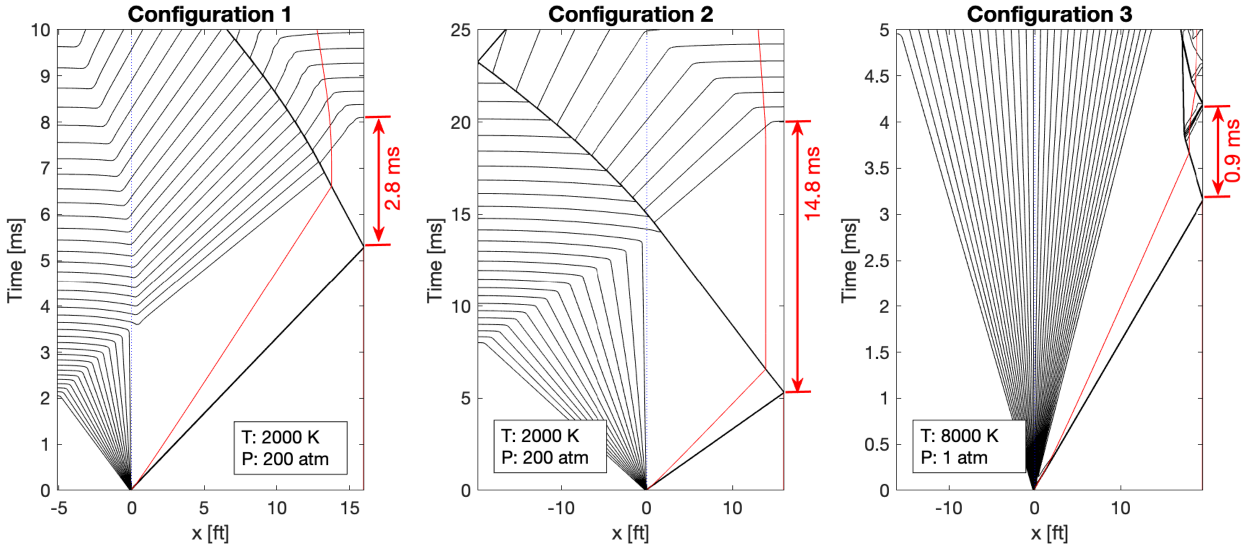

Figure D.1: Representative test times for each of the high-enthalpy shock tube configurations

tory space, driver and driven lengths were optimized to maximize the experimental test time for optical diagnostics behind the reflected shock waves. Utilizing this optimization script, the configurations listed in Table D.1 were selected for the desired operating conditions.

Configuration 1 and 2 are optimized to operate at temperatures less than 3000 K relevant to practical combustion devices (propulsion, internal combustion engines, power plants, etc.) and kinetic studies of fuel oxidation and pyrolysis. Configuration 1 uses the shortest driver length, thereby minimizing the amount of driver gas utilized for each experiment, which is often a consideration for gas consumption as the cost of helium increases. Configuration 2 provides extended test times for low-temperature kinetics by adding a driver length extension.

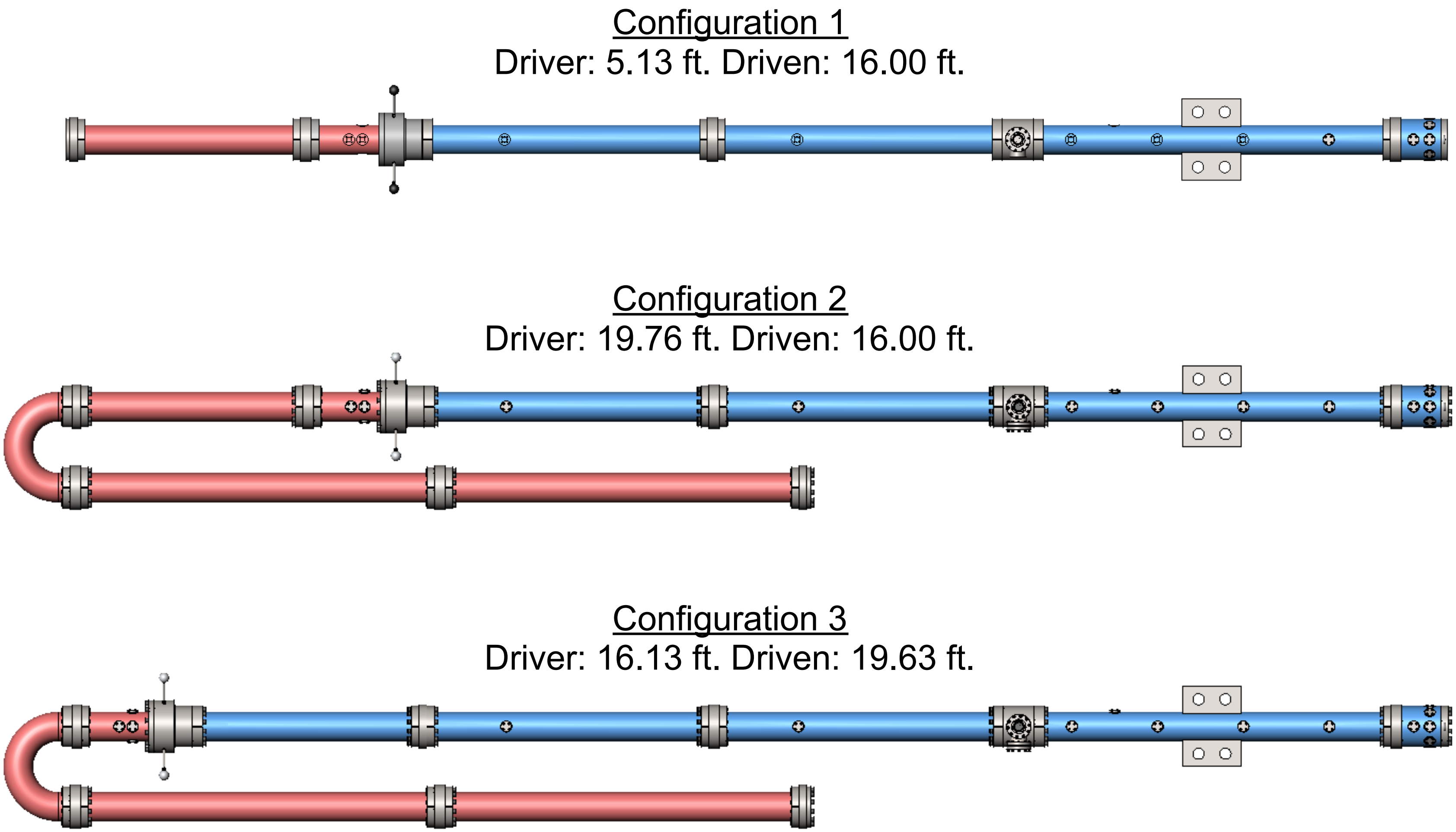

Figure D.2: CAD illustrations of the three high-enthalpy shock tube configurations

Configuration 3 is more suitable for studies pertaining to non-equilibrium radiative heat transfer found in hypersonics or planetary entry conditions. This configuration maximizes the driven length section in order to delay the contact surface arrival at extreme temperatures. Representative test times and CAD illustrations are shown for each configuration in Fig. D.1 and Fig. D.2.

D.1.2 Material selection

In choosing materials for shock tube devices, materials with high strength (for high-pressure applications), high corrosion resistance (to prevent degradation/oxidation over time–especially for combustion studies), and joinability (i.e. ability to be welded) are highly desired properties. As such, many shock tubes are manufactured out of stainless steel. Since there are many different types of stainless steel (304, 316, 440C, etc.), additional consideration must be given to differences in cost, availability, and manufacturability of these alloys. For all these reasons, the high-enthalpy shock tube at UCLA was manufactured out of 304/304L stainless steel. The main difference between 304 and 304L stainless steel alloys is the carbon content. 304 stainless steel has a maximum carbon content of 0.08%, whereas 304L stainless steel has a maximum carbon content of 0.03%. This difference has some implications on the corrosion resistance and mechanical properties of each alloy. In terms of mechanical properties 304L has a slight reduction in both the ultimate tensile strength (UTS) and yield strength–304L has a UTS of $\sim$70 ksi, whereas 304 has a UTS of $\sim$75 ksi. A similar difference is seen in the yield strength, where 304L has a yield strength of $\sim$25 ksi and 304 has a yield strength of $\sim$30 ksi. Please note that the strength values above are highly dependent on the processes used to form the material (annealing, hot/cold finish, etc.); therefore, in designing experiments, it is important to remain conservative and obtain material test reports (MTRs) for the specific stock material used for manufacturing. In terms of welding, 304L's lower carbon content minimizes/eliminates carbon precipitate during the welding process, eliminating the need to anneal the welded joints prior to use and, over time, preventing degradation of the joint. As a result 304L is preferable for welding operations. Since the high-enthalpy shock tube facility incorporates both welded an non-welded joints, the stock material chosen was dual certified for both 304 and 304L–taking advantage of the increase in mechanical properties of 304, while having the welding benefits of 304L.

D.1.3 High pressure weldless flanges

With three target configurations in mind, the high-enthalpy shock tube facility had to be designed to be modular enough to easily reconfigure in-between experiments. To achieve this, custom, low-profile weldless flanges were designed to be easily removable and minimize the overall footprint of a standard welded ASME ANSI flange (discussed in Sec. D.2.3). Additionally, the use of weldless flanges eliminates possible distortion of the tube from welding, which can affect the flow-field and perturb the shock wave as it travels along the tube. The weldless flanges on the high-enthalpy shock tube rely a double groove design that axially compresses and seals two tube sections, as seen in Fig. D.3. The design borrows from that of the High-Pressure Shock Tube at Texas A&M University as well as the well-known Gruvlok flanges, which are commonly used to join pipe sections in mining, oil, gas, slurry, sludge, and hydraulic systems. The entire flange assembly consists of: 2× clearance flanges (Flange_A), 2× threaded flanges (Flange_B), 1× alignment collar (Connector_A), and 12× 5/8-18×5.00 in. bolts and washers. An exploded view of a flange assembly connecting two tube sections is shown in Fig. D.4. The design can also be easily modified to connect a tube section to a blind end cap or other components.

The weldless flanges were designed using both SolidWorks Finite Element Analysis (FEA) and ANSYS FEA programs with the main optimization parameters being: the number of grooves, the depth and width of each groove, and the axial position of each groove. In order to minimize computational time, while still simulating all shock tube connections, all of the FEA was conducted on a simplified model of the shock tube assembly, which contained a tube-to-tube, tube-to-end cap, and tube-to-test section connection. An illustration of the CAD model used for FEA is shown in Fig. D.5. The simulations consisted of an internal pressure load of 200–300 bar applied radially and axially up to the mean diameter of the

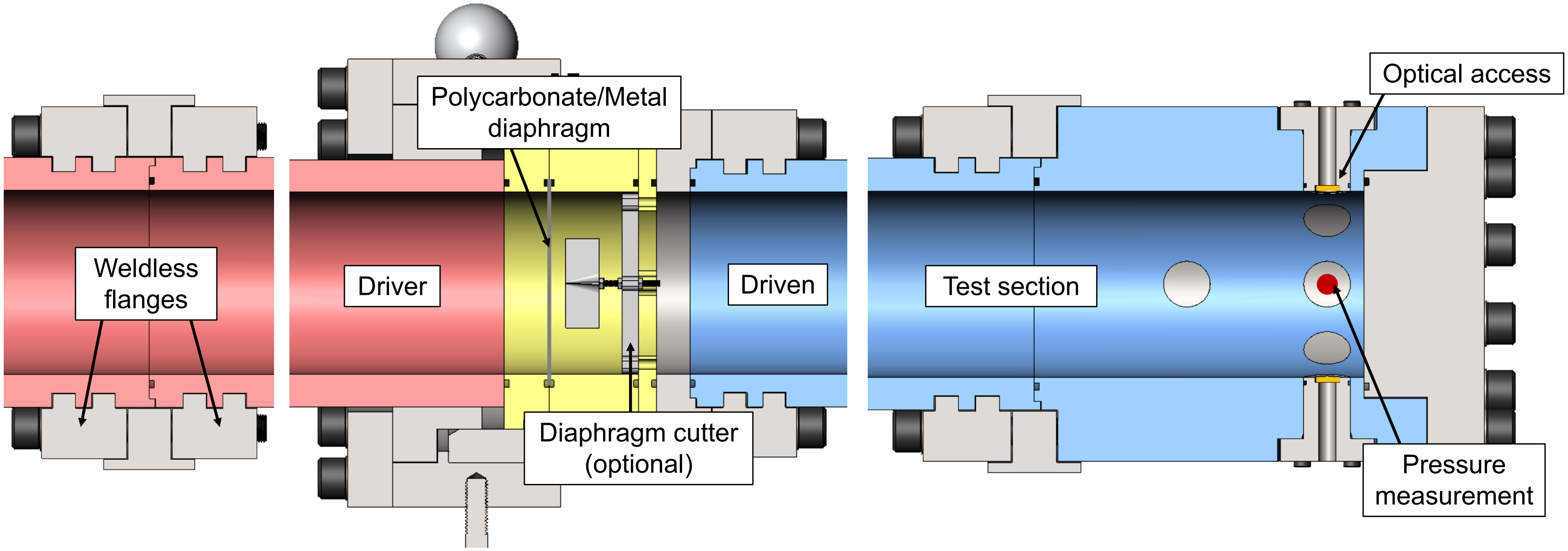

Figure D.3: Key design elements on the high-enthalpy shock tube facility include a high-pressure weldless flange design rated to 200 bar, an easily accessible diaphragm loading mechanism, and an optically accessible test section

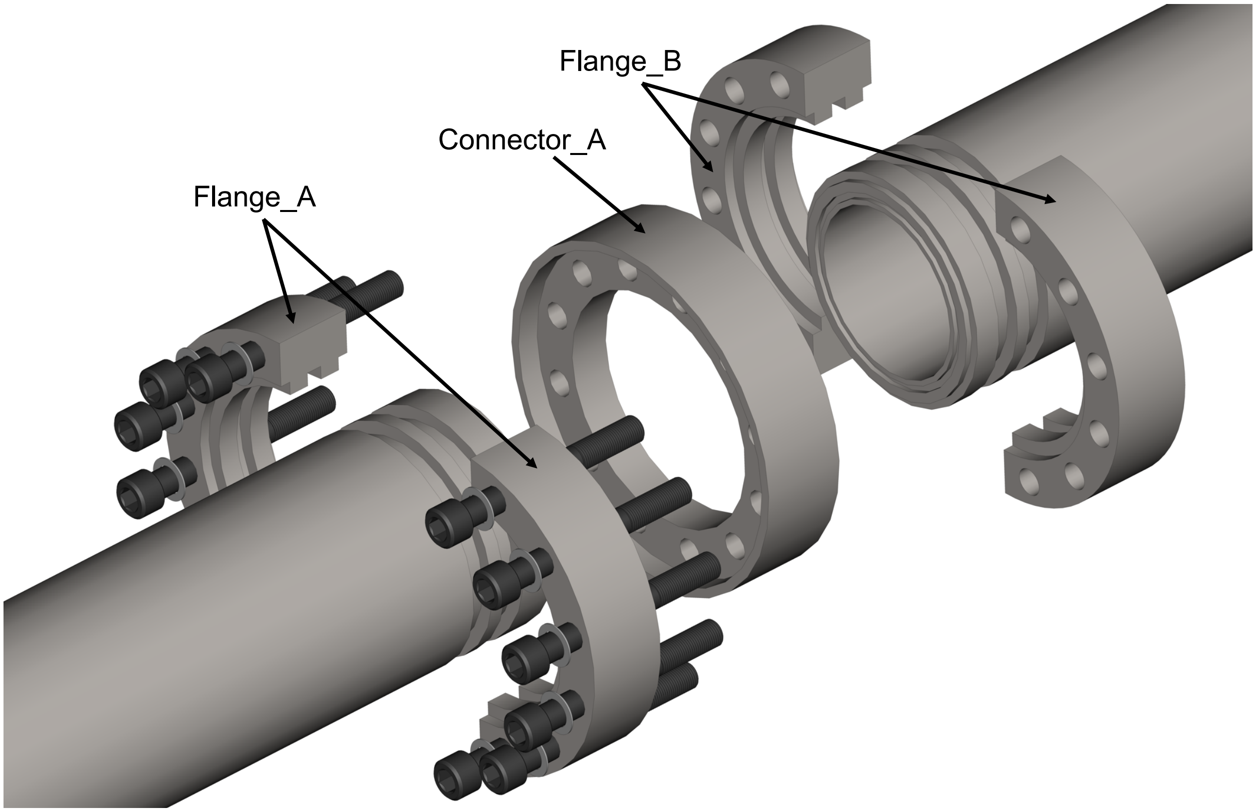

Figure D.4: Exploded view of the high-pressure weldless flange assembly used on the high-enthalpy shock tube facility. The flange assembly consists of: 2× clearance flanges (Flange_A), 2× threaded flanges (Flange_B), 1× alignment collar (Connector_A), and 12× 5/8-18×5.00 in. bolts and washers

o-rings used for sealing between connections (slightly larger than the tube inner diameter). By optimizing the parameters discussed above, it was found that a flange design with a single groove was not sufficient for the high pressures (200 bar) desired in this application (though suitable for pressures up to 100 bar as shown by the High Pressure Shock Tube at Texas A&M). As a result, a double groove design was necessary to increase the loading capability of the flange assembly. Since a double groove design requires two surface to come into contact, the tolerances on the flange and tube grooves shown in the drawing package are such that flange assembly and proper axial loading is possible considering tolerance stack-up. Once the aforementioned parameters were optimized on a relatively coarse mesh (to minimize computational time), the final design was determined by conducting a mesh

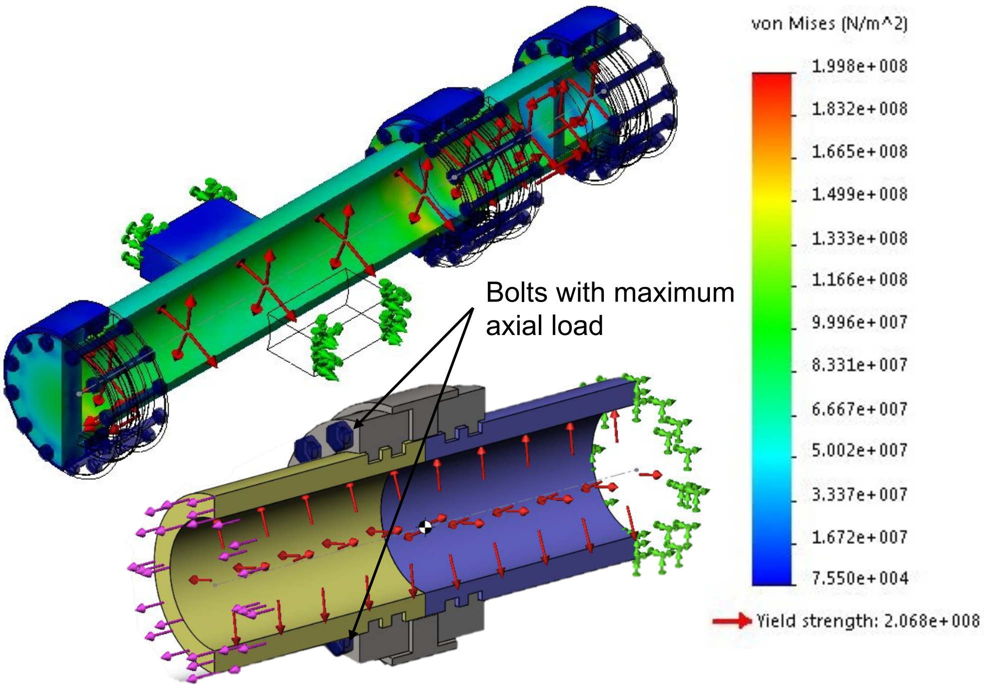

Figure D.5: Representative FEA results illustrating the simplified shock tube model used to optimize weldless flange parameters

convergence study (with a finer mesh at interfaces and contact points) while checking for convergence of the displacement field. It is important to note that when refining meshes near corners, theoretical stresses increase infinitely and create singularities, which are not present in actual features. Nonetheless, the displacement field was found to converge regardless of stress singularities.

In addition to using FEA to optimize the custom flange design, simulations were also useful in determining the loads through each of the 12× 5/8-18×5.00 in. bolts on the flange assembly. Since the flange design is split into two halves (Flange_A and Flange_B), for tube-to-tube connections, the axial load is not evenly distributed among each of the bolts and Eq. D.7 does not apply. For these connections, the bolts that experience the highest axial load are near the edge of the flanges, while those that experience the lowest are the furthest away from the edges, as labeled in Fig. D.5. Knowing the load distribution of the flange design allows for bolt failure calculations described in Sec. D.2.2. The tube-to-end cap and tube-to-test section connections only have split flanges on one side of the connection; therefore, the load is evenly distributed among all the bolts and FEA simply confirms the results given by Eq. D.7.

D.1.4 Shock tube sections

To preface this section, it is important to distinguish the difference between tubing and pipe. Tubing can refer to round, square, rectangular, and oval hollow sections used for transporting fluids, mechanical applications, and instrumentation systems. Tubing is specified by the outer diameter (OD) and wall thickness and typically has much higher tolerances on these parameters than pipe. As a result, tubing is commonly more expensive than pipe. However, it should be noted that since tubing is specified by the OD and wall thickness, the inner diameter (ID) (and its associated tolerance) is primarily constrained by the tolerance stack up of these two parameters. Pipes are tubular vessels used in pipeline systems to transport gases or fluids. Pipe is specified by a Nominal Pipe Size (NPS), a size standard established by the American National Standards Institute (ANSI), and Schedule (wall thickness). NPS can range from 1/8–24+; however, the standardized nominal OD for NPS 1/8–12 is different from the measured/actual OD. For NPS 12+, the standardized nominal OD is the same as the measured/actual OD. For every NPS, there are multiple pipe Schedules (wall thicknesses) available, including Schedule 10, 20, 40, 60, 120, XX, and many more depending on NPS. As the Schedule of the pipe increases for a given NPS, the OD remains the same and the wall thickness increases–decreasing the ID. Additionally, while the Schedule can be the same for different NPS, the actual wall thickness will be different. The standard combinations of NPS and Schedules are covered by the ASME B36.10 and ASME B36.19 specifications.

All tube sections on the high-enthalpy shock tube facility, with the exception of the 180-degree driver extension (Tube_F), are manufactured out of 304/304L tubing stock with 5-1/2 in. OD × 3/4 in. wall thickness–resulting in an ID of 4 in. All tube sections were then honed out to 4.063 ± 0.002 in. (10.32 ± 0.005 cm) with a surface finish of 32 RMS to eliminate any tolerance stack up present in the raw stock and minimize any mismatch of the tube sections at mating interfaces. The centerline radius of the 180-degree driver extension (Tube_F) was desired to be as small as possible to minimize the overall footprint of the shock tube facility in the laboratory. However, manufacturing a 180-degree bend on 5-1/2 in. OD × 3/4 in. wall thickness tubing is not feasible by any reasonable means; therefore, the 180-degree bend was manufactured by welding two 90-degree 5 in. Schedule XX (5.562 in. OD × 4.063 in. ID) pipe elbows. Additionally, the 90-degree pipe ends were welded, with full penetration welds, to 3-1/8 in. long tube sections with 4.063 ± 0.002 in. ID (as described above) to accommodate the high-pressure weldless flange features. All welds (both internal and external) were then ground smooth. This approach results in a highly compact assembly, where the centerline radius of the 180-degree return is 7-1/2 in.

In addition to honing out the tube sections to 4.063 ± 0.002 in., all tube sections were manufactured with male/female alignment grooves (seen on PipeEndDetail) on each end to ensure concentricity and minimize steps at mating interfaces. One end of each tube section has a male alignment groove, while the other end has a female alignment groove–enabling all tube sections to be interchanged throughout the entire assembly. Notably, since the tolerances on these features are tight, they have to be specified such that the male/female ends will always mate regardless of tolerance stack-up. After manufacturing, the tube sections (and all shock tube components) were passivated and electropolished. Passivation uses nitric or citric acid to remove free iron and contaminants from the surface, resulting in a protective oxide layer that is less likely to chemically react/corrode over time. Electropolishing is even more effective at eliminating any additional surface defects or contaminants embedded in the surface by precisely removing a 0.0001–0.0015 in. layer of metal, resulting in a micro-smooth, ultra-clean surface finish. In addition to preventing corrosion, these processes help mitigate boundary layer effects by minimizing perturbations/non-uniformities on the surface of the tube sections, which may perturb/attenuate the shock wave as it travels down the shock tube.

D.1.5 Port plugs

Port plugs are located throughout the entire shock tube assembly as a means of interfacing with fluid lines, instrumentation, optical access, etc. Multiple tube sections have port hole locations where port plugs can be installed using 4× 1/4-28×5/8 in. bolts. Two port plug designs are used (PortPlug_A and PortPlug_B) throughout the high-enthalpy shock tube, the main difference being the overall length of the part. PortPlug_B is longer than PortPlug_A and is used in the test section, which has a thicker wall than the rest of the shock tube assembly. Each port plug uses a radial o-ring seal that sits close to the tube section ID to minimize wetted surface area. Since tolerances on radial o-ring grooves are very tight, port plug installation is assisted by a 15-degree chamfer on every port hole (as seen in PortDetail). The angle of this chamfer was chosen such that the maximum OD of the port plug o-ring (considering tolerances) would be captured by the chamfer. As mentioned in Sec. D.1.4, all tube sections were honed and polished to an ID of 4.063 ± 0.002 in. This procedure was done with all the port plugs installed so that the contour of each port plug sits flush with the ID of each mating tube section. As such, each port plug and port hole is stamped with a label (A, B, C, etc.), which dictates the location and orientation of each port plug throughout the assembly. In addition to stamping each port plug and port hole, the actual location of the port hole along the tube should be requested from the manufacturer, as this location is critical to measuring shock velocities and having the specific location from the manufacturer will minimize any uncertainties in these calculations. On the high-enthalpy shock tube, port plugs are used for interfacing fluid lines, time-of-arrival sensors, optical windows, and high-speed pressure transducers. Drawings for these modifications are also included in Appendix F.

D.1.6 Test section

The test section (Tube_E) is located at the end of the driven section, where, as discussed in Sec. 2.2.5 and Sec. 2.3.5, the test time for reflected shock wave experiments is maximized. The test section was designed to accommodate 7 circumscribed port plugs (PortPlug_B) at

45-degree angles on the same axial plane for both optical and pressure measurements. The driven endwall (EndCap_A) mates to the test section (Tube_E) with 12×5/8-18×2 in. bolts and is designed such that the distance from the measurement plane is only ∼2 cm. To accommodate all these features, the OD of the test section had to be increased to 7.75 in. while keeping the ID the same; therefore, Tube_E was manufactured out of a solid piece of 304/304L stock. As a result, the flanges from the mating tube section (Tube_D) bolt directly into the test section using 12×5/8-18×3-3/4 in. bolts.

D.1.7 Poppet valve

To minimize the time it takes to vacuum down the assembly (maximizing test turnaround time), the high-enthalpy shock tube uses a poppet valve to connect the driven section to both roughing pumps (Adixen Alcatel 2021i) and turbomolecular pumps (Agilent Varian Turbo-V 550). The main components of the poppet valve assembly consist of a piston/poppet (Piston), a piston/poppet rod (PistonRod), and a piston/poppet valve guide (PistonGuide). A heavy duty linear pneumatic actuator (MDC: 661052) open and closes the entire poppet assembly and, when actuated, the poppet assembly provides a 2.50 in. diameter port for vacuuming. The piston/poppet is contoured to match the ID of the tube section (PoppetValveHousing) when closed and uses a face o-ring seal to isolate the driven section. It should be noted that since the piston/poppet is hard to reach once assembled and is actuated frequently, the face o-ring seal has a dovetail groove design to prevent the o-ring from coming out. The PoppetValveHousing connects to tube sections via 12×5/8-18×2-3/4 in. bolts and was designed to be modular enough such that it can be located at any location along the driven section. To maintain the piston/poppet in the correct orientation, a piston/poppet valve guide (PistonGuide) was manufactured out of a blank double-sided Del-Seal CF flange (MDC: 140022). Behind the poppet, Del-Seal CF flanges are used to connect various vacuum components (roughing pumps, turbopumps, ion gauges, etc.).

D.1.8 Diaphragm loading mechanism

The diaphragm loading mechanism consists of a breech canister (BreechCanister_A, BreechCanister_B, BreechCanister_C) and, depending on the desired operating pressures, several diaphragm inserts (DiaphragmCutter_A, DiaphragmSpacer_A, DiaphragmSpacer_B). The breech canister is threaded to facilitate switching out diaphragms in-between experiments. On the driver side, the breech canister is connected to Tube_B, which has a welded flange that interfaces with the canister. On the driven side, the breech canister features the female alignment groove discussed previously, which can be connected to any tube section via 12×5/8-18×1-3/4 in. bolts. Disengaging the breech canister pushes back the driver section, which sits on rollers, and allows user access to the inside of the breech canister. To prevent these threads from seizing, it is advisable to apply anti-seize thread lubricant, such as Loctite LB 8014 or Loctite LB C-200, on the exterior. The diaphragm mechanism allows for both polycarbonate and metal diaphragms, as discussed in Sec. D.6.1. Polycarbonate diaphragms can be used for driver pressures up to 100 psia (7 bar) and metal diaphragms for anything higher. When polycarbonate diaphragms are used, a four-bladed cutter is inserted into the breech canister (DiaphragmCutter_A) to facilitate rupturing of the diaphragm. When metal diaphragms are used, a square insert is inserted into the breech canister to prevent the metal petals from the diaphragm from shearing off when the diaphragm ruptures. More details on diaphragms and the associated procedure for different diaphragm materials are given in Sec. D.6.1.

D.2 Additional design considerations

D.2.1 Pressure vessel failures

In designing pressure vessels, the maximum hoop stress σ_θ, radial stress σ_r, and longitudinal stress σ_l must fall within the predetermined factors of safety to ensure safe and reliable operation. Often times, pressure vessels are categorized into either thin-walled cylinders or thick-walled cylinders. The distinction between the two is typically determined by the ratio between the mean radius $\bar{r}$ of the pressure vessel and the thickness of the wall t. The mean radius of the pressure vessel can be determined using inner and outer radius, r_i and r_o, respectively.

$$\bar{r} = \frac{r_i + r_o}{2} \tag{D.1}$$

If $\bar{r}/t > 10$, then the pressure vessel can be considered thin-walled. If the opposite is true, $\bar{r}/t < 10$, then the pressure vessel can be considered thick-walled. Shock tubes typically fall into the category of thick-walled pressure vessels. Therefore, for a thick-walled cylinder, the stresses at any radial location r can be determined by Lamé's equations:

$$\sigma_\theta = \frac{r_i^2 P_i - r_o^2 P_o}{(r_o^2 - r_i^2)} + \frac{(P_i - P_o) r_i^2 r_o^2}{(r_o^2 - r_i^2) r^2} \tag{D.2}$$

$$\sigma_r = \frac{r_i^2 P_i - r_o^2 P_o}{(r_o^2 - r_i^2)} - \frac{(P_i - P_o) r_i^2 r_o^2}{(r_o^2 - r_i^2) r^2} \tag{D.3}$$

$$\sigma_l = \frac{r_i^2 (P_i - P_o)}{(r_o^2 - r_i^2)} \tag{D.4}$$

where P_i is the internal pressure and P_o is the external pressure. Additionally, the maximum stress $\sigma_e^{\max}$ on a circular end cap with thickness t and bolt radius r_b can be found by:

$$\sigma_e^{\max} = \frac{3}{8} \left(\frac{r_b}{t} \right)^2 (P_i - P_o)(3 + \nu) \tag{D.5}$$

where ν is Poission's Ratio for the desired material. Note Eq. D.5 assumes the pressure acts over the entire bolt radius. In reality, the pressure will act on the area enclosed by the sealing mechanism (i.e. o-ring).

Since shock tubes may experience both internal ($P_i > P_o$) and external pressurization ($P_o > P_i$), both conditions should be evaluated in determining a proper design. As the hoops stress and radial stress varies with radial location r, the maximum location at which these

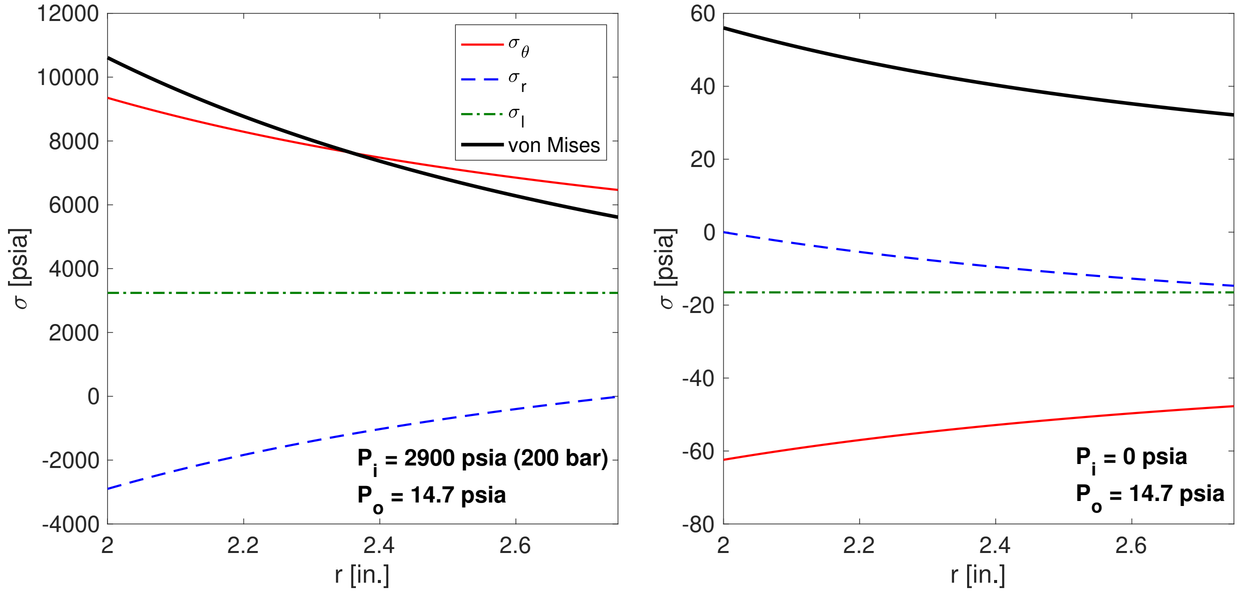

Figure D.6: Comparison of hoop, radial, longitudinal, and von Mises stresses in a pressure vessel with an inner radius of $r_i = 2.0$ in. and an outer radius of $r_i = 2.75$ in. for both internal and external loading configurations

stresses occur depends on the loading configuration. This illustrated in Fig. D.6, which shows the stresses for a thick-walled cylinder with inner radius of $r_i = 2$ in. and an outer radius $r_o = 2.75$ in. for external and internal loading configurations. As shown in Fig. D.6, the longitudinal stress does not depend on the radial distance r; therefore, this stress is experience at all radial points of the vessel. If internally pressurized the maximum hoop and radial stress occur on the inside surface at $r = r_i$. If externally pressurized the maximum hoop stress occurs at the same location but now the maximum radial stress occurs on the outside surface $r = r_o$. Additionally, it should be noted that for both loading configurations, the radial stress is acting in compression ($\sigma_r < 0$). However, for internal pressurization the hoop stress and longitudinal stress are acting in tension ($\sigma_\theta > 0$, $\sigma_l > 0$) and for external pressurization the hoop stress and longitudinal stress are acting in compression ($\sigma_\theta < 0$, $\sigma_l < 0$). To evaluate combined stresses, the von Mises failure criterion can calculated through:

$$\sqrt{\frac{(\sigma_\theta - \sigma_r)^2 + (\sigma_\theta - \sigma_l)^2 + (\sigma_r - \sigma_l)^2}{2}} \leq \sigma_y \tag{D.6}$$

where σ_y is the yield strength of the material. Since Eq. D.2–Eq. D.6 may be compared to the yield strength of the material for evaluating the factor of safety at the desired operating conditions.

In a shock tube driver and driven sections experience different loading configurations. Both sections can be subject to vacuum for several hours, depending on the desired ultimate pressure or when the facility is not in use. During a test, the driver section experiences a more sustained pressure loading prior to the diaphragm rupture and the driven section only experiences a brief (< 10 ms) pressure spike during the shock wave arrival. After the test, the entire facility may be at high or low pressures, depending on the targeting conditions. Nonetheless, the design requirement for these facilities should assume maximum expected pressure is sustained to ensure safe operation.

D.2.2 Bolt failures

Bolts can fail in a variety of ways; therefore, each failure mode must be evaluated to ensure safe operation. Bolts are typically used in shock tubes to connect different sections together or to hold port plugs/optical windows in place. To determine if a bolt will fail the first step is to calculate the total load the bolt F_{bolt} experiences. If assessing a symmetrical, continuous multi-bolt junction, such as a standard flange, this can easily be done by:

$$F_{\text{bolt}} = \frac{F_{\text{total}}}{N_{\text{bolt}}} \tag{D.7}$$

where F_{total} is the total force experienced by the junction and N_{bolt} is the number of bolts that split the load. However, if the junction is asymmetrical or discontinuous (i.e. if the flange is split into two halves), then each bolt will experience a different load, with the bolts closest to the discontinuity experiencing the highest loads. In this case, the maximum force experienced by the bolt can be determined via numerical tools, such as finite element analysis (FEA).

With the bolt load F_{bolt} determined, the following failure modes should be considered when the bolt is loaded along its primary axis: (1) tensile failure of the bolt itself, (2) external shear failure of the bolt threads, and (3) internal shear failure of the mating threads. To evaluate the tensile stress experienced by a bolt, the effective tensile strength area A_t [in.^{2}] must be calculated. Depending on the ultimate tensile strength σ_{ult} of the bolt material, this can be done through the following:

$$A_t = \begin{cases} 0.7854\left(D_{\text{B}} - \dfrac{0.9743}{n}\right)^2 & \text{if } \sigma_{\text{ult}} < 100 \text{ ksi} \\ \pi\left(\dfrac{E_{s,\min}}{2} - \dfrac{0.16238}{n}\right)^2 & \text{if } \sigma_{\text{ult}} > 100 \text{ ksi} \end{cases} \tag{D.8}$$

where D_{B} [in.] is the basic major diameter of the bolt, n is number of threads per inch, and $E_{s,\min}$ [in.] is the minimum pitch diameter of the external thread. Note, [ksi] is simply [ksi] = 1000×[]psi]. Values for D_{B} and $E_{s,\min}$ are tabulated in standard ASME B1.1-2003 and ASME B1.13M-2005. Using Eq. D.8, the tensile stress σ_t [psi] the bolt experiences and the resulting factor of safety can be evaluated through:

$$\sigma_t = \frac{F_{\text{bolt}}}{A_t} \tag{D.9}$$

$$FS = \frac{S_{\text{proof}}}{\sigma_t} = \frac{0.95 \times S_{\text{yield}}}{\sigma_t} \tag{D.10}$$

where S_{proof} [psi] is the bolt proof strength, typically defined as 95% of the bolt material yield strength S_{yield} [psi].

A similar analysis can be done for the external shear failure of the bolt threads. The external thread shear area $A_{s,\text{ext}}$ [in.^{2}] can be calculating through:

$$A_{s,\text{ext}} = \pi n L_e K_{n,\max}\left[\frac{1}{2n} + 0.57735\left(E_{s,\min} - K_{n,\max}\right)\right] \tag{D.11}$$

where L_e [in.] is the total thread engagement, $K_{n,\max}$ [in.] maximum minor diameter of the internal thread, and $E_{s,\text{min}}$ [in.] is the minimum pitch diameter of the external thread. These values can also be found tabulated in standard ASME B1.1-2003 and ASME B1.13M-2005. Using A_s, ext, the shear stress $\sigma_{s,\text{ext}}$ [psi] on the bolt threads and the resulting factor of safety can be evaluated through:

$$\sigma_{s,\text{ext}} = \frac{F_{\text{bolt}}}{A_{s,\text{ext}}} \tag{D.12}$$

$$FS = \frac{S_{\text{shear}}}{\sigma_{s,\text{ext}}} = \frac{\left(\dfrac{S_{\text{yield}}}{\sqrt{3}}\right)}{\sigma_{s,\text{ext}}} \tag{D.13}$$

where S_{shear} [psi] is the shear strength of the bolt material. If the shear strength of the bolt material is not readily available, a conservative estimate is to use $S_{\text{yield}}(\sqrt{3})^{-1}$ as a result of the von Mises yield criterion.

Finally, the same approach can be used to evaluate the internal shear failure of the mating threads. The internal thread shear area $A_{s,\text{int}}$ [in.^{2}] can be calculating through:

$$A_{s,\text{int}} = \pi n L_e D_{s,\text{min}} \left[\frac{1}{2n} + 0.57735\left(D_{s,\text{min}} - E_{n,\text{max}}\right)\right] \tag{D.14}$$

where $D_{s,\text{min}}$ [in.] minimum major diameter of the external thread, and $E_{n,\text{max}}$ [in.] is the maximum pitch diameter of the internal thread. These values can also be found tabulated in standard ASME B1.1 and ASME B1.13M. Using $A_{s,\text{int}}$, the shear stress $\sigma_{s,\text{int}}$ [psi] on the mating threads and the resulting factor of safety can be evaluated through:

$$\sigma_{s,\text{int}} = \frac{F_{\text{bolt}}}{A_{s,\text{int}}} \tag{D.15}$$

$$FS = \frac{S_{\text{shear}}}{\sigma_{s,\text{int}}} = \frac{\left(\dfrac{S_{\text{yield}}}{\sqrt{3}}\right)}{\sigma_{s,\text{int}}} \tag{D.16}$$

where S_{shear} [psi] is the shear strength of the material for the mating threads. Similarly, if the shear strength is not readily available, a conservative estimate is to use $S_{\text{yield}}(\sqrt{3})^{-1}$ as a result of the von Mises yield criterion.

D.2.3 Standard welded flanges

The American Society of Mechanical Engineers (ASME) provides standard flange sizes in ASME B16.5 for a wide range of operating pressures (up to 400+ bar) and temperatures. The flanges are available with the following end connections: weld neck, slip-on, socket weld, threaded, lap joint, or blind. The standard is organized by pressure class (150, 300, 400, 600, 900, 1500, or 2500), nominal pipe size (1/2–24), and operating temperature. As shock tubes only experience a brief temperature spike, room temperature can be used as the operating temperature. The use of standard welded flanges in the development of new shock tube facilities is attractive as it requires little design work to incorporate. However, consideration must be given to: (1) the distortion of the pipe as a result of the welding process and (2) the practical limitations in scaling the standard flanges to high pressures. Any distortion of the driven section portion of the shock tube is highly undesirable as it may significantly alter shock formation/propagation and amplify any non-ideal effects in the test conditions. Additionally, if the shock tube is being designed for high pressures, the standard welded flanges are large in size, which limits modularity and accessibility. Table D.2 shows the

Table D.2: Pressure ratings for steel pipe flanges according to ASME B16.5 - Group 1.2

	Class						
	150	**300**	**400**	**600**	**900**	**1500**	**2500**
Working pressure [bar]	19.8	51.7	68.9	103.4	155.1	258.6	430.9

Table D.3: Class 1500: carbon and stainless steel flange sizes

	Nominal Pipe Size							
	1	**1-1/4**	**1-1/2**	**2**	**2-1/2**	**3**	**4**	**5**
Flange OD [in.]	5-7/8	6-1/4	7	8-1/2	9-5/8	10-1/2	12-1/4	14-3/4
Pipe OD [in.]	1.32	1.66	1.90	2.38	2.88	3.50	4.50	5.56

required flange class for the desired pressure rating at room temperature operation.

As an example the high-enthalpy shock tube had a target operating pressure of 200 bar. From Table D.2, this would require a Class 1500 flange to ensure safe operation. Now using Table D.3, the flange size can be determined by the desired pipe size. If a pipe with an outer diameter of 5.56 in. is desired, the corresponding flange outer diameter would be 14.75 in. The physical size, along with the potential distortion of the tube, limits the practicality of using standard welded flanges for high-pressure shock tube applications with larger inner diameters. Therefore, custom welded or weldless flanges must be explored. The former is quite difficult to analyze as its very dependent on the application/procedure; thus, custom weldless flanges are preferred.

D.3 Shock tube hardware

Table D.4 lists relevant hardware (bolts, o-rings, valves, etc.) used throughout the high-enthalpy shock tube facility. Table D.4 can be used with Fig. D.18 to help identify valve type/locations. Please take note of appropriate pressure ratings and material compatibility as the hardware listed in Table D.4 may not be suitable for all experiments.

D.4 Factors of safety

Per the discussion in Sec. D.1 and Sec. D.2, Table D.5 lists the factors of safety FS for various components on the high-enthalpy shock tube at the maximum operating pressure, P_{max}. All values are computed at room temperatures using conservative values for the given yield strength S_{yield} of the material. If the listed failure mode is in shear, the shear strength of the material is estimated using the von Mises yield criterion ($S_{\text{shear}} = S_{\text{yield}}(\sqrt{3})^{-1}$).

Table D.4: Select hardware used on the high-enthalpy shock tube facility

Bolts

Description	Thread & Length	Material	Torque	Vendor	Part No.
Flange_A-to-Flange_B	5/8-18×5 in.[a]	Black-oxide steel alloy	45 lb-ft	McMaster-Carr	91251A490
BreechCanister_A	5/8-18×2-3/4 in.[a]	Black-oxide steel alloy	45 lb-ft	McMaster-Carr	91251A485
BreechCanister_B	5/8-18×1-3/4 in.[a]	Black-oxide steel alloy	45 lb-ft	McMaster-Carr	91251A400
PoppetValveHousing	5/8-18×2-3/4 in.[a]	Black-oxide steel alloy	45 lb-ft	McMaster-Carr	91251A485
EndCap_A	5/8-18×2 in.[a]	Black-oxide steel alloy	45 lb-ft	McMaster-Carr	91251A402
EndCap_B	5/8-18×3-3/4 in.[a]	Black-oxide steel alloy	45 lb-ft	McMaster-Carr	91251A506
Port Plugs	1/4-28×5/8 in.[b]	Black-oxide steel alloy	90 lb-in	McMaster-Carr	91251A439

O-rings

Description	Dash number	Material[c]	Hardness	Vendor	Part No.
Tube sections	2-245	Buna-N	Durometer 70A	McMaster-Carr	9452K195
Port plugs	2-020	Buna-N	Durometer 70A	McMaster-Carr	9452K74
Piston/poppet	2-232	Buna-N	Durometer 50A	McMaster-Carr	2418T187

Valves

Description	Pressure rating	Vendor	Part No.
High-pressure needle valve for driver fill	6000 psig	Swagelok	SS-3NRS4
Bellows needle valve for shock tube manifold	1000 psig	Swagelok	SS-6BK
Quarter-turn plug valves	3000 psig	Swagelok	SS-4P4T
Pneumatic ball valve	3000 psig	Swagelok	SS-43GS4-31C
Pneumatic roughing pump valve	–	MDC Precision	311073
Pneumatic turbo pump valve	–	MDC Precision	313041
Pneumatic actuator for piston/poppet	–	MDC Precision	661051

[a] Use with washer (McMaster-Carr: 91877A138)

[b] Use with washer (McMaster-Carr: 98019A228)

[c] Material may not be compatible/suitable for all gas mixtures

Table D.5: Factors of safety for various components on the high-enthalpy shock tube facility

Component	Failure mode	Material	S_{yield} [psi]	$P_{\max}$ [bar]	FS
High-pressure weldless flanges					
5/8-18 bolts	Thread tensile failure	Black-oxide steel alloy	170,000	200	9.1
5/8-18 bolts	External thread shear failure	Black-oxide steel alloy	170,000	200	15.6
5/8-18 bolts	Internal thread shear failure	304/304L stainless steel	30,000	200	3.8
Double-groove flange	Groove failure	304/304L stainless steel	30,000	200	1.4
Tube section	von Mises	304/304L stainless steel	30,000	200	2.7
Port plugs					
1/4-28 bolts	Thread tensile failure	Black-oxide steel alloy	170,000	200	7.5
1/4-28 bolts	External thread shear failure	Black-oxide steel alloy	170,000	200	8.8
1/4-28 bolts	Internal thread shear failure	304/304L stainless steel	30,000	200	2.8
Mixing Tank					
1/4-20 bolts	Single shear failure	Black-oxide steel alloy	170,000	69	3.7
Tank	von Mises	6061 aluminum	35,000	69	4.1
Tank	Bearing stress	6061 aluminum	35,000	69	2.7

D.5 Shock tube manufacturing and testing

The high-enthalpy shock tube was manufactured by Johansing Iron Works located in Benecia, CA. Upon manufacturing, the following test procedures were conducted:

1. Load press test of the weld on Tube_B and the high-pressure weldless flange assembly to the equivalent force of 280 bar
2. Hydrostatically test a simplified assembly, which contains the high-pressure weldless flanges, diaphragm loading mechanism, and port plugs to 265 bar
3. Hydrostatically test the entire high-enthalpy shock tube assembly to 240 bar

The high-enthalpy shock tube successfully completed testing, was delivered to UCLA, and the first shock was run on February 14th, 2018 (Valentine's Day).

D.6 Shock tube operation

D.6.1 Diaphragms

The high-enthalpy shock tube facility can accommodate either polycarbonate or metal diaphragms. Polycarbonate diaphragms are used for low-pressure experiments where the desired P_4 is less than 100 psia. Plastic diaphragms are typically bought as 2 ft.-by-4 ft. sheets and range in thickness from 0.005–0.020 in. in 0.005 in. increments with a thickness tolerance of ±10%. Prior to an experiment the plastic sheets are cut into diaphragms using a template. Caution must be taken to not damage the polycarbonate surface as the rupture pressure can be very sensitive to any imperfections in the material. Additionally, each sheet is covered with a thin film on either side, which should not be removed until the diaphragm is ready to be used.

When using plastic diaphragms with thicknesses between 0.005–0.015 in., the four-bladed cutter must be used to ensure consistent diaphragm rupture. The four-bladed cutter was manufactured out of a 1.0 in. thick 304 stainless steel block by using an electric discharge machine (EDM) to contour the blades such that the back has enough space for a mounting rod but the front is thin enough to be sharpened using course and ceramic knife sharpeners. When installing the four-bladed cutter, it is essential that all four blades are parallel to the diaphragm surface and that the distance between the cutter and the diaphragm is consistent. Small differences in the height of the blades can result in an uneven diaphragm rupture, precluding successful shock formation. Additionally, slight inconsistencies in the distance between the cutter and the diaphragm can increase or decrease the rupture pressure. If the cutter is too far, the diaphragm will deform too much before rupturing, typically resulting in loose diaphragm pieces in the tube. If the cutter is too close, the diaphragm will apply too much pressure on the cutter and can deform the mounting rod holding it in place. An adequate distance between the back of the cutter and the mounting location was found to be 0.500 in., as shown in Fig. D.7. When using polycarbonate diaphragms with a thickness of 0.020 in., the four-bladed cutter needs to be swapped with the arrowhead cutter and the diaphragms need to be scored. The 0.020 in. diaphragms cannot be used with the four-bladed cutter as its too thick for the cutter to rupture it. This can result in damage to both the cutter and the shock tube. The 0.020 in. thick diaphragms can be scored using a template and the arrowhead cutter should be mounted in a similar fashion to the four-bladed cutter. Once scored the 0.020 in. diaphragms rupture at a similar pressure as the 0.015 in.; therefore, when running experiments at pressure higher than what 0.015 in. diaphragm can produce, two scored 0.020 in. diaphragms must be stacked. The diaphragms can be stacked in such a way that the score marks are at 45 deg. from one other. This approach was found to be consistent in achieving even ruptures.

Above 100 psia, metal diaphragms are required and the remote filling station must be used. At the time of this writing, only aluminum and steel diaphragms have been used on the high-enthalpy shock tube facility; however, other materials, such as copper, can be explored if desired. Metal diaphragms are manufactured in-house using a waterjet and 3-axis CNC mill. The metal stock is typically purchased in 12 in.-by-12 in. sheets and each sheet can be used to produce four diaphragms. The diaphragms are first cut out on the waterjet and then

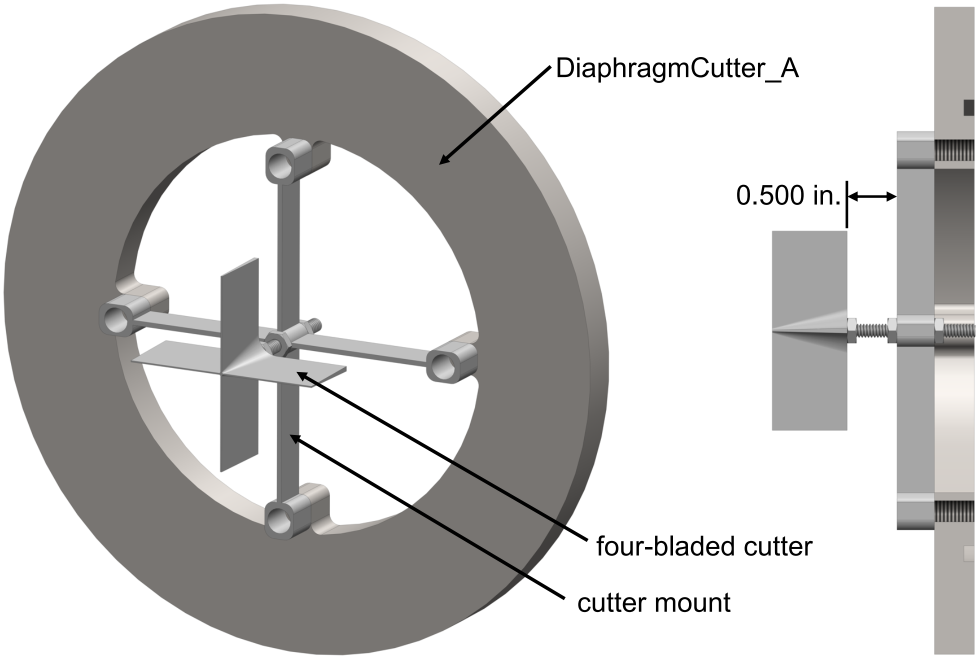

Figure D.7: Four-bladed diaphragm cutter used to rupture polycarbonate diaphragms on the high-enthalpy shock tube. 0.500 in. between the cutter and the mount was found to be an adequate distance for test repeatability

the edges are sanded to prepare for the CNC mill. When using the CNC mill, the diaphragm is placed in a high-precision tool that centers the diaphragms and ensure no lateral or vertical movement during the machining operations. The length of the score is the same dimension as the shock tube inner diameter (4.063 in.) and is machined using high-precision pointed endmill. The CNC mill can be used to score diaphragms to different depths depending on the desired rupture pressure. It should be noted that when manufacturing steel diaphragms, they must be dried immediately after operations on the waterjet or CNC as the water and coolant will cause the steel to rust fairly quickly. If the steel diaphragms are not being used immediately, they should be stored in a dry location. Before running an experiment with metal diaphragms, the cutter assembly must be removed from the shock tube and replaced with the square insert. The square insert ensures the metal petals hit a flat surface upon rupturing, which prevents petals from tearing at the base. When aligning the metal diaphragm in the shock tube, the scored side must face the driven section and the base of

Table D.6: Rupture pressures for polycarbonate, aluminum, and steel diaphragms

Material	Thickness [in.]	Min. Thickness [in.]	P_4 [psia]
Polycarbonate	0.005	–	25
Polycarbonate	0.010	–	45
Polycarbonate	0.015	–	65
Polycarbonate	0.020	0.015	65
Polycarbonate	0.020 (x2)	0.015	112
6061 Aluminum	0.050	0.020	277
6061 Aluminum	0.050	0.025	340
6061 Aluminum	0.050	0.030	491
6061 Aluminum	0.080	0.040	473
6061 Aluminum	0.080	0.050	611
6061 Aluminum	0.080	0.060	1017
6061 Aluminum	0.125	0.075	938
6061 Aluminum	0.125	0.080	973
6061 Aluminum	0.125	0.090	1164
6061 Aluminum	0.125	0.095	1561
6061 Aluminum	0.125	0.098	1925
6061 Aluminum	0.125	0.100	1992
6061 Aluminum	0.125	0.105	2401
6061 Aluminum	0.160	0.100	1378
6061 Aluminum	0.160	0.110	1467
4130 Alloy Steel	0.050	0.030	1414

the petals must align with the square insert, such that the score marks align with the corners of the insert. Fig. D.8 and Fig. D.9 show the correct placement for all of the diaphragm inserts in the breech canister when using either polycarbonate or metal diaphragms. Please note the order of the inserts changes depending on the diaphragm material.

A list of the rupture pressures for both polycarbonate and metal diaphragms with different score depths can be found in Table D.6. These score depths and thickness have been found to be consistent with clean ruptures. In trying new combinations or score depths it is advised that they are based off the percentage of material removed from what has worked before. In scoring diaphragms, it was found that too little of a score can result in small metal shrapnel from the rupture, which can considerably damage the shock tube, and too much of a score results in poor opening speeds as the petals do not fully open.

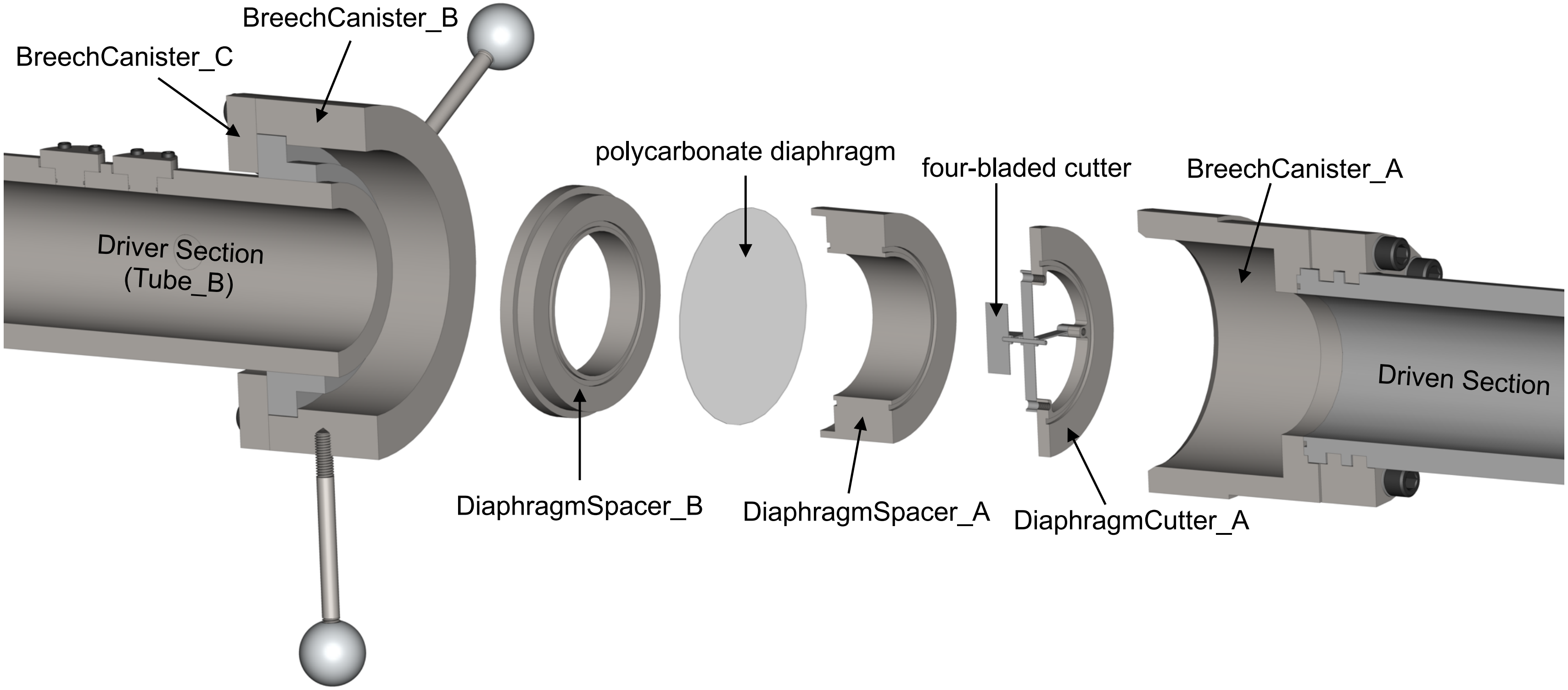

Figure D.8: Diaphragm inserts that get placed in BreechCanister_A when running shock tube experiments with polycarbonate diaphragms. The four-bladed cutter promotes repeatable diaphragm rupture and prevents polycarbonate from pieces from being sent into the driven section

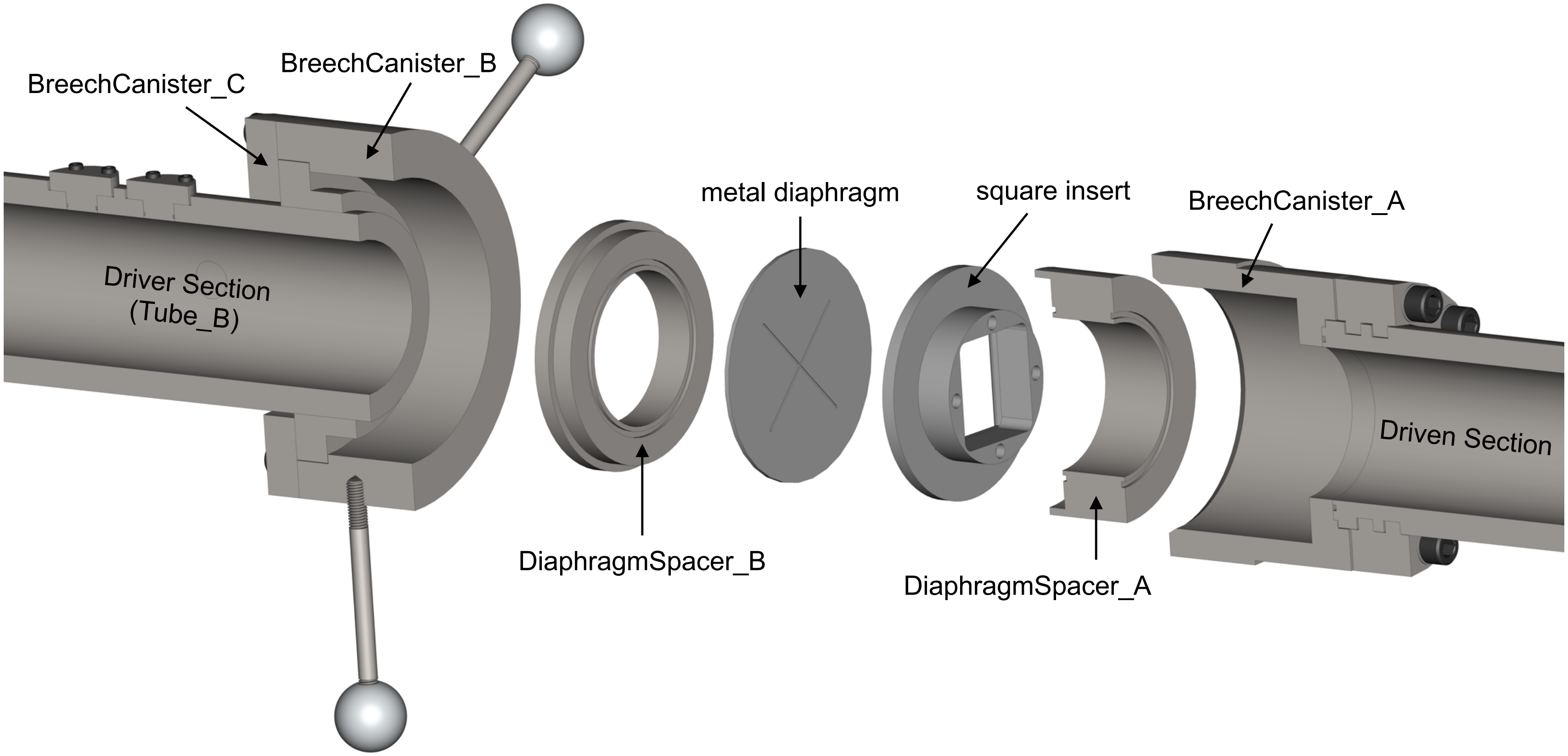

Figure D.9: Diaphragm inserts that get placed in BreechCanister_A when running shock tube experiments with metal diaphragms. Scoring metal diaphragms with a cross promotes repeatable diaphragm rupture. The square insert prevents the metal petals from the diaphragm from shearing off when it ruptures

D.6.2 Time-of-arrival sensors

As mentioned previously, it is possible to accurately determine (with $< \pm$ 1% uncertainty) the temperature and pressure behind the incident and reflected shock wave with a precise measurement of the incident shock speed. On the high-enthalpy shock tube, shock speed is determined by placing five fast-response, piezoelectric time-of-arrival sensors at different axial distances from the driven endwall. The time-of-arrival sensors are located at distances x = 3.79, 19.55, 35.55, 51.55, 67.55 in., where $x = 0$ corresponds to the driven endwall. The specific piezoelectric sensor used is shown in Fig. D.10 (CA-1135) and is purchased from Dynasen, Inc. located in Goleta, CA. These sensors operate over a wide range of pressures (sub-atmospheric–300 kbar) with a response time on the order of 10 nanoseconds. Sensors with different outer diameter brass casings are available (OD: 0.064, 0.093, 0.125 in.); however, the smaller the pin, the lower the uncertainty in shock location and, as a result, shock speed. Therefore, the high-enthalpy shock tube uses sensors with a 0.064 in. brass casing. Additionally, since the 0.064 in. brass casing is similar to standard 1/16 in. tubing, replacing sensors and interfacing with the shock tube port plugs is rather convenient.

To interface the sensors with the high-enthalpy shock tube, two mounting methods have been used, as shown in Fig. D.11. Mounting method 1 epoxies the sensors to a Swagelok

Figure D.10: Drawing of the piezoelectric sensor (CA-1135) used to measure shock speed on the high-enthalpy shock tube facility. The sensors, as well as this drawing, are obtained from Dynasen, Inc. located in Goleta, CA.

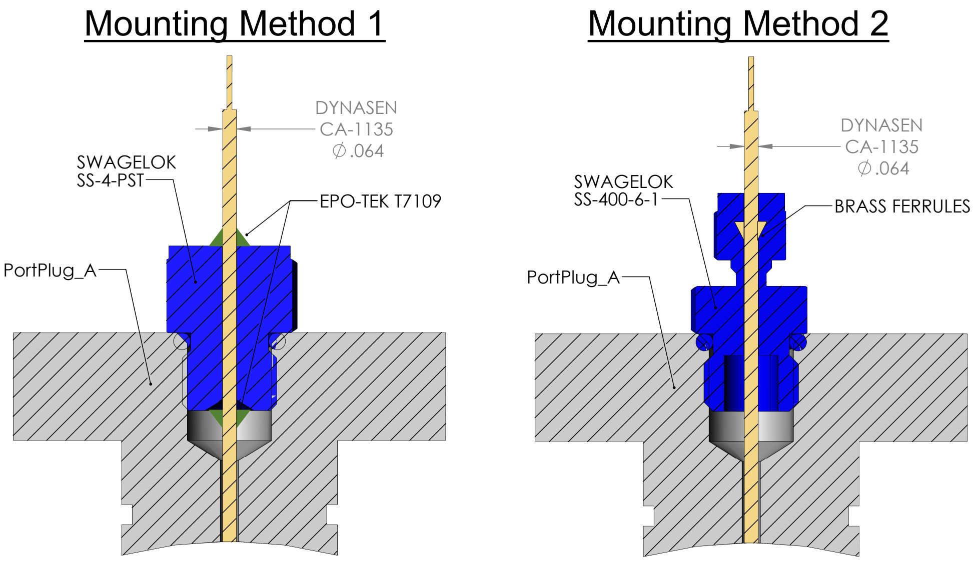

Figure D.11: Different mounting methods used for the time-of-arrival sensors. Method 1 uses epoxy to create a seal between the sensor and the fitting. Method 2 uses brass ferrules to seal off the sensor.

fitting (SS-4-PST), which directly threads into a port plug. The epoxy used is EPO-TEK T7109 sold by Epoxy Technology. It has a low vapor pressure to minimize outgassing under vacuum conditions and, as a result, is also used for installing optical windows. The Swagelok fitting (SS-4-PST) comes as a blank plug and, therefore, must be modified to interface with the sensor. To install the sensor, first install the Swagelok fitting onto the port plug. Afterwards, place the sensor inside the Swagelok fitting/port plug and apply epoxy to the exposed side of the fitting (top)–ensure the epoxy fully covers any air gaps/voids and that the sensor is flush with the contour of the port plug (minimizing how much the sensor protrudes into the driven section). The entire assembly is then baked in a furnace similar to optical windows (150-degree C for 20–30 minutes). Finally, remove the Swagelok fitting and sensor from the port plug, apply epoxy to the bottom of the fitting, and bake again. The sensor is now ready to be used on the shock tube.

Method 2 for mounting these sensors attaches 1/16 in. Swagelok ferrules directly to the brass casing of the sensor. Since the sensor casing is brass, 1/16 in. brass ferrules are used

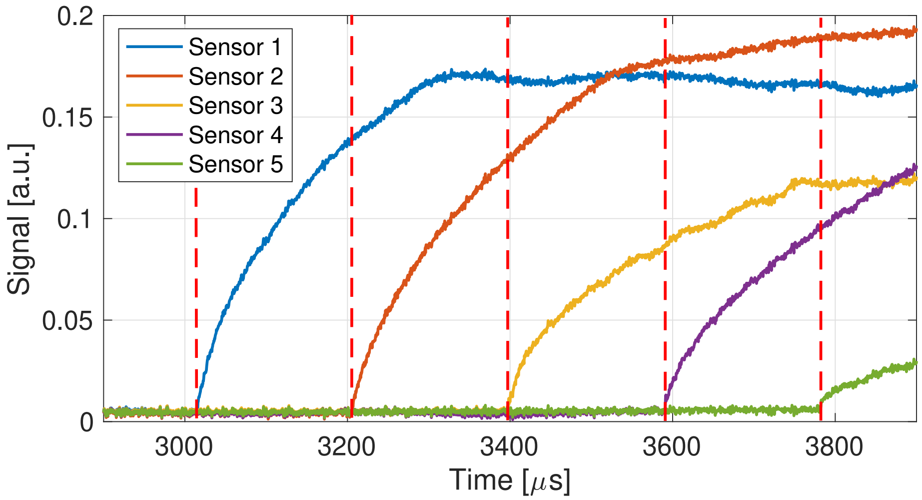

Figure D.12: Representative data obtained from the piezoelectric sensors from Dynasen, Inc. during a shock tube experiment. Dash lines indicate arrival of incident shock wave

to avoid damaging the sensor. Once the ferrules are installed, the sensor can be mounted on the port plug using a Swagelok fitting (SS-400-6-1). Please note that the brass ferrules should be installed onto the sensor while the Swagelok fitting is installed onto the port plug to ensure the sensor is flush with the contour of the port plug (minimizing how much the sensor protrudes into the driven section). Between the two methods, Method 2 is preferred as the installation process is less time consuming and replacing damaged sensors is much more convenient. Over time, sensors closest to the endwall tend to need replacement as they experience the highest temperatures and pressures during shock tube experiments.

Representative raw data for the time-of-arrival sensors is shown in Fig. D.12. These signals can be used to determine the velocity of the shock as it approaches the end wall, as seen in Fig. D.13. Typically, *if a shock is fully formed*, the velocity of the incident shock wave will decrease as it approaches the driven endwall due to boundary layer effects and viscous losses. However, *if a shock is not fully formed*, the velocity appears to increase as it approaches the driven endwall. Additional information on shock velocity trajectories can be found in [43]. The shock velocity at the driven endwall can then be extrapolated using a least-squares linear regression, which can be used to determine the test conditions and compared to the measured pressure trace, as illustrated previously in Fig. 2.8. Additionally,

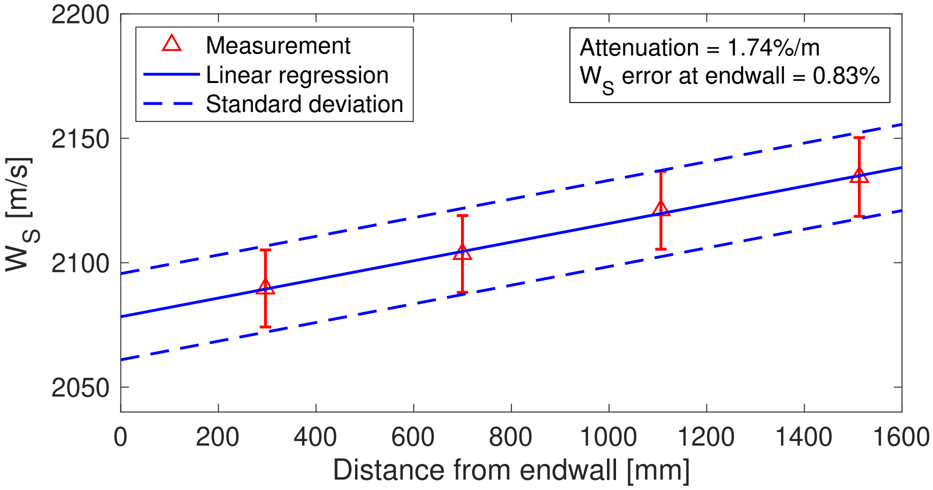

Figure D.13: Representative data for the shock attenuation on the high-enthalpy shock tube facility. The piezoelectric sensors from Dynasen, Inc. are used to determine the velocity profile of the incident shock wave

the uncertainty in the incident shock velocity obtained from the linear regression can be propagated to determine uncertainty in thermodynamic conditions.

D.6.3 Fast-response pressure transducer

To obtain pressure measurement data during shock tube experiments, the high-enthalpy shock tube uses a fast-response pressure transducer (Kistler 601B1) located on the driven sidewall, ∼2 cm away from driven endwall. As described in Sec. D.1.6, the fast-response pressure transducer is mounted on one of the seven port plugs that circumscribe the test section. This is done so that optical measurements and pressure measurements are taken at the same axial location of the shock tube. Because of the sidewall mounting location, the pressure transducer is susceptible to the boundary layer effects discussed in Sec. 2.3. As a result, although the relative changes in pressure are accurate, the overall magnitude of the pressure measurement can sometimes deviate from the pressure obtained from shock relations (using the measured incident shock velocity). As shock relations are known to provide well-known conditions, assuming non-ideal effects are accounted for (relaxation, attenuation, etc.), it is acceptable to simply use the measured pressure trace for relative changes in the test section. In other words, the pressure obtained from the Kistler 601B1 (at the moment the reflected shock wave passes) can be anchored to the pressure obtained from shock relations P_5. The measured pressure trace can then be used to determine any thermodynamic changes in the test section attributed to $\mathrm{d}P{*}/\mathrm{d}t$ or wave interactions.

The signal for the Kistler 601B1 is routed through a charge amplifier (Kistler 5018A), which enables the sensor to operate over a wide range of pressures (sub-atmospheric–15 ksi) with an uncertainty of 0.18% of the measurement. Additionally, the Kistler 601B1 has a rise time of 2 μs, which is sufficient for the majority of experiments; however, this may be insufficient to capture chemical/physical phenomena with shorter time scales. To make measurements, the Kistler 601B1 uses a quartz sensing element, which are ideally suited for dynamic pressure measurements. As a result, the sensor cannot perform truly static pressure measurements, which, for shock tube experiments, means the initial pressure in the driven section, P_1, must be added to the measured values.

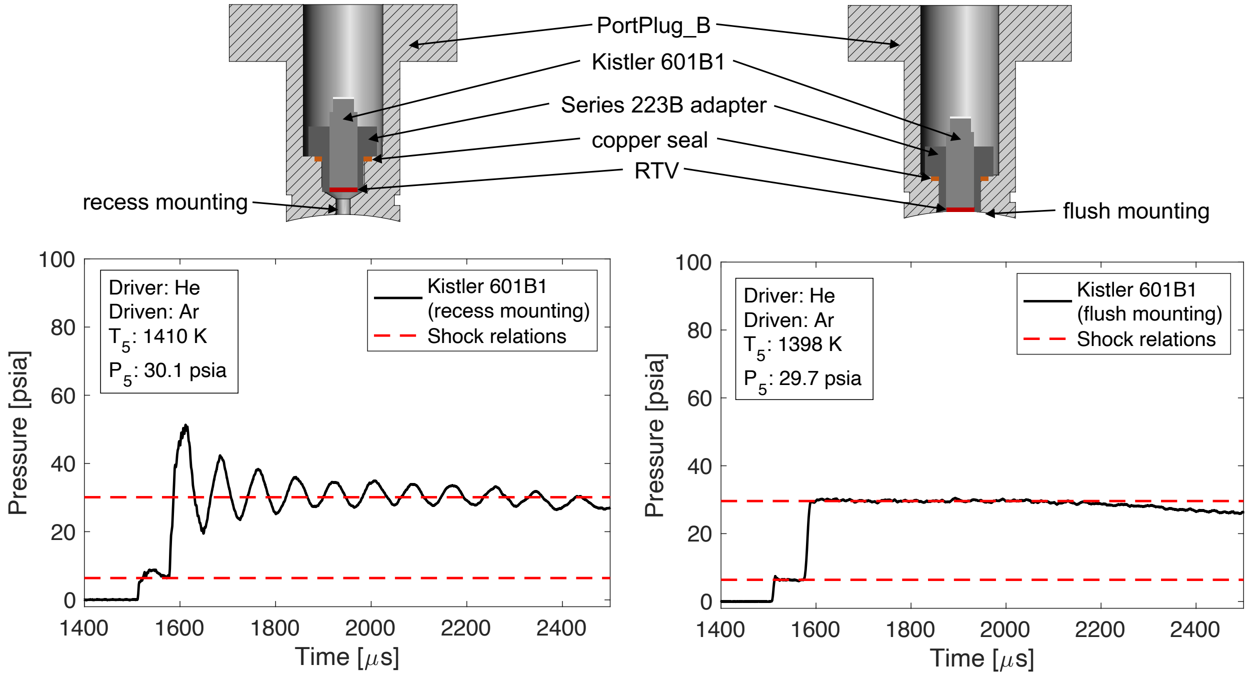

Figure D.14: Representative pressure traces obtained from the Kistler 601B1 sensor demonstrating acoustic resonance when a recess-mounted configuration is used

To protect the sensor from the high temperatures created in the reflected shock region, a layer of room-temperature-vulcanizing (RTV) silicone (Permatex 81160) is added on the diaphragm of the sensor. This is done by mounting the sensor in a Kistler Series 223B Standard Short Adapter, which leaves a recess for the RTV to be added. The sensor assembly (Kistler 601B1 + Series 223B adapter) is then mounted into a shock tube port plug, as shown in Fig. D.14, and the RTV is flush with the shock tube ID. Please note that both RTV application and the port plug mount design can cause artifacts in the measured pressure trace. As a result, the RTV may have to be removed and re-applied more than once. Regarding the port plug mount, the best results were obtained when the sensor assembly was flush with the ID of the shock tube. If an additional recess is created in the port plug, acoustic resonance may occur (organ pipe effect), as seen in Fig. D.14.

D.6.4 Mixture preparation

Gas mixtures for the high-enthalpy shock tube are barometrically prepared in an agitated mixing tank rated up to 1000 psia–the design of which is described in Appendix H. As seen in Fig. D.18, the shock tube manifold provides access to multiple gas sources, two Baratron capacitance manometers (1 torr and 1000 torr), and a high pressure (250 psia) Setra 225G pressure transducer. Using Dalton's law of partial pressures, mixtures containing multiple species can be easily prepared.

$$P_{\mathrm{MT}} = \sum_{i}^{n} P_{\mathrm{MT}} X_i \tag{D.17}$$

Here, P_{MT} is the final mixing tank pressure and X_i is mole fraction of species i. To prepare a mixture, the following steps can be taken–note valve descriptions refer to the P&ID in Fig. D.18:

1. Ensure all valves on the shock tube manifold are closed

2. Isolate the shock tube manifold from the shock tube itself by closing ST1 and ST2

3. Open the Setra 225G using SET1
4. Open the mixing tank ball valve, MT2
5. Slowly open the mixing tank needle valve, MT1–ensuring that the Setra 225G does not over-pressure (250 psia)
6. If mixing tank pressure <250 psia, fully open MT1
7. Vacuum out the shock tube manifold and the mixing tank by fully opening VAC1
8. Once the Setra 225G reads <19 psia, slowly open the 1000 torr Baratron via BAR1
9. Once the 1000 torr Baratron reads <1 torr, slowly open the 1 torr Baratron via BAR2
10. Wait until a desired ultimate vacuum is achieved (typically <5 mtorr)–note, depending on the initial pressure, this step may take several hours
11. Once ultimate vacuum is achieved, close the vacuum and the 1 torr Baratron via VAC1 and BAR2
12. Begin filling (slowly) the mixing tank with the first gas via SG2, SG3, SG4, TG, etc.–this step assumes the gas lines needed for the mixture have been previously vacuumed and pressurized up to the shock tube manifold needle valves. To minimize uncertainty in the mixture preparation, it is often desirable to fill gases in order of lowest concentration to highest.
13. *As a cautionary note*: gas filling should be done slowly. The temperature of the gas will change as its compressed in the mixing tank, which can result in inaccurate partial pressures (mole fractions) once it cools. Additionally, compressed gas cylinders often contain supercritical fluids; therefore, rapid expansions can cause rapid cooling/icing of the fluid lines
14. Once the desired pressure is achieved on the 1000 torr Baratron, close the fill line (SG2, SG3, SG4, TG, etc.)

15. Close the mixing tank ball valve, MT2
16. Vacuum out the shock tube manifold (up to MT2) using VAC1
17. Once the 1000 torr Baratron reads <1 torr, slowly open the 1 torr Baratron via BAR2
18. Once desired ultimate pressure is achieved (typically <5 mtorr), close VAC1 and BAR2
19. With the 1000 torr Baratron open, pressurize the shock tube manifold with the second gas (SG2, SG3, SG4, TG, etc.) at some pressure higher than the current mixing tank pressure–be very careful not to over-pressurize the Baratron
20. Slowly open the mixing tank, MT2
21. Continue to fill the mixing tank with the second gas (SG2, SG3, SG4, TG, etc.)
22. Repeat Steps 14–21 until the desired mixture is achieved

Note it is often desirable to prepare mixtures at pressures no higher than 1000 torr as the Baratron capacitance manometers have a much lower uncertainty than the Setra 225G. Any mixture uncertainty ultimately propagates into uncertainty in the calculated thermodynamic conditions obtained from shock relations (shock speed). Regardless, mixtures at pressures higher than 1000 torr are sometimes needed, in which case, the Setra 225G must be used. To determine the desired mixing tank pressure P_{MT}, it is convenient to calculate either: (1) the number of shocks N_{shocks} the mixing tank volume V_{MT} would yield if filling the shock tube driven section V_{ST} to some pressure P_1 or (2) the minimum mixing tank pressure P_{MT} to fill the driven section volume V_{ST} to some pressure P_1 for a single experiment.

$$N_{\mathrm{shocks}} = \frac{V_{\mathrm{MT}}}{V_{\mathrm{ST}}} \frac{T_1}{T_{\mathrm{MT}}} \left(\frac{P_{\mathrm{MT}}}{P_1} - 1 \right) \tag{D.18}$$

$$P_{\mathrm{MT}} = P_1 \left(\frac{V_{\mathrm{ST}}}{V_{\mathrm{MT}}} \frac{T_{\mathrm{MT}}}{T_1} + 1 \right) \tag{D.19}$$

The volumes for the different shock tube configurations, as well as the mixing tank, are given in Table D.7.

Table D.7: Volumes for the high-enthalpy shock tube configurations and mixing tank

Configuration	Driver [L]	Driven [L]	Mixing Tank [L]
1	13.08	40.81	11.10
2	50.40	40.81	11.10
3	41.14	50.07	11.10

D.6.5 Data acquisition

Depending on the desired sample rates and bandwidths, data on the high-enthalpy shock tube can be recorded on various data acquisition devices. For example, the five time-of-arrival sensors described previously are recorded on a National Instruments (NI) PXI-6133 multifunction I/O module. The PXI-6133 module provides 8 analog input channels with 14-bit resolution and a maximum sample rate of 2.5 MS/s per channel, which was found to be sufficient for capturing shock wave time-of-arrival. The PXI-6133 module is accessed via a NI PXIe-1073 chassis and a NI BNC-2090A rack mount connector. It should be noted that the PXI-6133 module is typically used for conducting differential-type measurements and, as a result, modifications must be made for measuring floating signal sources. A floating signal source is not connected in any way to the building ground system, such as the time-of-arrival sensors, but has an isolated ground-reference point. To conduct these measurements, the ground reference of a floating source signal must be tied to the ground of the data acquisition device to establish a local or on-device reference for the signal. This procedure must be done within the BNC-2090A rack mount connector, which interfaces with the PXI-6133 module. Fig. D.15 shows the onboard components for a differential analog input channel within the BNC-2090A rack mount. To properly ground the time-of-arrival sensors, a 10 MΩ and a 68 kΩ resistor had to be installed into component A (R32) and component B (R31),

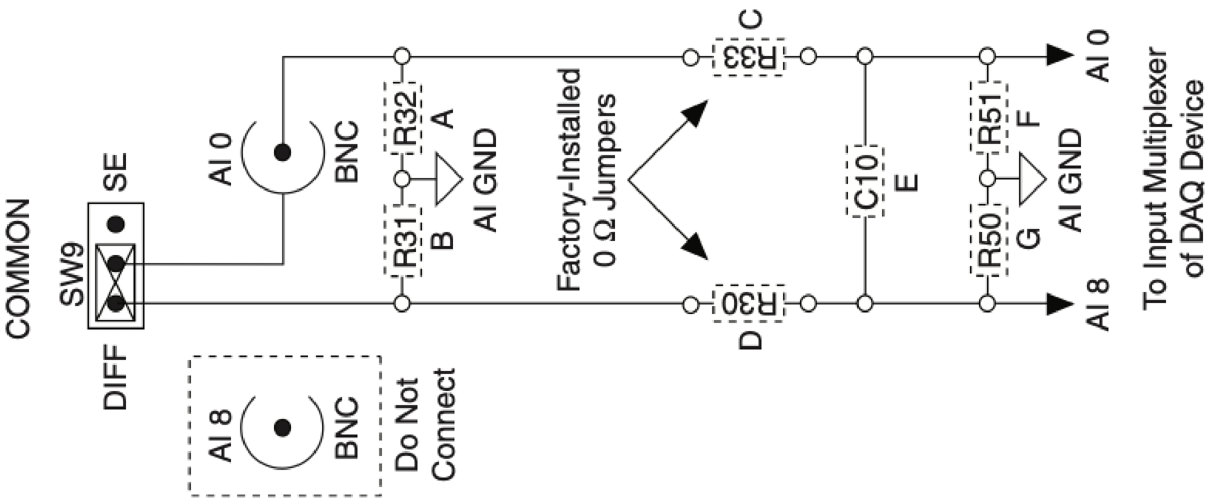

Figure D.15: Differential mode onboard components for analog input channel 0 (AI0)

respectively. These resistor values were found to be adequate enough to properly ground the floating sources, while still providing adequate signal. For example, if the resistance on component A (R32) is too low, the measurement signal will either always read the ground signal (due to being connected to AI GND via component A) or be too low. If the resistance on component A (R32) is too low the floating signal can build a charge and continue to float. The aforementioned procedure was applied to the five analog input channels used for measuring time-of-arrival data.

In addition to the PXI-6133 module, the PXIe-1073 chassis also has a PXI-6115 module, which provides 4 analog inputs with 12-bit resolution and 10 MS/s per channel. Unlike the PXI-6133 module, the PXI-6115 module measures pseudo-differential signals and, therefore, does not have the same issue with floating signal sources described above. When higher sample rates and bandwidths are desired, data is measured using either: (1) a PicoScope 4000 series with 8 analog input channels, a 20 MHz bandwidth, and a maximum samples rate of 80 MS/s, (2) a PicoScope 5000 series with 2 analog input channels, a 200 MHz bandwidth, and a maximum sample rate of 1 GS/s, or (3) a Tektronix 4 Series with 2 analog input channels, a 250 MHz bandwidth, and a maximum sample rate of 6.25 GS/s. Important to note is that as sample rate increases, bit-resolution often decreases; therefore, a trade-off must be made between the two. Additionally, to ensure pressure and optical measurements are in-sync during an experiment, it is desirable to record data using the same acquisition system, if possible. Otherwise, additional steps must be taken to ensure the timing of experimental events (incident shock arrival, reflected shock arrival, test time, etc.) across different data acquisition devices is the same.

D.6.6 Extended test times

As described in Sec. 2.3.5 and Sec. 2.3.6, the use of driver extensions, driver inserts, and driver gas tailoring are commonly used methods for mitigating non-ideal wave interactions and extending reflected shock test times. Combinations of these techniques have been successfully used to obtain test times as long as 25 ms at 640 K on the high-enthalpy shock tube facility, as seen in Fig. 2.15. To determine the driver gas tailoring condition, the following relationship must be satisfied [103]:

$$\frac{\gamma_4 \mathscr{M}_1 T_3}{\gamma_1 \mathscr{M}_4 T_2} = \frac{\left(1+\frac{\gamma_4+1}{\gamma_4-1}\frac{P_5}{P_2}\right)\left(\frac{2\gamma_4}{\gamma_4-1}\right)}{\left(1+\frac{\gamma_1+1}{\gamma_1-1}\frac{P_5}{P_2}\right)\left(\frac{2\gamma_1}{\gamma_1-1}\right)}\left[\frac{\left(\frac{2}{\gamma_1-1}\right)}{\left(\frac{2}{\gamma_4-1}\right)}\right]^2 \tag{D.20}$$

For a given driven gas ($\mathscr{M}_1$, γ_1), initial gas temperatures (T_4 and T_1), and a desired shock strength (P_5/P_2) (i.e. temperature T_5), Eq. D.20 can be satisfied by varying the driver gas composition ($\mathscr{M}_4$, γ_4). This is illustrated in Fig. D.16, which shows the driver gas tailoring condition for He and N_2 mixtures over a range of reflected shock temperatures (T_5). As shown in Fig. D.16, as reflected shock temperature increases, more helium is required in the driver gas composition to satisfy the tailored condition. He and N_2 are commonly used for driver gas mixtures; however, tailoring can be achieved with various gas combinations, as shown by [103]. In practice, driver gas mixtures can either be ordered or made in a mixing tank per the procedure listed in Sec. D.6.4. Achieving tailored conditions becomes more difficult at high temperatures, where the sensitivity to the gas mixture composition increases. As seen in Fig. D.16, as temperature increases, small changes in the driver gas composition

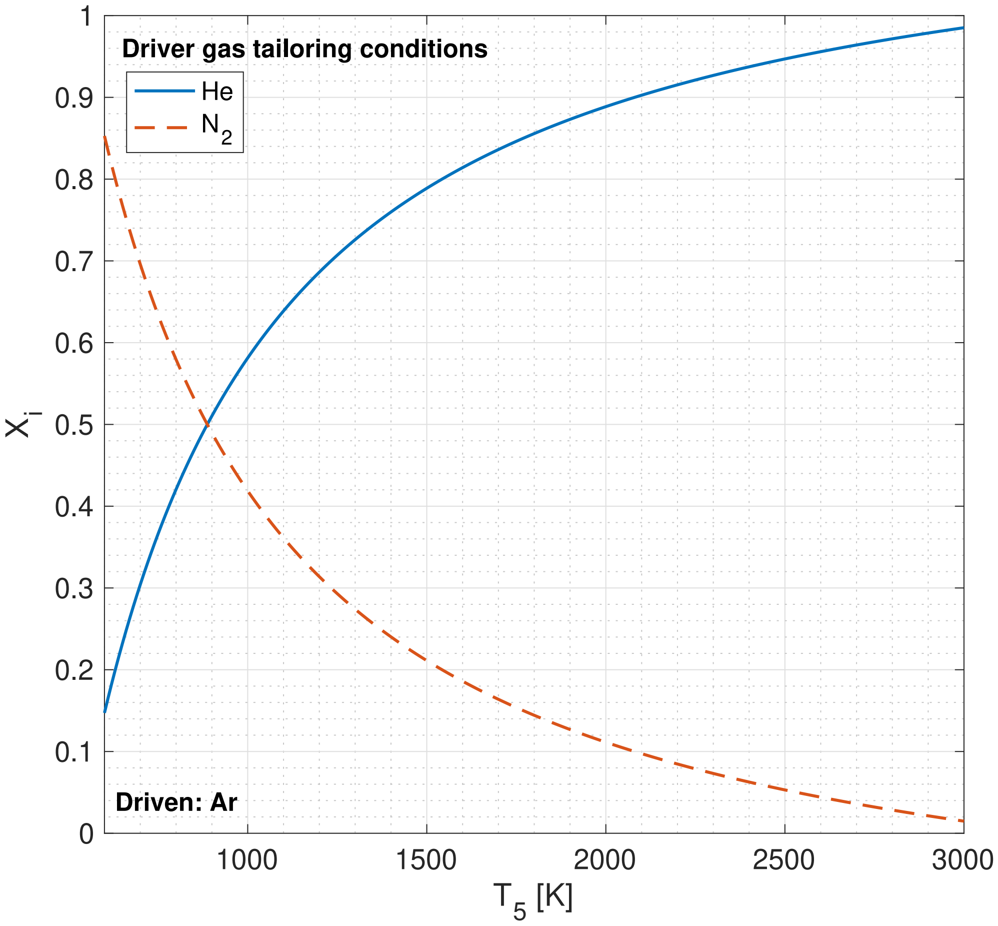

Figure D.16: Driver gas tailoring conditions for He and N_2 driver gas mixtures and Ar as the driven gas

can lead to large changes in the corresponding reflected shock temperature. As a result, it is beneficial to understand how mixtures should be modified. If the reflected shock test time ends due to a pressure increase (shock wave), the molecular weight of the mixture is too high; therefore, more of the lighter gas must be added. If the reflected shock test time ends due to a pressure decrease (expansion wave), the opposite is true and more of the heavy gas must be added. Additionally, from Fig. D.16, it is evident there exist test conditions–namely very low temperatures ($T_5 < 550$ K) and very high temperatures ($T_5 > 3200$ K)–for He/N_2 driver gas combinations where tailoring is not possible. Extending test times at high temperature, where tailoring is not possible, is achieved by extending the driven section, as discussed in Sec. D.1.1. This motivated Configuration 3 of the high-enthalpy shock tube facility.

In addition to using tailored driver gases for extended test times, the high-enthalpy shock tube can be used with variable-area driver inserts to mitigate any non-ideal $\mathrm{d}P_5/\mathrm{d}t$ present in the measured pressure trace. The driver inserts act as area changes and partially reflect expansion waves back towards the test section. The driver inserts used in the high-enthalpy shock tube are considered *positive* inserts and were manufactured out of PVC rods, consisting of multiple 3–6 in. sections of varying diameters from 1–2.5 in., as shown in Fig. D.17. *Negative* inserts involve the use of hollow cylinders, as opposed to rods, to introduce an area change. The inserts in the straight portion of the shock tube are supported by a 1/2 in. threaded rod and additional cross supports (shown in red) to maintain the insert assembly concentric with the tube. The inserts in the U-extension are attached to a nylon rope, which attaches to either of the straight portions via an eye bolt. In using driver inserts, the two main parameters are the location (distance from diaphragm) and size (diameter), which will vary depending on the desired test conditions (T_5, P_5). The insert location will determine how soon the expansion waves are partially reflected back to the test section. The closer the driver inserts are to the diaphragm, the sooner the partially reflected expansion waves are transmitted. As a result, the location should be chosen such that the partially reflected expansion waves arrive at the desired time during the test. The optimum location can be estimated by the use of x-t diagrams using the WiSTL code described in Sec. D.1.1. Producing an x-t diagram with the driver endwall location changed to the location of the first driver insert can be used to estimate the arrival time of the first reflected expansion wave. Typically, as the reflected shock temperature increase, the insert will have to sit closer to the diaphragm. The second parameter that can be modified is the diameter of the insert. A larger diameter insert will reflect more of the expansion wave and cause a larger pressure decrease in the test section. This is desirable when $\mathrm{d}P_5/\mathrm{d}t$ is high, as can happen at higher temperatures and/or pressures. Proper insert configurations for given thermodynamic conditions can be estimated with the help of numerical calculations but are often simply determined through trial and error.

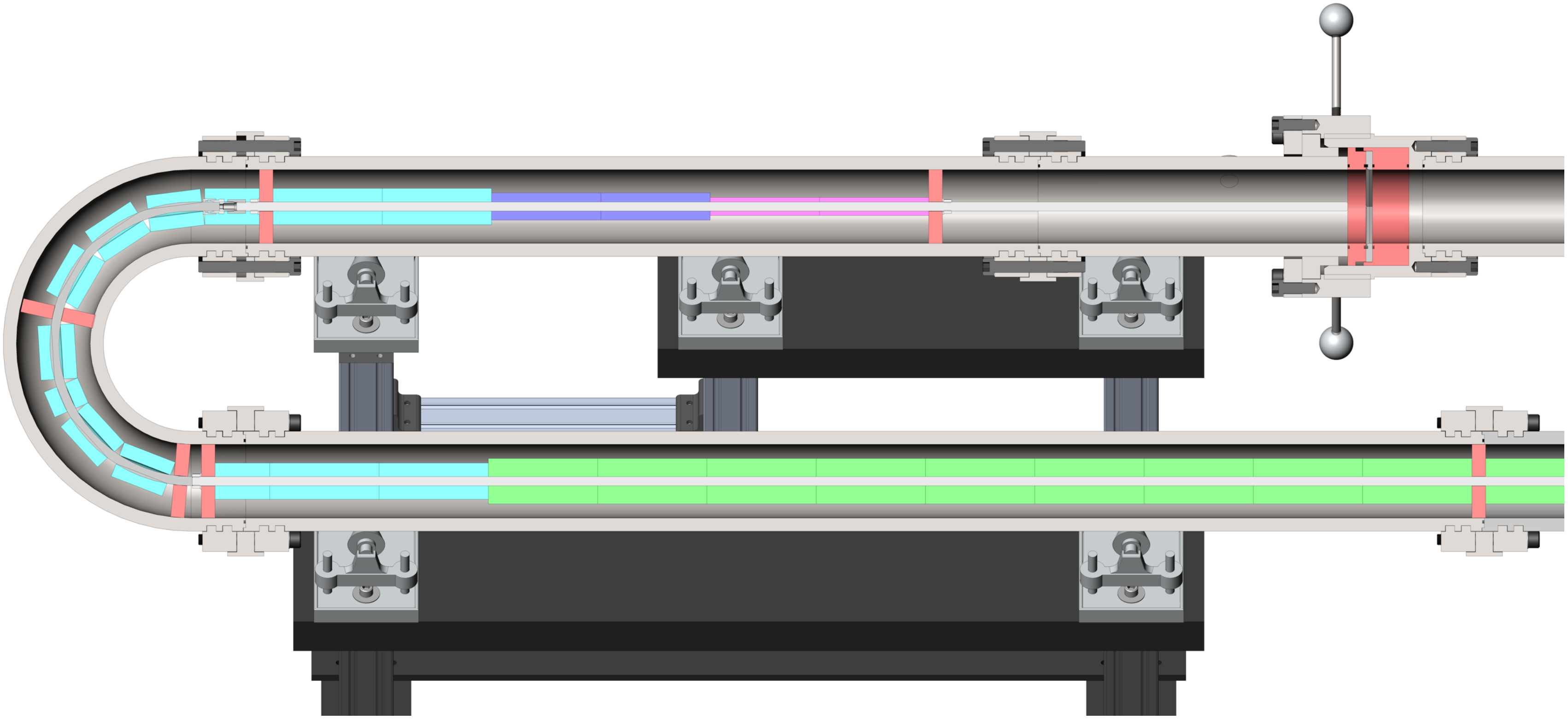

Figure D.17: Driver inserts used on the high-enthalpy shock tube facility to minimize $\mathrm{d}P_5/\mathrm{dt}$ and obtain extended test times

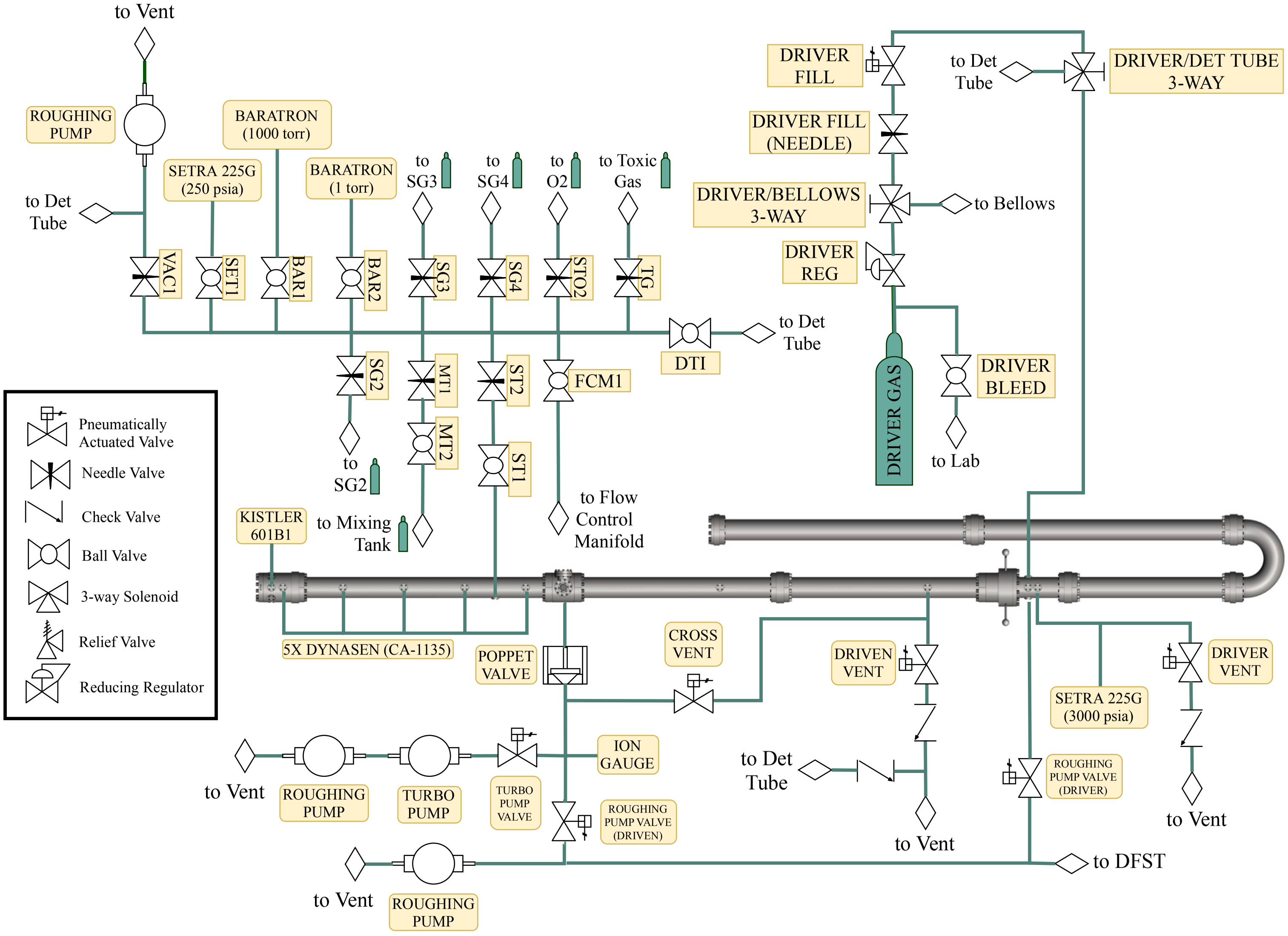

Figure D.18: Piping and instrumentation diagram (P&ID) of the high-enthalpy shock tube facility in the Laser Spectroscopy and Gas Dynamics Laboratory at UCLA.

D.6.7 Piping and instrumentation diagram (P&ID)

The piping and instrumentation diagram for the high-enthalpy shock tube facility is shown in Fig. D.18. Please note hardware/plumbing/instrumentation may have changed since the writing of this dissertation. For the most up-to-date schematic, please contact appropriate personnel in the Laser Spectroscopy and Gas Dynamics Laboratory at UCLA.

D.6.8 Standard operating procedure (SOP)

This section describes the standard operating procedure (SOP) for the high-enthalpy shock tube facility at UCLA. These steps are accurate for the equipment installed on the facility at the time of this writing. In general, new operators should first check with appropriate personnel prior to operating any equipment.

1. Change out diaphragm and close the breech canister
2. Close *Driven Vent* and *Driver Vent*
3. Open *Driven Roughing Pump* and *Driver Roughing Pump*
4. Open *Vacuum* needle valve when driver/driven pressure: ∼0 psia on Setra 225G
5. When vacuum stabilizes, close Vacuum needle valve
6. If **only** using Roughing Pump:
    a. Pump down until ultimate vacuum achieved
    b. Check leak rate:
        i. Close *Poppet Valve*
        ii. Close *Driven Roughing Pump* and *Driver Roughing Pump*
        iii. Observe leak rate on 1 torr Baratron for 2 minutes
    c. Open *Driven Roughing Pump* and *Driver Roughing Pump*
    d. Open *Poppet Valve* and *Vacuum needle valve*
    e. When vacuum stabilizes, close *Vacuum* needle valve

    f. When vacuum stabilizes, **close *Poppet Valve***
    g. Close *Driver Roughing Pump* and *Driven Roughing Pump*

7. If using Roughing Pump and Turbo Pump:
    a. If not already on, start turbo pump using turbo pump controller
    b. Check pressure on 1 torr Baratron and ensure it is $\leq$ 25 mtorr
    c. Close *Driven Roughing Pump*
    d. Open *Turbo Pump* valve
    e. Pump down until ultimate vacuum achieved
    f. Check leak rate:
        i. Close *Turbo Pump* Valve
        ii. Close *Poppet Valve* and *Driver Roughing Pump*
        iii. Observe leak rate on 1 torr Baratron for 2 minutes
    g. if $\leq$ 25 mtorr: open *Driver Roughing Pump*, *Poppet Valve*, and *Turbo Pump* valve
    h. if $\geq$ 25 mtorr: open *Driver Roughing Pump*, *Poppet Valve*, *Driven Roughing Pump*, and *Vacuum* needle valve–**return to *Step 5* without checking leak rate**
    i. When vacuum stabilizes, **close *Poppet Valve***
    j. Close *Turbo Pump* valve and *Driver Roughing Pump*
8. Fill driven section with test gas (*SG2/SG3/SG4/TG2/O2/MT*)–use *Vacuum* needle valve if needed
9. Close *ST1*, *ST2*, and *Baratron/Setra 225G* valves
10. Get DAQ program running and prepare for measurement
11. If using polycarbonate diaphragm:
    a. Make sure high-pressure driver regulator is disengaged

   b. Make sure driver bleed line is closed
   c. Make sure *Driver Fill* needle valve is closed and 3-way *Driver/Bellows* valve is pointing towards *Driver*
   d. Make sure 3-way *Driver/Detonation Tube* valve is pointing towards *Driver*
   e. Fully open driver gas cylinder–the high-pressure driver regulator should now read the cylinder pressure
   f. Engage the regulator and pressurize gas to ∼500 psig above expected burst pressure–**do not exceed 2800 psig**
   g. Make sure *Driver Fill* valve on the panel is open
   h. Open *Driver Fill* needle valve to rupture diaphragm
   i. Close *Driver Fill* needle valve when diaphragm ruptures

12. If using metal diaphragm:
   a. Make sure high-pressure driver regulator is disengaged
   b. Make sure driver bleed line is closed
   c. Make sure *Driver Fill* valve on both the main panel and remote panel is closed
   d. Make sure 3-way *Driver/Bellows* valve is pointing towards *Driver*
   e. Make sure 3-way *Driver/Detonation Tube* valve is pointing towards *Driver*
   f. Fully open driver gas cylinder–the high-pressure driver regulator should now read the cylinder pressure
   g. Fully open *Driver Fill* needle valve
   h. Engage the regulator and pressurize gas to ∼500 psig above expected burst pressure–**do not exceed 2800 psig**
   i. Remotely operate the shock tube from the remote panel and behind the blast shield
   j. Open *Driver Fill* valve on remote panel to rupture diaphragm

k. Close *Driver Fill* valve on remote panel when diaphragm ruptures

l. Open *Driven Vent* and *Driver Vent* on remote panel

m. When shock tube pressure $<$ 100 psia, close *Driven Vent* and *Driver Vent* on remote panel and approach shock tube

13. **If working with inert gases and shock tube pressure >14 psia:**

    a. Open *Driven Vent* and *Driver Vent* on main panel

    b. Open Setra 225G on the shock tube manifold

    c. Open *ST1* and *ST2*

    d. Ensure the Setra 225G on the shock tube manifold and the Setra 225G on the driver section read the same pressure

    e. Once tube is ∼14 psia, open *Breech Canister*

    f. Once tube is physically open to atmosphere, open *Cross Vent* on the main panel

    g. Wait ∼1 minute to equalize pressure behind the poppet valve and then open *Poppet Valve* on main panel

14. **If working with inert gases and shock tube pressure <14 psia:**

    a. Open Setra 225G on the shock tube manifold

    b. Open *ST1* and *ST2*

    c. Ensure the Setra 225G on the shock tube manifold and the Setra 225G on the driver section read the same pressure

    d. Fill tube with inert gas (Ar, N_2, He) via *SG2*/*SG3* until tube pressure ∼15 psia

    e. Open *Driven Vent* and *Driver Vent* on main panel

    f. Once tube is ∼14 psia, open *Breech Canister*

    g. Once tube is physically open to atmosphere, open *Cross Vent* on the main panel

h. Wait ∼1 minute to equalize pressure behind the poppet valve and then open *Poppet Valve* on main panel

15. **If working with toxic gases and shock tube pressure >14 psia:**

    a. Open *Driven Vent* and *Driver Vent* on main panel
    b. Open Setra 225G on the shock tube manifold
    c. Open *ST1* and *ST2*
    d. Ensure the Setra 225G on the shock tube manifold and the Setra 225G on the driver section read the same pressure
    e. Once tube is ∼14 psia, close *Driven Vent* and *Driver Vent* on main panel
    f. Open *Driver Roughing Pump* and *Vacuum* needle valve
    g. Once tube pressure <10 psia, close *Driver Roughing Pump* and *Vacuum* needle valve
    h. Open *Cross Vent* on the main panel
    i. Wait ∼1 minute to equalize pressure behind the poppet valve and then open *Poppet Valve* on main panel
    j. Open *Driver Roughing Pump*, *Driven Roughing Pump*, and *Vacuum* needle valve
    k. Open 1000 torr Baratron
    l. When pressure <1 torr, open 1 torr Baratron
    m. Vacuum tube down until ∼10 mtorr
    n. Close 1 torr Baratron and 1000 torr Baratron
    o. Close *Poppet Valve*, *Driver Roughing Pump*, *Driven Roughing Pump*, and *Vacuum* needle valve
    p. If toxic gas in the shock tube is greater than acceptable, dilute the gas in the tube even further

        - i. Fill tube with inert gas (Ar/He/N_2) via *SG2/SG3* until tube pressure: ∼10 psia
        - ii. Return to Step 15h above
    - q. If toxic gas in the shock tube is sufficiently low, fill tube with inert gas (Ar/He/N_2) via *SG2/SG3* until tube pressure: ∼15 psia
    - r. Open *Driven Vent* and *Driver Vent* on main panel
    - s. Once tube is ∼14 psia, open *Breech Canister*
    - t. Once tube is physically open to atmosphere, open *Cross Vent* on the main panel
    - u. Wait ∼1 minute to equalize pressure behind the poppet valve and then open *Poppet Valve* on main panel

16. **If working with toxic gases and shock tube pressure <14 psia:**
    - a. Open Setra 225G on the shock tube manifold
    - b. Open *ST1* and *ST2*
    - c. Ensure the Setra 225G on the shock tube manifold and the Setra 225G on the driver section read the same pressure
    - d. Open 1000 torr Baratron
    - e. Open *Cross Vent* on the main panel
    - f. Wait ∼1 minute to equalize pressure behind the poppet valve and then open *Poppet Valve* on main panel
    - g. Open *Driver Roughing Pump*, *Driven Roughing Pump*, and *Vacuum* needle valve
    - h. When pressure <1 torr, open 1 torr Baratron
    - i. Vacuum tube down until ∼10 mtorr
    - j. Close 1 torr Baratron and 1000 torr Baratron
    - k. Close *Poppet Valve*, *Driver Roughing Pump*, *Driven Roughing Pump*, and *Vacuum* needle valve

l. If toxic gas in the shock tube is greater than acceptable, dilute the gas in the tube even further
    i. Fill tube with inert gas (Ar/He/N_2) via *SG2/SG3* until tube pressure: ∼10 psia
    ii. Return to Step 16e above

m. If toxic gas in the shock tube is sufficiently low, fill tube with inert gas (Ar/He/N_2) via *SG2/SG3* until tube pressure: ∼15 psia

n. Open *Driven Vent* and *Driver Vent* on main panel

o. Once tube is ∼14 psia, open *Breech Canister*

p. Once tube is physically open to atmosphere, open *Cross Vent* on the main panel

q. Wait ∼1 minute to equalize pressure behind the poppet valve and then open *Poppet Valve* on main panel

Figure D.19: The high-enthalpy shock tube (HEST) facility in the Laser Spectroscopy and Gas Dynamics Laboratory at UCLA - Photograph 1/2

Figure D.20: The high-enthalpy shock tube (HEST) facility in the Laser Spectroscopy and Gas Dynamics Laboratory at UCLA - Photograph 2/2

APPENDIX E

Numerical scripts

This appendix provides some example codes used throughout this dissertation, including MATLAB scripts to solve for the thermodynamic conditions behind incident and reflected shock conditions using a FROzen SHock (FROSH) solver [64], MATLAB scripts to solve for the relaxation matrix W used to model line-mixing effects with the modified-exponential gap law, and a G-code for programming a 3-axis CNC mill used to score metal diaphragms.

E.1 Calculating post-shock thermodynamic conditions

```
clc;
clear;
close all;
format longG;
warning('off','all')
addpath ('../../../MATLAB Library')

%% INPUTS
run = 825; %run number
date = 091520; %date data was taken - used to find folder in directory
Uis = 'actual'; %actual/low/high - Uis = Uis +/- U_measured_std

%Save/Plot/Import
```

```
plot_output = 'yes'; %yes/no - plot output data
save_plot = 'no'; %yes/no - save plots
save_output = 'no'; %yes/no - save output data
import_input = 'no'; %yes/no - import inputs from previous runs

%ToA/Experiment Location
index_toa = [7541 8017 8496 8979 9458]; %if index == 0 then ToA automatically calculated
test_time = [260388 309037];

%Thermodynamic/Gas Conditions
P1 = 29.9; %torr - initial driven pressure
T1 = 296.45; %K - initial driven temperature

species_driven = {'Ar'}; %array of species in driven gas
X_driven = [1.0]; %vector of driven gas mole fractions
soln_method = 'FE'; %specifies EE, FE, or FF solution method
nasa_file = 'sandiaSmall.dat'; %string name of *.dat file containing NASA polynomial coefficients

%DAQ Data
SR_meas = 1E7; %sample rate on PXI 6115
SR_dynasen = 2.5E6; %sample rate on PXI 6133
samples_meas = 1E7; %number of samples on PXI 6115
samples_dynasen = 1.25E4; %number of samples on PXI 6133
pretrigger_dynasen = 20; %number of pretrigger samples on PXI 6133
kistler_scaling = 0.5; %bar/V - scaling on 5018 Charge Amp

```

```
%% CHECK INPUTS
fprintf('Checking Input\n')

if strcmp(import_input,'yes')
    load(sprintf('../../../../../Spearrin Lab Share/Data/HEST/Experimental Data/%06d/Plots/run%d_therm_inputs.mat',date,run), '-regexp', '^(?!()$).')
end

if strcmp(save_output,'yes')
    save(sprintf('../../../../../Spearrin Lab Share/Data/HEST/Experimental Data/%06d/Plots/run%d_therm_inputs.mat',date,run), '-regexp', '^(?!(import_input|post_process|save_output|save_plot|plot_output|Uis|soln_method)$).')
end

%% READING DYNASEN TIME OF ARRIVAL DATA
fprintf('Reading Dynasen Time of Arrival Data\n')

dynasen_meas = dlmread(sprintf('../../../../../Spearrin Lab Share/Data/HEST/Experimental Data/%06d/Raw Data/Dynasen_Measurement_%d.dat',date,run),'\t',0,0); %NI PXIe-1073
testsection_meas = dlmread(sprintf('../../../../../Spearrin Lab Share/Data/HEST/Experimental Data/%06d/Raw Data/TestSection_Measurement_%d.txt',date,run),'\t',7,1); %PicoScope 4000 Series
%testsection_meas = dlmread(sprintf('../../../../../Spearrin Lab Share/Data/HEST/Experimental Data/%06d/Raw Data/Measurement_%d.
```

```
dat',date,run),'\t',0,0); %NI PXIe-1073

dynasen_signal = dynasen_meas - repmat(mean(dynasen_meas(1:2000,:)),size(dynasen_meas,1),1); %background subtraction
kistler_signal = testsection_meas(:,1) - mean(testsection_meas(1:5E5,1)); %200000 background subtraction
kistler_pressure = (kistler_signal*kistler_scaling)/1.01325 + (P1/760); %atm - Kistler pressure

time_total_dynasen= samples_dynasen/SR_dynasen; %s - total measurement time
time_div_dynasen = time_total_dynasen/samples_dynasen; %s - time increment
time_dynasen = (0:time_div_dynasen:time_total_dynasen-time_div_dynasen)'*1000000; %?s - time matrix
samples_total_dynasen = 1:1:samples_dynasen;

time_total_meas = samples_meas/SR_meas; %s - total measurement time
time_div_meas = time_total_meas/samples_meas; %s - time increment
time_meas = (0:time_div_meas:time_total_meas-time_div_meas)'*1000000; %microseconds - time matrix
samples_total_meas = 1:1:samples_meas;

%FFT filter
%[detector_meas, f_meas, y_meas, y2_meas] = fftf(time_meas/1000000, detector_meas);
```

```
%[detector_back, f_back, y_back, y2_back] = fftf(time_meas
    /1000000, detector_back);

%% CALCULATING TIME OF ARRIVAL DATA
fprintf('Calculating Incident Shock Velocity\n')

%Plot Raw Dynasen Shock Traces
if strcmp(plot_output,'yes') || strcmp(save_plot,'yes')
    set(0,'DefaultFigureWindowStyle','docked')
    figure(1)
    plot(samples_total_dynasen, dynasen_signal)
    legend ('Dynasen 1', 'Dynasen 2', 'Dynasen 3', 'Dynasen 4', '
        Dynasen 5', 'Location', 'northwest')
    legend boxoff
    xlabel 'Index No.'
    ylabel 'Differential Voltage, V'
    xlim ([0 length(samples_total_dynasen)])
end

if strcmp(save_plot,'yes')
    savefig(sprintf('../../../../../Spearrin Lab Share/Data/HEST/
        Experimental Data/%06d/Plots/run%d_Figure1_ToA_raw.fig',
        date,run))
end

for i = 1:length(index_toa)
    mfnc = mean(dynasen_signal(1:pretrigger_dynasen,1));
    sfnc = std(dynasen_signal(1:pretrigger_dynasen,1));
```

```
    if index_toa(i) == 0
        index_toa(i) = cusum(dynasen_signal(:,i),10,1,mfnc,sfnc);
    end
    toa(i) = time_dynasen(index_toa(i));
end

length_dynasen = [16 16 16 15.763]; %inches - distance between each Dynasen sensor
Uis_meas = (length_dynasen./diff(toa/1000000))*0.0254; %m/s - incident shock speed - conversion from in/s to m/s
distance_endwall = [59.55 43.55 27.55 11.6685]*25.4; %mm - velocity distance from endwall - conversion from in to mm
U_meas_distance = [16 16 15.8815]; %in - distance travelled between each velocity measurement

%Error Propogation
delta_distance = [1/16 1/16 1/16 1/16]; %in - error in Dynasen locations - conversion from in to mm
delta_t = [3/SR_dynasen 3/SR_dynasen 3/SR_dynasen 3/SR_dynasen]; %s - error in ToA location
delta_U = Uis_meas.*sqrt((delta_distance./length_dynasen).^2 + (delta_t./diff(toa/1000000)).^2); %m/s - error in velocity measurements

[Uis_meas_int, Uis_meas_slope, sigma_int, sigma_slope] = york_fit(distance_endwall,Uis_meas,delta_distance*25.4,delta_U);
distance_fit = linspace(0, 1600);
Uis_fit = Uis_meas_slope*distance_fit + Uis_meas_int;
```

```
Uis_error = (sigma_int/Uis_meas_int)*100;
attenuation = (diff(Uis_meas)./Uis_meas(1:3))./(U_meas_distance*0.0254);
attenuation = mean(attenuation)*100;

if strcmp(Uis,'actual')
    Uis = Uis_fit(1);
elseif strcmp(Uis,'high')
    Uis = Uis_fit(1) + sigma_int;
elseif strcmp(Uis,'low')
    Uis = Uis_fit(1) - sigma_int;
end

%Plot Dynasen Shock Traces
if strcmp(plot_output,'yes') || strcmp(save_plot,'yes')
    figure(2)
    plot(time_dynasen, dynasen_signal)
    hold on
    legend ('Dynasen 1', 'Dynasen 2', 'Dynasen 3', 'Dynasen 4', 'Dynasen 5', 'Location', 'northwest')
    legend boxoff
    xlabel 'Time, \mus'
    ylabel 'Differential Voltage, V'

    %Plot Time of Arrival Locations
    for i = 1:length(index_toa)
        plot(toa(i), dynasen_signal(index_toa(i),i),'*r')
    end
```

```matlab
end

if strcmp(save_plot,'yes')
    savefig(sprintf('../../../../../Spearrin Lab Share/Data/HEST/Experimental Data/%06d/Plots/run%d_Figure2_ToA.fig',date,run))
end

%Plot Incident Shock Velocity Attentuation
if strcmp(plot_output,'yes') || strcmp(save_plot,'yes')
    figure(3)
    Plot_1 = plot(distance_endwall, Uis_meas,'*r');
    hold on
    %herrorbar(distance_endwall,Uis_meas,delta_distance*25.4,'r.')
    errorbar(distance_endwall,Uis_meas,delta_U,'r.')
    Plot_2 = plot(distance_fit,Uis_fit,'b');
    Plot_3 = plot(distance_fit,Uis_fit+sigma_int,'--b');
    plot(distance_fit,Uis_fit-sigma_int,'--b')
    legend ([Plot_1 Plot_2 Plot_3], 'Measured', 'Best Fit','Standard Deviation','Location','northwest')
    legend boxoff
    str = sprintf('Attenuation = %0.2f%%/m \nError at Endwall = %0.2f%%', abs(attenuation), Uis_error);
    annotation('textbox','String',str,'LineStyle','none', 'Position',[.65 .65 0.25 0.25])
    xlabel 'Distance from Endwall, mm'
    ylabel 'Incident Shock Velocity, m/s'
    ylim([Uis-4*sigma_int Uis_meas(1)+4*sigma_int])
```

```
end

if strcmp(save_plot,'yes')
    savefig(sprintf('../../../../../Spearrin Lab Share/Data/HEST/Experimental Data/%06d/Plots/run%d_Figure3_ShockAttenuation.fig',date,run))
end

%% INITIAL COMPUTATIONS
fprintf('Performing Initial Computations\n')

% rename and CAPITALIZE species vector
species_driven = upper(species_driven);
% CAPITALIZE solution method
soln_method = upper(soln_method);
% The velocity of the test gas relative to the shock in region 1 (u1) is
% equal to the incident shock velocity (Uis)
U1 = Uis; % m/s

%% FROSH
fprintf('Running FROSH\n')
[Tout, Pout, rhoOut, gammaOut, VsoundOut, Mout, Urs, phi] = frosh(Uis,P1,T1,species_driven,X_driven,soln_method,nasa_file);

%% ASSEMBLE OUTPUT VECTORS
fprintf('Assembling Output Vectors\n')

```

```
T2 = Tout(1); %temperature in region 5 (K)
T5 = Tout(2); %temperature in region 5 (K)
P2 = Pout(1); %pressure in region 5 (Pa)
P5 = Pout(2); %pressure in region 5 (Pa)
rho1 = rhoOut(1); %density in region 1 (kg/m3)
rho2 = rhoOut(2); %density in region 2 (kg/m3)
rho5 = rhoOut(3); %density in region 5 (kg/m3)
gamma1 = gammaOut(1); %cp5/cv5 in region 1
gamma2 = gammaOut(2); %cp5/cv5 in region 2
gamma5 = gammaOut(3); %cp5/cv5 in region 5
a1 = VsoundOut(1); %speed of sound in region 1 (m/s)
a2 = VsoundOut(2); %speed of sound in region 2 (m/s)
a5 = VsoundOut(3); %speed of sound in region 5 (m/s)
Mis = Mout(1); %Mach number of incident shock
Mrs = Mout(2); %Mach number of reflected shock

% change units
P1 = P1/760; %torr to atm
P2 = P2/101325; %Pa to atm
P5 = P5/101325; %Pa to atm

% output vectors
T = [T1 T2 T5]; % K
P = [P1 P2 P5]; % atm
rho = [rho1 rho2 rho5]; % kg/m3
gamma = [gamma1 gamma2 gamma5];
a = [a1 a2 a5]; % m/s
M = [Mis Mrs]; % m/s
```

```

%% EVALUATION KISTLER 601B1 PRESSURE TRACES
fprintf('Evaluating Kistler 601B1 Pressure Traces\n')

%Plot Kistler Pressure Traces Raw
if strcmp(plot_output,'yes') || strcmp(save_plot,'yes')
    figure(4)
    plot(kistler_pressure,'r')
    legend ('Kistler 601B1','Location','northeast')
    legend boxoff
    ylim([-0.1 max(kistler_pressure)])
    xlabel 'Index No.'
    ylabel 'Pressure, atm'
end

if strcmp(save_plot,'yes')
    savefig(sprintf('../../../../../Spearrin Lab Share/Data/HEST/Experimental Data/%06d/Plots/run%d_Figure4_Kistler_raw.fig',date,run))
end

%Plot Kistler Pressure Traces
if strcmp(plot_output,'yes') || strcmp(save_plot,'yes')
    figure(5)
    plot(time_meas, kistler_pressure,'r')
    hold on
    p = polyfit(time_meas(test_time(1):test_time(2)),kistler_pressure(test_time(1):test_time(2)),1);
```

```
    dPdt = p(1)*time_meas(test_time(1):test_time(2))+p(2);
    plot(time_meas(test_time(1):test_time(2)),dPdt,'k--','LineWidth',1.0)
    plot([min(time_meas) max(time_meas)],[P2 P2],'b--','LineWidth',1.0)
    plot([min(time_meas) max(time_meas)],[P5 P5],'b--','LineWidth',1.0)
    legend ('Kistler 601B1',sprintf('dP/dt = %0.2f%%/ms',100*1000*p(1)/kistler_pressure(test_time(1))),'Simulation','Location','northeast')
    legend boxoff
    ylim([-0.1 max(kistler_pressure)])
    xlabel 'Time, \mus'
    ylabel 'Pressure, atm'
end

if strcmp(save_plot,'yes')
    savefig(sprintf('../../../../../Spearrin Lab Share/Data/HEST/Experimental Data/%06d/Plots/run%d_Figure5_Kistler.fig',date,run))
end

Plot Kistler Pressure Traces with FFT
if strcmp(plot_output,'yes') || strcmp(save_plot,'yes')
    figure(6)
    FFT_Y = fft(kistler_signal);
    FFT_P2 = abs(FFT_Y/samples_meas);
    FFT_P1 = FFT_P2(1:samples_meas/2+1);
```

```
    FFT_P1(2:end-1) = 2*FFT_P1(2:end-1);
    FFT_f = SR_meas*(0:(samples_meas/2))/samples_meas;
    plot(FFT_f/1000,FFT_P1,'r')
    xlim([0 400])
    ylim([0 3E-3])
    xlabel('Signal Frequency (kHz)')
    ylabel('|P1(f)|')
end

if strcmp(save_plot,'yes')
    savefig(sprintf('../../Experimental Data/%06d/Plots/run%d_Figure6_KistlerFFT.fig',date,run))
end

%% SAVE DATA
if strcmp(save_output,'yes')
    save(sprintf('../../../../../Spearrin Lab Share/Data/HEST/Experimental Data/%06d/Post Process/run%d_SimulationTemperature.mat',date,run), 'T')
    save(sprintf('../../../../../Spearrin Lab Share/Data/HEST/Experimental Data/%06d/Post Process/run%d_SimulationPressure.mat',date,run), 'P')
    save(sprintf('../../../../../Spearrin Lab Share/Data/HEST/Experimental Data/%06d/Post Process/run%d_SimulationDensity.mat',date,run), 'rho')
    save(sprintf('../../../../../Spearrin Lab Share/Data/HEST/Experimental Data/%06d/Post Process/run%d_SimulationSpecificHeats.mat',date,run), 'gamma')
```

```
    save(sprintf('../../../../../Spearrin Lab Share/Data/HEST/Experimental Data/%06d/Post Process/run%d_SimulationSpeedOfSound.mat',date,run), 'a')
    save(sprintf('../../../../../Spearrin Lab Share/Data/HEST/Experimental Data/%06d/Post Process/run%d_SimulationMachNo.mat',date,run), 'M')
    save(sprintf('../../../../../Spearrin Lab Share/Data/HEST/Experimental Data/%06d/Post Process/run%d_KistlerPressure.mat',date,run), 'kistler_pressure')
    save(sprintf('../../../../../Spearrin Lab Share/Data/HEST/Experimental Data/%06d/Post Process/run%d_MeasurementTime.mat',date,run), 'time_meas')
end
```

E.2 Modeling spectroscopic line-mixing effects using the modified-exponential gap (MEG) law

```
clc;
clear all;
close all;
format longG;
warning('off','all')
addpath ('../../MATLAB Library')
set(0,'DefaultFigureWindowStyle','docked')
global a4 kv_fit n rho_diag vo_ h c k T E_lower gamma_self_T
    gamma_air_T Pshift_coef vo_diag P dipole v_range_sim X_gas

%% INPUTS
run = 260;
date = 110618;
save_output = 'no';
wn_shift = 0.0;

%Thermodynamic/Gas Conditions
L = 10.32; %cm - pathlength of measurement
MW = 27.994915; %g/mol - molecular weight of gas
X_gas = 1.0; %vector of driven gas mole fractions

%Simulation Inputs
v_start_sim = 4300; %cm-1 - start simulation frequency
v_end_sim = 4310; %cm-1 - end simulation frequency
v_start_meas = 4302.5; %cm-1 - start measurement frequency
v_end_meas = 4306.5; %cm-1 - end measurement frequency
```

```
wing_eval = 10; %cm-1 - wavenumber range of influence
dv = 0.001; %cm-1 - frequency resolution for absorbance

%% IMPORTING SHOCK CONDITIONS FROM hest_therm_solvr
fprintf('Importing Data from hest_therm_solvr\n')
load(sprintf('../../High-Enthalpy Shock Tube/Experimental Data/%06d/Post Process/run%d_IsentropicTemperature.mat',date,run))
load(sprintf('../../High-Enthalpy Shock Tube/Experimental Data/%06d/Post Process/run%d_IsentropicPressure.mat',date,run))
load(sprintf('../../High-Enthalpy Shock Tube/Experimental Data/%06d/Post Process/run%d_absorbance.mat',date,run))
load(sprintf('../../High-Enthalpy Shock Tube/Experimental Data/%06d/Post Process/run%d_wn.mat',date,run))
load(sprintf('../../High-Enthalpy Shock Tube/Experimental Data/%06d/Post Process/run%d_wnShift.mat',date,run))

P = P_isentropic(1)*760; %Torr
T = T_isentropic(1);
wn = v_detector + v_center + wn_shift;

%Constants
h = 6.626068e-34; %Planck's Constant in m^2*kg/s
k = 1.3806504e-23; %Boltzmann's Constant (J/K)
c = 2.99792458e10; %Speed of Light (cm/s)

T0 = 296;
fid = fopen('CO_HITEMP2010_spaced.par');
data1 = textscan(fid,'%f%f%f%f%f%f%f%f%f%f%f%f%s%f %*[^\n]'); %
```

```
    Read in first 9 columns of HITRAN file
fclose(fid);

fid = fopen('CO_HITEMP2010_degeneracy_upper.txt');
data2 = textscan(fid,'%f%*[^\n]'); % Read in first 9 columns of
    HITRAN file
fclose(fid);

fid = fopen('CO_HITEMP2010_degeneracy_lower.txt');
data3 = textscan(fid,'%f%*[^\n]'); % Read in first 9 columns of
    HITRAN file
fclose(fid);

vo_vect = data1{3};
S_vect = data1{4};
A_vect = data1{5};
gamma_air_vect = data1{6};
gamma_self_vect = data1{7};
E_lower_vect = data1{8};
n_air_vect = data1{9};
Pshift_vect = data1{10};
g_upper_vect = data2{1}; % upper state degeneracy
g_lower_vect = data3{1}; % lower state degeneracy
J_lower_vect = data1{14};
v_upper_vect = data1{11};
isotope_vect_1 = data1{1};
isotope_vect_2 = data1{2};
isotope_vect = str2num(strcat(num2str(isotope_vect_1),num2str(
```

```
    isotope_vect_2)));

% specify self-broadening temperature coefficient (not in HITRAN file)
n_self_vect = 0.5 .* ones(length(vo_vect),1);
m_shift_vect = 1.1 .* ones(length(vo_vect),1);

%Truncate the HITRAN data over the wavenumber range of interest
v_range_sim = [v_start_sim:dv:v_end_sim].';
v_range_meas = [v_start_meas:dv:v_end_meas].';
line_start_v = v_start_sim;
line_end_v = v_end_sim;
minIndex = min(find(vo_vect >= line_start_v));
maxIndex = find(vo_vect <= line_end_v, 1, 'last');

% Truncate data to range of interest
vo_ = vo_vect(minIndex:maxIndex);
S_ref = S_vect(minIndex:maxIndex);
A_coeff = A_vect(minIndex:maxIndex);
gamma_air = gamma_air_vect(minIndex:maxIndex);
gamma_self = gamma_self_vect(minIndex:maxIndex);
E_lower = E_lower_vect(minIndex:maxIndex);
E_upper = E_lower + vo_;
n_air = n_air_vect(minIndex:maxIndex);
Pshift = Pshift_vect(minIndex:maxIndex);
n_self = n_self_vect(minIndex:maxIndex);
m_shift = m_shift_vect(minIndex:maxIndex);
g_lower = g_lower_vect(minIndex:maxIndex);
```

```
g_upper = g_upper_vect(minIndex:maxIndex);
J_lower = J_lower_vect(minIndex:maxIndex);
v_upper = v_upper_vect(minIndex:maxIndex);
isotope = isotope_vect(minIndex:maxIndex);

for i = 1:length(vo_)
    if isotope(i) == 51 && v_upper(i) == 3 && J_lower(i) == 42
        gamma_self(i) = 0.01708;
        n_self(i) = 0.521;
        gamma_air(i) = 0.01236;
        n_air(i) = 0.485;
    elseif isotope(i) == 51 && v_upper(i) == 3 && J_lower(i) == 43
        gamma_self(i) = 0.01675;
        n_self(i) = 0.500;
        gamma_air(i) = 0.01205;
        n_air(i) = 0.455;
    elseif isotope(i) == 51 && v_upper(i) == 3 && J_lower(i) == 44
        gamma_self(i) = 0.01645;
        n_self(i) = 0.480;
        gamma_air(i) = 0.01209;
        n_air(i) = 0.478;
    elseif isotope(i) == 51 && v_upper(i) == 3 && J_lower(i) == 45
        gamma_self(i) = 0.01640;
        n_self(i) = 0.488;
        gamma_air(i) = 0.01155;
        n_air(i) = 0.425;
    elseif isotope(i) == 51 && v_upper(i) == 3 && J_lower(i) == 46
        gamma_self(i) = 0.01622;
```

```
        n_self(i) = 0.497;
        gamma_air(i) = 0.01157;
        n_air(i) = 0.455;
    elseif isotope(i) == 51 && v_upper(i) == 3 && J_lower(i) == 47
        gamma_self(i) = 0.01631;
        n_self(i) = 0.501;
        gamma_air(i) = 0.01137;
        n_air(i) = 0.429;
    elseif isotope(i) == 51 && v_upper(i) == 3 && J_lower(i) == 48
        gamma_self(i) = 0.01572;
        n_self(i) = 0.465;
        gamma_air(i) = 0.01126;
        n_air(i) = 0.429;
    elseif isotope(i) == 51 && v_upper(i) == 3 && J_lower(i) == 49
        gamma_self(i) = 0.01551;
        n_self(i) = 0.456;
        gamma_air(i) = 0.01110;
        n_air(i) = 0.422;
    elseif isotope(i) == 51 && v_upper(i) == 3 && J_lower(i) == 50
        gamma_self(i) = 0.01530;
        n_self(i) = 0.448;
        gamma_air(i) = 0.01094;
        n_air(i) = 0.414;
    elseif isotope(i) == 51 && v_upper(i) == 3 && J_lower(i) == 51
        gamma_self(i) = 0.01509;
        n_self(i) = 0.439;
        gamma_air(i) = 0.01078;
        n_air(i) = 0.406;
```

```
    elseif isotope(i) == 51 && v_upper(i) == 3 && J_lower(i) == 52
        gamma_self(i) = 0.01489;
        n_self(i) = 0.431;
        gamma_air(i) = 0.01062;
        n_air(i) = 0.398;
    elseif isotope(i) == 51 && v_upper(i) == 3 && J_lower(i) == 53
        gamma_self(i) = 0.01453;
        n_self(i) = 0.431;
        gamma_air(i) = 0.01047;
        n_air(i) = 0.390;
    elseif isotope(i) == 51 && v_upper(i) == 3 && J_lower(i) == 54
        gamma_self(i) = 0.01438;
        n_self(i) = 0.383;
        gamma_air(i) = 0.01029;
        n_air(i) = 0.401;
    elseif isotope(i) == 51 && v_upper(i) == 3 && J_lower(i) == 55
        gamma_self(i) = 0.01428;
        n_self(i) = 0.401;
        gamma_air(i) = 0.01025;
        n_air(i) = 0.393;
    elseif isotope(i) == 51 && v_upper(i) == 3 && J_lower(i) == 56
        gamma_self(i) = 0.01398;
        n_self(i) = 0.372;
        gamma_air(i) = 0.01018;
        n_air(i) = 0.379;
    elseif isotope(i) == 51 && v_upper(i) == 3 && J_lower(i) == 57
        gamma_self(i) = 0.01391;
        n_self(i) = 0.389;
```

```
            gamma_air(i) = 0.00988;
            n_air(i) = 0.359;
        elseif isotope(i) == 51 && v_upper(i) == 3 && J_lower(i) == 58
            gamma_self(i) = 0.01353;
            n_self(i) = 0.382;
            gamma_air(i) = 0.01000;
            n_air(i) = 0.355;
        end
end

% Remove isotope transition
index_remove = find(isotope ~= 51 | v_upper ~= 3);
vo_(index_remove) = [];
S_ref(index_remove) = [];
A_coeff(index_remove) = [];
gamma_air(index_remove) = [];
gamma_self(index_remove) = [];
E_lower(index_remove) = [];
E_upper(index_remove) = [];
n_air(index_remove) = [];
Pshift(index_remove) = [];
n_self(index_remove) = [];
m_shift(index_remove) = [];
g_lower(index_remove) = [];
g_upper(index_remove) = [];
J_lower(index_remove) = [];
v_upper(index_remove) = [];
isotope(index_remove) = [];
```

```

% Sort to increasing J"
J_lower_temp = sort(J_lower);
for i = 1:length(J_lower_temp)
    index = find(J_lower == J_lower_temp(i));
    vo_temp(i) = vo_(index);
    S_ref_temp(i) = S_ref(index);
    A_coeff_temp(i) = A_coeff(index);
    gamma_air_temp(i) = gamma_air(index);
    gamma_self_temp(i) = gamma_self(index);
    E_lower_temp(i) = E_lower(index);
    E_upper_temp(i) = E_upper(index);
    n_air_temp(i) = n_air(index);
    Pshift_temp(i) = Pshift(index);
    n_self_temp(i) = n_self(index);
    m_shift_temp(i) = m_shift(index);
    g_lower_temp(i) = g_lower(index);
    g_upper_temp(i) = g_upper(index);
    v_upper_temp(i) = v_upper(index);
    isotope_temp(i) = isotope(index);
end

vo_ = vo_temp';
S_ref = S_ref_temp';
A_coeff = A_coeff_temp';
gamma_air = gamma_air_temp';
gamma_self = gamma_self_temp';
E_lower = E_lower_temp';
```

```
E_upper = E_upper_temp';
n_air = n_air_temp';
Pshift = Pshift_temp';
n_self = n_self_temp';
m_shift = m_shift_temp';
g_lower = g_lower_temp';
g_upper = g_upper_temp';
J_lower = J_lower_temp;
v_upper = v_upper_temp';
isotope = isotope_temp';

% Get partition functions for CO at specified T, HITRAN 2008
Q_T = Q_CO(T);       % Partition function at T
Q_To = Q_CO(T0);     % Partition function at To
Q_ratio = Q_To/Q_T;

% Calculate temperature dependent HITRAN parameters for each line
for i = 1:length(vo_)
    dvo = Pshift(i)*(P/760)*(1-X_gas)*(T0/T)^m_shift(i); % Pressure shift [cm-1]
    Pshift_coef(i) = Pshift(i)*(T0/T)^m_shift(i); % Pressure shift coefficient
    vo(i) = vo_(i) + dvo; % New Linecenter [cm-1]
    [~,S_T(i)] = linestrength_Qrat(S_ref(i),E_lower(i),T,vo(i),Q_ratio); % Linestrength [cm-2/atm]

    if isotope(i) == 51 && v_upper(i) == 3 && J_lower(i) == 42
        gamma_self_T(i) = gamma_self(i)*(1500/T)^n_self(i); % Self
```

```
-broadening coefficient at T
        gamma_air_T(i) = gamma_air(i)*(1500/T)^n_air(i); % Air-broadening coefficient at T
    elseif isotope(i) == 51 && v_upper(i) == 3 && J_lower(i) == 43
        gamma_self_T(i) = gamma_self(i)*(1500/T)^n_self(i); % Self-broadening coefficient at T
        gamma_air_T(i) = gamma_air(i)*(1500/T)^n_air(i); % Air-broadening coefficient at T
    elseif isotope(i) == 51 && v_upper(i) == 3 && J_lower(i) == 44
        gamma_self_T(i) = gamma_self(i)*(1500/T)^n_self(i); % Self-broadening coefficient at T
        gamma_air_T(i) = gamma_air(i)*(1500/T)^n_air(i); % Air-broadening coefficient at T
    elseif isotope(i) == 51 && v_upper(i) == 3 && J_lower(i) == 45
        gamma_self_T(i) = gamma_self(i)*(1500/T)^n_self(i); % Self-broadening coefficient at T
        gamma_air_T(i) = gamma_air(i)*(1500/T)^n_air(i); % Air-broadening coefficient at T
    elseif isotope(i) == 51 && v_upper(i) == 3 && J_lower(i) == 46
        gamma_self_T(i) = gamma_self(i)*(1500/T)^n_self(i); % Self-broadening coefficient at T
        gamma_air_T(i) = gamma_air(i)*(1500/T)^n_air(i); % Air-broadening coefficient at T
    elseif isotope(i) == 51 && v_upper(i) == 3 && J_lower(i) == 47
        gamma_self_T(i) = gamma_self(i)*(1500/T)^n_self(i); % Self-broadening coefficient at T
        gamma_air_T(i) = gamma_air(i)*(1500/T)^n_air(i); % Air-broadening coefficient at T
```

```
    elseif isotope(i) == 51 && v_upper(i) == 3 && J_lower(i) == 48
        gamma_self_T(i) = gamma_self(i)*(1500/T)^n_self(i); % Self-broadening coefficient at T
        gamma_air_T(i) = gamma_air(i)*(1500/T)^n_air(i); % Air-broadening coefficient at T
    elseif isotope(i) == 51 && v_upper(i) == 3 && J_lower(i) == 49
        gamma_self_T(i) = gamma_self(i)*(1500/T)^n_self(i); % Self-broadening coefficient at T
        gamma_air_T(i) = gamma_air(i)*(1500/T)^n_air(i); % Air-broadening coefficient at T
    elseif isotope(i) == 51 && v_upper(i) == 3 && J_lower(i) == 50
        gamma_self_T(i) = gamma_self(i)*(1500/T)^n_self(i); % Self-broadening coefficient at T
        gamma_air_T(i) = gamma_air(i)*(1500/T)^n_air(i); % Air-broadening coefficient at T
    elseif isotope(i) == 51 && v_upper(i) == 3 && J_lower(i) == 51
        gamma_self_T(i) = gamma_self(i)*(1500/T)^n_self(i); % Self-broadening coefficient at T
        gamma_air_T(i) = gamma_air(i)*(1500/T)^n_air(i); % Air-broadening coefficient at T
    elseif isotope(i) == 51 && v_upper(i) == 3 && J_lower(i) == 52
        gamma_self_T(i) = gamma_self(i)*(1500/T)^n_self(i); % Self-broadening coefficient at T
        gamma_air_T(i) = gamma_air(i)*(1500/T)^n_air(i); % Air-broadening coefficient at T
    elseif isotope(i) == 51 && v_upper(i) == 3 && J_lower(i) == 53
        gamma_self_T(i) = gamma_self(i)*(1500/T)^n_self(i); % Self-broadening coefficient at T
```

```
            gamma_air_T(i) = gamma_air(i)*(1500/T)^n_air(i); % Air-
                broadening coefficient at T
        elseif isotope(i) == 51 && v_upper(i) == 3 && J_lower(i) == 54
            gamma_self_T(i) = gamma_self(i)*(1500/T)^n_self(i); % Self
                -broadening coefficient at T
            gamma_air_T(i) = gamma_air(i)*(1500/T)^n_air(i); % Air-
                broadening coefficient at T
        elseif isotope(i) == 51 && v_upper(i) == 3 && J_lower(i) == 55
            gamma_self_T(i) = gamma_self(i)*(1500/T)^n_self(i); % Self
                -broadening coefficient at T
            gamma_air_T(i) = gamma_air(i)*(1500/T)^n_air(i); % Air-
                broadening coefficient at T
        elseif isotope(i) == 51 && v_upper(i) == 3 && J_lower(i) == 56
            gamma_self_T(i) = gamma_self(i)*(1500/T)^n_self(i); % Self
                -broadening coefficient at T
            gamma_air_T(i) = gamma_air(i)*(1500/T)^n_air(i); % Air-
                broadening coefficient at T
        elseif isotope(i) == 51 && v_upper(i) == 3 && J_lower(i) == 57
            gamma_self_T(i) = gamma_self(i)*(1500/T)^n_self(i); % Self
                -broadening coefficient at T
            gamma_air_T(i) = gamma_air(i)*(1500/T)^n_air(i); % Air-
                broadening coefficient at T
        elseif isotope(i) == 51 && v_upper(i) == 3 && J_lower(i) == 58
            gamma_self_T(i) = gamma_self(i)*(1500/T)^n_self(i); % Self
                -broadening coefficient at T
            gamma_air_T(i) = gamma_air(i)*(1500/T)^n_air(i); % Air-
                broadening coefficient at T
        else
```

```
        gamma_self_T(i) = gamma_self(i)*(T0/T)^n_self(i); % Self-broadening coefficient at T
        gamma_air_T(i) = gamma_air(i)*(T0/T)^n_air(i); % Air-broadening coefficient at T
    end
end

%% SUBTRACT ABSORPTION THAT DOES NOT BELONG TO 1->3
absorbance_meas  = interp1(wn,absorbance_meas,v_range_meas);

[wn_adj, absorbance_adj] = spectraplot_CO_MEGlm_adj(T,P,X_gas,MW,L,v_start_sim,v_end_sim,wing_eval,dv);
v_start_adj = find(wn_adj == v_start_meas);
v_end_adj = find(wn_adj == v_end_meas);
absorbance_meas = absorbance_meas - absorbance_adj(v_start_adj:v_end_adj)';
kv_meas = absorbance_meas/L;

%% Line Mixing Model
n = ((X_gas*(P/760)*101325)/(k*T))/1E6; %molec/cm^3 - number density
rho = g_lower.*exp(-(h*c/k)*E_lower/T)/Q_T; %ni/n - Boltzmann population fraction
dipole = sqrt(S_T'./rho);%[cm^2/molec*cm]^1/2 - dipole moment

rho_diag = diag(rho);
vo_diag = diag(vo_);

```

```
%% GUESS VALUES FOR COEFFICIENTS
a1_guess = 0.0001;
a2_guess = 0.3;
a3_guess = 5.0;
a4 = 2;

%% SOLVE FOR COEFFICIENTS USING NONLINEAR FIT
Free_Parameters = [a1_guess a2_guess a3_guess];
lower_bound = [1E-6 1E-6 1E-6];
upper_bound = [20 20 20];

%options = optimoptions('lsqcurvefit','FinDiffType','central');
v_range_fit = v_range_meas;
[fit,resnorm,residual,exitflag,output,lambda,jacobian] =
    lsqcurvefit(@MEG_fit,Free_Parameters,v_range_meas,kv_meas,
    lower_bound,upper_bound);
fit_error = nlparci(fit,residual,'jacobian',jacobian);
fit_error = fit_error(:,2) - fit';

a1 = fit(1);
a2 = fit(2);
a3 = fit(3);

fprintf('a1: %d\n',a1)
fprintf('a2: %d\n',a2)
fprintf('a3: %d\n',a3)

if strcmp(save_output,'yes')
```

```
    save(sprintf('../../High-Enthalpy Shock Tube/Experimental Data/%06d/Post Process/run%d_MEGCoefficients_REV003.mat',date,run),'fit')
    save(sprintf('../../High-Enthalpy Shock Tube/Experimental Data/%06d/Post Process/run%d_MEGCoefficients_Error_REV003.mat',date,run),'fit_error')
end

%% PLOT MEASUREMENTS VS. SIMULATION
figure
hold on
plot(v_range_meas,kv_meas*L,'k','LineWidth',2)
plot(v_range_fit,kv_fit*L,'--r','LineWidth',2)
legend('Measurement','MEG Model')
title(sprintf('T: %0.0f K, P: %0.1f bar',T,P/760))
xlabel('Wavenumber, cm^{-1}')
ylabel('Absorbance')

%% PLOT MEASUREMENTS VS. SIMULATION W/ UPDATED COEFFICIENTS
[wn_adj, absorbance_adj] = spectraplot_CO_MEGlm_adj(T,P,X_gas,MW,L,v_start_sim,v_end_sim,wing_eval,dv);
v_start_adj = find(wn_adj == v_start_meas);
v_end_adj = find(wn_adj == v_end_meas);
absorbance_meas = absorbance_meas + absorbance_adj(v_start_adj:v_end_adj)';
[~, absorbance_lm] = spectraplot_CO_MEGlm(T,P,X_gas,MW,L,v_start_sim,v_end_sim,wing_eval,dv,a1_self,a2_self,a3_self,a4,m_self,a1,a2,a3);
```

```
[~, absorbance_HITEMP] = spectraplot_CO(T,P,X_gas,MW,L,v_start_sim,v_end_sim,wing_eval,dv);

figure
subplot(2,1,1)
hold on
plot(v_range_meas,absorbance_meas,'k','LineWidth',1.5)
plot(v_range_sim,absorbance_HITEMP,'-.g','LineWidth',1.5)
plot(v_range_sim,absorbance_lm,'--r','LineWidth',1.5)
legend('Measurement','HITEMP','MEG Model')
title(sprintf('T: %0.0f K, P: %0.1f bar',T,P/760))
xlim([v_start_meas v_end_meas])
xlabel('Wavenumber, cm^{-1}')
ylabel('Absorbance')

subplot(2,1,2)
plot(v_range_meas,100*(absorbance_meas - interp1(v_range_sim,absorbance_lm,v_range_meas))/max(absorbance_meas),'-r','LineWidth',0.5);
xlim([v_start_meas v_end_meas])
xlabel('Wavenumber, cm^{-1}')
ylabel('Residual [%]')
```

```
function [kv_fit] = MEG_fit(a,v_range_meas)
global a4 kv_fit n rho_diag vo_ h c k T E_lower gamma_self_T gamma_air_T Pshift_coef vo_diag P dipole v_range_sim X_gas

for i = 1:length(vo_)
    for j = 1:length(vo_)
```

```
        if j > i
            R_self(i,j) = -((a(1)*(T_ref/T)^m_self)*((1+a4*(h*c*E_lower(i)/(a(2)*k*T)))/(1+a4*(h*c*E_lower(i)/(k*T))))^2 * exp(-a(3)*(h*c*(E_lower(j)-E_lower(i)))/(k*T)));
            R_self(j,i) = rho_diag(i,i)/rho_diag(j,j)*R_self(i,j);
        elseif i == j
            R_self(i,j) = 0;
        end
    end
end

%for i = 1:length(vo_)
%    for j = 1:length(vo_)
%        if j > i
%            R_air(i,j) = -(a(1)*((1+a4*(h*c*E_lower(i)/(a(2)*k*T)))/(1+a4*(h*c*E_lower(i)/(k*T))))^2 * exp(-a(3)*(h*c*(E_lower(j)-E_lower(i)))/(k*T)));
%            R_air(j,i) = rho_diag(i,i)/rho_diag(j,j)*R_air(i,j);
%        elseif i == j
%            R_air(i,j) = 0;
%        end
%    end
%end

%% CONSTRUCT RELAXATION MATRIX
W_real_self = diag(gamma_self_T) + R_self;
W_imag_self = 1i*diag(Pshift_coef);
```

```
W_self = W_real_self + W_imag_self;

%W_real_air = diag(gamma_air_T) + R_air;
%W_imag_air = 1i*diag(Pshift_coef);
%W_air = W_real_air + W_imag_air;

W = X_gas*W_self;% + (1-X_gas)*W_air;

H = vo_diag + 1i*P/760*W;
[A, Ohm] = eig(H);
A_inv = inv(A);
wi = diag(Ohm);

b1 = dipole'*A;
b2 = A_inv*rho_diag*dipole;

for i = 1:length(v_range_sim)
    for j = 1:length(wi)
        kv_sum(j) = (b1(j)*b2(j))/(v_range_sim(i)-wi(j));
    end
    kv_fit(i,1) = n/pi*imag(sum(kv_sum));
end

v_start_fit = find(v_range_sim == v_range_meas(1));
v_end_fit = find(v_range_sim == v_range_meas(end));

kv_fit = kv_fit(v_start_fit:v_end_fit);
```

E.3 G-code for scoring metal diaphragms

This code is used to program a HAAS TM-2P 3-axis CNC mill for scoring metal diaphragms. The specific code included herein is for a score depth of 0.025 in. on an aluminum diaphragm. Please note, the origin should be placed at the center of the diaphragm with the top face being $Z = 0$ and the tool should be placed in slot 2 of the carousel.

```
O1000 (DIAPHRAGMSCORE_CNC)
N100 (COMPENSATION-WEAR)
N102 (REV-0.70)
N104 (OCT-15-2018-12:38:11PM)

N106 (TOOL 2 - DIA 0.375)

N1 G90 G17 G40 G80 G00
N108 M06 T2 ()
N110 (F-contour1)
N112 G00 G54 G90 X-2.0315 Y0. S2000 M03
N114 G43 H2 Z0.2
N116 Z0.04
N118 G01 Z-0.025 F2.
N120 X2.0315 F6.
N122 G00 Z2.
N124 X0. Y-2.0315
N126 G01 Z-0.025 F2.
N128 Y2.0315 F6.
N130 G00 Z0.04
N132 M05
N134 G00 G28 G91 Z0
```

```
N136 G00 G28 G91 Y0.
N138 G90
N140 M06 T2
N142 M30
```

APPENDIX F

High-enthalpy shock tube drawing package

University of California, Los Angeles
Laser Spectroscopy & Gas Dynamics Lab
High Enthalpy Shock Tube Facility (HEST)

Point of Contact:
Fabio Bendana
e: fbendana@ucla.edu
c: 650-255-8224

Package Contents:
Pages 1-7: Assembly drawings (to be used for reference only)
Page 8: Bill of Materials (Parts/Quantities interested in quoting)
Pages 9-39: Part Drawings
Pages 40-44: Reference Drawings

UCLA Configuration 1:
Driver Length: 5.13ft
Driven Length: 16.00ft

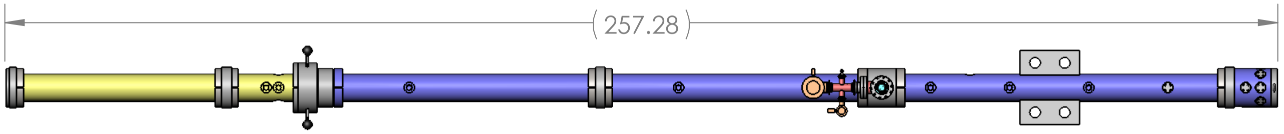

UCLA Configuration 2: Extended Test Times
Driver Length: 10+ ft
Driven Length: 16.00ft

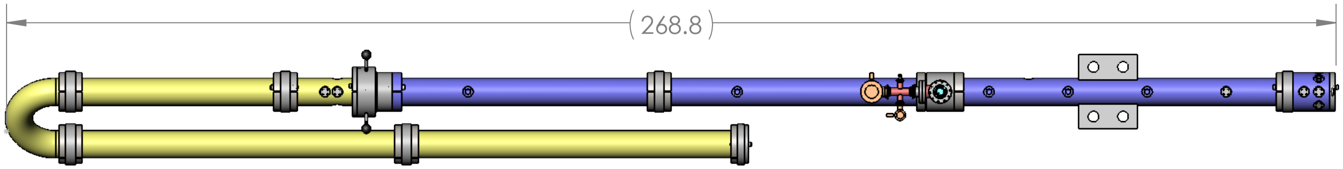

		UNLESS OTHERWISE SPECIFIED:		NAME	DATE	UCLA: Laser Spectroscopy & Gas Dynamics Lab
		DIMENSIONS ARE IN INCHES TOLERANCES: FRACTIONAL ± ANGULAR: MACH ± BEND ± TWO PLACE DECIMAL ± THREE PLACE DECIMAL ±	DRAWN	F. BENDANA	2/10/17	TITLE: HEST CONFIGURATIONS
			CHECKED			
			ENG APPR.			
			MFG APPR.			
		INTERPRET GEOMETRIC TOLERANCING PER:	Q.A.			
		MATERIAL 304 SS	COMMENTS:			SIZE A · DWG. NO. · REV 002
NEXT ASSY	USED ON	FINISH				
APPLICATION		DO NOT SCALE DRAWING				SCALE: 1:30 · SHEET 1 OF 7

PROPRIETARY AND CONFIDENTIAL
THE INFORMATION CONTAINED IN THIS DRAWING IS THE SOLE PROPERTY OF UCLA. ANY REPRODUCTION IN PART OR AS A WHOLE WITHOUT THE WRITTEN PERMISSION OF UCLA IS PROHIBITED.

SOLIDWORKS Educational Product. For Instructional Use Only

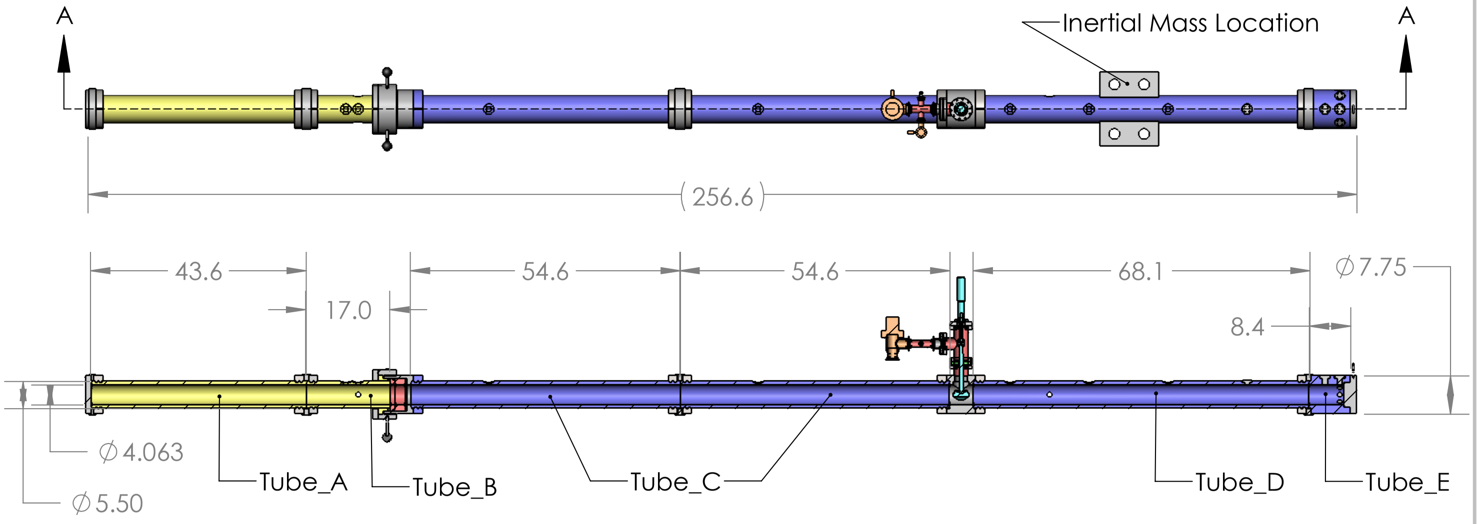

SECTION A-A

NOTE:
1. Tube_A,B,C,D are standard SS tubing honed out to the following dimensions (OD: 5.50" ID: 4.063")
2. Tube_E has OD: 7.75", ID: 4.063"
3. Dimensions above indicate approximate individual tube lengths
4. Material: 304 Stainless Steel
5. Finish on interior surface of tube: $\sqrt[32]{}$

UNLESS OTHERWISE SPECIFIED:		NAME	DATE
DIMENSIONS ARE IN INCHES TOLERANCES: FRACTIONAL ± ANGULAR: MACH ± BEND ± TWO PLACE DECIMAL ± THREE PLACE DECIMAL ±	DRAWN	F. BENDANA	2/10/17
	CHECKED		
	ENG APPR.		
	MFG APPR.		
INTERPRET GEOMETRIC TOLERANCING PER:	Q.A.		
MATERIAL 304 SS	COMMENTS:		
FINISH			
DO NOT SCALE DRAWING			

NEXT ASSY
USED ON
APPLICATION

UCLA: Laser Spectroscopy & Gas Dynamics Lab

TITLE:

HEST
OVERALL ASSEMBLY

SIZE A
DWG. NO.
REV 002
SCALE: 1:30
SHEET 2 OF 7

PAGE 2

PROPRIETARY AND CONFIDENTIAL
THE INFORMATION CONTAINED IN THIS DRAWING IS THE SOLE PROPERTY OF UCLA. ANY REPRODUCTION IN PART OR AS A WHOLE WITHOUT THE WRITTEN PERMISSION OF UCLA IS PROHIBITED.

SOLIDWORKS Educational Product. For Instructional Use Only

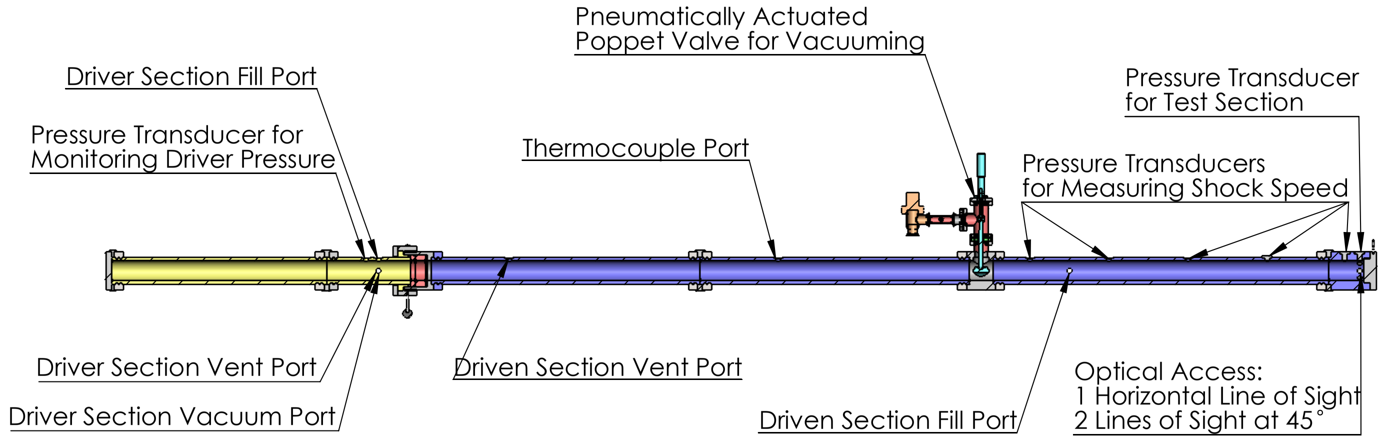

NOTE:

1. Optical access ports and pressure transducer for test section are located 2cm from endwall
2. Distance between pressure transducers for measuring shock speeds is ~16in
3. Pneumatically actuated poppet valve is connected to the roughing pump, the turbomolecular pump, and ambient

UNLESS OTHERWISE SPECIFIED:		NAME	DATE
DIMENSIONS ARE IN INCHES TOLERANCES: FRACTIONAL ± ANGULAR: MACH ± BEND ± TWO PLACE DECIMAL ± THREE PLACE DECIMAL ±	DRAWN	F. BENDANA	2/10/17
	CHECKED		
	ENG APPR.		
	MFG APPR.		
INTERPRET GEOMETRIC TOLERANCING PER:	Q.A.		
MATERIAL 304 SS	COMMENTS:		
FINISH			
DO NOT SCALE DRAWING			

NEXT ASSY	USED ON
APPLICATION	

UCLA: Laser Spectroscopy & Gas Dynamics Lab

TITLE:

HEST
PORT LOCATIONS

SIZE	DWG. NO.	REV
A		002
SCALE: 1:30		SHEET 3 OF 7

PROPRIETARY AND CONFIDENTIAL

THE INFORMATION CONTAINED IN THIS DRAWING IS THE SOLE PROPERTY OF <INSERT COMPANY NAME HERE>. ANY REPRODUCTION IN PART OR AS A WHOLE WITHOUT THE WRITTEN PERMISSION OF <INSERT COMPANY NAME HERE> IS PROHIBITED.

SOLIDWORKS Educational Product. For Instructional Use Only

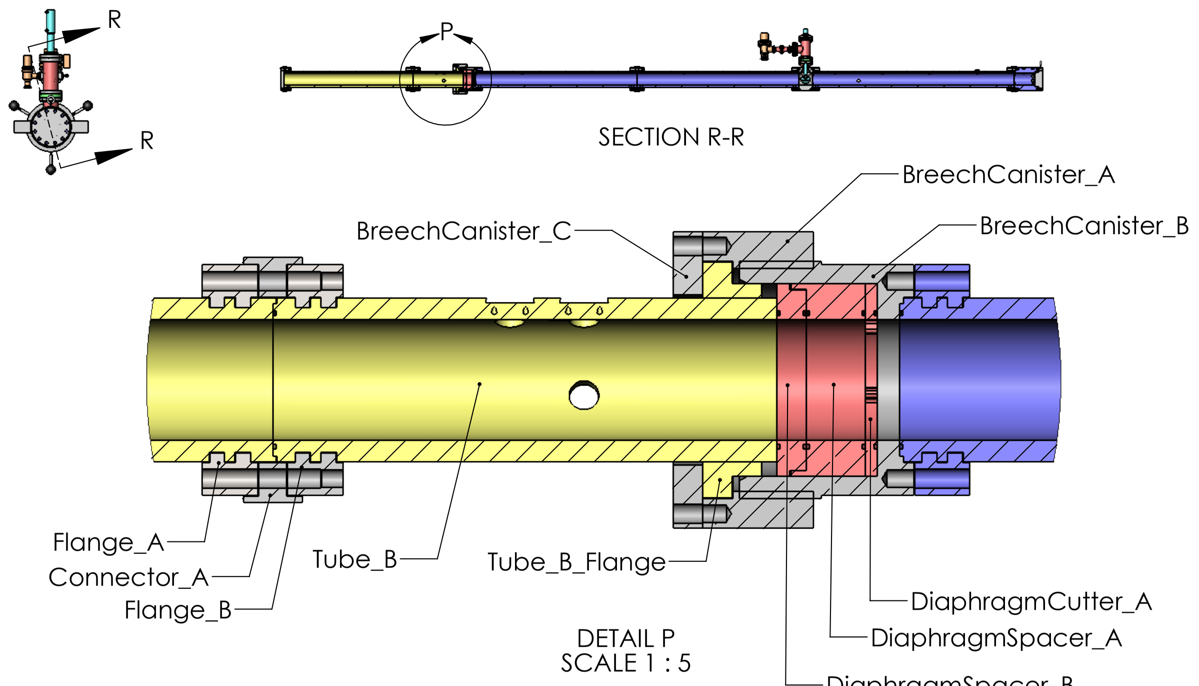

NOTE:
1. Tube_B and Tube_B_Flange are welded
2. BreechCanister_A and BreechCanister_B are threaded

	NAME	DATE
DRAWN	F. BENDANA	2/10/17
CHECKED		
ENG APPR.		
MFG APPR.		
Q.A.		
COMMENTS:		

UNLESS OTHERWISE SPECIFIED:
DIMENSIONS ARE IN INCHES
TOLERANCES:
FRACTIONAL ±
ANGULAR: MACH ± BEND ±
TWO PLACE DECIMAL ±
THREE PLACE DECIMAL ±
INTERPRET GEOMETRIC TOLERANCING PER:
MATERIAL
304 SS
FINISH
DO NOT SCALE DRAWING

NEXT ASSY
USED ON
APPLICATION

PROPRIETARY AND CONFIDENTIAL
THE INFORMATION CONTAINED IN THIS DRAWING IS THE SOLE PROPERTY OF UCLA. ANY REPRODUCTION IN PART OR AS A WHOLE WITHOUT THE WRITTEN PERMISSION OF UCLA IS PROHIBITED.

SOLIDWORKS Educational Product. For Instructional Use Only

UCLA: Laser Spectroscopy & Gas Dynamics Lab

TITLE:
HEST
DIAPHRAGM MECHANISM

SIZE A
DWG. NO.
REV 002
SCALE: 1:30
SHEET 4 OF 7

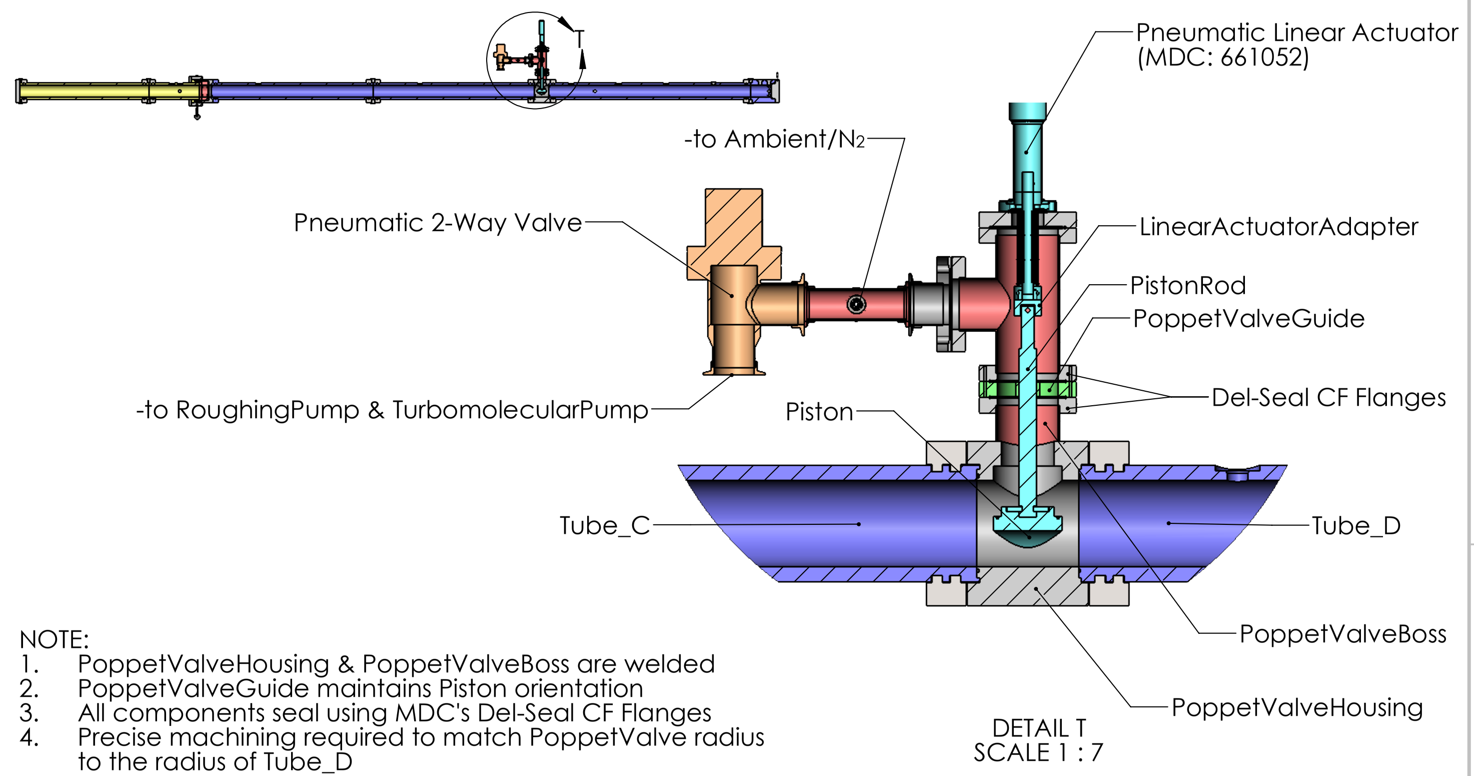

NOTE:
1. PoppetValveHousing & PoppetValveBoss are welded
2. PoppetValveGuide maintains Piston orientation
3. All components seal using MDC's Del-Seal CF Flanges
4. Precise machining required to match PoppetValve radius to the radius of Tube_D

PROPRIETARY AND CONFIDENTIAL

THE INFORMATION CONTAINED IN THIS DRAWING IS THE SOLE PROPERTY OF <INSERT COMPANY NAME HERE>. ANY REPRODUCTION IN PART OR AS A WHOLE WITHOUT THE WRITTEN PERMISSION OF <INSERT COMPANY NAME HERE> IS PROHIBITED.

NEXT ASSY
USED ON
APPLICATION

SOLIDWORKS Educational Product. For Instructional Use Only

UNLESS OTHERWISE SPECIFIED:
DIMENSIONS ARE IN INCHES
TOLERANCES:
FRACTIONAL ±
ANGULAR: MACH ± BEND ±
TWO PLACE DECIMAL ±
THREE PLACE DECIMAL ±
INTERPRET GEOMETRIC TOLERANCING PER:
MATERIAL 304 SS
FINISH
DO NOT SCALE DRAWING

	NAME	DATE
DRAWN	F. BENDANA	2/10/17
CHECKED		
ENG APPR.		
MFG APPR.		
Q.A.		

COMMENTS:

UCLA: Laser Spectroscopy & Gas Dynamics Lab

TITLE:

HEST
POPPET VALVE ASSEMBLY

SIZE A
DWG. NO.
REV 002
SCALE: 1:30
SHEET 5 OF 7

NOTE:
1. In the view below, some components are suppressed for better understanding of the assembly
2. PoppetValveGuide has a flat face to orient the valve

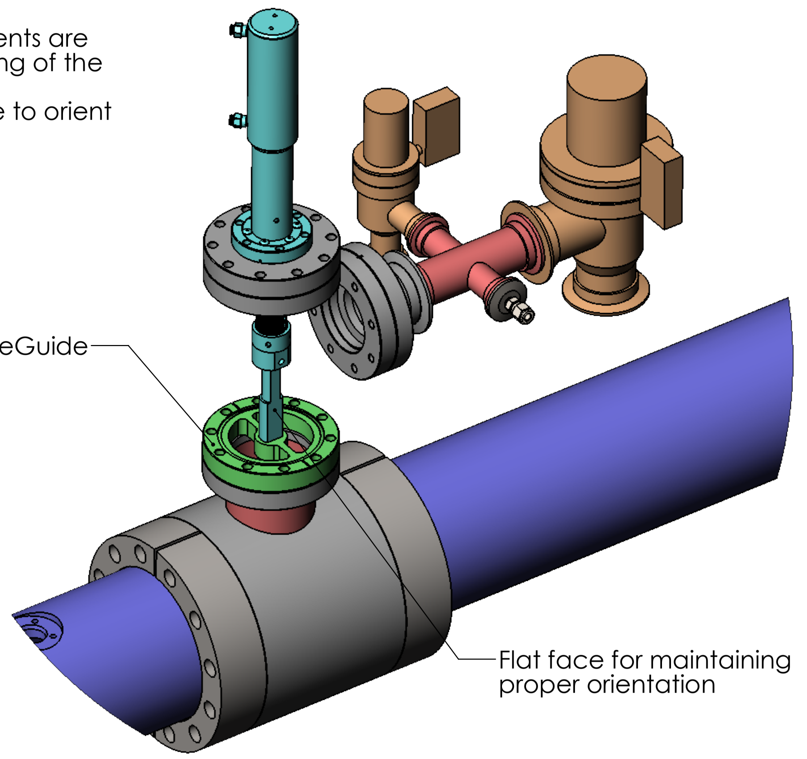

UNLESS OTHERWISE SPECIFIED:
DIMENSIONS ARE IN INCHES
TOLERANCES:
FRACTIONAL ±
ANGULAR: MACH ± BEND ±
TWO PLACE DECIMAL ±
THREE PLACE DECIMAL ±

INTERPRET GEOMETRIC TOLERANCING PER:

MATERIAL
304 SS

FINISH

DO NOT SCALE DRAWING

NEXT ASSY | USED ON
APPLICATION

	NAME	DATE
DRAWN	F. BENDANA	2/10/17
CHECKED		
ENG APPR.		
MFG APPR.		
Q.A.		

COMMENTS:

UCLA: Laser Spectroscopy & Gas Dynamics Lab

TITLE:

HEST
POPPET VALVE ASSEMBLY

SIZE **A** DWG. NO. REV 002

SCALE: 1:48 SHEET 6 OF 7

PROPRIETARY AND CONFIDENTIAL

THE INFORMATION CONTAINED IN THIS DRAWING IS THE SOLE PROPERTY OF <INSERT COMPANY NAME HERE>. ANY REPRODUCTION IN PART OR AS A WHOLE WITHOUT THE WRITTEN PERMISSION OF <INSERT COMPANY NAME HERE> IS PROHIBITED.

SOLIDWORKS Educational Product. For Instructional Use Only

2 1 B A

PAGE 6

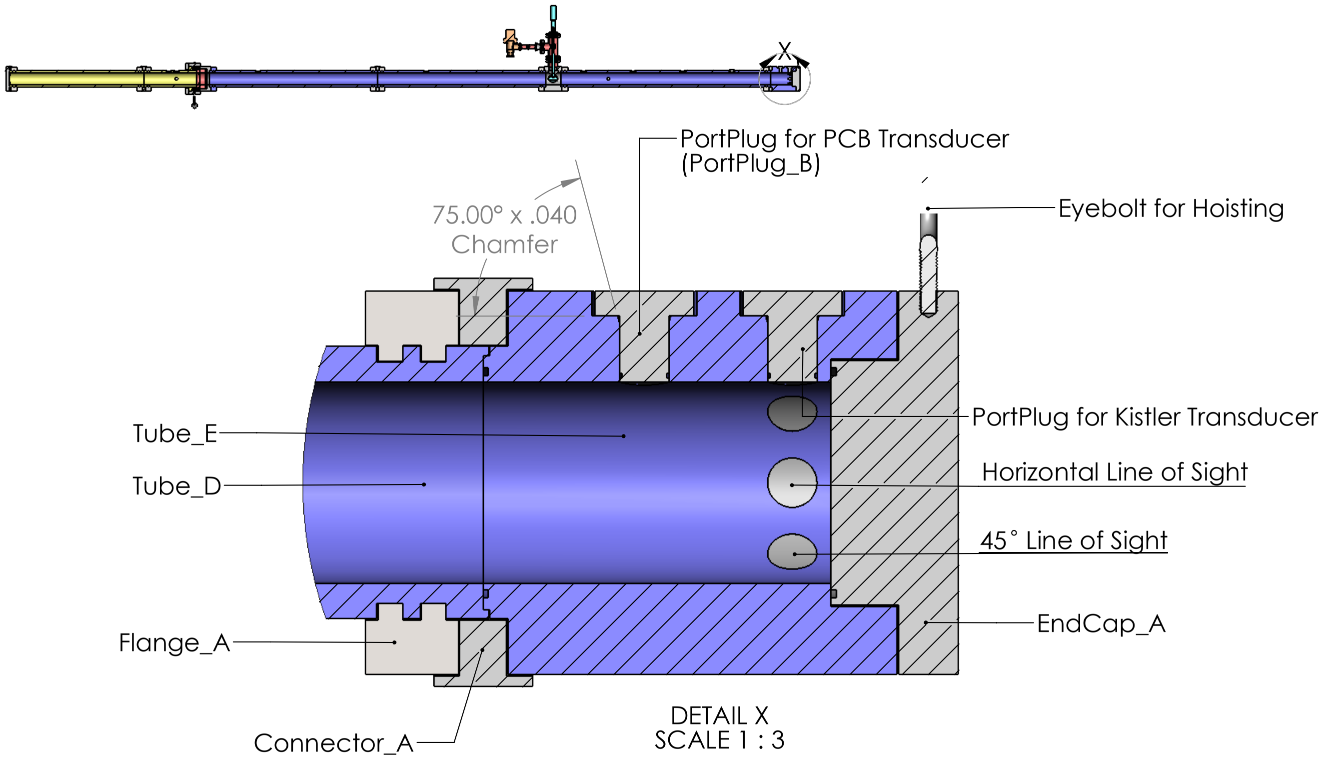

PROPRIETARY AND CONFIDENTIAL

THE INFORMATION CONTAINED IN THIS DRAWING IS THE SOLE PROPERTY OF <INSERT COMPANY NAME HERE>. ANY REPRODUCTION IN PART OR AS A WHOLE WITHOUT THE WRITTEN PERMISSION OF <INSERT COMPANY NAME HERE> IS PROHIBITED.

NEXT ASSY
USED ON
APPLICATION

SOLIDWORKS Educational Product. For Instructional Use Only

UNLESS OTHERWISE SPECIFIED:
DIMENSIONS ARE IN INCHES
TOLERANCES:
FRACTIONAL ±
ANGULAR: MACH ± BEND ±
TWO PLACE DECIMAL ±
THREE PLACE DECIMAL ±
INTERPRET GEOMETRIC TOLERANCING PER:
MATERIAL
304 SS
FINISH
DO NOT SCALE DRAWING

	NAME	DATE
DRAWN	F. BENDANA	2/10/17
CHECKED		
ENG APPR.		
MFG APPR.		
Q.A.		

COMMENTS:

UCLA: Laser Spectroscopy & Gas Dynamics Lab

TITLE:

HEST
TEST SECTION & PORT PLUG

SIZE A
DWG. NO.
REV 002
SCALE: 1:48
SHEET 7 OF 7

University of California, Los Angeles
Laser Spectroscopy & Gas Dynamics Lab
High Enthalpy Shock Tube Facility (HEST)

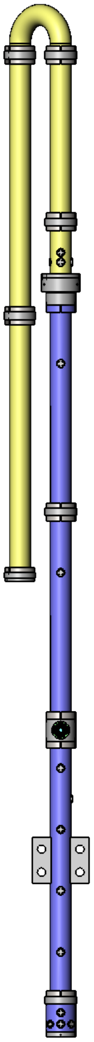

DWG. NO.	PART NUMBER	QTY.
1	Tube_A	1
2	Tube_B	1
3	Tube_C	2
4	Tube_D	1
5	Tube_E	1
6	Tube_F	1
7	Tube_G	2
8	Connector_A	6
9	Connector_B	1
10	Flange_A	18
11	Flange_B	12
12	DiaphragmCutter_A	1
13	DiaphragmSpacer_A	1
14	DiaphragmSpacer_B	1
15	DiaphragmSpacer_C	1
16	BreechCanister_A	1
17	BreechCanister_B	1
18	BreechCanister_C	1
19	PortPlug_A	11
20	PortPlug_B	8
21	EndCap_A	1
22	EndCap_B	1
23	PoppetValveHousing	1
24	PoppetValveBoss	1
25	Piston	1
26	PistonRod	1
27	RodClip_A	1
28	RodClip_B	1
29	PistonGuide	1
30	LinearActuatorAdapter	1
31	InertialMassAttachment_A	2

PROPRIETARY AND CONFIDENTIAL

THE INFORMATION CONTAINED IN THIS DRAWING IS THE SOLE PROPERTY OF UCLA. ANY REPRODUCTION IN PART OR AS A WHOLE WITHOUT THE WRITTEN PERMISSION OF UCLA IS PROHIBITED.

NEXT ASSY
USED ON
APPLICATION

DIMENSIONS ARE IN INCHES
TOLERANCES:
FRACTIONAL ±
ANGULAR: MACH ± BEND ±
TWO PLACE DECIMAL ±.010
THREE PLACE DECIMAL ±.005

MATERIAL

FINISH

DO NOT SCALE DRAWING

	NAME	DATE
DRAWN	F. BENDANA	2/10/17
CHECKED		
ENG APPR.		
MFG APPR.		
Q.A.		

COMMENTS:

UCLA: Laser Spectroscopy & Gas Dynamics Lab

HEST
BILL OF MATERIALS

SIZE A
DWG. NO.
REV. 002
SCALE:1:40
WEIGHT:
SHEET 1 OF 3

SOLIDWORKS Educational Product. For Instructional Use Only

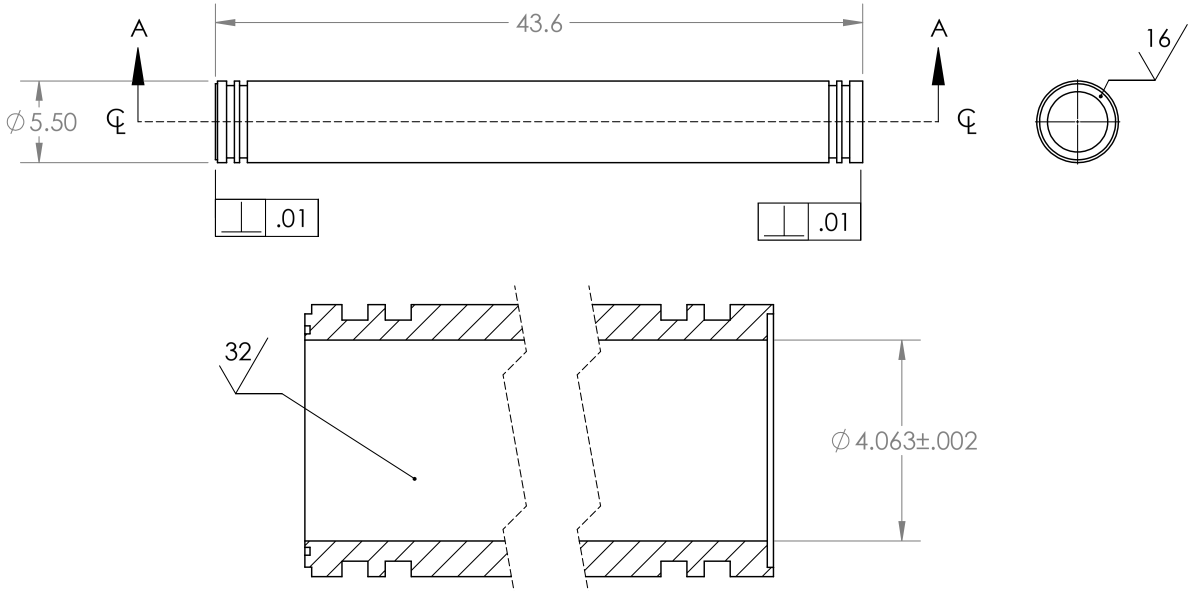

SECTION A-A
SCALE 1 : 3

NOTE:
1. O-RING GROOVE ONLY ON ONE SIDE
2. REFERENCE ORingGrooveDetail ON PAGE 40 FOR DIMENSIONS & SURFACE FINISHES
3. REFERENCE PipeEndDetail ON PAGE 44 FOR DIMENSIONS

PROPRIETARY AND CONFIDENTIAL

THE INFORMATION CONTAINED IN THIS DRAWING IS THE SOLE PROPERTY OF UCLA. ANY REPRODUCTION IN PART OR AS A WHOLE WITHOUT THE WRITTEN

NEXT ASSY
USED ON
APPLICATION

UNLESS OTHERWISE SPECIFIED:
DIMENSIONS ARE IN INCHES
TOLERANCES:
FRACTIONAL ±
ANGULAR: MACH ± BEND ±
ONE PLACE DECIMAL ±.100
TWO PLACE DECIMAL ±.010
THREE PLACE DECIMAL ±.005

INTERPRET GEOMETRIC TOLERANCING PER:

MATERIAL
304 SS

FINISH

DO NOT SCALE DRAWING

	NAME	DATE
DRAWN	F. BENDANA	2/10/17
CHECKED		
ENG APPR.		
MFG APPR.		
Q.A.		

COMMENTS:

UCLA: Laser Spectroscopy & Gas Dynamics Lab

TITLE:
Tube_A

SIZE	DWG. NO.	REV
A	1	002

SCALE: 1:10
SHEET 1 OF 3

SOLIDWORKS Educational Product. For Instructional Use Only

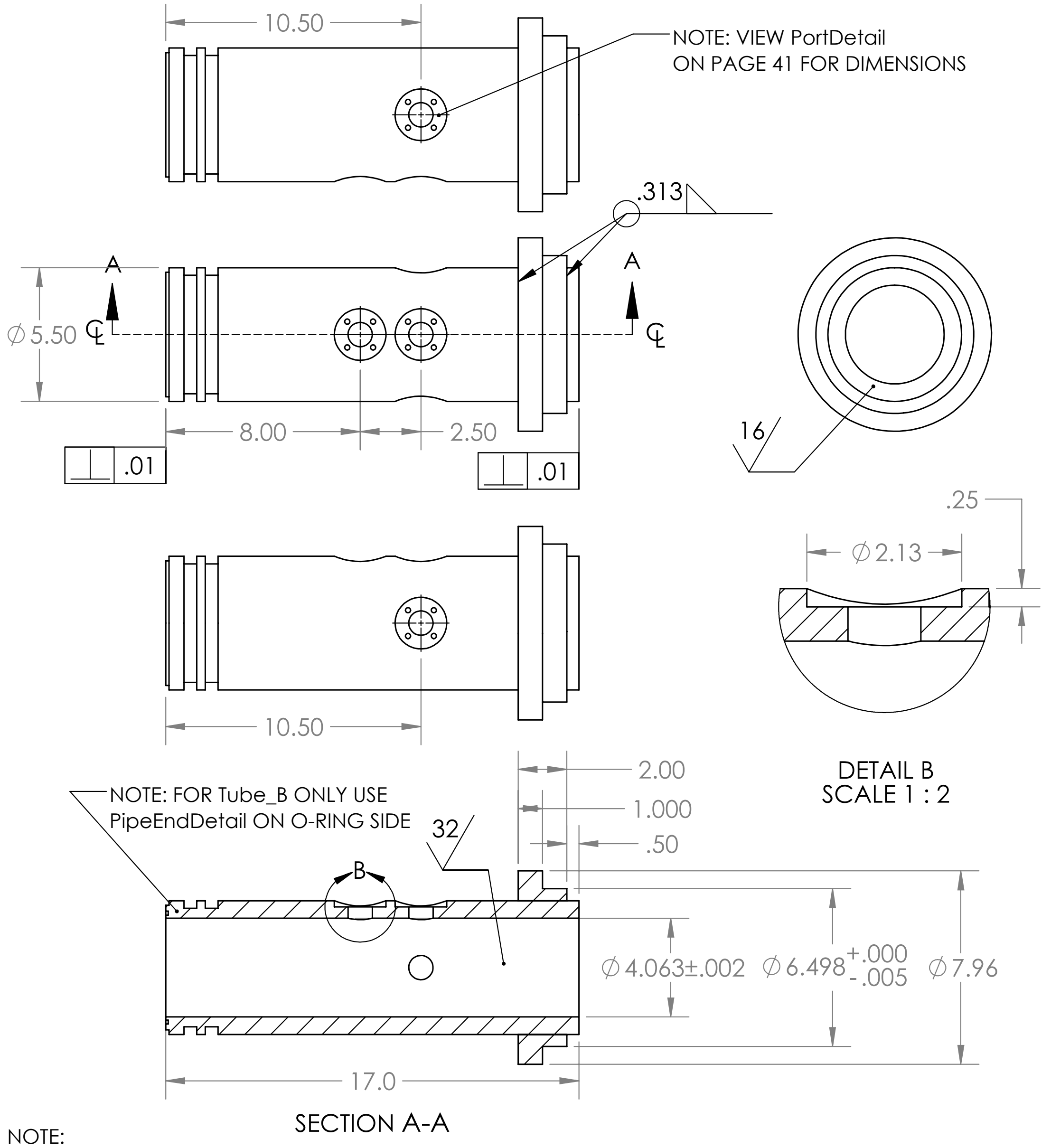

NOTE:
1. O-RING GROOVE ONLY ON ONE SIDE
2. REFERENCE ORingGrooveDetail ON PAGE 40 FOR DIMENSIONS & SURFACE FINISHES
3. REFERENCE PipeEndDetail ON PAGE 44 FOR DIMENSIONS

DIMENSIONS ARE IN INCHES
TOLERANCES:
FRACTIONAL ±
ANGULAR: MACH ± BEND ±
TWO PLACE DECIMAL ±.010
THREE PLACE DECIMAL ±.005

	NAME	DATE
DRAWN	F. BENDANA	2/10/17
CHECKED		
ENG APPR.		
MFG APPR.		
Q.A.		
COMMENTS:		

UCLA: Laser Spectroscopy & Gas Dynamics Lab

Tube_B

MATERIAL
304 SS

FINISH

NEXT ASSY
USED ON
APPLICATION
DO NOT SCALE DRAWING

PROPRIETARY AND CONFIDENTIAL
THE INFORMATION CONTAINED IN THIS DRAWING IS THE SOLE PROPERTY OF UCLA. ANY REPRODUCTION IN PART OR AS A WHOLE WITHOUT THE WRITTEN PERMISSION OF UCLA IS PROHIBITED.

SOLIDWORKS Educational Product. For Instructional Use Only

SIZE A
DWG. NO. 2
REV. 002
SCALE:1:6
WEIGHT:
SHEET 1 OF 1

2
1

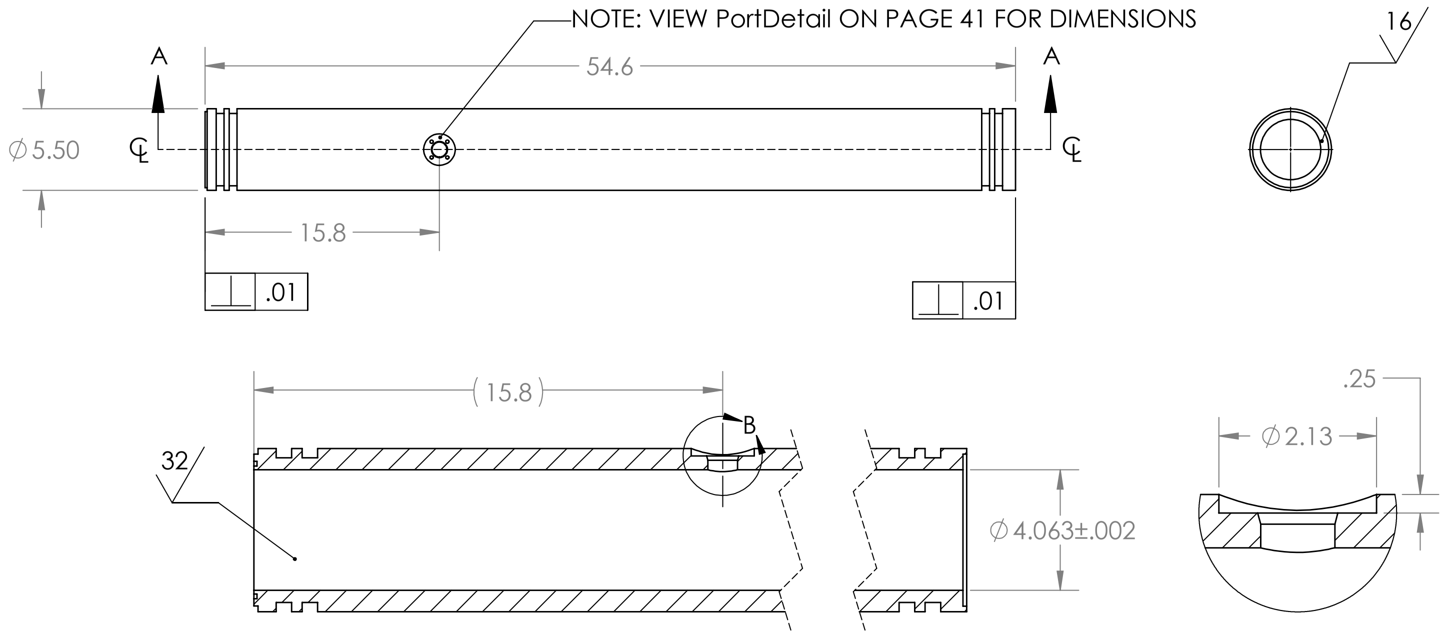

SECTION A-A
SCALE 1 : 5

DETAIL B
SCALE 1 : 2

NOTE:
1. O-RING GROOVE ONLY ON ONE SIDE
2. REFERENCE ORingGrooveDetail ON PAGE 40 FOR DIMENSIONS & SURFACE FINISHES
3. REFERENCE PipeEndDetail ON PAGE 44 FOR DIMENSIONS

PROPRIETARY AND CONFIDENTIAL
THE INFORMATION CONTAINED IN THIS DRAWING IS THE SOLE PROPERTY OF UCLA. ANY REPRODUCTION IN PART OR AS A WHOLE WITHOUT THE WRITTEN PERMISSION OF UCLA IS PROHIBITED.

SOLIDWORKS Educational Product. For Instructional Use Only

NEXT ASSY	USED ON
APPLICATION	

UNLESS OTHERWISE SPECIFIED:
DIMENSIONS ARE IN INCHES
TOLERANCES:
FRACTIONAL ±
ANGULAR: MACH ± BEND ±
ONE PLACE DECIMAL ±.100
TWO PLACE DECIMAL ±.010
THREE PLACE DECIMAL ±.005
INTERPRET GEOMETRIC TOLERANCING PER:
MATERIAL 304 SS
FINISH
DO NOT SCALE DRAWING

	NAME	DATE
DRAWN	F. BENDANA	2/10/17
CHECKED		
ENG APPR.		
MFG APPR.		
Q.A.		
COMMENTS:		

UCLA: Laser Spectroscopy & Gas Dynamics Lab

TITLE:
Tube_C

SIZE	DWG. NO.	REV
A	3	002
SCALE: 1:10		SHEET 1 OF 1

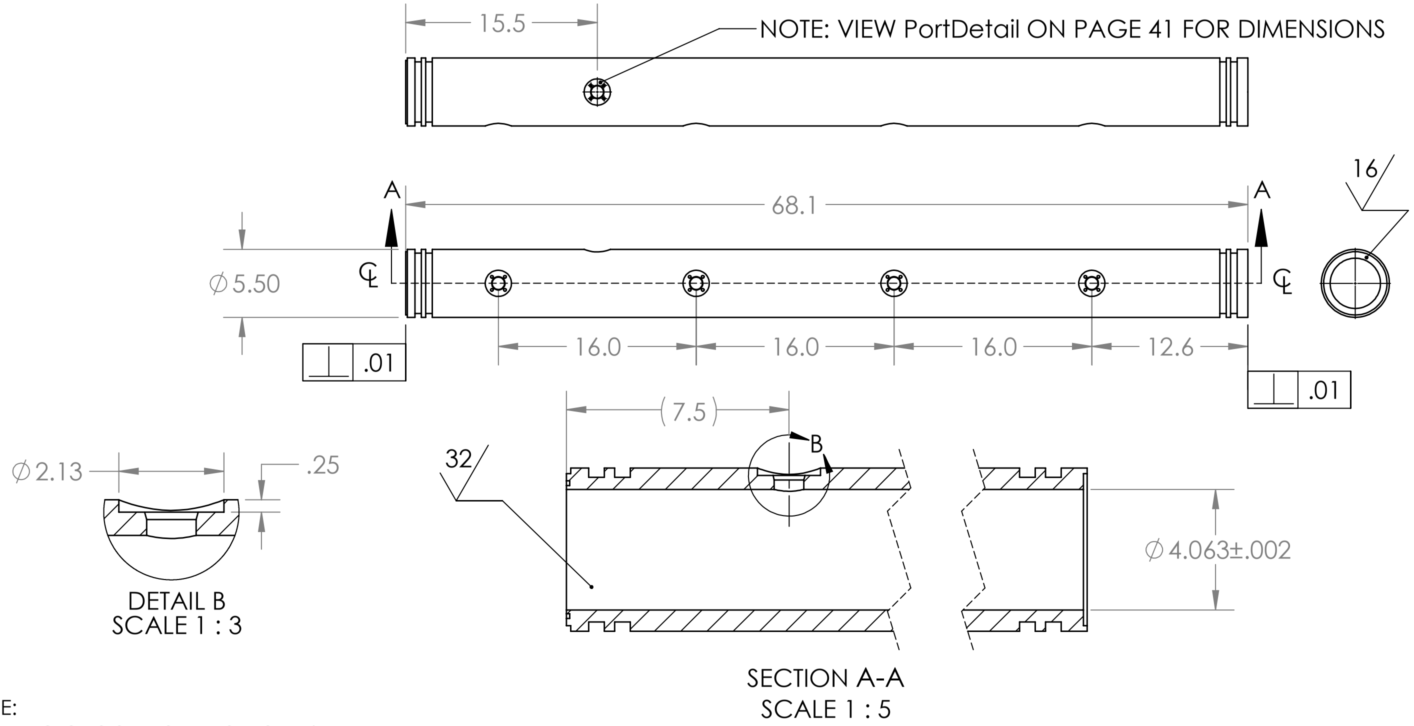

NOTE:
1. O-RING GROOVE ONLY ON ONE SIDE
2. REFERENCE ORingGrooveDetail ON PAGE 40 FOR DIMENSIONS & SURFACE FINISHES
3. REFERENCE PipeEndDetail ON PAGE 44 FOR DIMENSIONS

PROPRIETARY AND CONFIDENTIAL

THE INFORMATION CONTAINED IN THIS DRAWING IS THE SOLE PROPERTY OF UCLA. ANY REPRODUCTION IN PART OR AS A WHOLE WITHOUT THE WRITTEN

NEXT ASSY
USED ON
APPLICATION

SOLIDWORKS Educational Product. For Instructional Use Only

UNLESS OTHERWISE SPECIFIED:
DIMENSIONS ARE IN INCHES
TOLERANCES:
FRACTIONAL ±
ANGULAR: MACH ± BEND ±
ONE PLACE DECIMAL ±.100
TWO PLACE DECIMAL ±.010
THREE PLACE DECIMAL ±.005

INTERPRET GEOMETRIC TOLERANCING PER:

MATERIAL
304 SS

FINISH

DO NOT SCALE DRAWING

	NAME	DATE
DRAWN	F. BENDANA	2/10/17
CHECKED		
ENG APPR.		
MFG APPR.		
Q.A.		

COMMENTS:

UCLA: Laser Spectroscopy & Gas Dynamics Lab

TITLE:

Tube_D

SIZE	DWG. NO.	REV
A	4	002

SCALE: 1:12
SHEET 1 OF 1

PAGE 12

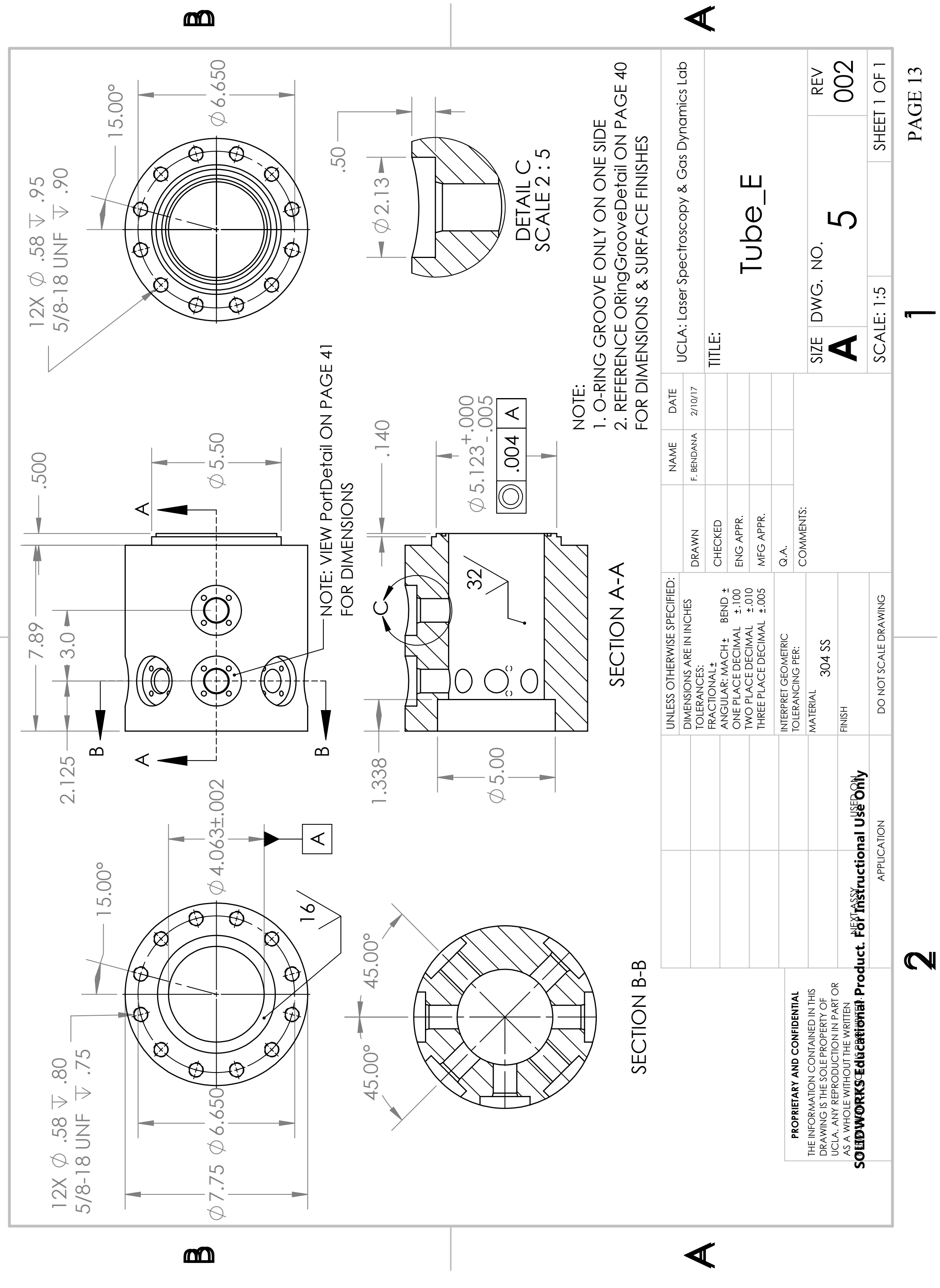
12X ⌀ .58 ↧ .95
5/8-18 UNF ↧ .90
15.00°
⌀ 6.650
.50
⌀ 2.13
DETAIL C
SCALE 2 : 5
NOTE:
1. O-RING GROOVE ONLY ON ONE SIDE
2. REFERENCE ORingGrooveDetail ON PAGE 40
FOR DIMENSIONS & SURFACE FINISHES
.500
⌀ 5.50
7.89
3.0
2.125
A
B
NOTE: VIEW PortDetail ON PAGE 41
FOR DIMENSIONS
.140
⌀ 5.123 +.000 -.005
.004 A
32
C
SECTION A-A
1.338
⌀ 5.00
12X ⌀ .58 ↧ .80
5/8-18 UNF ↧ .75
15.00°
⌀ 4.063±.002
A
16
⌀ 7.75
⌀ 6.650
45.00°
45.00°
SECTION B-B
UCLA: Laser Spectroscopy & Gas Dynamics Lab
TITLE:
Tube_E
SIZE A
DWG. NO. 5
REV 002
SCALE: 1:5
SHEET 1 OF 1
PAGE 13
NAME
DATE
DRAWN F. BENDANA 2/10/17
CHECKED
ENG APPR.
MFG APPR.
Q.A.
COMMENTS:
UNLESS OTHERWISE SPECIFIED:
DIMENSIONS ARE IN INCHES
TOLERANCES:
FRACTIONAL ±
ANGULAR: MACH ± BEND ±
ONE PLACE DECIMAL ±.100
TWO PLACE DECIMAL ±.010
THREE PLACE DECIMAL ±.005
INTERPRET GEOMETRIC TOLERANCING PER:
MATERIAL 304 SS
FINISH
DO NOT SCALE DRAWING
NEXT ASSY
USED ON
APPLICATION
PROPRIETARY AND CONFIDENTIAL
THE INFORMATION CONTAINED IN THIS DRAWING IS THE SOLE PROPERTY OF UCLA. ANY REPRODUCTION IN PART OR AS A WHOLE WITHOUT THE WRITTEN PERMISSION OF UCLA IS PROHIBITED.
SOLIDWORKS Educational Product. For Instructional Use Only
1
2
A
B

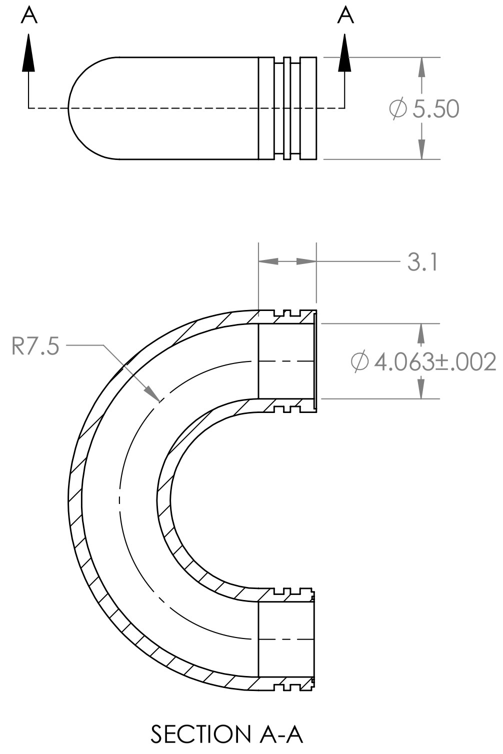

SECTION A-A

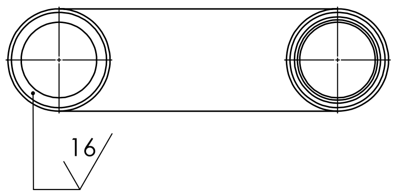

NOTE:
1. O-RING GROOVE ONLY ON ONE SIDE
2. REFERENCE ORingGrooveDetail ON PAGE 40 FOR DIMENSIONS & SURFACE FINISHES
3. REFERENCE PipeEndDetail ON PAGE 44 FOR DIMENSIONS

PROPRIETARY AND CONFIDENTIAL
THE INFORMATION CONTAINED IN THIS DRAWING IS THE SOLE PROPERTY OF UCLA. ANY REPRODUCTION IN PART OR AS A WHOLE WITHOUT THE WRITTEN PERMISSION OF UCLA IS PROHIBITED.

NEXT ASSY | USED ON
APPLICATION

UNLESS OTHERWISE SPECIFIED:
DIMENSIONS ARE IN INCHES
TOLERANCES:
FRACTIONAL ±
ANGULAR: MACH ± BEND ±
ONE PLACE DECIMAL ±.100
TWO PLACE DECIMAL ±.010
THREE PLACE DECIMAL ±.005
INTERPRET GEOMETRIC TOLERANCING PER:
MATERIAL 304 SS
FINISH
DO NOT SCALE DRAWING

	NAME	DATE
DRAWN	F. BENDANA	2/10/17
CHECKED		
ENG APPR.		
MFG APPR.		
Q.A.		

COMMENTS:

UCLA: Laser Spectroscopy & Gas Dynamics Lab
TITLE:
Tube_F
SIZE A
DWG. NO. 6
REV 002
SCALE: 1:8
SHEET 1 OF 1

SOLIDWORKS Educational Product. For Instructional Use Only

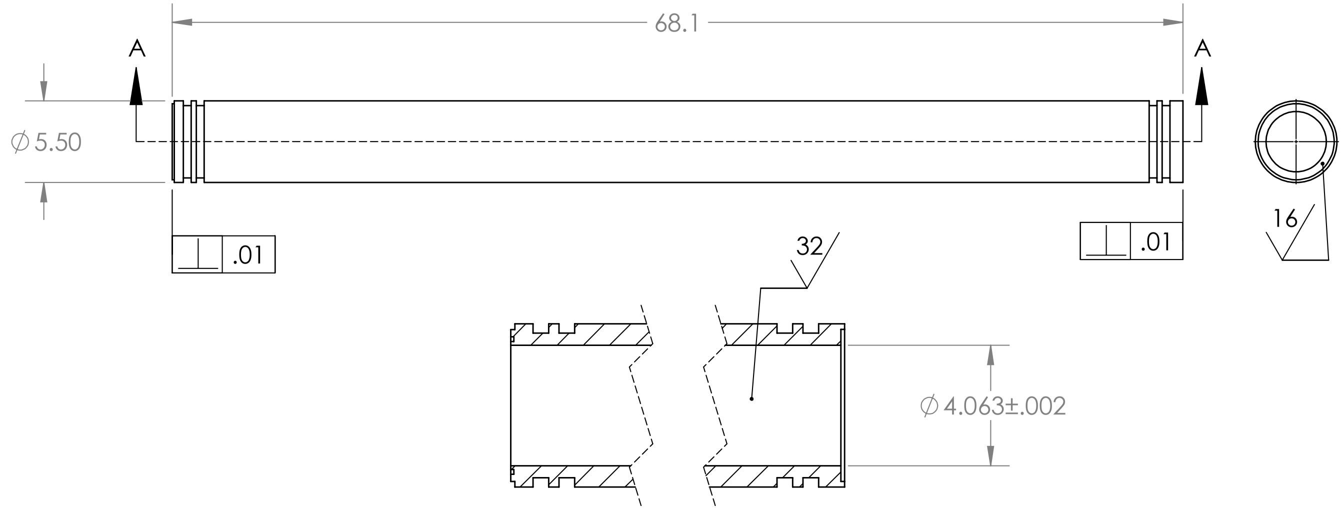

SECTION A-A
SCALE 1 : 5

NOTE:
1. O-RING GROOVE ONLY ON ONE SIDE
2. REFERENCE ORingGrooveDetail ON PAGE 40 FOR DIMENSIONS & SURFACE FINISHES
3. REFERENCE PipeEndDetail ON PAGE 44 FOR DIMENSIONS

PROPRIETARY AND CONFIDENTIAL

THE INFORMATION CONTAINED IN THIS DRAWING IS THE SOLE PROPERTY OF UCLA. ANY REPRODUCTION IN PART OR AS A WHOLE WITHOUT THE WRITTEN PERMISSION OF UCLA IS PROHIBITED.

NEXT ASSY	USED ON
APPLICATION	

UNLESS OTHERWISE SPECIFIED:
DIMENSIONS ARE IN INCHES
TOLERANCES:
FRACTIONAL ±
ANGULAR: MACH ± BEND ±
ONE PLACE DECIMAL ±.100
TWO PLACE DECIMAL ±.010
THREE PLACE DECIMAL ±.005

INTERPRET GEOMETRIC TOLERANCING PER:

MATERIAL
304 SS

FINISH

DO NOT SCALE DRAWING

	NAME	DATE
DRAWN	F. BENDANA	2/10/17
CHECKED		
ENG APPR.		
MFG APPR.		
Q.A.		

COMMENTS:

UCLA: Laser Spectroscopy & Gas Dynamics Lab

TITLE:
Tube_G

SIZE	DWG. NO.	REV
A	7	002

SCALE: 1:10
SHEET 1 OF 1

SOLIDWORKS Educational Product. For Instructional Use Only

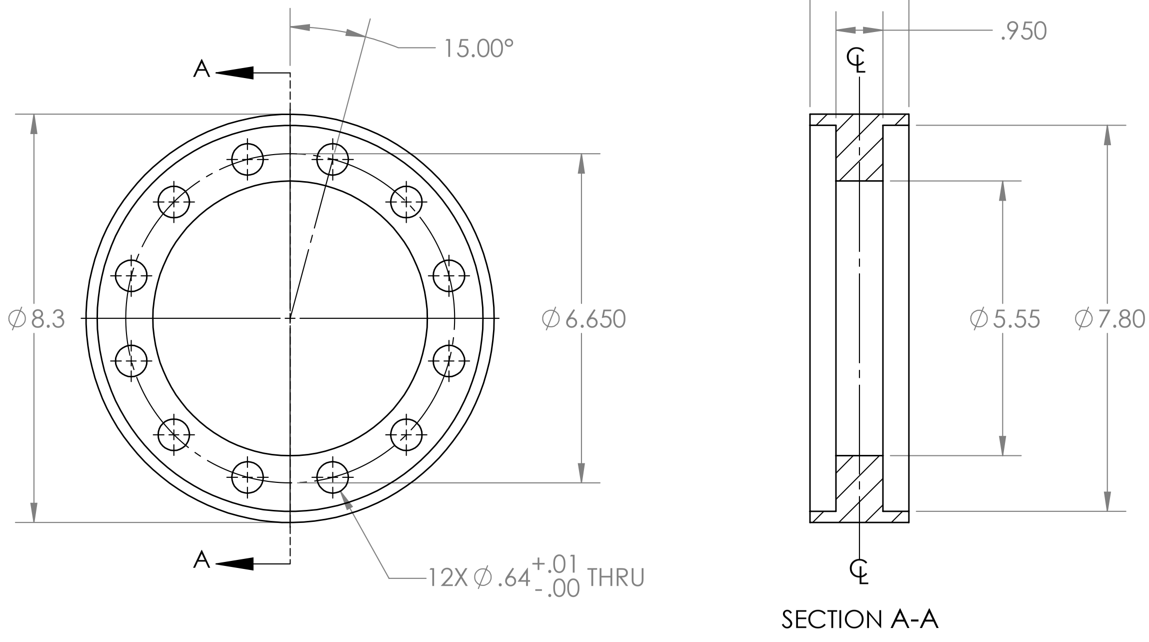

UNLESS OTHERWISE SPECIFIED:		NAME	DATE	UCLA: Laser Spectroscopy & Gas Dynamics Lab
DIMENSIONS ARE IN INCHES TOLERANCES: FRACTIONAL ± ANGULAR: MACH ± BEND ± ONE PLACE DECIMAL ±.100 TWO PLACE DECIMAL ±.010 THREE PLACE DECIMAL ±.005	DRAWN	F. BENDANA	2/10/17	TITLE: Connector_A
	CHECKED			
	ENG APPR.			
	MFG APPR.			
	Q.A.			
INTERPRET GEOMETRIC TOLERANCING PER:	COMMENTS:			SIZE A DWG. NO. 8 REV 002
MATERIAL 304 SS				
FINISH				
DO NOT SCALE DRAWING				SCALE: 1:3 SHEET 1 OF 1

NEXT ASSY | USED ON

APPLICATION

PROPRIETARY AND CONFIDENTIAL

THE INFORMATION CONTAINED IN THIS DRAWING IS THE SOLE PROPERTY OF UCLA. ANY REPRODUCTION IN PART OR AS A WHOLE WITHOUT THE WRITTEN PERMISSION OF UCLA IS PROHIBITED.

SOLIDWORKS Educational Product. For Instructional Use Only

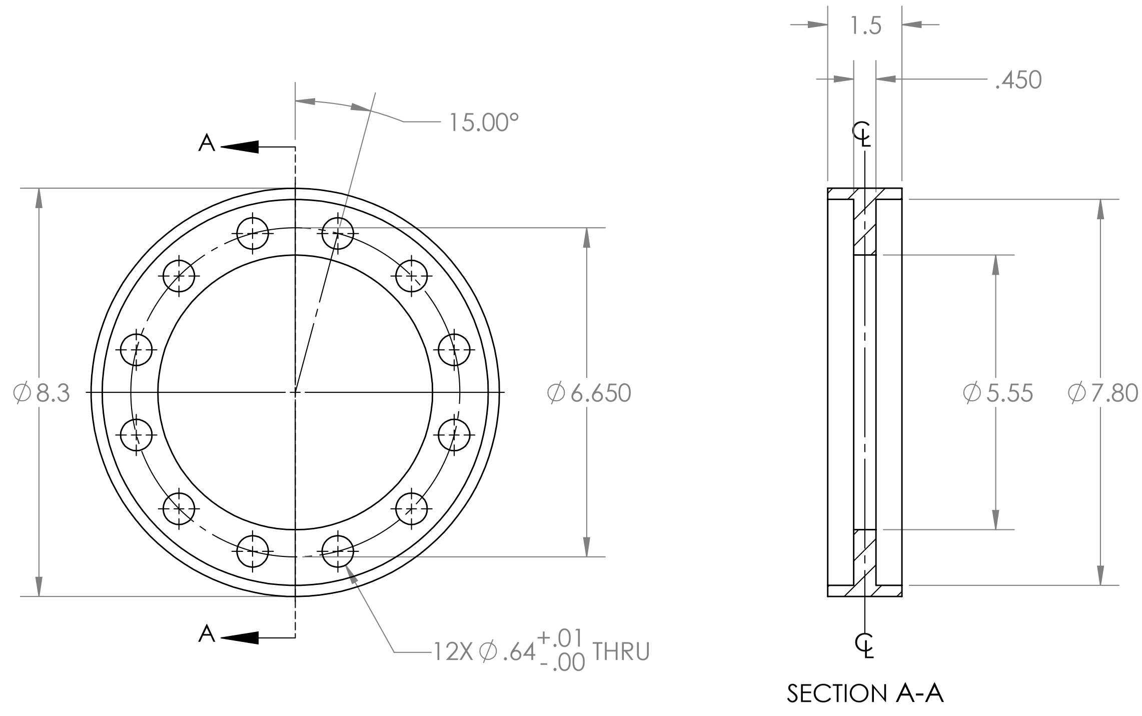

UNLESS OTHERWISE SPECIFIED:
DIMENSIONS ARE IN INCHES
TOLERANCES:
FRACTIONAL ±
ANGULAR: MACH ± BEND ±
ONE PLACE DECIMAL ±.100
TWO PLACE DECIMAL ±.010
THREE PLACE DECIMAL ±.005

INTERPRET GEOMETRIC TOLERANCING PER:

MATERIAL
304 SS

FINISH

DO NOT SCALE DRAWING

	NAME	DATE
DRAWN	F. BENDANA	2/10/17
CHECKED		
ENG APPR.		
MFG APPR.		
Q.A.		

COMMENTS:

UCLA: Laser Spectroscopy & Gas Dynamics Lab

TITLE:

Connector_B

SIZE A
DWG. NO. 9
REV 002

SCALE: 1:3
SHEET 1 OF 1

NEXT ASSY
USED ON
APPLICATION

PROPRIETARY AND CONFIDENTIAL

THE INFORMATION CONTAINED IN THIS DRAWING IS THE SOLE PROPERTY OF UCLA. ANY REPRODUCTION IN PART OR AS A WHOLE WITHOUT THE WRITTEN

SOLIDWORKS Educational Product. For Instructional Use Only

PAGE 17

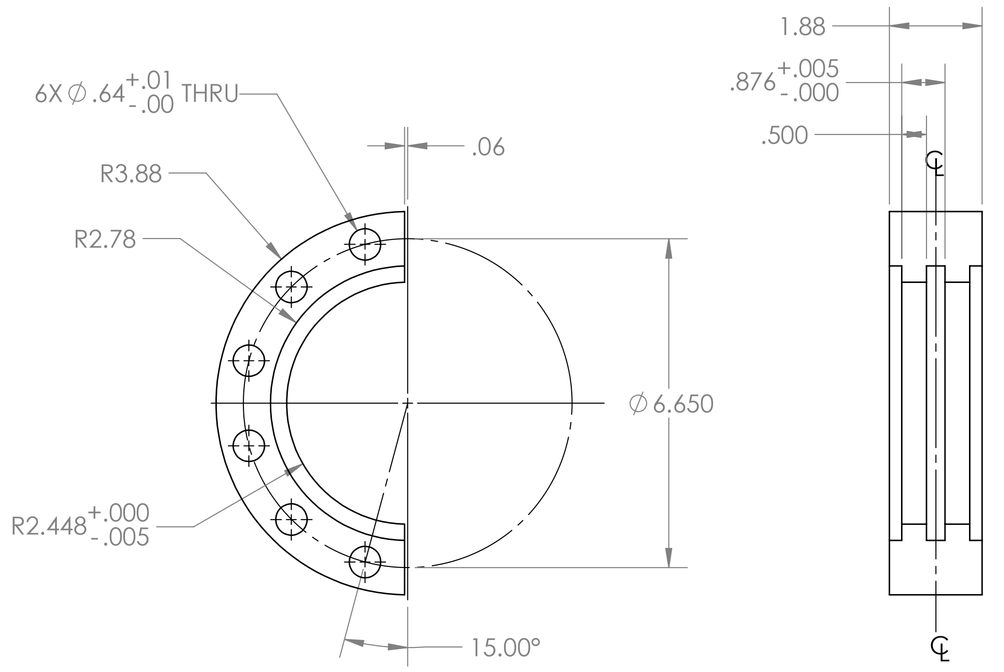

UNLESS OTHERWISE SPECIFIED:
DIMENSIONS ARE IN INCHES
TOLERANCES:
FRACTIONAL ±
ANGULAR: MACH ± BEND ±
TWO PLACE DECIMAL ±.010
THREE PLACE DECIMAL ±.005
INTERPRET GEOMETRIC TOLERANCING PER:
MATERIAL 304 SS
FINISH
DO NOT SCALE DRAWING

	NAME	DATE
DRAWN	F. BENDANA	2/10/17
CHECKED		
ENG APPR.		
MFG APPR.		
Q.A.		

COMMENTS:

UCLA: Laser Spectroscopy & Gas Dynamics Lab
TITLE:
Flange_A
SIZE A
DWG. NO. 10
REV 002
SCALE: 1:3
SHEET 1 OF 1

NEXT ASSY
USED ON
APPLICATION

PROPRIETARY AND CONFIDENTIAL
THE INFORMATION CONTAINED IN THIS DRAWING IS THE SOLE PROPERTY OF UCLA. ANY REPRODUCTION IN PART OR AS A WHOLE WITHOUT THE WRITTEN

SOLIDWORKS Educational Product. For Instructional Use Only

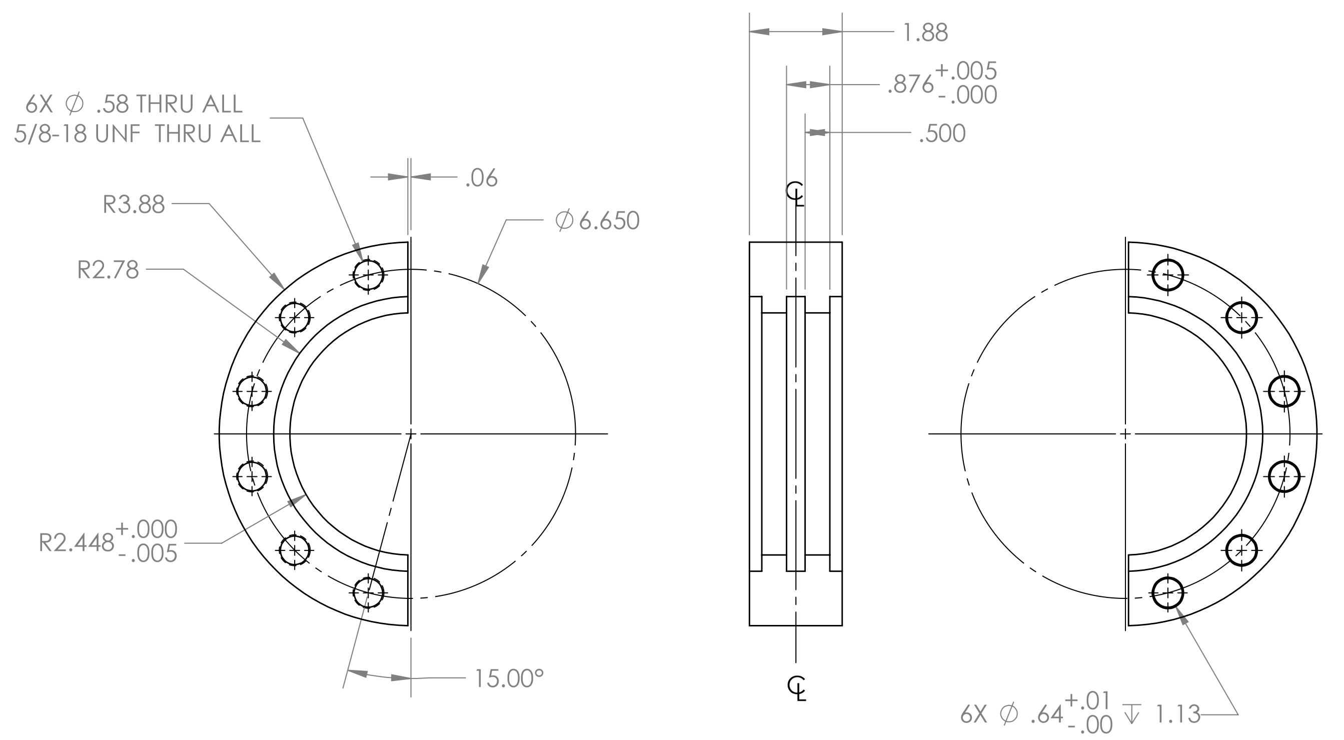

PROPRIETARY AND CONFIDENTIAL

THE INFORMATION CONTAINED IN THIS DRAWING IS THE SOLE PROPERTY OF UCLA. ANY REPRODUCTION IN PART OR AS A WHOLE WITHOUT THE WRITTEN

NEXT ASSY	USED ON
APPLICATION	

UNLESS OTHERWISE SPECIFIED:

DIMENSIONS ARE IN INCHES
TOLERANCES:
FRACTIONAL ±
ANGULAR: MACH ± BEND ±
TWO PLACE DECIMAL ±.010
THREE PLACE DECIMAL ±.005

INTERPRET GEOMETRIC TOLERANCING PER:

MATERIAL 304 SS

FINISH

DO NOT SCALE DRAWING

	NAME	DATE
DRAWN	F. BENDANA	2/10/17
CHECKED		
ENG APPR.		
MFG APPR.		
Q.A.		

COMMENTS:

UCLA: Laser Spectroscopy & Gas Dynamics Lab

TITLE:

Flange_B

SIZE	DWG. NO.	REV
A	11	002

SCALE: 1:3 SHEET 1 OF 1

SOLIDWORKS Educational Product. For Instructional Use Only

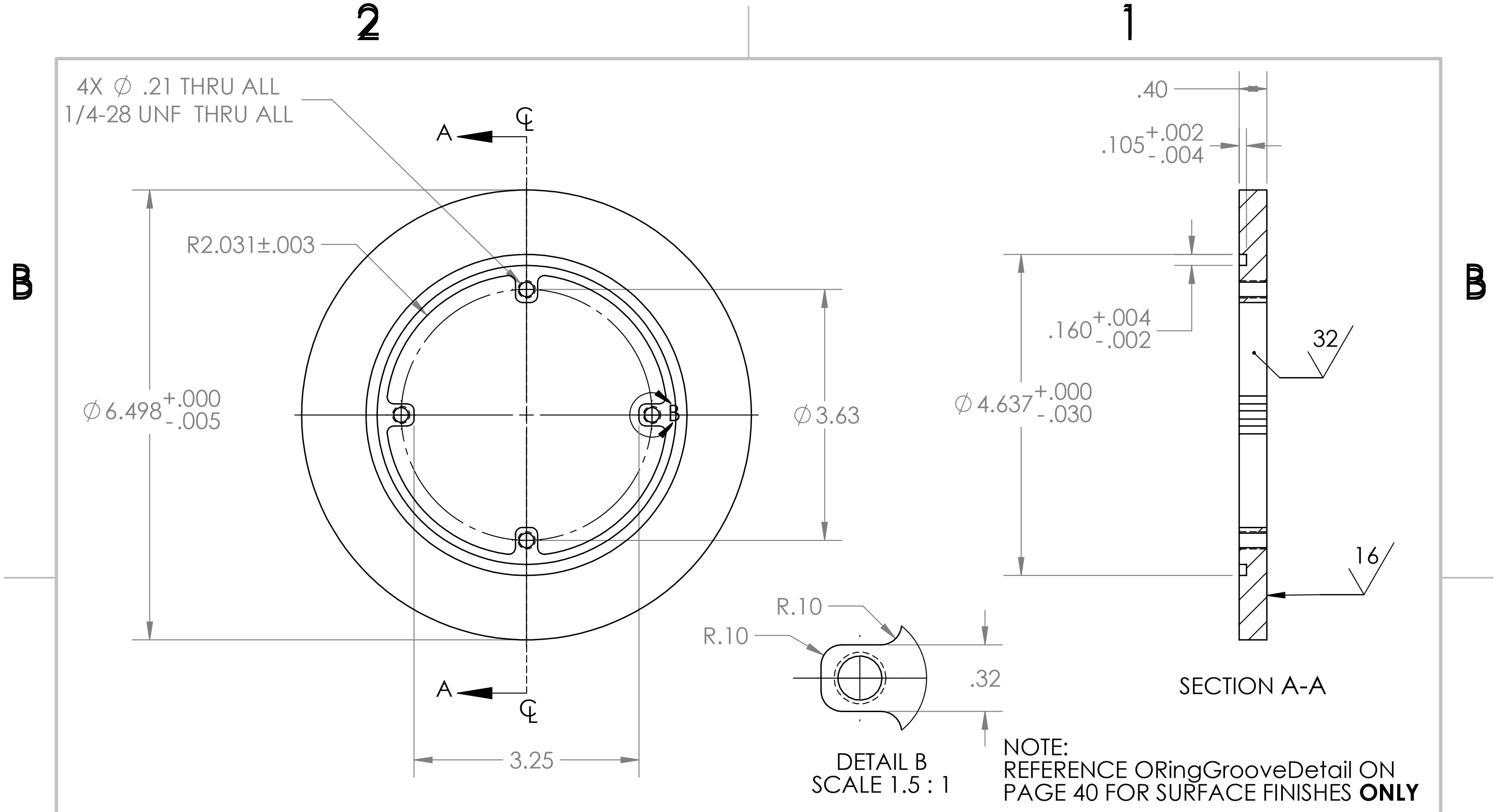

NOTE:
REFERENCE ORingGrooveDetail ON
PAGE 40 FOR SURFACE FINISHES **ONLY**

UNLESS OTHERWISE SPECIFIED:
DIMENSIONS ARE IN INCHES
TOLERANCES:
FRACTIONAL ±
ANGULAR: MACH ± BEND ±
TWO PLACE DECIMAL ±.010
THREE PLACE DECIMAL ±.005

INTERPRET GEOMETRIC TOLERANCING PER:

MATERIAL 304 SS

FINISH

DO NOT SCALE DRAWING

	NAME	DATE
DRAWN	F. BENDANA	2/10/17
CHECKED		
ENG APPR.		
MFG APPR.		
Q.A.		

COMMENTS:

UCLA: Laser Spectroscopy & Gas Dynamics Lab

TITLE:

DiaphragmCutter_A

SIZE A
DWG. NO. 12
REV 002
SCALE: 1:2
SHEET 1 OF 1

NEXT ASSY
USED ON
APPLICATION

PROPRIETARY AND CONFIDENTIAL

THE INFORMATION CONTAINED IN THIS DRAWING IS THE SOLE PROPERTY OF UCLA. ANY REPRODUCTION IN PART OR AS A WHOLE WITHOUT THE WRITTEN PERMISSION OF UCLA IS PROHIBITED.

SOLIDWORKS Educational Product. For Instructional Use Only

2
1

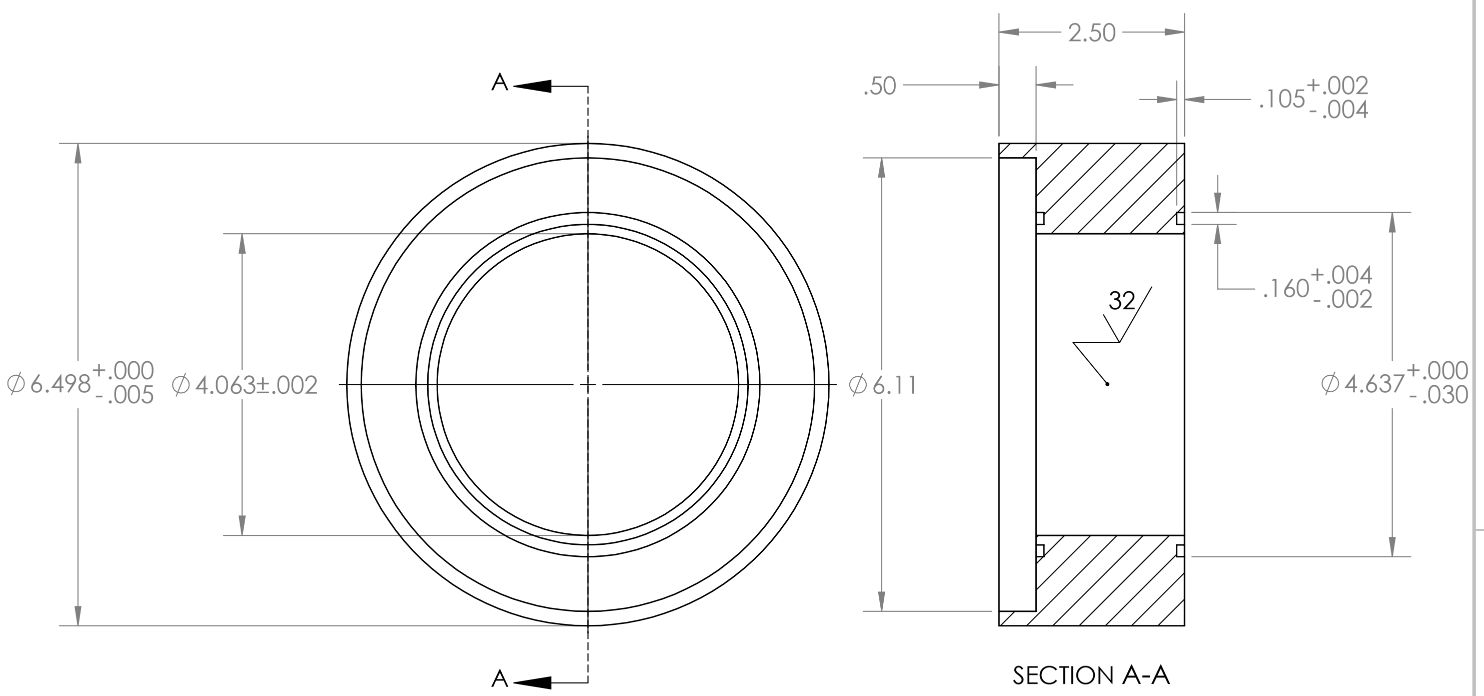

SECTION A-A

NOTE:
REFERENCE ORingGrooveDetail ON
PAGE 40 FOR SURFACE FINISHES **ONLY**

UNLESS OTHERWISE SPECIFIED:		NAME	DATE
DIMENSIONS ARE IN INCHES TOLERANCES: FRACTIONAL ± ANGULAR: MACH ± BEND ± TWO PLACE DECIMAL ±.010 THREE PLACE DECIMAL ±.005	DRAWN	F. BENDANA	2/10/17
	CHECKED		
	ENG APPR.		
	MFG APPR.		
INTERPRET GEOMETRIC TOLERANCING PER:	Q.A.		
MATERIAL 304 SS	COMMENTS:		
FINISH			
DO NOT SCALE DRAWING			

NEXT ASSY
USED ON
APPLICATION

UCLA: Gas Dynamics & Laser Spectroscopy Lab

TITLE:

DiaphragmSpacer_A

SIZE A
DWG. NO. 13
REV 002
SCALE: 1:2
SHEET 1 OF 1

PROPRIETARY AND CONFIDENTIAL

THE INFORMATION CONTAINED IN THIS DRAWING IS THE SOLE PROPERTY OF UCLA. ANY REPRODUCTION IN PART OR AS A WHOLE WITHOUT THE WRITTEN PERMISSION OF UCLA IS PROHIBITED.

SOLIDWORKS Educational Product. For Instructional Use Only

2
1
B
A

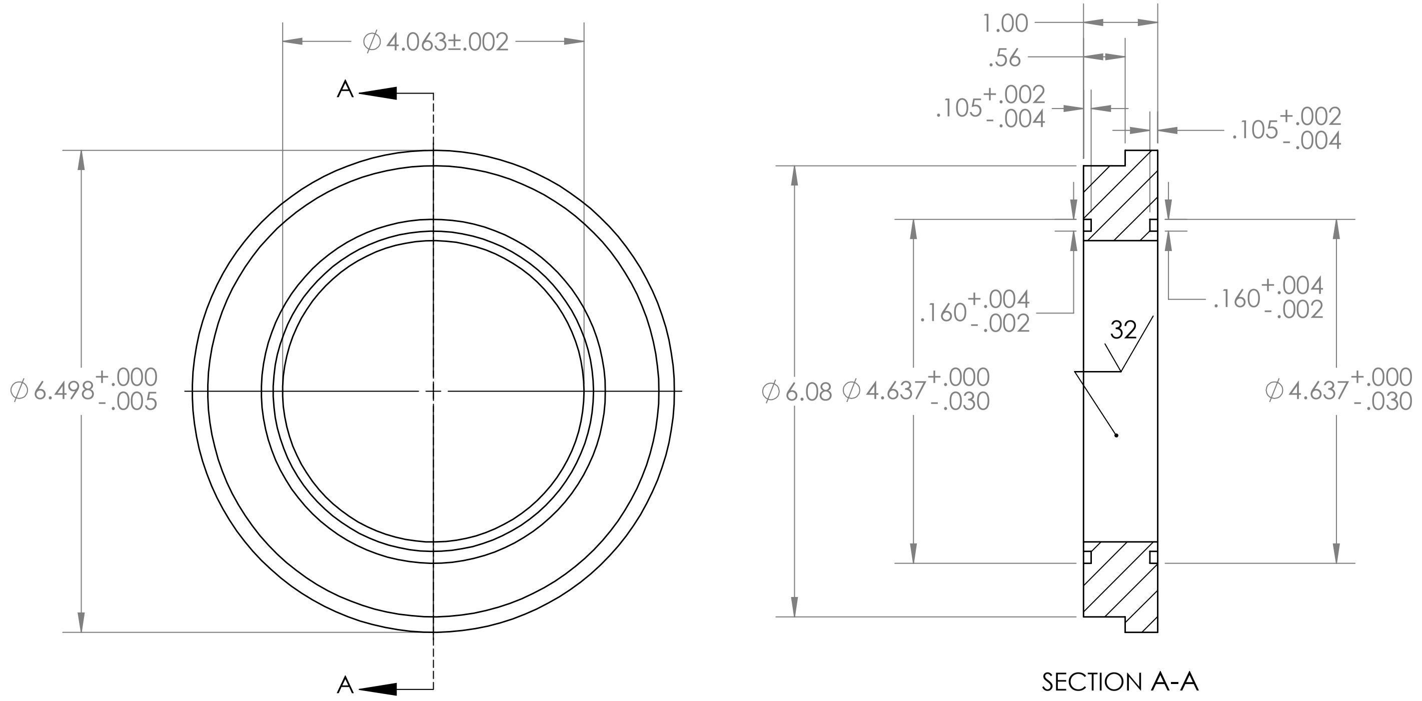

NOTE:
REFERENCE ORingGrooveDetail ON
PAGE 40 FOR SURFACE FINISHES **ONLY**

PROPRIETARY AND CONFIDENTIAL
THE INFORMATION CONTAINED IN THIS DRAWING IS THE SOLE PROPERTY OF UCLA. ANY REPRODUCTION IN PART OR AS A WHOLE WITHOUT THE WRITTEN PERMISSION OF UCLA IS PROHIBITED.

NEXT ASSY
USED ON
APPLICATION

UNLESS OTHERWISE SPECIFIED:
DIMENSIONS ARE IN INCHES
TOLERANCES:
FRACTIONAL ±
ANGULAR: MACH ± BEND ±
TWO PLACE DECIMAL ±.010
THREE PLACE DECIMAL ±.005
INTERPRET GEOMETRIC TOLERANCING PER:
MATERIAL 304 SS
FINISH
DO NOT SCALE DRAWING

	NAME	DATE
DRAWN	F. BENDANA	2/10/17
CHECKED		
ENG APPR.		
MFG APPR.		
Q.A.		

COMMENTS:

UCLA: Laser Spectroscopy & Gas Dynamics Lab
TITLE:
DiaphragmSpacer_B
SIZE A
DWG. NO. 14
REV 002
SCALE: 1:2
SHEET 1 OF 1

SOLIDWORKS Educational Product. For Instructional Use Only

PAGE 22

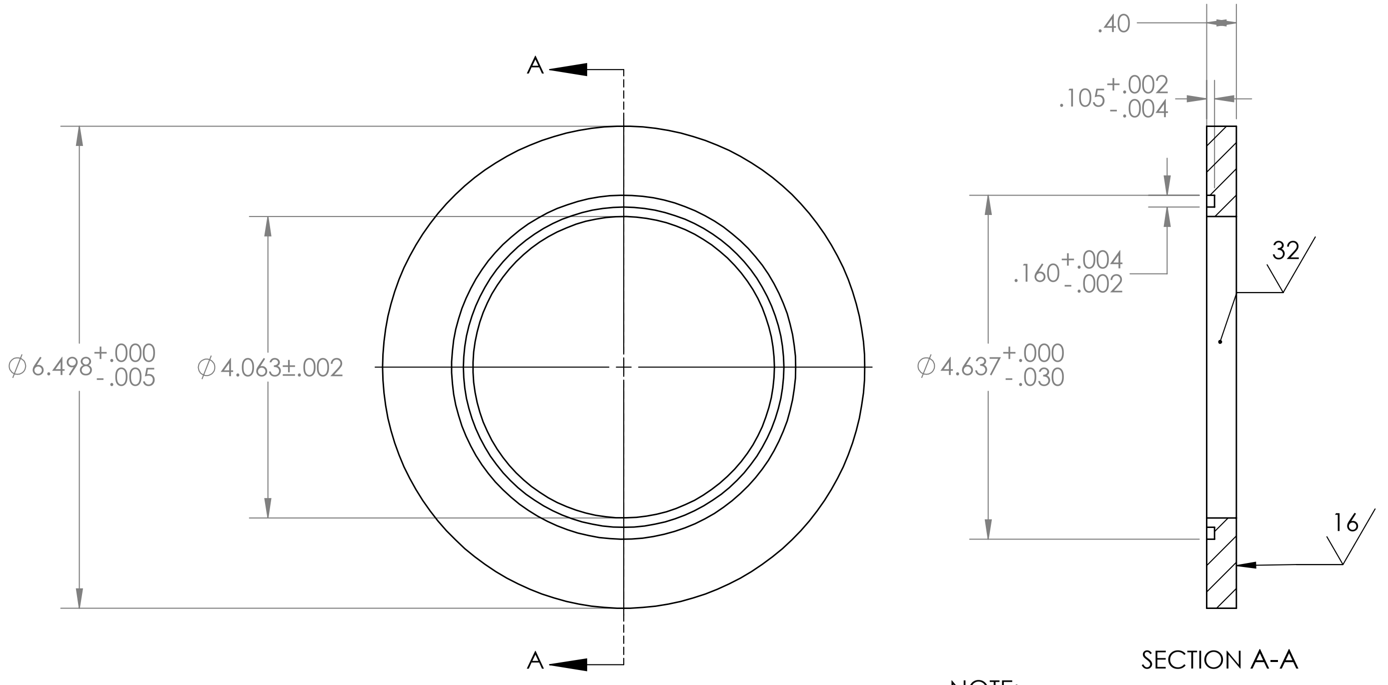

NOTE:
REFERENCE ORingGrooveDetail ON
PAGE 40 FOR SURFACE FINISHES **ONLY**

PROPRIETARY AND CONFIDENTIAL

THE INFORMATION CONTAINED IN THIS DRAWING IS THE SOLE PROPERTY OF UCLA. ANY REPRODUCTION IN PART OR AS A WHOLE WITHOUT THE WRITTEN PERMISSION OF UCLA IS PROHIBITED.

NEXT ASSY
USED ON
APPLICATION

UNLESS OTHERWISE SPECIFIED:
DIMENSIONS ARE IN INCHES
TOLERANCES:
FRACTIONAL ±
ANGULAR: MACH ± BEND ±
TWO PLACE DECIMAL ±.010
THREE PLACE DECIMAL ±.005
INTERPRET GEOMETRIC TOLERANCING PER:
MATERIAL 304 SS
FINISH
DO NOT SCALE DRAWING

	NAME	DATE
DRAWN	F. BENDANA	2/10/17
CHECKED		
ENG APPR.		
MFG APPR.		
Q.A.		

COMMENTS:

UCLA: Laser Spectroscopy & Gas Dynamics Lab

TITLE:

DiaphragmSpacer_C

SIZE A
DWG. NO. 15
REV 002
SCALE: 1:2
SHEET 1 OF 1

SOLIDWORKS Educational Product. For Instructional Use Only

NOTE: MAKE 8.0-4 UNC-2A X 3.0 THREADS
COMPATIBLE WITH BreechCanister_B ON PAGE 25

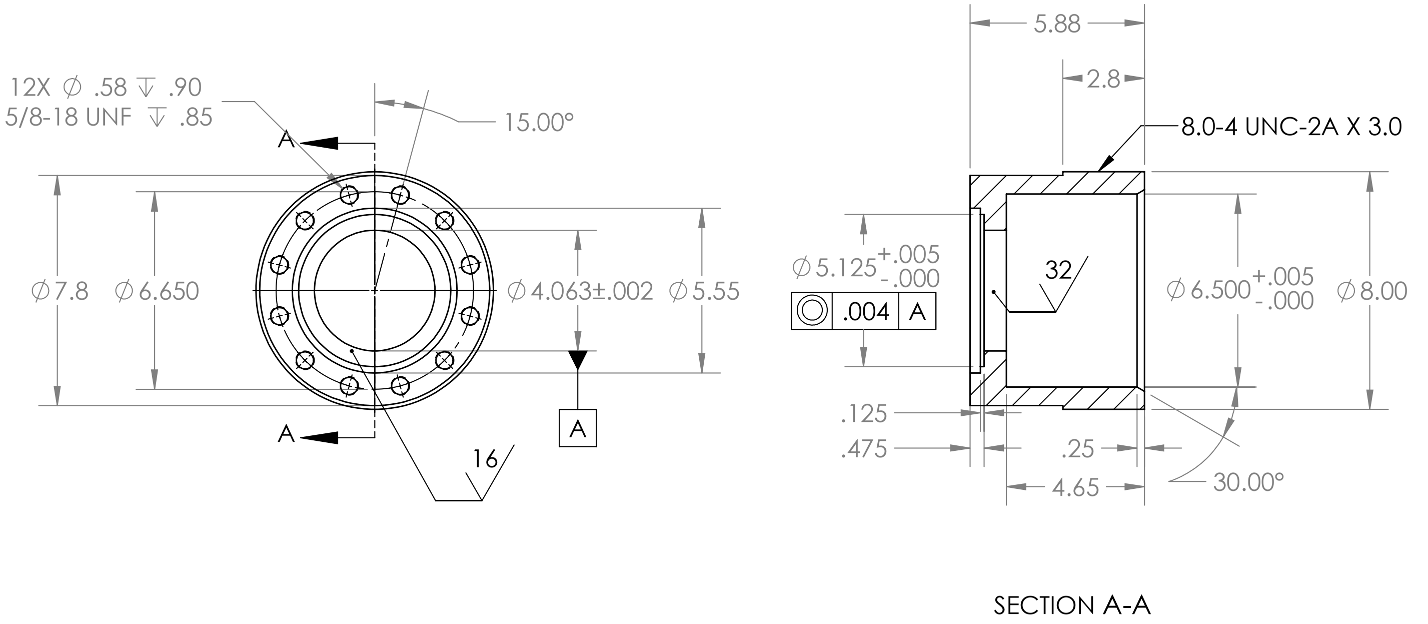

	NAME	DATE
DRAWN	F. BENDANA	2/10/17
CHECKED		
ENG APPR.		
MFG APPR.		
Q.A.		

COMMENTS:

UNLESS OTHERWISE SPECIFIED:
DIMENSIONS ARE IN INCHES
TOLERANCES:
FRACTIONAL ±
ANGULAR: MACH ± BEND ±
ONE PLACE DECIMAL ±.100
TWO PLACE DECIMAL ±.010
THREE PLACE DECIMAL ±.005

INTERPRET GEOMETRIC
TOLERANCING PER:

MATERIAL
304 SS

FINISH

DO NOT SCALE DRAWING

NEXT ASSY USED ON

APPLICATION

PROPRIETARY AND CONFIDENTIAL

THE INFORMATION CONTAINED IN THIS DRAWING IS THE SOLE PROPERTY OF UCLA. ANY REPRODUCTION IN PART OR AS A WHOLE WITHOUT THE WRITTEN PERMISSION OF UCLA IS PROHIBITED.

SOLIDWORKS Educational Product. For Instructional Use Only

UCLA: Laser Spectroscopy & Gas Dynamics Lab

TITLE:

BreechCanister_A

SIZE A
DWG. NO. 16
REV 002
SCALE: 1:5
SHEET 1 OF 1

NOTE: MAKE 8.0-4 UNC-2A X 2.7 THREADS
COMPATIBLE WITH BreechCanister_A ON PAGE 24

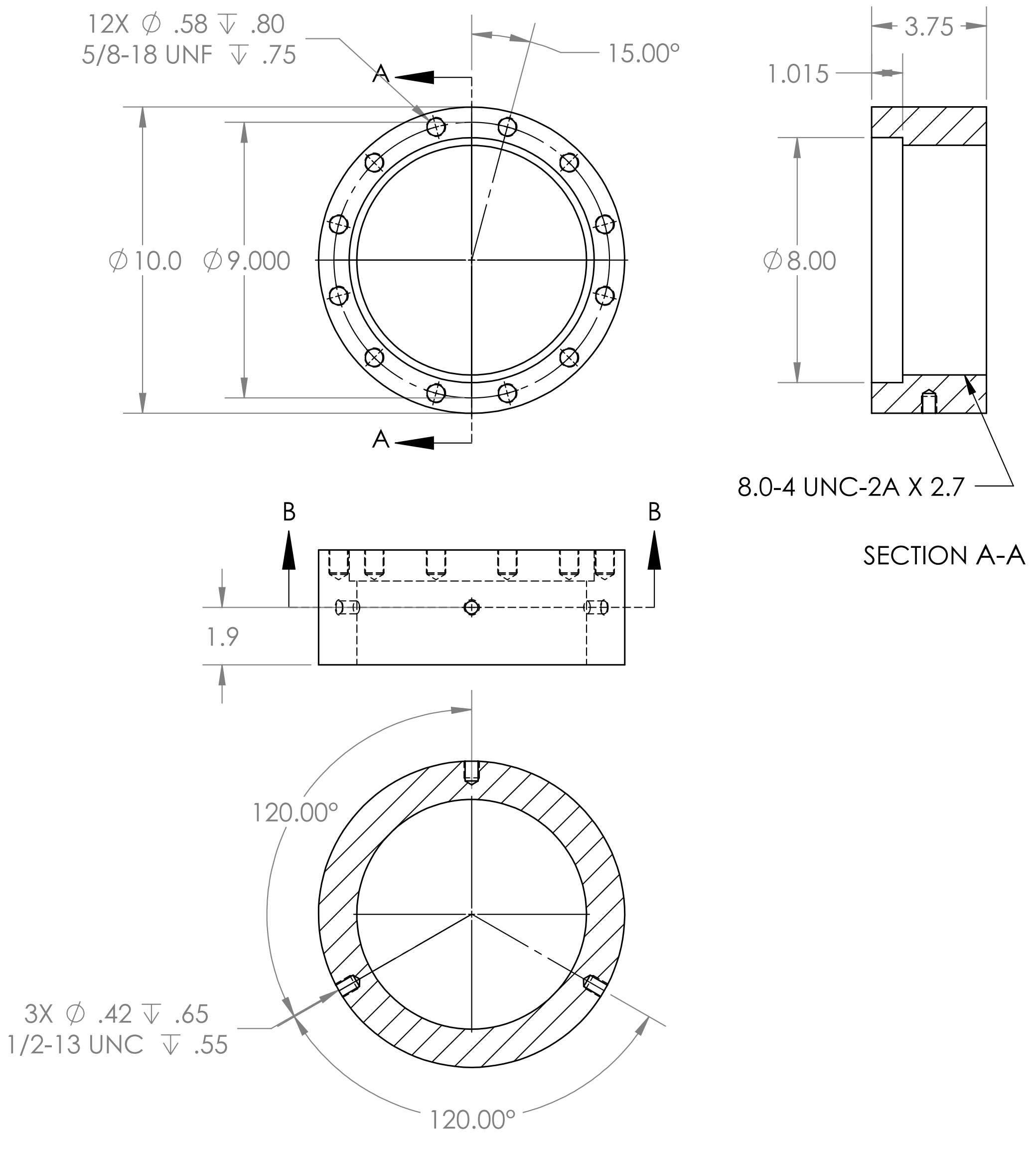

SECTION A-A

SECTION B-B

PROPRIETARY AND CONFIDENTIAL

THE INFORMATION CONTAINED IN THIS DRAWING IS THE SOLE PROPERTY OF UCLA. ANY REPRODUCTION IN PART OR AS A WHOLE WITHOUT THE WRITTEN PERMISSION OF UCLA IS PROHIBITED.

NEXT ASSY USED ON

APPLICATION

DIMENSIONS ARE IN INCHES
TOLERANCES:
FRACTIONAL ±
ANGULAR: MACH ± BEND ±
ONE PLACE DECIMAL ±.100
TWO PLACE DECIMAL ±.010
THREE PLACE DECIMAL ±.005

MATERIAL
304 SS

FINISH

DO NOT SCALE DRAWING

	NAME	DATE
DRAWN	F. BENDANA	2/10/17
CHECKED		
ENG APPR.		
MFG APPR.		
Q.A.		

COMMENTS:

UCLA: Laser Spectroscopy & Gas Dynamics Lab

BreechCanister_B

SIZE A DWG. NO. 17 REV. 002

SCALE:1:5 WEIGHT: SHEET 1 OF 1

SOLIDWORKS Educational Product. For Instructional Use Only

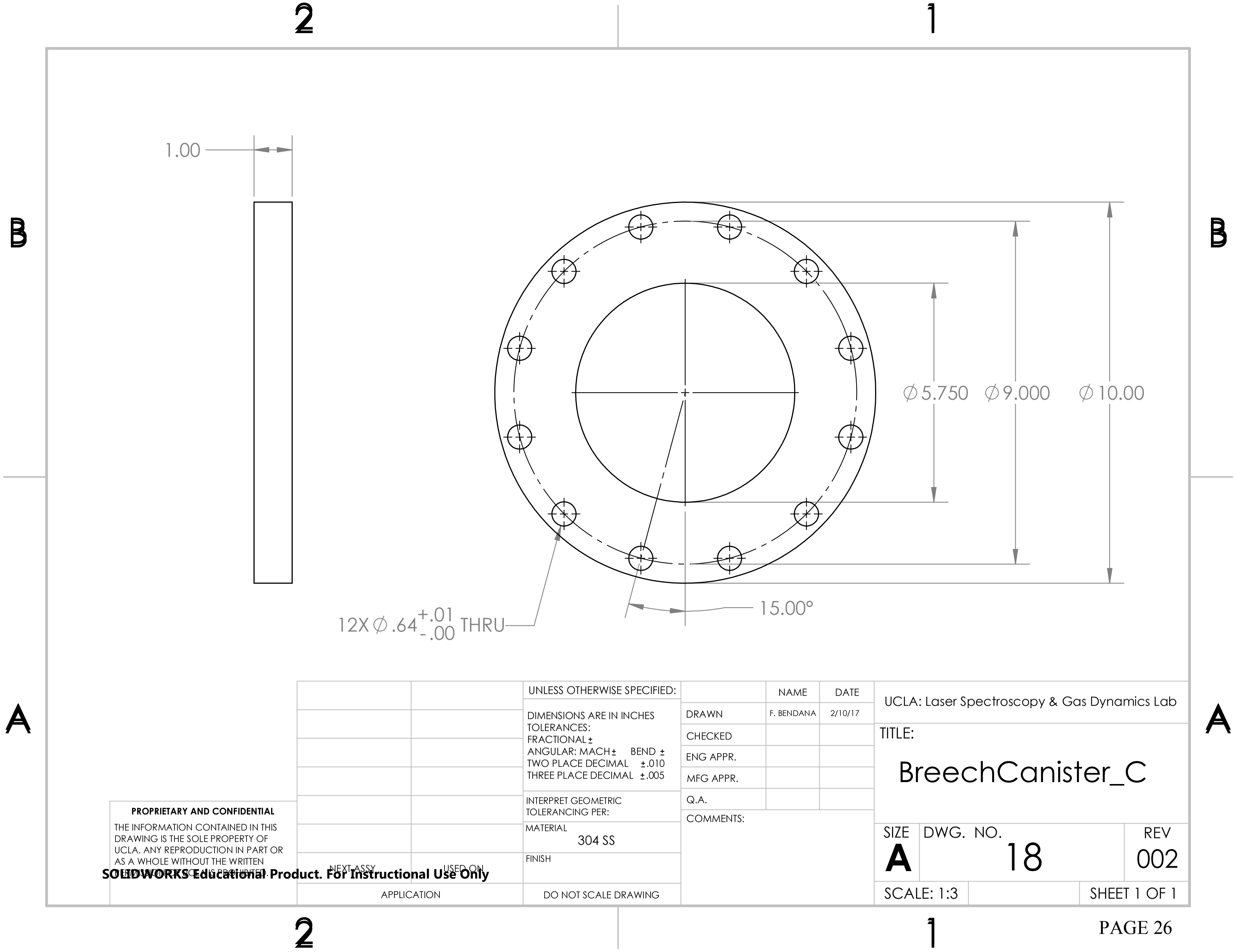
1.00
Ø5.750
Ø9.000
Ø10.00
15.00°
12X Ø.64 +.01 -.00 THRU
UNLESS OTHERWISE SPECIFIED:
DIMENSIONS ARE IN INCHES
TOLERANCES:
FRACTIONAL ±
ANGULAR: MACH ± BEND ±
TWO PLACE DECIMAL ±.010
THREE PLACE DECIMAL ±.005
INTERPRET GEOMETRIC TOLERANCING PER:
MATERIAL
304 SS
FINISH
DO NOT SCALE DRAWING
NEXT ASSY
USED ON
APPLICATION
NAME
DATE
DRAWN
F. BENDANA
2/10/17
CHECKED
ENG APPR.
MFG APPR.
Q.A.
COMMENTS:
UCLA: Laser Spectroscopy & Gas Dynamics Lab
TITLE:
BreechCanister_C
SIZE
A
DWG. NO.
18
REV
002
SCALE: 1:3
SHEET 1 OF 1
PROPRIETARY AND CONFIDENTIAL
THE INFORMATION CONTAINED IN THIS DRAWING IS THE SOLE PROPERTY OF UCLA. ANY REPRODUCTION IN PART OR AS A WHOLE WITHOUT THE WRITTEN
SOLIDWORKS Educational Product. For Instructional Use Only
1
2
A
B

PAGE 26

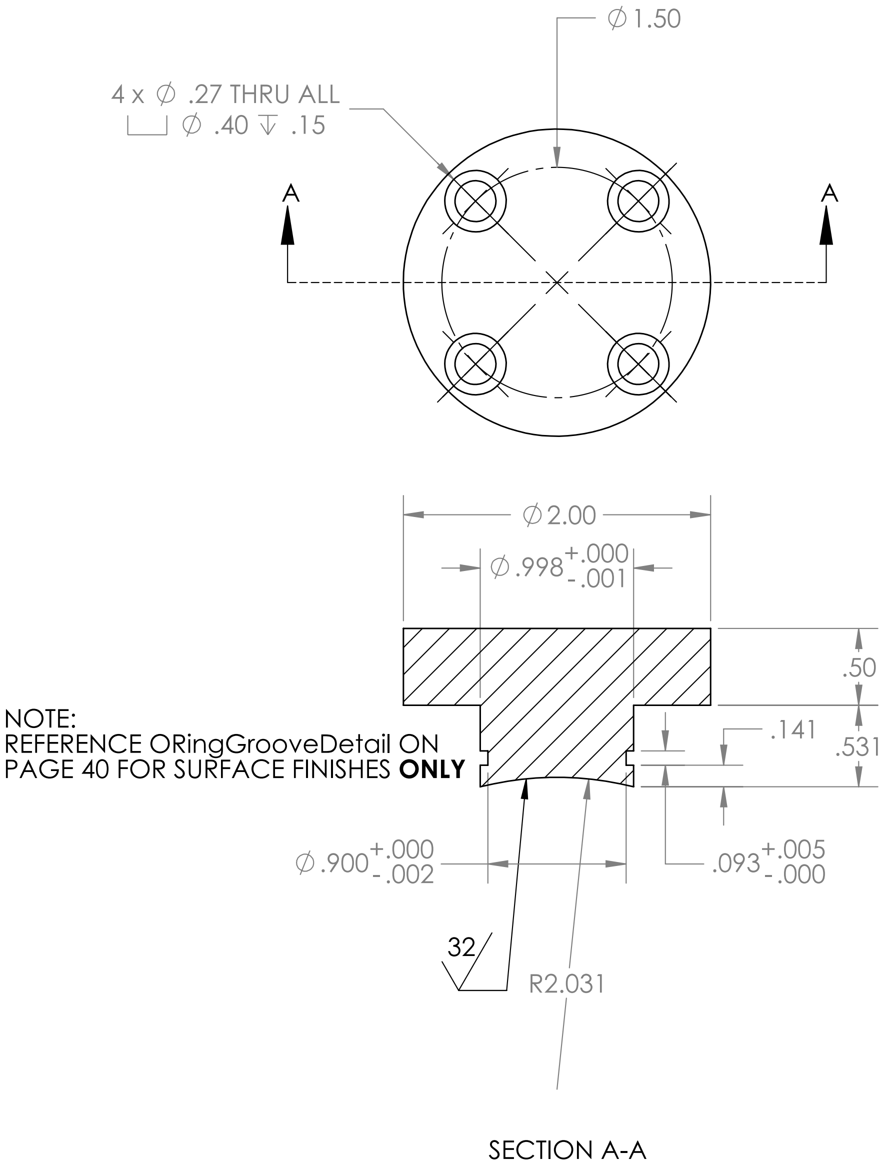

NOTE:
REFERENCE ORingGrooveDetail ON
PAGE 40 FOR SURFACE FINISHES **ONLY**

SECTION A-A

PROPRIETARY AND CONFIDENTIAL

THE INFORMATION CONTAINED IN THIS DRAWING IS THE SOLE PROPERTY OF UCLA. ANY REPRODUCTION IN PART OR AS A WHOLE WITHOUT THE WRITTEN PERMISSION OF UCLA IS PROHIBITED.

NEXT ASSY	USED ON	
APPLICATION		

DIMENSIONS ARE IN INCHES
TOLERANCES:
FRACTIONAL ±
ANGULAR: MACH ± BEND ±
TWO PLACE DECIMAL ±.010
THREE PLACE DECIMAL ±.005

MATERIAL
304 SS

FINISH

DO NOT SCALE DRAWING

	NAME	DATE
DRAWN	F. BENDANA	2/10/17
CHECKED		
ENG APPR.		
MFG APPR.		
Q.A.		

COMMENTS:

UCLA: Laser Spectroscopy & Gas Dynamics Lab

PortPlug_A

SIZE	DWG. NO.	REV.
A	19	002

SCALE:1:1 WEIGHT: SHEET 1 OF 1

SOLIDWORKS Educational Product. For Instructional Use Only

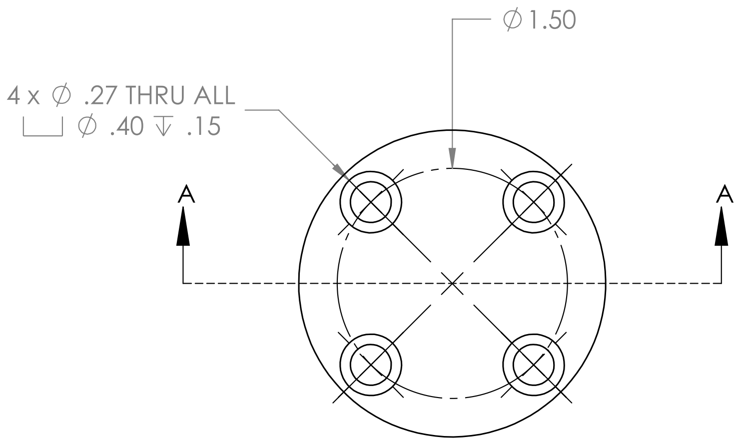

NOTE:
REFERENCE ORingGrooveDetail ON
PAGE 40 FOR SURFACE FINISHES **ONLY**

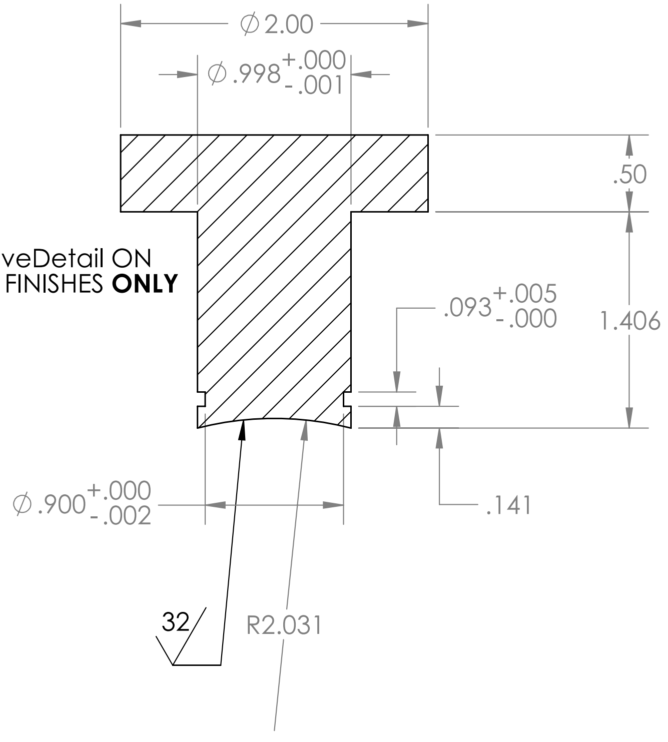

SECTION A-A

PROPRIETARY AND CONFIDENTIAL

THE INFORMATION CONTAINED IN THIS DRAWING IS THE SOLE PROPERTY OF UCLA. ANY REPRODUCTION IN PART OR AS A WHOLE WITHOUT THE WRITTEN PERMISSION OF UCLA IS PROHIBITED.

NEXT ASSY | USED ON

APPLICATION

DIMENSIONS ARE IN INCHES
TOLERANCES:
FRACTIONAL ±
ANGULAR: MACH ± BEND ±
TWO PLACE DECIMAL ±.010
THREE PLACE DECIMAL ±.005

MATERIAL
304 SS

FINISH

DO NOT SCALE DRAWING

	NAME	DATE
DRAWN	F. BENDANA	2/10/17
CHECKED		
ENG APPR.		
MFG APPR.		
Q.A.		

COMMENTS:

UCLA: Laser Spectroscopy & Gas Dynamics Lab

PortPlug_B

SIZE A | DWG. NO. 20 | REV. 002

SCALE:1:1 | WEIGHT: | SHEET 1 OF 1

SOLIDWORKS Educational Product. For Instructional Use Only

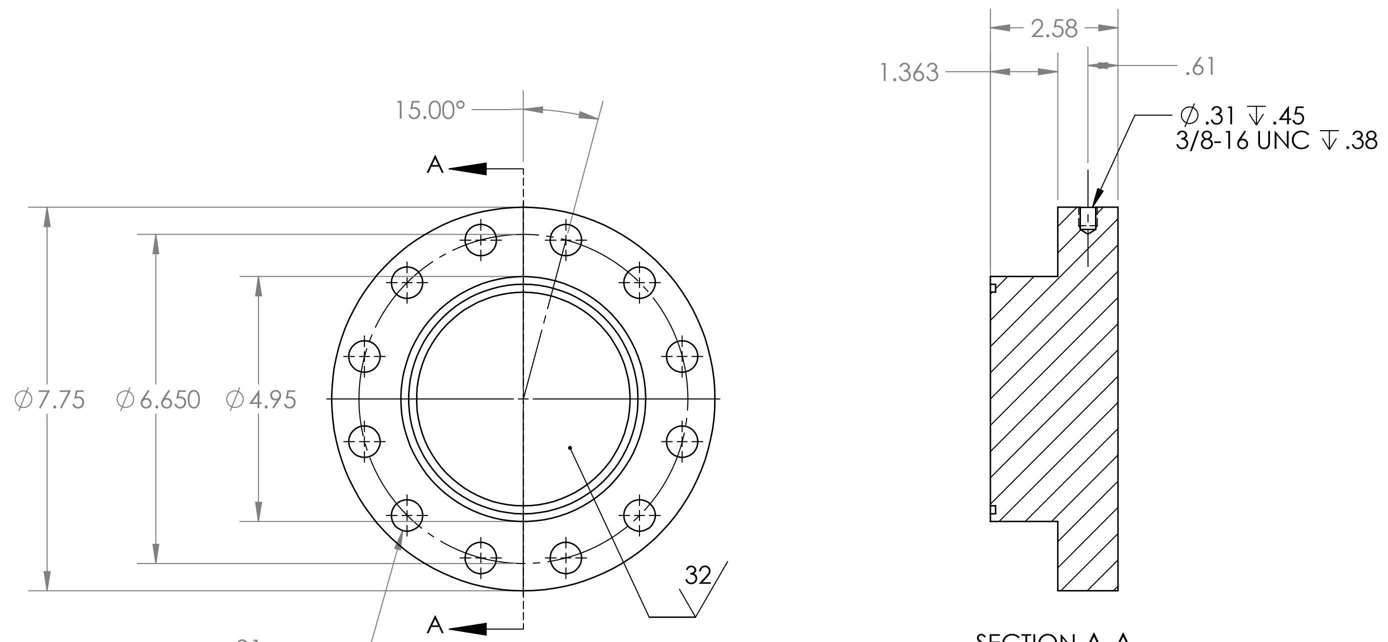

NOTE:
REFERENCE ORingGrooveDetail ON
PAGE 40 FOR SURFACE FINISHES & DIMENSIONS

PROPRIETARY AND CONFIDENTIAL

THE INFORMATION CONTAINED IN THIS DRAWING IS THE SOLE PROPERTY OF UCLA. ANY REPRODUCTION IN PART OR AS A WHOLE WITHOUT THE WRITTEN PERMISSION OF UCLA IS PROHIBITED.

SOLIDWORKS Educational Product. For Instructional Use Only

NEXT ASSY
USED ON
APPLICATION

UNLESS OTHERWISE SPECIFIED:
DIMENSIONS ARE IN INCHES
TOLERANCES:
FRACTIONAL ±
ANGULAR: MACH ± BEND ±
TWO PLACE DECIMAL ±.010
THREE PLACE DECIMAL ±.005
INTERPRET GEOMETRIC TOLERANCING PER:
MATERIAL 304 SS
FINISH
DO NOT SCALE DRAWING

	NAME	DATE
DRAWN	F. BENDANA	2/10/17
CHECKED		
ENG APPR.		
MFG APPR.		
Q.A.		

COMMENTS:

UCLA: Laser Spectroscopy & Gas Dynamics Lab
TITLE:
EndCap_A
SIZE A
DWG. NO. 21
REV 002
SCALE: 1:3
SHEET 1 OF 1

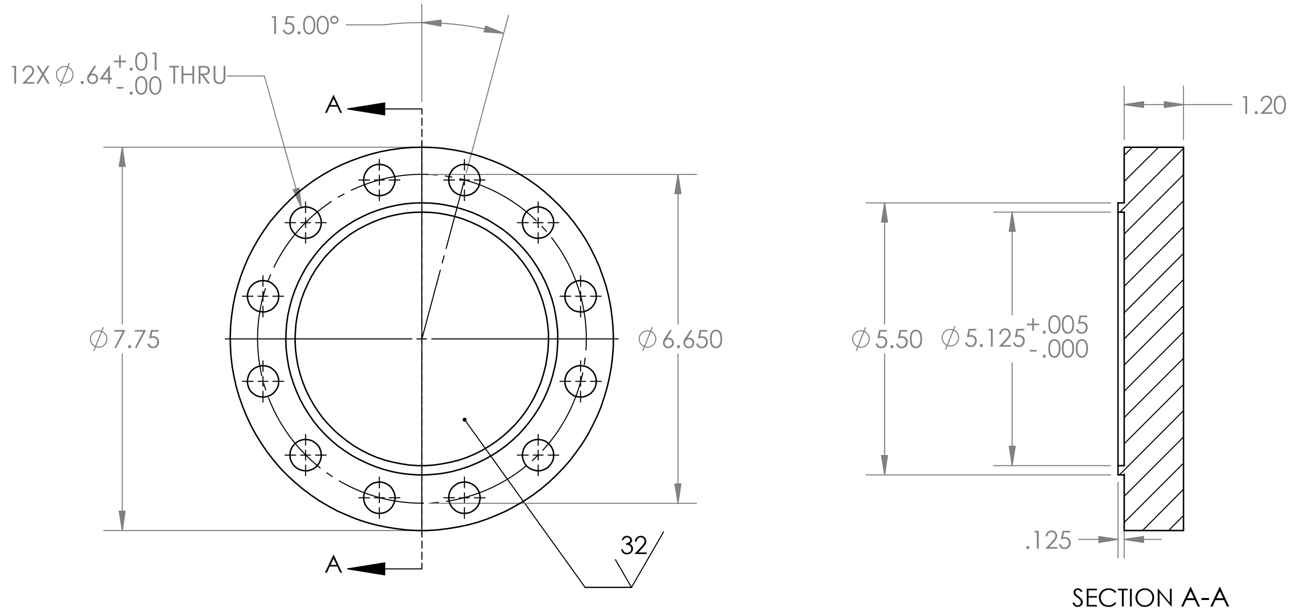

SECTION A-A

UNLESS OTHERWISE SPECIFIED:

DIMENSIONS ARE IN INCHES
TOLERANCES:
FRACTIONAL ±
ANGULAR: MACH ± BEND ±
TWO PLACE DECIMAL ±.010
THREE PLACE DECIMAL ±.005

INTERPRET GEOMETRIC TOLERANCING PER:

MATERIAL 304 SS

FINISH

DO NOT SCALE DRAWING

	NAME	DATE
DRAWN	F. BENDANA	2/10/17
CHECKED		
ENG APPR.		
MFG APPR.		
Q.A.		

COMMENTS:

UCLA: Laser Spectroscopy & Gas Dynamics Lab

TITLE:

EndCap_B

SIZE A
DWG. NO. 22
REV 002
SCALE: 1:3
SHEET 1 OF 2

NEXT ASSY
USED ON
APPLICATION

PROPRIETARY AND CONFIDENTIAL

THE INFORMATION CONTAINED IN THIS DRAWING IS THE SOLE PROPERTY OF UCLA. ANY REPRODUCTION IN PART OR AS A WHOLE WITHOUT THE WRITTEN PERMISSION OF UCLA IS PROHIBITED.

SOLIDWORKS Educational Product. For Instructional Use Only

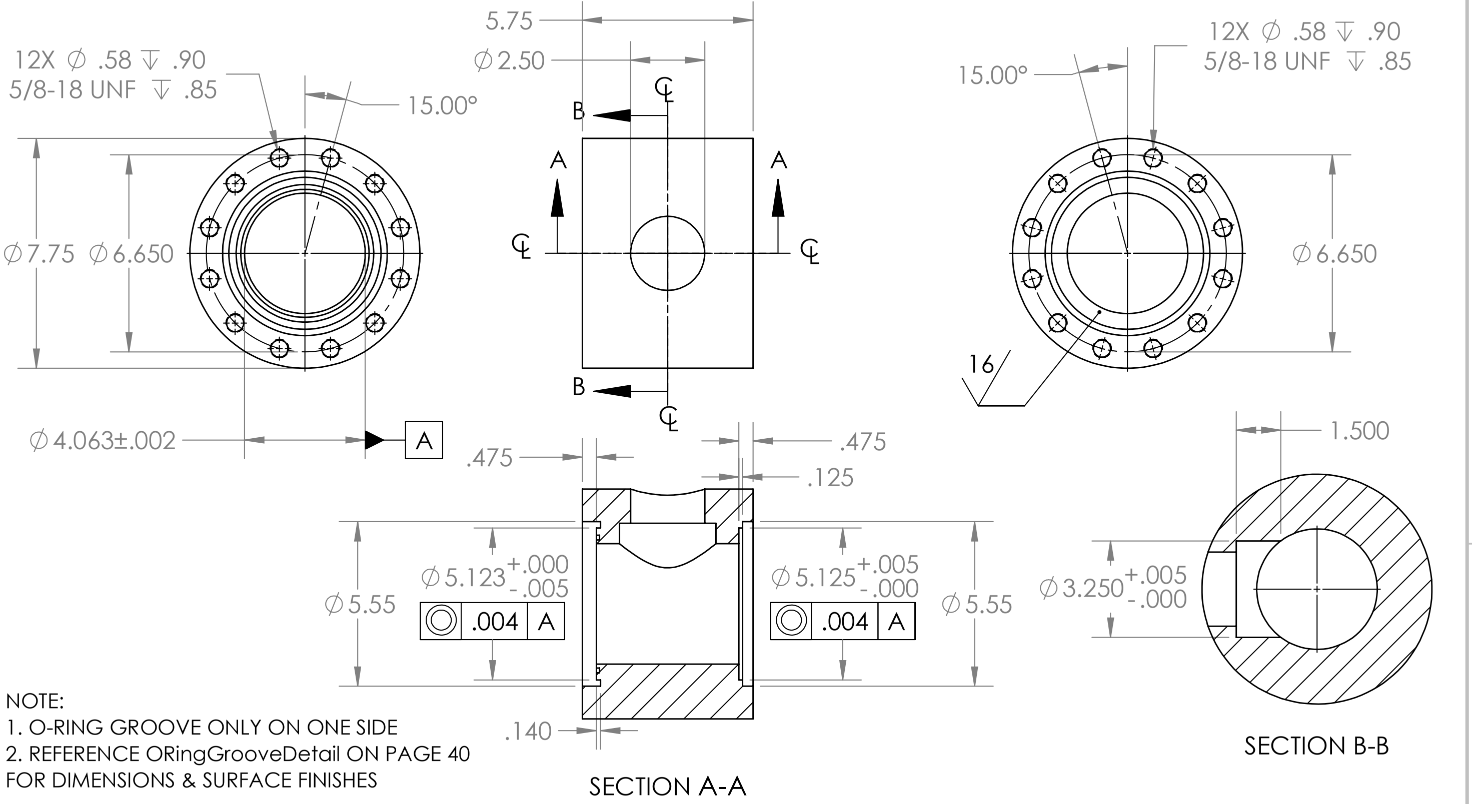

NOTE:
1. O-RING GROOVE ONLY ON ONE SIDE
2. REFERENCE ORingGrooveDetail ON PAGE 40
FOR DIMENSIONS & SURFACE FINISHES

UNLESS OTHERWISE SPECIFIED:		NAME	DATE
DIMENSIONS ARE IN INCHES TOLERANCES: FRACTIONAL ± ANGULAR: MACH ± BEND ± TWO PLACE DECIMAL ±.010 THREE PLACE DECIMAL ±.005	DRAWN	F. BENDANA	2/10/17
	CHECKED		
	ENG APPR.		
	MFG APPR.		
INTERPRET GEOMETRIC TOLERANCING PER:	Q.A.		
MATERIAL 304 SS	COMMENTS:		
FINISH			
DO NOT SCALE DRAWING			

NEXT ASSY
USED ON
APPLICATION

UCLA: Laser Spectroscopy & Gas Dynamics Lab

TITLE:

PoppetValveHousing

SIZE A
DWG. NO. 23
REV 002
SCALE: 1:5
SHEET 1 OF 1

PROPRIETARY AND CONFIDENTIAL

THE INFORMATION CONTAINED IN THIS DRAWING IS THE SOLE PROPERTY OF UCLA. ANY REPRODUCTION IN PART OR AS A WHOLE WITHOUT THE WRITTEN PERMISSION OF UCLA IS PROHIBITED.

SOLIDWORKS Educational Product. For Instructional Use Only

NOTE: TUBE WITH WELDED FLANGE WILL BE
PROVIDED BY MDC VACUUM PRODUCTS, LLC

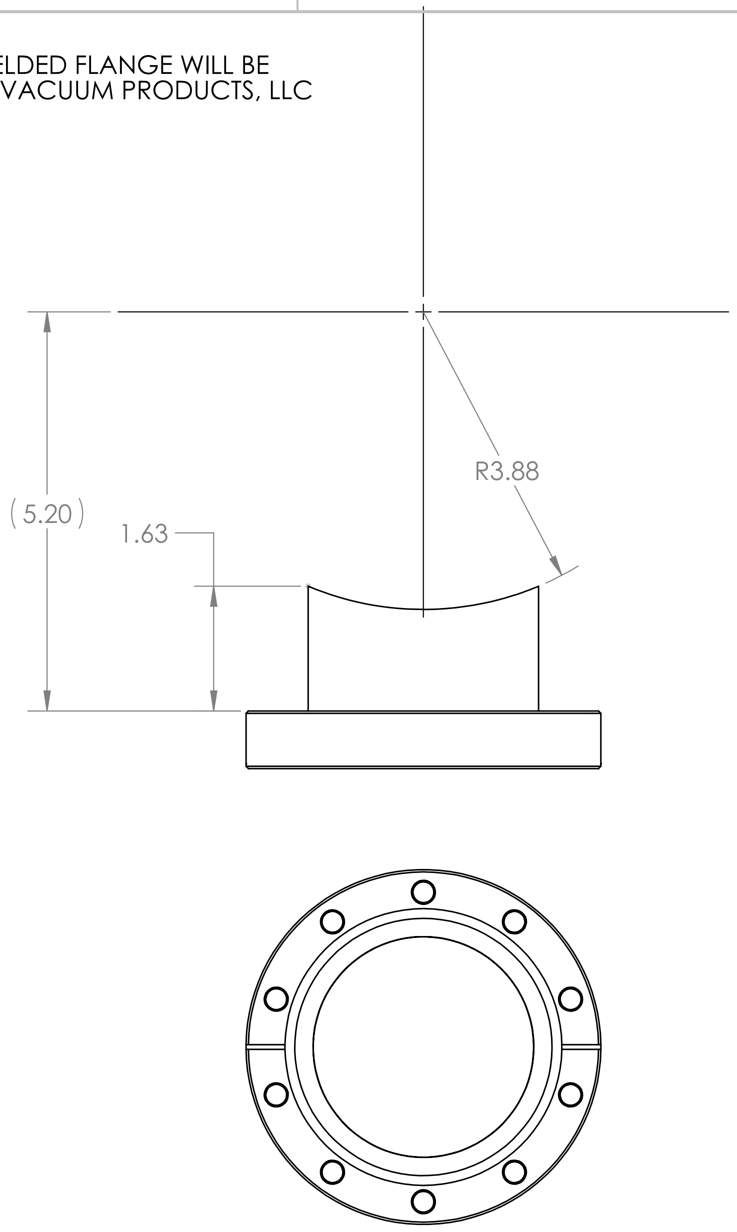

PROPRIETARY AND CONFIDENTIAL

THE INFORMATION CONTAINED IN THIS DRAWING IS THE SOLE PROPERTY OF UCLA. ANY REPRODUCTION IN PART OR AS A WHOLE WITHOUT THE WRITTEN PERMISSION OF UCLA IS PROHIBITED.

NEXT ASSY	USED ON
APPLICATION	

DIMENSIONS ARE IN INCHES
TOLERANCES:
FRACTIONAL ±
ANGULAR: MACH ± BEND ±
TWO PLACE DECIMAL ±.010
THREE PLACE DECIMAL ±.005

MATERIAL
304 SS

FINISH

DO NOT SCALE DRAWING

	NAME	DATE
DRAWN	F. BENDANA	2/10/17
CHECKED		
ENG APPR.		
MFG APPR.		
Q.A.		
COMMENTS:		

UCLA: Laser Spectroscopy & Gas Dynamics Lab

PoppetValveBoss

SIZE	DWG. NO.	REV.
A	24	002

SCALE:1:2 WEIGHT: SHEET 1 OF 1

SOLIDWORKS Educational Product. For Instructional Use Only

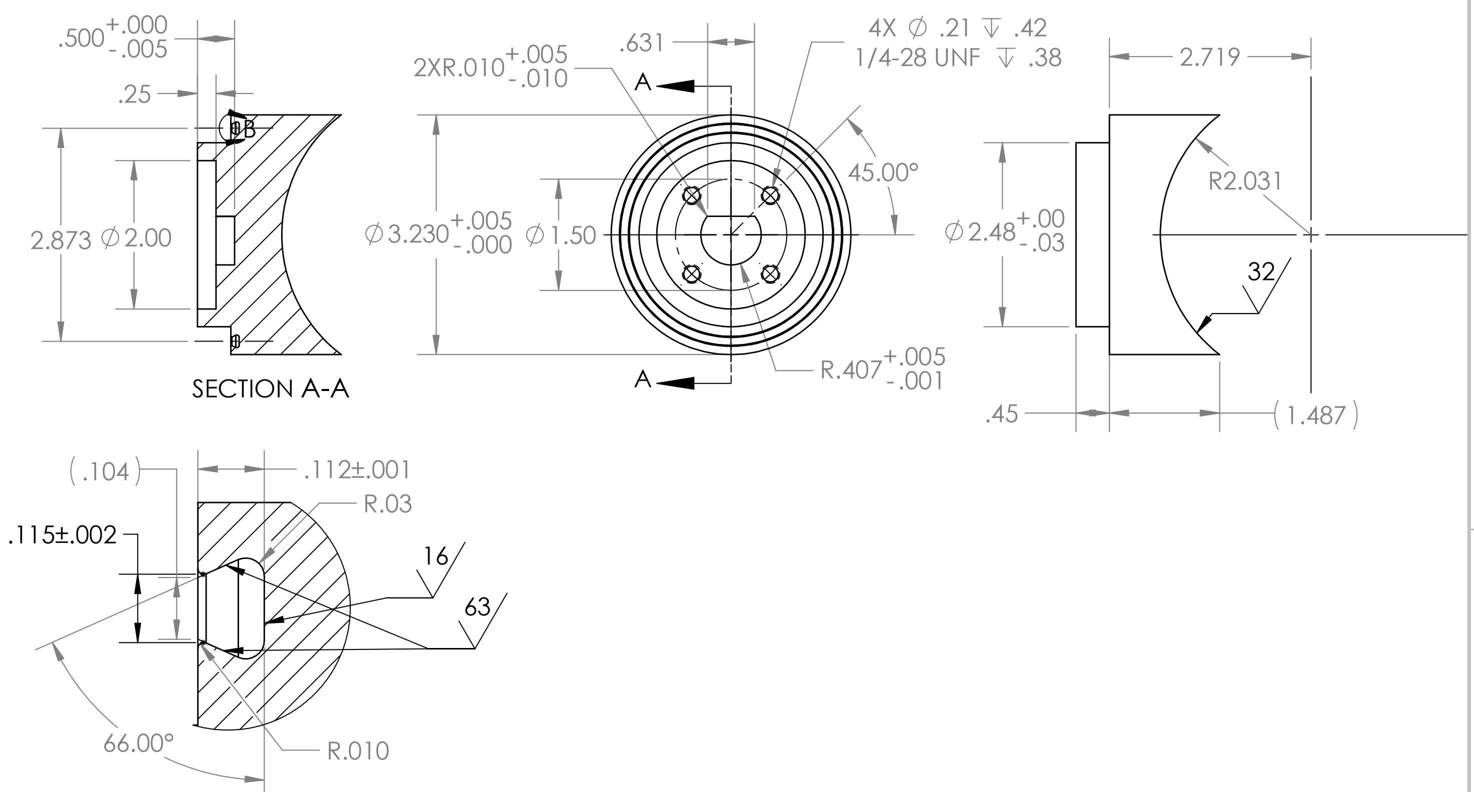

DETAIL B
SCALE 4 : 1

PROPRIETARY AND CONFIDENTIAL

THE INFORMATION CONTAINED IN THIS DRAWING IS THE SOLE PROPERTY OF UCLA. ANY REPRODUCTION IN PART OR AS A WHOLE WITHOUT THE WRITTEN PERMISSION OF UCLA IS PROHIBITED.

SOLIDWORKS Educational Product. For Instructional Use Only

NEXT ASSY
USED ON
APPLICATION

UNLESS OTHERWISE SPECIFIED:
DIMENSIONS ARE IN INCHES
TOLERANCES:
FRACTIONAL ±
ANGULAR: MACH ± BEND ±
TWO PLACE DECIMAL ±.010
THREE PLACE DECIMAL ±.005
INTERPRET GEOMETRIC TOLERANCING PER:
MATERIAL
304 SS
FINISH
DO NOT SCALE DRAWING

	NAME	DATE
DRAWN	F. BENDANA	2/10/17
CHECKED		
ENG APPR.		
MFG APPR.		
Q.A.		

COMMENTS:

UCLA: Laser Spectroscopy & Gas Dynamics Lab

TITLE:

Piston

SIZE A
DWG. NO. 25
REV 002
SCALE: 1:2
SHEET 1 OF 1

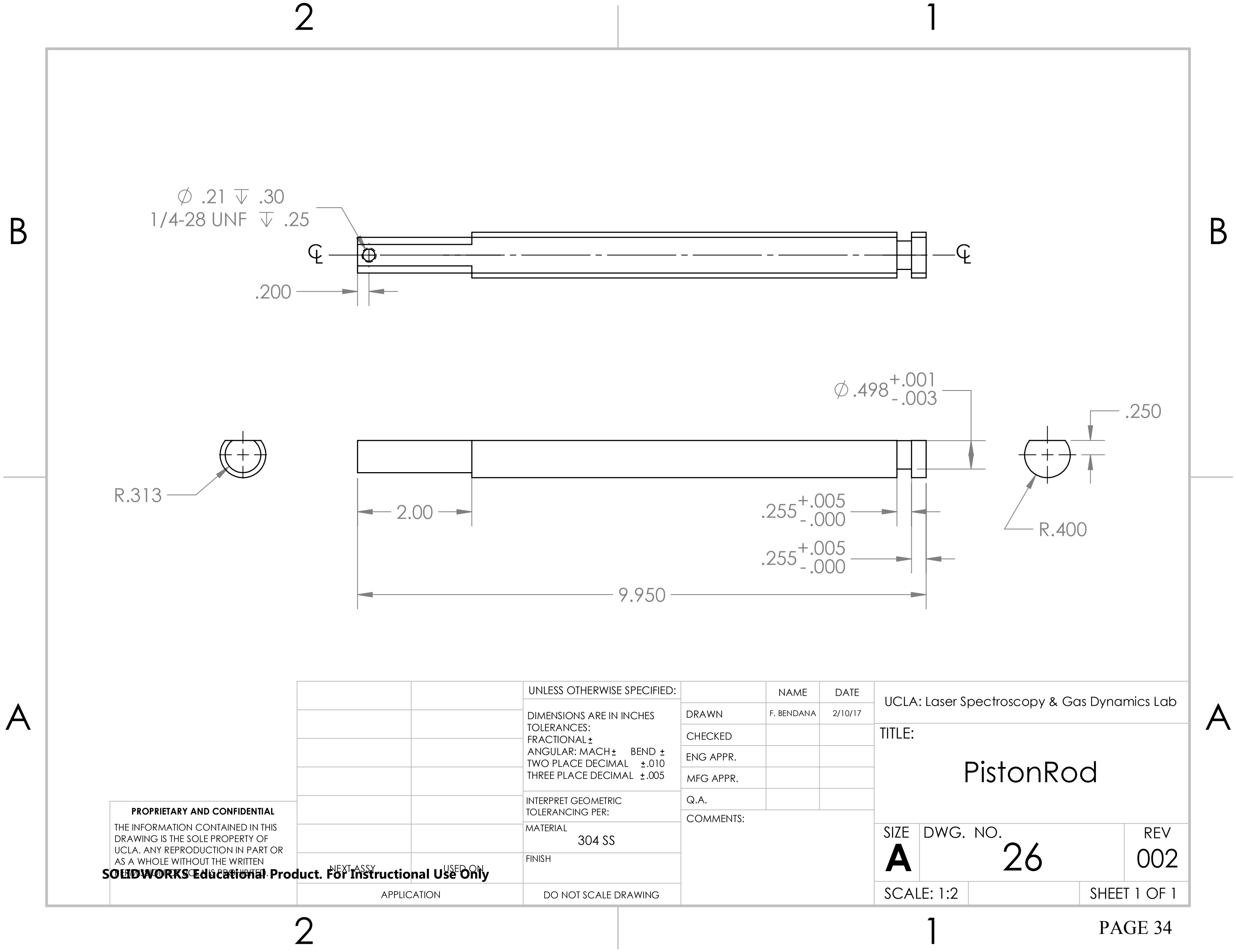

	NAME	DATE
DRAWN	F. BENDANA	2/10/17
CHECKED		
ENG APPR.		
MFG APPR.		
Q.A.		

COMMENTS:

UNLESS OTHERWISE SPECIFIED:

DIMENSIONS ARE IN INCHES
TOLERANCES:
FRACTIONAL ±
ANGULAR: MACH ± BEND ±
TWO PLACE DECIMAL ±.010
THREE PLACE DECIMAL ±.005

INTERPRET GEOMETRIC
TOLERANCING PER:

MATERIAL
304 SS

FINISH

DO NOT SCALE DRAWING

NEXT ASSY
USED ON
APPLICATION

UCLA: Laser Spectroscopy & Gas Dynamics Lab

TITLE:

PistonRod

SIZE A
DWG. NO. 26
REV 002

SCALE: 1:2
SHEET 1 OF 1

PROPRIETARY AND CONFIDENTIAL

THE INFORMATION CONTAINED IN THIS DRAWING IS THE SOLE PROPERTY OF UCLA. ANY REPRODUCTION IN PART OR AS A WHOLE WITHOUT THE WRITTEN PERMISSION OF UCLA IS PROHIBITED.

SOLIDWORKS Educational Product. For Instructional Use Only

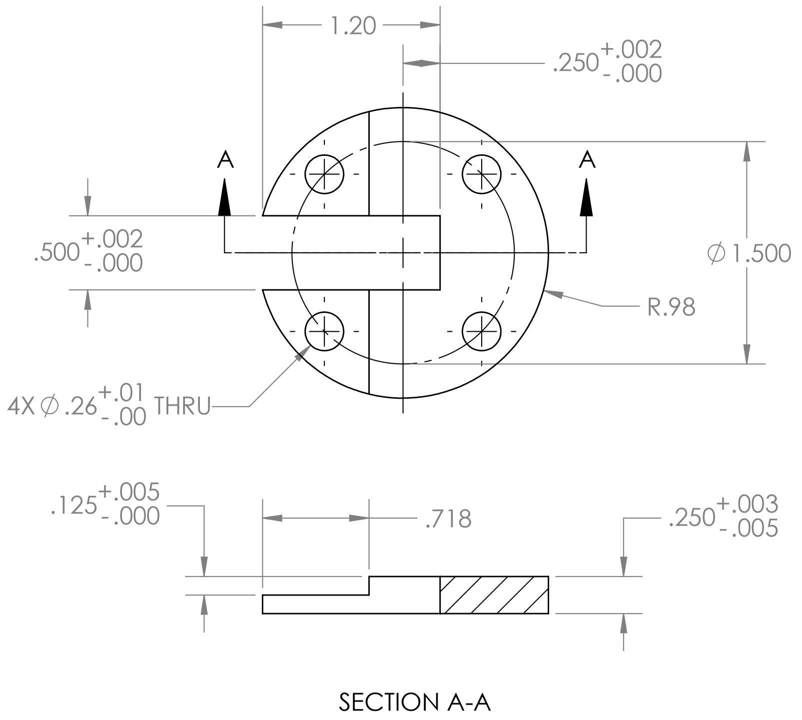

UNLESS OTHERWISE SPECIFIED:		NAME	DATE	UCLA: Laser Spectroscopy & Gas Dynamics Lab	
DIMENSIONS ARE IN INCHES TOLERANCES: FRACTIONAL ± ANGULAR: MACH ± BEND ± TWO PLACE DECIMAL ±.010 THREE PLACE DECIMAL ±.005	DRAWN	F. BENDANA	2/10/17	TITLE:	
	CHECKED			RodClip_A	
	ENG APPR.				
	MFG APPR.				
INTERPRET GEOMETRIC TOLERANCING PER:	Q.A.				
MATERIAL 304 SS	COMMENTS:			SIZE A DWG. NO. 27	REV 002
FINISH					
DO NOT SCALE DRAWING				SCALE: 1:1	SHEET 1 OF 1

NEXT ASSY | USED ON

APPLICATION

PROPRIETARY AND CONFIDENTIAL

THE INFORMATION CONTAINED IN THIS DRAWING IS THE SOLE PROPERTY OF UCLA. ANY REPRODUCTION IN PART OR AS A WHOLE WITHOUT THE WRITTEN PERMISSION OF UCLA IS PROHIBITED.

SOLIDWORKS Educational Product. For Instructional Use Only

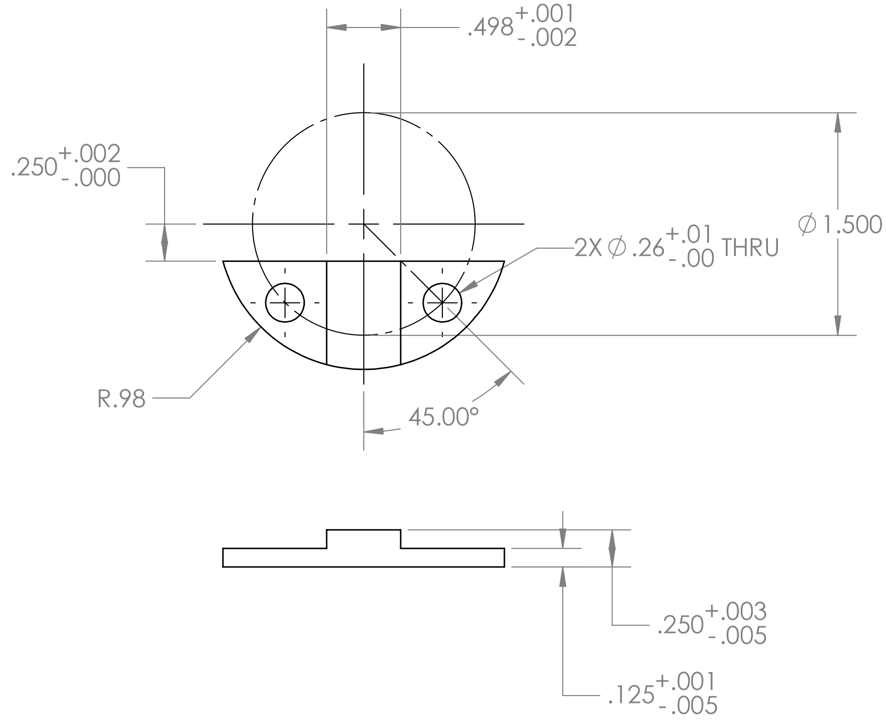

PROPRIETARY AND CONFIDENTIAL

THE INFORMATION CONTAINED IN THIS DRAWING IS THE SOLE PROPERTY OF UCLA. ANY REPRODUCTION IN PART OR AS A WHOLE WITHOUT THE WRITTEN PERMISSION OF UCLA IS PROHIBITED.

NEXT ASSY | USED ON

APPLICATION

UNLESS OTHERWISE SPECIFIED:
DIMENSIONS ARE IN INCHES
TOLERANCES:
FRACTIONAL ±
ANGULAR: MACH ± BEND ±
TWO PLACE DECIMAL ±.010
THREE PLACE DECIMAL ±.005

INTERPRET GEOMETRIC TOLERANCING PER:

MATERIAL
304 SS

FINISH

DO NOT SCALE DRAWING

	NAME	DATE
DRAWN	F. BENDANA	2/10/17
CHECKED		
ENG APPR.		
MFG APPR.		
Q.A.		

COMMENTS:

UCLA: Laser Spectroscopy & Gas Dynamics Lab

TITLE:
RodClip_B

SIZE A | DWG. NO. 28 | REV 002

SCALE: 1:1 | SHEET 1 OF 1

SOLIDWORKS Educational Product. For Instructional Use Only

NOTE: BLANK FLANGE WILL BE PROVIDED BY
MDC VACUUM, LLC

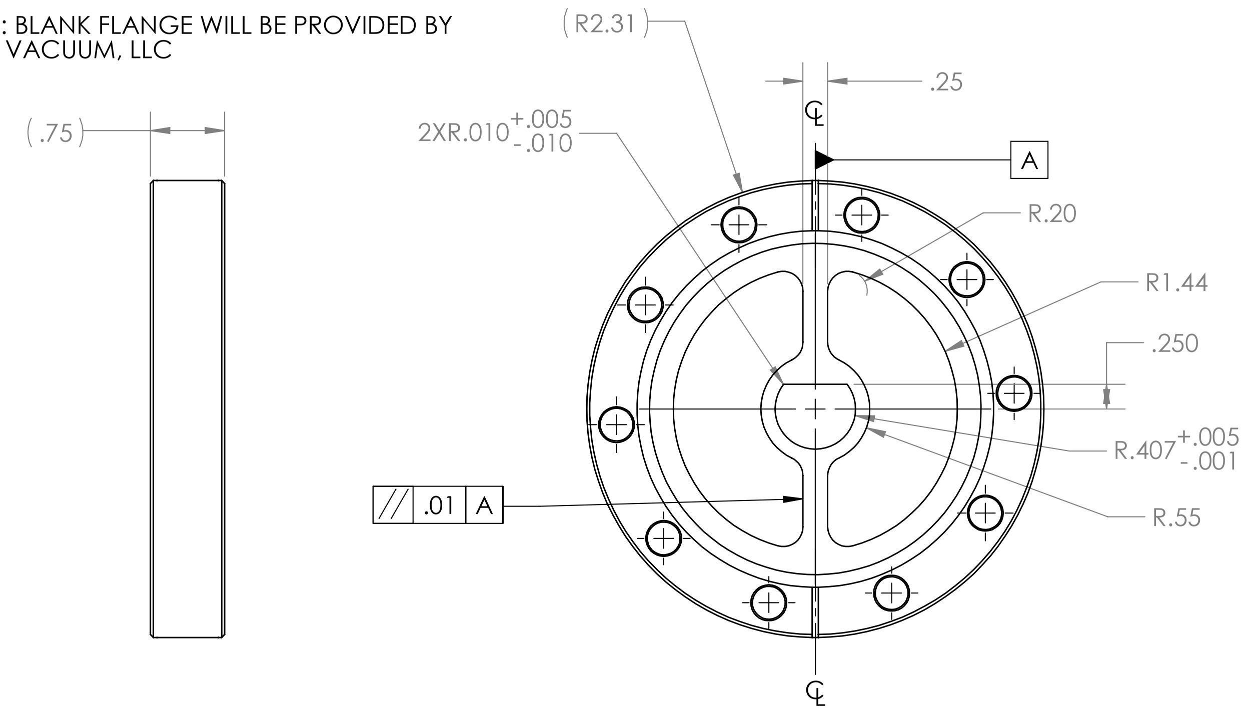

UNLESS OTHERWISE SPECIFIED:	NAME	DATE
DRAWN	F. BENDANA	2/10/17
CHECKED		
ENG APPR.		
MFG APPR.		
Q.A.		
COMMENTS:		

DIMENSIONS ARE IN INCHES
TOLERANCES:
FRACTIONAL ±
ANGULAR: MACH ± BEND ±
TWO PLACE DECIMAL ±.010
THREE PLACE DECIMAL ±.005

INTERPRET GEOMETRIC TOLERANCING PER:

MATERIAL
304 SS

FINISH

DO NOT SCALE DRAWING

NEXT ASSY USED ON

APPLICATION

UCLA: Laser Spectroscopy & Gas Dynamics Lab

TITLE:

PistonGuide

SIZE A DWG. NO. 29 REV 002

SCALE: 2:3 SHEET 1 OF 1

PROPRIETARY AND CONFIDENTIAL

THE INFORMATION CONTAINED IN THIS DRAWING IS THE SOLE PROPERTY OF UCLA. ANY REPRODUCTION IN PART OR AS A WHOLE WITHOUT THE WRITTEN PERMISSION OF UCLA IS PROHIBITED.

SOLIDWORKS Educational Product. For Instructional Use Only

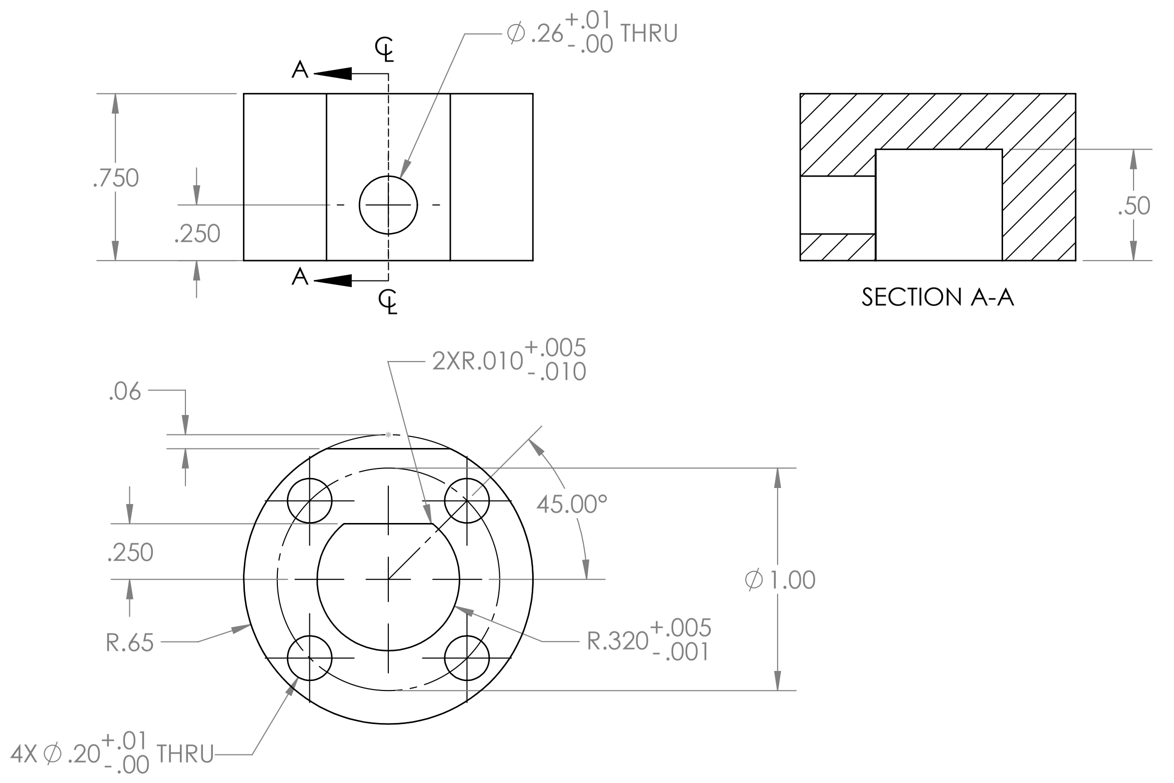

UNLESS OTHERWISE SPECIFIED:

DIMENSIONS ARE IN INCHES
TOLERANCES:
FRACTIONAL ±
ANGULAR: MACH ± BEND ±
TWO PLACE DECIMAL ±.010
THREE PLACE DECIMAL ±.005

INTERPRET GEOMETRIC
TOLERANCING PER:

MATERIAL
304 SS

FINISH

DO NOT SCALE DRAWING

NEXT ASSY
USED ON
APPLICATION

	NAME	DATE
DRAWN	F. BENDANA	2/10/17
CHECKED		
ENG APPR.		
MFG APPR.		
Q.A.		

COMMENTS:

UCLA: Laser Spectroscopy & Gas Dynamics Lab

TITLE:

LinearActuatorAdapter

SIZE A
DWG. NO. 30
REV 002
SCALE: 3:2
SHEET 1 OF 1

PROPRIETARY AND CONFIDENTIAL

THE INFORMATION CONTAINED IN THIS DRAWING IS THE SOLE PROPERTY OF UCLA. ANY REPRODUCTION IN PART OR AS A WHOLE WITHOUT THE WRITTEN PERMISSION OF UCLA IS PROHIBITED.

SOLIDWORKS Educational Product. For Instructional Use Only

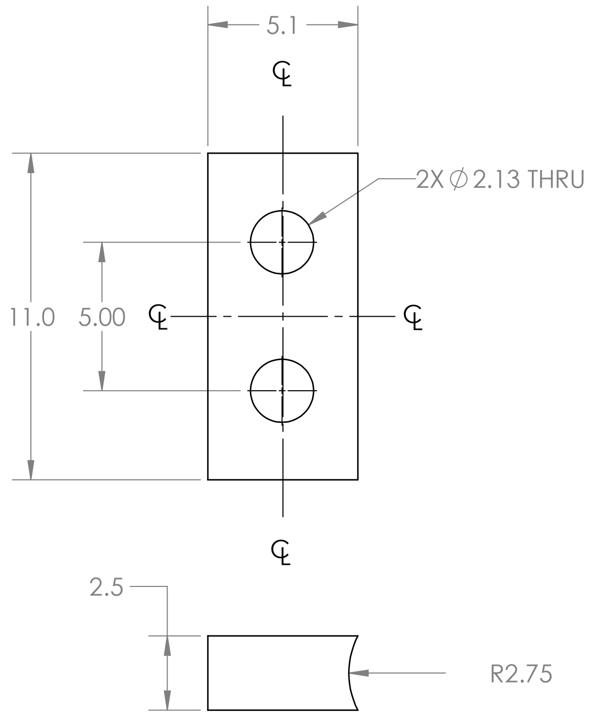

PROPRIETARY AND CONFIDENTIAL

THE INFORMATION CONTAINED IN THIS DRAWING IS THE SOLE PROPERTY OF UCLA. ANY REPRODUCTION IN PART OR AS A WHOLE WITHOUT THE WRITTEN PERMISSION OF UCLA IS PROHIBITED.

SOLIDWORKS Educational Product. For Instructional Use Only

NEXT ASSY	USED ON
APPLICATION	

UNLESS OTHERWISE SPECIFIED:
DIMENSIONS ARE IN INCHES
TOLERANCES:
FRACTIONAL ±
ANGULAR: MACH ± BEND ±
ONE PLACE DECIMAL ±.100
TWO PLACE DECIMAL ±.010
THREE PLACE DECIMAL ±.005

INTERPRET GEOMETRIC TOLERANCING PER:

MATERIAL: 304 SS

FINISH

DO NOT SCALE DRAWING

	NAME	DATE
DRAWN	F. BENDANA	2/10/17
CHECKED		
ENG APPR.		
MFG APPR.		
Q.A.		

COMMENTS:

UCLA: Laser Spectroscopy & Gas Dynamics Lab

TITLE:

InertialMassAttachement_A

SIZE	DWG. NO.	REV
A	31	002

SCALE: 1:5 SHEET 1 OF 1

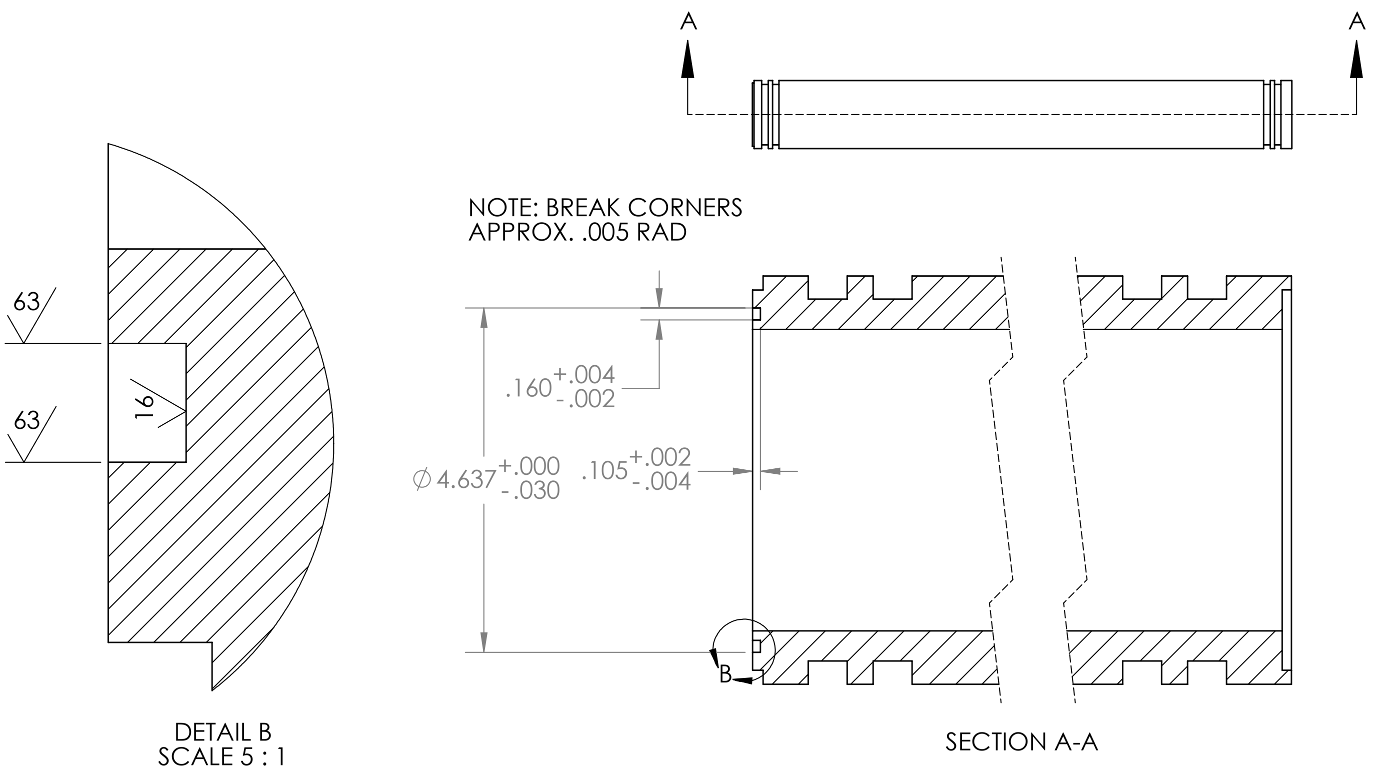

UNLESS OTHERWISE SPECIFIED:
DIMENSIONS ARE IN INCHES
TOLERANCES:
FRACTIONAL ±
ANGULAR: MACH ± BEND ±
ONE PLACE DECIMAL ±.100
TWO PLACE DECIMAL ±.010
THREE PLACE DECIMAL ±.005

INTERPRET GEOMETRIC
TOLERANCING PER:

MATERIAL

FINISH

DO NOT SCALE DRAWING

	NAME	DATE
DRAWN	F. BENDANA	2/10/17
CHECKED		
ENG APPR.		
MFG APPR.		
Q.A.		

COMMENTS:

UCLA: Laser Spectroscopy & Gas Dynamics Lab

TITLE:

ORingGrooveDetail

SIZE	REFERENCE DWG. NO.	REV
A	1, 2, 3, 4, 5, 6, 7, 12, 13, 14, 15, 19, 20, 21, 23	002

SCALE: 1:2

SHEET 2 OF 3

NEXT ASSY	USED ON
APPLICATION	

PROPRIETARY AND CONFIDENTIAL

THE INFORMATION CONTAINED IN THIS DRAWING IS THE SOLE PROPERTY OF UCLA. ANY REPRODUCTION IN PART OR AS A WHOLE WITHOUT THE WRITTEN PERMISSION OF UCLA IS PROHIBITED.

SOLIDWORKS Educational Product. For Instructional Use Only

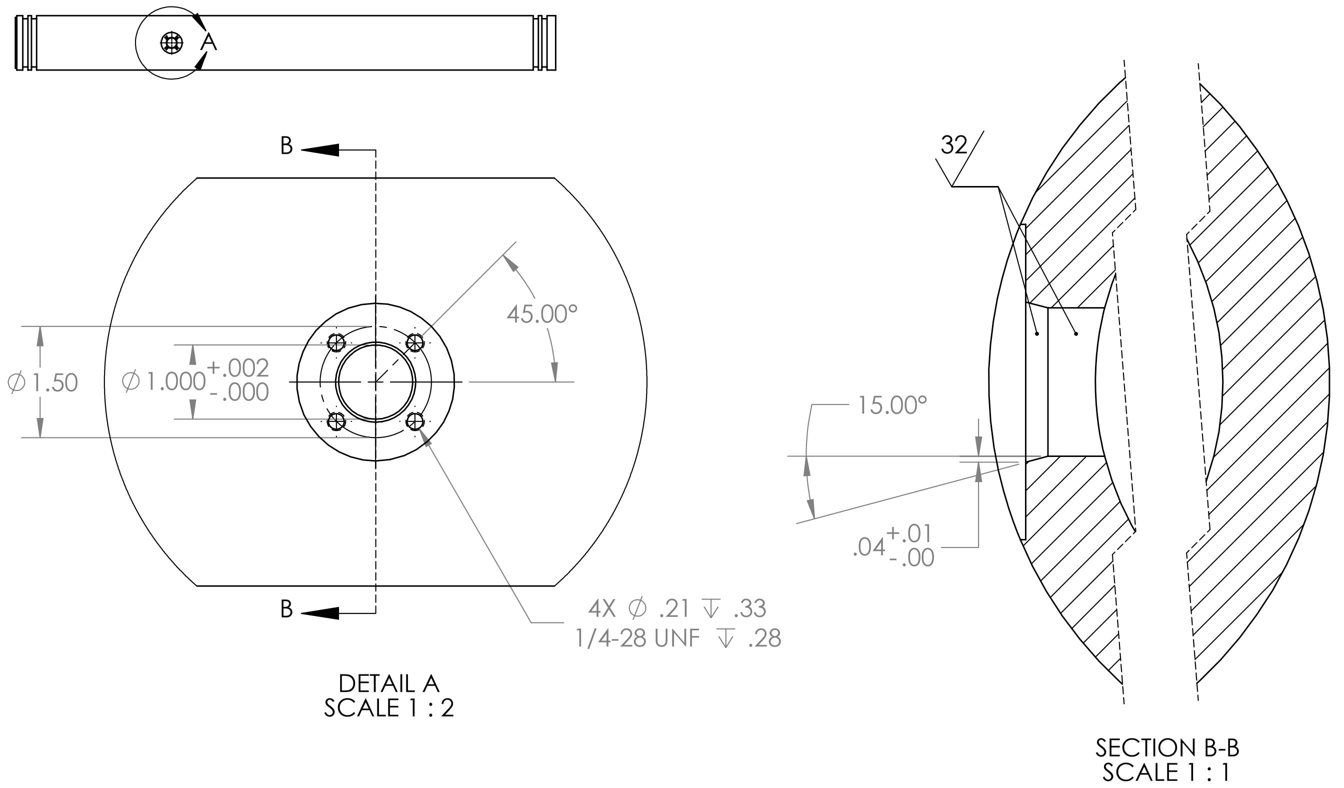

DETAIL A
SCALE 1 : 2

SECTION B-B
SCALE 1 : 1

UNLESS OTHERWISE SPECIFIED:		NAME	DATE	UCLA: Laser Spectroscopy & Gas Dynamics Lab
DIMENSIONS ARE IN INCHES TOLERANCES: FRACTIONAL ± ANGULAR: MACH ± BEND ± TWO PLACE DECIMAL ±.010 THREE PLACE DECIMAL ±.005	DRAWN	F. BENDANA	2/10/17	TITLE:
	CHECKED			PortDetail
	ENG APPR.			
	MFG APPR.			
INTERPRET GEOMETRIC TOLERANCING PER:	Q.A.			
MATERIAL	COMMENTS:			SIZE A REFERENCE DWG. NO. 2, 3, 4, 5 REV 002
FINISH				
DO NOT SCALE DRAWING				SCALE: 1:15 SHEET 2 OF 2

NEXT ASSY USED ON

APPLICATION

PROPRIETARY AND CONFIDENTIAL

THE INFORMATION CONTAINED IN THIS DRAWING IS THE SOLE PROPERTY OF UCLA. ANY REPRODUCTION IN PART OR AS A WHOLE WITHOUT THE WRITTEN PERMISSION OF UCLA IS PROHIBITED.

SOLIDWORKS Educational Product. For Instructional Use Only

PAGE 41

NOTE: Tube_D & InertialMassAttachment_A ARE WELDED

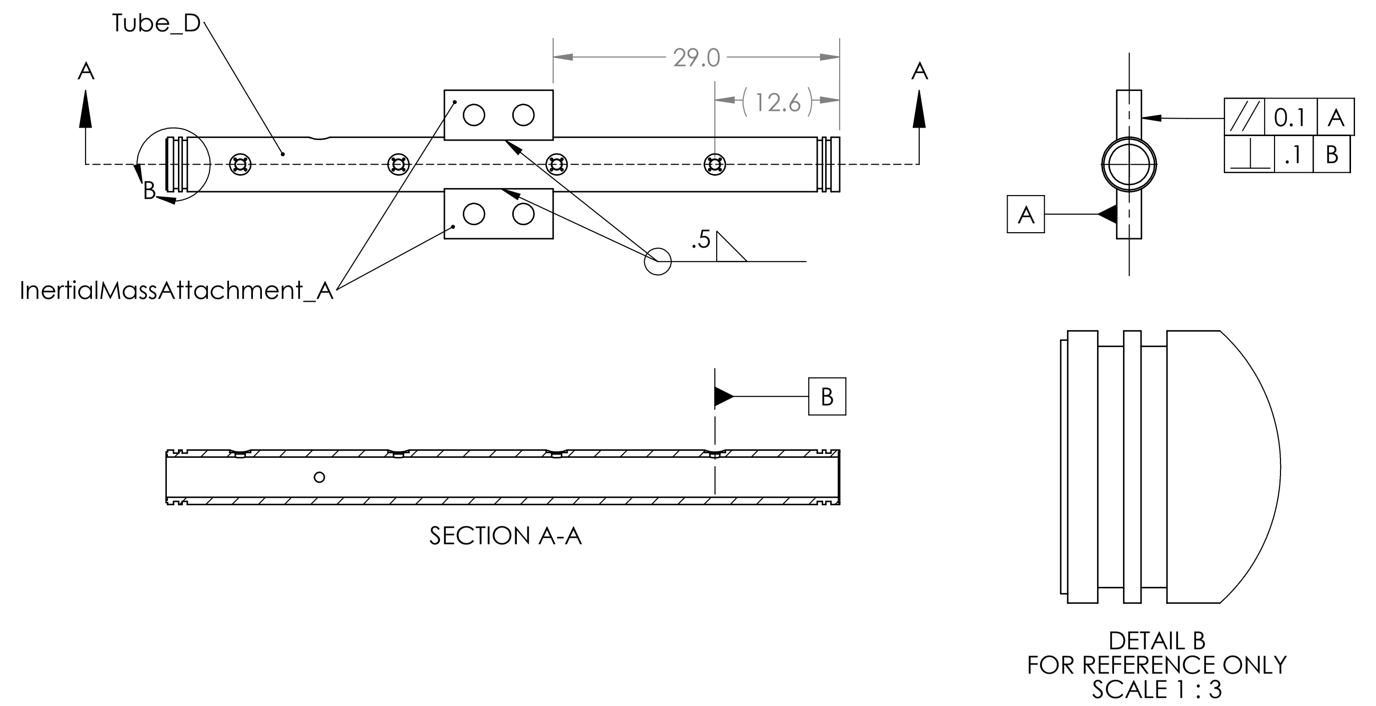

SECTION A-A

DETAIL B
FOR REFERENCE ONLY
SCALE 1 : 3

PROPRIETARY AND CONFIDENTIAL

THE INFORMATION CONTAINED IN THIS DRAWING IS THE SOLE PROPERTY OF UCLA. ANY REPRODUCTION IN PART OR AS A WHOLE WITHOUT THE WRITTEN PERMISSION OF UCLA IS PROHIBITED.

SOLIDWORKS Educational Product. For Instructional Use Only

		UNLESS OTHERWISE SPECIFIED:		NAME	DATE	UCLA: Laser Spectroscopy & Gas Dynamics Lab
		DIMENSIONS ARE IN INCHES TOLERANCES: FRACTIONAL ± ANGULAR: MACH ± BEND ± ONE PLACE DECIMAL ±.100 TWO PLACE DECIMAL ±.010 THREE PLACE DECIMAL ±.005	DRAWN	F. BENDANA	2/10/17	TITLE: Tube_D Assembly
			CHECKED			
			ENG APPR.			
			MFG APPR.			
		INTERPRET GEOMETRIC TOLERANCING PER:	Q.A.			
		MATERIAL 304 SS	COMMENTS:			SIZE A · REFERENCE DWG. NO. 4, 31 · REV 002
NEXT ASSY	USED ON	FINISH				
APPLICATION		DO NOT SCALE DRAWING				SCALE: 1:15 · SHEET 1 OF 1

.5

NOTE: PoppetValveBoss & PoppetValveHousing
ARE WELDED TOGETHER

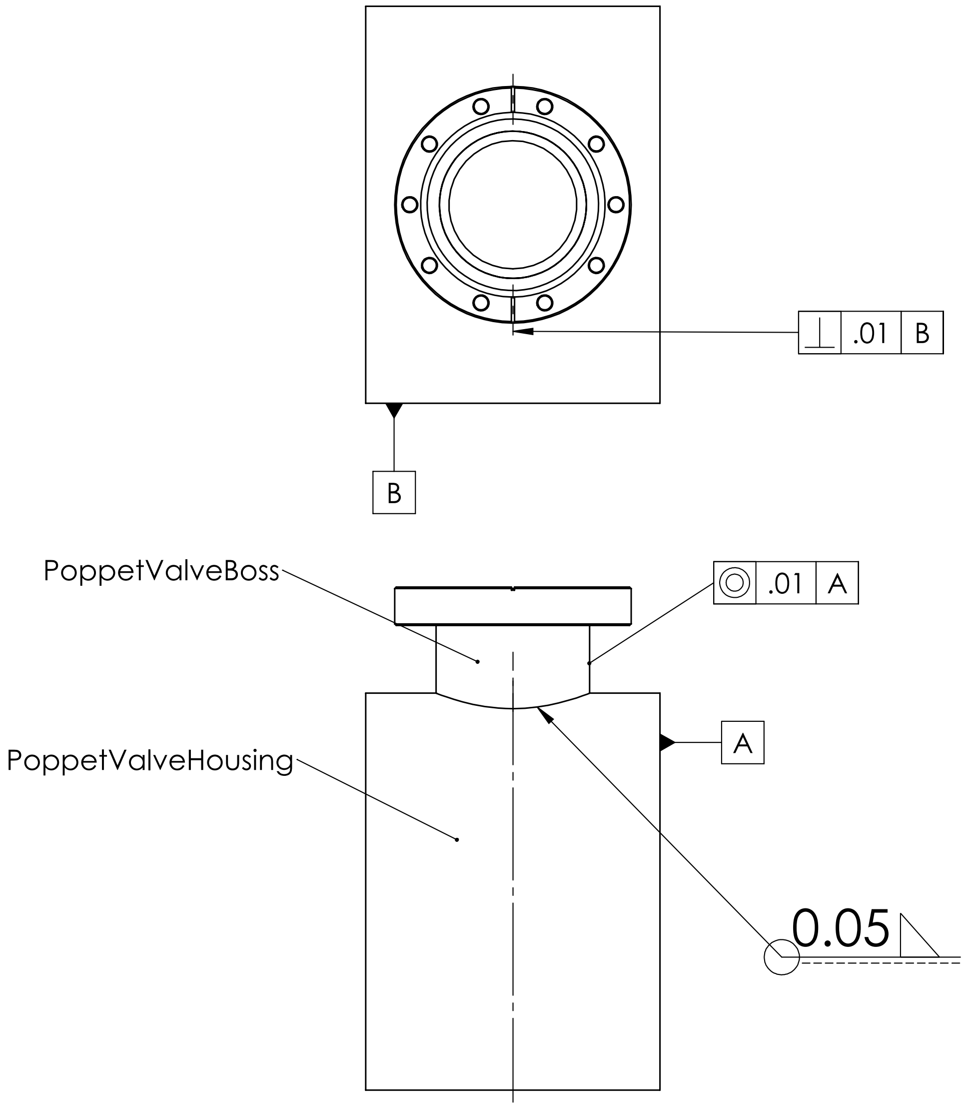

				NAME	DATE
	DIMENSIONS ARE IN INCHES TOLERANCES: FRACTIONAL ± ANGULAR: MACH ± BEND ± TWO PLACE DECIMAL ±.010 THREE PLACE DECIMAL ±.005	DRAWN	F. BENDANA	2/10/17	UCLA: Laser Spectroscopy & Gas Dynamics Lab
		CHECKED			
		ENG APPR.			PoppetValveHousing Assembly
		MFG APPR.			
	MATERIAL 304 SS	Q.A.			
	FINISH	COMMENTS:			SIZE A · REFERENCE DWG. NO. 23, 24 · REV. 002
NEXT ASSY · USED ON APPLICATION	DO NOT SCALE DRAWING				SCALE:1:3 · WEIGHT: · SHEET 1 OF 1

PROPRIETARY AND CONFIDENTIAL

THE INFORMATION CONTAINED IN THIS DRAWING IS THE SOLE PROPERTY OF UCLA. ANY REPRODUCTION IN PART OR AS A WHOLE WITHOUT THE WRITTEN PERMISSION OF UCLA IS PROHIBITED.

SOLIDWORKS Educational Product. For Instructional Use Only

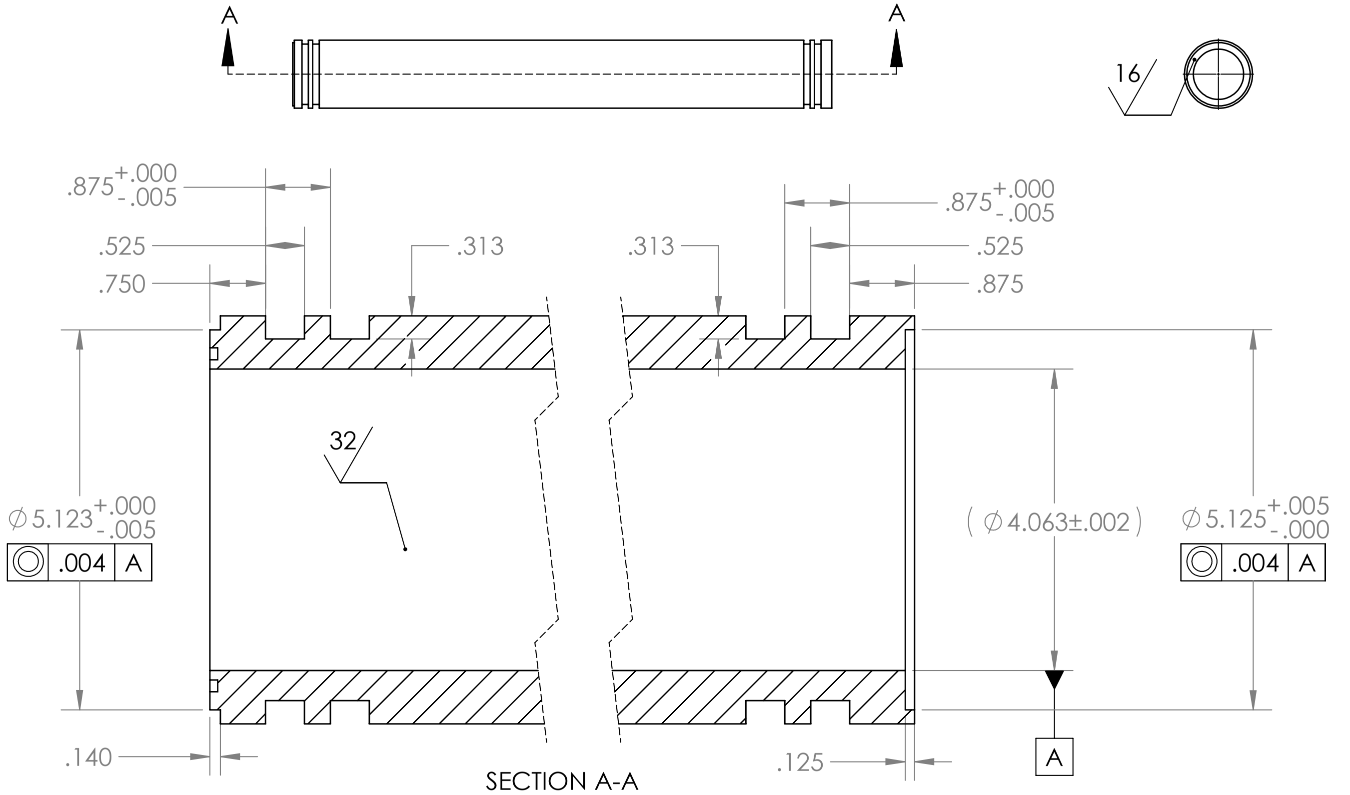

SECTION A-A

UNLESS OTHERWISE SPECIFIED:
DIMENSIONS ARE IN INCHES
TOLERANCES:
FRACTIONAL ±
ANGULAR: MACH ± BEND ±
ONE PLACE DECIMAL ±.100
TWO PLACE DECIMAL ±.010
THREE PLACE DECIMAL ±.005

INTERPRET GEOMETRIC TOLERANCING PER:
MATERIAL
FINISH
DO NOT SCALE DRAWING

NEXT ASSY
USED ON
APPLICATION

	NAME	DATE
DRAWN	F. BENDANA	2/10/17
CHECKED		
ENG APPR.		
MFG APPR.		
Q.A.		

COMMENTS:

UCLA: Laser Spectroscopy & Gas Dynamics Lab

TITLE:

PipeEndDetail

SIZE	REFERENCE DWG. NO.	REV
A	1, 2, 3, 4, 6, 7	002

SCALE: 1:2
SHEET 3 OF 3

PROPRIETARY AND CONFIDENTIAL

THE INFORMATION CONTAINED IN THIS DRAWING IS THE SOLE PROPERTY OF UCLA. ANY REPRODUCTION IN PART OR AS A WHOLE WITHOUT THE WRITTEN PERMISSION OF UCLA IS PROHIBITED.

SOLIDWORKS Educational Product. For Instructional Use Only

APPENDIX G

Diaphragmless shock tube drawing package

University of California, Los Angeles
Laser Spectroscopy & Gas Dynamics Laboratory
Diaphragmless Shock Tube

<u>Point of Contact:</u>
Fabio Bendana
e: fbendana@ucla.edu
c: 650-255-8224

<u>Package Contents:</u>
Pages 1-7: Assembly Drawings
(*for reference only*)
Page 8: Bill of Materials
(*parts/qty interested in quoting*)
Pages 9-21: Part Drawings

Internal Bellows Configuration

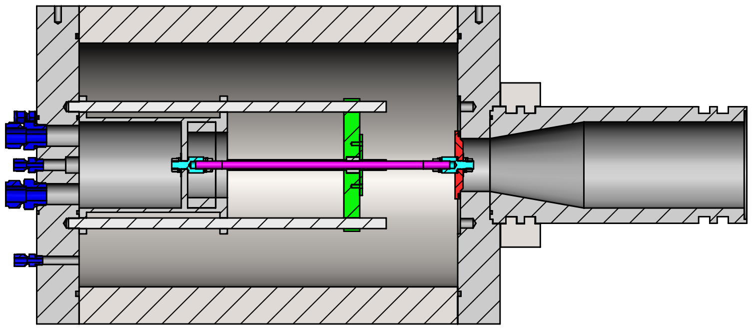

External Bellows Configuration

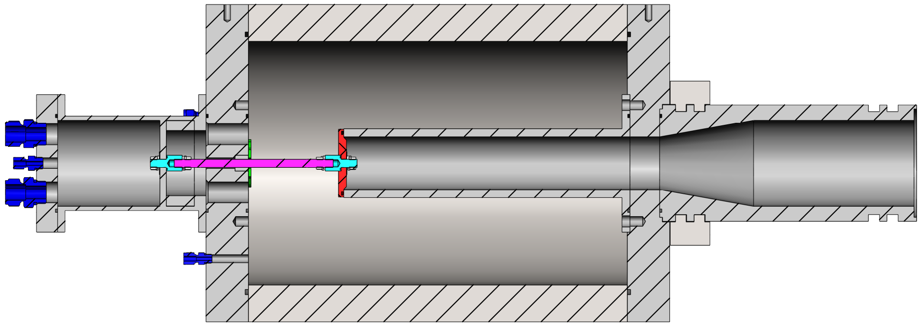

PROPRIETARY AND CONFIDENTIAL
THE INFORMATION CONTAINED IN THIS DRAWING IS THE SOLE PROPERTY OF UCLA. ANY REPRODUCTION IN PART OR AS A WHOLE WITHOUT THE WRITTEN PERMISSION OF UCLA IS PROHIBITED.

		UNLESS OTHERWISE SPECIFIED:		NAME	DATE	UCLA: Laser Spectroscopy & Gas Dynamics Lab
		DIMENSIONS ARE IN INCHES TOLERANCES: FRACTIONAL ± ANGULAR: MACH ± BEND ± ONE PLACE DECIMAL ±.100 TWO PLACE DECIMAL ±.010 THREE PLACE DECIMAL ±.005	DRAWN	F. BENDANA	3/11/19	TITLE: Diaphragmless Shock Tube Drawing Package
			CHECKED			
			ENG APPR.			
			MFG APPR.			
		INTERPRET GEOMETRIC TOLERANCING PER:	Q.A.			
		MATERIAL	COMMENTS:			SIZE A · DWG. NO. · REV 003
NEXT ASSY	USED ON	FINISH				
APPLICATION		DO NOT SCALE DRAWING				SCALE: 1:7 · SHEET 1 OF 8

SOLIDWORKS Educational Product. For Instructional Use Only.

Internal Bellows Configuration

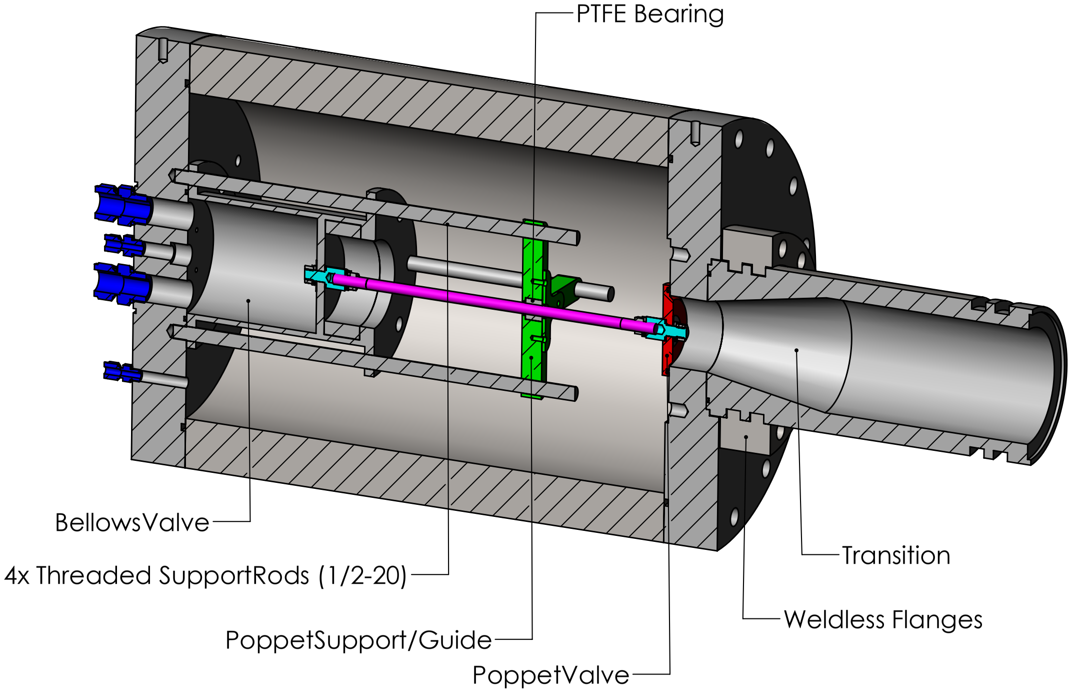

PROPRIETARY AND CONFIDENTIAL

THE INFORMATION CONTAINED IN THIS DRAWING IS THE SOLE PROPERTY OF UCLA. ANY REPRODUCTION IN PART OR AS A WHOLE WITHOUT THE WRITTEN PERMISSION OF UCLA IS PROHIBITED.

NEXT ASSY
USED ON
APPLICATION

UNLESS OTHERWISE SPECIFIED:
DIMENSIONS ARE IN INCHES
TOLERANCES:
FRACTIONAL ±
ANGULAR: MACH ± BEND ±
ONE PLACE DECIMAL ±.100
TWO PLACE DECIMAL ±.010
THREE PLACE DECIMAL ±.005
INTERPRET GEOMETRIC TOLERANCING PER:
MATERIAL
FINISH
DO NOT SCALE DRAWING

	NAME	DATE
DRAWN	F. BENDANA	3/11/19
CHECKED		
ENG APPR.		
MFG APPR.		
Q.A.		

COMMENTS:

UCLA: Laser Spectroscopy & Gas Dynamics Lab

TITLE:

Internal Bellows
Assembly

SIZE A
DWG. NO.
REV 003
SCALE: 1:5
SHEET 2 OF 8

PAGE 2

SOLIDWORKS Educational Product. For Instructional Use Only.

Internal Bellows Configuration

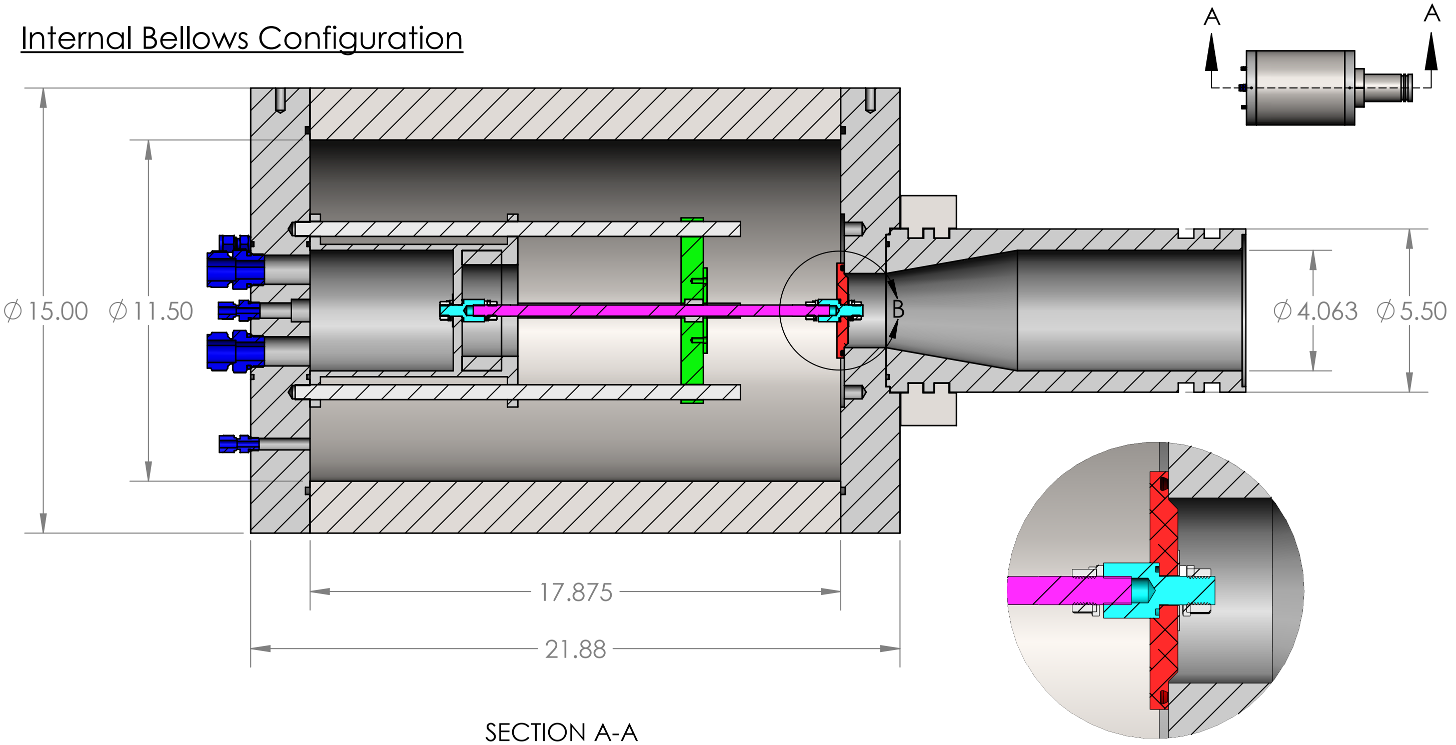

SECTION A-A

DETAIL B
SCALE 1 : 2

PROPRIETARY AND CONFIDENTIAL

THE INFORMATION CONTAINED IN THIS DRAWING IS THE SOLE PROPERTY OF UCLA. ANY REPRODUCTION IN PART OR AS A WHOLE WITHOUT THE WRITTEN PERMISSION OF UCLA IS PROHIBITED.

NEXT ASSY	USED ON

APPLICATION

UNLESS OTHERWISE SPECIFIED:
DIMENSIONS ARE IN INCHES
TOLERANCES:
FRACTIONAL ±
ANGULAR: MACH ± BEND ±
ONE PLACE DECIMAL ±.100
TWO PLACE DECIMAL ±.010
THREE PLACE DECIMAL ±.005

INTERPRET GEOMETRIC TOLERANCING PER:

MATERIAL

FINISH

DO NOT SCALE DRAWING

	NAME	DATE
DRAWN	F. BENDANA	3/11/19
CHECKED		
ENG APPR.		
MFG APPR.		
Q.A.		

COMMENTS:

UCLA: Laser Spectroscopy & Gas Dynamics Lab

TITLE:

Internal Bellows
Assembly

SIZE	DWG. NO.	REV
A		003

SCALE: 1:5

SHEET 3 OF 8

PAGE 3

SOLIDWORKS Educational Product. For Instructional Use Only.

Internal Bellows Configuration

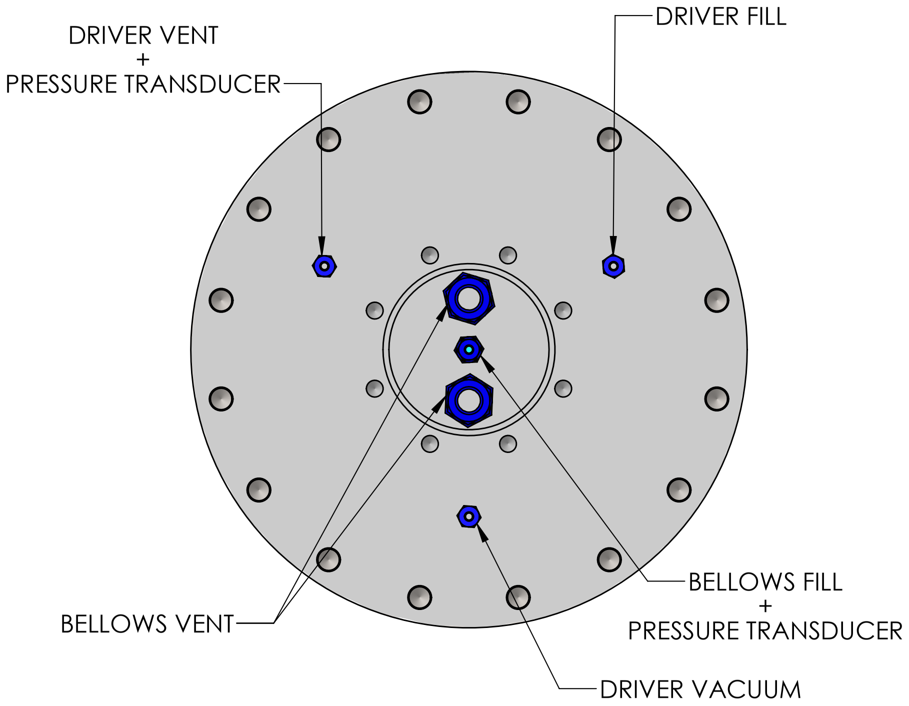

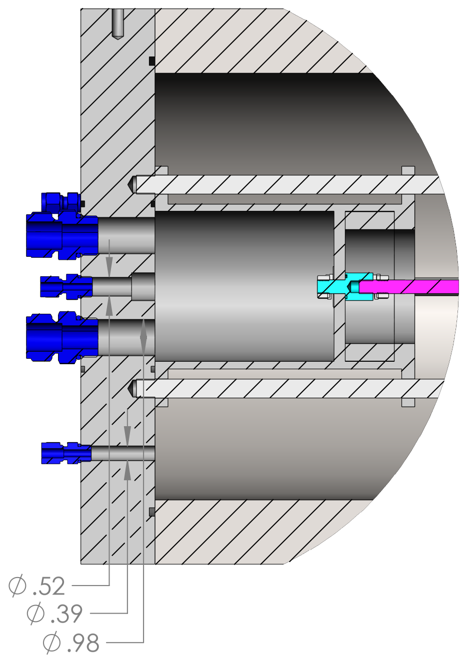

PROPRIETARY AND CONFIDENTIAL

THE INFORMATION CONTAINED IN THIS DRAWING IS THE SOLE PROPERTY OF UCLA. ANY REPRODUCTION IN PART OR AS A WHOLE WITHOUT THE WRITTEN PERMISSION OF UCLA IS PROHIBITED.

NEXT ASSY
USED ON
APPLICATION

UNLESS OTHERWISE SPECIFIED:
DIMENSIONS ARE IN INCHES
TOLERANCES:
FRACTIONAL ±
ANGULAR: MACH ± BEND ±
ONE PLACE DECIMAL ±.100
TWO PLACE DECIMAL ±.010
THREE PLACE DECIMAL ±.005
INTERPRET GEOMETRIC TOLERANCING PER:
MATERIAL
FINISH
DO NOT SCALE DRAWING

	NAME	DATE
DRAWN	F. BENDANA	3/11/19
CHECKED		
ENG APPR.		
MFG APPR.		
Q.A.		

COMMENTS:

UCLA: Laser Spectroscopy & Gas Dynamics Lab

TITLE:
Internal Bellows
Plumbing/Instrumentation

SIZE A
DWG. NO.
REV 003
SCALE: 1:4
SHEET 4 OF 8

PAGE 4

SOLIDWORKS Educational Product. For Instructional Use Only.

External Bellows Configuration

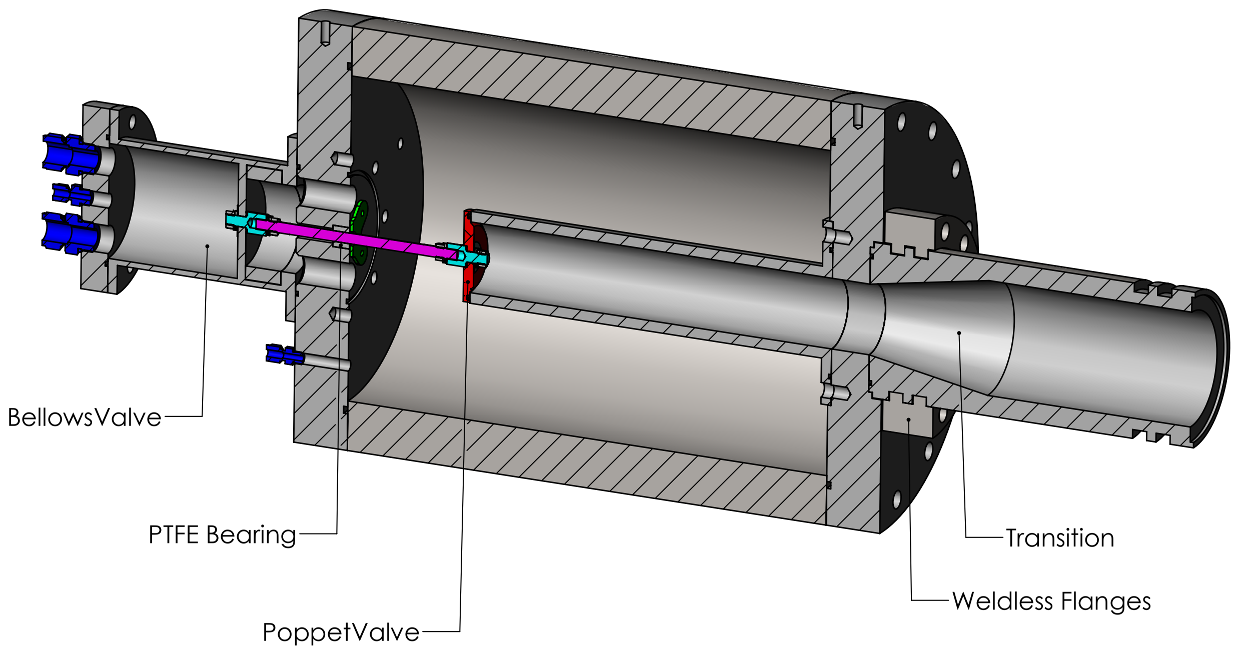

PROPRIETARY AND CONFIDENTIAL

THE INFORMATION CONTAINED IN THIS DRAWING IS THE SOLE PROPERTY OF UCLA. ANY REPRODUCTION IN PART OR AS A WHOLE WITHOUT THE WRITTEN PERMISSION OF UCLA IS PROHIBITED.

NEXT ASSY	USED ON
APPLICATION	

UNLESS OTHERWISE SPECIFIED:
DIMENSIONS ARE IN INCHES
TOLERANCES:
FRACTIONAL ±
ANGULAR: MACH ± BEND ±
ONE PLACE DECIMAL ±.100
TWO PLACE DECIMAL ±.010
THREE PLACE DECIMAL ±.005

INTERPRET GEOMETRIC TOLERANCING PER:
MATERIAL
FINISH
DO NOT SCALE DRAWING

	NAME	DATE
DRAWN	F. BENDANA	3/11/19
CHECKED		
ENG APPR.		
MFG APPR.		
Q.A.		
COMMENTS:		

UCLA: Laser Spectroscopy & Gas Dynamics Lab

TITLE:
External Bellows
Assembly

SIZE	DWG. NO.	REV
A		003

SCALE: 1:5
SHEET 5 OF 8

PAGE 5

SOLIDWORKS Educational Product. For Instructional Use Only.

External Bellows Configuration

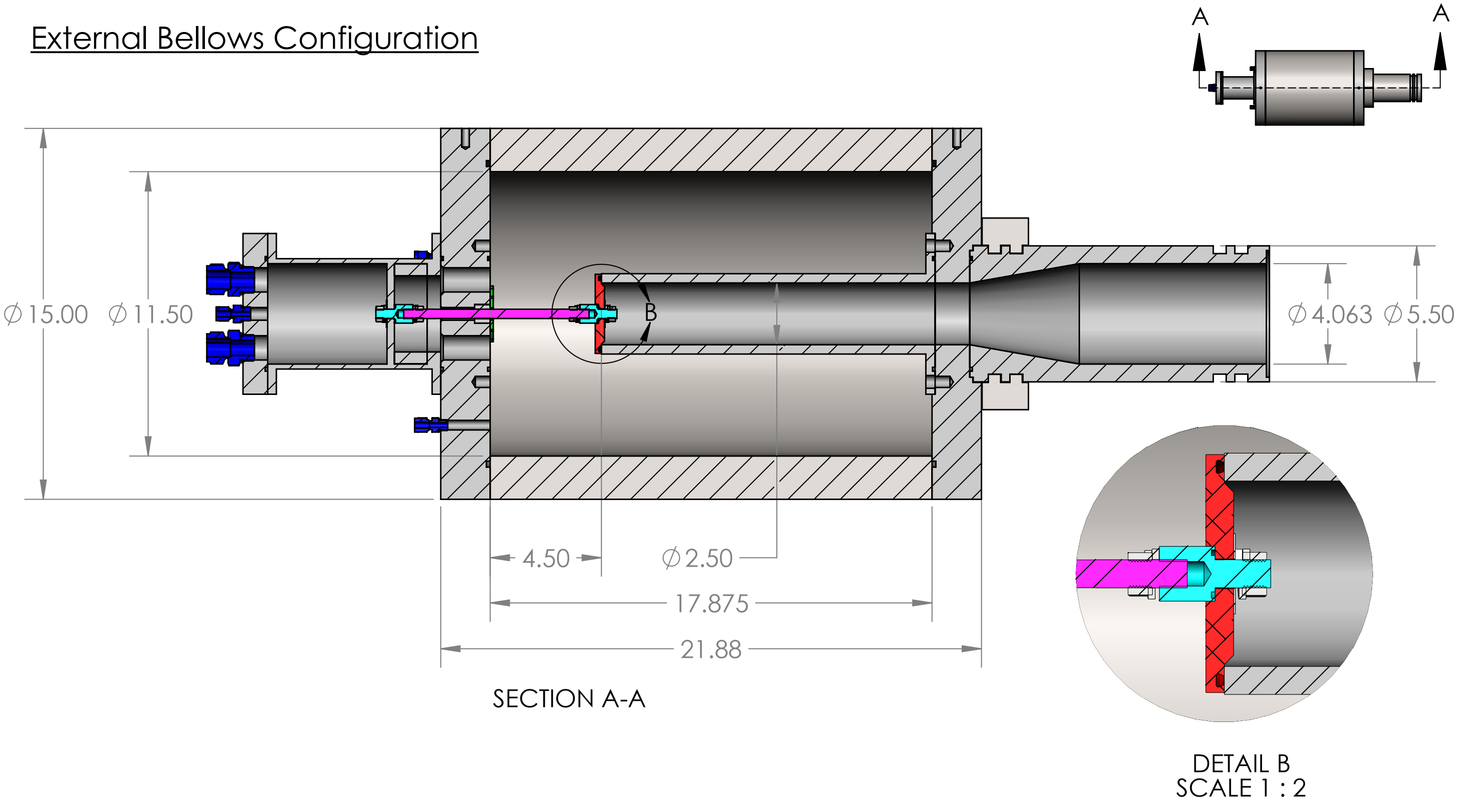

		UNLESS OTHERWISE SPECIFIED:		NAME	DATE
		DIMENSIONS ARE IN INCHES TOLERANCES: FRACTIONAL ± ANGULAR: MACH ± BEND ± ONE PLACE DECIMAL ±.100 TWO PLACE DECIMAL ±.010 THREE PLACE DECIMAL ±.005	DRAWN	F. BENDANA	3/11/19
			CHECKED		
			ENG APPR.		
			MFG APPR.		
		INTERPRET GEOMETRIC TOLERANCING PER:	Q.A.		
		MATERIAL	COMMENTS:		
NEXT ASSY	USED ON	FINISH			
APPLICATION		DO NOT SCALE DRAWING			

UCLA: Laser Spectroscopy & Gas Dynamics Lab

TITLE:

External Bellows
Assembly

SIZE A
DWG. NO.
REV 003

SCALE: 1:6
SHEET 6 OF 8

PROPRIETARY AND CONFIDENTIAL

THE INFORMATION CONTAINED IN THIS DRAWING IS THE SOLE PROPERTY OF UCLA. ANY REPRODUCTION IN PART OR AS A WHOLE WITHOUT THE WRITTEN PERMISSION OF UCLA IS PROHIBITED.

SOLIDWORKS Educational Product. For Instructional Use Only.

PAGE 6

External Bellows Configuration

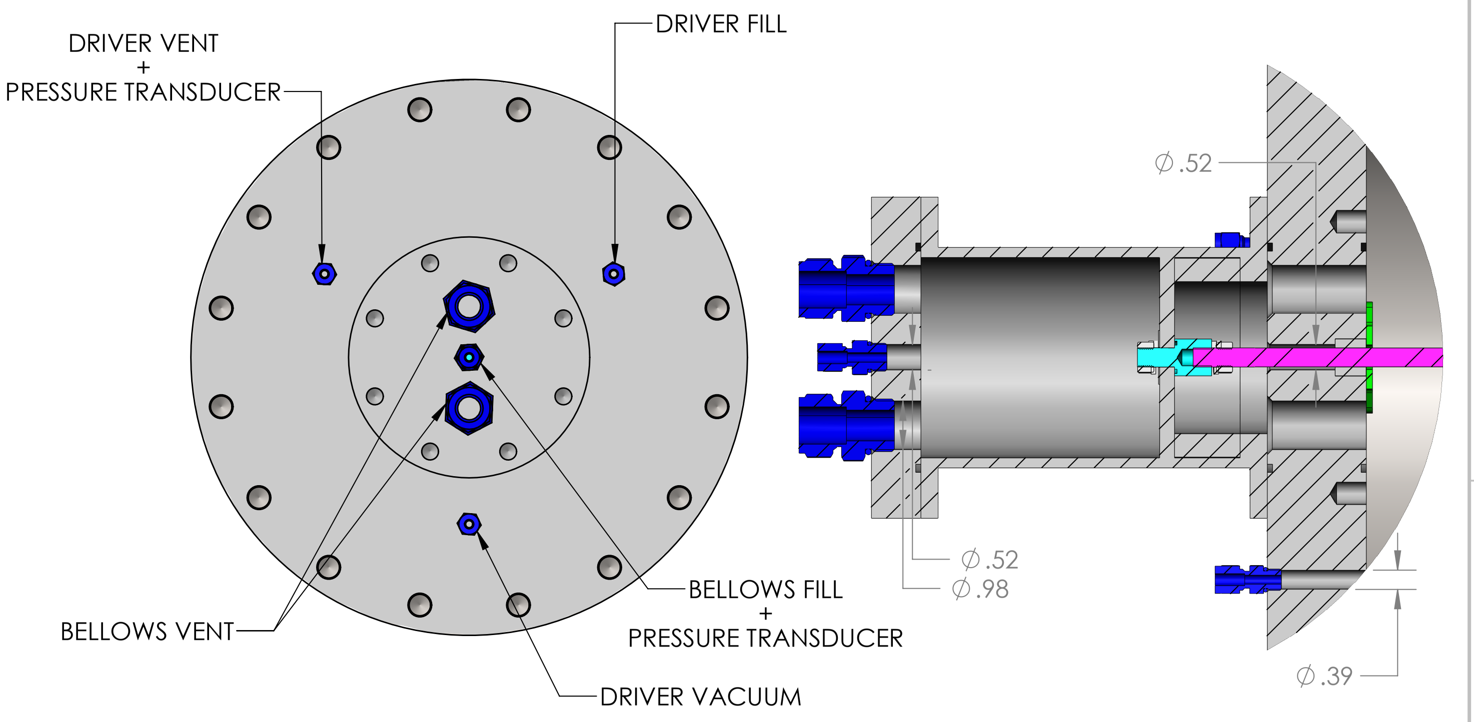

UNLESS OTHERWISE SPECIFIED:		NAME	DATE	UCLA: Laser Spectroscopy & Gas Dynamics Lab	
DIMENSIONS ARE IN INCHES TOLERANCES: FRACTIONAL ± ANGULAR: MACH ± BEND ± ONE PLACE DECIMAL ±.100 TWO PLACE DECIMAL ±.010 THREE PLACE DECIMAL ±.005	DRAWN	F. BENDANA	3/11/19	TITLE: External Bellows Plumbing/Instrumentation	
	CHECKED				
	ENG APPR.				
	MFG APPR.				
INTERPRET GEOMETRIC TOLERANCING PER:	Q.A.				
MATERIAL	COMMENTS:			SIZE A	DWG. NO. / REV 003
FINISH					
DO NOT SCALE DRAWING				SCALE: 1:4	SHEET 7 OF 8

NEXT ASSY	USED ON
APPLICATION	

PROPRIETARY AND CONFIDENTIAL

THE INFORMATION CONTAINED IN THIS DRAWING IS THE SOLE PROPERTY OF UCLA. ANY REPRODUCTION IN PART OR AS A WHOLE WITHOUT THE WRITTEN PERMISSION OF UCLA IS PROHIBITED.

SOLIDWORKS Educational Product. For Instructional Use Only.

PAGE 7

2 1

B

Internal Bellows Configuration

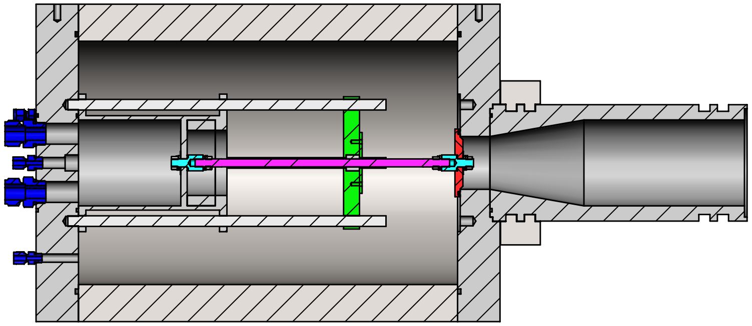

External Bellows Configuration

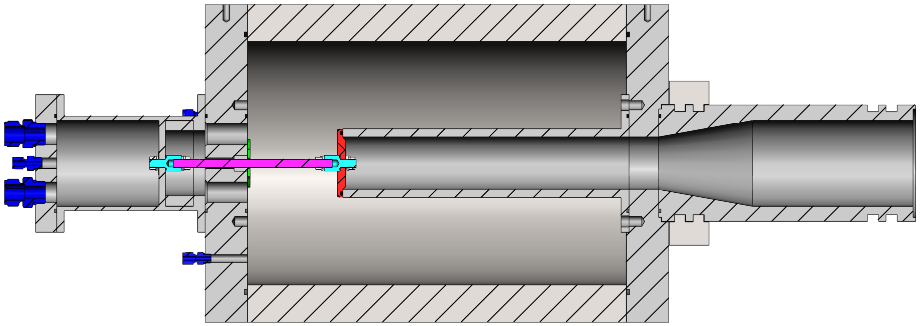

DWG. NO.	PART NUMBER	QTY.
1	Tube_J	1
2	EndCap_E	1
3	EndCap_F	1
4	Tube_K	1
5	SupportRod_A	1
6	PoppetValveSupport_A	1
7	PoppetValve_A	1
8	PoppetValve_B	2
9	Tube_L	1
10	EndCap_G	1
11	SupportRod_D	1

A

PROPRIETARY AND CONFIDENTIAL

THE INFORMATION CONTAINED IN THIS DRAWING IS THE SOLE PROPERTY OF UCLA. ANY REPRODUCTION IN PART OR AS A WHOLE WITHOUT THE WRITTEN PERMISSION OF UCLA IS PROHIBITED.

NEXT ASSY
USED ON
APPLICATION

UNLESS OTHERWISE SPECIFIED:
DIMENSIONS ARE IN INCHES
TOLERANCES:
FRACTIONAL ±
ANGULAR: MACH ± BEND ±
ONE PLACE DECIMAL ±.100
TWO PLACE DECIMAL ±.010
THREE PLACE DECIMAL ±.005
INTERPRET GEOMETRIC TOLERANCING PER:
MATERIAL
FINISH
DO NOT SCALE DRAWING

	NAME	DATE
DRAWN	F. BENDANA	3/11/19
CHECKED		
ENG APPR.		
MFG APPR.		
Q.A.		

COMMENTS:

UCLA: Laser Spectroscopy & Gas Dynamics Lab

TITLE:

Diaphragmless Shock Tube
Bill of Materials

SIZE A
DWG. NO.
REV 003

SCALE: 1:7
SHEET 8 OF 8

2 1

PAGE 8

SOLIDWORKS Educational Product. For Instructional Use Only.

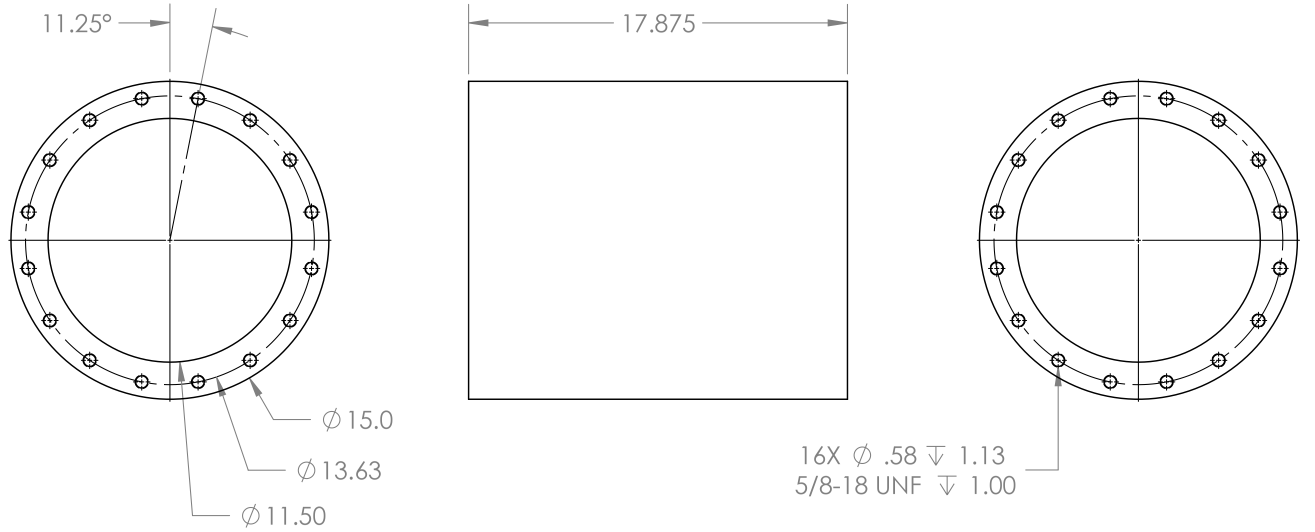

PROPRIETARY AND CONFIDENTIAL

THE INFORMATION CONTAINED IN THIS DRAWING IS THE SOLE PROPERTY OF UCLA. ANY REPRODUCTION IN PART OR AS A WHOLE WITHOUT THE WRITTEN PERMISSION OF UCLA IS PROHIBITED.

NEXT ASSY
USED ON
APPLICATION

UNLESS OTHERWISE SPECIFIED:
DIMENSIONS ARE IN INCHES
TOLERANCES:
FRACTIONAL ±
ANGULAR: MACH ± BEND ±
ONE PLACE DECIMAL ±.100
TWO PLACE DECIMAL ±.010
THREE PLACE DECIMAL ±.005

INTERPRET GEOMETRIC TOLERANCING PER:

MATERIAL
304 SS

FINISH

DO NOT SCALE DRAWING

	NAME	DATE
DRAWN	F. BENDANA	3/11/19
CHECKED		
ENG APPR.		
MFG APPR.		
Q.A.		

COMMENTS:

UCLA: Laser Spectroscopy & Gas Dynamics Lab

TITLE:
Tube_J

SIZE
A
DWG. NO.
1
REV
003

SCALE: 1:7
SHEET 1 OF 1

PAGE 9

SOLIDWORKS Educational Product. For Instructional Use Only.

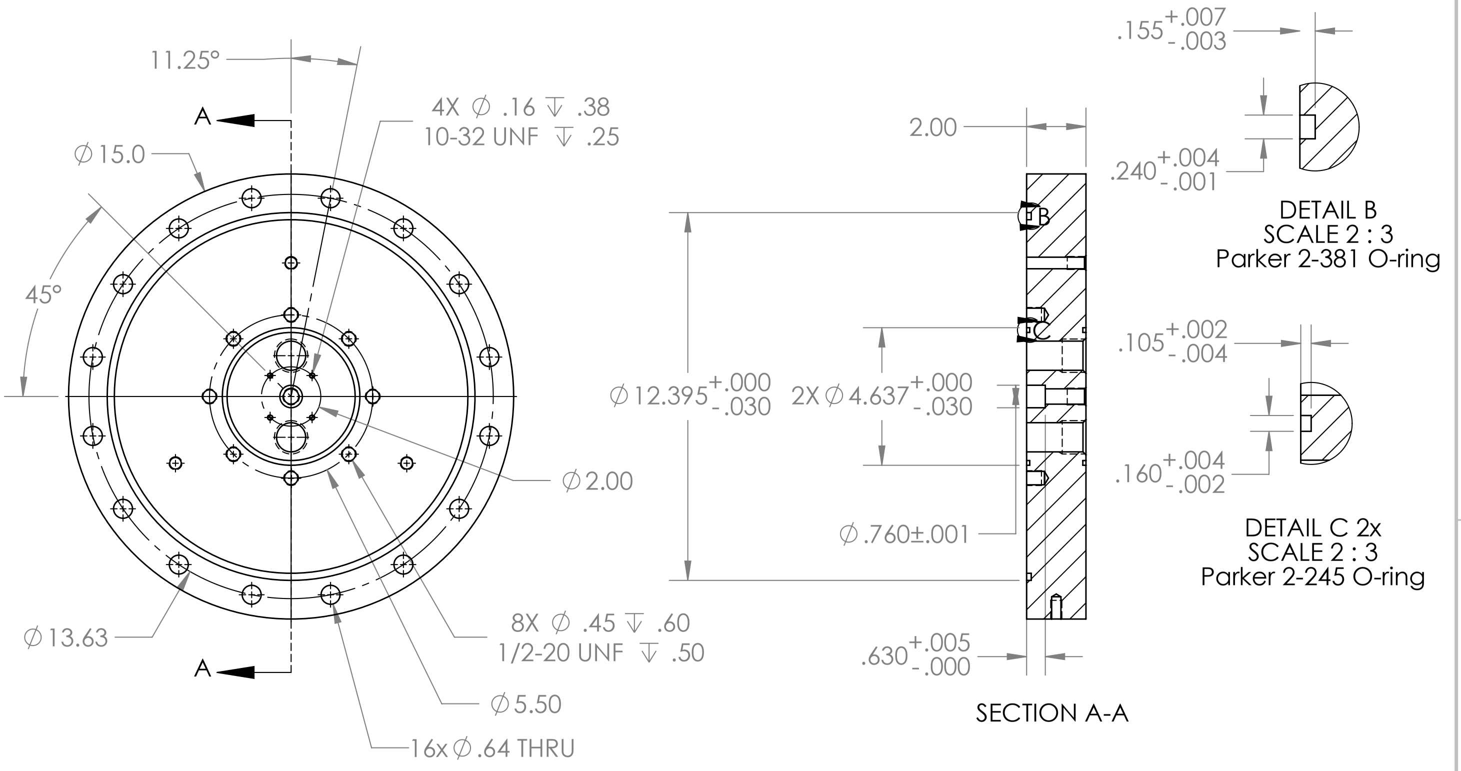

SECTION A-A

DETAIL B
SCALE 2 : 3
Parker 2-381 O-ring

DETAIL C 2x
SCALE 2 : 3
Parker 2-245 O-ring

PROPRIETARY AND CONFIDENTIAL

THE INFORMATION CONTAINED IN THIS DRAWING IS THE SOLE PROPERTY OF UCLA. ANY REPRODUCTION IN PART OR AS A WHOLE WITHOUT THE WRITTEN PERMISSION OF UCLA IS PROHIBITED.

NEXT ASSY
USED ON
APPLICATION

UNLESS OTHERWISE SPECIFIED:
DIMENSIONS ARE IN INCHES
TOLERANCES:
FRACTIONAL ±
ANGULAR: MACH ± BEND ±
ONE PLACE DECIMAL ±.100
TWO PLACE DECIMAL ±.010
THREE PLACE DECIMAL ±.005
INTERPRET GEOMETRIC TOLERANCING PER:
MATERIAL 304 SS
FINISH
DO NOT SCALE DRAWING

	NAME	DATE
DRAWN	F. BENDANA	3/11/19
CHECKED		
ENG APPR.		
MFG APPR.		
Q.A.		

COMMENTS:

UCLA: Laser Spectroscopy & Gas Dynamics Lab

TITLE:

EndCap_E

SIZE A
DWG. NO. 2
REV 003
SCALE: 1:5
SHEET 1 OF 2

2
1

SOLIDWORKS Educational Product. For Instructional Use Only.

PAGE 10

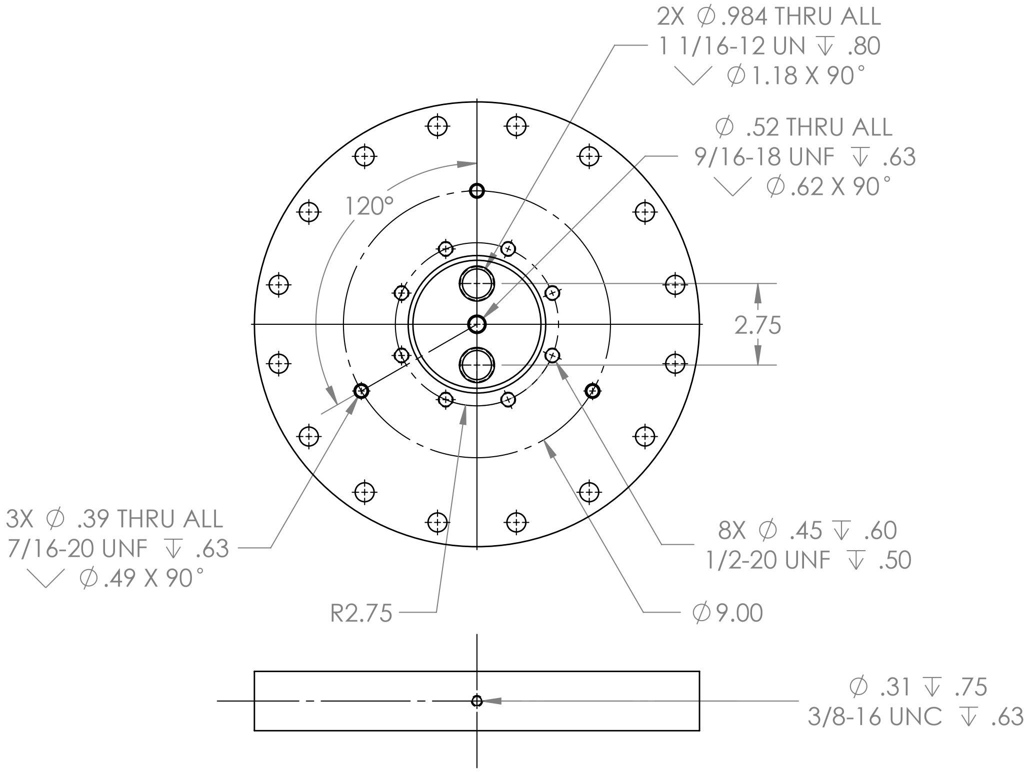

PROPRIETARY AND CONFIDENTIAL

THE INFORMATION CONTAINED IN THIS DRAWING IS THE SOLE PROPERTY OF UCLA. ANY REPRODUCTION IN PART OR AS A WHOLE WITHOUT THE WRITTEN PERMISSION OF UCLA IS PROHIBITED.

NEXT ASSY	USED ON	UNLESS OTHERWISE SPECIFIED: DIMENSIONS ARE IN INCHES TOLERANCES: FRACTIONAL ± ANGULAR: MACH ± BEND ± ONE PLACE DECIMAL ±.100 TWO PLACE DECIMAL ±.010 THREE PLACE DECIMAL ±.005		
APPLICATION		INTERPRET GEOMETRIC TOLERANCING PER:		
		MATERIAL 304 SS		
		FINISH		
		DO NOT SCALE DRAWING		

	NAME	DATE
DRAWN	F. BENDANA	3/11/19
CHECKED		
ENG APPR.		
MFG APPR.		
Q.A.		
COMMENTS:		

UCLA: Laser Spectroscopy & Gas Dynamics Lab

TITLE:

EndCap_E

SIZE	DWG. NO.	REV
A	2	003
SCALE: 1:5		SHEET 2 OF 2

SOLIDWORKS Educational Product. For Instructional Use Only.

PAGE 11

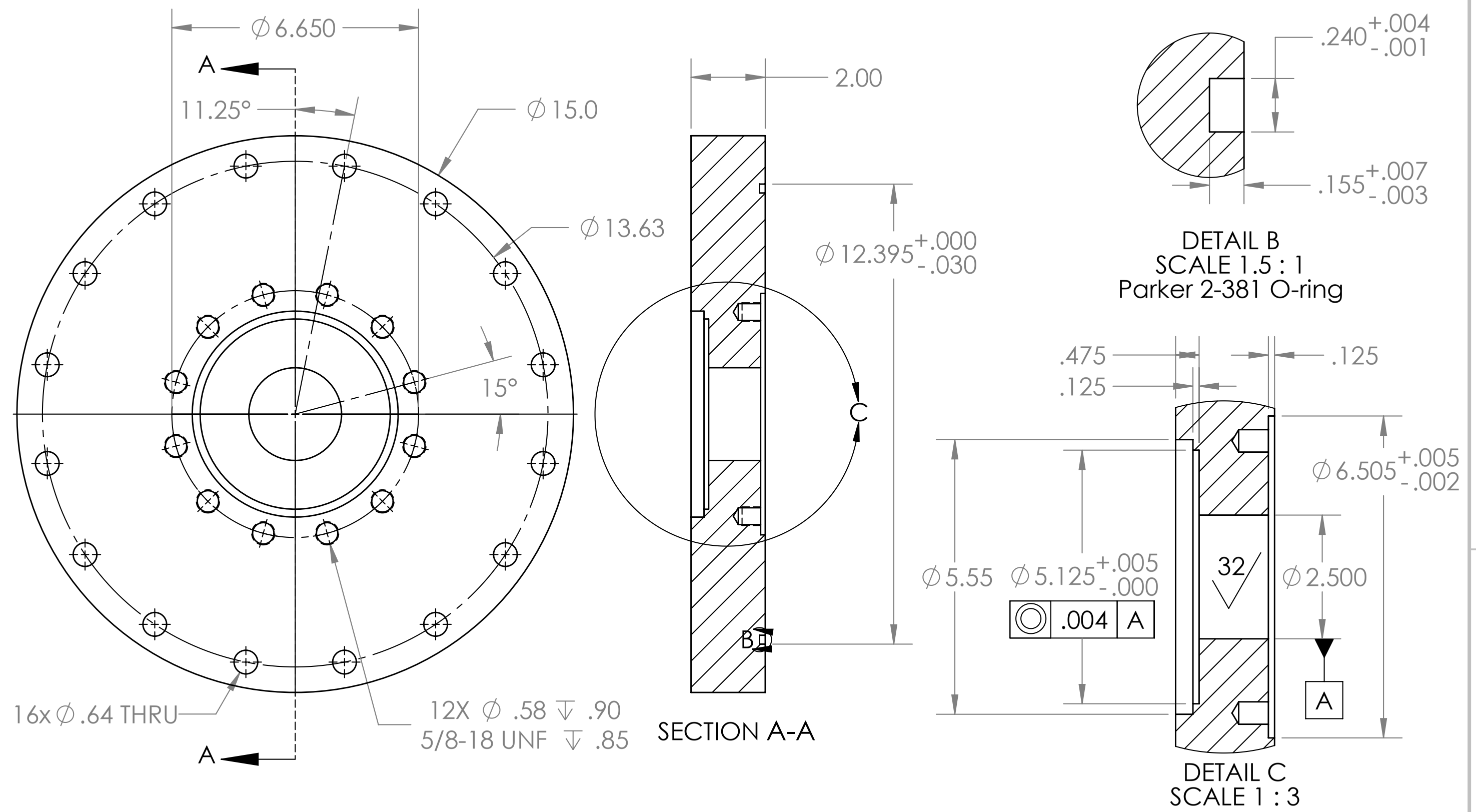

PROPRIETARY AND CONFIDENTIAL

THE INFORMATION CONTAINED IN THIS DRAWING IS THE SOLE PROPERTY OF UCLA. ANY REPRODUCTION IN PART OR AS A WHOLE WITHOUT THE WRITTEN PERMISSION OF UCLA IS PROHIBITED.

NEXT ASSY	USED ON
APPLICATION	

UNLESS OTHERWISE SPECIFIED:
DIMENSIONS ARE IN INCHES
TOLERANCES:
FRACTIONAL ±
ANGULAR: MACH ± BEND ±
ONE PLACE DECIMAL ±.100
TWO PLACE DECIMAL ±.010
THREE PLACE DECIMAL ±.005

INTERPRET GEOMETRIC TOLERANCING PER:

MATERIAL
304 SS

FINISH

DO NOT SCALE DRAWING

	NAME	DATE
DRAWN	F. BENDANA	3/11/19
CHECKED		
ENG APPR.		
MFG APPR.		
Q.A.		

COMMENTS:

UCLA: Laser Spectroscopy & Gas Dynamics Lab

TITLE:

EndCap_F

SIZE	DWG. NO.	REV
A	3	003

SCALE: 1:4 SHEET 1 OF 2

SOLIDWORKS Educational Product. For Instructional Use Only.

PAGE 12

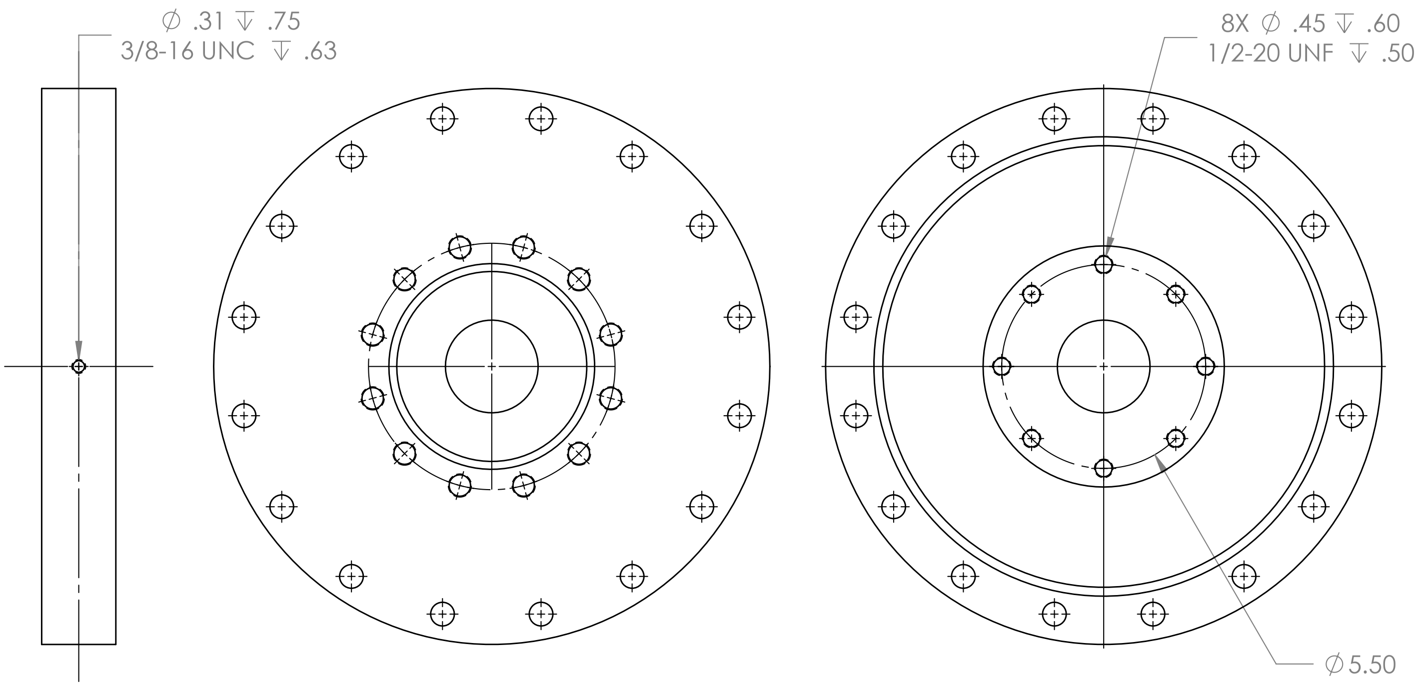

PROPRIETARY AND CONFIDENTIAL

THE INFORMATION CONTAINED IN THIS DRAWING IS THE SOLE PROPERTY OF UCLA. ANY REPRODUCTION IN PART OR AS A WHOLE WITHOUT THE WRITTEN PERMISSION OF UCLA IS PROHIBITED.

NEXT ASSY	USED ON
APPLICATION	

UNLESS OTHERWISE SPECIFIED:
DIMENSIONS ARE IN INCHES
TOLERANCES:
FRACTIONAL ±
ANGULAR: MACH ± BEND ±
ONE PLACE DECIMAL ±.100
TWO PLACE DECIMAL ±.010
THREE PLACE DECIMAL ±.005
INTERPRET GEOMETRIC TOLERANCING PER:
MATERIAL 304 SS
FINISH
DO NOT SCALE DRAWING

	NAME	DATE
DRAWN	F. BENDANA	3/11/19
CHECKED		
ENG APPR.		
MFG APPR.		
Q.A.		

COMMENTS:

UCLA: Laser Spectroscopy & Gas Dynamics Lab

TITLE:

EndCap_F

SIZE	DWG. NO.	REV
A	3	003

SCALE: 1:4 SHEET 2 OF 2

2 1

PAGE 13

SOLIDWORKS Educational Product. For Instructional Use Only.

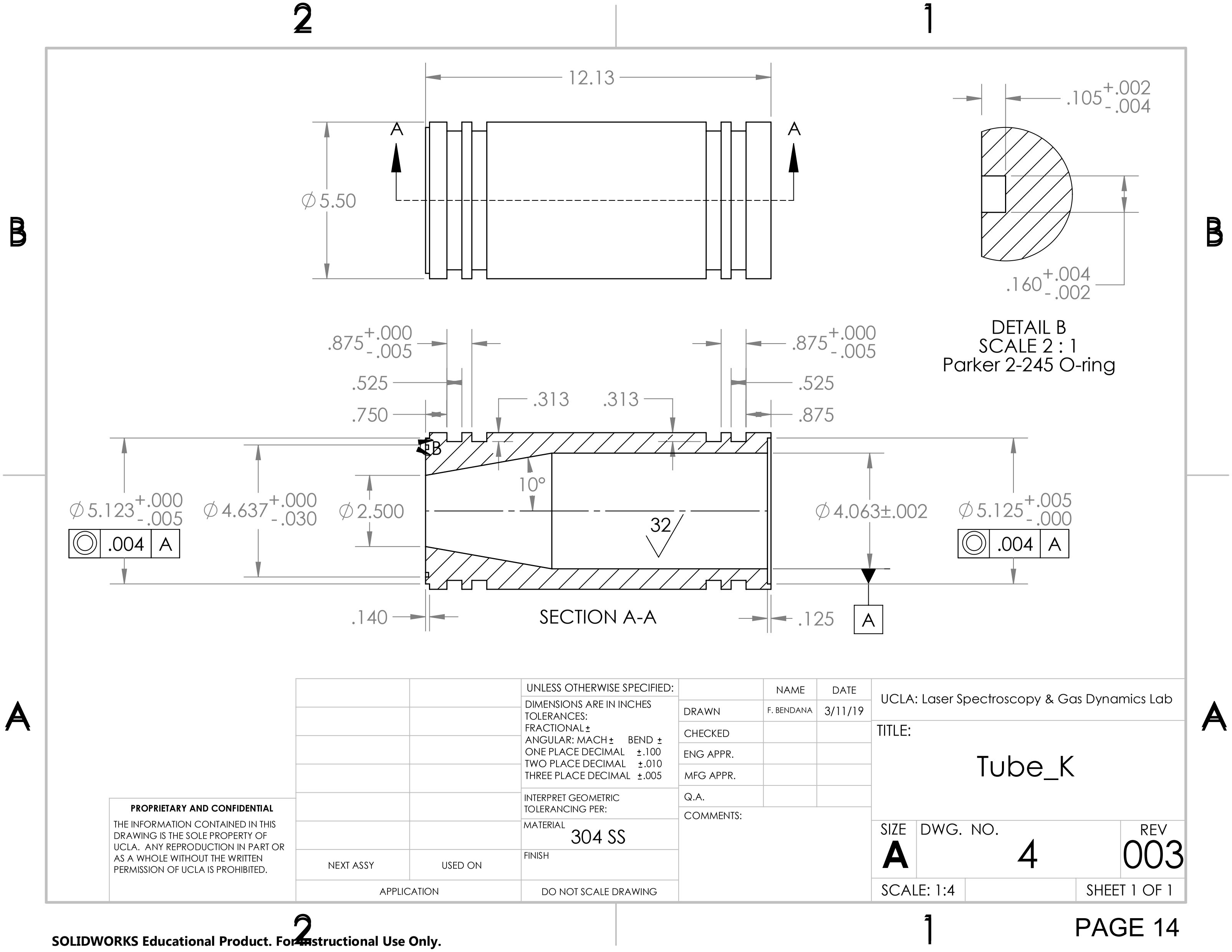

PAGE 14

SOLIDWORKS Educational Product. For Instructional Use Only.

Note: Straightness cannot deviate more than 0.005" over full length

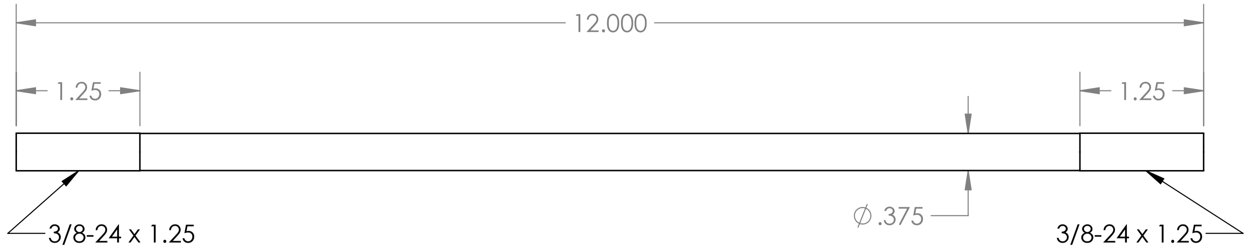

PROPRIETARY AND CONFIDENTIAL

THE INFORMATION CONTAINED IN THIS DRAWING IS THE SOLE PROPERTY OF UCLA. ANY REPRODUCTION IN PART OR AS A WHOLE WITHOUT THE WRITTEN PERMISSION OF UCLA IS PROHIBITED.

NEXT ASSY
USED ON
APPLICATION

UNLESS OTHERWISE SPECIFIED:
DIMENSIONS ARE IN INCHES
TOLERANCES:
FRACTIONAL ±
ANGULAR: MACH ± BEND ±
ONE PLACE DECIMAL ±.100
TWO PLACE DECIMAL ±.010
THREE PLACE DECIMAL ±.005
INTERPRET GEOMETRIC TOLERANCING PER:
MATERIAL
C55 Hardened 440C SS
FINISH
DO NOT SCALE DRAWING

	NAME	DATE
DRAWN	F. BENDANA	3/11/19
CHECKED		
ENG APPR.		
MFG APPR.		
Q.A.		

COMMENTS:

UCLA: Laser Spectroscopy & Gas Dynamics Lab

TITLE:

SupportRod_A

SIZE A
DWG. NO. 5
REV 003
SCALE: 1:1.5
SHEET 1 OF 1

SOLIDWORKS Educational Product. For Instructional Use Only.

PAGE 15

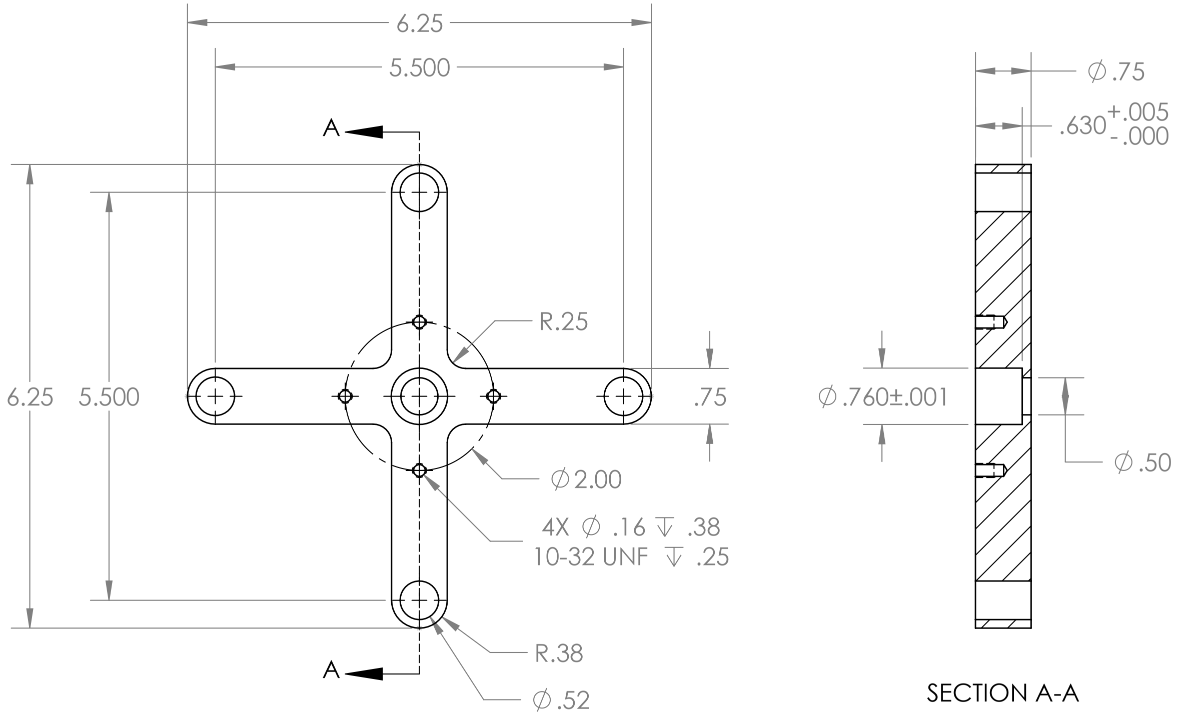

UNLESS OTHERWISE SPECIFIED:		NAME	DATE	UCLA: Laser Spectroscopy & Gas Dynamics Lab
DIMENSIONS ARE IN INCHES TOLERANCES: FRACTIONAL ± ANGULAR: MACH ± BEND ± ONE PLACE DECIMAL ±.100 TWO PLACE DECIMAL ±.010 THREE PLACE DECIMAL ±.005	DRAWN	F. BENDANA	3/11/19	TITLE:
	CHECKED			PoppetValveSupport_A
	ENG APPR.			
	MFG APPR.			
INTERPRET GEOMETRIC TOLERANCING PER:	Q.A.			
MATERIAL 304 SS	COMMENTS:			SIZE A DWG. NO. 6 REV 003
FINISH				
DO NOT SCALE DRAWING				SCALE: 1:2 SHEET 1 OF 1

NEXT ASSY	USED ON
APPLICATION	

PROPRIETARY AND CONFIDENTIAL

THE INFORMATION CONTAINED IN THIS DRAWING IS THE SOLE PROPERTY OF UCLA. ANY REPRODUCTION IN PART OR AS A WHOLE WITHOUT THE WRITTEN PERMISSION OF UCLA IS PROHIBITED.

PAGE 16

SOLIDWORKS Educational Product. For Instructional Use Only.

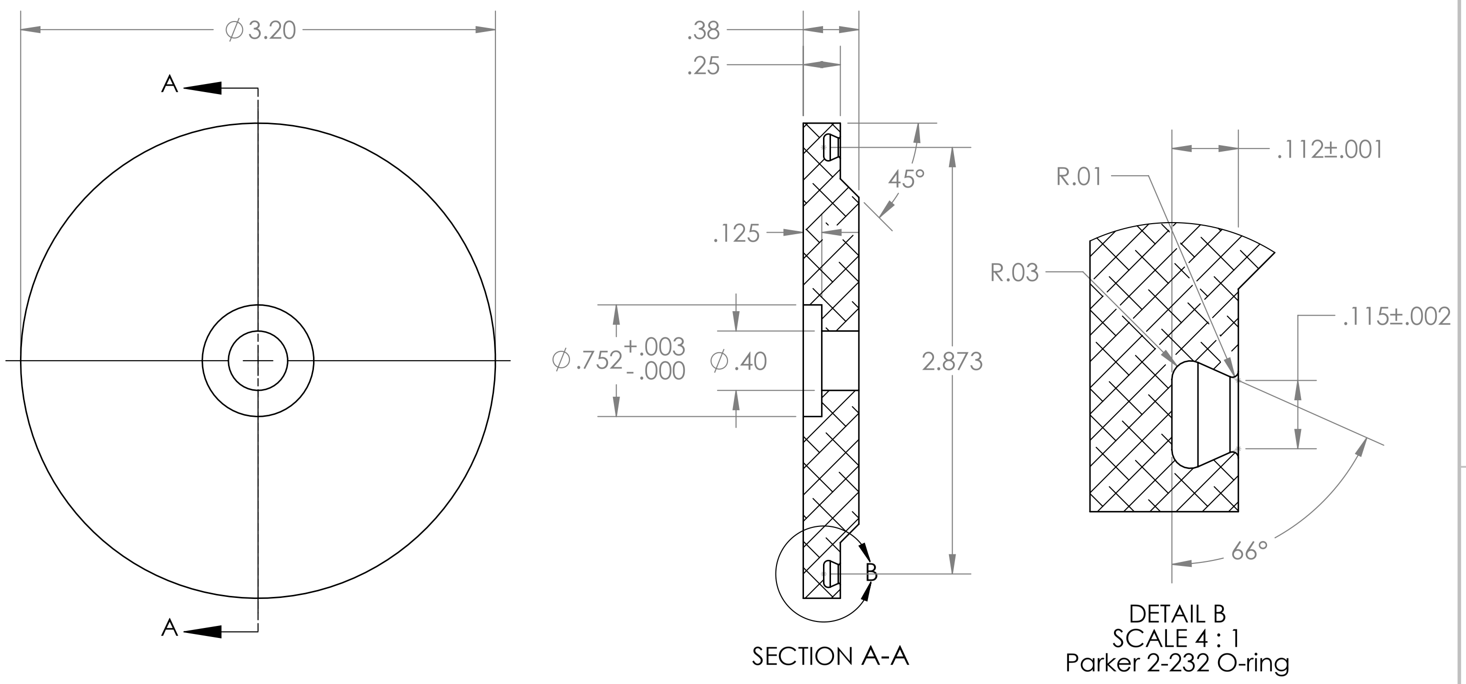

PROPRIETARY AND CONFIDENTIAL

THE INFORMATION CONTAINED IN THIS DRAWING IS THE SOLE PROPERTY OF UCLA. ANY REPRODUCTION IN PART OR AS A WHOLE WITHOUT THE WRITTEN PERMISSION OF UCLA IS PROHIBITED.

NEXT ASSY	USED ON
APPLICATION	

UNLESS OTHERWISE SPECIFIED:
DIMENSIONS ARE IN INCHES
TOLERANCES:
FRACTIONAL ±
ANGULAR: MACH ± BEND ±
ONE PLACE DECIMAL ±.100
TWO PLACE DECIMAL ±.010
THREE PLACE DECIMAL ±.005

INTERPRET GEOMETRIC TOLERANCING PER:

MATERIAL 7075-T6 Al

FINISH

DO NOT SCALE DRAWING

	NAME	DATE
DRAWN	F. BENDANA	3/11/19
CHECKED		
ENG APPR.		
MFG APPR.		
Q.A.		

COMMENTS:

UCLA: Laser Spectroscopy & Gas Dynamics Lab

TITLE:

PoppetValve_A

SIZE	DWG. NO.	REV
A	7	003

SCALE: 1:1 SHEET 1 OF 1

PAGE 17

SOLIDWORKS Educational Product. For Instructional Use Only.

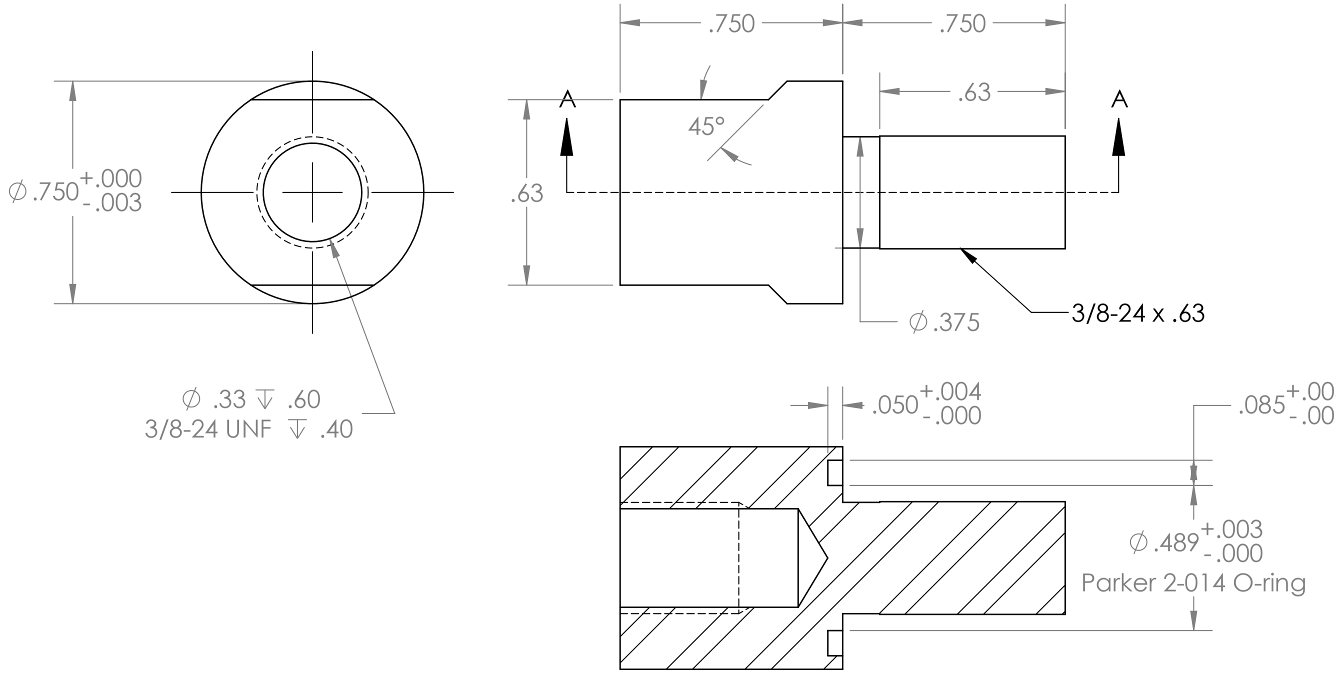

SECTION A-A

PROPRIETARY AND CONFIDENTIAL

THE INFORMATION CONTAINED IN THIS DRAWING IS THE SOLE PROPERTY OF UCLA. ANY REPRODUCTION IN PART OR AS A WHOLE WITHOUT THE WRITTEN PERMISSION OF UCLA IS PROHIBITED.

NEXT ASSY	USED ON
APPLICATION	

UNLESS OTHERWISE SPECIFIED:
DIMENSIONS ARE IN INCHES
TOLERANCES:
FRACTIONAL ±
ANGULAR: MACH ± BEND ±
ONE PLACE DECIMAL ±.100
TWO PLACE DECIMAL ±.010
THREE PLACE DECIMAL ±.005

INTERPRET GEOMETRIC TOLERANCING PER:

MATERIAL
C55 Hardened 440C SS

FINISH

DO NOT SCALE DRAWING

	NAME	DATE
DRAWN	F. BENDANA	3/11/19
CHECKED		
ENG APPR.		
MFG APPR.		
Q.A.		

COMMENTS:

UCLA: Laser Spectroscopy & Gas Dynamics Lab

TITLE:

PoppetValve_B

SIZE	DWG. NO.	REV
A	8	003

SCALE: 2:1 SHEET 1 OF 1

PAGE 18

SOLIDWORKS Educational Product. For Instructional Use Only.

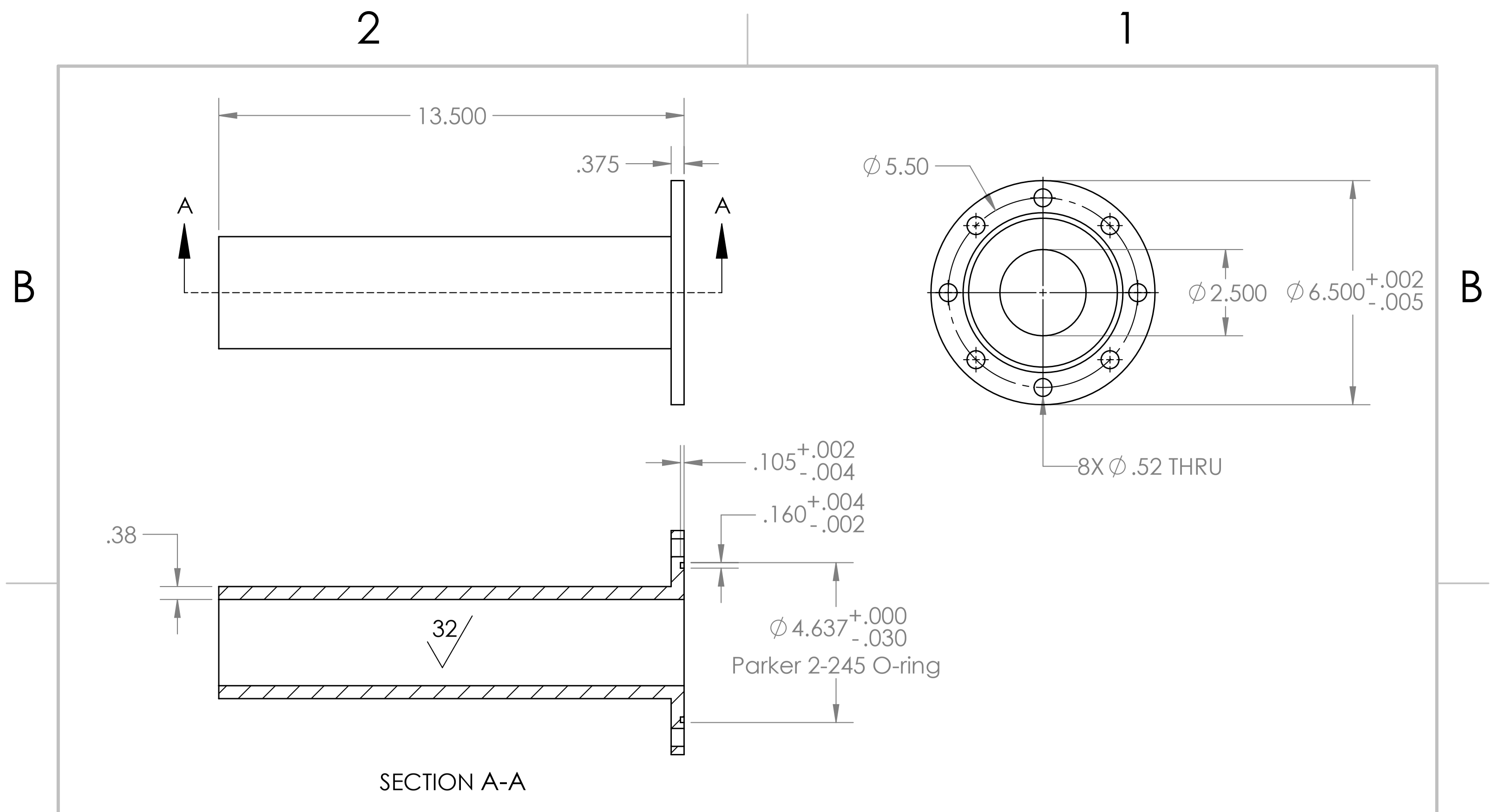

SECTION A-A

PROPRIETARY AND CONFIDENTIAL

THE INFORMATION CONTAINED IN THIS DRAWING IS THE SOLE PROPERTY OF UCLA. ANY REPRODUCTION IN PART OR AS A WHOLE WITHOUT THE WRITTEN PERMISSION OF UCLA IS PROHIBITED.

NEXT ASSY	USED ON
APPLICATION	

UNLESS OTHERWISE SPECIFIED:
DIMENSIONS ARE IN INCHES
TOLERANCES:
FRACTIONAL ±
ANGULAR: MACH ± BEND ±
ONE PLACE DECIMAL ±.100
TWO PLACE DECIMAL ±.010
THREE PLACE DECIMAL ±.005

INTERPRET GEOMETRIC TOLERANCING PER:

MATERIAL 304 SS

FINISH

DO NOT SCALE DRAWING

	NAME	DATE
DRAWN	F. BENDANA	3/11/19
CHECKED		
ENG APPR.		
MFG APPR.		
Q.A.		
COMMENTS:		

UCLA: Laser Spectroscopy & Gas Dynamics Lab

TITLE:

Tube_L

SIZE A
DWG. NO. 9
REV 003

SCALE: 1:4
SHEET 1 OF 1

2
1

SOLIDWORKS Educational Product. For Instructional Use Only.

PAGE 19

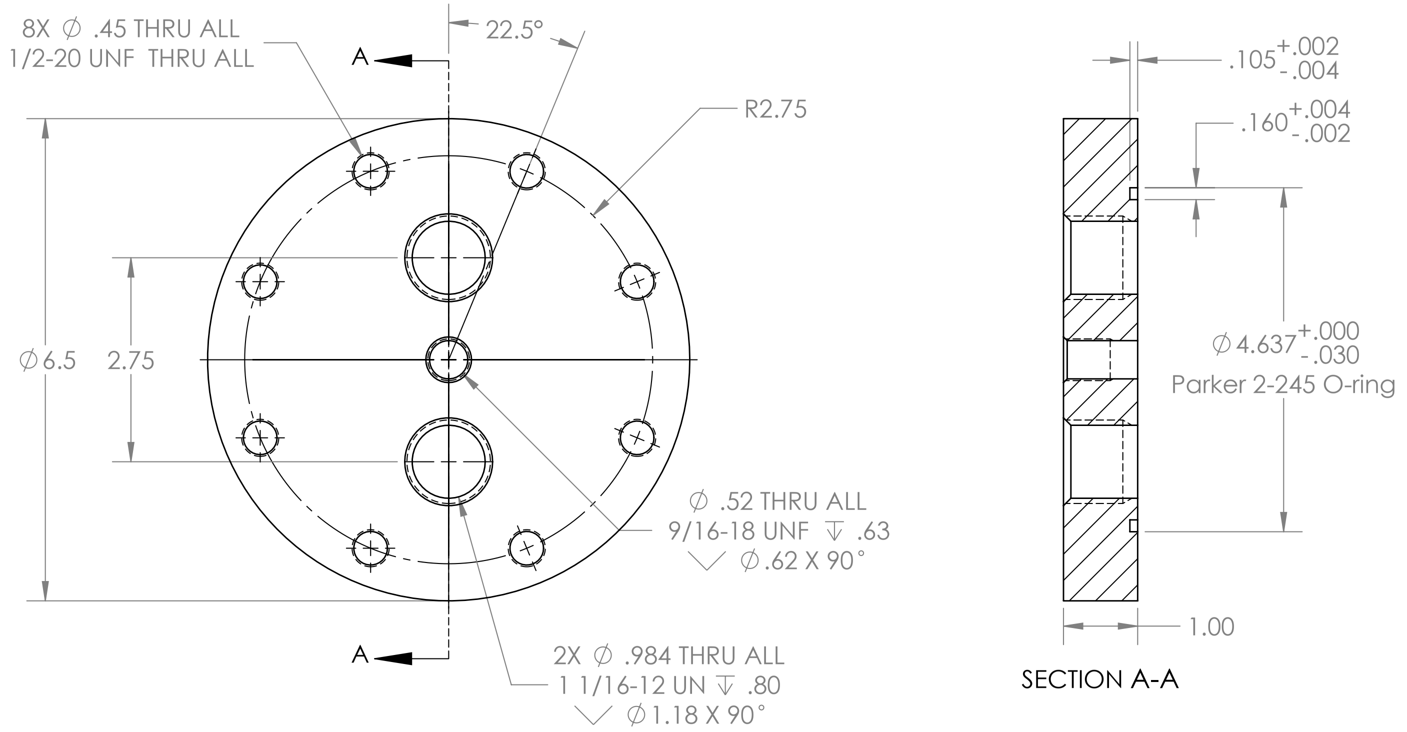

UNLESS OTHERWISE SPECIFIED:	
DIMENSIONS ARE IN INCHES TOLERANCES: FRACTIONAL ± ANGULAR: MACH ± BEND ± ONE PLACE DECIMAL ±.100 TWO PLACE DECIMAL ±.010 THREE PLACE DECIMAL ±.005	
INTERPRET GEOMETRIC TOLERANCING PER:	
MATERIAL	304 SS
FINISH	
DO NOT SCALE DRAWING	

	NAME	DATE
DRAWN	F. BENDANA	3/11/19
CHECKED		
ENG APPR.		
MFG APPR.		
Q.A.		
COMMENTS:		

NEXT ASSY	USED ON
APPLICATION	

PROPRIETARY AND CONFIDENTIAL

THE INFORMATION CONTAINED IN THIS DRAWING IS THE SOLE PROPERTY OF UCLA. ANY REPRODUCTION IN PART OR AS A WHOLE WITHOUT THE WRITTEN PERMISSION OF UCLA IS PROHIBITED.

UCLA: Laser Spectroscopy & Gas Dynamics Lab

TITLE:

EndCap_G

SIZE	DWG. NO.	REV
A	10	003
SCALE: 1:2		SHEET 1 OF 1

PAGE 20

SOLIDWORKS Educational Product. For Instructional Use Only.

2 1

B B

Note: Straightness cannot deviate more than 0.005" over full length

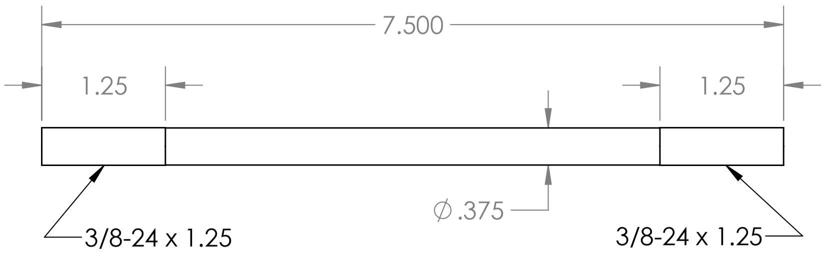

A A

PROPRIETARY AND CONFIDENTIAL

THE INFORMATION CONTAINED IN THIS DRAWING IS THE SOLE PROPERTY OF UCLA. ANY REPRODUCTION IN PART OR AS A WHOLE WITHOUT THE WRITTEN PERMISSION OF UCLA IS PROHIBITED.

NEXT ASSY | USED ON
APPLICATION

UNLESS OTHERWISE SPECIFIED:
DIMENSIONS ARE IN INCHES
TOLERANCES:
FRACTIONAL ±
ANGULAR: MACH ± BEND ±
ONE PLACE DECIMAL ±.100
TWO PLACE DECIMAL ±.010
THREE PLACE DECIMAL ±.005
INTERPRET GEOMETRIC TOLERANCING PER:
MATERIAL
C55 Hardened 440C SS
FINISH
DO NOT SCALE DRAWING

	NAME	DATE
DRAWN	F. BENDANA	3/11/19
CHECKED		
ENG APPR.		
MFG APPR.		
Q.A.		

COMMENTS:

UCLA: Laser Spectroscopy & Gas Dynamics Lab

TITLE:

SupportRod_D

SIZE A
DWG. NO. 11
REV 003
SCALE: 1:1.5
SHEET 1 OF 1

2 1

SOLIDWORKS Educational Product. For Instructional Use Only.

PAGE 21

APPENDIX H

Mixing tank drawing package

University of California, Los Angeles
Laser Spectroscopy & Gas Dynamics Lab
Mixing Tank

Point of Contact:
Fabio Bendana
e: fbendana@ucla.edu
c: 650-255-8224

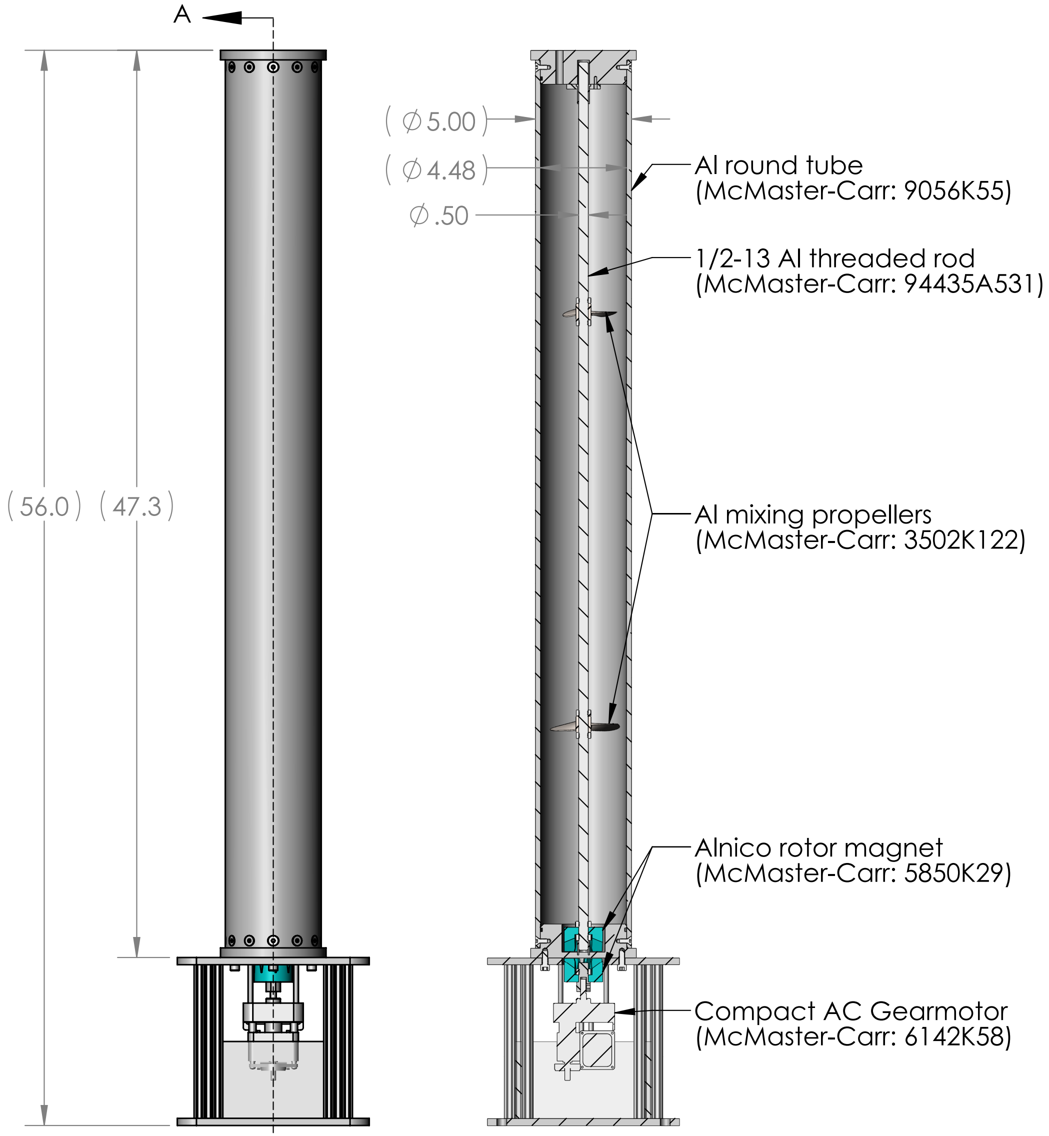

SECTION A-A

PROPRIETARY AND CONFIDENTIAL

THE INFORMATION CONTAINED IN THIS DRAWING IS THE SOLE PROPERTY OF UCLA. ANY REPRODUCTION IN PART OR AS A WHOLE WITHOUT THE WRITTEN PERMISSION OF UCLA IS PROHIBITED.

NEXT ASSY | USED ON
APPLICATION

DIMENSIONS ARE IN INCHES
TOLERANCES:
FRACTIONAL ±
ANGULAR: MACH ± BEND ±
TWO PLACE DECIMAL ±
THREE PLACE DECIMAL ±

MATERIAL

FINISH

DO NOT SCALE DRAWING

	NAME	DATE
DRAWN	F. BENDANA	12/13/20
CHECKED		
ENG APPR.		
MFG APPR.		
Q.A.		

COMMENTS:

UCLA: Laser Spectroscopy & Gas Dynamics Lab

Mixing Tank
Overall Assembly

SIZE A | DWG. NO. | REV. 001
SCALE:1:8 | WEIGHT: | SHEET 1 OF 6

SOLIDWORKS Educational Product. For Instructional Use Only.

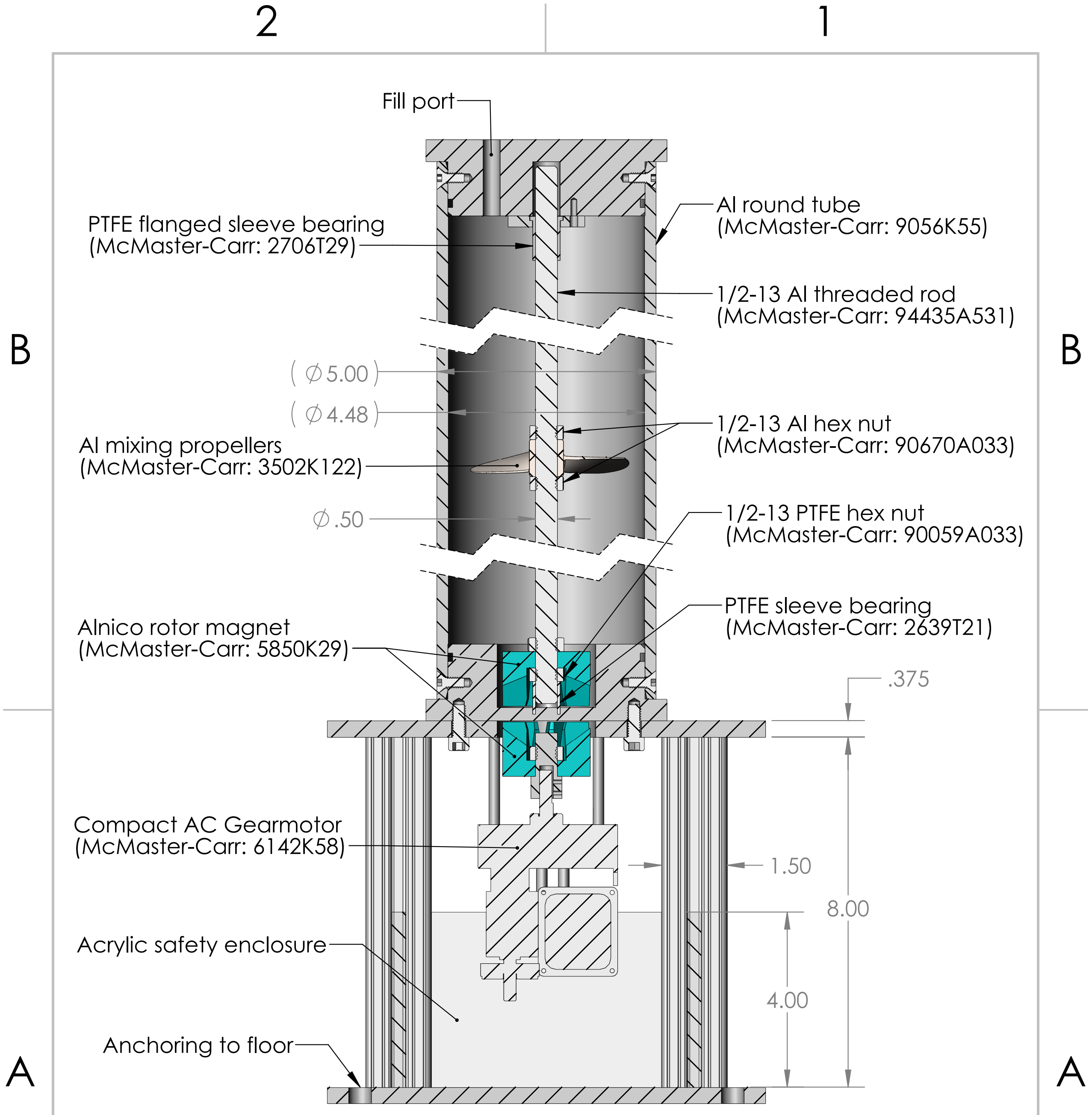

PROPRIETARY AND CONFIDENTIAL

THE INFORMATION CONTAINED IN THIS DRAWING IS THE SOLE PROPERTY OF UCLA. ANY REPRODUCTION IN PART OR AS A WHOLE WITHOUT THE WRITTEN PERMISSION OF UCLA IS PROHIBITED.

NEXT ASSY	USED ON
APPLICATION	

DIMENSIONS ARE IN INCHES
TOLERANCES:
FRACTIONAL ±
ANGULAR: MACH ± BEND ±
TWO PLACE DECIMAL ±
THREE PLACE DECIMAL ±

MATERIAL

FINISH

DO NOT SCALE DRAWING

	NAME	DATE
DRAWN	F. BENDANA	12/13/20
CHECKED		
ENG APPR.		
MFG APPR.		
Q.A.		

COMMENTS:

UCLA: Laser Spectroscopy & Gas Dynamics Lab

Mixing Tank Overall Assembly

SIZE	DWG. NO.	REV.
A		001

SCALE:1:3 WEIGHT: SHEET 2 OF 6

SOLIDWORKS Educational Product. For Instructional Use Only.

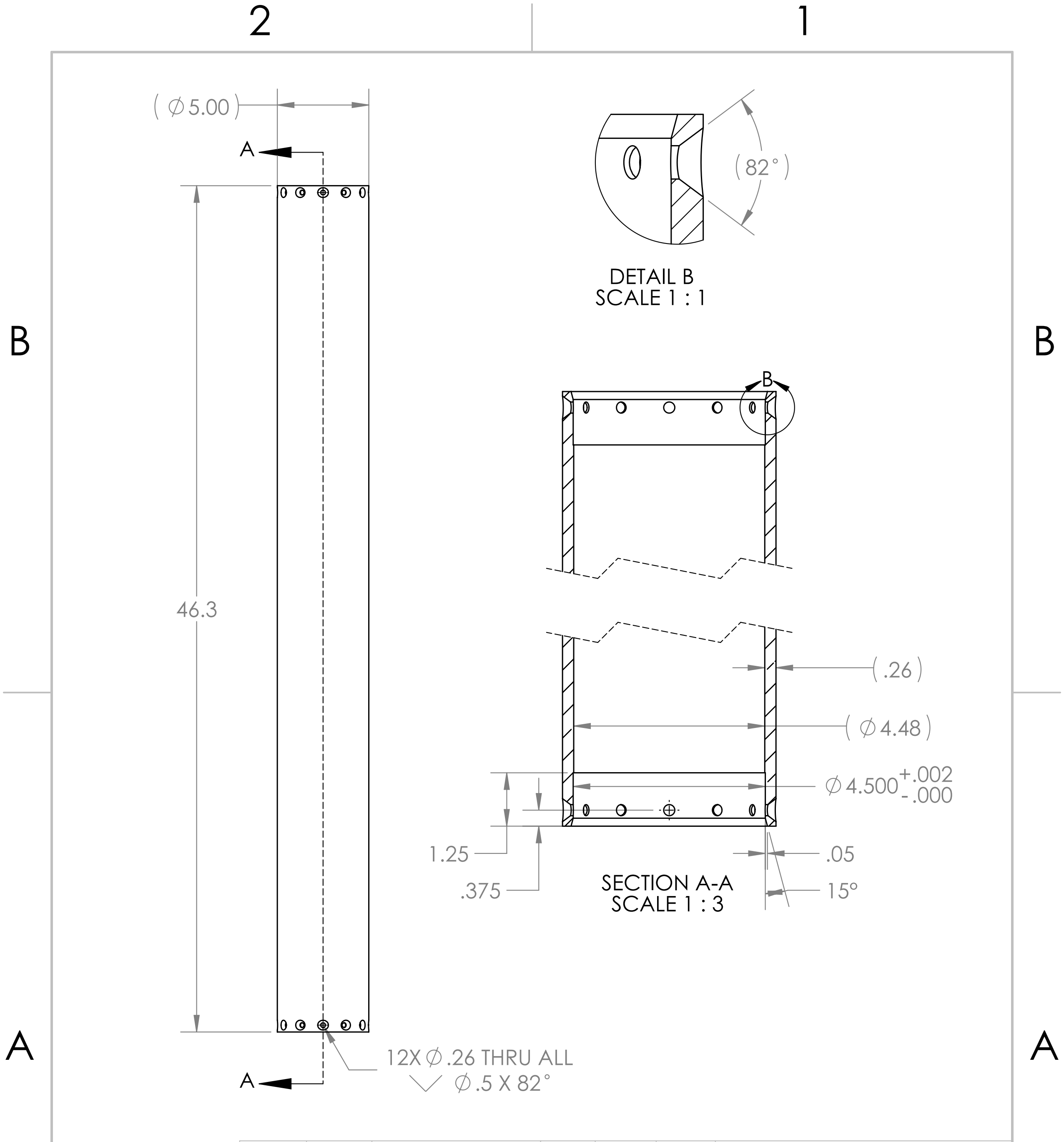

PROPRIETARY AND CONFIDENTIAL

THE INFORMATION CONTAINED IN THIS DRAWING IS THE SOLE PROPERTY OF UCLA. ANY REPRODUCTION IN PART OR AS A WHOLE WITHOUT THE WRITTEN PERMISSION OF UCLA IS PROHIBITED.

NEXT ASSY	USED ON
APPLICATION	

DIMENSIONS ARE IN INCHES
TOLERANCES:
FRACTIONAL ±
ANGULAR: MACH ± BEND ±
ONE PLACE DECIMAL ±.100
TWO PLACE DECIMAL ±.010
THREE PLACE DECIMAL ±.005

MATERIAL
6061 ALUMINUM

FINISH

DO NOT SCALE DRAWING

	NAME	DATE
DRAWN	F. BENDANA	12/13/20
CHECKED		
ENG APPR.		
MFG APPR.		
Q.A.		

COMMENTS:

UCLA: Laser Spectroscopy & Gas Dynamics Lab

Tube_I

SIZE A DWG. NO. REV. 001

SCALE:1:7 WEIGHT: SHEET 3 OF 6

SOLIDWORKS Educational Product. For Instructional Use Only.

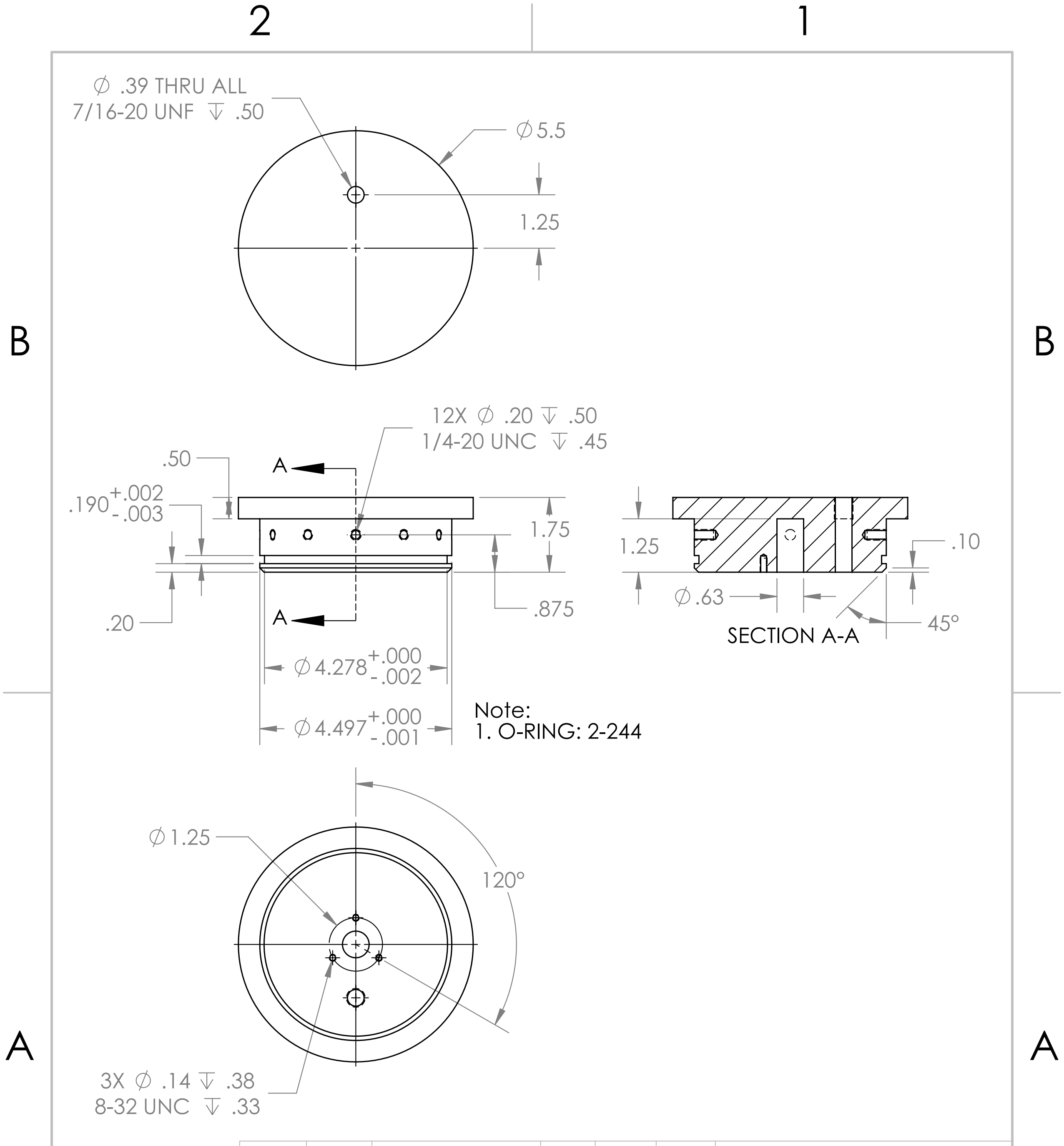

Note:
1. O-RING: 2-244

PROPRIETARY AND CONFIDENTIAL

THE INFORMATION CONTAINED IN THIS DRAWING IS THE SOLE PROPERTY OF UCLA. ANY REPRODUCTION IN PART OR AS A WHOLE WITHOUT THE WRITTEN PERMISSION OF UCLA IS PROHIBITED.

NEXT ASSY	USED ON
APPLICATION	

DIMENSIONS ARE IN INCHES
TOLERANCES:
FRACTIONAL ±
ANGULAR: MACH ± BEND ±
ONE PLACE DECIMAL ±.100
TWO PLACE DECIMAL ±.010
THREE PLACE DECIMAL ±.005

MATERIAL
6061 ALUMINUM

FINISH

DO NOT SCALE DRAWING

	NAME	DATE
DRAWN	F. BENDANA	12/13/20
CHECKED		
ENG APPR.		
MFG APPR.		
Q.A.		
COMMENTS:		

UCLA: Laser Spectroscopy & Gas Dynamics Lab

EndCap_D

SIZE	DWG. NO.	REV.
A		001

SCALE:1:3 WEIGHT: SHEET 4 OF 6

SOLIDWORKS Educational Product. For Instructional Use Only.

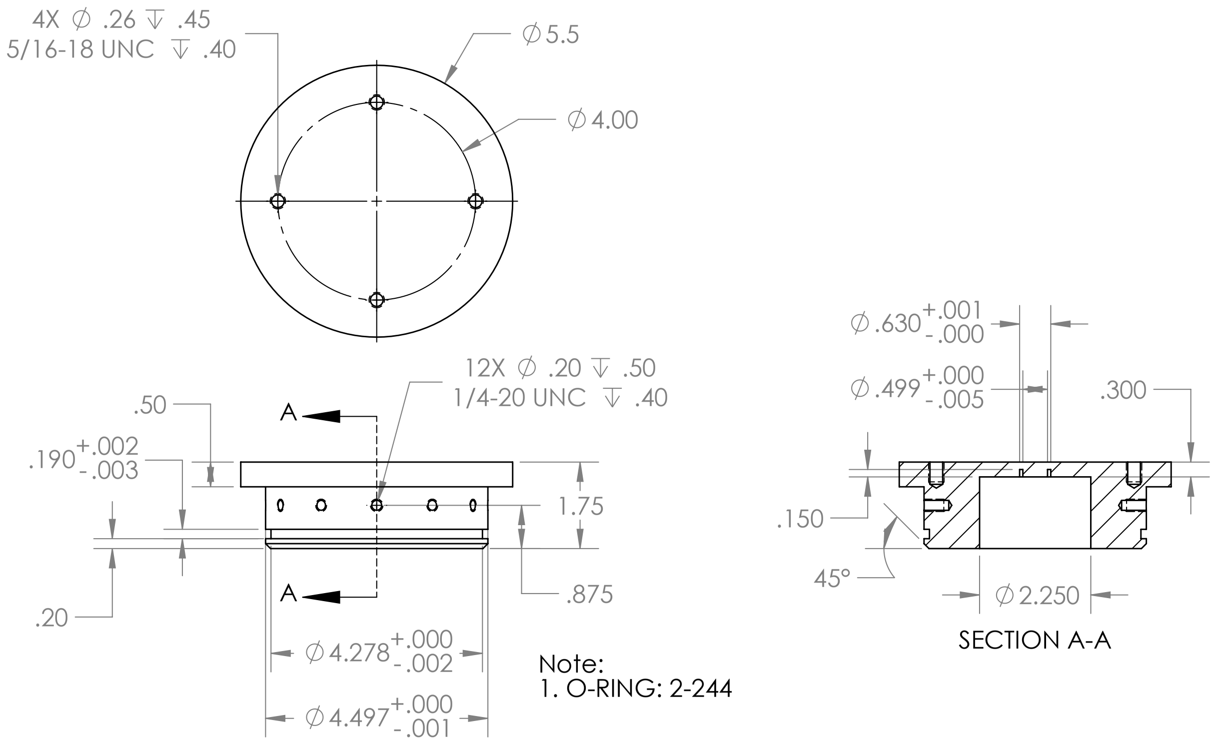

Note:
1. O-RING: 2-244

UNLESS OTHERWISE SPECIFIED:		NAME	DATE	UCLA: Laser Spectroscopy & Gas Dynamics Lab
DIMENSIONS ARE IN INCHES TOLERANCES: FRACTIONAL± ANGULAR: MACH± BEND ± ONE PLACE DECIMAL ±.100 TWO PLACE DECIMAL ±.010 THREE PLACE DECIMAL ±.005	DRAWN	F. BENDANA	12/13/20	TITLE: EndCap_C
	CHECKED			
	ENG APPR.			
	MFG APPR.			
INTERPRET GEOMETRIC TOLERANCING PER:	Q.A.			
MATERIAL 6061 ALUMINUM	COMMENTS:			SIZE A DWG. NO. REV 001
FINISH				
DO NOT SCALE DRAWING				SCALE: 1:3 WEIGHT: SHEET 5 OF 6

NEXT ASSY | USED ON

APPLICATION

PROPRIETARY AND CONFIDENTIAL

THE INFORMATION CONTAINED IN THIS DRAWING IS THE SOLE PROPERTY OF UCLA. ANY REPRODUCTION IN PART OR AS A WHOLE WITHOUT THE WRITTEN PERMISSION OF UCLA IS PROHIBITED.

SOLIDWORKS Educational Product. For Instructional Use Only.

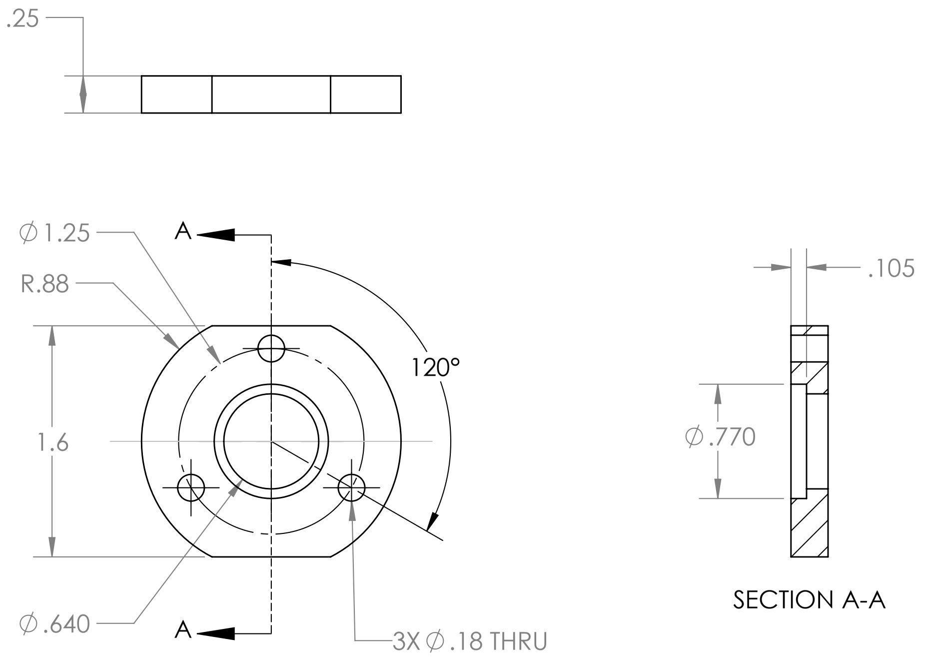

UNLESS OTHERWISE SPECIFIED:		NAME	DATE	UCLA: Laser Spectroscopy & Gas Dynamics Lab
DIMENSIONS ARE IN INCHES TOLERANCES: FRACTIONAL± ANGULAR: MACH± BEND ± ONE PLACE DECIMAL ±.100 TWO PLACE DECIMAL ±.010 THREE PLACE DECIMAL ±.005	DRAWN	F. BENDANA	12/13/20	TITLE: Bearing_C
	CHECKED			
	ENG APPR.			
	MFG APPR.			
INTERPRET GEOMETRIC TOLERANCING PER:	Q.A.			
MATERIAL 6061 ALUMINUM	COMMENTS:			SIZE A DWG. NO. REV 001
FINISH				
DO NOT SCALE DRAWING				SCALE: 1:1 WEIGHT: SHEET 6 OF 6

NEXT ASSY	USED ON
APPLICATION	

PROPRIETARY AND CONFIDENTIAL

THE INFORMATION CONTAINED IN THIS DRAWING IS THE SOLE PROPERTY OF UCLA. ANY REPRODUCTION IN PART OR AS A WHOLE WITHOUT THE WRITTEN PERMISSION OF UCLA IS PROHIBITED.

SOLIDWORKS Educational Product. For Instructional Use Only.

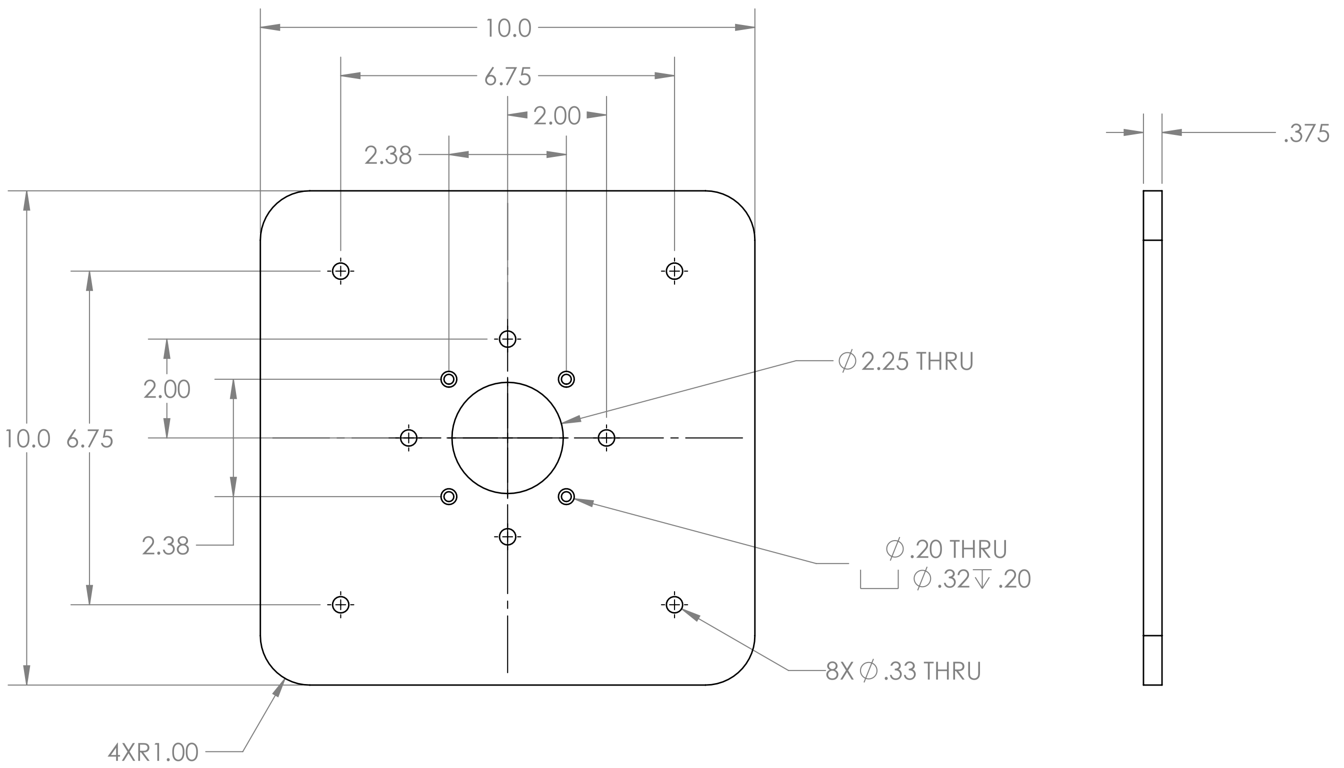

PROPRIETARY AND CONFIDENTIAL

THE INFORMATION CONTAINED IN THIS DRAWING IS THE SOLE PROPERTY OF UCLA. ANY REPRODUCTION IN PART OR AS A WHOLE WITHOUT THE WRITTEN PERMISSION OF UCLA IS PROHIBITED.

NEXT ASSY	USED ON
APPLICATION	

UNLESS OTHERWISE SPECIFIED:
DIMENSIONS ARE IN INCHES
TOLERANCES:
FRACTIONAL ±
ANGULAR: MACH ± BEND ±
ONE PLACE DECIMAL ±.1
TWO PLACE DECIMAL ±.01
THREE PLACE DECIMAL ±.005

INTERPRET GEOMETRIC TOLERANCING PER:

MATERIAL
.375" Aluminum

FINISH

DO NOT SCALE DRAWING

	NAME	DATE
DRAWN	F. BENDANA	5/24/17
CHECKED		
ENG APPR.		
MFG APPR.		
Q.A.		

COMMENTS:

UCLA: Laser Spectroscopy & Gas Dynamics Lab

TITLE:

EnclosurePlate_A

SIZE A
DWG. NO.
REV 001

SCALE: 1:3
SHEET 1 OF 1

SOLIDWORKS Educational Product. For Instructional Use Only.

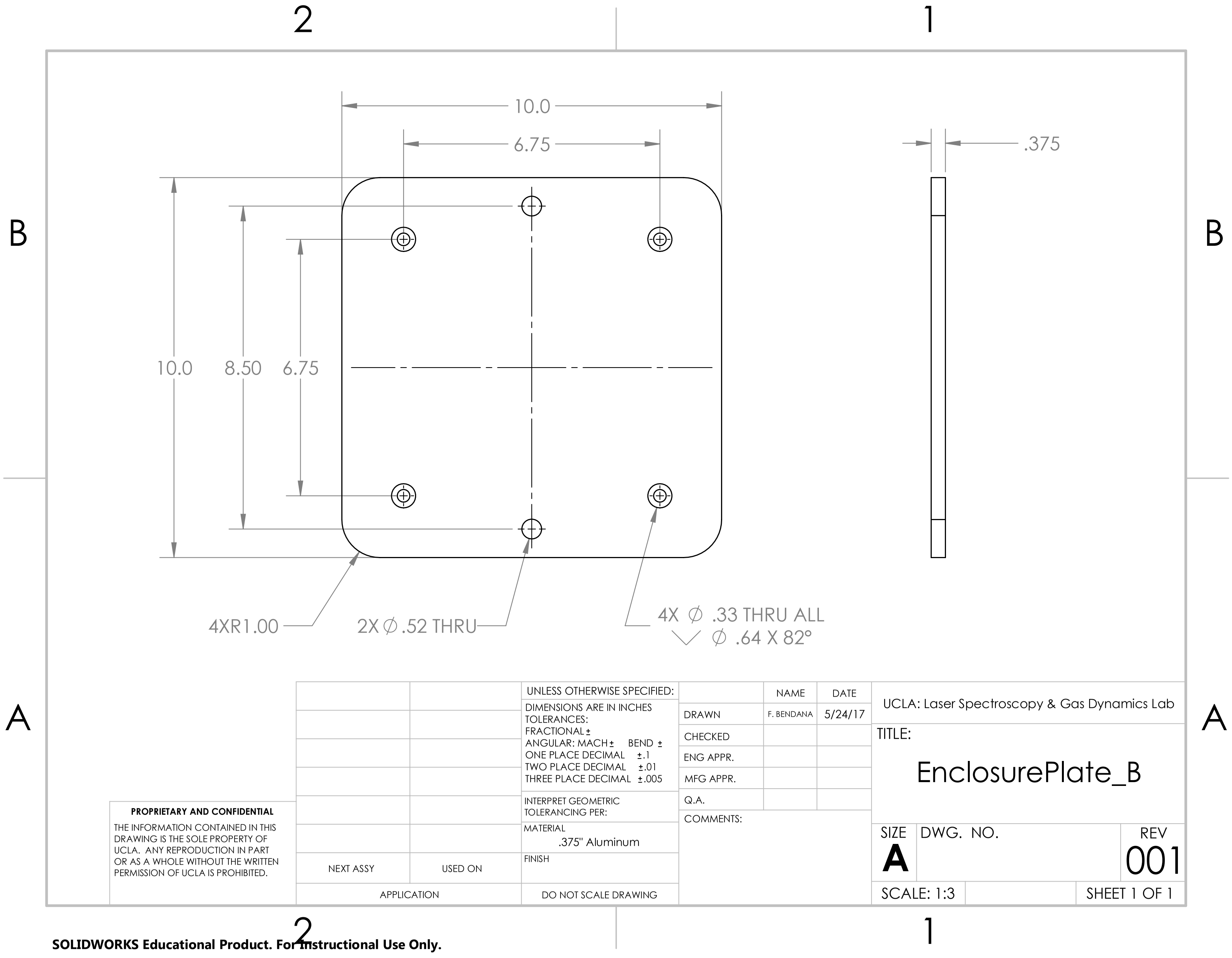

SOLIDWORKS Educational Product. For Instructional Use Only.

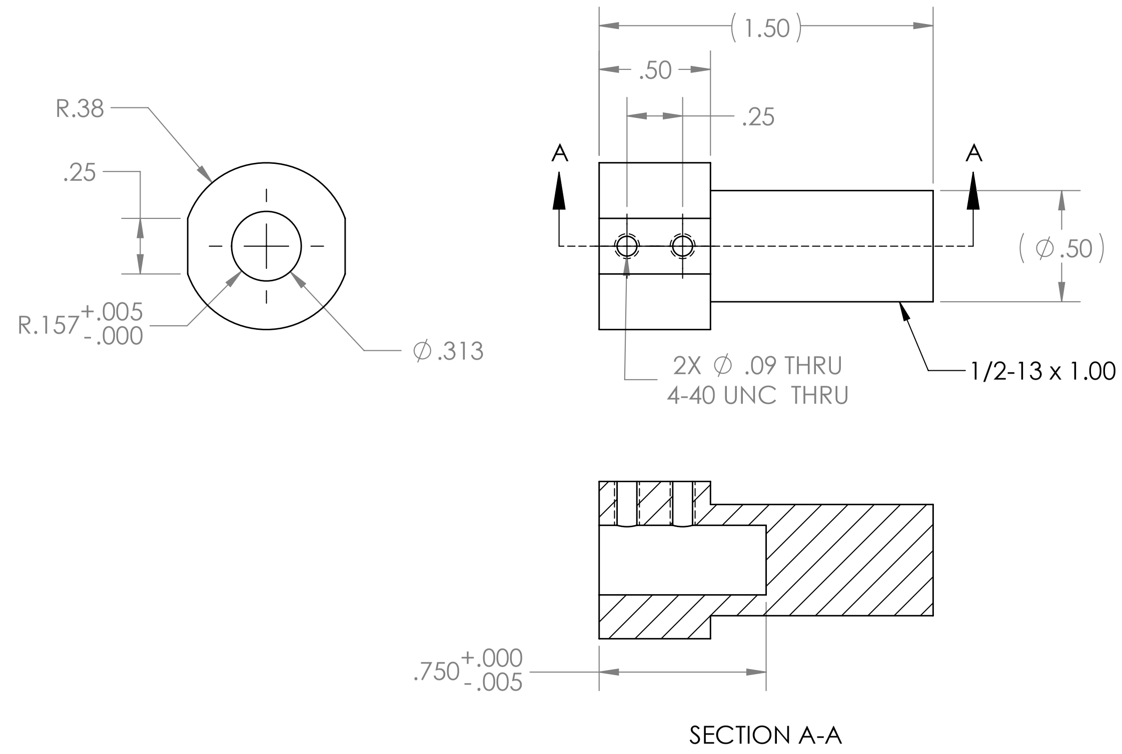

PROPRIETARY AND CONFIDENTIAL

THE INFORMATION CONTAINED IN THIS DRAWING IS THE SOLE PROPERTY OF UCLA. ANY REPRODUCTION IN PART OR AS A WHOLE WITHOUT THE WRITTEN PERMISSION OF UCLA IS PROHIBITED.

NEXT ASSY	USED ON
APPLICATION	

UNLESS OTHERWISE SPECIFIED:
DIMENSIONS ARE IN INCHES
TOLERANCES:
FRACTIONAL ±
ANGULAR: MACH ± BEND ±
ONE PLACE DECIMAL ±.1
TWO PLACE DECIMAL ±.01
THREE PLACE DECIMAL ±.005

INTERPRET GEOMETRIC TOLERANCING PER:

MATERIAL
6061 Aluminum

FINISH

DO NOT SCALE DRAWING

	NAME	DATE
DRAWN	F. BENDANA	5/24/17
CHECKED		
ENG APPR.		
MFG APPR.		
Q.A.		

COMMENTS:

UCLA: Laser Spectroscopy & Gas Dynamics Lab

TITLE:

ShaftCoupler_A

SIZE A
DWG. NO.
REV 001

SCALE: 3:2
SHEET 1 OF 1

SOLIDWORKS Educational Product. For Instructional Use Only.

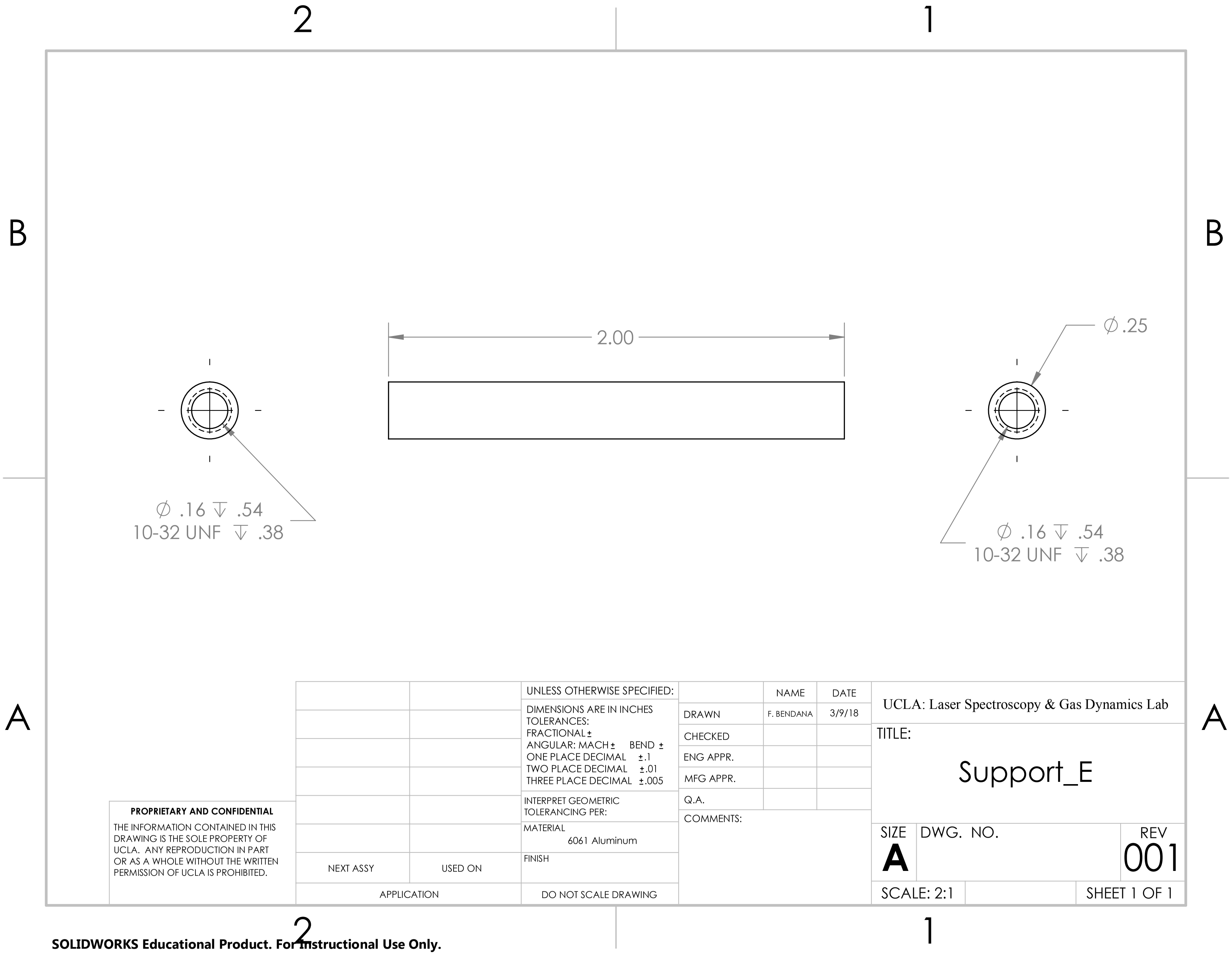
2
1
B
A
2.00
∅ .25
∅ .16 ↧ .54
10-32 UNF ↧ .38
∅ .16 ↧ .54
10-32 UNF ↧ .38
PROPRIETARY AND CONFIDENTIAL
THE INFORMATION CONTAINED IN THIS DRAWING IS THE SOLE PROPERTY OF UCLA. ANY REPRODUCTION IN PART OR AS A WHOLE WITHOUT THE WRITTEN PERMISSION OF UCLA IS PROHIBITED.
NEXT ASSY
USED ON
APPLICATION
UNLESS OTHERWISE SPECIFIED:
DIMENSIONS ARE IN INCHES
TOLERANCES:
FRACTIONAL ±
ANGULAR: MACH ± BEND ±
ONE PLACE DECIMAL ±.1
TWO PLACE DECIMAL ±.01
THREE PLACE DECIMAL ±.005
INTERPRET GEOMETRIC TOLERANCING PER:
MATERIAL
6061 Aluminum
FINISH
DO NOT SCALE DRAWING
NAME
DATE
DRAWN
F. BENDANA
3/9/18
CHECKED
ENG APPR.
MFG APPR.
Q.A.
COMMENTS:
UCLA: Laser Spectroscopy & Gas Dynamics Lab
TITLE:
Support_E
SIZE
A
DWG. NO.
REV
001
SCALE: 2:1
SHEET 1 OF 1
SOLIDWORKS Educational Product. For Instructional Use Only.

Bibliography

[1] D. K. Huzel and D. H. Huang, *Modern Engineering for Design of Liquid-Propellant Rocket Engines*. Washington DC: American Institute of Aeronautics and Astronautics, 1 1992.

[2] G. P. Sutton, "History of Liquid Propellant Rocket Engines in the United States," *Journal of Propulsion and Power*, vol. 19, pp. 978–1007, 11 2003.

[3] P. McRight, C. Popp, C. Pierce, A. Turpin, W. Urbanchock, and M. Wilson, "Confidence Testing of Shell-405 and S-405 Catalysts in a Monopropellant Hydrazine Thruster," in *41st AIAA/ASME/SAE/ASEE Joint Propulsion Conference & Exhibit*, no. July, American Institute of Aeronautics and Astronautics, 7 2005.

[4] E. J. Wucherer, T. Cook, M. Stiefel, R. Humphries, and J. Parker, "Hydrazine Catalyst Production - Sustaining S-405 Technology," in *39th AIAA/ASME/SAE/ASEE Joint Propulsion Conference and Exhibit*, no. July, American Institute of Aeronautics and Astronautics, 7 2003.

[5] M. Ventura and P. Mullens, "The use of hydrogen peroxide for propulsion and power," in *35th Joint Propulsion Conference and Exhibit*, no. June, American Institute of Aeronautics and Astronautics, 6 1999.

[6] E. W. Schmidt and E. J. Wucherer, "Hydrazine(S) vs. nontoxic propellants - Where do we stand now?," *European Space Agency, (Special Publication) ESA SP*, vol. 2004, no. 557, pp. 17–22, 2004.

[7] M. J. Casiano, J. R. Hulka, and V. Yang, "Liquid-Propellant Rocket Engine Throttling: A Comprehensive Review," *Journal of Propulsion and Power*, vol. 26, pp. 897–923, 9 2010.

[8] G. P. Sutton and O. Biblarz, *Rocket Propulsion Elements*. Hoboken, NJ, USA: John Wiley & Sons, Inc., 8th ed., 2010.

[9] M. A. Karabeyoglu, D. Altman, and B. J. Cantwell, "Combustion of Liquefying Hybrid Propellants: Part 1, General Theory," *Journal of Propulsion and Power*, vol. 18, pp. 610–620, 5 2002.

[10] M. A. Karabeyoglu and B. J. Cantwell, "Combustion of Liquefying Hybrid Propellants: Part 2, Stability of Liquid Films," *Journal of Propulsion and Power*, vol. 18, pp. 621–630, 5 2002.

[11] M. Karabeyoglu, B. Cantwell, and D. Altman, "Development and testing of paraffin-based hybrid rocket fuels," in *37th Joint Propulsion Conference and Exhibit*, no. c, (Reston, Virigina), American Institute of Aeronautics and Astronautics, 7 2001.

[12] A. Chandler, E. Jens, B. Cantwell, and G. S. Hubbard, "Visualization of the Liquid Layer Combustion of Paraffin Fuel for Hybrid Rocket Applications," in *48th AIAA/ASME/SAE/ASEE Joint Propulsion Conference & Exhibit*, no. August, (Reston, Virigina), American Institute of Aeronautics and Astronautics, 7 2012.

[13] E. T. Jens, A. A. Chandler, B. Cantwell, G. S. Hubbard, and F. Mechentel, "Combustion Visualization of Paraffin-Based Hybrid Rocket Fuel at Elevated Pressures," in *50th AIAA/ASME/SAE/ASEE Joint Propulsion Conference*, (Reston, Virginia), American Institute of Aeronautics and Astronautics, 7 2014.

[14] E. T. Jens, B. J. Cantwell, and G. S. Hubbard, "Hybrid Rocket Propulsion Systems for Outer Planet Exploration Missions," *Acta Astronautica*, vol. 128, pp. 119–130, 11 2016.

[15] G. Zilliac and M. Karabeyoglu, "Hybrid Rocket Fuel Regression Rate Data and Modeling," in *42nd AIAA/ASME/SAE/ASEE Joint Propulsion Conference and Exhibit*, no. July, (Reston, Virginia), pp. 1–21, American Institute of Aeronautics and Astronautics, 7 2006.

[16] A. C. Karp, B. Nakazono, G. Story, J. Chaffin, and G. Zilliac, "Hybrid Propulsion

Technology Development for a Potential Near- Term Mars Ascent Vehicle," in *2019 IEEE Aerospace Conference*, vol. 2019-March, pp. 1–8, IEEE, 3 2019.

[17] Y.-S. Chen and B. Wu, "Development of a Small Launch Vehicle with Hybrid Rocket Propulsion," in *2018 Joint Propulsion Conference*, no. July, (Reston, Virginia), pp. 9–11, American Institute of Aeronautics and Astronautics, 7 2018.

[18] E. T. Jens, A. C. Karp, J. Rabinovitch, A. Conte, B. Nakazono, and D. A. Vaughan, "Design of Interplanetary Hybrid CubeSat and SmallSat Propulsion Systems," in *2018 Joint Propulsion Conference*, (Reston, Virginia), pp. 1–18, American Institute of Aeronautics and Astronautics, 7 2018.

[19] R. W. Conversano, J. Rabinovitch, N. J. Strange, N. Arora, E. Jens, and A. C. Karp, "SmallSat Missions Enabled by Paired Low- Thrust Hybrid Rocket and Low-Power Long-Life Hall Thruster," in *2019 IEEE Aerospace Conference*, vol. 2019-March, pp. 1–8, IEEE, 3 2019.

[20] R. K. Hanson, "Applications of quantitative laser sensors to kinetics, propulsion and practical energy systems," *Proceedings of the Combustion Institute*, vol. 33, no. 1, pp. 1–40, 2011.

[21] D. Salgues, A.-G. Mouis, S.-Y. Lee, D. Kalitan, S. Pal, and R. Santoro, "Shear and Swirl Coaxial Injector Studies of LOX/GCH4 Rocket Combustion Using Non-Intrusive Laser Diagnostics," in *44th AIAA Aerospace Sciences Meeting and Exhibit*, vol. 12, pp. 9159–9172, American Institute of Aeronautics and Astronautics, 1 2006.

[22] B. K. McMillin, J. L. Palmer, and R. K. Hanson, "Temporally resolved, two-line fluorescence imaging of NO temperature in a transverse jet in a supersonic cross flow," *Applied Optics*, vol. 32, p. 7532, 12 1993.

[23] A. Ben-Yakar and R. K. Hanson, "Cavity Flame-Holders for Ignition and Flame Stabilization in Scramjets: An Overview," *Journal of Propulsion and Power*, vol. 17, pp. 869–877, 7 2001.

[24] J. Smith, D. Klimenko, W. Clauss, and W. Mayer, "Supercritical LOX/Hydrogen Rocket Combustion Investigations Using Optical Diagnostics," in *38th AIAA/ASME/SAE/ASEE Joint Propulsion Conference & Exhibit*, no. July, American Institute of Aeronautics and Astronautics, 7 2002.

[25] F. Grisch, E. Bertseva, M. Habiballah, E. Jourdanneau, F. Chaussard, R. Saint-Loup, T. Gabard, and H. Berger, "CARS spectroscopy of CH4 for implication of temperature measurements in supercritical LOX/CH4 combustion," *Aerospace Science and Technology*, vol. 11, pp. 48–54, 1 2007.

[26] F. Grisch, P. Bouchardy, and W. Clauss, "CARS thermometry in high pressure rocket combustors," *Aerospace Science and Technology*, vol. 7, pp. 317–330, 6 2003.

[27] C. S. Goldenstein, R. M. Spearrin, J. B. Jeffries, and R. K. Hanson, "Infrared laser absorption sensors for multiple performance parameters in a detonation combustor," *Proceedings of the Combustion Institute*, vol. 35, no. 3, pp. 3739–3747, 2015.

[28] R. M. Spearrin, C. S. Goldenstein, J. B. Jeffries, and R. K. Hanson, "Mid-infrared Laser Absorption Diagnostics for Detonation Studies," in *29th International Symposium on Shock Waves 1*, pp. 259–264, Cham: Springer International Publishing, 2015.

[29] W. Y. Peng, S. J. Cassady, C. L. Strand, C. S. Goldenstein, R. M. Spearrin, C. M. Brophy, J. B. Jeffries, and R. K. Hanson, "Single-ended mid-infrared laser-absorption sensor for time-resolved measurements of water concentration and temperature within the annulus of a rotating detonation engine," *Proceedings of the Combustion Institute*, vol. 37, no. 2, pp. 1435–1443, 2019.

[30] A. P. Nair, D. D. Lee, D. I. Pineda, J. Kriesel, W. A. Hargus, J. W. Bennewitz, S. A. Danczyk, and R. M. Spearrin, "MHz laser absorption spectroscopy via diplexed RF modulation for pressure, temperature, and species in rotating detonation rocket flows," *Applied Physics B*, vol. 126, p. 138, 8 2020.

[31] M. L. Huber, E. W. Lemmon, L. S. Ott, and T. J. Bruno, "Preliminary Surrogate Mixture Models for the Thermophysical Properties of Rocket Propellants RP-1 and RP-2," *Energy & Fuels*, vol. 23, pp. 3083–3088, 6 2009.

[32] Z. Hong, D. F. Davidson, and R. K. Hanson, "An improved H2/O2 mechanism based on recent shock tube/laser absorption measurements," *Combustion and Flame*, vol. 158, pp. 633–644, 4 2011.

[33] Z. Hong, D. Davidson, E. Barbour, and R. Hanson, "A new shock tube study of the H+O2→OH+O reaction rate using tunable diode laser absorption of H2O near 2.5μm," *Proceedings of the Combustion Institute*, vol. 33, no. 1, pp. 309–316, 2011.

[34] Y. Hidaka, S. Kazutaka, Y. Henmi, H. Tanaka, and K. Inami, "Shock-tube and modeling study of methane pyrolysis and oxidation," *Combustion and Flame*, vol. 118, pp. 340–358, 8 1999.

[35] S. Vasu, D. Davidson, Z. Hong, V. Vasudevan, and R. Hanson, "n-Dodecane oxidation at high-pressures: Measurements of ignition delay times and OH concentration time-histories," *Proceedings of the Combustion Institute*, vol. 32, no. 1, pp. 173–180, 2009.

[36] J. Shao, R. Choudhary, Y. Peng, D. F. Davidson, and R. K. Hanson, "A shock tube study of n-heptane, iso-octane, n-dodecane and iso-octane/n-dodecane blends oxidation at elevated pressures and intermediate temperatures," *Fuel*, vol. 243, no. January, pp. 541–553, 2019.

[37] H.-P. S. Shen, J. Steinberg, J. Vanderover, and M. A. Oehlschlaeger, "A Shock Tube Study of the Ignition of n-Heptane, n-Decane, n-Dodecane, and n-Tetradecane at Elevated Pressures," *Energy & Fuels*, vol. 23, pp. 2482–2489, 5 2009.

[38] D. Davidson, D. Haylett, and R. Hanson, "Development of an aerosol shock tube for kinetic studies of low-vapor-pressure fuels," *Combustion and Flame*, vol. 155, pp. 108–117, 10 2008.

[39] M. F. Campbell, T. Parise, A. M. Tulgestke, R. M. Spearrin, D. F. Davidson, and R. K. Hanson, "Strategies for obtaining long constant-pressure test times in shock tubes," *Shock Waves*, vol. 25, pp. 651–665, 11 2015.

[40] J. D. Anderson, *Modern Compressible Flow.* McGraw-Hill, 3rd ed., 2002.

[41] E. L. Resler, S. Lin, and A. Kantrowitz, "The Production of High Temperature Gases in Shock Tubes," *Journal of Applied Physics*, vol. 23, pp. 1390–1399, 12 1952.

[42] A. Gaydon and I. Hurle, *The shock tube in high-temperature chemical physics.* New York: Reinhold Pub. Corp, 1963.

[43] E. M. Rothkopf and W. Low, "Shock formation distance in a pressure driven shock tube," *Physics of Fluids*, vol. 19, no. 12, p. 1885, 1976.

[44] D. R. White, "Influence of diaphragm opening time on shock-tube flows," *Journal of Fluid Mechanics*, vol. 4, pp. 585–599, 11 1958.

[45] "Wisconsin x-t Diagram Tool."

[46] H. Li, Z. C. Owens, D. F. Davidson, and R. K. Hanson, "A simple reactive gasdynamic model for the computation of gas temperature and species concentrations behind reflected shock waves," *International Journal of Chemical Kinetics*, vol. 40, pp. 189–198, 4 2008.

[47] D. F. Davidson and R. K. Hanson, "Recent advances in shock tube/laser diagnostic methods for improved chemical kinetics measurements," *Shock Waves*, vol. 19, pp. 271–283, 8 2009.

[48] C. WITTLIFF, "Hypersonic shock tunnel heat transfer tests of the Space Shuttle SILTS pod configuration," in *18th Thermophysics Conference*, American Institute of Aeronautics and Astronautics, 7 1983.

[49] R. C. Evans, "Operation and performance of a shock tube with heated driver," Tech. Rep. 48, GALCIT, 1959.

[50] A. Hertzberg and W. E. Smith, “A Method for Generating Strong Shock Waves,” *Journal of Applied Physics*, vol. 25, pp. 130–131, 1 1954.

[51] J. BELANGER and H. HORNUNG, “A combustion driven shock tunnel to complement the free piston shocktunnel T5 at GALCIT,” in *28th Joint Propulsion Conference and Exhibit*, (Reston, Virigina), American Institute of Aeronautics and Astronautics, 7 1992.

[52] H. r. Yu, B. Esser, M. Lenartz, and H. Grönig, “Gaseous detonation driver for a shock tunnel,” *Shock Waves*, vol. 2, pp. 245–254, 12 1992.

[53] Y. Hongru, “Oxyhydrogen combustion and detontion,” *Acta Mechanica Sinica*, vol. 15, no. 2, pp. 98–107, 1999.

[54] R. J. STALKER, “A study of the free-piston shock tunnel.,” *AIAA Journal*, vol. 5, pp. 2160–2165, 12 1967.

[55] R. J. Stalker, “Recent developments with free piston drivers,” in *AIP Conference Proceedings*, vol. 208, pp. 96–107, AIP, 1990.

[56] S. Gai, “Free piston shock tunnels: developments and capabilities,” *Progress in Aerospace Sciences*, vol. 29, pp. 1–41, 1 1992.

[57] J. C. Camm and P. H. Rose, “Electric Arc-Driven Shock Tube,” *Physics of Fluids*, vol. 6, no. 5, p. 663, 1963.

[58] R. G. Fowler, J. S. Goldstein, and B. E. Clotfelter, “Luminous Fronts in Pulsed Gas Discharges,” *Physical Review*, vol. 82, pp. 879–882, 6 1951.

[59] A. C. Kolb, “Production of High-Energy Plasmas by Magnetically Driven Shock Waves,” *Physical Review*, vol. 107, pp. 345–350, 7 1957.

[60] D. Bershader, “Some Remarks on Electric-Discharge Shock-Tube Diagnostics,” *Reviews of Modern Physics*, vol. 32, pp. 780–784, 10 1960.

[61] D. W. Koopman, “Performance Studies with an Electrically Driven Shock Tube,” *Physics of Fluids*, vol. 7, no. 10, p. 1651, 1964.

[62] D. E. Bloxsom, “Electrically Driven Shock Tube,” *Journal of Applied Physics*, vol. 29, pp. 1128–1129, 7 1958.

[63] S. P. Sharma and C. Park, “Operating Characteristics of a 60- and 10-cm Electric Arc-Driven Shock Tube-Part I: The Driver,” *Journal of Thermophysics and Heat Transfer*, vol. 4, pp. 259–265, 7 1990.

[64] M. F. Campbell, K. G. Owen, D. F. Davidson, and R. K. Hanson, “Dependence of Calculated Postshock Thermodynamic Variables on Vibrational Equilibrium and Input Uncertainty,” *Journal of Thermophysics and Heat Transfer*, vol. 31, pp. 586–608, 7 2017.

[65] R. E. Mitchell and R. J. Kee, “A general-purpose computer code for predicting chemical-kinetic behavior behind incident and reflected shocks,” tech. rep., NASA STI/Recon Technical Report N, 1982.

[66] D. F. Davidson and R. K. Hanson, “Real Gas Corrections in Shock Tube Studies at High Pressures,” *Israel Journal of Chemistry*, vol. 36, no. 3, pp. 321–326, 1996.

[67] H. A. Bethe and E. Teller, “Deviations from thermal equilibrium in shock waves,” tech. rep., Engineering Research Inst., Univ. of Mich.; Cornell Univ.; George Washington Univ., 1953.

[68] R. C. Millikan and D. R. White, “Systematics of Vibrational Relaxation,” *The Journal of Chemical Physics*, vol. 39, pp. 3209–3213, 12 1963.

[69] W. J. Hooker and R. C. Millikan, “Shock-Tube Study of Vibrational Relaxation in Carbon Monoxide for the Fundamental and First Overtone,” *The Journal of Chemical Physics*, vol. 38, pp. 214–220, 1 1963.

[70] D. R. WHITE and R. C. MILLIKAN, "Vibrational relaxation in air," *AIAA Journal*, vol. 2, pp. 1844–1846, 10 1964.

[71] P. F. Zittel and D. E. Masturzo, "Vibrational relaxation of H2O from 295 to 1020 K," *The Journal of Chemical Physics*, vol. 90, pp. 977–989, 1 1989.

[72] R. E. Center and J. F. Newton, "Vibrational relaxation of N2 by H2O," *The Journal of Chemical Physics*, vol. 68, pp. 3327–3333, 4 1978.

[73] R. C. Millikan, "Carbon Monoxide Vibrational Relaxation in Mixtures with Helium, Neon, and Krypton," *The Journal of Chemical Physics*, vol. 40, pp. 2594–2596, 5 1964.

[74] E. M. Rothkopf and W. Low, "Diaphragm opening process in shock tubes," *Physics of Fluids*, vol. 17, no. 6, p. 1169, 1974.

[75] C. J. S. M. Simpson, "Effect on Shock Trajectory of the Opening Time of Diaphragms in a Shock Tube," *Physics of Fluids*, vol. 10, no. 9, p. 1894, 1967.

[76] I. I. GLASS and G. N. PATTERSON, "A Theoretical and Experimental Study of Shock-Tube Flows," *Journal of the Aeronautical Sciences*, vol. 22, pp. 73–100, 2 1955.

[77] H. MIRELS, "Shock tube test time limitation due to turbulent wall boundary layer," *AIAA Journal*, vol. 2, pp. 84–93, 1 1964.

[78] D. Nativel, S. P. Cooper, T. Lipkowicz, M. Fikri, E. L. Petersen, and C. Schulz, "Impact of shock-tube facility-dependent effects on incident- and reflected-shock conditions over a wide range of pressures and Mach numbers," *Combustion and Flame*, vol. 217, pp. 200–211, 7 2020.

[79] E. L. Petersen and R. K. Hanson, "Nonideal effects behind reflected shock waves in a high-pressure shock tube," *Shock Waves*, vol. 10, pp. 405–420, 1 2001.

[80] R. J. Emrich and C. W. Curtis, "Attenuation in the Shock Tube," *Journal of Applied Physics*, vol. 24, pp. 360–363, 3 1953.

[81] J. E. Drewry and Z. A. Walenta, "Determination of Diaphragm Opening-Times and Use of Diaphragm Particle Traps in a Hypersonic Shock Tube," Tech. Rep. 90, UTIAS Technical Note, 1965.

[82] Z. S. Duntsova, I. V. Ershov, V. T. Kireev, and E. I. Ruzavin, "Calculation of shock wave motion and flow parameters for a noninstantaneous shock tube diaphragm opening," *Fluid Dynamics*, vol. 4, no. 2, pp. 81–87, 1972.

[83] K. TAJIMA, E. OUTA, and G. NAKADA, "Some Investigations of Shock Tube Flow : On the Propagation Behavior of the Initial Shock Front," *Bulletin of JSME*, vol. 11, no. 43, pp. 116–124, 1968.

[84] H. Mirels, "Attenuation in a shock tube due to unsteady-boundary-layer action," *NACA Tech. Note 1333*, 1957.

[85] H. MIRELS, "Boundary Layer Behind Shock or Thin Expansion Wave Moving Into Stationary Fluid," *NACA Tech. Note 3712*, 1956.

[86] H. Mirels, "Test Time in Low-Pressure Shock Tubes," *Physics of Fluids*, vol. 6, no. 9, p. 1201, 1963.

[87] J. J. Jones, "Experimental Investigation of Attenuation of Strong Shock Waves in a Shock Tube with Hydrogen and Helium as Driver Gases," tech. rep., National Advisory Committee for Aeronautics, Washington, 1957.

[88] L. Davies and J. L. Wilson, "Influence of Reflected Shock and Boundary-Layer Interaction on Shock-Tube Flows," *Physics of Fluids*, vol. 12, no. 5, pp. I–37, 1969.

[89] H. Mark, "The Interaction of a Reflected Shock Wave with the Boundary Layer in a Shock Tube," *NACA Tech. Mem. 1418*, 1958.

[90] R. A. Strehlow and C. T. Case, "Limitations of the Reflected Shock Technique for Studying Fast Chemical Reactions," *The Journal of Chemical Physics*, vol. 35, pp. 1506–1507, 10 1961.

[91] S. Byron and N. Rott, “On the interaction of the reflected shock wave with the laminar boundary layer on the shock tube walls,” in *Proceedings of the 1961 Heat Transfer and Fluid Mechanics Institute*, p. 38, Stanford University, Press Stanford, 1961.

[92] N. Rott and R. Hartunian, *On the heat transfer to the walls of a shock tube.* PhD thesis, Cornell University Ithaca NY, 1955.

[93] E. L. Petersen and R. K. Hanson, “Measurement of Reflected-shock Bifurcation Over a Wide Range of Gas Composition and Pressure,” *Shock Waves*, vol. 15, pp. 333–340, 8 2006.

[94] K. A. Heufer and H. Olivier, “Determination of ignition delay times of different hydrocarbons in a new high pressure shock tube,” *Shock Waves*, vol. 20, pp. 307–316, 8 2010.

[95] H. Ciezki and G. Adomeit, “Shock-tube investigation of self-ignition of n-heptane-air mixtures under engine relevant conditions,” *Combustion and Flame*, vol. 93, pp. 421–433, 6 1993.

[96] D. Davidson, B. Gauthier, and R. Hanson, “Shock tube ignition measurements of iso-octane/air and toluene/air at high pressures,” *Proceedings of the Combustion Institute*, vol. 30, pp. 1175–1182, 1 2005.

[97] S. S. Vasu, D. F. Davidson, Z. Hong, and R. K. Hanson, “Shock Tube Study of Methylcyclohexane Ignition over a Wide Range of Pressure and Temperature,” *Energy & Fuels*, vol. 23, pp. 175–185, 1 2009.

[98] K. Heufer, R. Fernandes, H. Olivier, J. Beeckmann, O. Röhl, and N. Peters, “Shock tube investigations of ignition delays of n-butanol at elevated pressures between 770 and 1250K,” *Proceedings of the Combustion Institute*, vol. 33, no. 1, pp. 359–366, 2011.

[99] K.-Y. Lam, Z. Hong, D. Davidson, and R. Hanson, “Shock tube ignition delay time measurements in propane/O2/argon mixtures at near-constant-volume conditions,” *Proceedings of the Combustion Institute*, vol. 33, no. 1, pp. 251–258, 2011.

[100] S. Gates, A. McCartt, J. Jeffries, R. Hanson, L. Hokama, and K. Mortelmans, "Extension of Bacillus endospore gas dynamic heating studies to multiple species and test conditions," *Journal of Applied Microbiology*, vol. 111, pp. 925–931, 10 2011.

[101] G. Pang, D. Davidson, and R. Hanson, "Experimental study and modeling of shock tube ignition delay times for hydrogen–oxygen–argon mixtures at low temperatures," *Proceedings of the Combustion Institute*, vol. 32, no. 1, pp. 181–188, 2009.

[102] Z. Hong, D. F. Davidson, and R. K. Hanson, "Contact surface tailoring condition for shock tubes with different driver and driven section diameters," *Shock Waves*, vol. 19, pp. 331–336, 8 2009.

[103] A. R. Amadio, M. W. Crofton, and E. L. Petersen, "Test-time extension behind reflected shock waves using CO2–He and C3H8–He driver mixtures," *Shock Waves*, vol. 16, pp. 157–165, 12 2006.

[104] Z. Hong, G. A. Pang, S. S. Vasu, D. F. Davidson, and R. K. Hanson, "The use of driver inserts to reduce non-ideal pressure variations behind reflected shock waves," *Shock Waves*, vol. 19, pp. 113–123, 6 2009.

[105] M. F. Campbell, S. Wang, C. S. Goldenstein, R. M. Spearrin, A. M. Tulgestke, L. T. Zaczek, D. F. Davidson, and R. K. Hanson, "Constrained reaction volume shock tube study of n -heptane oxidation: Ignition delay times and time-histories of multiple species and temperature," *Proceedings of the Combustion Institute*, vol. 35, no. 1, pp. 231–239, 2015.

[106] M. F. Campbell, A. M. Tulgestke, D. F. Davidson, and R. K. Hanson, "A second-generation constrained reaction volume shock tube," *Review of Scientific Instruments*, vol. 85, p. 055108, 5 2014.

[107] L. Z. Dumitrescu, "An Attenuation-Free Shock Tube," *Physics of Fluids*, vol. 15, no. 1, p. 207, 1972.

[108] H. Polachek and R. J. Seeger, “On Shock-Wave Phenomena; Refraction of Shock Waves at a Gaseous Interface,” *Physical Review*, vol. 84, pp. 922–929, 12 1951.

[109] W. J. Hooker, “Testing Time and Contact-Zone Phenomena in Shock-Tube Flows,” *Physics of Fluids*, vol. 4, no. 12, p. 1451, 1961.

[110] A. Roshko and D. Baganoff, “A Novel Device for Bursting Shock-Tube Diaphragms,” *Physics of Fluids*, vol. 4, no. 11, p. 1445, 1961.

[111] J. H. Spurk and E. J. Gion, “Fast Acting Diaphragm Cutter,” *Review of Scientific Instruments*, vol. 39, pp. 348–351, 3 1968.

[112] R. S. Hickman, L. C. Farrar, and J. B. Kyser, “Behavior of burst diaphragms in shock tubes,” *Physics of Fluids*, vol. 18, no. 10, p. 1249, 1975.

[113] O. Kosing, F. Barbosa, and B. Skews, “A new, friction controlled, piston actuated diaphragmless shock tube driver,” *Shock Waves*, vol. 9, pp. 69–72, 2 1999.

[114] M. S. Downey, T. J. Cloete, and A. D. B. Yates, “A rapid opening sleeve valve for a diaphragmless shock tube,” *Shock Waves*, vol. 21, pp. 315–319, 8 2011.

[115] Y. Takano and T. Akamatsu, “A diaphragmless shock tube,” *Journal of Physics E: Scientific Instruments*, vol. 17, pp. 644–646, 8 1984.

[116] S. M. Hurst and S. H. Bauer, “A piston-actuated shock-tube, with laser–Schlieren diagnostics,” *Review of Scientific Instruments*, vol. 64, pp. 1342–1346, 5 1993.

[117] K. A. Huefer, H. Olivier, S. Drumm, and H. Murrenhoff, “A new fast acting valve for diaphragmless shock tubes,” in *28th international symposium on shock waves*, pp. 535–540, Springer, Berlin, Heidelberg, 2012.

[118] R. S. Tranter and B. R. Giri, “A diaphragmless shock tube for high temperature kinetic studies,” *Review of Scientific Instruments*, vol. 79, no. 9, p. 094103, 2008.

[119] J. B. Randazzo and R. S. Tranter, "Note: An improved driver section for a diaphragmless shock tube," *Review of Scientific Instruments*, vol. 86, p. 016117, 1 2015.

[120] R. S. Tranter and P. T. Lynch, "A miniature high repetition rate shock tube," *Review of Scientific Instruments*, vol. 84, p. 094102, 9 2013.

[121] E. L. Petersen, *A Shock Tube and Diagnostics for Chemistry Measurements at Elevated Pressures with Application to Methane Ignition.* PhD thesis, Stanford University, 1998.

[122] B. Gauthier, D. Davidson, and R. Hanson, "Shock tube determination of ignition delay times in full-blend and surrogate fuel mixtures," *Combustion and Flame*, vol. 139, pp. 300–311, 12 2004.

[123] S. S. Vasu, D. F. Davidson, and R. K. Hanson, "Jet fuel ignition delay times: Shock tube experiments over wide conditions and surrogate model predictions," *Combustion and Flame*, vol. 152, pp. 125–143, 1 2008.

[124] W. Ren, D. F. Davidson, and R. K. Hanson, "IR laser absorption diagnostic for C2H4 in shock tube kinetics studies," *International Journal of Chemical Kinetics*, vol. 44, no. 6, pp. 423–432, 2012.

[125] S. S. Vasu, D. F. Davidson, and R. K. Hanson, "Shock-Tube Experiments and Kinetic Modeling of Toluene Ignition," *Journal of Propulsion and Power*, vol. 26, pp. 776–783, 7 2010.

[126] R. S. Tranter, K. Brezinsky, and D. Fulle, "Design of a high-pressure single pulse shock tube for chemical kinetic investigations," *Review of Scientific Instruments*, vol. 72, pp. 3046–3054, 7 2001.

[127] R. SIVARAMAKRISHNAN, K. BREZINSKY, H. VASUDEVAN, and R. S. TRANTER, "A SHOCK-TUBE STUDY OF THE HIGH-PRESSURE THERMAL DECOMPOSITION OF BENZENE," *Combustion Science and Technology*, vol. 178, pp. 285–305, 1 2006.

[128] R. Sivaramakrishnan, R. Tranter, and K. Brezinsky, "A high pressure model for the oxidation of toluene," *Proceedings of the Combustion Institute*, vol. 30, pp. 1165–1173, 1 2005.

[129] S. Gudiyella and K. Brezinsky, "High pressure study of n-propylbenzene oxidation," *Combustion and Flame*, vol. 159, pp. 940–958, 3 2012.

[130] R. Tranter, H. R. Amoorthy, A. Raman, K. Brezinsky, and M. Allendorf, "High-pressure single-pulse shock tube investigation of rich and stoichiometric ethane oxidation," *Proceedings of the Combustion Institute*, vol. 29, pp. 1267–1275, 1 2002.

[131] T. Malewicki and K. Brezinsky, "Experimental and modeling study on the pyrolysis and oxidation of n-decane and n-dodecane," *Proceedings of the Combustion Institute*, vol. 34, pp. 361–368, 1 2013.

[132] S. Gudiyella and K. Brezinsky, "The high pressure study of n-propylbenzene pyrolysis," *Proceedings of the Combustion Institute*, vol. 34, pp. 1767–1774, 1 2013.

[133] S. Gudiyella and K. Brezinsky, "High pressure study of 1,3,5-trimethylbenzene oxidation," *Combustion and Flame*, vol. 159, pp. 3264–3285, 11 2012.

[134] S. P. Sharma and C. Park, "Operating Characteristics of a 60- and 10-cm Electric Arc-Driven Shock Tube-Part II: The Driven Section," *Journal of Thermophysics and Heat Transfer*, vol. 4, pp. 266–272, 7 1990.

[135] B. A. Cruden, D. Prabhu, and R. Martinez, "Absolute Radiation Measurement in Venus and Mars Entry Conditions," *Journal of Spacecraft and Rockets*, vol. 49, pp. 1069–1079, 11 2012.

[136] A. M. Brandis, R. G. Morgan, T. J. McIntyre, and P. A. Jacobs, "Nonequilibrium Radiation Intensity Measurements in Simulated Titan Atmospheres," *Journal of Thermophysics and Heat Transfer*, vol. 24, pp. 291–300, 4 2010.

[137] A. M. Brandis, C. O. Johnston, B. A. Cruden, and D. K. Prabhu, "Equilibrium Radiative Heating from 9.5 to 15.5 km/s for Earth Atmospheric Entry," *Journal of Thermophysics and Heat Transfer*, vol. 31, pp. 178–192, 1 2017.

[138] J. H. Grinstead, M. J. Wright, D. W. Bogdanoff, and G. A. Allen, "Shock radiation measurements for Mars aerocapture radiative heating analysis," *Journal of Thermophysics and Heat Transfer*, vol. 23, no. 2, pp. 249–255, 2009.

[139] B. A. Cruden, "Electron Density Measurement in Reentry Shocks for Lunar Return," *Journal of Thermophysics and Heat Transfer*, vol. 26, pp. 222–230, 4 2012.

[140] R. Hanson and D. Davidson, "Recent advances in laser absorption and shock tube methods for studies of combustion chemistry," *Progress in Energy and Combustion Science*, vol. 44, pp. 103–114, 10 2014.

[141] D. F. Davidson and R. K. Hanson, "Interpreting shock tube ignition data," *International Journal of Chemical Kinetics*, vol. 36, pp. 510–523, 9 2004.

[142] G. P. Smith, D. M. Golden, M. Frenklach, N. W. Moriarty, B. Eiteneer, M. Goldenberg, C. T. Bowman, R. K. Hanson, S. Song, W. C. Gardiner, V. V. Lissianski, and Z. Qin, "GRI-MECH 3.0," 1999.

[143] H. Wang, X. You, A. V. Joshi, S. G. Davis, A. Laskin, F. Egolfopoulos, and C. K. Law, "USC Mech Version II. High-Temperature Combustion Reaction Model of H2/CO/C1-C4 Compounds," 2007.

[144] W. K. Metcalfe, S. M. Burke, S. S. Ahmed, and H. J. Curran, "A Hierarchical and Comparative Kinetic Modeling Study of C1-C2 Hydrocarbon and Oxygenated Fuels," *International Journal of Chemical Kinetics*, vol. 45, pp. 638–675, 10 2013.

[145] M. Mehl, W. J. Pitz, C. K. Westbrook, and H. J. Curran, "Kinetic modeling of gasoline surrogate components and mixtures under engine conditions," *Proceedings of the Combustion Institute*, vol. 33, no. 1, pp. 193–200, 2011.

[146] K. K. Schwarm, H. Q. Dinh, C. S. Goldenstein, D. I. Pineda, and R. M. Spearrin, "High-pressure and high-temperature gas cell for absorption spectroscopy studies at wavelengths up to 8 µm," *Journal of Quantitative Spectroscopy and Radiative Transfer*, vol. 227, pp. 145–151, 4 2019.

[147] R. K. Hanson, R. M. Spearrin, and C. S. Goldenstein, *Spectroscopy and Optical Diagnostics for Gases*. Cham: Springer International Publishing, 2016.

[148] C. S. Goldenstein, R. M. Spearrin, J. B. Jeffries, and R. K. Hanson, "Infrared laser-absorption sensing for combustion gases," *Progress in Energy and Combustion Science*, vol. 60, pp. 132–176, 5 2017.

[149] I. Gordon, L. Rothman, C. Hill, R. Kochanov, Y. Tan, P. Bernath, M. Birk, V. Boudon, A. Campargue, K. Chance, B. Drouin, J.-M. Flaud, R. Gamache, J. Hodges, D. Jacquemart, V. Perevalov, A. Perrin, K. Shine, M.-A. Smith, J. Tennyson, G. Toon, H. Tran, V. Tyuterev, A. Barbe, A. Császár, V. Devi, T. Furtenbacher, J. Harrison, J.-M. Hartmann, A. Jolly, T. Johnson, T. Karman, I. Kleiner, A. Kyuberis, J. Loos, O. Lyulin, S. Massie, S. Mikhailenko, N. Moazzen-Ahmadi, H. Müller, O. Naumenko, A. Nikitin, O. Polyansky, M. Rey, M. Rotger, S. Sharpe, K. Sung, E. Starikova, S. Tashkun, J. V. Auwera, G. Wagner, J. Wilzewski, P. Wcisło, S. Yu, and E. Zak, "The HITRAN2016 molecular spectroscopic database," *Journal of Quantitative Spectroscopy and Radiative Transfer*, vol. 203, pp. 3–69, 12 2017.

[150] L. Rothman, I. Gordon, R. Barber, H. Dothe, R. Gamache, A. Goldman, V. Perevalov, S. Tashkun, and J. Tennyson, "HITEMP, the High-Temperature Molecular Spectroscopic Database," *Journal of Quantitative Spectroscopy and Radiative Transfer*, vol. 111, pp. 2139–2150, 10 2010.

[151] S. W. Sharpe, T. J. Johnson, R. L. Sams, P. M. Chu, G. C. Rhoderick, and P. A. Johnson, "Gas-Phase Databases for Quantitative Infrared Spectroscopy," *Applied Spectroscopy*, vol. 58, pp. 1452–1461, 12 2004.

[152] N. Jacquinet-Husson, R. Armante, N. Scott, A. Chédin, L. Crépeau, C. Boutammine, A. Bouhdaoui, C. Crevoisier, V. Capelle, C. Boonne, N. Poulet-Crovisier, A. Barbe, D. Chris Benner, V. Boudon, L. Brown, J. Buldyreva, A. Campargue, L. Coudert, V. Devi, M. Down, B. Drouin, A. Fayt, C. Fittschen, J.-M. Flaud, R. Gamache, J. Harrison, C. Hill, O. Hodnebrog, S.-M. Hu, D. Jacquemart, A. Jolly, E. Jiménez, N. Lavrentieva, A.-W. Liu, L. Lodi, O. Lyulin, S. Massie, S. Mikhailenko, H. Müller, O. Naumenko, A. Nikitin, C. Nielsen, J. Orphal, V. Perevalov, A. Perrin, E. Polovtseva, A. Predoi-Cross, M. Rotger, A. Ruth, S. Yu, K. Sung, S. Tashkun, J. Tennyson, V. Tyuterev, J. Vander Auwera, B. Voronin, and A. Makie, "The 2015 edition of the GEISA spectroscopic database," *Journal of Molecular Spectroscopy*, vol. 327, pp. 31–72, 9 2016.

[153] J. Humlíček, "Optimized computation of the voigt and complex probability functions," *Journal of Quantitative Spectroscopy and Radiative Transfer*, vol. 27, pp. 437–444, 4 1982.

[154] M. Kuntz, "A new implementation of the Humlicek algorithm for the calculation of the Voigt profile function," *Journal of Quantitative Spectroscopy and Radiative Transfer*, vol. 57, no. 6, pp. 819–824, 1997.

[155] W. Ruyten, "Comment on "A new implementation of the Humlicek algorithm for the calculation of the Voigt profile function" by M. Kuntz [JQSRT 57(6) (1997) 819–824]," *Journal of Quantitative Spectroscopy and Radiative Transfer*, vol. 86, pp. 231–233, 6 2004.

[156] A. McLean, C. Mitchell, and D. Swanston, "Implementation of an efficient analytical approximation to the Voigt function for photoemission lineshape analysis," *Journal of Electron Spectroscopy and Related Phenomena*, vol. 69, pp. 125–132, 9 1994.

[157] J. M. Hartmann, C. Boulet, and D. Robert, *Collisional Effects on Molecular Spectra*. Elsevier, 2008.

[158] W. Cai and C. F. Kaminski, "Tomographic Absorption Spectroscopy for the study of Gas Dynamics and Reactive Flows," *Progress in Energy and Combustion Science*, vol. 59, pp. 1–31, 3 2017.

[159] A. Guha and I. M. Schoegl, "Tomographic Imaging of Flames: Assessment of Reconstruction Error Based on Simulated Results," *Journal of Propulsion and Power*, vol. 30, pp. 350–359, 3 2014.

[160] M. Deutsch and I. Beniaminy, "Inversion of Abel's Integral Equation for Experimental Data," *Journal of Applied Physics*, vol. 54, pp. 137–143, 1 1983.

[161] E. O. Åkesson and K. J. Daun, "Parameter selection methods for axisymmetric flame tomography through Tikhonov regularizaron," *Applied Optics*, vol. 47, no. 3, pp. 407–416, 2008.

[162] K. J. Daun, K. A. Thomson, F. Liu, and G. J. Smallwood, "Deconvolution of axisymmetric flame properties using Tikhonov regularization," *Applied Optics*, vol. 45, p. 4638, 7 2006.

[163] C. J. Dasch, "One-dimensional tomography: a comparison of Abel, onion-peeling, and filtered backprojection methods," *Applied Optics*, vol. 31, p. 1146, 3 1992.

[164] P. C. Hansen, *The L-Curve and its Use in the Numerical Treatment of Inverse Problems*, vol. 4. WIT Press, 2000.

[165] D. D. Cox and P. C. Hansen, "Rank-Deficient and Discrete III-Posed Problems: Numerical Aspects of Linear Inversion," *Journal of the American Statistical Association*, vol. 94, p. 1388, 12 1999.

[166] D. I. Pineda, F. A. Bendana, K. K. Schwarm, and R. M. Spearrin, "Multi-isotopologue laser absorption spectroscopy of carbon monoxide for high-temperature chemical kinetic studies of fuel mixtures," *Combustion and Flame*, vol. 207, pp. 379–390, 9 2019.

[167] R. W. Dibble, *Laser probing of excited CO Products from shock wave initiated oxidation of carbon disulfide.* PhD thesis, University of Wisconsin - Madison, 1975.

[168] C.-L. Yu, C. Wang, and M. Frenklach, "Chemical Kinetics of Methyl Oxidation by Molecular Oxygen," *The Journal of Physical Chemistry*, vol. 99, pp. 14377–14387, 9 1995.

[169] W. Ren, A. Farooq, D. F. Davidson, and R. K. Hanson, "CO concentration and temperature sensor for combustion gases using quantum-cascade laser absorption near 4.7 μm," *Applied Physics B*, vol. 107, pp. 849–860, 6 2012.

[170] R. M. Spearrin, W. Ren, J. B. Jeffries, and R. K. Hanson, "Multi-band infrared CO2 absorption sensor for sensitive temperature and species measurements in high-temperature gases," *Applied Physics B*, vol. 116, pp. 855–865, 9 2014.

[171] W. Ren, R. Mitchell Spearrin, D. F. Davidson, and R. K. Hanson, "Experimental and Modeling Study of the Thermal Decomposition of C3–C5 Ethyl Esters Behind Reflected Shock Waves," *The Journal of Physical Chemistry A*, vol. 118, pp. 1785–1798, 3 2014.

[172] Y. Tao, G. P. Smith, and H. Wang, "Critical kinetic uncertainties in modeling hydrogen / carbon monoxide , methane , methanol , formaldehyde , and ethylene combustion," *Combustion and Flame*, vol. 195, pp. 18–29, 2018.

[173] C. R. Mulvihill, S. A. Alturaifi, and E. L. Petersen, "High-temperature He- and O2-broadening of the R(12) line in the $1\leftarrow0$ band of carbon monoxide," *Journal of Quantitative Spectroscopy and Radiative Transfer*, vol. 217, pp. 432–439, 9 2018.

[174] O. Mathieu, C. R. Mulvihill, and E. L. Petersen, "Assessment of modern detailed kinetics mechanisms to predict CO formation from methane combustion using shock-tube laser-absorption measurements," *Fuel*, vol. 236, pp. 1164–1180, 1 2019.

[175] S. M. Sarathy, A. Farooq, and G. T. Kalghatgi, "Recent progress in gasoline surrogate fuels," *Progress in Energy and Combustion Science*, vol. 65, pp. 67–108, 2018.

[176] H. Wang, R. Xu, K. Wang, C. T. Bowman, R. K. Hanson, D. F. Davidson, K. Brezinsky, and F. N. Egolfopoulos, "A physics-based approach to modeling real-fuel combustion chemistry - I. Evidence from experiments, and thermodynamic, chemical kinetic and statistical considerations," *Combustion and Flame*, vol. 193, pp. 502–519, 7 2018.

[177] R. Xu, K. Wang, S. Banerjee, J. Shao, T. Parise, Y. Zhu, S. Wang, A. Movaghar, D. J. Lee, R. Zhao, X. Han, Y. Gao, T. Lu, K. Brezinsky, F. N. Egolfopoulos, D. F. Davidson, R. K. Hanson, C. T. Bowman, and H. Wang, "A physics-based approach to modeling real-fuel combustion chemistry – II. Reaction kinetic models of jet and rocket fuels," *Combustion and Flame*, vol. 193, pp. 520–537, 7 2018.

[178] E. V. Anslyn and D. A. Dougherty, *Modern Physical Organic Chemistry.* University Science Books, 2006.

[179] A. Eveleigh and N. Ladommatos, "Isotopic Tracers for Combustion Research," *Combustion Science and Technology*, vol. 189, no. 4, pp. 660–682, 2017.

[180] P. Ghosh and W. A. Brand, "Stable isotope ratio mass spectrometry in global climate change research," *International Journal of Mass Spectrometry*, vol. 228, no. 1, pp. 1–33, 2003.

[181] R. H. Michener and K. Lajtha, *Stable Isotopes in Ecology and Environmental Science.* Oxford, UK: Blackwell Publishing Ltd, 7 2007.

[182] D. A. McQuarrie and J. D. Simon, *Physical Chemistry: A Molecular Approach.* University Science Books, illustrate ed., 1997.

[183] D. D. Lee, F. A. Bendana, S. A. Schumaker, and R. M. Spearrin, "Wavelength modulation spectroscopy near 5 μm for carbon monoxide sensing in a high-pressure kerosene-fueled liquid rocket combustor," *Applied Physics B*, vol. 124, p. 77, 5 2018.

[184] C. Wei, D. I. Pineda, C. S. Goldenstein, and R. M. Spearrin, "Tomographic Laser Absorption Imaging of Combustion Species and Temperature in the Mid-wave Infrared," *Optics Express*, vol. 26, p. 20944, 8 2018.

[185] C. Wei, D. I. Pineda, L. Paxton, F. N. Egolfopoulos, and R. M. Spearrin, “Mid-infrared laser absorption tomography for quantitative 2D thermochemistry measurements in premixed jet flames,” *Applied Physics B*, vol. 124, p. 123, 6 2018.

[186] K. Kohse-Höinghaus, “Clean combustion: Chemistry and diagnostics for a systems approach in transportation and energy conversion,” *Progress in Energy and Combustion Science*, vol. 65, pp. 1–5, 2018.

[187] P. L. Varghese and R. K. Hanson, “Collisional narrowing effects on spectral line shapes measured at high resolution,” *Applied Optics*, vol. 23, p. 2376, 7 1984.

[188] D. York, N. M. Evensen, M. L. Martinez, and J. De Basabe Delgado, “Unified equations for the slope, intercept, and standard errors of the best straight line,” *American Journal of Physics*, vol. 72, pp. 367–375, 3 2004.

[189] D. G. Goodwin, H. K. Moffat, and R. L. Speth, “Cantera: An object-oriented software toolkit for chemical kinetics, thermodynamics, and transport processes,” 2018.

[190] C. K. Law, *Combustion Physics.* New York: Cambridge University Press, 2006.

[191] J. Warnatz, U. Maas, and R. Dibble, *Combustion: Physical and Chemical Fundamentals, Modeling and Simulation, Experiments, Pollutant Formation.* Berlin, Germany: Springer, 4th ed., 2006.

[192] R. M. Spearrin, C. S. Goldenstein, J. B. Jeffries, and R. K. Hanson, “Quantum cascade laser absorption sensor for carbon monoxide in high-pressure gases using wavelength modulation spectroscopy,” *Applied Optics*, vol. 53, p. 1938, 3 2014.

[193] C. F. Goldsmith, L. B. Harding, Y. Georgievskii, J. A. Miller, and S. J. Klippenstein, “Temperature and Pressure-Dependent Rate Coefficients for the Reaction of Vinyl Radical with Molecular Oxygen,” *Journal of Physical Chemistry A*, vol. 119, no. 28, pp. 7766–7779, 2015.

[194] D. I. Pineda, F. A. Bendana, and R. Mitchell Spearrin, "Competitive oxidation of methane and C2 hydrocarbons discerned by isotopic labeling and laser absorption spectroscopy of CO isotopologues in shock-heated mixtures," *Combustion and Flame*, 11 2020.

[195] F. L. Dryer, "Chemical kinetic and combustion characteristics of transportation fuels," *Proceedings of the Combustion Institute*, vol. 35, no. 1, pp. 117–144, 2015.

[196] M. D. Boot, M. Tian, E. J. Hensen, and S. Mani Sarathy, "Impact of fuel molecular structure on auto-ignition behavior – Design rules for future high performance gasolines," *Progress in Energy and Combustion Science*, vol. 60, pp. 1–25, 2017.

[197] E. Ranzi, M. Dente, A. Goldaniga, G. Bozzano, and T. Faravelli, "Lumping procedures in detailed kinetic modeling of gasification, pyrolysis, partial oxidation and combustion of hydrocarbon mixtures," *Progress in Energy and Combustion Science*, vol. 27, no. 1, pp. 99–139, 2001.

[198] S. C. Li, B. Varatharajan, and F. A. Williams, "Chemistry of JP-10 ignition," *AIAA Journal*, vol. 39, no. 12, pp. 2351–2356, 2001.

[199] C. K. Westbrook, W. J. Pitz, O. Herbinet, H. J. Curran, and E. J. Silke, "A comprehensive detailed chemical kinetic reaction mechanism for combustion of n-alkane hydrocarbons from n-octane to n-hexadecane," *Combustion and Flame*, vol. 156, no. 1, pp. 181–199, 2009.

[200] W. Liu, A. P. Kelley, and C. K. Law, "Flame propagation and counterflow nonpremixed ignition of mixtures of methane and ethylene," *Combustion and Flame*, vol. 157, no. 5, pp. 1027–1036, 2010.

[201] W. Lowry, J. De Vries, M. Krejci, E. Petersen, Z. Serinyel, W. Metcalfe, H. Curran, and G. Bourque, "Laminar flame speed measurements and modeling of pure alkanes and alkane blends at elevated pressures," *Journal of Engineering for Gas Turbines and Power*, vol. 133, no. 9, pp. 1–9, 2011.

[202] S. Ravi, T. G. Sikes, A. Morones, C. L. Keesee, and E. L. Petersen, "Comparative study on the laminar flame speed enhancement of methane with ethane and ethylene addition," *Proceedings of the Combustion Institute*, vol. 35, no. 1, pp. 679–686, 2015.

[203] C. K. Westbrook, "An Analytical Study of the Shock Tube Ignition of Mixtures of Methane and Ethane," *Combustion Science and Technology*, vol. 20, no. 1-2, pp. 5–17, 1979.

[204] E. L. Petersen, J. M. Hall, S. D. Smith, J. de Vries, A. R. Amadio, and M. W. Crofton, "Ignition of lean methane-based fuel blends at gas turbine pressures," *Journal of Engineering for Gas Turbines and Power*, vol. 129, no. 4, pp. 937–944, 2007.

[205] M. M. Holton, P. Gokulakrishnan, M. S. Klassen, R. J. Roby, and G. S. Jackson, "Autoignition delay time measurements of methane, ethane, and propane pure fuels and methane-based fuel blends," *Journal of Engineering for Gas Turbines and Power*, vol. 132, no. 9, pp. 1–9, 2010.

[206] C. J. Aul, W. K. Metcalfe, S. M. Burke, H. J. Curran, and E. L. Petersen, "Ignition and kinetic modeling of methane and ethane fuel blends with oxygen: A design of experiments approach," *Combustion and Flame*, vol. 160, no. 7, pp. 1153–1167, 2013.

[207] J. Shao, D. F. Davidson, and R. K. Hanson, "A shock tube study of ignition delay times in diluted methane, ethylene, propene and their blends at elevated pressures," *Fuel*, vol. 225, no. March, pp. 370–380, 2018.

[208] M. Baigmohammadi, V. Patel, S. Nagaraja, A. Ramalingam, S. Martinez, S. Panigrahy, A. A. E. S. Mohamed, K. P. Somers, U. Burke, K. A. Heufer, A. Pekalski, and H. J. Curran, "Comprehensive Experimental and Simulation Study of the Ignition Delay Time Characteristics of Binary Blended Methane, Ethane, and Ethylene over a Wide Range of Temperature, Pressure, Equivalence Ratio, and Dilution," *Energy and Fuels*, vol. 34, no. 7, pp. 8808–8823, 2020.

[209] A. V. Joshi and H. Wang, “Master equation modeling of wide range temperature and pressure dependence of CO + OH → products,” *International Journal of Chemical Kinetics*, vol. 38, pp. 57–73, 1 2006.

[210] S. H. Pyun, W. Ren, K. Y. Lam, D. F. Davidson, and R. K. Hanson, “Shock tube measurements of methane, ethylene and carbon monoxide time-histories in DME pyrolysis,” *Combustion and Flame*, vol. 160, no. 4, pp. 747–754, 2013.

[211] F. Sen, B. Shu, T. Kasper, J. Herzler, O. Welz, M. Fikri, B. Atakan, and C. Schulz, “Shock-tube and plug-flow reactor study of the oxidation of fuel-rich CH4/O2 mixtures enhanced with additives,” *Combustion and Flame*, vol. 169, pp. 307–320, 2016.

[212] C. R. Mulvihill, C. L. Keesee, T. Sikes, R. S. Teixeira, O. Mathieu, and E. L. Petersen, “Ignition delay times, laminar flame speeds, and species time-histories in the H2S/CH4 system at atmospheric pressure,” *Proceedings of the Combustion Institute*, vol. 37, no. 1, pp. 735–742, 2019.

[213] D. He, D. Nativel, J. Herzler, J. B. Jeffries, M. Fikri, and C. Schulz, “Laser-based CO concentration and temperature measurements in high-pressure shock-tube studies of n-heptane partial oxidation,” *Applied Physics B: Lasers and Optics*, vol. 126, no. 8, pp. 1–11, 2020.

[214] D. He, L. Shi, D. Nativel, J. Herzler, M. Fikri, and C. Schulz, “CO-concentration and temperature measurements in reacting CH4/O2 mixtures doped with diethyl ether behind reflected shock waves,” *Combustion and Flame*, vol. 216, pp. 194–205, 2020.

[215] N. J. Labbe, R. Sivaramakrishnan, C. F. Goldsmith, Y. Georgievskii, J. A. Miller, and S. J. Klippenstein, “Weakly Bound Free Radicals in Combustion: Prompt Dissociation of Formyl Radicals and Its Effect on Laminar Flame Speeds,” *Journal of Physical Chemistry Letters*, vol. 7, no. 1, pp. 85–89, 2016.

[216] N. J. Labbe, R. Sivaramakrishnan, C. F. Goldsmith, Y. Georgievskii, J. A. Miller, and S. J. Klippenstein, “Ramifications of including non-equilibrium effects for HCO in

flame chemistry," *Proceedings of the Combustion Institute*, vol. 36, no. 1, pp. 525–532, 2017.

[217] M. Röhrig, E. L. Petersen, D. F. Davidson, and R. K. Hanson, "A shock tube study of the pyrolysis of NO2," *International Journal of Chemical Kinetics*, vol. 29, no. 7, pp. 483–493, 1997.

[218] M. F. Campbell, K. G. Owen, D. F. Davidson, and R. K. Hanson, "Dependence of Calculated Postshock Thermodynamic Variables on Vibrational Equilibrium and Input Uncertainty," *Journal of Thermophysics and Heat Transfer*, vol. 31, pp. 586–608, 7 2017.

[219] F. A. Bendana, D. D. Lee, C. Wei, D. I. Pineda, and R. M. Spearrin, "Line mixing and broadening in the v(1→3) first overtone bandhead of carbon monoxide at high temperatures and high pressures," *Journal of Quantitative Spectroscopy and Radiative Transfer*, vol. 239, p. 106636, 12 2019.

[220] D. D. Lee, F. A. Bendana, A. P. Nair, D. I. Pineda, and R. M. Spearrin, "Line mixing and broadening of carbon dioxide by argon in the v3 bandhead near 4.2 µm at high temperatures and high pressures," *Journal of Quantitative Spectroscopy and Radiative Transfer*, vol. 253, p. 107135, 9 2020.

[221] M. A. Oehlschlaeger, D. F. Davidson, and J. B. Jeffries, "Temperature measurement using ultraviolet laser absorption of carbon dioxide behind shock waves," *Applied Optics*, vol. 44, p. 6599, 11 2005.

[222] G. P. Smith, Y. Tao, and H. Wang, "Foundational Fuel Chemistry Model Version 1.0 (FFCM-1)," 2016.

[223] C. W. Zhou, Y. Li, E. O'Connor, K. P. Somers, S. Thion, C. Keesee, O. Mathieu, E. L. Petersen, T. A. DeVerter, M. A. Oehlschlaeger, G. Kukkadapu, C. J. Sung, M. Alrefae, F. Khaled, A. Farooq, P. Dirrenberger, P. A. Glaude, F. Battin-Leclerc, J. Santner,

Y. Ju, T. Held, F. M. Haas, F. L. Dryer, and H. J. Curran, “A comprehensive experimental and modeling study of isobutene oxidation,” *Combustion and Flame*, vol. 167, pp. 353–379, 2016.

[224] K. Narayanaswamy, G. Blanquart, and H. Pitsch, “A consistent chemical mechanism for oxidation of substituted aromatic species,” *Combustion and Flame*, vol. 157, no. 10, pp. 1879–1898, 2010.

[225] D. F. Davidson, Y. Zhu, J. Shao, and R. K. Hanson, “Ignition delay time correlations for distillate fuels,” *Fuel*, vol. 187, pp. 26–32, 2017.

[226] F. A. Bendana, I. C. Sanders, J. J. Castillo, C. G. Hagström, D. I. Pineda, and R. M. Spearrin, “In-situ thermochemical analysis of hybrid rocket fuel oxidation via laser absorption tomography of $$\text {CO}$$, $$\text {CO}_{2}$$, and $$\text {H}_{2}\text {O}$$,” *Experiments in Fluids*, vol. 61, p. 190, 9 2020.

[227] A. Mazzetti, L. Merotto, and G. Pinarello, “Paraffin-based Hybrid Rocket Engines Applications: A Review and a Market Perspective,” *Acta Astronautica*, vol. 126, pp. 286–297, 9 2016.

[228] A. Karabeyoglu, “Challenges in the Development of Large-scale Hybrid Rockets,” *International Journal of Energetic Materials and Chemical Propulsion*, vol. 16, no. 3, pp. 243–261, 2017.

[229] H. Tian, X. Li, P. Zeng, N. Yu, and G. Cai, “Numerical and experimental studies of the hybrid rocket motor with multi-port fuel grain,” *Acta Astronautica*, vol. 96, pp. 261–268, 3 2014.

[230] S. Kim, J. Lee, H. Moon, J. Kim, H. Sung, and O. C. Kwon, “Regression Characteristics of the Cylindrical Multiport Grain in Hybrid Rockets,” *Journal of Propulsion and Power*, vol. 29, pp. 573–581, 5 2013.

[231] C. Lee, Y. Na, J.-W. Lee, and Y.-H. Byun, "Effect of induced swirl flow on regression rate of hybrid rocket fuel by helical grain configuration," *Aerospace Science and Technology*, vol. 11, pp. 68–76, 1 2007.

[232] C. Carmicino and A. Russo Sorge, "Experimental Investigation into the Effect of Solid-Fuel Additives on Hybrid Rocket Performance," *Journal of Propulsion and Power*, vol. 31, pp. 699–713, 3 2015.

[233] A. Karabeyoglu, G. Zilliac, B. Cantwell, S. De Zilwa, and P. Castellucci, "Scale-up Tests of High Regression Rate Liquefying Hybrid Rocket Fuels," in *41st Aerospace Sciences Meeting and Exhibit*, no. January, (Reston, Virigina), pp. 1–19, American Institute of Aeronautics and Astronautics, 1 2003.

[234] X. Sun, H. Tian, Y. Li, N. Yu, and G. Cai, "Regression rate behaviors of HTPB-based propellant combinations for hybrid rocket motor," *Acta Astronautica*, vol. 119, pp. 137–146, 2 2016.

[235] T.-V. Chelaru and F. Mingireanu, "Hybrid rocket engine, theoretical model and experiment," *Acta Astronautica*, vol. 68, pp. 1891–1902, 6 2011.

[236] G. D. Di Martino, C. Carmicino, S. Mungiguerra, and R. Savino, "The Application of Computational Thermo-Fluid-Dynamics to the Simulation of Hybrid Rocket Internal Ballistics with Classical or Liquefying Fuels: A Review," *Aerospace*, vol. 6, p. 56, 5 2019.

[237] D. R. Greatrix, "Regression rate estimation for standard-flow hybrid rocket engines," *Aerospace Science and Technology*, vol. 13, pp. 358–363, 10 2009.

[238] E. T. Jens, A. C. Karp, V. A. Miller, G. S. Hubbard, and B. J. Cantwell, "Experimental Visualization of Hybrid Combustion: Results at Elevated Pressures," *Journal of Propulsion and Power*, vol. 36, pp. 33–46, 1 2020.

[239] E. T. Jens, V. A. Miller, and B. J. Cantwell, "Schlieren and OH* chemiluminescence

imaging of combustion in a turbulent boundary layer over a solid fuel," *Experiments in Fluids*, vol. 57, p. 39, 3 2016.

[240] C. Dunn, G. Gustafson, J. Edwards, T. Dunbrack, and C. Johansen, "Spatially and temporally resolved regression rate measurements for the combustion of paraffin wax for hybrid rocket motor applications," *Aerospace Science and Technology*, vol. 72, pp. 371–379, 1 2018.

[241] I. Gordon, L. Rothman, C. Hill, R. Kochanov, and others, "The HITRAN2016 molecular spectroscopic database," *Journal of Quantitative Spectroscopy and Radiative Transfer*, vol. 203, pp. 3–69, 12 2017.

[242] D. I. Pineda, J. L. Urban, and R. M. Spearrin, "Interband Cascade Laser Absorption of Hydrogen Chloride for High-Temperature Thermochemical Analysis of Fire-resistant Polymer Reactivity," *Applied Optics*, vol. 59, p. 2141, 3 2020.

[243] F. A. Bendana, J. J. Castillo, C. G. Hagström, and R. M. Spearrin, "Thermochemical structure of a hybrid rocket reaction layer based on laser absorption tomography," in *AIAA Propulsion and Energy 2019 Forum*, American Institute of Aeronautics and Astronautics, 8 2019.

[244] B. J. McBride and S. Gordon, *Computer Program for Calculation of Complex Chemical Equilibrium Compositions and Applications.* No. January, NASA, 1996.

[245] C. S. Goldenstein, R. M. Spearrin, J. B. Jeffries, and R. K. Hanson, "Wavelength-modulation spectroscopy near 2.5 μm for H2O and temperature in high-pressure and -temperature gases," *Applied Physics B*, vol. 116, pp. 705–716, 9 2014.

[246] K.-P. Cheong, L. Ma, Z. Wang, and W. Ren, "Influence of Line Pair Selection on Flame Tomography Using Infrared Absorption Spectroscopy," *Applied Spectroscopy*, vol. 73, pp. 529–539, 5 2019.

[247] J. Benesty, J. Chen, Y. Huang, and I. Cohen, "Pearson Correlation Coefficient," pp. 1–4, Springer, Berlin, Heidelberg, 2009.

[248] R. D. Stephens and S. H. Cadle, "Remote Sensing Measurements of Carbon Monoxide Emissions from On-Road Vehicles," *Journal of the Air & Waste Management Association*, vol. 41, pp. 39–46, 1 1991.

[249] J. Fishman, K. W. Bowman, J. P. Burrows, A. Richter, K. V. Chance, D. P. Edwards, R. V. Martin, G. A. Morris, R. B. Pierce, J. R. Ziemke, J. A. Al-Saadi, J. K. Creilson, T. K. Schaack, and A. M. Thompson, "Remote Sensing of Tropospheric Pollution from Space," *Bulletin of the American Meteorological Society*, vol. 89, pp. 805–822, 6 2008.

[250] R. M. Spearrin, C. S. Goldenstein, I. A. Schultz, J. B. Jeffries, and R. K. Hanson, "Simultaneous sensing of temperature, CO, and CO2 in a scramjet combustor using quantum cascade laser absorption spectroscopy," *Applied Physics B*, vol. 117, pp. 689–698, 11 2014.

[251] J. R. Howell, R. Siegel, and M. P. Mengüç, *Thermal Radiation Heat Transfer*. Boca Raton, FL: CRC Press, 5th ed., 2011.

[252] R. Sur, K. Sun, J. B. Jeffries, and R. K. Hanson, "Multi-species laser absorption sensors for in situ monitoring of syngas composition," *Applied Physics B*, vol. 115, pp. 9–24, 4 2014.

[253] X. Chao, J. B. Jeffries, and R. K. Hanson, "Absorption sensor for CO in combustion gases using 2.3 µm tunable diode lasers," *Measurement Science and Technology*, vol. 20, p. 115201, 11 2009.

[254] F. A. Bendana, D. D. Lee, R. M. Spearrin, S. A. Schumaker, and S. A. Danczyk, "Infrared laser absorption thermometry and CO sensing in high-pressure rocket combustion flows from 25 to 105 bar," in *AIAA Scitech 2019 Forum*, no. January, American Institute of Aeronautics and Astronautics, 1 2019.

[255] J.-M. Hartmann, H. Tran, R. Armante, C. Boulet, A. Campargue, F. Forget, L. Gianfrani, I. Gordon, S. Guerlet, M. Gustafsson, J. T. Hodges, S. Kassi, D. Lisak,

F. Thibault, and G. C. Toon, “Recent advances in collisional effects on spectra of molecular gases and their practical consequences,” *Journal of Quantitative Spectroscopy and Radiative Transfer*, vol. 213, pp. 178–227, 7 2018.

[256] P. Sinclair, P. Duggan, R. Berman, J. R. Drummond, and A. May, “Line Broadening in the Fundamental Band of CO in CO–He and CO–Ar Mixtures,” *Journal of Molecular Spectroscopy*, vol. 191, pp. 258–264, 10 1998.

[257] Q. Zou and P. Varanasi, “New laboratory data on the spectral line parameters in the 1-0 and 2-0 bands of relevant to atmospheric remote sensing,” *Journal of Quantitative Spectroscopy and Radiative Transfer*, vol. 75, pp. 63–92, 8 2002.

[258] A. Predoi-Cross, J. P. Bouanich, D. C. Benner, A. D. May, and J. R. Drummond, “Broadening, shifting, and line asymmetries in the 2←0 band of CO and CO–N2: Experimental results and theoretical calculations,” *The Journal of Chemical Physics*, vol. 113, pp. 158–168, 7 2000.

[259] J.-P. Bouanich, “On the temperature dependence of self-broadening in the first overtone band of CO,” *Journal of Quantitative Spectroscopy and Radiative Transfer*, vol. 31, pp. 561–567, 6 1984.

[260] J. J. BelBruno, J. Gelfand, W. Radigan, and K. Verges, “Helium and self-broadening in the first and second overtone bands of 12C16O,” *Journal of Molecular Spectroscopy*, vol. 94, pp. 336–342, 8 1982.

[261] V. Devi, D. Benner, M. Smith, C. Rinsland, and A. Mantz, “Determination of self- and H2-broadening and shift coefficients in the 2-0 band of using a multispectrum fitting procedure,” *Journal of Quantitative Spectroscopy and Radiative Transfer*, vol. 75, pp. 455–471, 11 2002.

[262] V. Malathy Devi, D. Chris Benner, M. Smith, A. Mantz, K. Sung, L. Brown, and A. Predoi-Cross, “Spectral line parameters including temperature dependences of self-

and air-broadening in the 2←0 band of CO at 2.3 μm," *Journal of Quantitative Spectroscopy and Radiative Transfer*, vol. 113, pp. 1013–1033, 7 2012.

[263] R. H. Hunt, R. A. Toth, and E. K. Plyler, "High-Resolution Determination of the Widths of Self-Broadened Lines of Carbon Monoxide," *The Journal of Chemical Physics*, vol. 49, pp. 3909–3912, 11 1968.

[264] S. Wójtewicz, K. Stec, P. Masłowski, A. Cygan, D. Lisak, R. Trawiński, and R. Ciuryło, "Low pressure line-shape study of self-broadened CO transitions in the (3←0) band," *Journal of Quantitative Spectroscopy and Radiative Transfer*, vol. 130, pp. 191–200, 11 2013.

[265] A. Predoi-Cross, C. Hnatovsky, K. Strong, J. Drummond, and D. Chris Benner, "Temperature dependence of self- and N2-broadeningand pressure-induced shifts in the 3←0 band of CO," *Journal of Molecular Structure*, vol. 695-696, pp. 269–286, 6 2004.

[266] G. Kowzan, K. Stec, M. Zaborowski, S. Wójtewicz, A. Cygan, D. Lisak, P. Masłowski, and R. Trawiński, "Line positions, pressure broadening and shift coefficients for the second overtone transitions of carbon monoxide in argon," *Journal of Quantitative Spectroscopy and Radiative Transfer*, vol. 191, pp. 46–54, 4 2017.

[267] V. Malathy Devi, D. Chris Benner, M. A. H. Smith, A. W. Mantz, K. Sung, and L. R. Brown, "Spectral line parameters including temperature dependences of air-broadening for the 2←0 bands of 13C16O and 12C18O at 2.3\$μ\$m," *Journal of Molecular Spectroscopy*, vol. 276-277, pp. 33–48, 6 2012.

[268] T. L. Hill, *An Introduction to Statistical Thermodynamics*. Addison-Wesley Publishing Co, 1960.

[269] U. Fano, "Pressure Broadening as a Prototype of Relaxation," *Physical Review*, vol. 131, pp. 259–268, 7 1963.

[270] M. Baranger, "Problem of Overlapping Lines in the Theory of Pressure Broadening," *Physical Review*, vol. 111, pp. 494–504, 7 1958.

[271] A. S. Pine and J. P. Looney, “Self-broadening and line mixing in HCN Q branches,” *The Journal of Chemical Physics*, vol. 96, pp. 1704–1714, 2 1992.

[272] L. L. Strow and D. Reuter, “Effect of line mixing on atmospheric brightness temperatures near 15 μm,” *Applied Optics*, vol. 27, p. 872, 3 1988.

[273] R. G. Gordon and R. P. McGinnis, “Line Shapes in Molecular Spectra,” *The Journal of Chemical Physics*, vol. 49, pp. 2455–2456, 9 1968.

[274] R. G. Gordon, “Semiclassical Theory of Spectra and Relaxation in Molecular Gases,” *The Journal of Chemical Physics*, vol. 45, pp. 1649–1655, 9 1966.

[275] J. Boissoles, C. Boulet, D. Robert, and S. Green, “State-to-state rotational phase coherence effect on the vibration–rotation band shape: An accurate quantum calculation for CO–He,” *The Journal of Chemical Physics*, vol. 90, pp. 5392–5398, 5 1989.

[276] M. L. Koszykowski, L. A. Rahn, R. E. Palmer, and M. E. Coltrin, “Theoretical and experimental studies of high-resolution inverse Raman spectra of N2 at 1-10 atm,” *Journal of Physical Chemistry*, vol. 91, pp. 41–46, 1 1987.

[277] L. Rahn, R. Palmer, M. Koszykowski, and D. Greenhalgh, “Comparison of rotationally inelastic collision models for Q-branch Raman spectra of N2,” *Chemical Physics Letters*, vol. 133, pp. 513–516, 2 1987.

[278] J. O. Hirschfelder, C. F. Curtiss, and R. B. Bird, *Molecular Theory of Gases and Liquids.* New York: John Wiley & Sons, Inc., 2nd ed., 1964.

[279] G. J. Rosasco, L. A. Rahn, W. S. Hurst, R. E. Palmer, and S. M. Dohne, “Measurement and prediction of Raman Q -branch line self-broadening coefficients for CO from 400 to 1500 K,” *The Journal of Chemical Physics*, vol. 90, pp. 4059–4068, 4 1989.

[280] J. Looney, G. Rosasco, L. Rahn, W. Hurst, and J. Hahn, “Comparison of rotational relaxation rate laws to characterize the Raman Q-branch spectrum of CO at 295 K,” *Chemical Physics Letters*, vol. 161, pp. 232–238, 9 1989.

[281] A. Ben-Reuven, "Impact Broadening of Microwave Spectra," *Physical Review*, vol. 145, pp. 7–22, 5 1966.

[282] J. I. Steinfeld, P. Ruttenberg, G. Millot, G. Fanjoux, and B. Lavorel, "Scaling laws for inelastic collision processes in diatomic molecules," *The Journal of Physical Chemistry*, vol. 95, pp. 9638–9647, 11 1991.

[283] J. M. Hartmann, L. Rosenmann, M. Y. Perrin, and J. Taine, "Accurate calculated tabulations of CO line broadening by H2O, N2, O2, and CO2 in the 200–3000-K temperature range," *Applied Optics*, vol. 27, p. 3063, 8 1988.

[284] J.-P. Bouanich and C. Haeusler, "Linewidths of carbon monoxide self-broadening and broadened by argon and nitrogen," *Journal of Quantitative Spectroscopy and Radiative Transfer*, vol. 12, pp. 695–702, 4 1972.

[285] D. Romanini and K. K. Lehmann, "Line-mixing in the 106←000 overtone transition of HCN," *The Journal of Chemical Physics*, vol. 105, pp. 81–88, 7 1996.

[286] J. Wu, R. Huang, M. Gong, A. Saury, and E. Carrasquillo M., "Rotational energy transfer in highly vibrationally excited HCN," *The Journal of Chemical Physics*, vol. 99, pp. 6474–6482, 11 1993.

[287] F. A. Bendana, D. D. Lee, S. A. Schumaker, S. A. Danczyk, and R. M. Spearrin, "Cross-band infrared laser absorption of carbon monoxide for thermometry and species sensing in high-pressure rocket flows," *Applied Physics B*, vol. 125, p. 204, 11 2019.

[288] D. Paez, "SpaceX's Starship Engine Shattered a Long-Standing Russian Rocket Record," 2019.

[289] P. G. Hill and C. R. Peterson, *Mechanics and Thermodynamics of Propulsion*. Reading, MA: Addison-Wesley Publishing Co, 2nd ed., 1992.

[290] A. Caswell, S. Sanders, and M. Chiaverini, "Swept-Wavelength Laser Absorption Tomography for Imaging Rocket Plume Gas Properties," in *41st AIAA/AS-*

ME/SAE/ASEE Joint Propulsion Conference & Exhibit, (Reston, Virigina), American Institute of Aeronautics and Astronautics, 7 2005.

[291] A. S. Makowiecki, T. R. Hayden, M. R. Nakles, N. H. Pilgram, N. A. MacDonald, W. A. Hargus, and G. B. Rieker, "Wavelength modulation spectroscopy for measurements of temperature and species concentration downstream from a supersonic nozzle," in *53rd AIAA/SAE/ASEE Joint Propulsion Conference*, (Reston, Virginia), American Institute of Aeronautics and Astronautics, 7 2017.

[292] J. Locke, S. Pal, R. Woodward, and R. Santoro, "Diode Laser Absorption Spectroscopy Measurements in a Gaseous Hydrogen / Oxygen Rocket," *49th AIAA Aerospace Sciences Meeting including the New Horizons Forum and Aerospace Exposition*, 1 2011.

[293] H. Zeng, F. Li, X. Yu, D. Ou, and L. Chen, "Measurement of multispecies concentration and gas temperature in an ammonium-dinitramide-based thruster by tunable diode lasers," *Applied Optics*, vol. 57, p. 1321, 2 2018.

[294] D. D. Lee, F. A. Bendana, and R. M. Spearrin, "Laser Absorption Spectroscopy of Carbon Monoxide near 4.97 μm for Temperature and Species Measurements in Hydrocarbon-Fueled Rockets," in *2018 AIAA Aerospace Sciences Meeting*, no. 210059, American Institute of Aeronautics and Astronautics, 1 2018.

[295] L. H. Ma, L. Y. Lau, and W. Ren, "Non-uniform temperature and species concentration measurements in a laminar flame using multi-band infrared absorption spectroscopy," *Applied Physics B*, vol. 123, p. 83, 3 2017.

[296] G. B. Rieker, J. B. Jeffries, and R. K. Hanson, "Calibration-free wavelength-modulation spectroscopy for measurements of gas temperature and concentration in harsh environments," *Applied Optics*, vol. 48, pp. 5546–5560, 10 2009.

[297] K. Sun, X. Chao, R. Sur, C. S. Goldenstein, J. B. Jeffries, and R. K. Hanson, "Analysis of calibration-free wavelength-scanned wavelength modulation spectroscopy for prac-

tical gas sensing using tunable diode lasers," *Measurement Science and Technology*, vol. 24, no. 12, p. 125203, 2013.

[298] J. M. Kriesel, N. Gat, B. E. Bernacki, R. L. Erikson, B. D. Cannon, T. L. Myers, C. M. Bledt, and J. A. Harrington, "Hollow core fiber optics for mid-wave and long-wave infrared spectroscopy," in *Proceedings of SPIE - The International Society for Optical Engineering*, vol. 8018, p. 80180V, 5 2011.

[299] E. B. Coy, "A Method for Eliminating Beam Steering Error for the Modulated Absorption-Emission Thermometry Technique," *53rd AIAA Aerospace Sciences Meeting*, pp. 1–12, 1 2015.

[300] B. J. McBride and S. Gordon, *Computer Program for Calculation of Complex Chemical Equilibrium Compositions and Applications.* No. January, NASA, 1996.

[301] T. Dreier, G. Schiff, and A. A. Suvernev, "Collisional effects in Q branch coherent anti-Stokes Raman spectra of N 2 and O 2 at high pressure and high temperature," *The Journal of Chemical Physics*, vol. 100, pp. 6275–6289, 5 1994.

[302] J. Bonamy, L. Bonamy, D. Robert, M. L. Gonze, G. Millot, B. Lavorel, and H. Berger, "Rotational relaxation of nitrogen in ternary mixtures N 2 –CO 2 –H 2 O: Consequences in coherent anti-Stokes Raman spectroscopy thermometry," *The Journal of Chemical Physics*, vol. 94, pp. 6584–6589, 5 1991.

[303] F. Beyrau, A. Datta, T. Seeger, and A. Leipertz, "Dual-pump CARS for the simultaneous detection of N2, O2 and CO in CH4 flames," *Journal of Raman Spectroscopy*, vol. 33, pp. 919–924, 11 2002.

[304] H. W. Coleman and W. G. Steele, *Experimentation, Validation, and Uncertainty Analysis for Engineers.* Hoboken, NJ, USA: John Wiley & Sons, Inc., 3rd ed., 2009.

[305] X. Ouyang and P. L. Varghese, "Line-of-sight absorption measurements of high temperature gases with thermal and concentration boundary layers," *Applied Optics*, vol. 28, p. 3979, 9 1989.

[306] B. Sumpf, J. P. Burrows, A. Kissel, H. D. Kronfeldt, O. Kurtz, I. Meusel, J. Orphal, and S. Voigt, “Line Shift Investigations for Different Isotopomers of Carbon Monoxide,” *Journal of Molecular Spectroscopy*, vol. 190, no. 2, pp. 226–231, 1998.

[307] C. Luo, R. Wehr, J. R. Drummond, A. D. May, F. Thibault, J. Boissoles, J. M. Launay, C. Boulet, J.-P. P. Bouanich, and J.-M. M. Hartmann, “Shifting and broadening in the fundamental band of CO highly diluted in He and Ar: A comparison with theory,” *The Journal of Chemical Physics*, vol. 115, pp. 2198–2206, 8 2001.

[308] R. Wehr, A. Vitcu, F. Thibault, J. R. Drummond, and A. D. May, “Collisional line shifting and broadening in the fundamental P-branch of CO in Ar between 214 and 324 K,” *Journal of Molecular Spectroscopy*, vol. 235, no. 1, pp. 69–76, 2006.

[309] M. L. Koszykowski, R. L. Farrow, and R. E. Palmer, “Calculation of collisionally narrowed coherent anti-Stokes Raman spectroscopy spectra,” *Optics Letters*, vol. 10, p. 478, 10 1985.